OFFICE OF CIVILIAN RADIOACTIVE WASTE MANAGEMENT
ANALYSIS/MODEL COVER SHEET

1. QA: QA

Page: 1 of: ~~342~~ 334

Complete Only Applicable Items

1/31/02 DLS

2. ☑ Analysis — Check all that apply

Type of Analysis	☐ Engineering ☐ Performance Assessment ☑ Scientific
Intended Use of Analysis	☐ Input to Calculation ☑ Input to another Analysis or Model ☑ Input to Technical Document ☑ Input to other Technical Products

Describe use:
Report available ambient field testing data in underground drifts for input to Uunsaturated Zone Analysis Modeling Reports.

3. ☐ Model — Check all that apply

Type of Model	☐ Conceptual Model ☐ Abstraction Model ☐ Mathematical Model ☐ System Model ☐ Process Model
Intended Use of Model	☐ Input to Calculation ☐ Input to another Model or Analysis ☐ Input to Technical Document ☐ Input to other Technical Products

Describe use:

4. Title:
In Situ Field Testing of Processes

5. Document Identifier (including Rev. No. and Change No., if applicable):
ANL-NBS-HS-000005 REV01

6. Total Attachments:
8

7. Attachment Numbers - No. of Pages in Each:
See Block 12

	Printed Name	Signature	Date
8. Originator	Joseph Wang	SIGNATURE ON FILE	12/14/01
9. Checker	Peter Persoff	SIGNATURE ON FILE	12/14/01
10. Lead/Supervisor	Joseph Wang	SIGNATURE ON FILE	12/14/01
11. Responsible Manager	G.S. Bodvarsson	SIGNATURE ON FILE	12/14/01

12. Remarks:

Attachments: I (6 p), II (18 p), III (6 p), IV (6 p), V (8 p), VI (6 p), VII (4 p), VIII (10 p)

Contributors:

Section 6.1: Paul Cook
Section 6.2: Robert Trautz, Steve Flexser
Section 6.3: Max Hu
Section 6.4: Max Hu
Section 6.5: Paul Cook
Section 6.6: Rohit Salve
Section 6.7: Rohit Salve
Section 6.8: Rohit Salve
Section 6.9: Rohit Salve
Section 6.10: Rohit Salve, David Hudson, Paul Cook, Max Hu, Mark Conrad
Section 6.11: Yvonne Tsang, Paul Cook
Section 6.12: Rohit Salve, David Hudson, Ken Williams
Section 6.13: Wendy Soll, Jake Turin, Ken Williams

2. Analysis or Model Title:

In Situ Field Testing of Processes

3. Document Identifier (including Rev. No. and Change No., if applicable):

ANL-NBS-HS-000005 REV01

4. Revision/Change No.	5. Description of Revision/Change
REV 00	Initial Issue
REV 01	Complete revision. Numerous changes have been made throughout the document. Table and figure identifiers have been changed throughout. The main revisions are: • Section 4 “Inputs” has been revised to update data inputs and to associate subsections with the various analyses presented in the Section 6 subsections. • Section 5 “Assumptions” has been revised to update assumptions and to associate subsections with the various analyses presented in the Section 6 subsections. • Section 6.1 is revised (1) to include air-permeability data of Niche CD 1620 - Section 6.1.2.2, and (2) to analyze the permeability changes - Section 6.1.2.3. • Section 6.2 is revised (1) to present flow path observations at Niche CD 1620 - Section 6.2.1.2, (2) to present long-term seepage-test data - Section 6.2.1.3, and (3) to compare the seepage threshold data from Niche 4788 with short-term seepage threshold data from Niche 3650 - Section 6.2.2. • Section 6.3 is revised to present additional tracer distribution data on samples collected from the ceiling of Niche 3650 - Section 6.3.1.2. • Section 6.4 is revised to present laser ablation - induced coupled plasma mass spectrometry data for chemical tracer transport and sorption - Section 6.4.3. • Section 6.5 to Section 6.9 are not revised. • Section 6.10 is revised (1) to present data of construction water tracer migration below invert - Section 6.10.1.3, and (2) to present observations of non-ventilated Cross Drift - Section 6.10.2. • Section 6.11 on systematic hydrologic characterization is a new section. • Section 6.12 on fault test at Alcove 8 and Niche 3107 is a new section. • Section 6.13 on Busted Butte unsaturated zone transport test is a new section.

CONTENTS

Page

1. PURPOSE 25
1.1 OBJECTIVES AND PROCESSES ANALYZED BY THE AMBIENT FIELD TESTING ACTIVITIES 25
1.2 LOCATIONS OF TEST SITES 26
1.3 CONSTRAINTS, CAVEATS, AND LIMITATIONS 30
2. QUALITY ASSURANCE 31
3. COMPUTER SOFTWARE AND MODEL USAGE 33
4. INPUTS 35
4.1 DATA AND PARAMETERS 35
4.2 CRITERIA 44
4.3 CODES AND STANDARDS 44
5. ASSUMPTIONS 45
5.1 ASSUMPTIONS USED IN BOREHOLE AIR-PERMEABILITY CALCULATIONS 46
5.2 ASSUMPTIONS USED IN ANALYZING AND INTERPRETING THE NICHE LIQUID-RELEASE AND SEEPAGE TEST DATA 47
5.2.1 Assumptions Used in Estimating Saturated Hydraulic Conductivity Using Air Permeability 47
5.2.2 Assumption Used in Deriving the Capillary Strength of the Fractures, Based on Philip's Capillary Barrier Solution 48
5.2.3 Assumptions Used in Deriving the Estimated Volumetric Water Content for the Fractures Based on Braester's Wetted-Profile Solution 49
5.3 APPROXIMATIONS USED IN TRACER-MIGRATION DELINEATION AT NICHE 3650 49
5.4 APPROXIMATIONS USED IN ANALYSES OF TRACER PENETRATION AND WATER IMBIBITION INTO WELDED TUFF MATRIX 50
5.5 APPROXIMATIONS USED IN CROSSHOLE CONNECTIVITY ANALYSES 50
5.6 APPROXIMATIONS USED IN ANALYSES OF FRACTURE FLOW IN FRACTURE-MATRIX TEST BED AT ALCOVE 6 51
5.7 APPROXIMATIONS USED IN ANALYSES OF FLOW THROUGH THE FAULT AND MATRIX IN THE TEST BED AT ALCOVE 4 51

CONTENTS (CONTINUED)

Page

5.8 APPROXIMATIONS USED IN WATER-POTENTIAL MEASUREMENTS IN NICHES 52

5.9 APPROXIMATIONS USED IN MONITORING CONSTRUCTION-WATER MIGRATION 52

5.10 APPROXIMATIONS USED IN MOISTURE MONITORING AND WATER ANALYSIS IN UNDERGROUND DRIFTS 52

5.11 APPROXIMATIONS USED IN ANALYZING AND INTERPRETING THE SYSTEMATIC HYDROLOGICAL CHARACTERIZATION DATA 53

5.12 APPROXIMATIONS USED IN PRELIMINARY OBSERVATIONS FROM THE FAULT TEST AT ALCOVE 8 – NICHE 3107 54

5.13 ASSUMPTIONS USED IN THE BUSTED BUTTE UNSATURATED ZONE TRANSPORT TEST 54

6. ANALYSES 57

6.1 AIR-PERMEABILITY DISTRIBUTIONS AND EXCAVATION-INDUCED ENHANCEMENTS 62

6.1.1 Niche Test Site and Borehole Configuration 62

6.1.1.1 Site Selection 62

6.1.1.2 Borehole Configuration 64

6.1.2 Air-Permeability Spatial Distribution and Statistical Analysis 67

6.1.2.1 Data Reduction and Air-Permeability Determination 68

6.1.2.2 Pre- and Post-Excavation Permeability Profiles 69

6.1.2.3 Permeability Change as a Function of Initial Permeability 78

6.1.2.4 Statistical Comparison of Air-Permeability Distributions 82

6.2 ANALYSIS AND INTERPRETATION OF THE NICHE LIQUID-RELEASE AND SEEPAGE-TEST DATA 87

6.2.1 Review of Data Obtained from Liquid-Release and Seepage Tests Conducted at Niches 88

6.2.1.1 Pre-Excavation Liquid-Release Test Data 88

6.2.1.2 Niche Excavation Activities 89

6.2.1.3 Post-Excavation Seepage Tests 92

6.2.2 Niche Seepage Threshold and Fracture Characteristic Curve 102

6.2.2.1 Post-Excavation Liquid-Release and Niche Seepage Threshold 102

6.2.2.2 Capillary Strength (α^{-1}) of Fractures 105

6.2.2.3 Estimated Volumetric Water Content (θ) of Fractures 108

6.2.2.4 Estimated Water Potentials (ψ) of Fractures 111

6.2.2.5 Fracture-Water Characteristic Curves 113

CONTENTS (CONTINUED)

Page

6.3 ANALYSES OF TRACER-MIGRATION DELINEATION AT NICHE 3650 116
6.3.1 Tracer Distribution from the Tracer-Migration Test 116
6.3.1.1 Field Studies at Niche 3650 116
6.3.1.2 Tracer-Migration Test 116
6.3.2 Delineation of Tracer Distributions from Previous Liquid-Release Tests 118
6.3.2.1 Detection of Tracers 118
6.3.2.2 Distribution of Dyes 122

6.4 ANALYSES OF TRACER PENETRATION AND WATER IMBIBITION INTO WELDED TUFF MATRIX 128
6.4.1 Penetration of Dyes into Rocks from the Niches 128
6.4.1.1 Field Observations 128
6.4.1.2 Dye Penetrations into Rocks 130
6.4.1.3 Fast Fracture Flow 131
6.4.1.4 Concentration of Dye Tracer at Saturated Contact 132
6.4.2 Retardation and Tracer Front Movement 135
6.4.2.1 Dye Retardation Factor Determined by Front Separation 135
6.4.2.2 Dye Retardation Factor Measured at Saturated Contact 138
6.4.2.3 Extent of Fracture-Matrix Interaction 139
6.4.2.4 Travel-Front Separation 139
6.4.3 Application of LA-ICP-MS to Investigate Chemical Transport and Sorption 140

6.5 CROSSHOLE ANALYSES OF AIR-INJECTION TESTS 142
6.5.1 Crosshole Responses in Welded Tuff 143
6.5.2 Permeability Distributions and Crosshole Responses in Nonwelded Tuff 147

6.6 ANALYSES OF FRACTURE FLOW IN FRACTURE-MATRIX TEST BED AT ALCOVE 6 151
6.6.1 Liquid-Release Tests in Low- and High-Permeability Zones 152
6.6.1.1 The Test Bed 152
6.6.1.2 Instrumentation 153
6.6.1.3 Liquid-Release Experiments 153
6.6.2 Observations of Wetting Front Migration and Fracture Flow 155
6.6.2.1 Liquid-Release Rates 155
6.6.2.2 Formation Wetting and Drying 157
6.6.2.3 Seepage into the Slot 161
6.6.2.4 Tracer Recovery 165

CONTENTS (CONTINUED)

Page

6.7 ANALYSES OF FLOW THROUGH THE FAULT AND MATRIX IN THE TEST BED AT ALCOVE 4 167
6.7.1 Flow Tests in Paintbrush Tuff Unit Layers and Fault 167
6.7.1.1 The Test Bed 167
6.7.1.2 Instrumentation 170
6.7.1.3 Liquid-Release Experiments 171
6.7.2 Observations of Fault Flow and Matrix Flow 172
6.7.2.1 Fault Responses 172
6.7.2.2 Matrix Responses 177

6.8 COMPILATION OF WATER-POTENTIAL MEASUREMENTS IN NICHES 179
6.8.1 Location and Timing of Water-Potential Measurements at Niches 179
6.8.2 Observations of Dryout in Niche Boreholes 182
6.8.2.1 Niche 3566 (Pre-Excavation) 184
6.8.2.2 Niche 3566 (Post-Excavation) 185
6.8.2.3 Niche 3650 (Pre-Excavation) 186
6.8.2.4 Niche 3107 186

6.9 OBSERVATIONS OF CONSTRUCTION-WATER MIGRATION 187
6.9.1 Equipment Set-Up for Construction-Water Monitoring 187
6.9.1.1 Starter Tunnel Borehole 187
6.9.1.2. Electrical Resistivity Probes and Psychrometers 188
6.9.1.3 Drift Monitoring at the Cross-Over Point 189
6.9.2 Wetting Front Detection and Monitoring Below the ECRB Cross Drift 190
6.9.2.1 Wetting Front Detection at the Starter Tunnel 190
6.9.2.2 Wetting Front Monitoring at the Cross-Over Point 199

6.10 MOISTURE MONITORING AND WATER ANALYSIS IN UNDERGROUND DRIFTS 200
6.10.1 Construction Induced Effects from Drift Excavation 200
6.10.1.1 Status of the ESF Moisture-Monitoring Study 200
6.10.1.2 Moisture Conditions and Perturbations Observed in Drifts 203
6.10.1.3 Construction Water Migration Below Invert from Excavation 207
6.10.2 Analysis and Observation of Non-Ventilated ECRB Cross Drift 208
6.10.2.1 Water-Potential Measurements and Drift Relative Humidity and Temperature Variations 209
6.10.2.2 Observations 209
6.10.2.3 Observations of Wet Zones During Bulkhead Entries 215
6.10.2.4 Chemical and Isotopic Analysis of Water Samples Collected During Bulkhead Entries 219

CONTENTS (CONTINUED)

Page

6.11 ANALYSES AND INTERPRETATIONS OF SYSTEMATIC HYDROLOGICAL CHARACTERIZATION 225
6.11.1 Systematic Borehole Testing Setup 225
6.11.1.1 Systematic Borehole Configuration 225
6.11.1.2 Equipment 226
6.11.2 Systematic Testing Results and Observations 231
6.11.2.1 Air-Injection Tests and Liquid-Release Tests in LA2, Initiated on May 11, 2000 231
6.11.2.2 Liquid-Release Test in Zone 1, Zone 2, and Zone 3 in LA2, Initiated on May 17, 2000 234
6.11.2.3 Liquid-Release Test in Zone 1, Zone 2, and Zone 3 in LA2, Initiated on May 23, 2000 235
6.11.2.4 Liquid-Release Test in Zone 2 and Zone 3 in LA2: October 23–December 1, 2000 239
6.11.2.5 Liquid-Release Test in Zone 2 of LA1: December 20, 2000 – January 2, 2001 241
6.11.2.6 Liquid-Release Test in Zone 2 of LA1: February 28 – April 30, 2001 243
6.11.3 Systematic Testing Discussion and Interpretation 244
6.11.3.1 Participation of Lithophysal Cavities in Storage and Flow Paths 245
6.11.3.2 Estimation of the Steady-State Nonintersecting Flow around the Drift 246
6.11.3.3 Minimum Injection Rate Needed to Induce Seepage 248
6.11.3.4 Estimation of Evaporation from within the Fracture System 249
6.12 PRELIMINARY OBSERVATIONS FROM THE FAULT TEST AT ALCOVE 8-NICHE 3107 249
6.12.1 Drift-to-Drift Fault Test Setup 250
6.12.1.1 Test Sequence of Liquid and Tracer Releases 250
6.12.1.2 The Test Bed 251
6.12.1.3 Instrumentation 254
6.12.2 Fault Liquid Test Observations 254
6.12.2.1 Fault Intake Rates 255
6.12.2.2 Wetting-Front Migration 255
6.12.2.3 Seepage in Niche 3107 256
6.12.3 Geophysical Imaging of the Drift-to-Drift Test Block 257
6.12.3.1 Background and Ground-Penetrating-Radar Experimental Approach 257
6.12.3.2 Results of the Radar Data Acquisition 258
6.12.3.3 Comparison with Seismic Tomography 261

CONTENTS (CONTINUED)

Page

6.13 BUSTED BUTTE UNSATURATED ZONE TRANSPORT TEST 262
6.13.1 Overview of Unsaturated Zone Transport Test 263
6.13.1.1 Unsaturated Zone Transport Test Location 263
6.13.1.2 Unsaturated Zone Transport Test Objectives 263
6.13.1.3 Unsaturated Zone Transport Test Concept 263
6.13.1.4 Test Design 264
6.13.1.5 Site Characterization 265
6.13.1.6 Borehole Injection and Sampling Systems 266
6.13.1.7 Electrical-Resistance Moisture Sensors 267
6.13.1.8 Nonreactive and Reactive Tracers and Microspheres 268
6.13.1.9 Phase 1 Tracers 268
6.13.1.10 Phase 2 Tracers 271
6.13.1.11 Synthetic Pore-Water Recipe 273
6.13.2 Field-Scale Tracer Transport—Phase 1 273
6.13.2.1 Test Phase 1A 273
6.13.2.2 Test Phase 1B 274
6.13.3 Field-Scale Tracer Transport – Phase 2 280
6.13.3.1 Test Configuration 280
6.13.3.2 Additional Coring 282
6.13.3.3 Mineback 282
6.13.3.4 Pad Analyses 283
6.13.3.5 Moisture Movement 284
6.13.3.6 Scaling/Travel Distance 284
6.13.3.7 Heterogeneity 284
6.13.3.8 Transverse Dispersion 286
6.13.3.9 Sorption/Retardation 287
6.13.4 Tomographic Studies: Geophysical Techniques at the Busted Butte Unsaturated Zone Test Facility 288
6.13.4.1 Busted Butte Ground Penetrating Radar Tomography 288
6.13.4.2 Electrical-Resistance Tomography 297

7. CONCLUSIONS 301

7.1 SUMMARY AND CONCLUSIONS OF AIR-PERMEABILITY DISTRIBUTION AND EXCAVATION-INDUCED ENHANCEMENT IN NICHES 305

7.2 SUMMARY AND CONCLUSIONS OF LIQUID-RELEASE AND SEEPAGE TESTS IN NICHES 305
7.2.1 Pre-Excavation Liquid-Release Testing and Niche Excavation Activities 305
7.2.2 Post-Excavation Seepage Tests at Niche 3650 and Niche 4788 306
7.2.3 Constraints, Caveats, and Limitations of the Niche Seepage Test Results 307

CONTENTS (CONTINUED)

Page

7.3 SUMMARY AND CONCLUSIONS OF TRACER-MIGRATION DELINATION AT NICHE 3650 308

7.4 SUMMARY AND CONCLUSIONS ON TRACER PENETRATION AND WATER IMBIBITION INTO WELDED TUFF MATRIX 308

7.5 SUMMARY AND CONCLUSIONS OF SINGLE-HOLE PERMEABILITY DISTRIBUTIONS AND CROSSHOLE CONNECTIVITY ANALYSES 309

7.6 SUMMARY AND CONCLUSIONS OF FRACTURE FLOW IN FRACTURE-MATRIX TEST BED AT ALCOVE 6 310

7.7 SUMMARY AND CONCLUSIONS OF FLOW THROUGH THE FAULT AND MATRIX IN THE TEST BED AT ALCOVE 4 311

7.8 SUMMARY AND CONCLUSIONS OF WATER-POTENTIAL MEASUREMENTS IN THE NICHES 312

7.9 SUMMARY AND CONCLUSIONS OF MONITORING THE CONSTRUCTION-WATER MIGRATION 312

7.10 SUMMARY AND CONCLUSIONS OF ANALYSES OF CONSTRUCTION EFFECTS 313

7.11. SUMMARY AND CONCLUSIONS OF SYSTEMATIC HYDROLOGICAL CHARACTERIZATION ALONG ECRB CROSS DRIFT 314

7.12 SUMMARY AND CONCLUSIONS OF DRIFT-TO-DRIFT TEST BETWEEN ALCOVE 8 AND NICHE 3107 315

7.13 SUMMARY AND CONCLUSIONS OF BUSTED BUTTE UNSATURATED ZONE TRANSPORT TEST 315

8. INPUTS AND REFERENCES 317

8.1 CITED DOCUMENTS 317

8.2 CODES, STANDARDS, REGULATIONS, AND PROCEDURES 325

8.3 SOURCE DATA, LISTED BY DATA TRACKING NUMBER 326

8.4 OUTPUT DATA, LISTED BY DATA TRACKING NUMBER 333

ATTACHMENTS

ATTACHMENT I AUTOMATED AIR INJECTION SYSTEM I-1

I.1 AUTOMATIC PNEUMATIC INJECTION PACKERS I-3

I.2 AIR-INJECTION FLOW INSTRUMENTATION I-4

I.3 INITIAL SETUP IN TESTING REGIMEN I-5

I.4 AUTOMATION I-5

CONTENTS (CONTINUED)

Page

ATTACHMENT II. COMPUTATION TABLES FOR NICHE STUDIES II-1

ATTACHMENT III COMPARISON OF LIQUID AND AIR-DERIVED SATURATED HYDRAULIC CONDUCTIVITIES III-1

ATTACHMENT IV WATER CONTENT PROFILE EVALUATION IV-1
- IV.1 EVALUATION OF ASSUMPTION OF ONE-DIMENSIONAL (1-D) FLOW IV-3
- IV.2 EVALUATION OF ASSUMPTION OF DOWNWARD TRANSLATION OF THE WETTED PROFILE AT CONSTANT VELOCITY IV-3

ATTACHMENT V LABORATORY MEASUREMENTS OF RETARDATION AND FRONT SEPARATION V-1
- V.1 WATER IMBIBITION V-3
- V.2 ROCK SAMPLING AND TRACER EXTRACTION V-3
- V.3 MEASUREMENT OF AQUEOUS TRACER CONCENTRATION V-4
- V.4 EVALUATION OF DRILLING TECHNIQUE V-5

ATTACHMENT VI FIELD EQUIPMENT FOR CONTROLLED WATER RELEASE, WETTING FRONT DETECTION AND SEEPAGE COLLECTION VI-1
- VI.1 FLUID INJECTION VI-3
- VI.2 BOREHOLE MONITORING VI-4
- VI.3 SEEPAGE COLLECTION VI-5

ATTACHMENT VII MEASUREMENT OF WATER POTENTIAL USING PSYCHROMETERS VII-1

ATTACHMENT VIII GEOLOGY, MINERALOGY, AND HYDROLOGIC PROPERTIES — BUSTED BUTTE APPLICABILITY VIII-1
- VIII.1 GEOLOGY OF THE BUSTED BUTTE TEST FACILITY VIII-3
- VIII.2 STRATIGRAPHIC SETTING OF BUSTED BUTTE VIII-4
- VIII.3 LITHOLOGY OF THE CALICO HILLS FORMATION VIII-5
  - VIII.3.1 Informal Units of the Calico Hills Formation VIII-5
- VIII.4 CRITERIA OF UNIT IDENTIFICATION VIII-5
- VIII.5 EVALUATION OF PETROGRAPHIC PARAMETERS VIII-6
- VIII.6 IMPLICATIONS FOR BUSTED BUTTE APPLICABILITY VIII-7
- VIII.7 MINERALOGIC PROPERTIES VIII-8
- VIII.8 HYDROLOGIC PROPERTIES VIII-8

FIGURES

Page

1.2-1. Schematic Illustration of Alcove and Niche Locations in the Exploratory Studies Facility at Yucca Mountain 27
1.2-2. Schematic Illustration of ESF and ECRB Cross Drift 28
1.2-3. Schematic Illustration of East-West Distribution of Hydrogeologic Units Intersected by the Potential Repository Horizon (Tptpmn, Tptpll, and Tptpln) 29
1.2-4. Photo of Yucca Mountain Ridge, Fran Ridge, and Busted Butte, taken from the Southwest across the Solitario Canyon Fault 30
6-1. Schematic Illustration of Flow Tests in the Exploratory Studies Facility at Yucca Mountain 59
6-2. Schematic Illustration of the Cross-Over Point of ECRB Cross Drift with the Main Drift 60
6.1.1-1. Location Map for Niche 3107, Niche 3566, Niche 3650, Niche 4788 and Niche CD 1620 63
6.1.1-2. Schematic Illustration of the End View of Borehole Clusters at Niche Sites 65
6.1.1-3. Schematic Illustration of the Plan View of Borehole Clusters at Niche Sites 66
6.1.1-4. Schematic Illustration of the End and Plan Views of Borehole Clusters at Niche CD 1620 67
6.1.2-1. Pre-Excavation Air-Permeability Profiles along Axial Boreholes at Niche 3566 70
6.1.2-2. Post-Excavation Air-Permeability Profiles along Radial Boreholes at Niche 3566 71
6.1.2-3. Pre- and Post-Excavation Air-Permeability Profiles along Upper Boreholes at Niche 3650 72
6.1.2-4. Pre-Excavation Air-Permeability Profiles along Middle and Bottom Boreholes at Niche 3650 73
6.1.2-5. Pre- and Post-Excavation Air-Permeability Profiles along Upper Boreholes at Niche 3107 74
6.1.2-6. Pre-Excavation Air-Permeability Profiles along Middle and Bottom Boreholes at Niche 3107 75
6.1.2-7. Pre- and Post-Excavation Air-Permeability Profiles along Upper Boreholes at Niche 4788 76
6.1.2-8. Pre-Excavation Air-Permeability Profiles along Middle and Bottom Boreholes at Niche 4788 77
6.1.2-9. Pre- and Post-Excavation Air-Permeability Profiles along Upper Boreholes at Niche CD 1620 79
6.1.2-10. Pre- and Post-Excavation Air-Permeability Profiles along AK Side Boreholes at Niche CD 1620 80
6.1.2-11. Change Ratio Plot for Niche CD 1620 Overhead Boreholes 80
6.1.2-12. Change Ratio Plots for Niche CD 1620 AK Boreholes 81
6.1.2-13. Change Ratio Plot for Niche 3650 81
6.1.2-14. Change Ratio Plot for Niche 3107 82
6.1.2-15. Change Ratio Plot for Niche 4788 82

FIGURES (CONTINUED)

Page

6.2.1-1. Photographic Illustrations of Flow Paths Observed During Niche Excavations: a) ambient flow path at Niche 3566, b) blue dyed flow path at Niche 3566, c) pink dyed flow path at Niche CD 1620, d) pink stain on the floor of a lithophysal cavity at Niche CD 1620 91
6.2.1-2. Mass of Water Released Versus Aspect Ratio 92
6.2.1-3. Schematic Illustration of Seepage Capture System and Test Intervals at Niche 3650 94
6.2.1-4. Relative Humidity and Temperature Inside Niche 3107 96
6.2.1-5. Relative Humidity and Temperature Inside Niche 4788 97
6.2.1-6. Stabilized Flow Rates Observed during Test #1 1-5-00 Conducted on Test Interval UR at Niche 4788 98
6.2.1-7. Wetting-Front Sequences Overlying Fracture Map of Niche 4788 Crown from Seepage Test Begun June 26, 2000 100
6.2.1-8. Wetting-Front area (m^2) versus Time (s) for the Seepage Test Shown in Figure 6.2.1-7 101
6.2.1-9. Square Root of Area (m) Plotted versus Perimeter (m) for each of the Wetting Fronts in the Niche 4788 Seepage Test 101
6.2.2-1. Liquid-Release Flux Versus Seepage Percentage 103
6.2.2-2. Niche Seepage Threshold 105
6.2.2-3. Water Retention Curves for Fractures 114
6.2.2-4. Effect of Wetting History on Water Retention Curves for Test Interval N3650 UM 4.27-4.57 m 115
6.3.1-1. Schematic of Sampling Borehole Array: (a) Plan View with Liquid-Release/Dye-Application History, and (b) Three-Dimensional View from inside the Niche 117
6.3.2-1. Dye Detection along Borehole 7: (a) FD&C Blue No. 1, and (b) Sulpho Rhodamine B 120
6.3.2-2. Dye Detection of: (a) Pyranine Along Borehole 11, and (b) Acid Yellow 7 along Borehole 2 121
6.3.2-3. Three-Dimensional View of FD&C Blue No. 1 Detection Related to the Release Intervals above the Niche 122
6.3.2-4. Three-Dimensional View of Sulpho Rhodamine B Detection Related to the Release Intervals above the Niche 123
6.3.2-5. Three-Dimensional View of Pyranine Detection Related to the Release Interval above the Niche 124
6.3.2-6. Three-Dimensional View of Acid Yellow 7 Detection Related to the Release Interval above the Niche 125
6.3.2-7. Three-Dimensional View of Amino G Acid Detection Related to the Release Interval above the Niche 126
6.3.2-8. Three-Dimensional View of FD&C Yellow No. 6 Detection Related to the Release Intervals above the Niche 127

FIGURES (CONTINUED)

Page

6.4.1-1. Photograph showing the wall face with fracture network and sampling location of rock. Stained by FD&C Blue No. 1 during Niche Excavation at Niche 4788 129
6.4.1-2. Sulpho Rhodamine B Penetration Profiles into Rock Matrix from the Fracture Surface 130
6.4.1-3. Tracer Penetration Profile into Rock Matrix from the Fracture Surface: (a) FD&C Blue No.1 at Niche 3650, (b) FD&C Blue No.1 at Niche 4788 134
6.4.2-1. Comparison of Tracer Concentration Profiles in a Low-Initial-Saturation Core: (a) Bromide, (b) FD&C Blue No. 1, (c) Sulpho Rhodamine B. Core D had initial saturation of 12.5% and was in contact with saturated boundary for 19.5 hours 136
6.4.2-2. Comparison of Tracer Concentration Profiles in a High-Initial-Saturation Core: (a) Bromide, (b) FD&C Blue No. 1, (c) Sulpho Rhodamine B. Core H had initial saturation of 75.8% and was in contact with saturated boundary for 17.9 hours 137
6.4.3-1. Spatial Distribution along the Tracer Solution Contact Surface of Applied Tracers and the Distribution of Intrinsic Tuff Elements Profiled Using LA-ICP-MS 141
6.4.3-2. Spatial Distribution Normal to the Tracer Solution Contact Surface (in the Direction of Liquid Imbibition) of Applied Tracers and Distribution of Intrinsic Tuff Elements Profiled Using LA-ICP-MS 142
6.5.1-1. Cross-Hole Responses for the Borehole Cluster in Niche 4788 144
6.5.1-2. Air-Permeability Profiles along Boreholes in Alcove 6 145
6.5.1-3. Crosshole Responses for the Borehole Cluster in Alcove 6 146
6.5.2-1. Perspective Illustration of Alcove 4 Test Bed 147
6.5.2-2. Air-Permeability Profiles along Boreholes in Alcove 4 149
6.5.2-3. Crosshole Responses for Borehole Cluster at Alcove 4 PTn Test Bed with All Response Pressure (Resp.) Ratios below 0.2 Included 150
6.5.2-4. Crosshole Responses for Borehole Cluster at Alcove 4 PTn Test Bed with Small Response Pressure (Resp.) Ratios Filtered 151
6.6.1-1. Schematic Illustration of (a) Plan view of Location and (b) Vertical View of Layout of Test Bed at Alcove 6 in the ESF at Yucca Mountain. 153
6.6.2-1. Water Intake Rates Observed in the Low Permeability Zone 156
6.6.2-2. Water Intake Rates Observed in the High Permeability Zone 156
6.6.2-3. Changes in Electrical Resistance and Water Potential Detected during Liquid Release into the Low Permeability Zone. The legend identifies the sensor location in borehole (C & D) and distance of sensor from the borehole collar. Shaded zones indicate the duration of liquid-release events. Note resistance axis is inverted. 158
6.6.2-4. Changes in Electrical Resistance and Water Potential Detected during Liquid Release into the High Permeability Zone 160

FIGURES (CONTINUED)

Page

6.6.2-5. Seepage into Slot: (a) Percentage of Injected Water Recovered and (b) Seepage Rates for Various Release Rates 162
6.6.2-6. Seepage into Collection Trays in the Slot: (a) Tray Configuration and (b) Percentages of Injected Water Recovered for Different Trays 164
6.6.2-7. Volume of Water Recovered in the Slot after Liquid Injection at Various Rates into the High Permeability Zone was Stopped 165
6.6.2-8. Tracer Concentrations in Seepage Water Following Injection into the High Permeability Zone 166
6.7.1-1. Geological Sketch for the North Face of Alcove 4 in the ESF at Yucca Mountain 168
6.7.1-2. Perspective Illustration of Three-Dimensional View of the Boreholes, Slot, and Lithological Unit Contacts in the Alcove 4 Test Bed 170
6.7.2-1. Intake Rates along the 0.3-m Zone Located on the Fault in Borehole 12 173
6.7.2-2. Wetting Front Arrival in Borehole 11 Following Liquid Released into the Fault in Borehole 12 174
6.7.2-3. Changes in Electrical Resistance in Borehole 11 in Response to Liquid Released into the Fault in Borehole 12 175
6.7.2-4. Changes in Electrical Resistance in Borehole 2 in Response to Liquid Released into the Fault in Borehole 12 176
6.7.2-5. Intake Rates along a 0.3-m Zone in the Matrix Located 2.44–2.74 m from the Collar in Borehole 5 177
6.7.2-6. Changes in Electrical Resistance in Borehole 6 in Response to Liquid Released in Borehole 5 178
6.8.1-1. Schematic Illustration of the Location of Psychrometers in Niche 3566 (a) in Pre-Excavation and (b) in Post-Excavation Conditions 180
6.8.1-2. Schematic Illustration of Location of Psychrometers in Niche 3650 181
6.8.1-3. Schematic Illustration of Location of Psychrometers in Niche 3107 (Pre-Excavation) 182
6.8.2-1. Pre-Excavation Water Potential Measured along Borehole U in Niche 3566 185
6.8.2-2. Water Potential Measured along Borehole UM in Niche 3107 186
6.9.1-1. Schematic Illustration of the Location of Wetting Monitoring Borehole at the Starter Tunnel of the ECRB Cross Drift 187
6.9.1-2. Schematic Illustration of the Borehole Wetting Front Monitoring System with Psychrometers and Electrical Resistivity Probes 188
6.9.1-3. Schematic Illustration of Sensor Arrays for Wetting Front Monitoring 189
6.9.2-1. Changes in Water Potential Observed along the Wetting Front Monitoring Borehole at the Starter Tunnel of ECRB Cross Drift 195
6.9.2-2. Changes in Electrical Resistance Observed along the Wetting-Front Monitoring Borehole at the Starter Tunnel of the ECRB Cross Drift 196
6.9.2-3. Comparison of Performance of Electrical Resistivity Probe and Psychrometer 198
6.9.2-4. Example of Time Domain Reflectometry Probe Data at the Cross-Over Point in the ESF Main Drift 200

FIGURES (CONTINUED)

Page

6.10.1-1. Relative Humidity Temporal Variations in the ECRB Cross Drift 206
6.10.1-2. Relative Humidity Spatial Variations along the ECRB Cross Drift 206
6.10.1-3. Construction Water Distribution below Exploratory Studies Facility Drift 207
6.10.2-1. Schematic Illustration of Moisture Monitoring Stations in the ECRB Cross Drift 208
6.10.2-2. Water potential measurements along the ECRB Cross Drift: a) Station 15+00; b) Station 20+00; c) Station 25+00 210
6.10.2-3. Barometric-Pressure Measured along the ECRB Cross Drift 211
6.10.2-4. Temperature Measured in the Four ECRB Cross Drift Stations 212
6.10.2-5. Relative Humidity Measured in the Four ECRB Cross Drift Stations 214
6.10.2-6 As-Built Cross Section of the Terminal End of the ECRB Cross Drift (23+00 m to 26+81 m) Showing the Bulkhead Locations 216
6.10.2-7. Chemical Analyses of Liquid Samples Collected during Bulkhead Entries 220
6.10.2-8. Comparison of Chemical Signatures 221
6.10.2-9. Plot of the Hydrogen and Oxygen Isotope Compositions of Water Samples Collected from the ECRB Cross Drift 224
6.11.1-1. Schematic of Borehole Configuration in the ECRB Cross Drift for Systematic Characterization of the Lower Lithophysal Unit 226
6.11.1-2 A Schematic of the Equipment System: Packer Assembly, Water Supply and Air-Injection Component, Seepage Collection Component, and Data Acquisition and Control 227
6.11.1-3. Front Panel for Control Interface on Computer 230
6.11.2-1. Pressure Responses (Red, Orange, and Green) to Constant Mass Flow of Air-Injection (Blue) for Estimation of Fracture Permeability in ECRB-SYBT LA#2 232
6.11.2-2 Cumulative Water Supplied to ECRB-SYBT-LA#2 Zone 1 and Cumulative Seeped Water into the ECRB Cross Drift for Test Performed on May 11–May 12, 2000 233
6.11.2-3. Cumulative Water Supplied to ECRB-SYBT-LA#2 Zone 1, Zone 2, and Zone 3 and Cumulative Seeped Water into the ECRB Cross Drift for Tests Performed on May 17–May 18, 2000 235
6.11.2-4. Cumulative Water Supplied to ECRB-SYBT-LA#2 Zone 1 and Cumulative Seeped Water into the ECRB Cross Drift for Tests Performed on May 23–June 1, 2000 236
6.11.2-5. Cumulative Water Supplied to ECRB-SYBT-LA#2 Zone 2 and Cumulative Seeped Water into ECRB Cross Drift for Tests Performed on May 23-June 8, 2000. (a) May 23-June 1, 2000 (b) June 1–June 8, 2000. 237

FIGURES (CONTINUED)

Page

6.11.2-6. Cumulative Water Supplied to ECRB-SYBT-LA#2 Zone 3 and Cumulative Seeped Water into ECRB Cross Drift for Tests Performed on May 23-June 27, 2000. (a) May 23-June 1 (b) June 1 to June 3 (c) June 14-June 18 (d) June 18–June 27. 238
6.11.2-7. Cumulative Water Supplied to ECRB-SYBT-LA#2 Zone 2 and Zone 3 and Cumulative Seeped Water into ECRB Cross Drift for Test Performed on October 23, 2000 to December 1, 2000..... 240
6.11.2-8. Supply Rate, Seepage Rate and Relative Humidity and Temperature for Liquid-Release Test Performed in ECRB-SYBT-LA#2 Zone 2 on October 23, 2000 to December 1, 2000 240
6.11.2-9. Supply Rate, Seepage Rate, and Relative Humidity and Temperature for Liquid-Release Test Performed in ECRB-SYBT-LA#2 Zone 3 on October 23, 2000 to December 1, 2000 241
6.11.2-10. (a) Cumulative Water Supplied to ECRB-SYBT-LA#1 Zone 2 for Test Performed on December 20, 2000 to January 2, 2001. Also shown are humidity and (b) temperature, and the water level in the evaporation pan. 242
6.11.2-11. (a) Cumulative Water Supplied to and Seeped from ECRB-SYBT-LA#1 Zone 2 for Test Performed on February 28 to April 30, 2001, (b) Water Supply Rate and Seeped Rate, (c) Humidity, Temperature and the Water Level in the Evaporation Pan. 244
6.12.1-1. Schematic Illustration of Liquid Release and Seepage Collection Test Sequence..... 251
6.12.1-2. Schematic Illustration of the Test Bed for the Alcove 8-Niche 3107 Tests..... 252
6.12.1-3. Schematic Illustration of the Infiltration Zones along the Floor of Alcove 8 253
6.12.1-4. Schematic Illustration of Monitoring Boreholes in Niche 3107 253
6.12.2-1. Infiltration Rates along Fault in Alcove 8 255
6.12.2-2. Wetting Front Arrival Detected in Borehole 10 in Niche 3107.. 256
6.12.2-3. Cumulative Seepage (Blue) from All Collection Trays in Niche 3107 and the Seepage Rate Observed (Red) along a Section of Fault in Niche 3107 (as Measured in Tray U3-B4). 257
6.12.3-1. Radar Velocity Tomograms between Alcove 8 Well Pairs..... 260
6.12.3-2. Radar Velocity Tomograms between Alcove 8 and Niche 3107 Well Pairs..... 261
6.12.3-3. Seismic Tomograms between Alcove 8 and Niche 3107..... 262
6.13.1-1. Busted Butte Unsaturated Zone Transport Test 266
6.13.1-2. Vertical Cross-Section of Injection and Collection System Configuration..... 267
6.13.1-3. Schematic of Phase-1A Borehole Numbers and Relative Locations 269
6.13.1-4. Phase-1B and Phase-2 Borehole Numbers and Relative Locations 269
6.13.2-1. Phase-1B Pad Extraction/Analysis Scheme 276

FIGURES (CONTINUED)

Page

6.13.2-2a. Bromide Concentrations in Borehole 6 for Phase 1B 277
6.13.2-2b. 2,6-DFBA Concentrations in Borehole 6 for Phase 1B 278
6.13.2-2c. Fluorescein Concentrations in Borehole 6 for Phase 1B 278
6.13.2-2d. Pyridone Concentrations in Borehole 6 for Phase 1B 279
6.13.2-2e. Lithium Concentrations in Borehole 6 for Phase 1B 279
6.13.3-1. Borehole Configuration on the Collection Face 281
6.13.3-2. Locations of Phase 2 Post-Test Overcores 283
6.13.3-3. Moisture Front Precedes Tracer Front 285
6.13.3-4. Influence of Scaling/Travel Distance on Tracer Transport in UZTT Phase 2 286
6.13.3-5. Influence of Rock Heterogeneity on Tracer Transport in UZTT Phase 2 286
6.13.3-6. Extent of Transverse Dispersion on Tracer Transport Measured in Borehole 16 of the UZTT Phase 2 287
6.13.3-7. Effect of Sorption/Retardation on Tracer Transport in UZTT Phase 2 288
6.13.4-1. Tomography (GPR-T) Results for Well Pair 46-16 from December 1998; March 1999; and April 1999 292
6.13.4-2. Tomography (GPR-T) Results for Well Pair 46-9 from April 1999; February 2000; and July 2000 294
6.13.4-3. Tomography (GPR-T) Results for Well Pair 11-47 from September 1999; February 2000; and November 2000. 295
6.13.4-4. Tomography (GPR-T) Results for Well Pair 13-15 from April 1999; February 2000; and July 2000 296
6.13.4-5. Electrical-Resistance Tomography Layout 298
6.13.4-6. Electrical-Resistance Tomography Electrode Assignments 298
6.13.4-7. Electrical-Resistance Tomography Images of the Test Block Viewed from Test Alcove: Baseline and August Differences 300
6.13.4-8 Electrical-Resistance Tomography Images of the Test Block Viewed from Alcove: September Differences 300
I-1. Schematic Sketch of Automatic Packer Design. I-3
I-2. Schematic Illustration of the Permutation Scheme for Automatic Packers. I-4
III-1. Comparison of Liquid and Air-Derived Saturated Hydraulic Conductivities. III-5
V-1. Comparison of Measured Detection Ratio from the Opposite Drilling Directions for Core D with Lower Initial Sw: (a) Bromide, (b) Sulpho Rhodamine B. V-6
V-2. Comparison of Measured Detection Ratio from the Opposite Drilling Directions for Core H with Higher Initial Sw: (a) Bromide, (b) Sulpho Rhodamine B. V-7
VI-1. Schematic Illustration of Liquid Release System for Constant-Head and Constant-Rate Injections. VI-4
VI-2. Schematic Illustration of Borehole Monitoring System. VI-5
VI-3. Schematic Illustration of Water Collection System Installed in Slot. VI-6

FIGURES (CONTINUED)

Page

VII-1. Effect of Cooling Current on Psychrometer Output Curve (PSY-732)..... VII-3
VII-2. Effect of Dust Coating on Psychrometer Output Curve (PSY-731)..... VII-4
VIII-1. Busted Butte Geologic Map VIII-4

TABLES

		Page
3-1.	Software and Routines	33
4.1-1.	Data Used to Support Analysis of Air-Permeability Distributions and Excavation-Induced Enhancements	36
4.1-2.	Data Used to Support Analysis and Interpretation of the Niche Liquid-Release and Seepage-Test Data	37
4.1-3.	Data Used to Support Analyses of Tracer-Migration Delineation at Niche 3650	37
4.1-4.	Data Used to Support Analyses of Tracer Penetration and Water Imbibition into Welded Tuff Matrix	38
4.1-5.	Data Used to Support Cross-Hole Analysis of Air Injection Tests	38
4.1-6.	Data Used to Support Analysis of Fracture Flow in Fracture-Matrix Test Bed at Alcove 6	38
4.1-7.	Data Used to Support Analysis of Flow Through the Fault and Matrix in the Test Bed at Alcove 4	39
4.1-8.	Data Used to Support Compilation of Water-Potential Measurements in Niches	39
4.1-9.	Data Used to Support Observations of Construction-Water Migration	39
4.1-10.	Data Used to Support Moisture Monitoring and Water Analysis in Underground Drifts	40
4.1-11.	Data Used to Support Analyses and Interpretations of Systematic Hydrological Characterization	42
4.1-12.	Data Used to Support Preliminary Observations from the Fault Test at Alcove8-Niche3107	42
4.1-13.	Data Used to Support Busted Butte Unsaturated Zone Transport Test	43
5-1.	Assumptions	45
6-1.	Scientific Notebooks	61
6.1.2-1.	Statistical Analyses of Air-Permeability along Boreholes above Niches	84
6.1.2-2.	Statistical Analyses of Air-Permeability along Boreholes above Niche CD 1620	85
6.1.2-3.	Comparison of Geometric Means and Standard Deviations of Niches and Alcoves in the Exploratory Studies Facility at Yucca Mountain	86
6.2.2-1.	Seepage Threshold Fluxes (K_{o*})	104
6.2.2-2.	Alpha (α) Values Estimated for the Fractures	107
6.2.2-3.	Estimated Changes in Volumetric Water Content ($\Delta\theta$)	110
6.2.2-4.	Estimated Water Potential (ψ) for the Fractures	112
6.3.2-1.	Compilation of Tracer Detection Versus Borehole Location	119
6.4.1-1.	Liquid Release Tests and Experimental Conditions	131
6.4.1-2.	Post-Excavation Tracer Release Tests at Niche 3650	131
6.4.1-3.	Compilation of C/C_0 Value for Rock Drilling Taken at the 0–1 mm Interval	133
6.4.2-1.	Measured Properties for Core Samples	138
6.6.1-1.	Amount of Water and Types of Tracers Released into the Injection Borehole	155

TABLES (CONTINUED)

Page

6.6.2-1. Summary of Liquid-Injection Tests in the High Permeability Zone. 161
6.7.1-1. Summary of Liquid Releases into the Fault Zone in Borehole 12 171
6.8.2-1. Water-Potential Measurements in Niche 3566 183
6.8.2-2. Water-Potential Measurements in Niche 3650 184
6.8.2-3. Water-Potential Measurements in Niche 3107 184
6.9.2-1. Psychrometers Response to Excavation at the Starter Tunnel of the ECRB Cross Drift 191
6.9.2-2. Electrical Resistivity Probe Responses to Excavation at the Starter Tunnel of the ECRB Cross Drift 192
6.10.1-1. Moisture-Monitoring Stations in the Exploratory Studies Facility 201
6.10.1-2. Water-Potential Measurements in the Exploratory Studies Facility 202
6.10.1-3. Saturation Measurements in the Exploratory Studies Facility 203
6.10.2-1 Rock Unit Contacts Intersected by the Bulkhead Sections (All within the Topopah Spring Tuff) 217
6.10.2-2. Chemical and Isotopic Data for Liquid Samples Collected in the ECRB Cross Drift 222
6.11.2-1. Air-Permeability Estimates for the Three Zones in Borehole LA2 232
6.13.1-1. Tracer C_0 Values for Phase 1B Injection 270
6.13.1-2. Summary of Concentrations Used for Phase 1 Injections 270
6.13.1-3. Summary of Concentrations Used for Phase 2A Injections 271
6.13.1-4. Summary of Concentrations Used for Phase 2B Injections 272
6.13.1-5. Summary of Concentrations Used for Phase 2C Injections 272
6.13.2-1. Phase 1A Samples Taken from the 90-cm Mineback Face at Borehole 3 274
II-1. Computation of Aspect Ratio (depth to lateral distance) II-3
II-2. Computation of Distance from Borehole to Niche Ceiling at Niche 4788, a Niche Study II-4
II-3a. Computation of Liquid Release Flux for Post-Excavation Seepage Tests at Niche 3107, Niche Studies II-6
II-3b. Computation of Liquid Release Flux for Post-Excavation Seepage Tests at Niche 4788, Niche Studies II-7
II-4. Summary of Regression Equations and Computation of Seepage Threshold Fluxes (K_{o*}) and Saturated Hydraulic Conductivities (K l), a Niche Study II-8
II-4a. Data Used in Linear Regression Analysis (y' vs. ln qs) II-9
II-4b. Linear Regression Summary (Output) for Niche 3107 UM 4.88-5.18 ..... II-10
II-4c. Linear Regression Summary (Output) for Niche 4788 UL 7.62-7.93 ..... II-11
II-4d. Linear Regression Summary (Output) for Niche 4788 UM 6.10-6.40 ..... II-12
II-4e. Linear Regression Summary (Output) for Niche 4788 UR 5.18-5.48 ..... II-13
II-5. Computation of Θ-Values, a Niche Study II-14
II-6. Computed Values of the Maximum Dimensionless Potential, Θ max II-15
II-7. Computation of Estimated Water Potentials, a Niche Study II-17
II-8. Computation of Estimated Water Content Change, Niche Studies II-18

TABLES (CONTINUED)

Page

IV-1. Time to Steady-State Moisture Conditions. IV-5
VIII-1. Calico Hills Formation Lithostratigraphy VIII-7
VIII-2. Rock Mineralogic Composition and Fe and Mn Oxide Contents in Stratigraphic Units Present in UZTT Phase-2 Block VIII-8
VIII-3. Hydrogeologic Properties of Busted Butte Units VIII-9

ACRONYMS AND ABBREVIATIONS

1-D	one-dimensional
2-D	two-dimensional
3-D	three-dimensional
ACC	Accession Number
AMR	Analysis/Model Report
AP	Administrative Procedure (DOE)
B	Bottom borehole
BBTF	Busted Butte Test Facility
BST	Borehole Sensor Tray
CD	ECRB Cross Drift
CDCS	Cross Drift Construction Station
CRWMS	Civilian Radioactive Waste Management System
CS	Construction Station (ESF main loop)
DOE	U.S. Department of Energy
DTN	Data Tracking Number
ECM	Effective Continuum Method
ECRB	Enhanced Characterization of Repository Block
ERP	Electrical Resistivity Probe
ERT	Electrical Resistance Tomography
ESF	Exploratory Studies Facility
FBA	Flourobenzoic Acid
FD&C	Food, Drug and Cosmetics
FY	Fiscal Year
GPR	Ground Penetrating Radar
GPR-T	Ground Penetrating Radar Tomography
HPZ	High Permeability Zone
ICPAES	Inductively Couples Plasma Atomic Emission Spectrometry
LA	License Application
LA-ICP-MS	Laser Ablation analyzed by Inductively Coupled Plasma-Mass Spectrometry
LANL	Los Alamos National Laboratory
LBNL	Lawrence Berkeley National Laboratory
LPZ	Low Permeability Zone

ACRONYMS AND ABBREVIATIONS (CONTINUED)

M	Middle borehole
M&O	Management and Operating Contractor
M&TE	Measuring and Test Equipment
ML	Middle Left borehole
MFC	Mass Flow Controller
MR	Middle Right borehole
NTS	Nevada Test Site
OCRWM	Office of Civilian Radioactive Waste Management
PA	Performance Assessment
PMR	Process Model Report
PTn	Paintbrush non-welded hydrogeologic unit
PVC	Polyvinyl Chloride
Q	Qualified
QA	Quality Assurance
QAP	Administrative Procedure (M&O)
QARD	Quality Assurance Requirements and Description
QIP	Quality Implementing Procedure
RIS	Records Information System
SR	Site Recommendation
SLPM	Standard Liter Per Minute
TBM	Tunnel Boring Machine
TBV	To Be Verified
TCO	Test Coordination Office
TCw	Tiva Canyon welded hydrogeologic unit
TDMS	Technical Data Management System
TDR	Time Domain Reflectometry
TSPA	Total System Performance Assessment
U	Upper borehole
UL	Upper Left borehole
UM	Upper Middle borehole
UR	Upper Right borehole
USGS	United States Geological Survey
UV/Vis	Ultraviolet and Visible
UZ	Unsaturated Zone
UZTT	Unsaturated Zone Transport Test

ACRONYMS AND ABBREVIATIONS (CONTINUED)

YAP	Administrative Procedure (YMP)
YMP	Yucca Mountain Site Characterization Project

1. PURPOSE

The purpose of this Analysis/Model Report (AMR) is to update and document the data and subsequent analyses from ambient field-testing activities performed in underground drifts of the Yucca Mountain Site Characterization Project (YMP). This revision updates data and analyses presented in the initial issue of this AMR (CRWMS M&O 2000 [141400]). This AMR was developed in accordance with the *Technical Work Plan for Unsaturated Zone (UZ) Flow and Transport Process Model Report* (BSC 2001 [155051]) and *Technical Work Plan for UZ Flow, Transport, and Coupled Processes Process Model Report* (BSC 2001 [157107]). These activities were performed to investigate *in situ* flow and transport processes. The evaluations provide the necessary framework to: (1) refine and confirm the conceptual model of matrix and fracture processes in the unsaturated zone (UZ) and (2) analyze the impact of excavation (including use of construction water and effect of ventilation) on the UZ flow and transport processes. This AMR is intended to support revisions to *Conceptual and Numerical Models for UZ Flow and Transport* CRWMS M&O 2000 [141187] and *Unsaturated Zone Flow and Transport Model Process Model Report* (CRWMS M&O 2000 [151940]).

In general, the results discussed in this AMR are from studies conducted using a combination or a subset of the following three approaches: (1) air-injection tests, (2) liquid-release tests, and (3) moisture monitoring using in-drift sensors or in-borehole sensors, to evaluate the impact of excavation, ventilation, and construction-water usage on the surrounding rocks. The liquid-release tests and air-injection tests provide an evaluation of *in situ* fracture flow and the competing processes of matrix imbibition. Only the findings from testing and data not covered in the *Seepage Calibration Model and Seepage Testing Data* (CRWMS M&O 2001 [153045]) are analyzed in detail in this AMR.

1.1 OBJECTIVES AND PROCESSES ANALYZED BY THE AMBIENT FIELD TESTING ACTIVITIES

The field-test findings and their implications for drift seepage, fracture flow, matrix imbibition, moisture evolution and radionuclide transport can be used to address Performance Assessment (PA) uncertainties and potential repository design issues. In Total System Performance Assesment (TSPA) for the Viability Assessment uncertainty analyses, the fraction of waste packages contacted by seepage water is the most important parameter in determining peak dose rates in 10,000, 100,000, and 1,000,000-year periods (DOE 1998 [100550], Section 4.3.2, Figure 4-34, pp. 4-73 through 4-74). The significance to TSPA of uncertainties in this fraction is categorized as high (DOE 1998 [100550], Section 6.4, Table 6-1, p. 6-12; DOE 1998 [100551], Section 2.2.4.1, Table 2-2, p. 2–20). The UZ flow and transport model and the drift-scale model need field data for partitioning UZ flux into a fast fracture-flow component and a slow matrix-flow component in the potential repository within the Topopah Spring welded tuff unit (TSw) and throughout the UZ. This partitioning is controlled by the fracture-matrix interaction. The damping of infiltration pulses and diversion by the Paintbrush nonwelded tuff unit (PTn) above the TSw are potential mechanisms for infiltration and percolation flux redistribution. In the vicinity of the potential repository, perturbations by drift excavation, air ventilation, and water usage can change the hydrologic regime in the UZ. Retardation by rock mass and dispersion through fractures are processes affecting the migration of tracers and the dilution of potential

radionuclides below the drifts to the water table. Some of these processes and related uncertainties, issues, and concerns are addressed by the ambient testing program at underground test sites at Yucca Mountain.

1.2 LOCATIONS OF TEST SITES

The Exploratory Study Facility (ESF) provides underground access to tuff units at and above the potential repository level. *In situ* testing and monitoring studies are being conducted to directly assess and evaluate the potential waste-emplacement environment and the UZ natural barriers to radionuclide transport at Yucca Mountain. This AMR summarizes the progress and status of ambient studies of UZ flow conducted at various test sites along the ESF, as illustrated in Figure 1.2-1. The ECRB Cross Drift over the potential repository block provides access to different subunits of TSw for Enhanced Characterization of Repository Block (ECRB), as illustrated in Figure 1.2-2 and Figure 1.2-3.

Figure 1.2-1 illustrates the locations of four alcoves (Alcoves 1, 2, 3, and 4) along the North Ramp, and three alcoves (Alcoves 5, 6, and 7) and four niches (Niches 3107, 3566, 3650, and 4788) along the Main Drift of the ESF. The numerical identification for each niche denotes the distance in meters from the North Portal. The ECRB Cross Drift branches out from the North Ramp, crosses over the Main Drift near Niche 3107, and reaches the western boundary of the potential repository block, as illustrated in Figure 1.2-2. Two additional niches with fracture-matrix test beds and three additional alcoves are planned for excavation in the ECRB Cross Drift. Figure 1.2-3 illustrates how the ECRB accesses all the hydrogeologic units encountered by the potential repository: the Topopah Spring middle nonlithophysal (Tptpmn), lower lithophysal (Tptpll), and lower nonlithophysal (Tptpln) units (stratigraphic nomenclature of Buesch et al. 1996 [100106], Table 2, pp. 5–8). Most of the emplacement drifts will be in the lower tuff units. The lower units could have distinctly different tuff characteristics with unknown effects on seepage fraction and fracture-matrix flow partition. A systematic study with transient air injection and pulse liquid release along boreholes into the crown of the ECRB Cross Drift is on-going to supplement the niche and alcove tests. The ECRB Cross Drift entrance is in the TSw upper lithophysal (Tptpul) unit. One alcove (Alcove 8) in Tptpul and one niche (Niche CD 1620 with CD denoting ECRB Cross Drift) in Tptpll have been excavated in the ECRB Cross Drift.

Figure 1.2-4 provides a panoramic view of the Yucca Mountain ridge, with Fran Ridge and Busted Butte to the east and south of the potential repository block. The ECRB Cross Drift penetrates the Yucca Mountain block to reach the Solitario Canyon fault. The ECRB Cross Drift is currently sealed by three bulkheads, as illustrated in Figure 1.2-3, to isolate sections including the fault. The Calico Hills tuff unit, not accessible by either the ESF Main Drift or the ECRB Cross Drift, is exposed at Busted Butte, 8 kilometers southeast of the potential repository area. This Busted Butte outcrop is the site of the Unsaturated Zone Tracer Test (UZTT), which is described in Section 6.13 of this AMR.

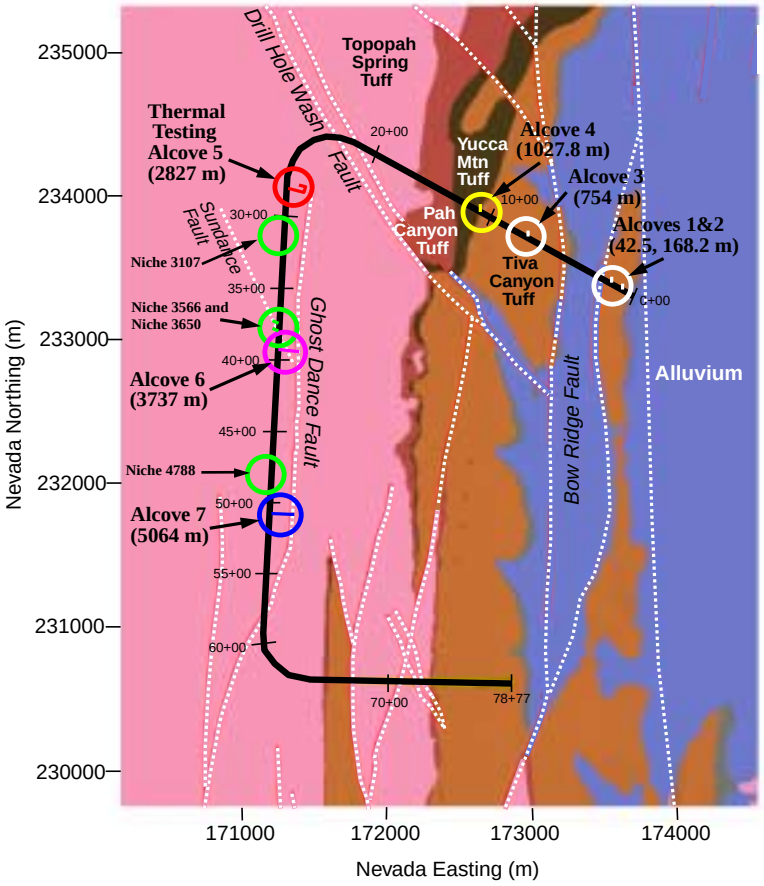

Figure 1.2-1. Schematic Illustration of Alcove and Niche Locations in the Exploratory Studies Facility at Yucca Mountain

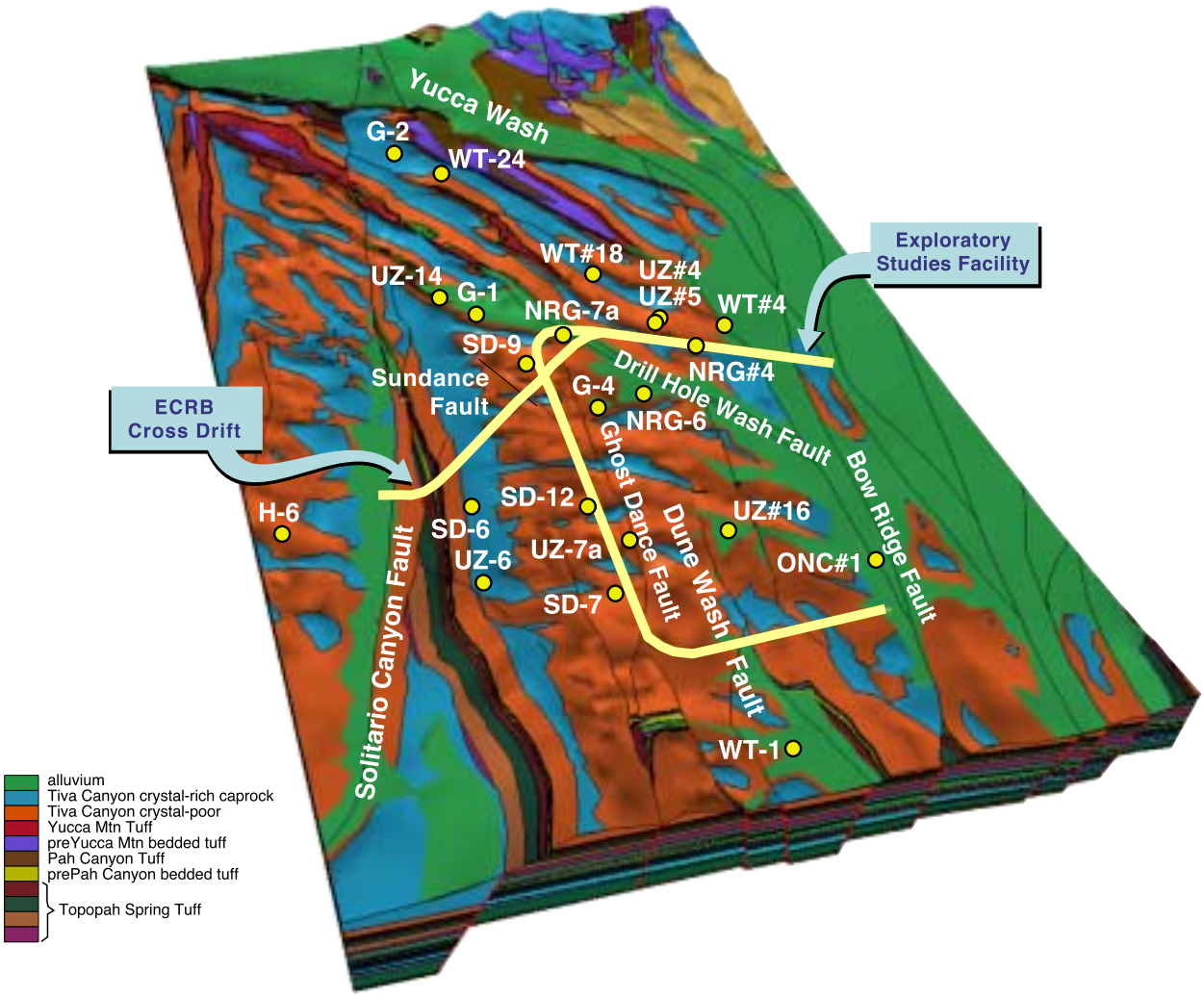

NOTE: The ECRB Cross Drift branches out from the North Ramp of the Exploratory Studies Facility, crosses over the Main Drift, and accesses the western fault boundary of the potential repository block at Yucca Mountain

Figure 1.2-2. Schematic Illustration of the ESF and ECRB Cross Drift

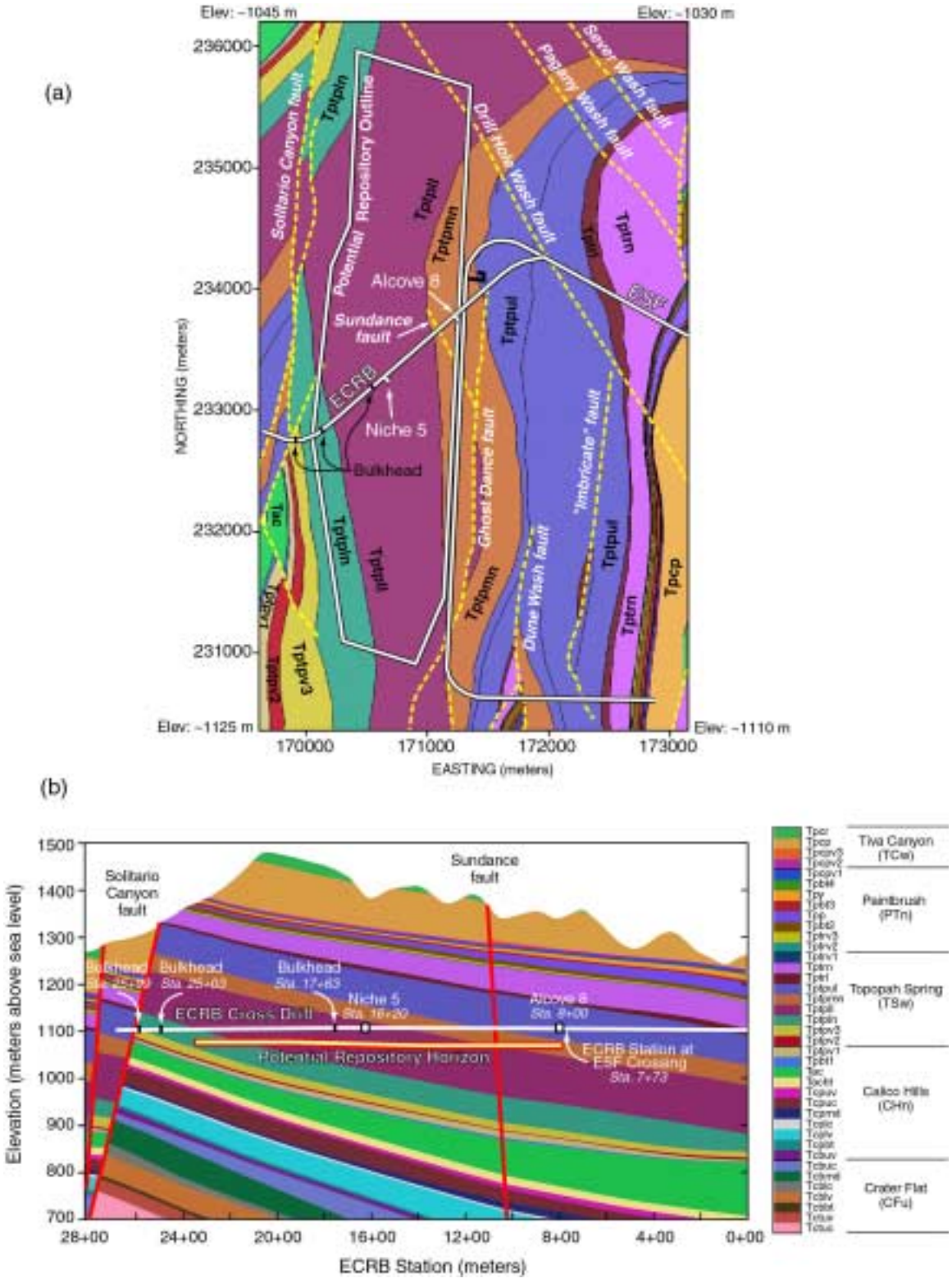

Figure 1.2-3. Schematic Illustration of East-West Distribution of Hydrogeologic Units Intersected by the Potential Repository Horizon (Tptpmn, Tptpll, and Tptpln)

Figure 1.2-4. Photo of Yucca Mountain Ridge, Fran Ridge, and Busted Butte, taken from the Southwest across the Solitario Canyon Fault

1.3 CONSTRAINTS, CAVEATS, AND LIMITATIONS

The field-testing activities and the associated analyses are subject to the constraints and limitations of spatial locations and temporal durations for tests conducted in the underground drifts. One niche has been excavated in the Tptpll unit. Most of the other existing testing alcoves and niches in the ESF (shown in Figure 1.2-3) are located at and above the horizon of the Tptpmn unit. Test results and analyses from these provide information for the alcoves and niches upper tuff units. Some of the active flow tests were conducted within a few hours to a few days because of limited accessibility to the test beds in the evenings and weekends. Depending on the system characteristics, the establishment of steady-state conditions requires longer tests. Some tests used automatic data acquisition systems for long term monitoring and liquid releases, subject to power interruptions and equipment malfunctions. These constraints, caveats, and limitations are addressed in the analyses, if applicable.

2. QUALITY ASSURANCE

The activities documented in this AMR were evaluated under Administrative Procedure (AP)-2.21Q, *Quality Determinations and Planning for Scientific, Engineering, and Regulatory Compliance Activities*, and were determined to be subject to the requirements of the United States Department of Energy (U.S. DOE) Office of Civilian Radioactive Waste Management (OCRWM) *Quality Assurance Requirements and Description* (QARD) (DOE 2000 [149540]). This evaluation is documented in BSC (2001 [155051], Attachment 1), and BSC (2001 [157107], Attachment 1). Electronic management of information was evaluated in accordance with AP-SV.1Q, *Control of the Electronic Management of Information*, and controlled under YMP-LBNL-QIP-SV.0, *Management of YMP-LBNL Electronic Data*. This evaluation is documented in the Technical Work Plan (TWP) (BSC 2001 [155051], Attachment 2).

This AMR reports on natural barriers (the Tiva Canyon welded, Paintbrush nonwelded, Topopah Springs welded, and Calico Hills nonwelded hydrogeologic units) that have been included in the *Q-List* (YMP 2000 [149733]) as items important to waste isolation. The AMR contributes to the analyses and modeling data used to support performance assessment. The conclusions of this AMR do not affect the repository design or permanent items as discussed in QAP-2-3, *Classification of Permanent Items.*

The activities documented in this AMR were conducted in accordance with the quality assurance program of the Yucca Mountain Site Characterization Project (YMP) using OCRWM APs and YMP Quality Implementing Procedures (QIPs) as identified in the TWP (BSC 2001 [155051], Table 6-1).

INTENTIONALLY LEFT BLANK

3. COMPUTER SOFTWARE AND MODEL USAGE

The software used in this study is listed in Table 3-1. All qualified software was obtained from Software Configuration Management (SCM), in accordance with AP-3.10Q, Attachment 1, Section 3, is appropriate for its intended use, and is used only within the range of validation in accordance with AP-SI.1Q, *Software Management.*

For data collection, only acquired software embedded as an integral part of the measuring and Test Equipment (M&TE), and controlled by AP-12.1Q, *Control of Measuring and Test Equipment and Calibration Standards*, was utilized. Embedded software are exempted from AP.SI.1Q requirements.

Table 3-1. Software and Routines

Software Name and Version	Software Tracking Number (STN)	DIRS Reference Number	Platform and Operating System
EARTHVISION-2 V4.0	30035-2 V4.0	152835	PC, UNIX
ECRB-XYZ V.03	30093 V.03	147402	PC, Windows 98

No models were used for the analyses performed in this AMR.

Microsoft Excel 97 and Microsoft Excel Version 7 were used to plot data for this AMR. These programs are exempted from the requirements of AP.SI.1Q.

INTENTIONALLY LEFT BLANK

4. INPUTS

Field data collected from underground drifts that characterize ambient and *in situ* field testing conditions include the following:

- Pneumatic pressure and air-permeability data from Alcoves 4 and 6
- Pneumatic pressure and air-permeability data (pre- and post-excavation) for ESF niches
- Laboratory dye measurements and sorptivity data
- Seepage and liquid-release data
- Water-potential data from drift walls and boreholes
- Fracture aperture and frequency data
- Unsaturated Zone transport testing data from Busted Butte.

The properties resulting from the analyses of the above field data include air-permeability distribution, fracture network connectivity, fracture flow-path distribution, seepage percentage, seepage threshold, fracture characteristic curve, formation intake rate, wetting-front travel time, fracture porosity, fracture volume, fracture flow fraction, tracer distribution, matrix imbibition, retardation factor, fault and matrix flow, water-potential distribution, construction-water migration, relative humidity, and moisture conditions.

4.1 DATA AND PARAMETERS

The Q-status of all inputs and a description of the data are shown in the Technical Data Management System (TDMS). The inputs to the AMR were obtained from the TDMS. This AMR was revised to reflect the most recent available *in situ* field-testing data. The data tracking numbers (DTNs) presented in the following tables include the most recent data. For this reason, the data used in this AMR are considered the most appropriate source for *in situ* field testing data to be used in the analyses presented in Chapter 6 of this AMR.

The input data used in this AMR are summarized in the following tables, which are organized to correspond to equivalent subsections in Chapter 6. DTNs used as sources for output DTNs developed in this AMR are indicated by notations in the following tables. DTNs used to corroborate output DTNs developed in this AMR are also indicated in notations to these tables.

Table 4.1-1 Data Used to Support Analysis of Air-Permeability Distributions and Excavation-Induced Enhancements

Inputs	Used in	Description
*LB0011AIRKTEST.001 [153155]	Table 6.1.2-1 Table 6.1.2-3 Figures 6.1.2-1,-2,-3,-4	Air permeability measurements in Niches 3566 and 3650 of the ESF.
*LB0012AIRKTEST.001 [154586]	Figure 6.1.2-9	Air permeability testing in Niche CD 1620
*LB002181233124.001 [146878]	Figure 6.1.2-10	Air permeability and pneumatic pressure data collected from Niche CD 1620
*LB0110AK23POST.001 [156905]	Figure 6.1.2-10	Air permeability measurement in Niche CD 1620
*LB0110AKN5POST.001 [156904]	Figure 6.1.2-9	Air permeability measurement in Niche CD 1620
LB980101233124.002 [105818]	Table 6.1.2-1	Statistical analysis of air-permeability along boreholes.
LB980901233124.004 [105855]	Table 6.1.2-3	Pneumatic pressure and air permeability data from Alcove 6 in the ESF
LB980901233124.009 [105856]	Table 6.1.2-3	Pneumatic pressure and air permeability data from Alcove 4 in the ESF
+LB980901233124.101 [136593]	Figure 6.1.2-5,-6,-7,-8 Table 6.1.2-1 Table 6.1.2-3	Pneumatic pressure and air permeability data from Niche 3107 and Niche 4788 in the ESF
LB980912332245.001 [110828]	Table 6.1.2-3	Air injection data from Niche 3107 of the ESF
*LB990601233124.001 [105888]	Figure 6.1.2-5 Figure 6.1.2-7 Table 6.1.2-1 Table 6.1.2-3	Seepage data feed to UZ drift-scale flow model for TSPA-SR
LB990901233124.004 [123273]	Table 6.1.2-1 Table 6.1.2-3	Air permeability cross-hole connectivity in Alcove 6, Alcove 4, and Niche 4788 of the ESF Pneumatic pressure and air permeability data from Niche 4788, Alcove 4, and Alcove 6 of the ESF; this data set also includes statistical analyses of air permeability data from Niches 3650, 3107, and 4788, as well as Alcoves 4 and 6.

NOTE: * Input DTNs for DTN: LB0110AIRK0015.001 [Output].
+ Corroborative data supporting DTN: LB0110AIRK0015.001 [Output].

Table 4.1-2 Data Used to Support Analysis and Interpretation of the Niche Liquid-Release and Seepage-Test Data

Inputs	Used in	Description
*LB0010NICH3LIQ.001 [153144]	Section 6.2.1.3.2	Niche 3107 seepage test
*# LB0010NICH4LIQ.001 [153145]	Section 6.2.1.3.3 Figure 6.2.1-5,-6,1-7,-8, and -9 Figure 6.2.2-2 Attachment II	Niche 4788 seepage tests measuring injected and captured water masses over time. Time spans include considerations for pumping time, wetting front arrival time, and dripping duration
*LB0102NICH5LIQ.001 [155681]	Sections 6.2.1.1 and 6.2.1.2 Figure 6.2.1-2 Attachment II	Niche CD 1620 seepage tests - pre excavation
+LB980001233124.004 [136583]	Sections 6.2.1.1, 6.2.1.2, 6.2.1.3.1, and 6.2.2.1, 6.2.2.3, 6.2.2.4 Figure 6.2.2-2 Figure 6.2.1-2 Table 6.2.2-4	Liquid release test data from Niche 3566 and Niche 3650 of the ESF
+LB980901233124.003 [105592]	Sections 6.2.1.1 and 6.2.1.2 Figure 6.2.1-2 Table 6.2.2-1,-2,-3,-4 Figure 6.2.2-1,-2,-3,-4	Liquid release and tracer tests in Niches 3566, 3650, 3107, and 4788 in the ESF. Fracture flow and seepage testing in the ESF
*LB990601233124.001 [105888]	Attachment II	Seepage data feed to UZ drift-scale flow model for TSPA-SR
*MO0107GSC01069.000 [156941]	Attachment II	ESF Niche 4788 borehole as-built information.

NOTE: * Input DTNs for DTN: LB0110LIQR0015.001 [Output].
+ Corroborative data supporting DTN: LB0110LIQR0015.001 [Output].
# Input DTN for LB0110NICH4LIQ.001 [Output].

Table 4.1-3 Data Used to Support Analyses of Tracer-Migration Delineation at Niche 3650

Inputs	Used in	Description
LB990601233124.003 [106051]	Table 6.3.2-1 Figure 6.3.2-1,-2,-3.,-4,-5,-6.,-7, and -8	Tracer detection data from core samples for tracers injected in Niche 3650 in the ESF

Table 4.1-4 Data Used to Support Analyses of Tracer Penetration and Water Imbibition into Welded Tuff Matrix

Inputs	Used in	Description
LB0110TUFTRACR.001 [156979]	Figure 6.4.3-1 Figure 6.4.3-2	Spatial distribution of applied tracers and the distribution of intrinsic tuff elements profiled using LA-ICP-MS.
LB980001233124.004 [136583]	Table 6.4.1-1 Table 6.4.1-2	Liquid-release tests performed to determine if a capillary barrier exists in Niche 3566 and Niche 3650
LB980901233124.003 [105592]	Table 6.4.1-1	Liquid release and tracer tests in niches 3566, 3650, 3107, and 4788 in the ESF.
LB990901233124.003 [155690]	Figure 6.4.1-2 Table 6.4.1-1, -2, and -3 Section 6.4.1.4 Figure 6.4.1-3 Figure 6.4.2-1 Figure 6.4.2-2 Table 6.4.2-1	Tracer lab analyses of dye penetration in Niches 3650 and 4788 of the ESF

Table 4.1-5 Data Used to Support Cross-Hole Analysis of Air Injection Tests

Inputs	Used in	Description
LB980901233124.004 [105855]	Figure 6.5.1-2	Pneumatic pressure and air permeability data from Alcove 6 in the ESF
LB990901233124.004 [123273]	Figure 6.5.1-1 Figure 6.5.1-3 Figure 6.5.2-2,-3, and -4	Air permeability crosshole connectivity in Alcove 6, Alcove 4, and Niche 4788 of the ESF

Table 4.1-6 Data Used to Support Analysis of Fracture Flow in Fracture-Matrix Test Bed at Alcove 6

Inputs	Used in	Description
LB990901233124.002 [146883]	Table 6.6.1-1 Figure 6.6.2-1,-2,-3,-4,-5,-6, and -7 Table 6.6.2-1	Alcove 6 flow data, including electrical resistance, water injection, intake rate, and water potential measurements
LB990901233124.001 [155694]	Figure 6.6.2-8	Alcove 6 tracer tests: the breakthrough of tracers, relating to the volume and the measured tracer concentration of the collected liquid at four collection trays in Alcove 6 experiments

Table 4.1-7 Data Used to Support Analysis of Flow Through the Fault and Matrix in the Test Bed at Alcove 4

Inputs	Used in	Description
GS960908314224.020 [106059]	Section 6.7.1.1	Analysis report: geology of the north ramp - stations 4+00 to 28+00 data: detailed line survey and full-periphery geotechnical map - Alcoves 3 (UPCA) and 4 (LPCA), and comparative geologic cross section - Stations 0+60 to 28+00
LB990901233124.005 [146884]	Table 6.7.1-1 Figure 6.7.2-1,-2,-3,-4,-5, and-6	Alcove 4 flow data, including electrical resistance, water injection, intake rate measurements

Table 4.1-8 Data Used to Support Compilation of Water-Potential Measurements in Niches

Inputs	Used in	Description
LB980001233124.001 [105800]	Table 6.8.2-1 Table 6.8.2-2 Table 6.8.2-3 Figure 6.8.2-1 Figure 6.8.2-2	Water-potential measurements in Niches 3566, 3650, and 3107 of the ESF

Table 4.1-9 Data Used to Support Observations of Construction-Water Migration

Inputs	Used in	Description
LB980901233124.014 [105858]	Figure 6.9.2-1 Figure 6.9.2-2 Figure 6.9.2-3 Figure 6.9.2-4	Borehole monitoring at the single borehole in the ECRB and ECRB crossover point in the ESF

Table 4.1-10 Data Used to Support Moisture Monitoring and Water Analysis in Underground Drifts

Inputs	Used in	Description
GS970208312242.001 [135119]	Table 6.10.1-1	Moisture monitoring in the ESF
GS970708312242.002 [135123]	Table 6.10.1-1	Moisture monitoring in the ESF
GS970808312232.005 [105978]	Table 6.10.1-2	USW NRG-7a, UE-25 UZ#4, UE-25 UZ#5, USW UZ-7a and USW SD-12
GS971108312232.007 [105980]	Table 6.10.1-2	USW NRG-7a, UE-25 UZ#4, UE-25 UZ#5, USW UZ-7a and USW SD-12
GS980308312242.001 [135181]	Table 6.10.1-3	TDR measurements
GS980308312242.002 [135163]	Table 6.10.1-2	Heat-dissipation-probe drill holes
GS980308312242.003 [135180]	Table 6.10.1-3	Borehole samples
GS980308312242.004 [107172]	Table 6.10.1-2	18 North Ramp boreholes, 3 Alcove 4 boreholes, and 46 South Ramp boreholes, HQ, 2-m length
GS980308312242.005 [107165]	Table 6.10.1-3	Borehole samples
GS980908312242.022 [135157]	Table 6.10.1-2	heat dissipation probe drill holes
GS980408312232.001 [105982]	Table 6.10.1-2	USW NRG-7a, UE-25 UZ#4, UE-25 UZ#5, USW UZ-7a and USW SD-12
GS980908312242.018 [135170]	Table 6.10.1-3	3 main boreholes, 6 lateral boreholes in Niche 3566 and 7 main boreholes in Niche 3650
GS980908312242.020 [135172]	Table 6.10.1-3	3 main boreholes, 6 lateral boreholes in Niche 3566 and 7 main boreholes in Niche 3650
GS980908312242.024 [135132]	Table 6.10.1-1	Moisture monitoring in the ESF
GS980908312242.028 [135176]	Table 6.10.1-3	3 boreholes in Alcove 6, 1 borehole in Alcove 7
GS980908312242.029 [135175]	Table 6.10.1-3	3 boreholes in Alcove 6, 1 borehole in Alcove 7
GS980908312242.030 [135224]	Table 6.10.1-3	1 slant borehole core
GS980908312242.032 [107177]	Table 6.10.1-2 Table 6.10.1-3	1 core hole in Alcove 3, 2 core holes in Alcove 4
GS980908312242.033 [107168]	Table 6.10.1-2 Table 6.10.1-3	1 core hole in Alcove 3, 2 core holes in Alcove 4
GS980908312242.035 [135133]	Table 6.10.1-1	Moisture monitoring in the ECRB
GS980908312242.036 [119820]	Table 6.10.1-2	6 heat-dissipation-probe drill holes
GS981208312232.002 [156505]	Table 6.10.1-2	USW NRG-7a, UE-25 UZ#4, UE-25 UZ#5, USW UZ-7a and USW SD-12
GS990408314224.006 [108409]	Table 6.10.2-1	Full periphery geologic maps for Station 20+00 to 26+81, ECRB Cross Drift
LAJF831222AQ98.007 [122730]	Figure 6.10.1-3	Chloride, Bromide, and Sulfate analysis of salts leached from ECRB-CWAT#1, #2, and #3 drill core.
LB0011CO2DST08.001 [153460]	Figure 6.10.2-9	Contents of gas samples collected from the following drift-scale test holes: 57, 58, 59, 60, 61, 74, 75, 76, 77, 78, 185; and the following control areas: Heater Drift #2 and AO drift air

Table 4.1-10 Data Used to Support Moisture Monitoring and Water Analysis in Underground Drifts (Continued)

Inputs	Used in	Description
LB0108CO2DST05.001 [156888]	Figure 6.10.2-9	Concentration data for CO_2 from gas samples collected from hydrology holes in drift-scale test.
LB0110ECRBH2OA.001 [156886]	Figure 6.10.2-7, -8 Table 6.10.2-2	Anion-cation measurements for water samples from non-ventilated sections of the ECRB.
LB0110ECRBH2OI.001 [156887]	Figure 6.10.2-9 Table 6.10.2-2	Deuterium and DEL O-18 measurements for water samples from non-ventilated sections of the ECRB.
LB0110ECRBH2OP.001 [156883]	Figure 6.10.2-2	Measurements of water potential at three locations between successive bulkhead doors in the ECRB
LB0110ECRBRHTB.001 [156885]	Figure 6.10.2-3 Figure 6.10.2-4 Figure 6.10.2-5	Measurements of relative humidity, temperature, and barometric pressure at four locations between successive bulkhead doors in the ECRB
LB960800831224.001 [105793]	Table 6.10.1-1 Section 6.10.1.2.1	Relative humidity, temperature, and pressure in ESF monitoring stations
LB970300831224.001 [105794]	Table 6.10.1-1 Section 6.10.1.2.1	Moisture data report from October
LB970801233124.001 [105796]	Table 6.10.1-1	Moisture monitoring data collected at ESF sensor stations
LB970901233124.002 [105798]	Table 6.10.1-1	Moisture monitoring data collected at stationary moisture stations
LB980001233124.001 [105800]	Table 6.10.1-2	3 main boreholes, 5 lateral boreholes in Niche 3566
LB980901233124.014 [105858]	Table 6.10.1-2 Table 6.10.1-3	43 psychrometers on ESF drift walls, 1 slant borehole below the invert 43 TDR probes on ESF drift walls
LB990901233124.006 [135137]	Figure 6.10.1-1 Figure 6.10.1-2 Table 6.10.1-1	Moisture data from the ECRB cross drift; relative humidity data from various cross-drift moisture stations
GS990908314224.010 [152631]	Figure 6.10.2-6	Comparative cross section along the ECRB Cross Drift
MO0006J13WTRCM.000 [151029]	Figure 6.10.2-8	J-13 well water composition

Table 4.1-11 Data Used to Support Analyses and Interpretations of Systematic Hydrological Characterization

Inputs	Used in	Description
*LB000900122l3U.001 [153141]	Section 6.11.2.1 Table 6.11.2-1 Figure 6.11.2-1	Two sets of air k (pneumatic conductivity) tests at 3 intervals in title borehole. Air k derived from steady state pressure response.
*LB000900122l3U.002 [153154]	Figure 6.11.2-2,-3, -4, -5, -6	Eleven sets of seepage tests. Liquid release tests from borehole SYBT-ECRB-LA#2 at CS 17+26 in cross drift.
*LB0110ECRBLIQR.001 [156878]	Figure 6.11.2-10	Measurements of seepage from injection tests in boreholes located in the drift crown of the ECRB.
*LB0110ECRBLIQR.002 [156879]	Figure 6.11.2-11	Measurements of seepage from injection tests in boreholes located in the drift crown of the ECRB.
LB980912332245.002 [105593]	Section 6.11.3.1	Gas tracer data from Niche 3107 of the ESF.
LB0110COREPROP.001 [157169]	Section 6.11.3.1	Data measured from cores drilled in the ecrb: porosity, saturation, bulk density, gravimetric water content, particle density.
*LB0110ECRBLIQR.003 [156877]	Figure 6.11.2-7 Figure 6.11.2-8 Figure 6.11.2-9	Measurements of seepage from injection tests in boreholes located in the drift crown of the ECRB.

NOTE: * Input DTNs for DTN: LB0110SYST0015.001 [Output].

Table 4.1-12 Data Used to Support Preliminary Observations from the Fault Test at Alcove8-Niche3107

Inputs	Used in	Description
LB0110A8N3GPRB.001 [156912]	Figures 6.12.3-1, -2, -3	Pre-seepage test ground penetrating radar tomography in radial borehole arrays between Alcove 8 (ECRB) and Niche 3107 (ESF).
*MO9901MWDGFM31.000 [103769]	Section 6.12.1.2	Geologic Framework Model. Version GFM 3.1.
LB0110A8N3LIQR.001 [157001]	Figure 6.12.2-2 Figure 6.12.2-3	Seepage data from Alcove 8/Niche 3107.
GS010608312242.003 [157119]	Figure 6.12.2-1	Crossover Alcove/Seepage into Niche 3.

*Note: The TDMS shows DTN: MO9901MWDGFM31.000 [103769] to be superseded by DTN: MO0012MWDGFM02.002 [153777], however, the new DTN does not include the data used for development of this analysis. The comment section on the Technical Data Information Form for the more recent DTN also contains the statement, “GFM2000” does not invalidate GFM3.1. This AMR maintains the use of the original DTN.

Table 4.1-13 Data Used to Support Busted Butte Unsaturated Zone Transport Test

Inputs	Used in	Description
GS990308312242.007 [107185]	Attachment VIII.8	Laboratory and centrifuge measurements of physical and hydraulic properties of core samples from Busted Butte boreholes.
GS990708312242.008 [109822]	Attachment VIII.8	Physical and hydraulic properties of core samples from Busted Butte boreholes.
LA9909WS831372.001 [122739]	6.13.2.2, Figure 6.13.2-2b-e	Busted Butte UZ transport test: Phase 1 collection pad extract concentrations
LA9909WS831372.002 [122741]	6.13.2.2, Figure 6.13.2-2b-e	Busted Butte UZ transport test: Phase 1 collection pad extract concentrations
LA9909WS831372.015 [140089]	6.13.1.11	ICPAES porewater analysis for rock samples from Busted Butte (used in AMR as ref for pore water composition)
LA9909WS831372.016 [140093]	6.13.1.11	Ion chromatography porewater analysis for rock samples from Busted Butte (used in AMR as ref for pore water composition)
LA9909WS831372.017 [140097]	6.13.1.11	pH of porewater of rock samples from Busted Butte (used in AMR as ref for pore water composition)
LA9909WS831372.018 [140101]	6.13.1.11	Gravimetric moisture content of rock samples from Busted Butte (used in AMR as ref for pore water composition)
LA9910WS831372.008 [147156]	6.13.2.1, Table 6.13.2-1	Busted Butte UZ transport test: gravimetric moisture content and bromide concentration in selected Phase 1A rock samples
LA9912WS831372.001 [156586]	6.13.3.9	Sorption of fluorinated benzoic acids and lithium on rock samples form Busted Butte
LB00032412213U.001 [149214]	Figure 6.13.4-1, -2, -3, and -4	Busted Butte ground penetrating radar data collected June 1998 through February 2000 at the unsaturated zone transport test (UZTT): GPR velocity data
LB0110BSTBTGPR.001 [156913]	Figure 6.13.4-3 Figure 6.13.4-4	Busted Butte Ground Penetrating Radar (GPR) Data
LL990612704244.098 [147168]	6.13.4.2.1 Figure 6.13.4-7, -8	Electrical Resistance Tomography (ERT) data for Busted Butte
LA0112WS831372.001 [157100]	Figure 6.13.3-3, -4, -5, -6, and-7	Quantitative pad tracer load data collected from Busted Butte Phase II UZTT.
LA0112WS831372.002 [157115]	Figure 6.13.3-3, -4, -5, -6, and-7	Quantitative pad tracer load data collected from Busted Butte Phase II UZTT.
LA0112WS831372.003 [157106]	Figure 6.13.3-3, -4, -5, -6, and-7	Quantitative normalized collection pad tracer concentrations from Busted Butte Phase II UZTT.
MO0004GSC00167.000 [150300]	Figure 6.13.4-1, Figure 6.13.4-2	As-built coordinate of boreholes in the test Alcove and running drift, Busted Butte test facility (BBTF)

4.2 CRITERIA

This AMR complies with 66 FR 55732. Subparts of the final rule that apply to this analysis or modeling activity are those pertaining to the characterization of the Yucca Mountain Site (Subpart B, Section 63.15). The compilation of information regarding geology of the site is in support of the License Application (Subpart B, Section 63.21(c)(1)(ii), and the definition of geologic parameters and the conceptual model used in the performance assessment (Subpart E, Section 63.114(a)).

4.3 CODES AND STANDARDS

No specific formally established standards have been identified as applying to this analysis.

5. ASSUMPTIONS

This AMR on ambient field testing of processes presents data collected in underground drifts at Yucca Mountain and its vicinity. The first group of four testing activities contributes to the drift seepage study to characterize fracture systems at niche sites, to determine seepage thresholds, and to evaluate tracer distributions. The second group of three activities involves flow and transport tests in two slotted test beds. The third group of three activities concerns the effects induced by ventilation and construction-water usage along underground drifts. The fourth group of three activities describes relatively large-scale tests for flow and transport processes.

The assumptions used in analyses of field-testing data are documented in this section. Depending on the status of the testing activities, the list of assumptions varies among different activities. Each of the 13 activities is discussed in its own subsection. The subsections in Section 5 (on assumptions) correspond to subsections in Section 6 (on analyses) and in Section 7 (on conclusions) (i.e., Sections 5.1, 6.1, and 7.1 are on Activity 1; 5.2, 6.2, and 7.2 on Activity 2). The assumption subsection contents range from specific discussion of the equation used in data analysis to general comment on the uncertainties, approximations, and approaches used in interpreting the test results. Some cross references to the main text in Section 6 on analyses are presented, especially for activities entering the stage of intensive interaction between data collection and test interpretation. The specific assumptions used in analyzing the test results are assigned ordering numbers for cross referencing, with the main descriptions summarized in Table 5-1. Approximations and approaches are summarized in bulleted lists.

Table 5-1. Assumptions

Ordering Number	Summary Description	Application Context	Justification or Evaluation Section	Assumption Used in Section
5.1-1	Air as ideal gas	Air-permeability calculation formula	5.1	6.1.2.1 6.1.2.2
5.1-2	Flow around finite line source			
5.1-3	Air-flow through fractures, Darcy's law			
5.2-1	Saturated liquid permeability equal to air permeability	Saturated hydraulic conductivity estimation	5.2	6.2.2.2
5.2-2	Gravity-driven liquid-flow, Darcy's law			
5.2-3	Steady downward flow through homogeneous, isotropic, infinite porous medium	Philip's capillary-barrier solution	5.2	6.2.2.2
5.2-4	One-dimensional flow	Braester's wetted profile solution	5.2	6.2.2.3
5.2-5	Downward translation of wetted profile at constant velocity			

Ordering Number	Summary Description	Application Context	Justification or Evaluation Section	Assumption Used in Section
5.13-1	Representativeness of Busted Butte	Mineralogic comparison	5.13	6.13
5.13-2	Natural conditions	Minimal construction effects		
5.13-3	Borehole influence	Numerical evaluation		
5.13-4	Steady-state background	Moisture distribution		
5.13-5	Uniform injection	Emitter design		
5.13-6	Non-reactive tracer	Laboratory evaluation		

5.1 ASSUMPTIONS USED IN BOREHOLE AIR-PERMEABILITY CALCULATIONS

In air-permeability tests, permeability values were obtained from pressure changes and flow rates using an analytic formula (modified Hvorslev's solution given in Section 6.1.2.1) derived from the following assumptions.

Assumption 5.1-1: Air behaves as an ideal gas.

This assumption is very nearly true at the ambient temperatures and pressures used in the air-permeability tests. No justification or evaluation of this assumption is required for the ambient field-testing conditions. This assumption is used in the equation presented in Section 6.1.2.1.

Assumption 5.1-2: A finite line source is used to represent a borehole injection interval.

This assumption is applied to the borehole injection interval, where all air flow is assumed to be in the radial direction and none in the axial direction. This assumption is justified because in the air-permeability tests, the length of injection zone was 0.3048 m and the radius of the borehole was 0.0381 m. The injection zone is a long, thin cylinder. Flows along axial directions were blocked by packers, and occurrences of packer leaks were monitored by pressures in adjacent borehole intervals, as described in Attachment I.

Although the fractured tuff of the niches is not a homogenous or infinite medium, the equation provides a consistent method of obtaining a permeability value for an equivalent homogeneous case and enables comparison of the test results for various injection locations, which is the focus of these tests. Because the heterogeneity of the surrounding medium is not known *a priori*, the permeabilities calculated by analytic formula are estimates of effective values around the injection borehole intervals. The results of the air-permeability tests are used to characterize the heterogeneity of the medium of niche sites and test beds. The main test results using this assumption are presented in Section 6.1.2.1 and Section 6.1.2.2 for the niches.

Assumption 5.1-3: Air flows are mainly through fractures and are governed by Darcy's law.

The justification for this assumption is as follows: Under the ambient unsaturated conditions in fractured tuff at Yucca Mountain, capillary forces confine the liquid mainly mainly to the matrix. This leaves the fracture network, which is more permeable than the tuff matrix, available for gas flow. Darcy's law is used to relate flux to pressure gradients (Bear 1972 [156269]).

Deviations from Darcy's law may result from either turbulent flow or from gas slip-flow phenomena (Klinkenberg 1942 [106105]); both these effects are assumed to be negligible. This assumption is justified as follows: Slip flow is significant only in pores whose dimensions are similar to the mean free path of air molecules (Bear 1972 [156269]); apertures of fractures in Yucca Mountain are much larger than the molecular mean free path. Pressure drop is proportional to flow rate in laminar flow, which is required for Darcy's law, but not in turbulent flow (Bear 1972 [156269]. These experiments were conducted at multiple flow rates to detect any evidence of deviation from Darcy's law due to turbulence, and none was found.

No further justification of this assumption of Darcy's law for air flows in fractures is required for the ambient field-testing conditions. The analytic equation is used in Section 6.1.2.2. Small effects potentially associated with movement of residual water within the fractures and the multi-rate approach to check packer leak-by and other nonlinear effects (e.g., turbulence) are discussed in Attachment I.4.

5.2 ASSUMPTIONS USED IN ANALYZING AND INTERPRETING THE NICHE LIQUID-RELEASE AND SEEPAGE TEST DATA

In liquid tests for seepage quantification, the saturated conductivities are estimated from air permeability values, the fracture capillarities are estimated from the seepage threshold fluxes, and the water potentials are estimated for the flow paths from the liquid-release interval to the niche ceiling. The following assumptions are used to derive the seepage parameters.

5.2.1 Assumptions Used in Estimating Saturated Hydraulic Conductivity Using Air Permeability

Permeability is an intrinsic parameter characterizing the resistance to flow by the rock medium. For laboratory test conditions with a well-defined unidirectional flow path through a core specimen, the permeability value is independent of the fluid used in the measurement. In the field conditions associated with localized injections, the flow path followed by the air is different from the flow path followed by the liquid. The following assumptions, together with detailed evaluation in Attachment III, address the relationship between air permeability and liquid permeability in the niche seepage tests.

Assumption 5.2-1: Saturated liquid permeability is equal to air permeability.

For locally saturated conditions such as in the immediate vicinity of a liquid-filled borehole interval, the saturated permeability to liquid flow is assumed to be equal to the permeability measured in air-injection tests. The saturated liquid flux is then estimated from the measured air-permeability value and the wetted area of the borehole, as described in Attachment III.

The estimations of saturated liquid permeability are evaluated in Attachment III from available data collected in the niche studies. The evaluation compares the estimated flux values with measured flux values for cases where there is evidence that the borehole intervals tested are actually saturated , with return flows observed. With liquid flow mainly through fractures below the borehole interval (results from gravity drainage and air flow into fractures all around the borehole interval driven by pressure gradient), the liquid permeability and air permeability represent the effective values of different fracture flow paths. The evaluation of the difference between liquid permeability and air permeability is documented in Attachment III, where it is shown that the saturated liquid permeability is within one order of magnitude of the air permeability. This assumption is used in Section 6.2, where this approximation is acceptable. This evaluation also requires the following assumption:

Assumption 5.2-2: Gravity-driven flow is the primary flow mechanism in fractures with weak capillarity, and liquid fracture flows are governed by Darcy's law.

Under unsaturated conditions, capillary forces and gravity are the driving mechanisms for flow. Because fracture apertures are much larger than tuff matrix pores, the effect of capillarity is much less than the effect of gravity on liquid fracture flow. This justifies use of this assumption to neglect fracture capillarity and use the gravity gradient to estimate flux. The small fracture capillarity is evaluated in Section 6.2.2.2. No further justification or evaluation of using Darcy's law for fracture flows is required for the ambient field testing conditions. This assumption is used in Attachment III and in Section 6.2.2.1 where seepage threshold fluxes are compared with estimated hydraulic conductivities.

5.2.2 Assumption Used in Deriving the Capillary Strength of the Fractures, Based on Philip's Capillary Barrier Solution

Philip et al. (1989 [105743]) developed an analytical solution describing under what conditions water will flow from an unsaturated porous medium into a buried cylindrical cavity. The solution is used in Section 6.2.2.2 to compute the sorptive number, α, a hydraulic parameter that is related to the strength of the capillary forces exerted by the porous medium. Philip et al. (1989 [105743], pp. 16–18) assumed the following in the analysis:

Assumption 5.2-3: Steady downward flow of water through a homogeneous, isotropic, unsaturated porous medium is assumed. Far from the cavity, the flow velocity is spatially uniform. The flow region is infinite in extent.

These conditions underlie the derivation of Philip's capillary-barrier solution. Furthermore, Philip et al. (1989 [105743], Section 1.5, p. 17) note that the requirement for homogeneity is relatively weak. Analytic solutions are generally derived in most cases with simplified descriptions and assumptions about the flow domain in the surrounding medium. Results derived from an analytic solution represent effective values. The description, evaluation, and justification of Philip's capillary-barrier solution are presented in Section 6.2.2.2.

5.2.3 Assumptions Used in Deriving the Estimated Volumetric Water Content for the Fractures Based on Braester's Wetted-Profile Solution

Braester (1973 [106088]) derived a time-dependent solution for the average volumetric-water-content distribution in a porous medium caused by the water release from a surface source of constant flux. This solution is described and used to estimate the volumetric water content of the fractures in Section 6.2.2.3. In addition to using Darcy's law for an unsaturated fractured medium, similar to Assumption 5.1-3 and Assumption 5.2-2 described above, the following assumptions were used by Braester (1973 [106088]) to derive the solution.

Assumption 5.2-4: A one-dimensional (1-D) formulation of Richards' equation, which includes both gravity and capillary-driven components of flow, is used to describe flow through an unsaturated porous medium.

The 1-D flow approximation can be evaluated and justified by (1) the weak fracture capillarity values described in Section 6.2.2.2, (2) the roughly 1-D flow paths observed during niche excavation described in Section 6.2.1.2, and (3) the limited spatial spread of seepage fluxes observed during post-excavation seepage tests described in Section 6.2.1.3.1. The evaluation of this assumption is addressed further in Attachment IV.1.

Assumption 5.2-5: The downward translation of a wetted profile is at constant velocity.

The average value of the water content at the infiltrating surface over time is assumed by Braester (1973 [106088], p. 688) to be equal to the average value of water content over the wetted depth. This approximation becomes valid if the solution of water content takes the form of a downward translation of the entire wetted profile at constant velocity. This would generally occur after the capillary forces near the source have diminished and the volumetric water content at the soil surface reaches its steady-state limit, with the gravity gradient driving the liquid flux. The times needed to reach steady state and the evaluations of this assumption of downward translation of wetted profiles at constant velocity are addressed further in Attachment IV.

The following approximations are also used in Section 6.2.2.3 with Braester's solution to estimate water content:

- Residual water content in fractures is negligible. This approximation is reasonable for fracture flow paths, which are likely to be dry under ambient conditions, with liquid mainly residing in the matrix.

- A linearized solution is used to provide a reasonable approximation of the water content at the infiltrating surface and the advance of the wetting front. The evaluations of the solutions by Braester's solution are discussed in Section 6.2.2.3.

5.3 APPROXIMATIONS USED IN TRACER-MIGRATION DELINEATION AT NICHE 3650

Tracer measurements were conducted on cores collected at Niche 3650. Twelve boreholes were drilled around the last liquid-release point. Core analyses delineated the spatial distributions of

the specific tracers released in the last liquid-release event as well as tracers used in previous tests in the fractured rock mass above the niche ceiling. The following approximations were used in the analysis and interpretation of tracer results.

- Iodine and various dye tracers were used in the liquid-release tests and were analyzed on samples along the boreholes. Iodine was treated as a nonreactive conservative tracer. Dyes were used to trace the main flow paths through the fractures.

- Higher ratios of detected tracer concentration to the background concentration indicated the stronger presence of tracers. The ratio representation was used to minimize the dependence of test results on measurement sensitivity and tracer purity associated with different dyes and chemicals.

- Locations of subsamples were estimated from rock-sample-packet information. The spatial resolutions were poor, especially for fragmented samples.

- The absence of tracers in the twelve surrounding boreholes was used to indicate the localization of liquid released in the central borehole.

- The presence of iodine in rock chips collected on the niche ceiling directly below the release point was used to confirm the arrival of wetting front.

5.4 APPROXIMATIONS USED IN ANALYSES OF TRACER PENETRATION AND WATER IMBIBITION INTO WELDED TUFF MATRIX

Tracer-stained rock samples were collected during niche excavation for laboratory analyses. Clean rock samples collected from the same stratigraphic unit were used to evaluate the relative extents of dye penetration, tracer penetration, and water imbibition. The following approximations were used in the analysis and interpretation of test results:

- Dye-stained rock samples collected during niche excavations were associated with liquid-release tests conducted before niche excavations.

- Initial concentrations of tracers were derived from weights of tracers divided by water volumes.

- Rock powders from drilling into field samples and lab cores to different depths were used in determining tracer profiles.

- Visual observations on cores were used to determine water penetration.

5.5 APPROXIMATIONS USED IN CROSSHOLE CONNECTIVITY ANALYSES

The crosshole data were acquired at the same time as the single-hole data (as described in Section 5.1), by logging the steady-state pressure response in all the noninjected (observation) zones while performing an injection. Observation response pressure is a function of the injection pressure, the connectivity between zones, and the distance between zones. In practice, it is not

well understood how to normalize response to distance in the fractured rock. Attempts at dividing pressure response by any function of distance result in the apparent connectivity being skewed to the more distant zones. Distance is thus not included in the approximation used in crosshole analyses. The approximation uses the simple ratio of observation-response pressure to injection pressure. If a test is performed at low pressures at twice the injection pressure change, the response change should also be twice. The ratio is

$$\Delta P_{res} \Big/ \Delta P_{inj} \qquad \text{Eq. 5.5-1}$$

where

ΔP_{res} is the steady-state pressure rise above ambient at the observation location, and

ΔP_{inj} is the steady-state pressure rise in the injection zone.

The ratio provides a measure of how well a response zone is connected to an injection zone. The value enables all the observation responses from all injections at a site to be directly compared, so that they can all be viewed on a single three-dimensional (3-D) diagram instead of individual diagrams for each tested injection zone.

5.6 APPROXIMATIONS USED IN ANALYSES OF FRACTURE FLOW IN FRACTURE-MATRIX TEST BED AT ALCOVE 6

Flow tests were conducted in a test bed at Alcove 6 in the ESF within the Tptpmn unit. This test bed has a slot excavated below a cluster of boreholes. Wetting-front detectors in monitoring boreholes and seepage collection trays in the slot were developed to evaluate the evolution of flow field in response to liquid releases and injections into localized zones along an injection borehole. The following approximations were used in the interpretation and analysis of test results:

- Wetting-front arrivals were indicated by decreases in electrical resistance of probes in contact with the borehole walls and by increases in water potentials measured by psychrometers.
- Seepage arrivals in the slot within minutes to hours after liquid injections were interpreted to be associated with fracture flow paths.
- Drainage into the slot after termination of injection for each test was interpreted to be a measure of the volume of the fracture flow paths.

5.7 APPROXIMATIONS USED IN ANALYSES OF FLOW THROUGH THE FAULT AND MATRIX IN THE TEST BED AT ALCOVE 4

Flow tests were conducted in a test bed at Alcove 4 in the ESF within the PTn unit. The test bed has a series of horizontal boreholes underlain by a single slot. Water was injected into isolated

zones within some of these boreholes, and the resulting water plume was then monitored as it migrated past adjacent boreholes. The following approximations were used in the interpretation and analysis of the test results:

- Wetting-front arrivals were indicated by decreases in electrical resistance of probes in contact with the borehole walls and increases in water potentials measured by psychrometers.

- Fast travel times, observed following injection of water in the borehole through the fault, were interpreted to be associated with flow through the fault.

5.8 APPROXIMATIONS USED IN WATER-POTENTIAL MEASUREMENTS IN NICHES

Water potential measurements were measured in boreholes with psychrometers, with the following approximation:

- Psychrometers in the boreholes were in approximate equilibrium with the moisture in the borehole interval.

5.9 APPROXIMATIONS USED IN MONITORING CONSTRUCTION-WATER MIGRATION

Construction-water migrations were monitored at the starter tunnel of the ECRB Cross Drift and at the cross-over point in the Main Drift, with the following indications:

- Construction-water arrivals at a borehole below the invert were indicated by decreases in electrical resistance of probes in contact with the borehole walls and increases in water potential measured by psychrometers.

- Construction-water arrivals to the Main Drift below the ECRB Cross Drift would be indicated by wetting of the drift walls and seepage into a water-collection system.

5.10 APPROXIMATIONS USED IN MOISTURE MONITORING AND WATER ANALYSIS IN UNDERGROUND DRIFTS

Moisture data collected by moisture-monitoring stations could be used to estimate the moisture removal rate, if the ventilation rate were known or estimated. The pertinent estimations involve the following approximations:

- Vapor density was determined by the relative humidity multiplied by the saturated vapor density, as determined by the temperature from a standard steam table.

- Equivalent evaporation rate could be calculated with vapor-density differences multiplied by the ventilation flow rate and divided by the total drift wall area between two stations.

Water collected in boreholes drilled below the drifts and in containers in the sealed drifts were analyzed for the presence of lithium bromide and other chemical compositions and isotopic signatures. The implications are:

- Presence of bromide was interpreted as a signature for the presence of construction water, which was traced with lithium bromide.

- Absence of lithium bromide and other chemicals was treated as an indication that the water was originated from condensation caused by temperature and relative humidity variations along sealed drifts.

5.11 APPROXIMATIONS USED IN ANALYZING AND INTERPRETING THE SYSTEMATIC HYDROLOGICAL CHARACTERIZATION DATA

Volumes and rates of released water and collected seepage, together with data on the wetting front arrival and estimated evaporation loss, were used to characterize systematically the lower lithophysal zone of the Topopah Spring welded tuff. The estimations involve the following approximations:

- The capacity of the fractured-porous-lithophysal welded tuff to take in water was determined by the volume of water released into the borehole section, minus the volume of water returned (from overflow should the delivery rate prove to be too high).

- The volume of water introduced to the formation up to the first appearance of wetting on the drift ceiling was the volume required to establish “fast paths” between injection and seepage locations. This volume includes both the porosity of the fast path and that of the matrix blocks into which water has imbibed, as well as the portions of the lithophysal cavities into which water has entered and remained.

- Not all seepage water was recorded by the seepage collection system because of evaporation, since the relative humidity in the drift was typically far below 100%. A measure of the amount of seepage water lost to evaporation were obtained from the average evaporation rate from the open evaporation-pan measurement coupled with the estimated area of wetting on the drift ceiling.

- After establishment of steady-state seepage (and for subsequent brief pauses of water release), “fast paths” drained during pauses and refill following resumption of water release.

    - The porosity of the fast paths could be estimated from the volume of water introduced from the time of resumption of water released into the borehole section up to the re-establishment of seepage collection.

    - The difference between the volume of seepage water collected during the pause of water supply and the volume of water needed to occupy the porosity of “fast paths” could be used to estimate the volume of water diverted around the drift (when the effect of seepage water lost to evaporation was accounted for).

5.12 APPROXIMATIONS USED IN PRELIMINARY OBSERVATIONS FROM THE FAULT TEST AT ALCOVE 8 – NICHE 3107

The drift-to-drift tests used a combination of techniques to quantify the flow processes and to map the structure of the test beds:

- The arrivals of released water from Alcove 8 in boreholes above Niche 3107 were indicated by decreases in electrical resistance of probes installed in borehole intervals.
- The liquid-release rate and the seepage rate were quantified by infiltrometer and by transducers in the seepage collection system.
- The ground-penetrating-radar tomograph and seismic tomograph techniques were used to confirm the presence of the lithologic contact between the ECRB and the ESF.

5.13 ASSUMPTIONS USED IN THE BUSTED BUTTE UNSATURATED ZONE TRANSPORT TEST

The Busted Butte Unsaturated Zone Transport Test (UZTT) uses the following assumptions:

Assumption 5.13-1 (identical to Assumption (11) in CRWMS M&O 2001 [154024], Section 5): The rocks identified as Calico Hills vitric (CHv) and Topopah Spring welded (TSw) hydrogeologic units at Busted Butte are part of the same-named units that exist under the repository and are also representative of those same units under the repository.

The basis for this assumption is the equivalent location of the units within the rock sequence at Busted Butte and Yucca Mountain (including the repository), as well as an understanding of the geologic processes that formed the region. Mineralogic analyses of samples from Busted Butte compared to those collected from boreholes on Yucca Mountain support this assumption (Bussod et al. 1999 [155695], Section 2.2 and 2.3). This assumption is used in Attachment VIII of this AMR.

Assumption 5.13-2 (identical to Assumption (15) in CRWMS M&O 2001 [154024], Section 5): The test block was minimally disturbed (saturation, *in situ* water distribution, fractures, faults) during construction of the test and is assumed to represent natural conditions.

Precautions, such as dry drilling, were taken to avoid disturbance of the test block during construction, and no unexpected disturbances have been observed during visual inspection of the integrity of the test block. On this basis, plus the assessment that the effects of an undetected disturbance on subsequent tests will be small compared to intentionally induced effects, the assumption does not require further confirmation. This assumption is used in Section 6.13 of this AMR.

Assumption 5.13-3 (identical to Assumption (12) in CRWMS M&O 2001 [154024], Section 5): The presence of boreholes does not unduly influence the results of the transport test.

This assumption has been tested through numerical assessment of borehole influence, as shown in the AMR *Unsaturated Zone and Saturated Zone Transport Properties* (CRWMS M&O 2001 [154024], Section 6.8.2). The AMR shows that solute travel time is disturbed by less than 20% (CRWMS M&O 2001 [154024], Figure 42). This assumption does not require further confirmation. This assumption is used in Section 6.13 of this AMR.

Assumption 5.13-4 (identical to Assumption (16) in CRWMS M&O 2001 [154024], Section 5): The UZTT test blocks were at a steady-state background moisture distribution before injection.

The UZTT is located in an otherwise undisturbed area of the Yucca Mountain site. It is assumed that the construction of the UZTT and the test design caused minimal disturbance of the system (see previous assumption), and that any change caused by construction would quickly return to an equilibrium state within the time between tunnel excavation and beginning injection. A modeling study by Soll (1997 [149146], p. 21, Phase 1A results) found that perturbations caused by construction would be insignificant by 14 days. This result is sufficient justification for the assumption; more than 14 days elapsed between construction and injection. This assumption is used in Section 6.13 of this AMR.

Assumption 5.13-5 (identical to Assumption (17) in CRWMS M&O 2001 [154024], Section 5): The different emitters in any given borehole are all injecting at the same rate.

All emitters are identical. Total injection quantity is carefully monitored, and any variation can be identified and incorporated into analyses. Because each emitter is designed to be identical, this assumption does not require confirmation. This assumption is used in Section 6.13 of this AMR.

Assumption 5.13-6 (identical to Assumption (18) in CRWMS M&O 2001 [154024], Section 5): In selecting the tracers, fluorescein, bromide, and FBAs were assumed to be effectively nonsorbing.

This assumption is based on values from the refereed literature (DTN: LB991220140160.019 [146601]), and no further confirmation is required. This assumption is used in Section 6.13 of this AMR.

INTENTIONALLY LEFT BLANK

6. ANALYSES

This section describes the field-testing results of unsaturated zone (UZ) processes in underground drifts at Yucca Mountain and its vicinity. The field activities range from drift seepage tests over decimeter scale above niches, fracture-matrix interaction tests over meter scale above slots in alcoves, flow and transport tests over decameter scale along or between drifts, to moisture monitoring studies over kilometers along drifts. Niches are room-size excavations, slots are excavations below test beds in alcove walls, and alcoves are side drifts along the ESF Main Loop and ECRB Cross Drift.

Specifically, Section 6.1 and Section 6.5 present the test-site characteristics of niches and alcoves from pneumatic air-permeability test results. Section 6.2 shows that drift-seepage thresholds exist and that seepage threshold data can be interpreted using the capillary-barrier theory. It also presents liquid-flow-path data for niche sites. Section 6.3 and Section 6.4 present laboratory-measurement results for tracer migration and matrix imbibition for welded tuff samples from the ESF. Section 6.6 presents the results of two series of fracture-matrix interaction tests to quantify the partitioning of flux into fast and slow components. Section 6.7 presents the results for flow tests in the Paintbrush nonwelded tuff (PTn) test bed. Sections 6.8–6.10 summarize data collected on ambient water-potential distribution, construction-water migration, and moisture conditions. Section 6.11 presents the results from systematic hydrologic characterization using slanted boreholes along the Cross Drift. Section 6.12 presents the results of drift-to-drift tests from liquid releases in Alcove 8 and wetting-front and seepage detection at Niche 3107. Section 6.13 presents the results of different phases of transport tests at Busted Butte.

The tests performed in niches and alcoves along the ESF are illustrated in Figure 6-1. Seepage into drifts at the potential-repository level is related to water percolating down from the ground surface. Drift seepage tests at niche sites quantify the seepage from liquid pulses released above the niches. Percolation flux has a fast fracture-flow component and a slow matrix-flow component. This partitioning of flow is evaluated at the fracture-matrix test bed in Alcove 6. The heterogeneous hydrogeologic setting with alternating tuff layers determines the percolation distribution throughout the UZ, with input from infiltration at the ground surface boundary. The mechanism of redistributing near-surface fracture flow by the porous PTn, especially the flow-damping process by the PTn unit, is studied in a test bed in Alcove 4 that consisted of layered, altered, and bedded tuffs that were transected by a fault. Wetter climate conditions increase the infiltration, as quantified in an artificial infiltration test in Alcove 1 and in moisture monitoring at depth in Alcove 7. The seepage threshold data from niches and from systematic hydrologic characterization are inputs to CRWMS M&O 2001 [153045].

Figure 6-1 lists major TSPA issues (DOE 1998 [100550]) related to UZ flow processes of seepage, percolation, and infiltration. The tests illustrated in Figure 6-1 focus on different issues to quantify the functional relationships among these processes. Seepage is smaller than the percolation flux because of capillarity-induced drift diversion (CRWMS M&O 2001 [153045], Section 6), and percolation may be smaller than infiltration because of lateral diversion of percolating water along tuff interfaces to bounding faults (BSC 2001 [156609], Section 6.4.3). All tests use tracers to assist the characterization of plume migration.

Figure 6-2 illustrates the ECRB Cross Drift to ESF Main Drift seepage collection system to study the migration of water and tracer flow from one drift to another. The cross-over point is located in the northern part of the ESF, as illustrated in Figure 6-2 and Figure 6.1.1-1. In 1998, the seepage monitoring system was used to monitor the migration of construction water from the ECRB Cross Drift. Niche 3107, originally excavated and used for the drift seepage study, is currently part of the drift-to-drift study as a seepage collection site. The existing horizontal boreholes at Niche 3107 are used for wetting-front monitoring for liquid released from Alcove 8 excavated horizontally from the ECRB Cross Drift and directly above Niche 3107.

Since neither the ESF drift nor the ECRB Cross Drift reaches the Calico Hills hydrogeologic tuff unit (CHn) below the potential repository block, a dedicated drift complex was excavated at Busted Butte, 8 km southeast of Yucca Mountain, to evaluate the flow and transport processes in vitric CHn. Early results were first reported in the AMR *Unsaturated Zone and Saturated Zone Transport Properties (U0100)* (CRWMS M&O 2001 [154024]). The different field-testing phases and recent updates are presented in Section 6.13.

Each testing activity has unique findings to contribute to the assessment of unsaturated flow and transport processes at Yucca Mountain. The progress and analyses of field-test results are presented in the following thirteen subsections for thirteen testing activities. Key scientific notebooks (with relevant page numbers) used for recording the ESF Field Testing activities and analyses described in this AMR are listed in Table 6-1.

This AMR provides data that are used directly to support seepage modeling. *Seepage into Emplacement Drifts* is classified as a principal factor for the postclosure safety case. Therefore, this AMR is assigned primary (Level 1) importance.

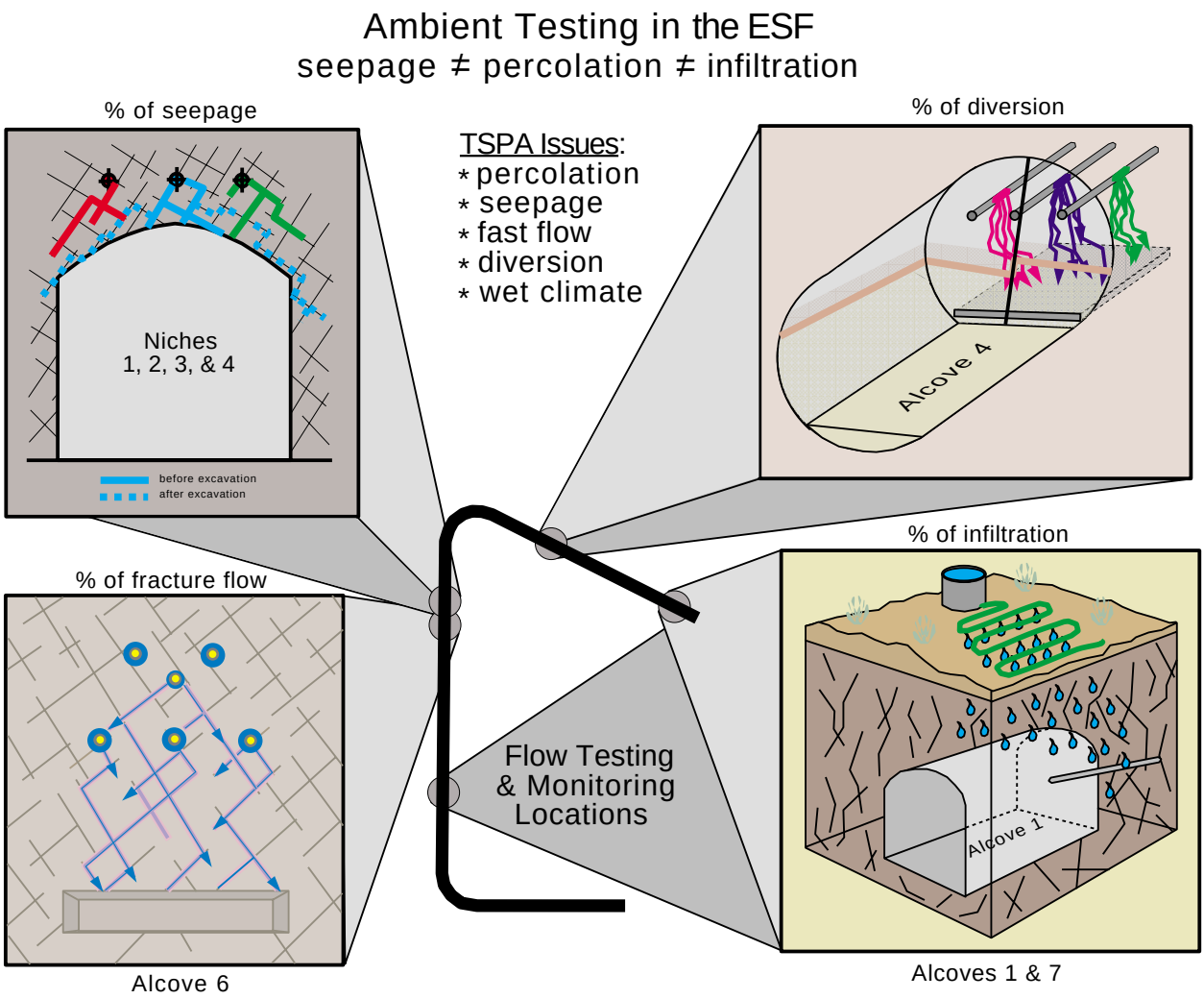

NOTE: The tests evaluate functional relationships between unsaturated zone processes to resolve TSPA issues.

Figure 6-1. Schematic Illustration of Flow Tests in the Exploratory Studies Facility at Yucca Mountain

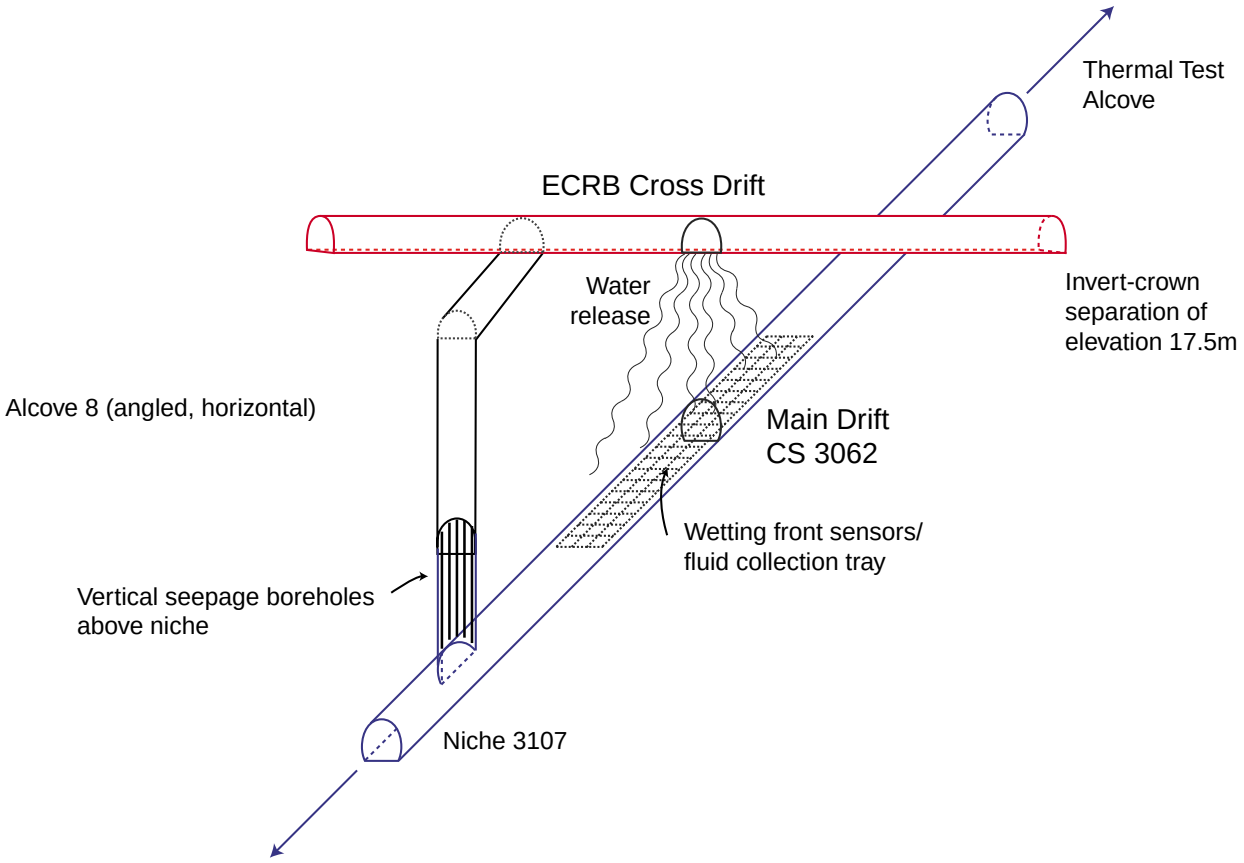

NOTE: Wetting-front sensors and fluid collection trays monitored the construction-water migration. Both the ECRB Cross Drift and the Main Drift, together with Alcove 8 and Niche 3107 and its boreholes, are horizontal in this illustration. Alcove 8 is directly above Niche 3107.

Figure 6-2. Schematic Illustration of the Cross-Over Point of ECRB Cross Drift with the Main Drift

Table 6-1. Scientific Notebooks

LBNL Scientific Notebook ID	YMP M&O Scientific Notebook ID	Page Numbers	Citation
YMP-LBNL-JSW-6	SN-LBNL-SCI-065-V1	pp. 1-156	Wang 1997 [156530]
YMP-LBNL-JSW-6A	SN-LBNL-SCI-066-V1	pp. 1-156	Wang 1997 [156534]
YMP-LBNL-JSW-6B	SN-LBNL-SCI-121-V1	pp. 1-156	Wang 1999 [156538]
YMP-LBNL-JSW-6C	SN-LBNL-SCI-122-V1	pp. 1-156	Wang 1999 [153449]
YMP-LBNL-JSW-QH-1	SN-LBNL-SCI-089-V1	pp. 1-156	Hu 1999 [156539]
YMP-LBNL-JSW-QH-1A	SN-LBNL-SCI-090-V1	pp. 20-22, 37-48, 54, 68-82, 86-99, 103-126	Hu 1999 [156540]
YMP-LBNL-JSW-QH-1B	SN-LBNL-SCI-091-V1	pp. 9, 27, 35, 40, 42, 48-73, 77, 81-94, 107-110, 115, 118-119, 123-142, 149, 154-155	Hu 1999 [156541]
YMP-LBNL-JSW-QH-1C	SN-LBNL-SCI-092-V1	pp. 13, 16-25, 39-41, 51-102, 105-112, 116, 128-133, 139-140, 143-145	Hu 1999 [156542]
YMP-LBNL-JSW-QH-1D	SN-LBNL-SCI-093-V1	pp. 3-151	Hu 1999 [155691]
YMP-LBNL-JSW-QH-1E	SN-LBNL-SCI-154-V1	pp. 3-16	Hu 2000 [156473]
YMP-LBNL-JSW-PJC-6.2	SN-LBNL-SCI-078-V1	pp. 1-99, 104,109,110,115,116,120–125,132-135,144,146	Cook 2001 [156902]
YMP-LBNL-JSW-RS-1	SN-LBNL-SCI-102-V1	pp. 1-115	Salve 1999 [155692]
YMP-LBNL-JSW-RS-1A	SN-LBNL-SCI-104-V1	pp. 1-39	Salve 1999 [156547]
YMP-LBNL-JSW-RS-2	SN-LBNL-SCI-105-V1	pp. 1-7	Salve 2000 [156548]
YMP-LBNL-JW-1.2	SN-LBNL-SCI-048-VI	pp. 103-152	Salve 1999 [156552]
YMP-LBNL-JW-1.2A	SN-LBNL-SCI-133-V1	pp. 1-43	Salve 1999 [156555]
YMP-LBNL-JSW-JJH-1	SN-LBNL-SCI-088-V1	pp. 1-68	Hinds 2000 [156557]
YMP-LBNL-JSW-CMO-1	SN-LBNL-SCI-042-V1	pp. 1-59	Oldenburg 2000 [156558]
YMP-LBNL-JSW-4.3	SN-LBNL-SCI-116-V1	pp. 1-24, 61-67, 74-81	Wang 2000 [156559]
YMP-LBNL-JSW-JS-1	SN-LBNL-SCI-150-V1	pp. 18, 148	Stepek 2000 [156561]
YMP-LBNL-RCT-1	SN-LBNL-SCI-113-V1	pp. 62-73, 88-150	Trautz 1999 [156563]
YMP-LBNL-RCT-2	SN-LBNL-SCI-156-V1	pp. 27-34	Trautz 2001 [156903]
YMP-LBNL-RCT-3	SN-LBNL-SCI-177-V1	pp. 79, 84	Trautz 2001 [157022]

6.1 AIR-PERMEABILITY DISTRIBUTIONS AND EXCAVATION-INDUCED ENHANCEMENTS

Pneumatic air-permeability tests were undertaken over a three year period (1997-2000) at various locations in the ESF to characterize the potential fluid flow paths in the rock. The potential repository host rock consists predominantly of unsaturated, fractured welded tuff. As discussed in Section 5.1, air flows are mainly through the fractures. Air-permeability tests are utilized to study the fracture heterogeneity. Air-permeability tests can characterize fractured systems efficiently. Once the injections stop, the pressure field returns to its ambient conditions within minutes, under most field-test conditions.

To determine potential flow paths in the test sites, packer assemblies were used to isolate intervals in clusters of boreholes drilled into the fractured rock to perform pneumatic testing. In these tests, air is injected into specific intervals at constant mass flux while pressure responses are monitored in other intervals. The objectives for pneumatic testing include profiling the air permeability of boreholes along their length, investigating the effects of nearby excavation on the permeability of a rock mass, and enabling a site-to-site comparison of air-permeability statistics and related scale effects. Two basic types of data are readily available from pneumatic testing and are used to satisfy these testing objectives: (1) single-borehole air permeability profiles, which are used for borehole-to-borehole and site-to-site comparisons, and (2) cross-hole pressure-response data, which enable a determination of connectivity through fracture networks between locations at a given site. This section focuses on the permeability profiles for boreholes in five niche sites. Permeability profiles before niche excavation are compared with profiles measured after niche excavation. Section 6.5 focuses on crosshole data analyses.

6.1.1 Niche Test Site and Borehole Configuration

Extensive air-permeability measurements have been made in borehole clusters at five niches and at three alcoves within the ESF tunnel, as part of a program to select locations for liquid-release tests. The air permeability along each borehole in a cluster serves as a guide to the selection of the liquid-release intervals.

6.1.1.1 Site Selection

The niche sites were selected for study based on fracture and hydrologic data collected in the ESF, as illustrated in Figure 6.1.1-1. Four niches were excavated along the Main Drift of the ESF and a fifth in the ECRB Cross Drift. The first niche site is located at Construction Station (CS) 35+66 (hereafter referred to as Niche 3566, located at 3,566 m from the ESF north portal), in a brecciated zone between the Sundance fault and a cooling joint where a preferential flow path is believed to be present (based on elevated $^{36}Cl/Cl$ ratios described in BSC 2001 [154874] the AMR on geochemistry data). Niche 3566 was sealed with a bulkhead to conduct long-term monitoring of *in situ* conditions. The second niche site is located at CS 36+50 (Niche 3650) in a competent rock mass with lower fracture density than Niche 3566. The third niche is located at CS 31+07 (Niche 3107) in close proximity to the crossover point located at CS 30+62. A test alcove (Alcove 8) has been excavated from the ECRB Cross Drift to a position immediately above Niche 3107 so that a large-scale drift-to-drift test can be conducted at this location. The fourth niche site is located at CS 47+88 (Niche 4788) in a 950 m long exposure of the middle

nonlithophysal zone, referred to by Buesch and Spengler (1998 [101433], p. 19) as the intensely fractured zone. The fifth niche is located at ECRB Cross Drift CS 16+20 (Niche CD 1620) near the center of the potential repository block. The first four niches described above were excavated on the west side of the ESF main drift within the middle nonlithophysal zone of the Topopah Spring welded tuff unit (TSw). The fifth niche in the ECRB Cross Drift is excavated in the lower lithophysal zone of TSw, which is the tuff unit where most of the potential repository emplacement drifts are planned to be.

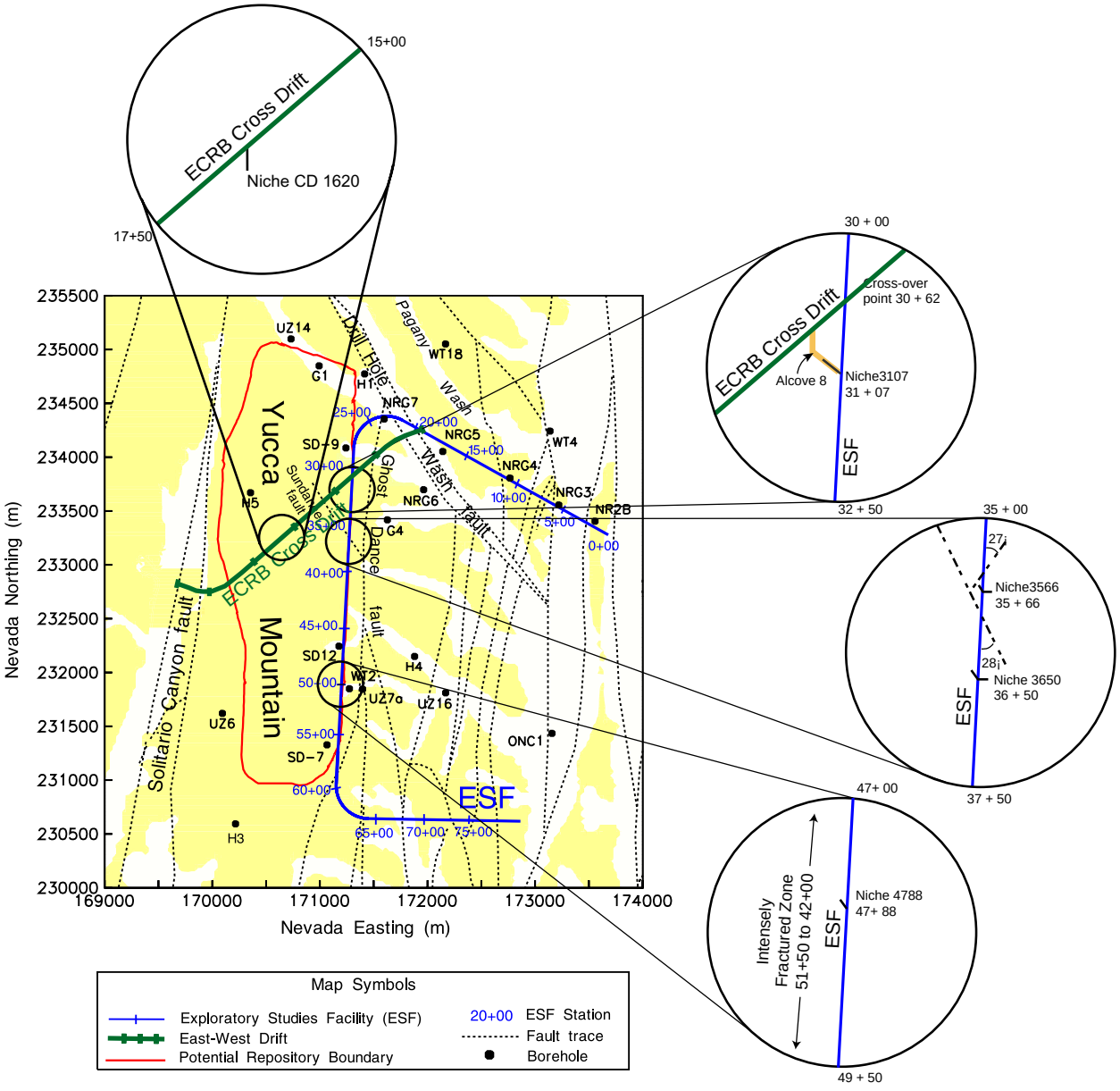

Figure 6.1.1-1. Location Map for Niche 3107, Niche 3566, Niche 3650, Niche 4788 and Niche CD 1620

6.1.1.2 Borehole Configuration

Three boreholes were drilled at Niche 3566, and seven boreholes per niche were drilled at Niche 3650, Niche 3107, and Niche 4788 prior to excavation to gain access to the rock for testing and monitoring purposes. Figure 6.1.1-2 shows the schematics of borehole clusters tested at the first four niche sites. At the niches, boreholes were drilled before excavation into both the rock to be excavated and the surrounding rock. Both types of boreholes were tested before niche excavation, and the surrounding boreholes were retested after excavation, allowing a study of excavation effects on the permeability of the surrounding rock. All boreholes shown in Figure 6.1.1-2 are parallel to the niche axis as illustrated in Figure 6.1.1-3.

Figure 6.1.1-2a and Figure 6.1.1-3a show that three boreholes were originally installed at Niche 3566 along the same vertical plane coincident with the center of the niche.[1] The three boreholes were assigned the designation U, M, and B, corresponding to the upper, middle, and bottom borehole, respectively. Borehole M and borehole B were subsequently removed when the rock was mined out to create the niche, and borehole U still remains.

Figure 6.1.1-2b and Figure 6.1.1-3b show the location of the seven boreholes installed at Niche 3650. Three of the boreholes, designated UL, UM, and UR (upper left, upper middle, and upper right), were installed approximately one meter apart and 0.65 m above the crown of the niche in the same horizontal plane. The remaining boreholes (ML, MR, BL, and BR) were drilled within the boundaries of the proposed niche and were subsequently mined out when the niche was excavated as planned.

Figure 6.1.1-2c and Figure 6.1.1-3c show the final configuration of the seven boreholes installed at Niche 3107. The original intent was to install the middle borehole ML and borehole MR beyond the limits of the proposed excavation to monitor the movement of moisture around the niche during subsequent testing. Unfortunately, the middle boreholes were not installed at the correct elevation above Niche 3107 and were partially mined away during excavation.

Figure 6.1.1-2d and Figure 6.1.1-3d show the final configuration of the seven boreholes installed at Niche 4788. A misinterpretation of a survey mark, along with bad ground conditions (i.e., falling rock or collapsing ground conditions) at Niche 4788, also resulted in the partial loss of borehole ML at this site. The original plan was to install the U and M series boreholes outside the excavation.

After the excavation of Niche 3566, a special set of horizontal boreholes was drilled from within the niche into the walls and end of the niche in a radial pattern. A similar scheme was used at Niche 3107 after its excavation.

Recently, air-permeability testing has been performed at Niche CD 1620. Special boreholes to discern the effects of excavation on permeability were drilled alongside the proposed excavation

[1]Figures 6.1.1-2, 6.1.1-3, and 6.1.1-4 were generated using field measurements recorded in scientific notebooks (YMP-LBNL-JSW-6 (Wang 1997 [156530]), YMP-LBNL-JSW-6A (Wang 1997 [156534]), YMP-LBNL-JSW-6B (Wang 1999 [156538]), YMP-LBNL-JSW-6C (Wang 1999 [153449]), and YMP-LBNL-RCT-1 (Trautz 1999 [156563])) and/or using pre-built plans for niche construction. Therefore, these figures show the idealized shape of the niches and approximate locations of the boreholes.

site, parallel to the niche wall to-be. These boreholes were designated "AK" because they were intended mainly for air permeability (K) use. Figure 6.1.1-4a and Figure 6.1.1-4c show in plan and elevation view respectively, three boreholes designated AK1, AK2 and AK3 that were drilled 1 m apart in a horizontal plane, with the first borehole 1 m from the proposed niche wall about the elevation of the springline. Before the inner excavation at Niche CD 1620, seven additional boreholes were drilled, shown in Figure 6.1.1-4b, Figure 6.1.1-4d, and Figure 6.1.1-4e in plan, elevation, and side view respectively, designated B1.75, ML, MM, MR, UL, UM, UR. All of these boreholes except B1.75 were drilled above the proposed inner-niche location. Subsequent excavation of the inner part of the niche mined out the borehole B1.75.

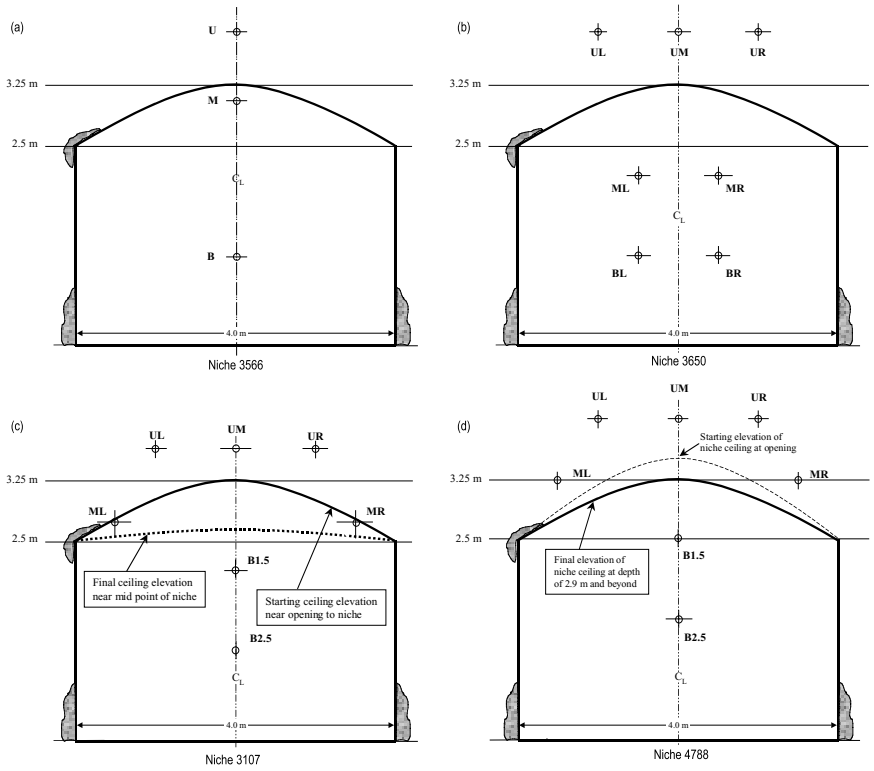

NOTE: The niche faces are on the west wall of the Main Drift of the Exploratory Studies Facility.

Figure 6.1.1-2. Schematic Illustration of the End View of Borehole Clusters at Niche Sites

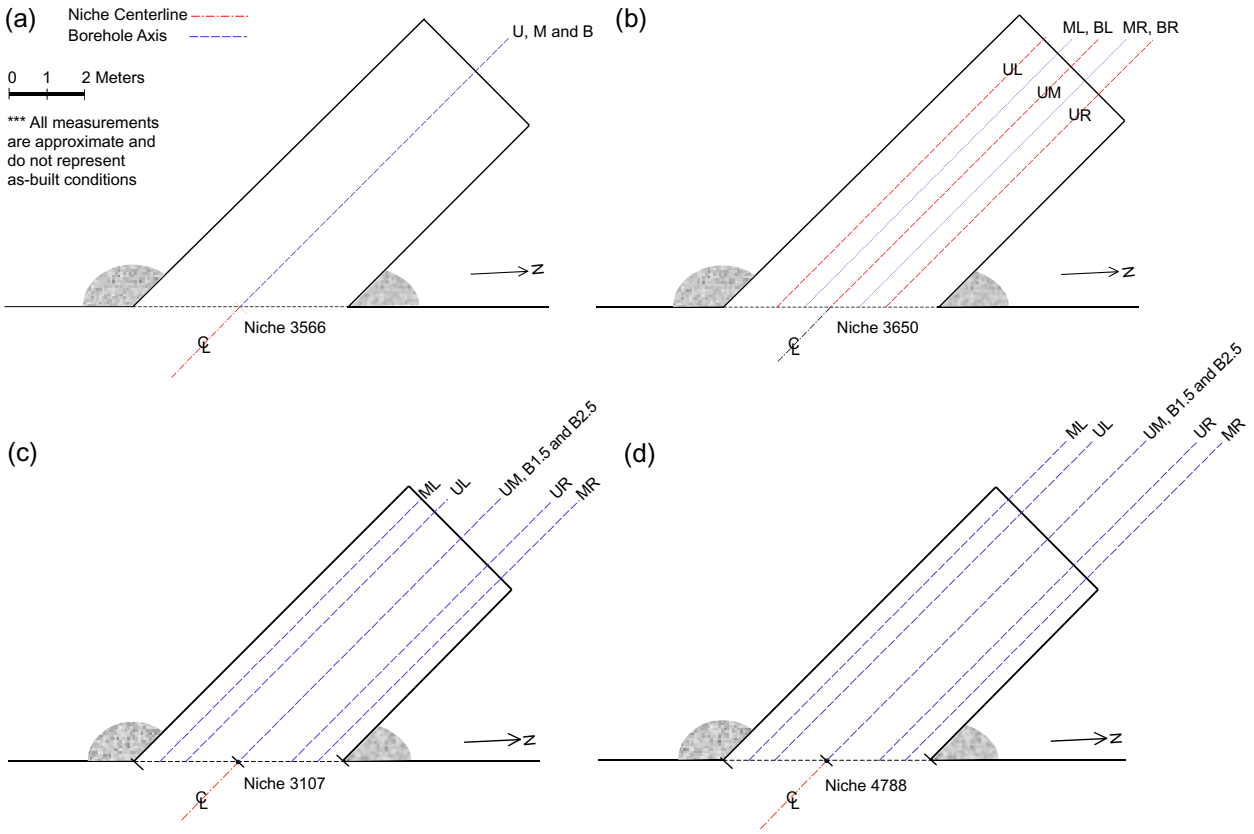

NOTE: The boreholes shown are oriented horizontally in the northwestern direction parallel to the niche axis.

Figure 6.1.1-3. Schematic Illustration of the Plan View of Borehole Clusters at Niche Sites

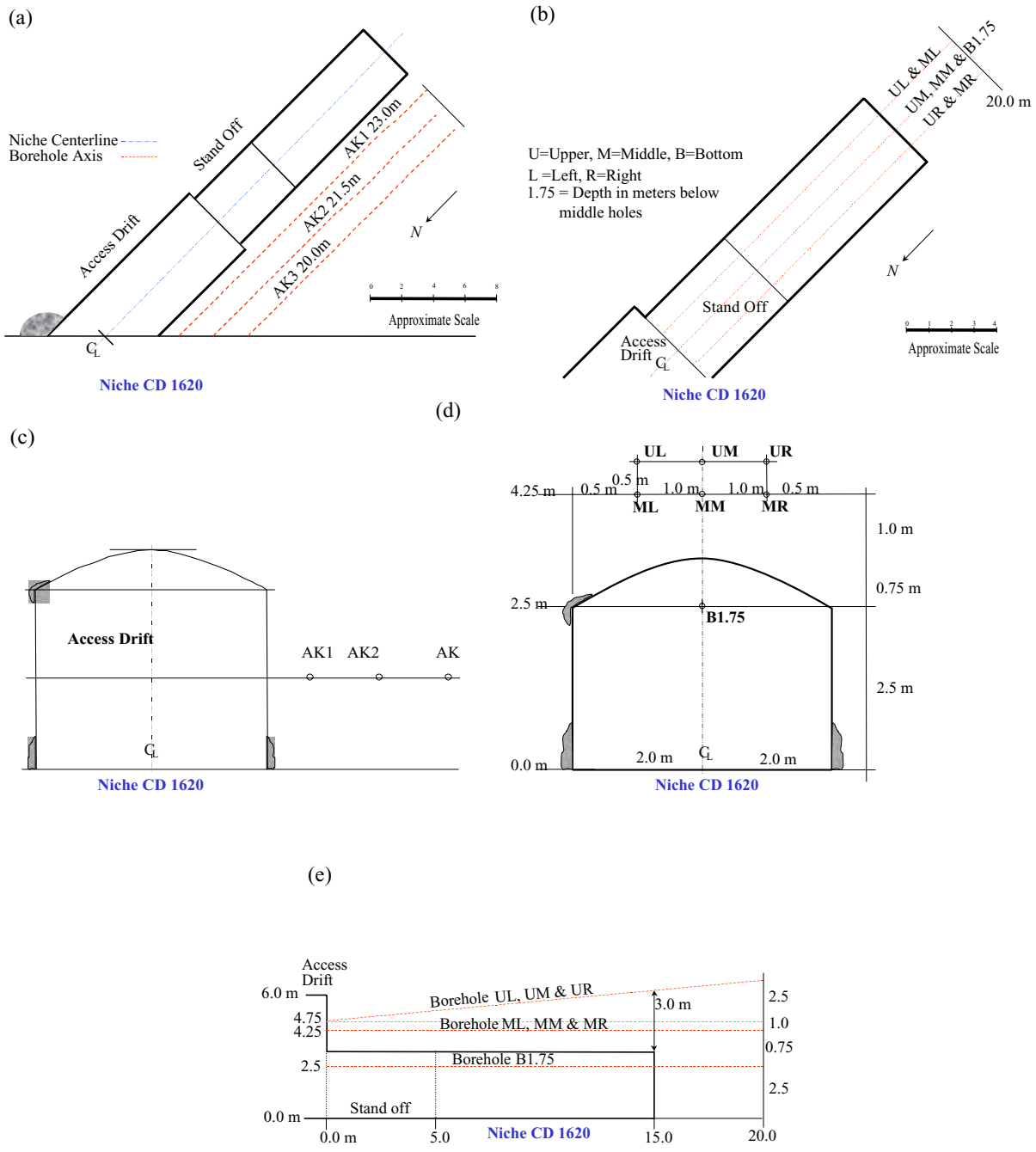

NOTE: The niche face is on the southeast wall of the ECRB Cross Drift.

Figure 6.1.1-4. Schematic Illustration of the End and Plan Views of Borehole Clusters at Niche CD 1620

6.1.2 Air-Permeability Spatial Distribution and Statistical Analysis

To date, an estimated 3,500 separate air injections have been undertaken in the *in situ* studies underground at Yucca Mountain. Nearly a quarter-million pressure-response curves have been logged in the studies. The number of tests lends itself to visualization and statistical comparison

of the flow connections and the distributions of permeability in the rock mass. The specially designed equipment for pneumatic testing is described in Attachment I. With the equipment, it is feasible to conduct tests for site-to-site and borehole-to-borehole comparisons both before and after nearby excavations.

6.1.2.1 Data Reduction and Air-Permeability Determination

Data in the field were acquired in the form of voltage output from the various instruments and converted in real time or post-test time to physical units, using each instrument's calibration data. At Niche 3107, Niche 4788, and Niche CD 1620, data acquisition was fully automated, so that log entries for each individual injection test could be done by computer and correlation with the data files linked. Each of these tests was given three minutes to reach steady state. Based on previous experience with other tests, the maximum flow rate that did not cause the interval pressure to exceed the packer leak-by pressure was chosen for the purpose of the permeability calculation.

Because each injection test was repeated to accommodate two different observation-packer configurations, there are two tests for each injection location from which to choose flow and pressure data for the single-borehole results. When graphed, the two are usually indistinguishable. Preference is given to the lower of the two if there is a significant difference, because this higher value is likely caused by leaks in the packer sealing.

Reported data consist of the acquisition filename, test location, time, date, channel or interval number, flow rate, ambient pressure, and steady-state injection pressure. The derived steady-state single-borehole permeability can be obtained using the expression described below, with Assumption 5.1-1, Assumption 5.1-2 and Assumption 5.1-3 discussed in Section 5.1.

In air-permeability tests to characterize the fracture heterogeneity of the test sites, permeability values are obtained from pressure changes and flow rates using the following modified Hvorslev's formula (LeCain 1995 [101700], Equation 15, p. 10):

$$k = \frac{P_{sc} Q_{sc} \mu \ell n\left(\frac{L}{r_w}\right) T_f}{\pi L\left(P_2^2 - P_1^2\right) T_{sc}} \qquad \text{(Eq. 6.1.2-1)}^{[a]}$$

k permeability, m^2

P_{sc} standard pressure, Pa

Q_{sc} flow-rate at standard conditions, m^3/s

[a] The solution is derived for the steady state ellipsoidal flow field around a finite line source. If the length L in the natural logarithm term in Equation 6.1.2-1 is replaced by an external radius R_e, this formula is identical to the cylindrical flow solution with an ambient constant pressure boundary at the external radius (Muskat 1982 [134132], p. 734). This replacement is used in Section 6.2.2.1 to estimate the saturated hydraulic conductivity for post-excavation liquid flow paths from the borehole interval to the niche ceiling.

μ dynamic viscosity of air, Pa-s

L length of zone, m

r_w radius of bore, m

T_f temperature of formation, K

P_2 injection zone pressure at steady-state, Pa

P_1 ambient pressure, Pa

T_{sc} standard temperature, K

ℓn natural log

For the purpose of calculation, standard pressure is 1.013E+05 Pa (one atmosphere). The dynamic viscosity of air used is 1.78E-05 Pa-s. Temperature contributions to Equation 6.1.2-1 are negligible with $T_f \sim T_{sc.}$ for ambient temperature testing conditions.

6.1.2.2 Pre- and Post-Excavation Permeability Profiles

All boreholes at niches as illustrated in Figure 6.1.1-2 and Figure 6.1.1-3 are nominally 10 m long and 0.0762 m in diameter. Those in Figure 6.1.1-4 were nominally 15 m long and 0.0762 m in diameter. The boreholes were drilled dry with compressed air to remove drill cuttings. The packer interval length and the test interval length are 0.3 m.

Permeability profiles along boreholes at the five niches show the permeability value from each test interval, plotted against the location of the middle of the test interval (zone). Figure 6.1.2-1 illustrates three Niche 3566 permeability profiles along the upper, middle, and bottom boreholes, which are parallel to the niche axis. The air-permeability tests were conducted before niche excavation. Niche 3566, the first niche excavated in the ESF, is located in the vicinity of the Sundance fault.. All three boreholes penetrated brecciated zones in the last one-third of the boreholes, with broken rock pieces preventing packer penetration. A wet feature in a brecciated zone was observed at the end of this niche right after completion of dry excavation (Wang et al. 1999 [106146], Figure (4c), p. 331). The width of the wet feature is comparable to the borehole-interval length of 0.3 m, used in the air-permeability tests (this section) and liquid-release seepage tests (Section 6.2).

After niche excavation, six additional horizontal boreholes were drilled from the inside of the niche, fanning out radially in different directions. Only two radial holes were tested and analyzed in this niche. This niche was sealed for moisture monitoring after testing these two boreholes, and further seepage testing in this niche has been deferred. The permeability profiles for two radial boreholes on the left side of the niche are illustrated in Figure 6.1.2-2. These boreholes also penetrated brecciated zones. The absence of data from the deeper portion of one of the boreholes in Figure 6.1.2-2 is related to the intrinsic difficulties of brecciated zone testing due to poor borehole conditions, which prevent the maintenance of a proper seal (see also Attachment I.4 for discussion about issues of packer leak-by in testing). On average, the permeability values

along the radial boreholes are higher than the average values in the three axial boreholes. The comparison is based on measurements in boreholes at different locations in the same niche site.

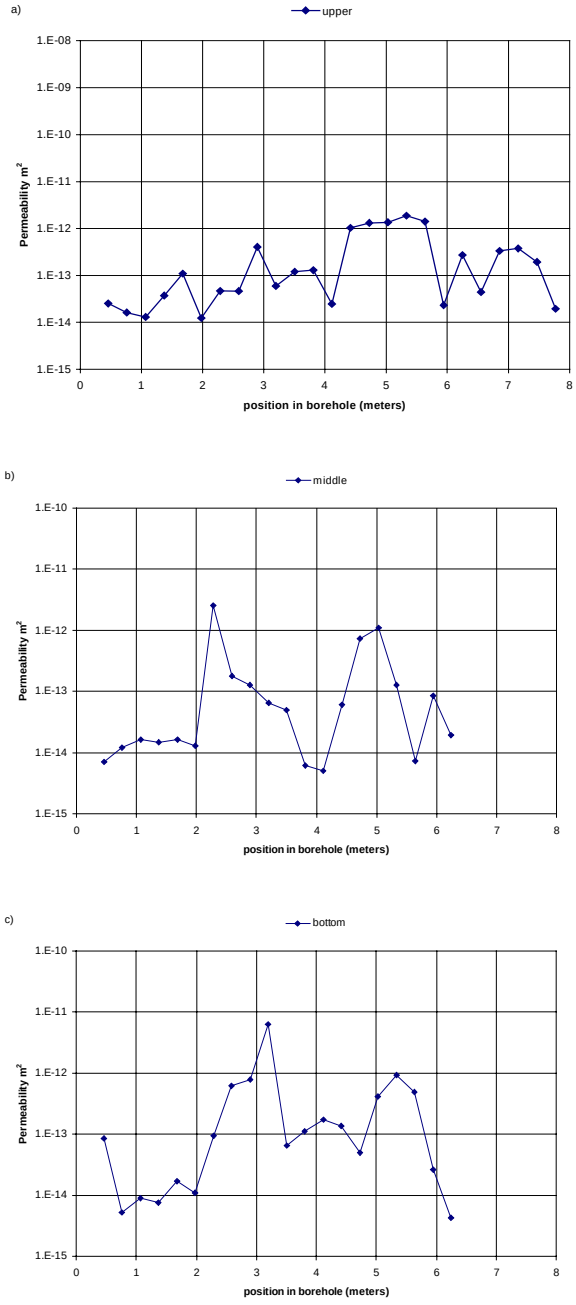

DTN: LB0011AIRKTEST.001 [153155]

NOTE: In DTN: LB0011AIRKTEST.001 [153155], zone numbers are reported, rather than actual position in the borehole. Zone 1 is centered at 0.5 m and each successive zone is 0.3 m farther into the borehole (e.g., zone 2 is centered at 0.8 m).

Figure 6.1.2-1. Pre-Excavation Air-Permeability Profiles along Axial Boreholes at Niche 3566

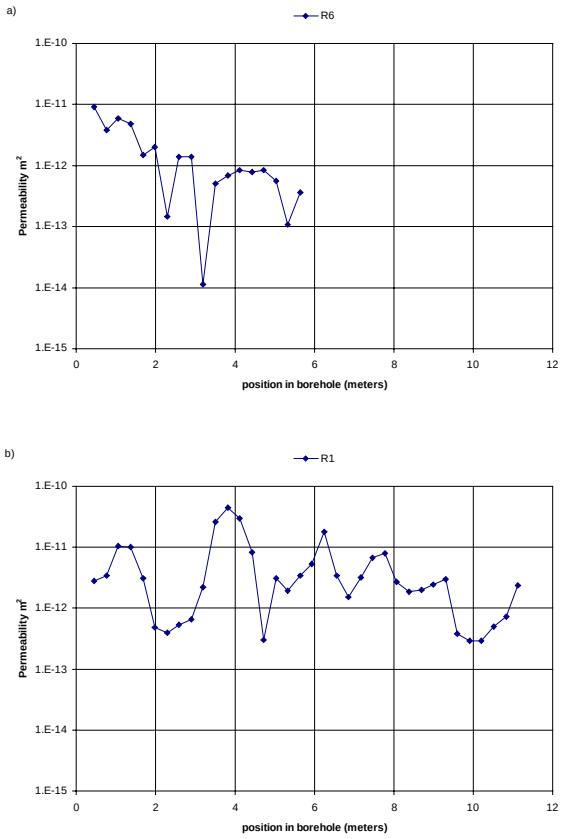

DTN: LB0011AIRKTEST.001 [153155]

NOTE: In DTN: LB0011AIRKTEST.001 [153155], zone numbers are reported, rather than actual position in the borehole. Zone 1 is centered at 0.5 m and each successive zone is 0.3 m farther into the borehole (e.g., zone 2 is centered at 0.8 m).

Figure 6.1.2-2. Post-Excavation Air-Permeability Profiles along Radial Boreholes at Niche 3566

Figure 6.1.2-3 illustrates both the pre- and post-excavation permeability profiles along three upper boreholes at Niche 3650. On all the plots with both pre- and post-excavation data, a line is drawn through the profiles to indicate the geometric mean of each. This mean includes only intervals that were tested both before and after excavation.

The permeability increases could be interpreted as the opening of pre-existing fractures induced by stress releases associated with niche excavation (Wang and Elsworth 1999 [104366], pp. 752–756). The niches were excavated using an Alpine Miner, a mechanical device with a rotary head cutting the rocks below the upper-level boreholes, as illustrated in Figure 6.1.1-2.

Intervals with high pre-excavation permeability recorded the smallest post-excavation permeability changes. In additional to mechanical effects, some of the permeability increases could be related to the intersection of previously dead-ended fractures with the excavated free surface. For borehole intervals, beyond the extent of the niche excavation, the permeability values are less altered. Figure 6.1.2-4 illustrates the pre-excavation permeability profiles of the other four boreholes. The middle- and bottom-level boreholes were available for air-injection testing only before niche excavation, since they were subsequently removed by excavation.

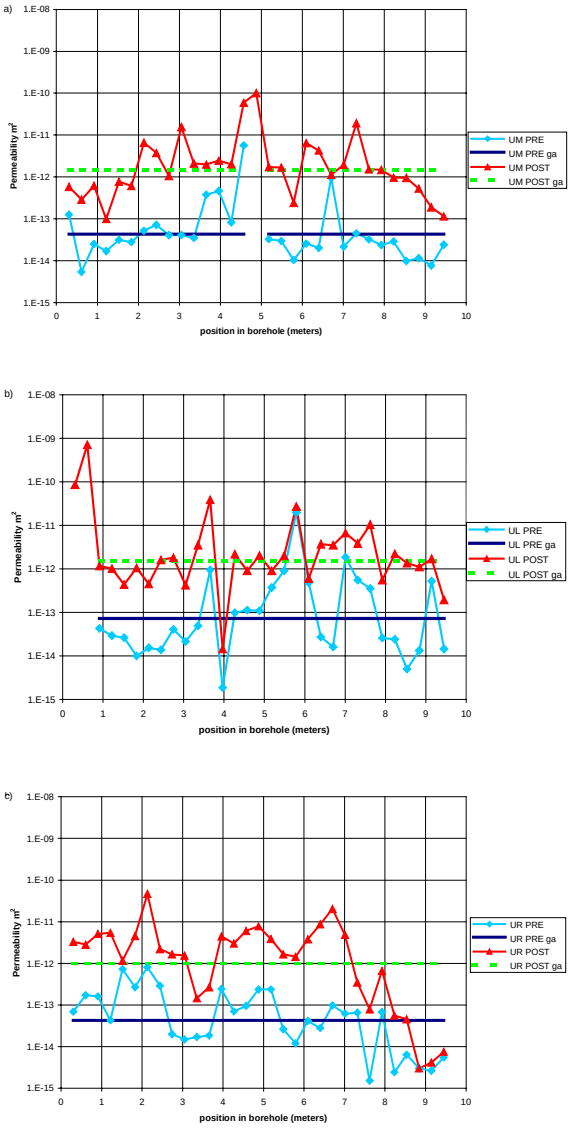

DTN: LB0011AIRKTEST.001 [153155]

NOTE: "ga" is the geometric average.

In DTN: LB0011AIRKTEST.001 [153155], zone numbers are reported, rather than actual position in the borehole. Zone 1 is centered at 0.5 m and each successive zone is 0.3 m farther into the borehole (e.g., zone 2 is centered at 0.8 m).

Figure 6.1.2-3. Pre- and Post-Excavation Air-Permeability Profiles along Upper Boreholes at Niche 3650

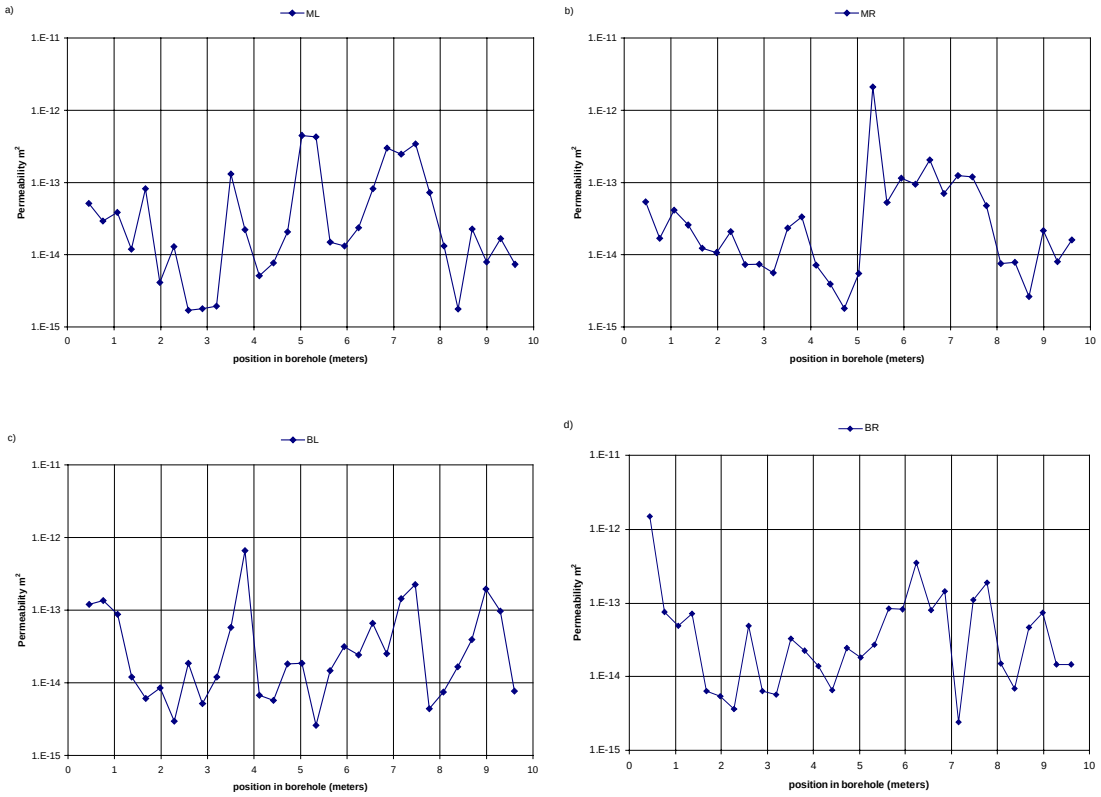

DTN: LB0011AIRKTEST.001 [153155]

NOTE: In DTN: LB0011AIRKTEST.001 [153155], zone numbers are reported, rather than actual position in the borehole. Zone 1 is centered at 0.5 m and each successive zone is 0.3 m farther into the borehole (e.g., zone 2 is centered at 0.8 m).

Figure 6.1.2-4. Pre-Excavation Air-Permeability Profiles along Middle and Bottom Boreholes at Niche 3650

To compare with Niche 3650, the corresponding results of the permeability profiles are presented for Niche 3107 in Figure 6.1.2-5 and Figure 6.1.2-6, and for Niche 4788 in Figure 6.1.2-7 and Figure 6.1.2-8. Figure 6.1.2-5 and Figure 6.1.2-7, similar to Figure 6.1.2-3, are for the upper boreholes, with both pre-excavation and post-excavation values presented for the evaluation of excavation-induced enhancements in permeabilities. Figure 6.1.2-6 and Figure 6.1.2-8 are pre-excavation permeability profiles for the middle- and lower-level boreholes of Niche 3107 and Niche 4788. The borehole layouts for these two niches are modified from the layout in Niche 3650, as illustrated in Figure 6.1.1-2.

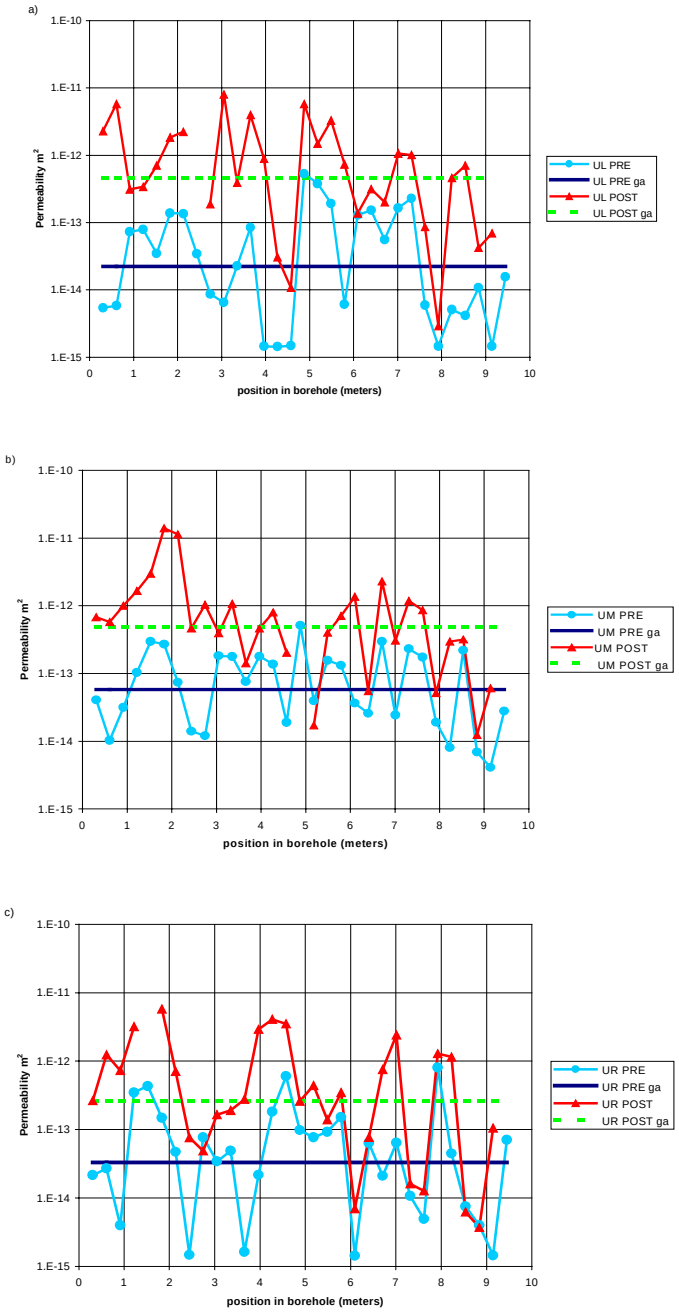

DTNs: LB980901233124.101 [136593] for pre-excavation data,
LB990601233124.001 [105888] for post-excavation data

NOTE: Intervals tested are 0.3 m long, position plotted is farther end of tested interval.

Figure 6.1.2-5. Pre- and Post-Excavation Air-Permeability Profiles along Upper Boreholes at Niche 3107

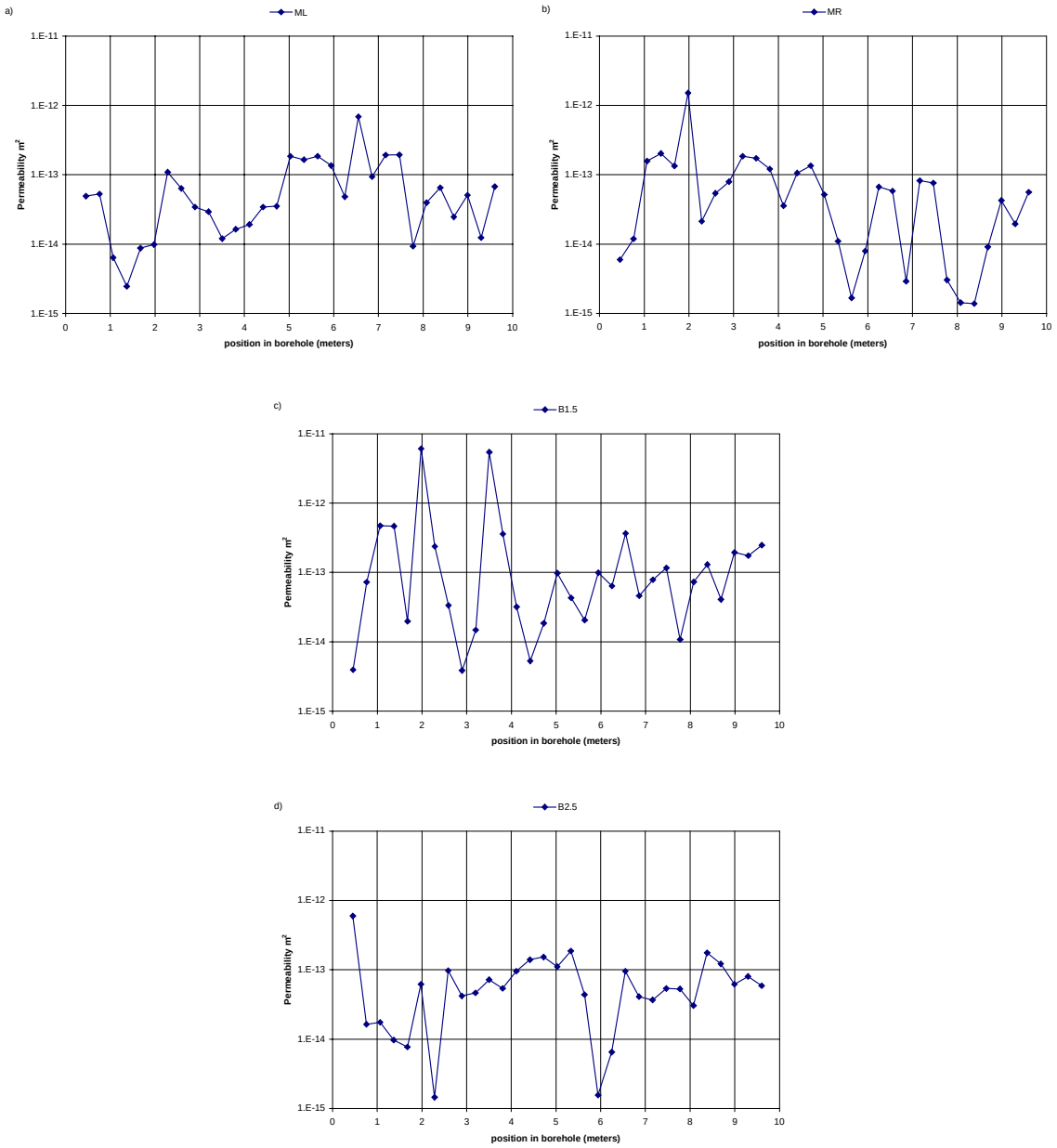

DTN: LB980901233124.101 [136593]

Figure 6.1.2-6. Pre-Excavation Air-Permeability Profiles along Middle and Bottom Boreholes at Niche 3107

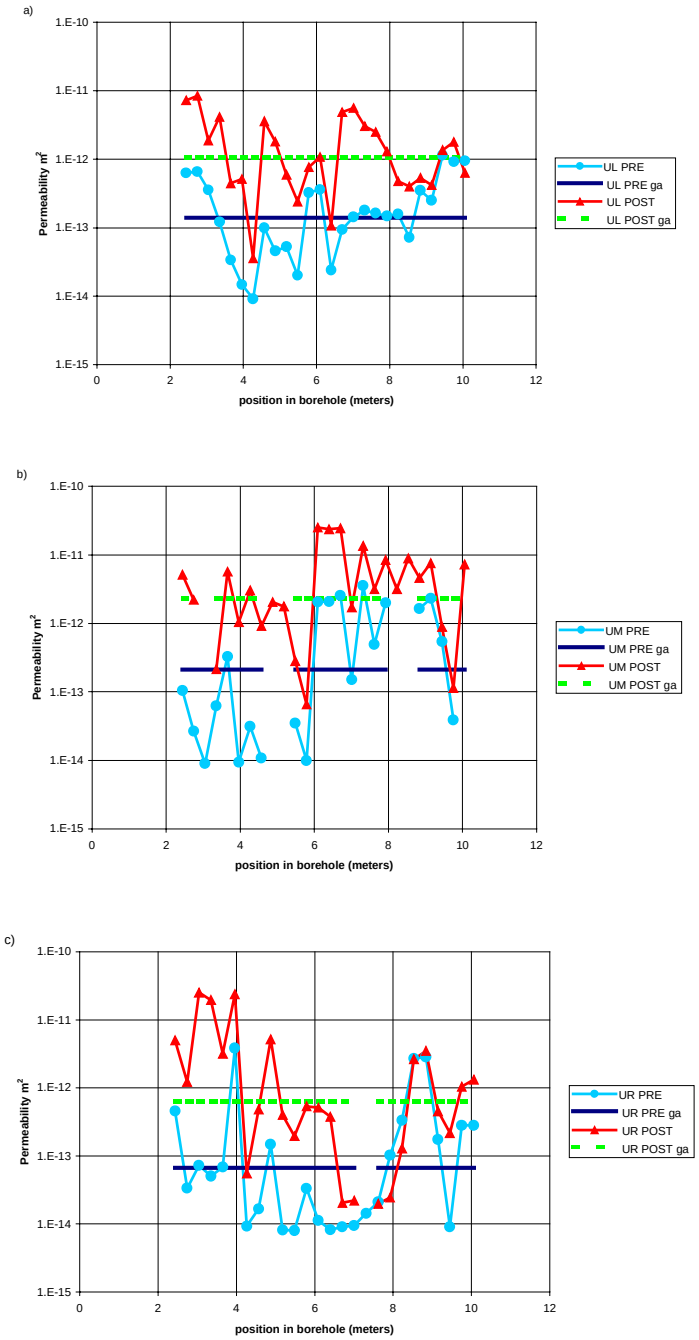

DTNs: LB980901233124.101 [136593] for pre-excavation data,
LB990601233124.001 [105888] for post-excavation data

Figure 6.1.2-7. Pre- and Post-Excavation Air-Permeability Profiles along Upper Boreholes at Niche 4788

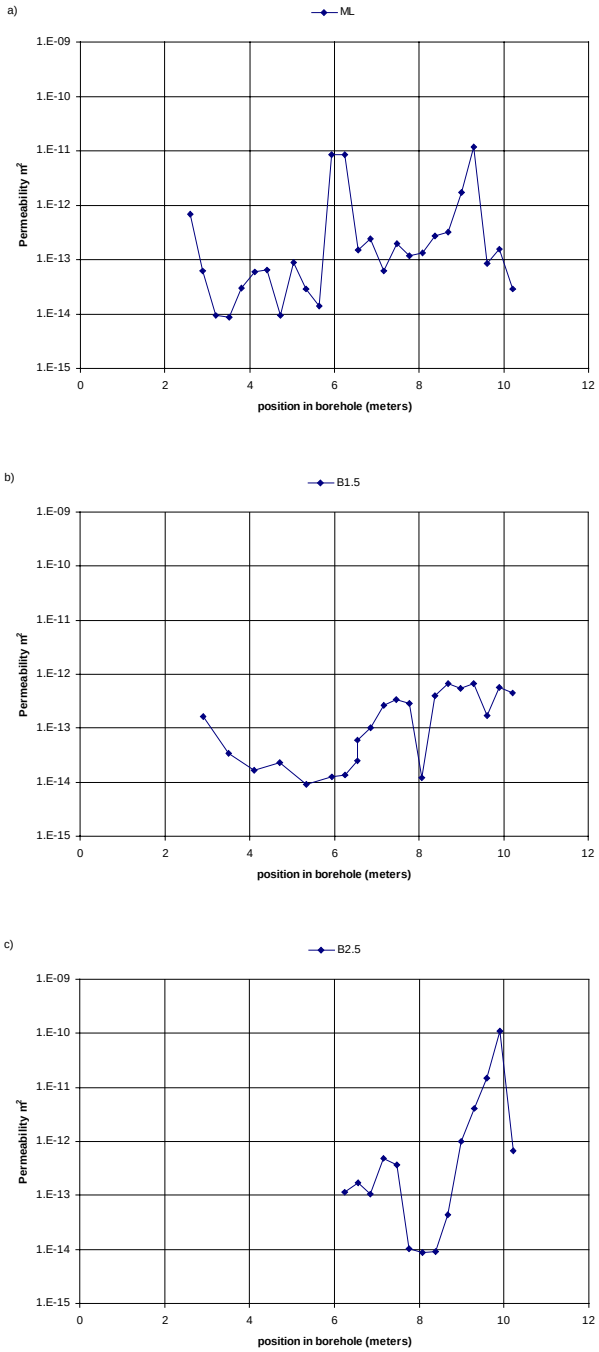

DTN: LB980901233124.101 [136593]

NOTE: Two or more measurements were made at each position. The least value of calculated permeability is reported here as being the most likely to be unaffected by leak-by.

Figure 6.1.2-8. Pre-Excavation Air-Permeability Profiles along Middle and Bottom Boreholes at Niche 4788

At Niche CD 1620, measurements taken before and after excavation at the inner niche area and alongside the outer niche area allowed comparison of excavation effects on permeability profiles

for boreholes situated above excavation versus those situated alongside excavation. Profiles were taken of borehole UL, borehole UM, and borehole ML over the inner niche area both before and after the inner niche excavation, as illustrated in Figure 6.1.2-9. The AK borehole closest to the proposed niche wall became blocked close to the collar before any measurements could be taken. The other two, AK2 and AK3, were successfully profiled with air-k measurements at 0.3 m intervals. After excavation of the outer niche the AK boreholes were again profiled. In Figure 6.1.2-10, comparison of the profiles for the two AK boreholes does not show as big a change as the boreholes above the niche in Figure 6.1.2-9. For the overhead boreholes, certain borehole parts change more than other parts. The change in geometric average (subscript "ga" in figures) for the AK boreholes alongside the excavation is smaller than it is for the overhead boreholes. The UL borehole and the AK2 borehole are roughly the same distance from their respective mined surfaces of the niche, but show a marked difference in change of geometric average of permeability.

6.1.2.3 Permeability Change as a Function of Initial Permeability

Another type of plot can highlight the difference in character of permeability change in these boreholes caused by excavation. The post-excavation permeability divided by the pre-excavation permeability for a particular interval in a borehole is the change ratio due to excavation. A plot of the log change ratio versus the log pre-excavation permeability value can show a dependence of the change on the initial value. Figure 6.1.2-11 and Figure 6.1.2-12 show the changes for three of the overhead boreholes at Niche CD 1620 and for two of the side boreholes respectively. The overhead boreholes show some trend that the initially low permeability zones have the most change. For the side boreholes, however, there is a much weaker trend. The R^2 values on the change ratio plots indicate a measure of the trend.

Change ratios for the pre- and post-excavation testing previously undertaken at Niche 3650, Niche 3107 and Niche 4788 (all in overhead boreholes) are shown in Figure 6.1.2–13 through Figure 6.1.2-15. The change ratio plots for these niches in the middle nonlithophysal zone of TSw show stronger correlation between initial permeability and change ratio. Additionally, from the geometric averages in the profile plots, it can be seen that all these middle nonlithophysal niches show a larger average excavation effect than the boreholes at Niche CD 1620 in the lower lithophysal zone of the TSw.

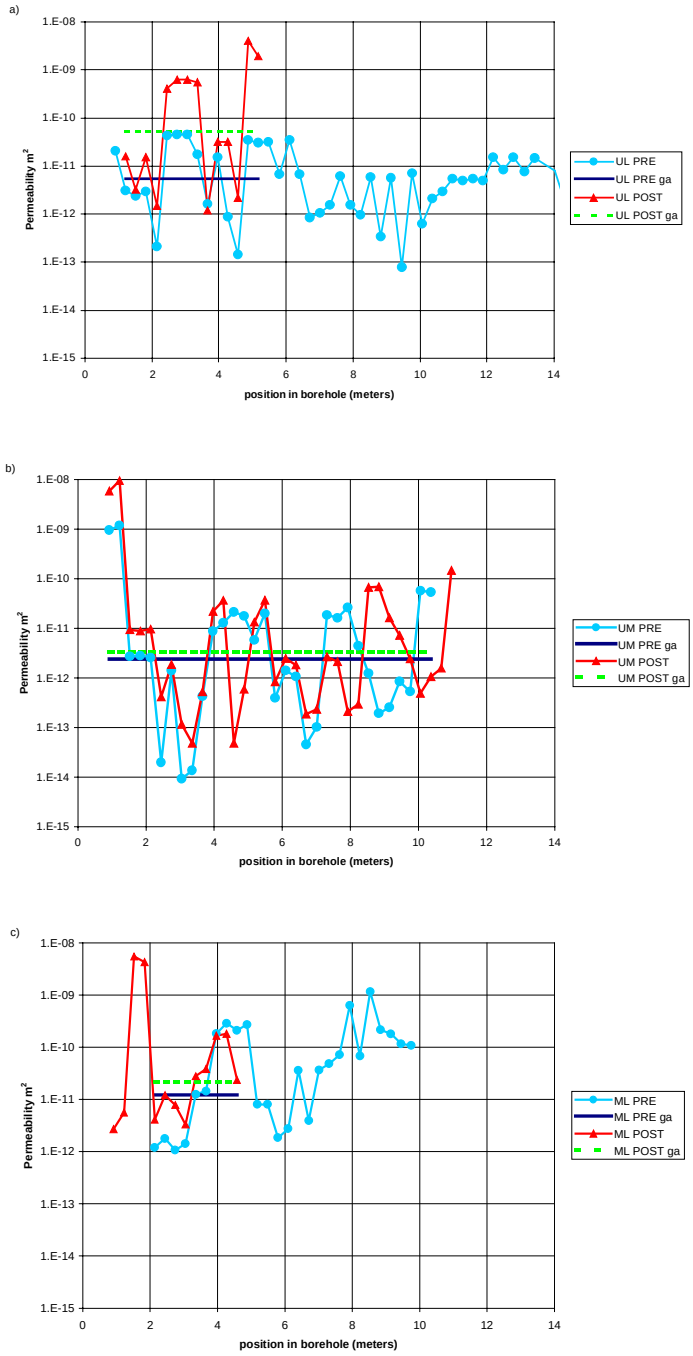

DTN: LB0012AIRKTEST.001 [154586] for pre-excavation data;
LB0110AKN5POST.001 [156904] for post-excavation data

Figure 6.1.2-9. Pre- and Post-Excavation Air-Permeability Profiles along Upper Boreholes at Niche CD 1620

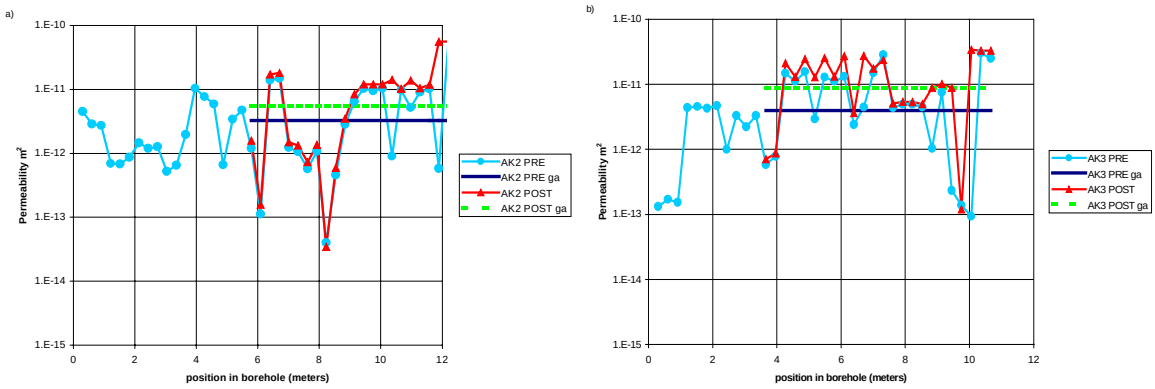

DTN: LB002181233124.001 [146878]; DTN: LB0110AK23POST.001 [156905]

Figure 6.1.2-10. Pre- and Post-Excavation Air-Permeability Profiles along AK Side Boreholes at Niche CD 1620

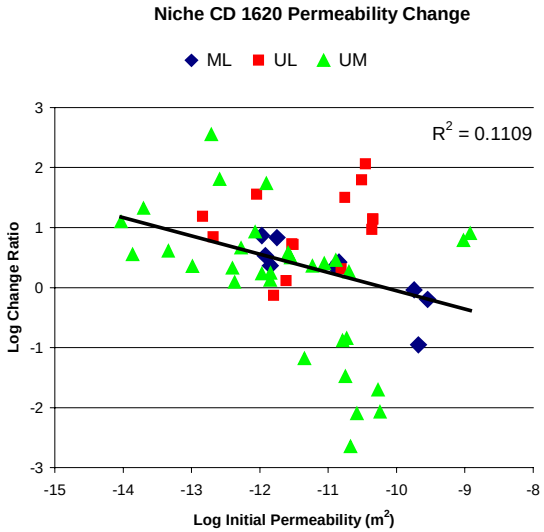

DTN: LB0110AIRK0015.001 [OUTPUT]

Figure 6.1.2-11. Change Ratio Plot for Niche CD 1620 Overhead Boreholes

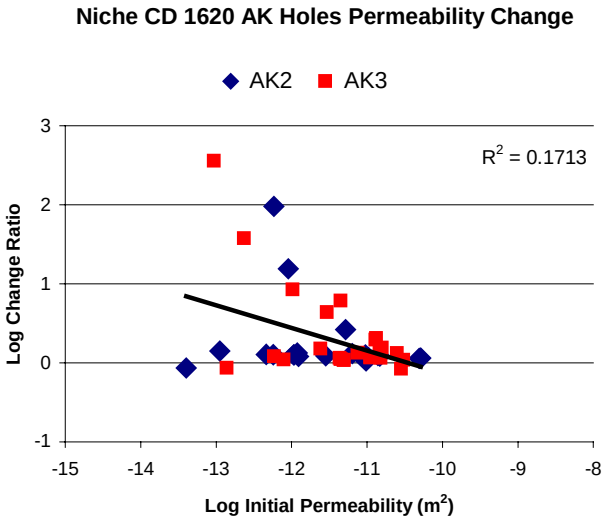

DTN: LB0110AIRK0015.001 [OUTPUT]

Figure 6.1.2-12. Change Ratio Plots for Niche CD 1620 AK Boreholes

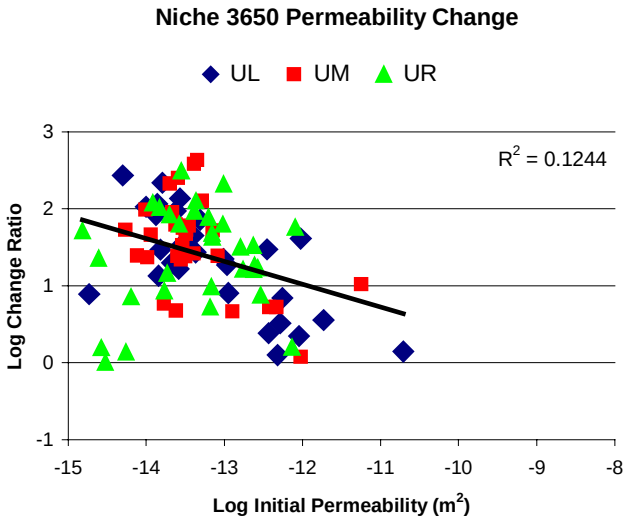

DTN: LB0110AIRK0015.001 [OUTPUT]

Figure 6.1.2-13. Change Ratio Plot for Niche 3650

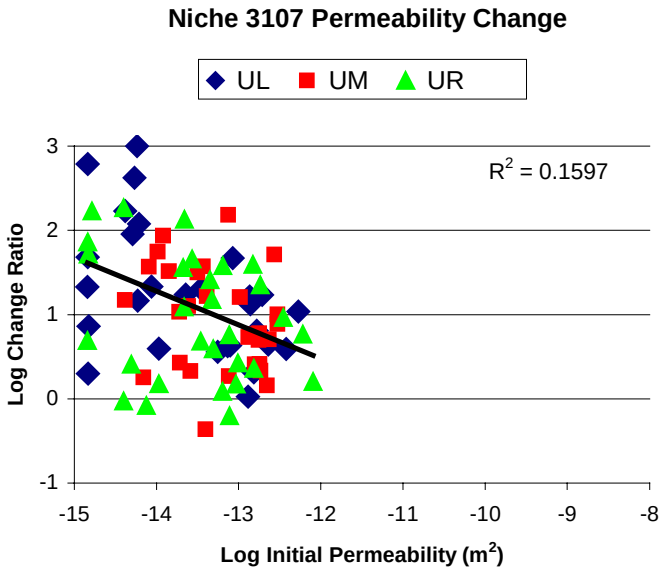

DTN: LB0110AIRK0015.001 [OUTPUT]

Figure 6.1.2-14. Change Ratio Plot for Niche 3107

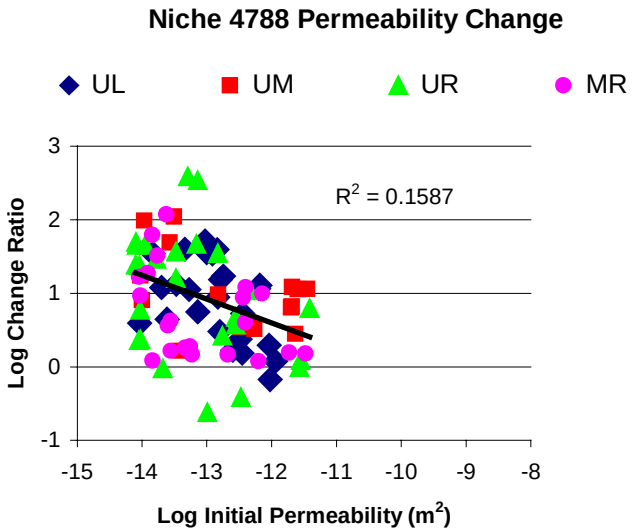

DTN LB0110AIRK0015.001 [OUTPUT]

Figure 6.1.2-15. Change Ratio Plot for Niche 4788

6.1.2.4 Statistical Comparison of Air-Permeability Distributions

Table 6.1.2-1 summarizes the average (arithmetic and geometric) values, standard deviations, and ranges of variations in pre- and post-excavation permeability of individual boreholes and of whole niche sites. Also included are the averages, deviations, and ranges of interval change ratios for individual boreholes and whole niches. (The ratios are calculated from the pre- and

post-excavation permeability values for each interval before the statistical analyses.) Table 6.1.2-2 shows similar information for the overhead boreholes at Niche CD 1620. For assessing the excavation-induced impacts, the analyses in Table 6.1.2-1 and Table 6.1.2-2 are on the upper boreholes only. Drift-scale variations along boreholes and among different boreholes within the same niche test site are larger than differences among different sites.

Table 6.1.2-3 summarizes the geometric means and standard deviations of all clusters of boreholes tested in the ESF, except for Niche CD 1620. Each niche has a distinct air-permeability character. The spatial variabilities are significant in the borehole-interval scale of 0.3 m before averaging over the 10 m scale along the boreholes and the 100 m^3 volume over the borehole clusters (3 or 7 boreholes). Niche 3107 and Niche 3566 each have a "radial" entry in the table, which indicates boreholes that are drilled from inside the niches after excavation. Permeability values from these boreholes for Niche 3107 (profiles not shown) vary little from those of the pre-excavation boreholes, indicative of the uniformity of the formation around Niche 3107. For Niche 3566, however, the radial boreholes that were tested ran through the brecciated zone within the niche wall and so exhibited higher permeability than that for the pre-excavation boreholes. (The entries in Table 6.1.2-3 for Alcove 4 and Alcove 6 are included for completeness and will be discussed in Section 6.5.)

The permeability values from the middle and bottom boreholes are included in the averaging results presented in Table 6.1.2-3. Pre-excavation (log geometric) means and standard deviations were derived from averaging over all seven boreholes in each niche cluster. The middle- and lower-level boreholes supplement the upper boreholes to characterize the 3-D space in the niche test beds and locate flow paths under pre-excavation conditions. After excavation with only upper boreholes in a horizontal plane left, the air-permeability tests can characterize only the zones above the niche ceilings.

Table 6.1.2-1. Statistical Analyses of Air-Permeability along Boreholes above Niches

Borehole	Niche 3650			Niche 3107			Niche 4788		
	Pre-Excavation	Post-Excavation	Post/Pre Ratio*	Pre-Excavation	Post-Excavation	Post/Pre Ratio*	Pre-Excavation	Post-Excavation	Post/Pre Ratio*
Geometric Mean									
UL	7.26E-14	2.09E-12	20.75	2.22E-14	4.55E-13	20.51	1.41E-13	1.07E-12	7.62
UM	4.29E-14	1.64E-12	33.29	5.81E-14	4.82E-13	8.72	1.81E-13	2.56E-12	11.09
UR	4.27E-14	1.01E-12	23.56	3.32E-14	2.64E-13	8.94	6.27E-14	6.27E-13	9.42
All 3	5.07E-14	1.51E-12	25.38	3.50E-14	3.87E-13	11.69	1.05E-13	1.20E-12	9.42
Arithmetic Mean									
UL	8.59E-12	2.98E-11	47.06	8.12E-14	1.46E-12	135.48	2.82E-13	2.07E-12	14.28
UM	1.01E-12	7.78E-12	72.98	1.14E-13	1.55E-12	21.36	8.59E-13	6.19E-12	26.43
UR	1.27E-13	4.59E-12	53.62	1.14E-13	1.04E-12	30.95	4.42E-13	3.79E-12	45.09
All 3	3.24E-12	1.40E-11	57.89	1.03E-13	1.35E-12	62.60	5.05E-13	3.99E-12	28.55
Minimum Value									
UL	1.86E-15	1.45E-14	0.67	1.44E-15	2.90E-15	1.06	9.16E-15	3.57E-14	0.67
UM	5.40E-15	9.88E-14	1.19	4.10E-15	1.24E-14	0.43	8.99E-15	6.56E-14	1.64
UR	1.53E-15	3.02E-15	1.01	1.43E-15	3.72E-15	0.63	8.01E-15	1.98E-14	0.24
All 3	1.53E-15	3.02E-15	0.67	1.43E-15	2.90E-15	0.43	8.01E-15	1.98E-14	0.24
Maximum Value									
UL	1.27E-10	7.15E-10	271.15	5.32E-13	7.99E-12	1229.23	1.15E-12	8.44E-12	51.54
UM	2.28E-11	1.01E-10	427.91	5.15E-13	1.40E-11	153.02	3.56E-12	2.50E-11	110.52
UR	8.07E-13	4.66E-11	310.67	8.06E-13	5.80E-12	184.13	3.83E-12	2.51E-11	386.90
All 3	1.27E-10	7.15E-10	427.91	8.06E-13	1.40E-11	1229.23	3.83E-12	2.51E-11	386.90
Range of Log									
UL	4.83	4.69	2.61	2.57	3.44	3.06	2.10	2.37	1.89
UM	3.63	3.01	2.56	2.10	3.05	2.55	2.60	2.58	1.83
UR	2.72	4.19	2.49	2.75	3.19	2.47	2.68	3.10	3.21
All 3	4.92	5.38	2.80	2.75	3.68	3.45	2.68	3.10	3.21
Std. Dev. of Log									
UL	1.18	0.84	0.69	0.81	0.83	0.83	0.58	0.57	0.54
UM	0.80	0.70	0.62	0.57	0.71	0.61	0.95	0.70	0.58
UR	0.73	1.05	0.66	0.79	0.90	0.74	0.85	0.94	0.84
All 3	0.93	0.88	0.66	0.74	0.82	0.75	0.79	0.78	0.67

Input: Niche 3650 Pre- and Post-Excavation DTN: LB0011AIRKTEST.001 [153155], Post-Excavation DTN: LB980101233124.002 [105818]

Niche 3107 Pre-Excavation DTN: LB980901233124.101 [136593], Post Excavation DTN: LB990601233124.001 [105888]

Niche 4788 Pre-Excavation DTN: LB980901233124.101 [136593], Post-Excavation DTN: LB990601233124.001 [105888]

Summary: DTN: LB990901233124.004 [123273]

NOTE: *The post/pre ratio is the ratio of post-excavation to pre-excavation permeabilities. This ratio was calculated for each interval in each borehole. Values reported are the statistical measures (maximum, minimum, mean, etc.) of all post/pre ratios calculated for each borehole. For example, mean of (post/pre) ratio is not the same as the ratio of mean(post)/mean(pre).

*Where more than one measurement of permeability was made at a position, the least value is used in averaging.

Table 6.1.2-2. Statistical Analyses of Air-Permeability along Boreholes above Niche CD 1620

Niche CD 1620			
Borehole	**Of Pre**	**Of Post**	**Of Change Ratio**
Geometric Mean			
ML	1.23E-11	2.14E-11	1.75
UL	5.54E-12	5.48E-11	9.89
UM	2.40E-12	3.32E-12	1.38
All 3	3.88E-12	9.19E-12	2.37
Arithmetic Mean			
ML	7.88E-11	5.15E-11	2.93
UL	1.75E-11	5.90E-10	22.75
UM	7.58E-11	4.90E-10	17.84
All 3	6.14E-11	4.44E-10	16.65
Minimum			
ML	1.06E-12	3.30E-12	0.11
UL	1.46E-13	1.19E-12	0.74
UM	9.28E-15	4.82E-14	0.00
All 3	9.28E-15	4.82E-14	0.00
Maximum			
ML	2.86E-10	1.82E-10	7.33
UL	4.53E-11	4.03E-09	115.10
UM	1.19E-09	9.51E-09	354.12
All 3	1.19E-09	9.51E-09	354.12
Range of Log			
ML	2.43	1.74	1.82
UL	2.49	3.53	2.19
UM	5.11	5.30	5.19
All 3	5.11	5.30	5.19
Std Dev of Log			
ML	1.03	0.63	0.57
UL	0.87	1.22	0.63
UM	1.25	1.25	1.19
All 3	1.14	1.27	1.04

DTN: LB0110AIRK0015.001 [OUTPUT]

Table 6.1.2-3. Comparison of Geometric Means and Standard Deviations of Niches and Alcoves in the Exploratory Studies Facility at Yucca Mountain

Borehole Cluster	Type of Site	log(k) (m^2)	
		Mean	Standard Deviation
Niche 3566 Pre-Excavation	Intersects brecciated zone	-13.0	0.92
Niche 3566 Radial	Predominantly within brecciated zone	-11.8	0.66
Niche 3650 Pre-Excavation	Moderately fractured welded tuff	-13.4	0.81
Niche 3650 Post-Excavation	Post-excavation welded tuff	-11.8	0.88
Niche 3107 Pre-Excavation	Moderately fractured welded tuff	-13.4	0.70
Niche 3107 Post-Excavation	Post-excavation welded tuff	-12.4	0.82
Niche 3107 Radial	Moderately fractured welded tuff	-13.8	0.92
Niche 4788 Pre-Excavation	Highly fractured welded tuff	-13.0	0.85
Niche 4788 Post-Excavation	Post-excavation welded tuff	-11.9	0.78
Alcove 4	Discretely faulted and fractured non-welded tuff	-13.0	0.93
Alcove 6	Highly fractured post-excavation welded tuff	-11.9	0.67

Input: DTNs: LB0011AIRKTEST.001 [153155], LB980901233124.101 [136593], LB990601233124.001 [105888], LB980901233124.004 [105855], LB980901233124.009 [105856], LB980912332245.001 [110828]
Summary: DTN: LB990901233124.004 [123273]

6.2 ANALYSIS AND INTERPRETATION OF THE NICHE LIQUID-RELEASE AND SEEPAGE-TEST DATA

The ESF Drift Seepage Test and Niche Moisture Study characterize the seepage process and further our understanding of how moisture could seep into drifts. Specific objectives of the study include:

- Measuring *in situ* hydrologic properties of the potential repository host rock for use in *Seepage Calibration Model and Seepage Testing Data* (CRWMS M&O 2001 [153045]) and *Seepage Model for PA Including Drift Collapse* (CRWMS M&O 2000 [153314]).
- Providing a database of liquid-release and seepage data that can be used to evaluate seepage and other related UZ processes
- Evaluating drift-scale seepage processes to quantify the extent to which seepage is excluded from entering an underground cavity
- Determining the seepage threshold below which percolating water will not seep into a drift.

The objectives of the study are realized through a combination of field experiments, including air-injection, liquid-release, and seepage tests. Assumptions used in the analyses are described in Section 5.2.

Analytic solutions are used in the data analyses presented in this section to estimate the seepage thresholds, capillary strengths, water-potential values, and characteristic relationships along seepage flow paths. Local homogeneity is the main assumption in the analytic solutions used in estimating the air-permeability values and liquid seepage flow field. Numerical models have been formulated in the AMR U0080 *Seepage Calibration Model and Seepage Testing Data* (CRWMS M&O 2001 [153045]) to evaluate the effects of spatial heterogeneity on the effective seepage parameters, with the heterogeneity field based on the air-permeability distribution (described in Section 6.1, with local homogeneity assumption described in Section 5.1). The seepage calibration model is the basis for other AMRs in estimating the seepage fraction and distribution over the potential waste-emplacement drifts. The subsequent AMRs include U0075 *Seepage Model for PA Including Drift Collapse* (CRWMS M&O 2000 [153314]) and U0120 *Abstraction of Drift Seepage* (CRWMS M&O 2001 [154291]).

Some of the early results based on short-duration releases of pulses above the first niche tested are enhanced by later tests in other niches with long durations so that the liquid-release rates and seepage rates can approach steady states. The short-duration tests, originally designed to simulate the arrivals of episodic percolation events through fast-flow paths into ventilated drifts, do not provide the data sets needed by the seepage calibration model and other PA models, which emphasize the steady-state conditions in sealed drifts under post-emplacement conditions.

6.2.1 Review of Data Obtained from Liquid-Release and Seepage Tests Conducted at Niches

This section provides a general overview of the tests, including field activities performed prior to, during, and after the niches were excavated.

6.2.1.1 Pre-Excavation Liquid-Release Test Data

Before seepage tests in excavated niches, the niche test sites are characterized by air-permeability tests (Section 6.1) and by liquid-release tests. The pre-excavation liquid-release tests introduce a finite amount of dyed water to characterize the flow paths within the niche space. The main objective is to determine the relative strengths between the gravity force that moves the liquid downward and the capillary forces that tend to spread the liquid laterally. The characterization of the flow paths is conducted during niche excavation (Section 6.2.1.2).

Hundreds of air-injection tests were conducted in the boreholes at niche sites prior to excavation. The test results were used to determine the distribution of single-borehole air permeabilities within the rock mass (refer to Section 6.1 in this AMR). These data were then used to select test intervals for subsequent liquid-release tests. The intervals selected for liquid-release testing exhibited a wide range of air permeabilities, including both high and low values.

Liquid-release tests were conducted in the same boreholes as the air-injection tests by pumping water containing colored or fluorescent dyes at a constant rate into various 0.3 m long test intervals. A finite amount of dye-spiked water, typically 1 liter, was introduced into each test interval at a low flow rate to minimize buildup of fluid pressure in the test interval. Various colored and fluorescent tracers were used during the study to document the flow path traveled by the wetting front. Hereafter, the term “water” will be used to describe the test fluid, which may or may not have contained tracer.

Pre-excavation liquid-release tests were performed during early June and early August 1997, in boreholes installed prior to the excavation of Niche 3566 and Niche 3650, respectively. Pre-excavation liquid-release tests were performed at Niche 3107 and Niche 4788, starting in late April and late June 1998, respectively. Pre-excavation liquid-release tests were also performed at Niche CD 1620 in the lower lithophysal zone in April 2000. The data from these pre-excavation tests, including the mass of water released, pumping rates and times, liquid-release rates, were tabulated and entered into the TDMS, and assigned DTN: LB980001233124.004 [136583] for Niche 3566 and Niche 3650; DTN: LB980901233124.003 [105592] for Niche 3107 and Niche 4788; and DTN: LB0102NICH5LIQ.001 [155681] for Niche CD 1620. The tables include directly measured mass, pumping rates, and return flow rates, and derived quantities of average liquid release rates from the differences of the measured rates.

6.2.1.2 Niche Excavation Activities

The niches were excavated using minimal water and with an Alpine Miner, a mechanical device, to observe and photograph the distribution of fractures and dye within the welded tuff. As reported in DTN: LB980001233124.004 [136583], dye was observed along individual fractures as well as along intersecting fractures to depths ranging 0 to 2.6 m below the liquid-release points at the Niche 3566 and Niche 3650 sites. Dye was observed at a maximum depth of about 1.2 m below the release point at Niche 3107 and about 1.8 m at Niche 4788, as reported in DTN: LB980901233124.003 [105592]. Dye was observed at a maximum depth of about 1.4 m below the release point at Niche CD 1620, as reported in DTN: LB0102NICH5LIQ.001 [155681]. (In this AMR, TDMS DTN and data report table name are both identified if many files are in a given DTN.) Flow of water through a relatively undisturbed fracture-matrix system was documented in this manner.

During the mining operation at Niche 3566 and Niche 3650, two types of flow paths were observed in the field based on the observed pattern of dye, including: (1) flow through individual or small groups of high-angle fractures; and (2) flow through several interconnected low- and high-angle fractures, creating a fracture network. Dye was observed along individual fractures and fracture networks to a maximum depth of 2.6 m below the release points in the middle nonlithophysal zone (Tptpmn) of TSw. The vertically elongated dye pattern suggests that water is predominantly flowing downwards. In contrast, an approximately spherical dye pattern centered at the release point was observed at Niche CD 1620, located in the lower lithophysal zone (Tptpll) of TSw. Dye was observed in fractures and lithophysae to a maximum depth of 1.4 m. Here the dye patterns were more symmetric, with the lateral edges of the wetted area lying about equal distance from the release point.

Figure 6.2.1-1 compares examples of flow paths observed in the Tptpmn at Niche 3566 with dye patterns observed in the Tptpll at Niche CS 1620 (See Section 6.1.2.2 for the observation of a damp feature included in the figure). The observed damp feature and the dye patterns suggest that flow through fractures in the Tptpmn is predominately gravity-driven. In contrast, the symmetry of the dye patterns observed in the Tptpll suggests that capillary forces may be more important in this zone.

Dye was observed in numerous lithophysae in the Tptpll. There was no direct field evidence that water accumulated and dripped into the cavities, even though the liquid-release fluxes applied during the test were 1,000 times greater than the natural flux estimated at 10 mm/yr. No dye stains on the ceiling were observed to line up directly above stains on the floor of the cavities. An example of dye observed on the floor of a lithophysal cavity is illustrated in Figure 6.2.1-1d, suggesting capillary induced upward fluid movement is a likely mechanism to introduce fluid into the cavity.

It is surprising that capillary forces appear to be stronger in the Tptpll, because the average air-permeability of the Tptpll is greater than the Tptpmn. Typically, capillary forces are less important in higher-permeability media than in lower-permeability materials. This may indicate that the air-permeability measurements performed in the Tptpll are influenced by the lithophysal cavities, which may connect relatively large fractures with smaller fractures, effectively contributing to the relatively strong capillarity.

Note that some of the lithophysae had a thick layer of drill cuttings (i.e., dust) coating their surfaces. This layer of dust could influence the flow (dye) patterns and depth of wetting-front migration observed in the Tptpll. This dust was introduced into the cavities intersecting the borings when the boreholes were air cored. The dust could act as a highly transmissive surface zone (compared to the rock matrix) that could enhance the uniform spread of the wetting front. The dust could also impede the movement of water and dye through the fractures by imbibing and retaining the moisture close to the point of release.

In general, the maximum distance that the wetting front traveled through the Tptpmn from the point of injection to the furthest point of observation increased with the mass of water injected. The data did not show that the type of flow (i.e., network or vertical fracture flow) had any significant influence on the maximum travel distance. Figure 6.2.1-2 shows that on average, the wetting front traveled much deeper (i.e., had a larger aspect ratio) for tests conducted in the Tptpmn compared to tests performed in the Tptpll. (Computation of the aspect ratio was performed in the Excel spreadsheet documented in Attachment II, Table II-1). The average line for Tptpll in Figure 6.2.1-2 is influenced by a single data point with high aspect ratio. Without this data point, the average is much closer to 1 (i.e., the aspect ratio of a spherical pattern.)

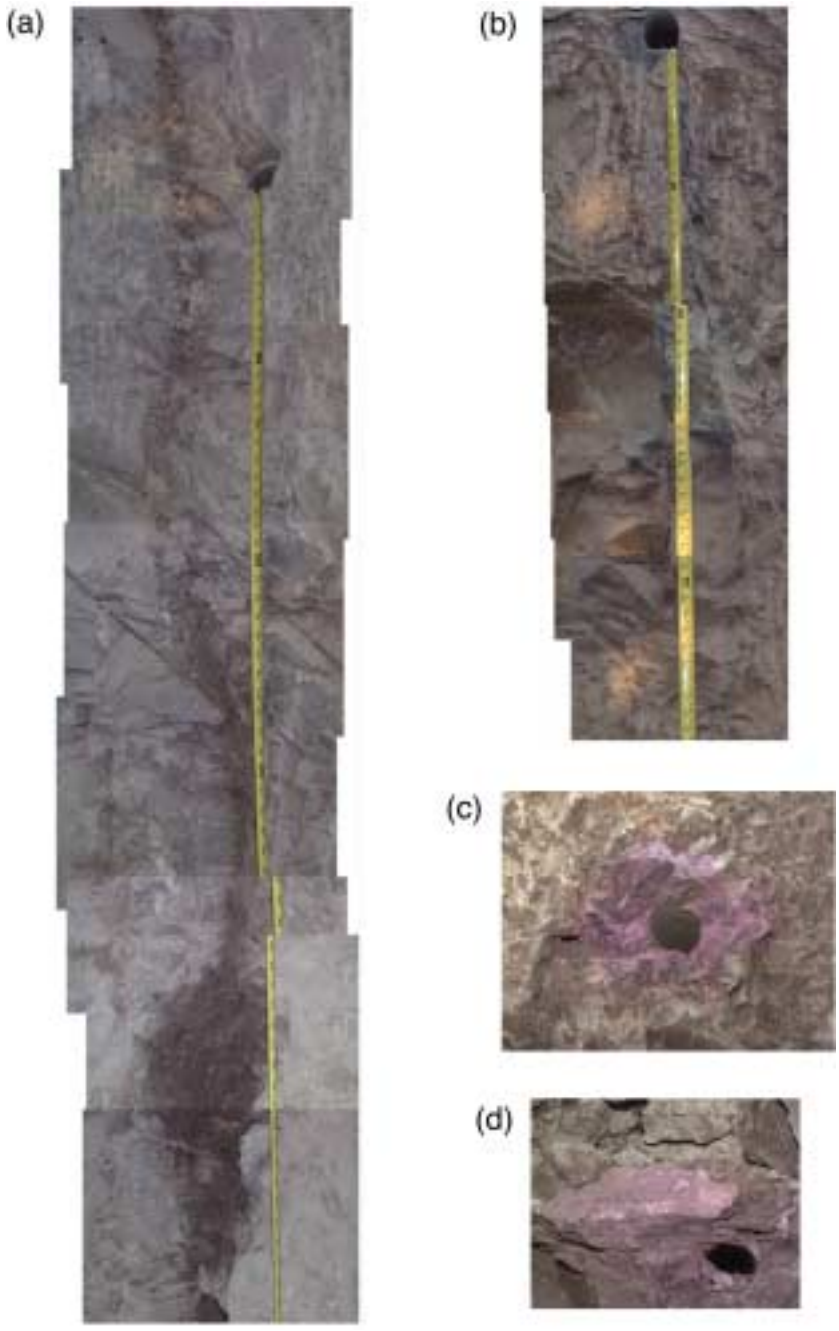

SOURCE: Wang et al. 1999 [106146], Figures 4a, 4c], scientific notebook YMP-LBNL-RCT-3 (Trautz 2001 [157022] pp. 79, 84).

Figure 6.2.1-1. Photographic Illustrations of Flow Paths Observed During Niche Excavations: a) ambient flow path at Niche 3566, b) blue dyed flow path at Niche 3566, c) pink dyed flow path at Niche CD 1620, d) pink stain on the floor of a lithophysal cavity at Niche CD 1620.

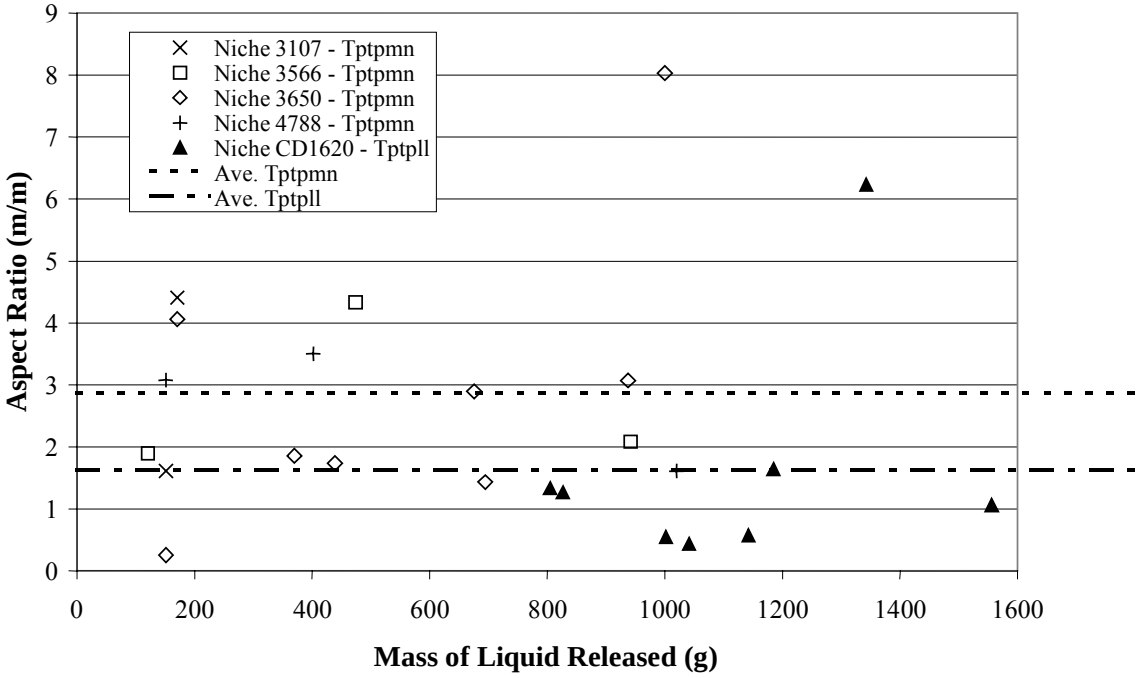

DTNs: LB980001233124.004 [136583], LB980901233124.003 [105592], LB0102NICH5LIQ.001 [155681], LB0110LIQR0015.001 [OUTPUT]

Figure 6.2.1-2. Mass of Water Released Versus Aspect Ratio

6.2.1.3 Post-Excavation Seepage Tests

A series of seepage tests was performed at Niche 3107, Niche 3650, and Niche 4788. In general, the tests were used to quantify the amount of water seeping into the drift from a localized source of water of known duration and intensity. The tests were also used to establish the niche seepage-threshold (K_{o*}), defined as the largest flux of water that can be introduced into the test borehole without resulting in seepage into the niche. The borehole flux values were derived from the pumping rate and the wetted area estimated for the borehole interval. This definition of niche seepage threshold is different from the definition used by PA, with the seepage threshold related to the steady-state background percolation flux averaged over drift scale and site scale areas.

The seepage tests were conducted after the niches were excavated by pumping water into select test intervals in borehole UL, borehole UM, and borehole UR located above each niche. The distance from the test intervals to the niche ceiling ranges from 0.58 to 1.23 m for all the niche sites. (Computation of the distance is inserted in an Excel spreadsheet documented in Attachment II, Table II-2.) The tests were performed by sealing a short interval of borehole using an inflatable packer system, similar to the system used in air-injection tests as described in Attachment I. Any water that migrated from the borehole to the niche ceiling and dripped into the opening was captured and weighed.

For each packer interval, a liquid-return (overflow) line prevented pressure buildup of excess pressure. If the liquid injection rate was high and return flow was observed, the liquid-release rate was determined by the difference between injection flow rate and return flow rate (if any). The observation of return flows inferred that the pumping rate exceeded the saturated hydraulic conductivity of the borehole interval. (For tests with small liquid volume in cases with significant storage in the borehole interval, no return flow did not imply that the pumping conditions represented unsaturated conditions.)

6.2.1.3.1 Niche 3650 Seepage-Test Data

Forty niche seepage tests were performed on 16 test intervals positioned above Niche 3650 beginning in late 1997 and ending in early 1998. Water migrated through the rock and seeped into the niche in 10 out of the 16 zones tested. The niche seepage threshold was determined for the 10 zones that seeped. Seepage and liquid-release data were tabulated and entered into the TDMS, where it was assigned DTN: LB980001233124.004 [136583].

The mass of water released to the formation was computed by mass balance. In turn, the liquid-release rate (Q_s) for each test was computed by dividing the mass released by the respective duration of each test; thus, these values represent time-averaged rates. The rate at which water was released to the formation ranged from 0.007 to 2.892 g/s, and the total mass released ranged from 274.5 to 5597.5 g per test, as summarized in DTN: LB980001233124.004 [136583].

When water appeared at the niche ceiling during a test and dripped into the opening, it was collected in the capture system and weighed. Figure 6.2.1-3 shows the approximate location of the capture system and test intervals relative to the niche boundaries, and the sequence of dyes and number of tests performed on each test interval. The wetting front typically arrived at the niche ceiling directly below the test zone. Most of the water was typically captured in only one or two 0.3 × 0.3 m cells located directly beneath the test interval.

In the immediate vicinity at the intersection of the niche ceiling and the conducting fractures, the relative humidity could be high from local evaporation. However, the localized humid conditions were not met everywhere within the niche and/or the ESF Main Drift. Maintenance of high relative humidity conditions was important for long-term seepage tests, since the evaporation effects could have a substantial impact on the analysis of seepage data, with models assuming post-emplacement high humidity conditions in seepage threshold estimation. The potential impact of evaporation effects are discussed in Section (6.3) and Section (6.4) of AMR U0080 *Seepage Calibration Model and Seepage Testing Data* (CRWMS M&O 2001 [153045]).

The mass of water captured ranged from 0.0 to 568.6 g per test as reported in DTN: LB980001233124.004 [136583]. The niche seepage percentage is defined as the mass of water that dripped into the capture system divided by the mass of water released to the rock:

$$\textit{Niche Seepage Percentage} = 100 \times \frac{\text{"}\textit{Mass Captured}\ (g)\text{"}}{\text{"}\textit{Mass Released}\ (g)\text{"}} \qquad \text{(Eq. 6.2.1-1)}$$

The niche seepage percentage ranged from 0% for zones that did not seep to 56.2% for a predominantly gravity-driven flow through a highly saturated fracture (DTN: LB980001233124.004 [136583]).

The niche seepage tests at Niche 3650 were conducted with relatively small amount of liquid over short duration, with multiple tests over multiple borehole intervals. To address the model needs of steady-state data in controlled relative humidity conditions, the later tests in Niche 3107 and Niche 4788 were conducted in selected borehole intervals with large amount of liquid over long duration, as described in the following two sections.

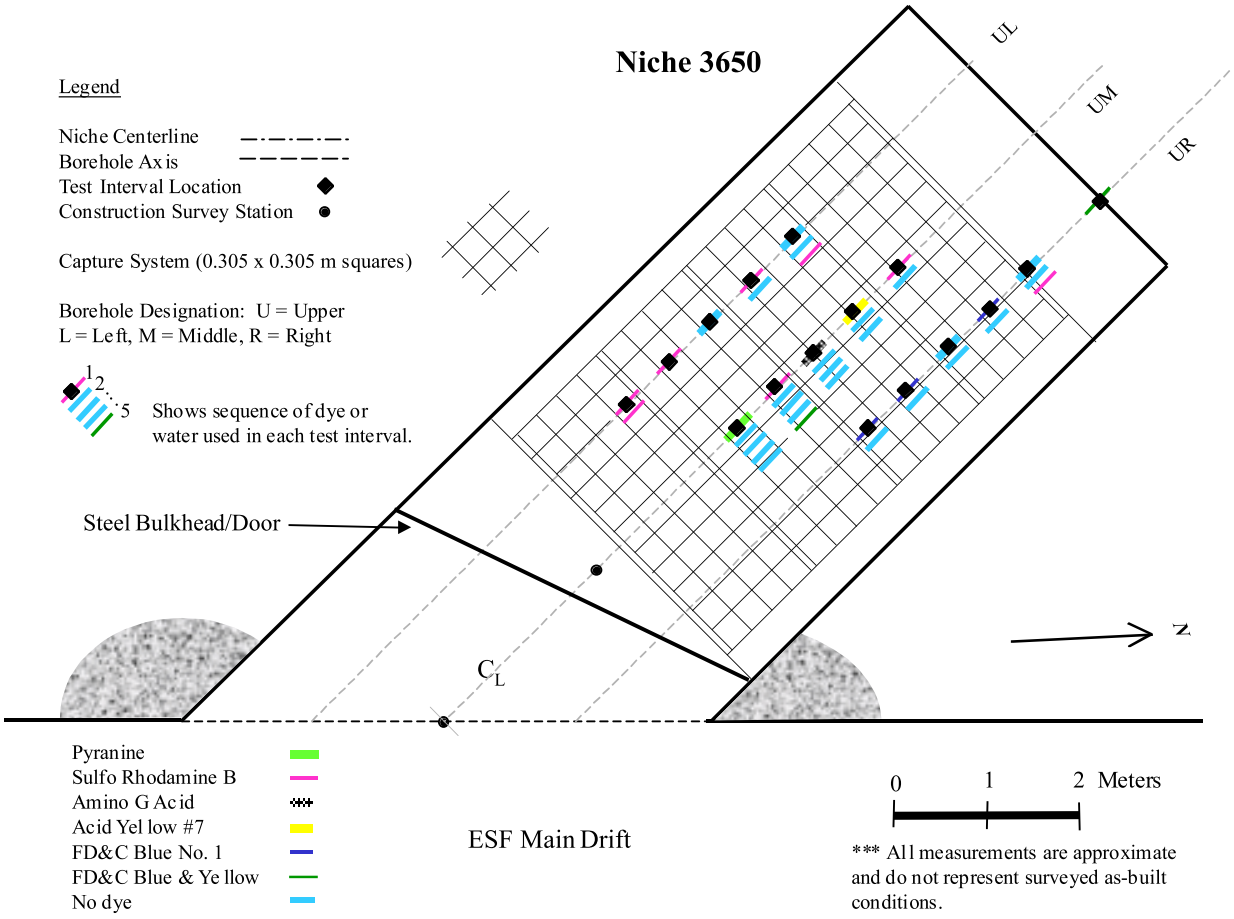

Figure 6.2.1-3. Schematic Illustration of Seepage Capture System and Test Intervals at Niche 3650

6.2.1.3.2 Niche 3107 Seepage Test Data

Beginning in early 1999 and ending in late 1999, twelve niche seepage tests were performed on two test intervals positioned above Niche 3107. Water migrated through the rock and seeped into the niche for one out of the two zones tested. Niche seepage threshold was determined for the zone that seeped. The seepage and liquid-release data were tabulated and entered into the TDMS, where it was assigned DTN: LB0010NICH3LIQ.001 [153144]. As noted in Section 6.2.1.3.1, the borehole flux values were derived from the pumping rate and the wetted area estimated for the borehole interval. This definition of niche seepage threshold is different from the definition

used by PA, with the seepage threshold related to the steady-state, background percolation flux averaged over drift scale and site scale areas.

As with Niche 3650, the mass of water released to the formation was computed by mass balance. The liquid release-rate (Q_s) for each test was computed by dividing the mass released by the respective duration of each test; thus, these values represent time-averaged rates. The rate at which water was released to the formation ranged from 0.014 to 0.102 g/s for all of the tests, and the mass released ranged from 4,229.5 to 23,831.4 g per test.

When water appeared at the niche ceiling during a test and dripped into the opening, it was collected in the capture system and weighed. The wetting front typically arrived at the niche ceiling directly below the test zone. Most of the water was typically captured in only one or two 0.3 × 0.3 m cells located directly beneath the test interval. The mass of water captured ranged from 0.0 to 15,715.1 g per test. The seepage percentage defined by Equation 6.2.1-1 ranged from 0% for zones that did not seep to 70.1%.

The niche seepage tests were conducted with the bulkhead doors at the entrance to the niche closed and sealed. Also, the air space within the niche was artificially humidified to increase the relative humidity as high as practical to minimize the effects of evaporation resulting from ESF ventilation. One open-faced water bath was placed inside the niche to freely supply moisture to the niche space. The water loss volume resulting from evaporation was used to estimate the average evaporation rate over the niche space. The test conditions (e.g., high humidity and low evaporation rates) are representative of steady seepage into a drift that could potentially occur after the repository is closed, the heat load and temperature rise from the decaying waste have dissipated, and air in the sealed repository equilibrates with the surrounding rock at or near 100% relative humidity. The relative humidity and temperature within Niche 3107 is shown in Figure 6.2.1-4.

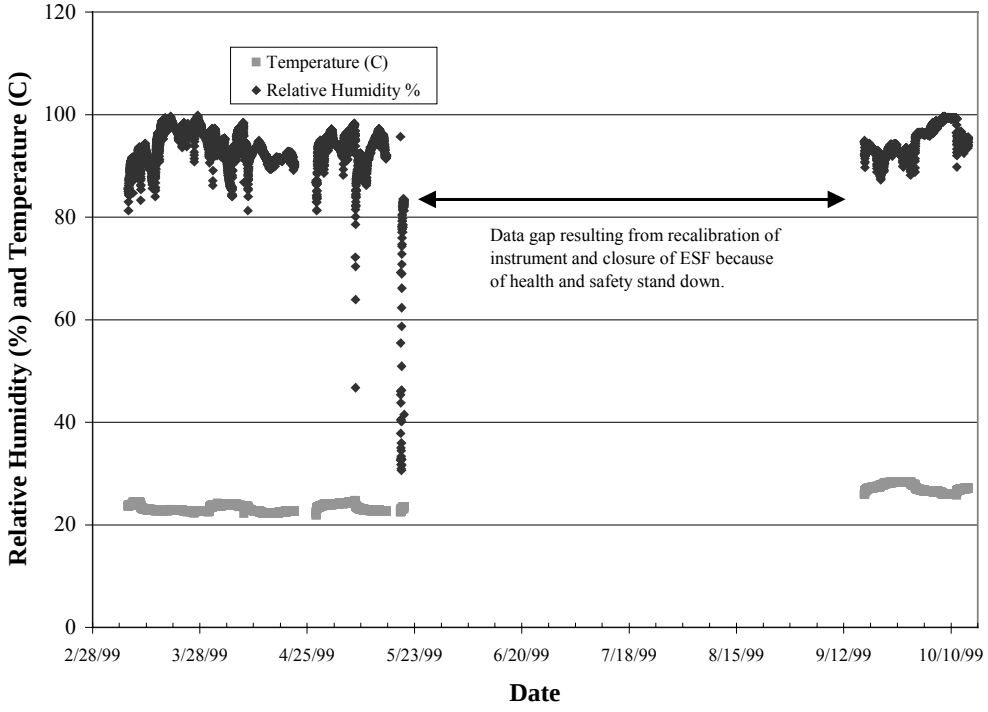

DTN: LB0010NICH3LIQ.001 [153144]

Figure 6.2.1-4. Relative Humidity and Temperature Inside Niche 3107

6.2.1.3.3 Niche 4788 Seepage Test Data

Beginning in late 1999 and ending in mid-2000, thirteen niche seepage tests were performed on three test intervals positioned above Niche 4788. Water migrated through the rock and seeped into the niche from all zones tested. The niche seepage threshold was determined for two of the three zones that seeped. The seepage and liquid-release data were tabulated and entered into the TDMS, where it was assigned DTN: LB0010NICH4LIQ.001 [153145]. As noted in Section 6.2.1.3.1 for Niche 3650 and Section 6.2.1.3.2 for Niche 3107, the borehole flux values for Niche 4788 were derived from the pumping rate and the wetted area estimated for the borehole interval. This definition of niche seepage threshold is different from the definition used by PA, with the seepage threshold related to the steady-state background percolation flux averaged over drift scale and site scale areas.

The long-duration data from Niche 4788 were analyzed in details in Section 6.4 of AMR U0080 *Seepage Calibration Model and Seepage Testing Data* (CRWMS M&O 2001 [153045]). The seepage calibration model analyzed the transient behavior, storage effects, and memory effects between separate tests to determine the effective seepage parameters. The parameters were then used in AMR U0075 *Seepage Model for PA Including Drift Collapse* (CRWMS M&O 2000

[153314]) to determine the seepage threshold flux relative to percolation flux. The final input to TSPA is evaluated in U0120 *Abstraction of Drift Seepage* (CRWMS M&O 2001 [154291]).

As with Niche 3107 and Niche 3650, the mass of water released to the formation was computed by mass balance. The liquid-release rate (Q_s) for each test was computed by dividing the mass released by the respective duration of each test; thus, these values represent time-averaged rates. The rate at which water was released to the formation ranged from 0.008 to 0.092 g/s for all of the tests, and the mass released ranged from 1,474.9 to 39,514.6 g per test.

When water appeared at the niche ceiling during a test and dripped into the opening, it was collected in the capture system and weighed. The wetting front typically arrived at the niche ceiling directly below the test zone. Most of the water was typically captured in only one or two 0.3 × 0.3 m cells located directly beneath the test interval. The mass of water captured ranged from 0.0 to 15,555.1 g per test. The niche seepage percentage defined by Equation 6.2.1-1 ranged from 0% to 68.7%.

Again, the seepage tests were conducted with the bulkhead doors at the entrance to the niche closed and sealed, and the air space within the niche was artificially humidified to minimize evaporation. Figure 6.2.1-5 shows the relative humidity and temperature inside of Niche 4788.

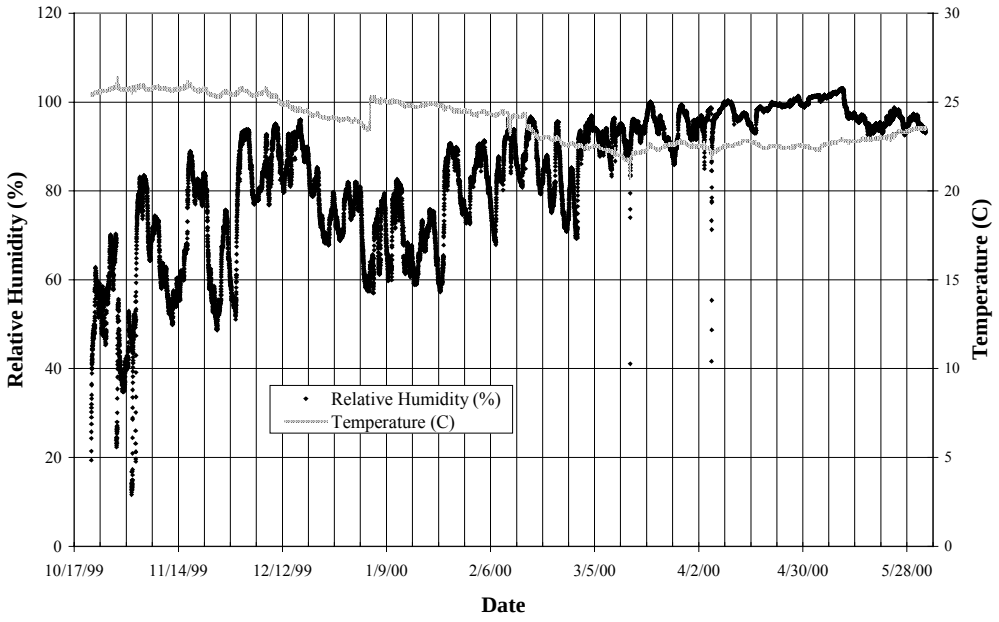

DTN: LB0010NICH4LIQ.001 [153145]

NOTE: Raw data, files Niche4 h&T 3-10-00.csv, Niche4 RH&T 4-1-00.csv, and Niche4788 R&T 6-8-00.csv; data report S00429_007.

Figure 6.2.1-5. Relative Humidity and Temperature Inside Niche 4788

Figure 6.2.1-6 illustrates the release rate into a borehole interval, the return rate, and the stabilization of niche seepage rate of water collected in the niche trays. If tests were not long

enough before niche stabilization, the niche seepage ratio was not well defined. Various operating conditions and niche moisture conditions may contribute to the fluctuations observed in the early time data. The execution of long-duration tests to ensure quasi-steady conditions contributed to the robustness of seepage quantification at selected borehole intervals.

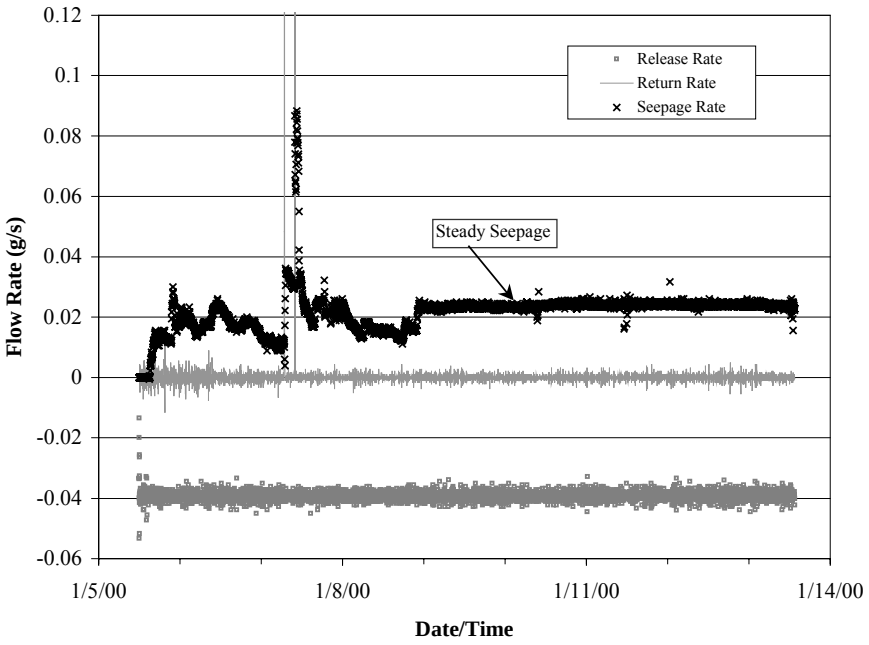

DTN: LB0010NICH4LIQ.001 [153145]

NOTE: Raw data, file Niche 4788 UR 5.18-5.48m 1-5-2000.csv; data report S00429_007.

Figure 6.2.1-6. Stabilized Flow Rates Observed during Test #1 1-5-00 Conducted on Test Interval UR at Niche 4788

6.2.1.3.4 Niche 4788 Wetting Area Data

In this section, an example of niche wetting-area data from a seepage test run in Niche 4788 is discussed. The progression of the wetting fronts with time was recorded on videotape, and still images from the videos were captured and digitized. Wetting fronts were traced from these captured still images; they were later adjusted by reference to marked grid points and other features on the niche crown, and to sketches made during the tests, to correct for distortion caused by the camera's oblique angle of view to the niche crown. They were then superimposed over corresponding areas of a fracture map of the niche crown (Trautz 2001 [156903], pp. 57-62).

Figure 6.2.1-7 shows the wetting-front sequence for a seepage test begun June 26, 2000, with water released from the interval 7.62–7.93 m from the collar of the borehole UL. The release rate

at the borehole interval was 0.02 g/s, and the seepage into the niche corresponded to 14% of the water released.

Several observations can be made from Figure 6.2.1-7. With regard to fractures, their presence has a variable impact on progression of the wetting fronts. Influence of fractures appears relatively minor in the June 26, 2000 test (although a general upper-left-to-lower-right elongation of the fronts may reflect preferred fracture orientation). Also, the initial wetting fronts in these tests are displaced laterally from the vertical projections (the shortest paths) of the release intervals onto the crown, and the wetting fronts overall are not symmetrical about those projections, which suggest a role for fractures in directing flow in the niche crown.

Figure 6.2.1-8 shows the wetting-front growth with time for the seepage test. Each data point corresponds to one of the numbered contours in Figure 6.2.1-7. The x-axis refers to time elapsed since the first wet spot appeared on the crown, rather than from the first release of water.

The plot in Figure 6.2.1-9 pertains to the shape progression of the wet spot. If a front's 2-D shape remained constant as it grew, with subsequent fronts expanding uniformly and maintaining shape similarity between them, the slope of its line in Figure 6.2.1-9 would be constant. This is nearly the case through the early part of the test, with somewhat greater irregularity seen after the 8^{th} or 9^{th} front (or data point). The average value of the slope for this test is ~0.25, somewhat less than the 0.28 slope, which would apply for a circle; this reflects the slightly elongated wetting fronts observed for this test.

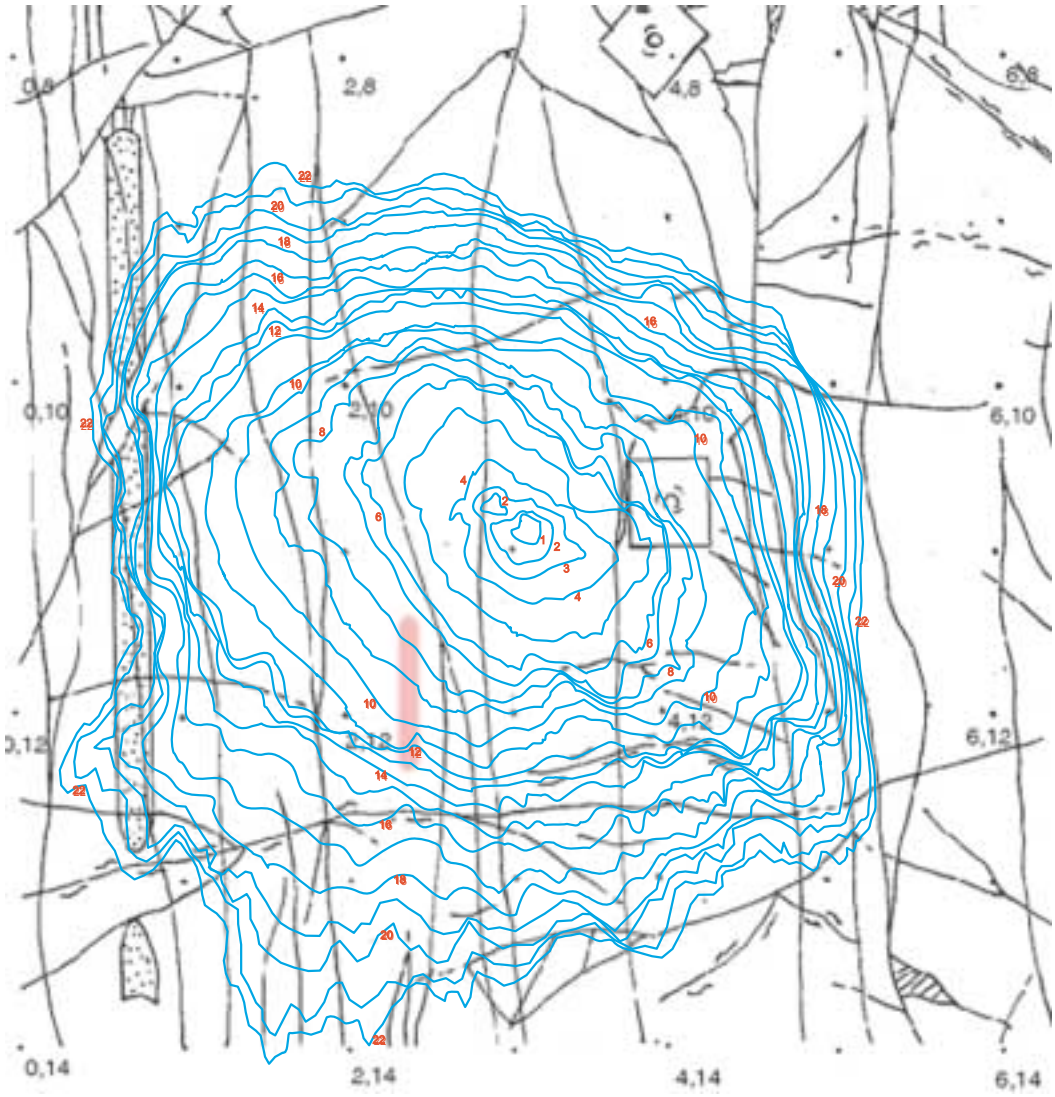

Map symbols:

fractures

rock bolt

grid points at 1-ft intervals

breccia

hole

borehole partly cut by crown

DTN: LB0110NICH4LIQ.001 [OUTPUT]

NOTE: Blue contours are outlines of wetting fronts. Numbers along wetting fronts correlate with the order of data points in Figure 6.2.1-8, and the time corresponding to each front can be determined from that figure. Pink bars indicate approximate positions of release intervals in boreholes above niche, projected onto crown.

Figure 6.2.1-7. Wetting-Front Sequences Overlying Fracture Map of Niche 4788 Crown from Seepage Test Begun June 26, 2000

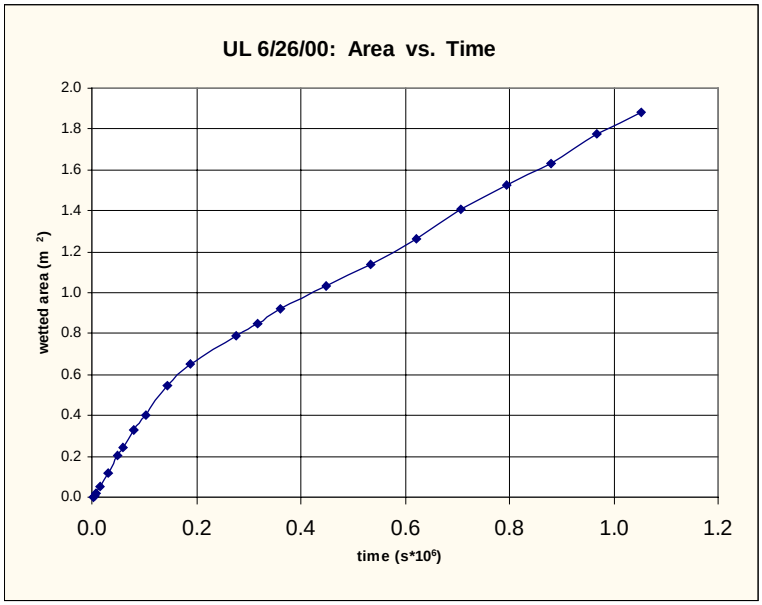

DTN: LB0010NICH4LIQ.001 [153145]

NOTE: Each plotted point represents data for one of the numbered curves shown in Figure 6.2.1-7.

Figure 6.2.1-8. Wetting-Front area (m^2) versus Time (s) for the Seepage Test Shown in Figure 6.2.1-7

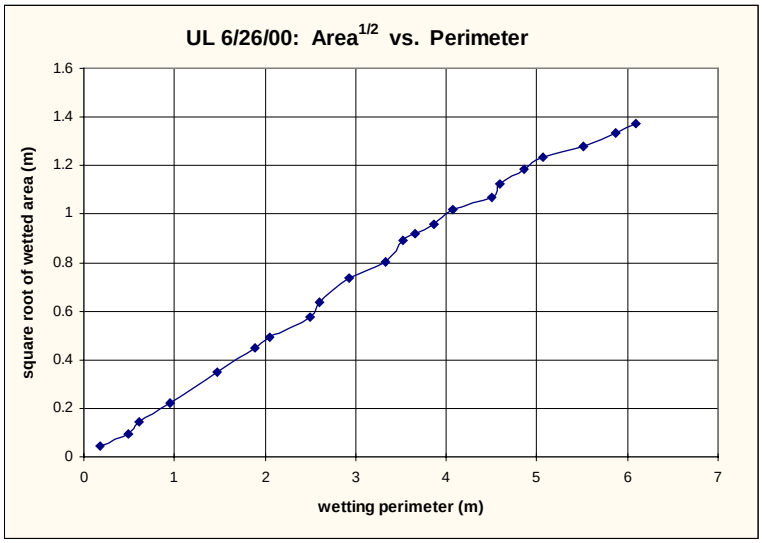

DTN: LB0010NICH4LIQ.001 [153145]

NOTE: Data points correspond to those in Figure 6.2.1-8.

Figure 6.2.1-9. Square Root of Area (m) Plotted versus Perimeter (m) for each of the Wetting Fronts in the Niche 4788 Seepage Test

6.2.1.3.5 Niche CD 1620

A seepage test was initiated at Niche CD 1620 in late February 2001 and ended approximately 39 days later in early April 2001. Water did not seep nor did the wetting front appear at the niche ceiling during this test. Additional seepage tests are planned for Niche CD 1620.

6.2.2 Niche Seepage Threshold and Fracture Characteristic Curve

The niche seepage data collected from short-duration tests in ten intervals at Niche 3560, long-term tests in one interval at Niche 3107, and long-term tests in three intervals at Niche 4788 are analyzed in this section. As stated in Section 6.2.1.3.1, Section 6.2.1.3.2, and Section 6.2.1.3.3, the niche seepage threshold is defined in terms of the pumping rate and the wetted area estimated for the borehole interval. This definition of niche seepage threshold is different from the definition used by PA with the seepage threshold related to the steady-state background percolation flux averaged over drift-scale and site-scale areas.

6.2.2.1 Post-Excavation Liquid-Release and Niche Seepage Threshold

For a given test interval, seepage tests were initially conducted at high liquid-release rates (injection rates into borehole interval without excessive pressure buildup). Subsequent tests were performed at lower liquid-release rates to determine whether a threshold could be estimated below which seepage into the cavity would no longer occur.

Figure 6.2.2-1 shows a plot of the seepage percentages observed during four tests conducted at different q_s in borehole UM at the same interval, located 5.49–5.79 m from the borehole collar at Niche 3650. A linear regression was performed on the four data points to compute the equation for the trendline and the R-squared values (R^2) reported in Figure 6.2.2-1 and tabulated in Table 6.2.2-1. This exercise was repeated for the intervals tested at all the niches to produce the regression data reported in Table 6.2.2-1 for all the zones that seeped. The R-squared values were computed separately for each interval and are listed for those intervals where three or more data points are available. (The linear regression was performed in an Excel spreadsheet documented in Attachment II, Tables II-3a through -4e.)

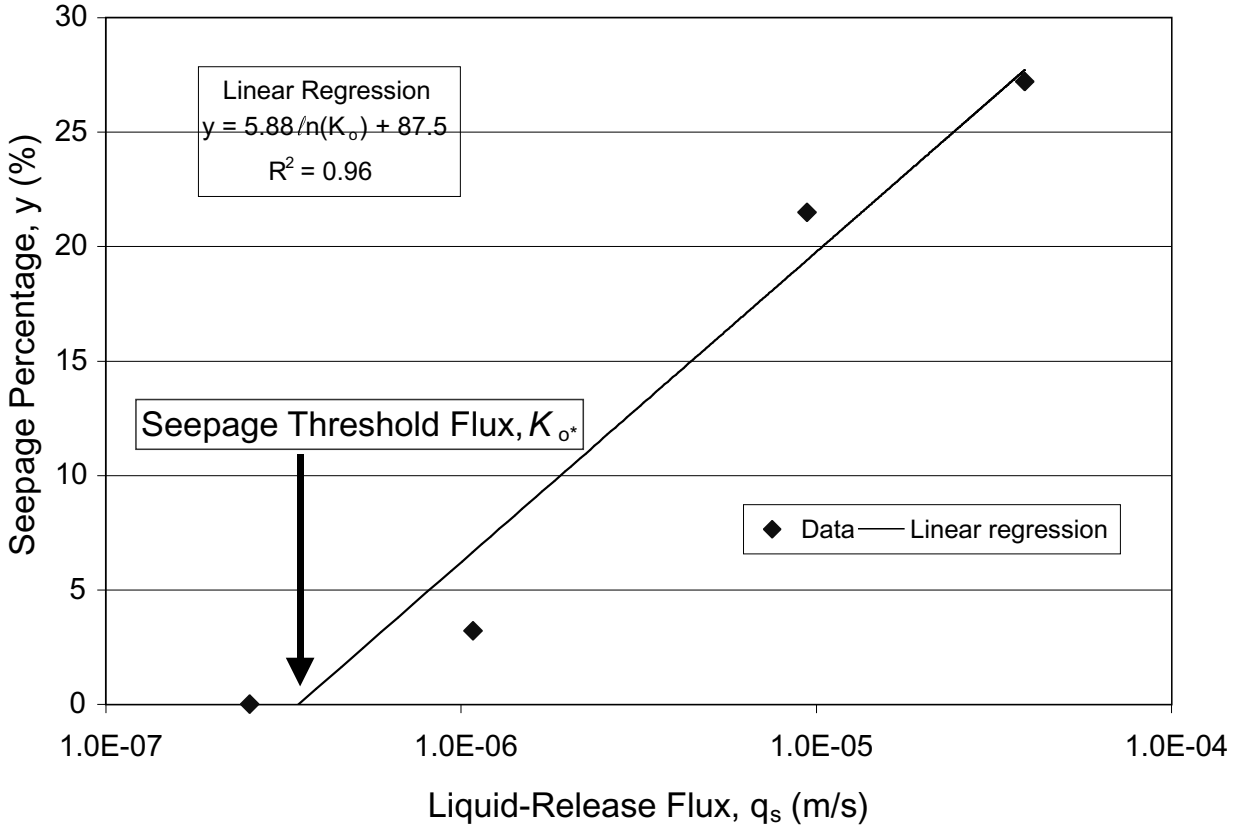

DTN: LB980901233124.003 [105592]

NOTE: Seepage tests were conducted for the interval 5.49-5.79 m from the collar for the upper middle borehole at Niche 3650.

Figure 6.2.2-1. Liquid-Release Flux Versus Seepage Percentage

Table 6.2.2-1. Seepage Threshold Fluxes (K_{o*}).

Niche	Borehole and Depth (m)	Linear Regression Equation	Data Points	Correlation Coefficient (R^2)	Niche Seepage Threshold K_o^* (m/s)	Saturated Hydraulic Conductivity K_l (m/s)
3107	UM 4.88-5.18	$y = 30.440\ln(K_o) + 456.085$	8	0.820	3.11E-07	NA
3650	UL 7.01-7.32	$y = 0.6833\ln(K_o) + 8.5742$	2	NR	3.55E-06	8.98E-05
	UL 7.62-7.92	$y = 5.7394\ln(K_o) + 92.627$	3	0.979	9.80E-08	1.51E-04
	UM 4.27-4.57	$y = 5.2757\ln(K_o) + 79.443$	4	0.921	2.89E-07	2.62E-05
	UM 4.88-5.18	$y = 2.304\ln(K_o) + 31.767$	3	0.975	1.03E-06	2.52E-03
	UM 5.49-5.79	$y = 5.8876\ln(K_o) + 87.528$	4	0.963	3.50E-07	2.16E-05
	UR 4.27-4.57	$y = 0.314\ln(K_o) + 4.3283$	2	NR	1.03E-06	4.08E-05
	UR 4.88-5.18	$y = 0.3165\ln(K_o) + 4.3751$	2	NR	9.92E-07	9.87E-05
	UR 5.49-5.79	$y = 28.419\ln(K_o) + 351.09$	2	NR	4.31E-06	1.71E-05
	UR 6.10-6.40	$y = 4.2169\ln(K_o) + 79.596$	2	NR	6.35E-09	3.01E-05
	UR 6.71-7.01	$y = 10.574\ln(K_o) + 165.28$	3	0.974	1.63E-07	2.28E-04
4788	UL 7.62-7.93	$y = 9.273\ln(K_o) + 148.119$	4	0.929	1.16E-07	2.46E-05
	UM 6.10-6.40	$y = 15.697\ln(K_o) + 243.611$	4	0.980	1.82E-07	2.45E-04
	UR 5.18-5.48	$y = 25.415\ln(K_o) + 410.285$	3	0.970	9.75E-08	3.92E-06

DTN: LB980901233124.003 [105592] and LB0110LIQR0015.001 [OUTPUT]

NOTES: Various data sets were used to generate Table 6.2.2-1. Refer to Tables II-3 and II-4 in Attachment II for details.
NA = not applicable, the test could not be completed as planned because of rock properties outside the equipment's measurable range.
NR = not reported because two data points result in perfect correlation (R^2 =1.0), therefore, correlation coefficient is meaningless.
y = predicted seepage percentage (%)
K_o = net downward liquid-release flux from regression model (m/s)
ln = natural logarithm

Table 6.2.2-1 also summarizes the niche seepage threshold (K_o^*), defined as the liquid-release flux below which water will not seep into the drift (i.e., see K_o^* defined on Figure 6.2.2-1). The K_o^* values were determined using the regression equations provided in Table 6.2.2-1 by setting the seepage percentage, *y*, equal to 0, then solving for $K_o = K_o^*$ [$K_o^* = K_o(y=0)$.] Here, the symbol K_o is used to denote the liquid-release flux used in the regression model to distinguish it from the liquid-release flux computed using the field data (q_s). In terms of K_o and K_o^*, the niche seepage threshold is defined as follows:

- If the liquid-release flux exceeds the seepage threshold flux ($K_o > K_o^*$) for the given interval, then water will seep into the drift.

- If the liquid-release flux is less than the seepage threshold flux ($K_o < K_o^*$), then water will not enter the cavity.

Figure 6.2.2-2 shows a log-log plot of K_o^* versus the saturated hydraulic conductivity (K_l) for 10 test intervals at Niche 3650 and 3 test intervals at Niche 4788 where seepage occurred. For each

test interval, multiple tests with different release rates were conducted to estimate the niche seepage threshold. The air permeabilities obtained from the post-excavation gas-injection tests were converted into equivalent saturated hydraulic conductivities (DTN: LB980001233124.004 [136583]) as shown in Scientific Notebook YMP-LBNL-JSW-6c, pp. 34–38 (Wang 1999 [153449]) for Niche 3650, to produce the values recorded in Table 6.2.2-1 and plotted in Figure 6.2.2-2. (Computation of K_o^* and K_l was performed in an Excel spreadsheet documented in Attachment II, Table II-4. K_l could not be calculated for Niche 3107 because the air-permeability test could not be completed as planned: the rock properties were outside the equipment's measurable range). The straight line in Figure 6.2.2-2 is derived from an analytic solution described in Section 6.2.2.2. The estimation of saturated hydraulic conductivity using air-permeability test data is evaluated in Attachment III.

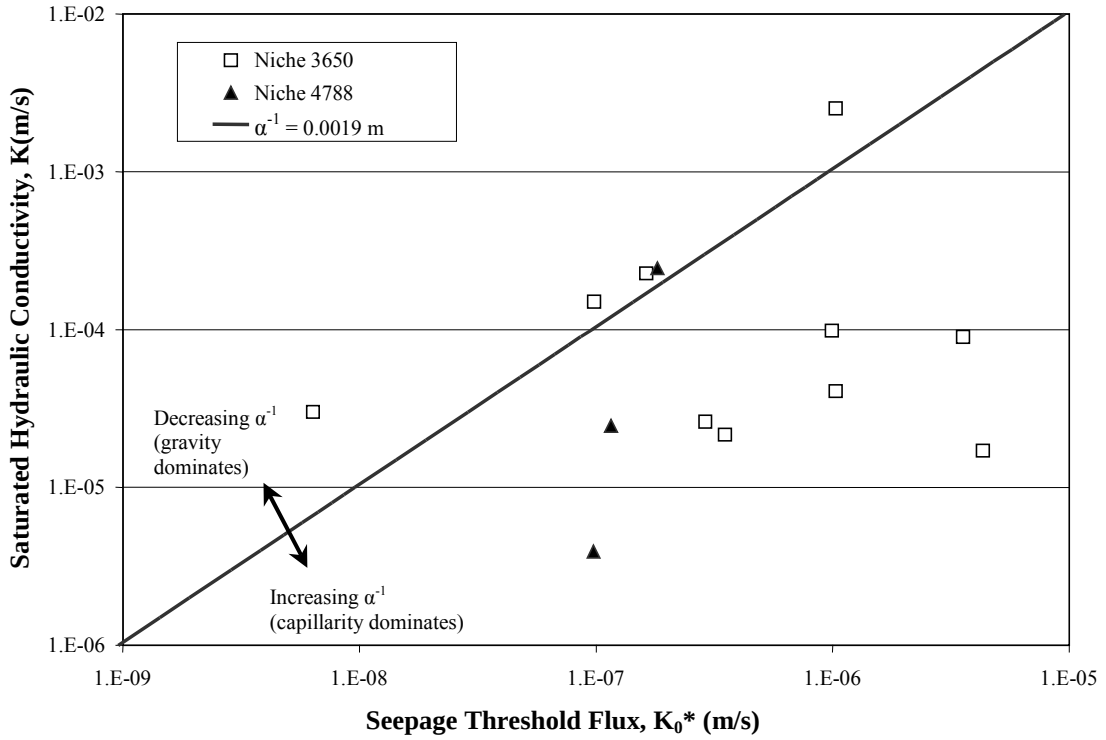

DTN: LB980001233124.004 [136583]; LB0010NICH4LIQ.001 [153145]; LB980901233124.003 [105592]; LB0110LIQR0015.001 [OUTPUT]

Note: Various Data sets were used to generate this figure. Refer to Table II-4 in Attachment II for details.

Figure 6.2.2-2. Niche Seepage Threshold

6.2.2.2 Capillary Strength (α^{-1}) of Fractures

Philip et al. (1989 [105743]) recognized that buried cylindrical cavities are obstacles to flow, preventing water from entering the cavity. Given Assumption 5.2-3 in Section 5.2.2, the following theoretical relation between K_o^* and K_l was provided by Philip et al. (1989 [105743], Section 3.4, p. 19):

$$K_{o*} = K_l \left[\vartheta_{\max}(s)\right]^{-1} \quad \text{(Eq. 6.2.2-1)}$$

where s is the value of the dimensionless cavity length and ϑ_{max} is the maximum value of the dimensionless potential ϑ at the boundary of the cavity. Philip et al. (1989 [105743], Equation 56, p. 20) shows that ϑ_{max} occurs at the apex or crown of a cylindrical cavity. The dimensionless cavity length, s, is a measure of the relative importance of gravity and capillarity in determining flow. As $s \rightarrow 0$, capillarity dominates, whereas gravity dominates as $s \rightarrow \infty$.

An exponential functional relation between unsaturated hydraulic conductivity, $K(\psi)$, and water potential, ψ, is used (Philip et.al. 1989 [105743], Equation 12, p. 18):

$$K(\psi) = K_l \, e^{\alpha(\Psi - \Psi_e)} \quad \text{(Eq. 6.2.2-2)}$$

K_l is the saturated hydraulic conductivity (Pullan 1990 [106141], p. 1221). ψ_e. is the air entry potential, K_l is the conductivity at $\psi = \psi_e$ and α^{-1} is the capillary strength parameter.

This Gardner exponential functional relation is used by Philip et al. (1989 [105743], Equation 12, p. 18) and by Braester (1973 [106088], Equation 5, p. 688) to transform and linearize the unsaturated governing equations. Equation 6.2.2-2 is also used in Section 6.2.2.4 to estimate water potential.

Another model for unsaturated hydraulic conductivity and water potential is the van Genuchten model with its own capillary-strength parameter and pore-size distribution parameter (CRWMS M&O 2001 [153045], Section 6.3.2.3). The distinction between model-dependent capillary-strength parameters should be noted in comparing results from the analysis presented in this section and the results from the seepage calibration model and other PA models.

Philip et al. (1989 [105743], Equation 14, p. 18) notes that the dimensionless cavity length s in Equation 6.2.2-1 is related to the capillary strength parameter α^{-1} (Equation 6.2.2-2) and a characteristic length of the cavity ℓ by the following expression:

$$s = 0.5 \alpha \ell \quad \text{(Eq. 6.2.2-3)}$$

When s is large, Philip et al. (1989 [105743], Section 6, pp. 23–25) demonstrate that a boundary layer adjoining the ceiling of the cavity surface will develop. This allows the steady flow equation to be replaced by a boundary-layer equation that is readily solved. The asymptotic expansion of ϑ_{max} for large values of s yields (Philip et al. 1989 [105743], Equation 84, p. 23):

$$\vartheta_{\max} = 2s + 2 - \frac{1}{s} + \frac{2}{s^2} - \ldots \quad \text{(Eq. 6.2.2-4)}$$

Philip et al. (1989 [105743], Table 1, Section 6, p. 25) note that when $s \geq 1$, the first three terms on the right-hand side of Equation 6.2.2-4 produce an adequate estimate that is within 12% or

better of the exact value of ϑ_{max}. Therefore, using appropriate values for K_{o*}, ℓ, and K_l, we can estimate the capillary strength (α^{-1}) for the porous medium from Equation 6.2.1-1, Equation 6.2.1-3 and the first three terms in Equation 6.2.2-4. This technique was utilized to compute the α^{-1} values reported in Table 6.2.2-2 using the values for K_{o*} derived in Section 6.2.2.1. The K_l values were derived from post-excavation air-injection tests summarized in Table 6.2.2-1 and a value of 2 meters was used for ℓ, which is approximately equal to the radius of the curvature of the niche ceiling. By taking the reciprocal of the α^{-1} reported in Table 6.2.2-2, which in our case also equals s, all the s-values with the exception of Niche 3107 UM 4.88-5.18 m are greater than one, justifying the use of Equation 6.2.2-4. The s-value for Niche 3107 UM 4.88-5.18 m is slightly less than one (i.e., 0.43), implying that the use of Equation 6.2.2-4 will result in a larger error in α^{-1} for this test.

Table 6.2.2-2. Alpha (α) Values Estimated for the Fractures

Niche	Borehole and Interval (m)	Output Capillary Strength α^{-1} (m)
3650	UL 7.01-7.32	0.0855
	UL 7.62-7.92	0.0013
	UM 4.27-4.57	0.0225
	UM 4.88-5.18	0.0008
	UM 5.49-5.79	0.0334
	UR 4.27-4.57	0.0532
	UR 4.88-5.18	0.0205
	UR 5.49-5.79	0.71
	UR 6.10-6.40	0.0004
	UR 6.71-7.01	0.0014
4788	UL 7.62-7.93	0.0095
	UM 6.10-6.40	0.0015
	UR 5.18-5.48	0.0523
Theoretical limit		0.0019

DTN: LB980901233124.003 [105592]; LB990601233124.001 [105888]

NOTE: Various data sets were used to derive α^{-1}. Refer to Attachment II, Table II-5 for detail.

An early analysis based on visual inspection and straight-line fitting of Niche 3650 short-duration test data in Figure 6.2.2-2 is documented in Trautz and Wang (2000 [157161]). In this section of this AMR, the Niche 3650 data analyses are compared with the results of long-duration tests at Niche 4788.

Philip (1989 [156974]) reports that α^{-1} ranges from 0.05 m or less for coarse-grained soils to 5 m or more for fine-textured soils. In comparison, the values reported in Table 6.2.2-2 range from 0.001 to 0.71 m for the fractures tested, with the lower bound below that normally reported in the literature for soils. Philip (1989 [156974]) and White and Sully (1987 [106152], p. 1514)

recognized that α^{-1} is a K-weighted mean soil-water potential directly related to the macroscopic capillary length, or pore radius r of the medium, as follows:

$$2\alpha^{-1} = \frac{2\gamma\cos(\theta)}{\rho g r} \qquad \text{(Eq. 6.2.2-5)}$$

where γ, ρ, and θ are the surface tension, density, and contact angle of the fluid, respectively, and g is gravitational acceleration. The right-hand-side of Equation 6.2.2-5 is known as Laplace's capillary formula, which is equal to the height of fluid rise in a small diameter cylindrical tube. Equation 6.2.2-5 can also be used to estimate the height of fluid rise between two smooth parallel plates (analogous to a fracture) by substituting the aperture b, or separation distance between plates for r in Equation 6.2.2-5.

Bouwer (1966 [155682], p. 733) and Raats and Gardner (1971 [155683], p. 922) described the macroscopic capillary length, and hence $2\alpha^{-1}$, as a "mean" height of capillary rise above a water table, or the "mean" air-entry head. In our case, the significance of $2\alpha^{-1}$ is that it represents the mean height that water can be retained in the fractures above the drift (without seeping) because of the capillary barrier.

Figure 6.2.2-2 was generated by plotting the K_o^* values derived in Section 6.2.2.1 along with their corresponding K_l values reported in Table 6.2.2-1. The significance of the line in Figure 6.2.2-2 is that it corresponds to the smallest value of α^{-1} that can be obtained, given the limited range of validity for the capillary mechanism using Laplace's formula. Wang and Narasimhan (1993 [106793], p. 329) show that when the fracture aperture is very large, the radial curvature of the fluid meniscus between two parallel plates will be very large and the capillary effect will be negligible. Using Laplace's formula, they determined for a wetting fluid of contact angle zero (i.e., $\theta = 0$ in Equation 6.2.2-5) that the capillary mechanism is no longer valid when the maximum aperture b_{max} between two smooth-walled parallel plates exceeds

$$b_{max} = \left(\frac{2\gamma}{\rho g}\right)^{1/2} \qquad \text{(Eq. 6.2.2-6)}$$

For $\gamma = 0.072$ kg/s^2, $\rho = 998$ kg/m^3, and $g = 9.8$ m/s^2 the nominal aperture size is 3.84 mm, which, using Equation 6.2.2-5, corresponds to a limiting value for α^{-1} equal to 0.0019 m. The line in Figure 6.2.2-2 represents the practical limit of Equation 6.2.2-1 calculated using the limiting value of α^{-1} derived from Equation 6.2.2-5 and Equation 6.2.2-6. Therefore, values of α^{-1} less than 0.0019 m correspond to nominal apertures that are greater than 3.84 mm, the point at which capillary forces vanish and gravity forces dominate flow. Several data points are slightly above the line in Figure 6.2.2-2. This implies that gravity forces dominate fluid flow through these features.

6.2.2.3 Estimated Volumetric Water Content (θ) of Fractures

Another useful piece of information that can be derived using the niche seepage data includes estimates of the change in volumetric water content θ, where θ = (volume of water in

fractures)/(bulk volume of fractured tuff) of the fractures. Direct measurement of fracture θ in the field is difficult at best using conventional hydrologic techniques (e.g., using neutron moisture logs). Therefore, an alternative method of measuring average volumetric water contents indirectly, using wetting-front arrival times observed at the niche ceiling during the seepage tests, is described below. Assumptions used in the analyses are described in Section 5.2.3.

Based on mass conservation along the vertical flow path, the depth of the wetting front below the water source is:

$$z_p = \frac{q_s\, t}{(\theta_{ave} - \theta_n)} \qquad \text{(Eq. 6.2.2-7)}$$

where z_p is the depth from the water-supply surface to the leading edge of the wetting front, t is the arrival time of the front at depth z_p, q_s is the constant flux of water supplied at the source, and θ_n is the initial or antecedent (or residual) water content.

Using the arrival time for the wetting front observed at the niche ceiling (DTN: LB980001233124.004 [136583]) and the q_s data (DTN: LB980001233124.004 [136583]), it is possible to estimate the change in volumetric water content change $\Delta\theta = \theta_{ave} - \theta_n$ for each seepage test by applying Equation 6.2.2-7. (Computation of $\Delta\theta$ was performed in an Excel spreadsheet documented in Attachment II, Table II-8 for Niche 4788. The $\Delta\theta$ was not computed for Niche 3107—refer to Section 6.2.2.4). Table 6.2.2-3 provides a summary of the estimated $\Delta\theta$ values for zones where three or more seepage tests were conducted. With the approximation (described in Section 5.2.3) that the initial, antecedent, or residual moisture content θ_n is negligible compared to θ_{ave}, then $\Delta\theta$ becomes a measure of the average volumetric water content.

The water-content values shown in Table 6.2.2-3 range from 0.09 to 5.0%. Surprisingly, this indicates that the saturated water contents or porosities of the fractures could be as high as 5.0%, which is greater than expected. In turn, these values could influence travel-time calculations computed for the unsaturated zone, since travel time is proportional to water content. Using larger water content for the fractures would result in longer travel times.

Assumption 5.2-4 and Assumption 5.2-5 in Section 5.2.3 are used to estimate water contents for the fractures. These two assumptions are evaluated in Attachment IV.

Table 6.2.2-3. Estimated Changes in Volumetric Water Content ($\Delta\theta$)

Niche	Depth (m)	Test Name	Liquid Release Flux q_s, (m/s)	Average Water Content Change $\Delta\theta = \theta_{ave} - \theta_n$ (m^3/m^3)
3650	UL 7.62-7.92	Test #2 1-6-98	9.49E-06	0.0101
	UL 7.62-7.92	Test #1 2-12-98	1.89E-06	0.0017
	UL 7.62-7.92	Test #1 3-4-98	2.33E-07	0.0009
	UM 4.27-4.57	Test 5 Niche 3650 (11-13-97)	3.78E-05	0.0242
	UM 4.27-4.57	Test #1 12-3-97	9.42E-06	0.0146
	UM 4.27-4.57	Test #2 12-3-97	9.47E-06	0.0075
	UM 4.27-4.57	Test #1 1-7-98	8.82E-07	0.0120
	UM 4.27-4.57	Test #2 2-10-98	3.09E-07	0.0063
	UM 4.88-5.18	Test 1 Niche 3650 (11-12-97)	5.41E-05	0.0150
	UM 4.88-5.18	Test #1 12-4-97	9.49E-06	0.0043
	UM 4.88-5.18	Test #2 12-5-97	2.70E-06	0.0040
	UM 4.88-5.18	Test #1 1-8-98	8.75E-07	0.0082
	UM 4.88-5.18	Test #1 3-6-98	2.48E-07	0.0083
	UM 5.49-5.79	Test 4 Niche 3650 (11-13-97)	3.87E-05	0.0124
	UM 5.49-5.79	Test #2 12-4-97	9.43E-06	0.0061
	UM 5.49-5.79	Test #1 1-9-98	1.08E-06	0.0046
	UM 5.49-5.79	Test #1 2-11-98	2.55E-07	0.0040
	UR 6.71-7.01	Test #1 1-13-98	3.68E-06	0.0024
	UR 6.71-7.01	Test #1 2-3-98	1.91E-06	0.0018
	UR 6.71-7.01	Test #1 3-5-98	2.48E-07	0.0017
4788	UL 7.62-7.93	Test #1 11/3/99	1.65E-06	0.0200
	UL 7.62-7.93	Test #1 11-30-99 Niche 4788	9.22E-07	0.0057
	UL 7.62-7.93	Test #1 6-26-2000	3.59E-07	0.0101
	UL 7.62-7.93	Test #1 01-24-00	1.46E-07	0.0115
	UM 6.10-6.40	Test #1 Niche 4788 11/16/99	1.72E-06	0.0489
	UM 6.10-6.40	Test #1 Niche 4788 12-10-99	7.33E-07	0.0503
	UM 6.10-6.40	Test #1 06-08-2000	3.83E-07	0.0331
	UM 6.10-6.40	Test #1 3-14-2000	1.66E-07	0.0355
	UR 5.18-5.48	Test #1 Niche 4788 12/7/99	1.69E-06	0.0092
	UR 5.18-5.48	Test #1 1/5/2000	7.11E-07	0.0055
	UR 5.18-5.48	Test #1 02-14-2000	1.65E-07	0.0055

DTN: LB980901233124.003 [105592] and LB0110LIQR0015.001 [OUTPUT]

6.2.2.4 Estimated Water Potentials (ψ) of Fractures

The direct measurement of water potentials is difficult to make in unsaturated fractures because hydrologic instruments are not readily adaptable to measuring such small features. Therefore, an indirect measure of the water potential (ψ) was formulated using the α-values computed in Section 6.2.2.2, the liquid-release fluxes, air-derived saturated hydraulic conductivities, employing Equation 6.2.2-2 with $q_s = K(\psi)$, and solving for ψ as shown below:

$$\psi = \frac{\ell n(q_s / K_l)}{\alpha} \qquad \text{(Eq. 6.2.2-8)}$$

Using the values for q_s and K_l reported in DTN: LB980001233124.004 [136583] and the α-values from Table 6.2.2-2, ψ was computed for several Niche 3650 tests by employing Equation 6.2.2-8. (Computation of ψ was performed in an Excel spreadsheet documented in Attachment II, Table II-7 for Niche 4788. ψ was not computed for Niche 3107 because a value for K_l could not be computed: the corresponding air k value was not measurable with the equipment used). A summary of the resulting ψ values is provided in Table 6.2.2-4.

Table 6.2.2-4. Estimated Water Potential (ψ) for the Fractures

Niche	Borehole/Depth (m)	Test Name	Absolute Value of the Water Potential ψ (m)
3650	UL 7.62-7.92	Test #2 1-6-98	3.59E-03
	UL 7.62-7.92	Test #1 2-12-98	5.68E-03
	UL 7.62-7.92	Test #1 3-4-98	8.39E-03
	UM 4.27-4.57	Test 5 Niche 3650 (11-13-97)	8.26E-03
	UM 4.27-4.57	Test #1 12-3-97	2.30E-02
	UM 4.27-4.57	Test #2 12-3-97	2.29E-02
	UM 4.27-4.57	Test #1 1-7-98	7.64E-02
	UM 4.27-4.57	Test #2 2-10-98	1.00E-01
	UM 4.88-5.18	Test 1 Niche 3650 (11-12-97)	3.13E-03
	UM 4.88-5.18	Test #1 12-4-97	4.56E-03
	UM 4.88-5.18	Test #2 12-5-97	5.58E-03
	UM 4.88-5.18	Test #1 1-8-98	6.50E-03
	UM 4.88-5.18	Test #1 3-6-98	7.53E-03
	UM 5.49-5.79	Test 4 Niche 3650 (11-13-97)	1.95E-02
	UM 5.49-5.79	Test #2 12-4-97	2.77E-02
	UM 5.49-5.79	Test #1 1-9-98	1.00E-01
	UM 5.49-5.79	Test #1 2-11-98	1.48E-01
	UR 6.71-7.01	Test #1 1-13-98	5.90E-03
	UR 6.71-7.01	Test #1 2-3-98	6.84E-03
	UR 6.71-7.01	Test #1 3-5-98	9.76E-03
4788	UL 7.62-7.93	Test #1 11/3/99	2.56E-02
	UL 7.62-7.93	Test #1 11-30-99 Niche 4788	3.12E-02
	UL 7.62-7.93	Test #1 6-26-2000	4.01E-02
	UL 7.62-7.93	Test #1 01-24-00	4.86E-02
	UM 6.10-6.40	Test #1 Niche 4788 11/16/99	7.38E-03
	UM 6.10-6.40	Test #1 Niche 4788 12-10-99	8.65E-03
	UM 6.10-6.40	Test #1 06-08-2000	9.61E-03
	UM 6.10-6.40	Test #1 3-14-2000	1.09E-02
	UR 5.18-5.48	Test #1 Niche 4788 12/7/99	4.41E-02
	UR 5.18-5.48	Test #1 1/5/2000	8.93E-02
	UR 5.18-5.48	Test #1 02-14-2000	1.66E-01

DTN: LB980001233124.004 [136583]; LB980901233124.003 [105592]

NOTE: Various data sets were used to generate this table. Refer to Table II-7 in Attachment II for details.

6.2.2.5 Fracture-Water Characteristic Curves

The volumetric water-content values from Section 6.2.2.3 and the water-potential values derived in Section 6.2.2.4 are plotted on Figure 6.2.2-3 to create a water-characteristic curve for the fractures. Only those test intervals where three or more tests were conducted are included in the figure. (Inclusion of zones having only two data points joined by a straight line contributes little to understanding of the functional relation between θ and ψ.)

Although Assumption 5.2-3, Assumption 5.2-4, and Assumption 5.2-5 described in Section 5.2.2 and Section 5.2.3 were used to derive these curves, note that the data fall into two groups, exhibiting similar water-retention characteristics. The first group (N3650 UL 7.62-7.92 m, N3650 UR 6.71-7.01 m and N3650 4.88-5.18 m) consists of high-permeability fractures that drain over a narrow range of water potentials and appear to have low residual water contents of about 0.001 to 0.002. The second group (N3650 UM 4.27-4.57 m, N3650 UM 5.49-5.79 m, N4788 UM 6.10-6.40 m, N4788 UL 7.62-7.93 m, and N4788 UR 5.18-5.48 m) consists of lower-permeability fractures that drain over a relatively larger range of water potentials and appear to have a slightly larger residual water content of about 0.005.

Residual water remaining in the fracture after the initial test can cause subsequent test data (collected during a test performed at a similar rate) to shift to the left, parallel to the x-axis, as shown in Figure 6.2.2-4 for zone N3650 UM 4.27-4.57 m. The second and third tests from this interval were conducted at nearly identical fluxes (9.42E-06 versus 9.47E-06 m/s) separated in time by less than 2 hours. The wetting front arrived at the niche ceiling during the second test in about half the time as the first test, resulting in a $\Delta\theta$ value that is half that for the second test compared to the first. The fourth and fifth tests in the sequence were performed approximately one and two months later, respectively. Evidence of the effects of wetting history is not readily apparent for these tests, which were conducted at lower fluxes (corresponding to lower water contents), indicating that the fractures drained or dried out prior to retesting.

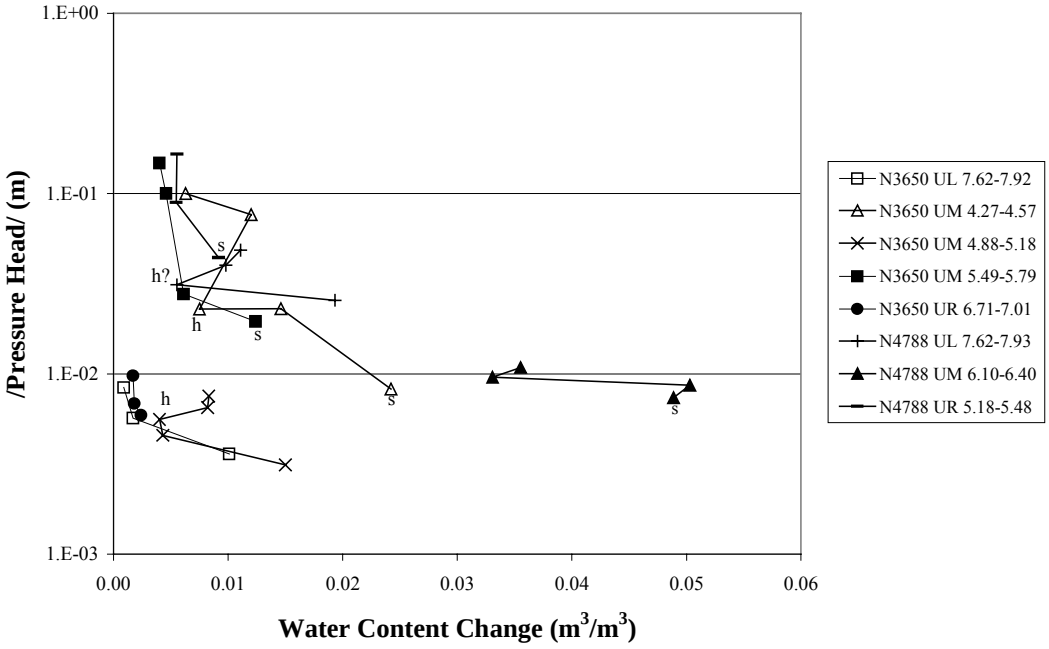

s = saturated conditions
h = data point influenced by wetting history

DTN: LB980901233124.003 [105592] and LB0110LIQR0015.001 [OUTPUT]

NOTE: Various data sets were used to generate this Figure. Refer to Tables II-7 and -8 in Attachment II for details.

Figure 6.2.2-3. Water Retention Curves for Fractures

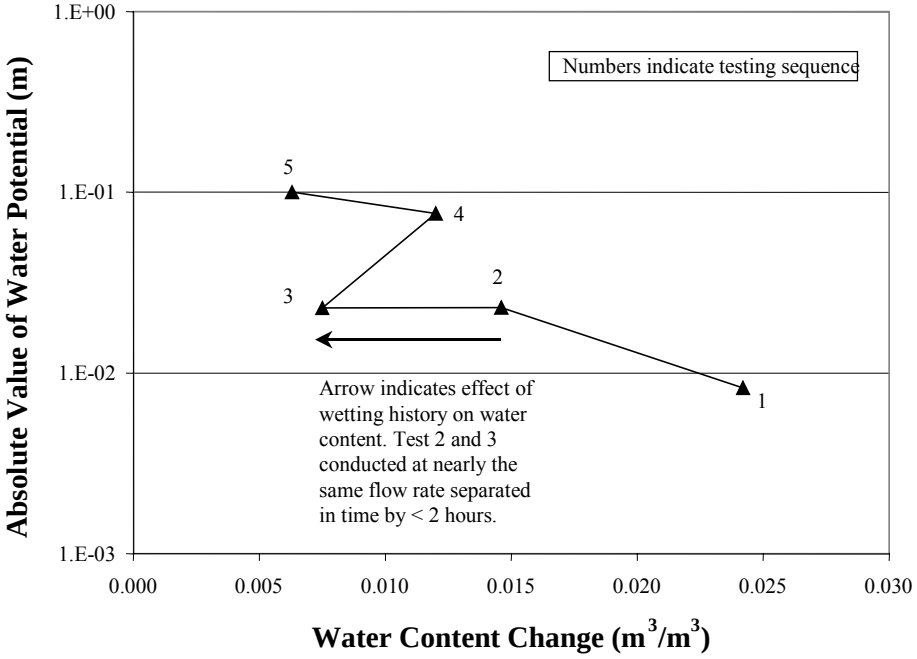

DTN: LB980901233124.003 [105592]

NOTE: Various data sets were used to generate this Figure. Refer to Tables II-7 and -8 in Attachment II for details.

Figure 6.2.2-4. Effect of Wetting History on Water Retention Curves for Test Interval N3650 UM 4.27-4.57 m

6.3 ANALYSES OF TRACER-MIGRATION DELINEATION AT NICHE 3650

An additional episodic tracer-migration test was conducted at drift-seepage test site Niche 3650 in the ESF to elucidate the flow paths above the niche ceiling. The distribution of tracers from both the tracer-migration test and previous liquid-release and seepage-threshold tests are presented in this section.

6.3.1 Tracer Distribution from the Tracer-Migration Test

6.3.1.1 Field Studies at Niche 3650

Seven 0.0762 m diameter boreholes were drilled at Niche 3650. Three of these boreholes, designated UL, UM, and UR, were drilled approximately one meter apart and 0.65 m above the niche ceiling in the same horizontal plane as shown in Figure 6.1.1-2b. An array of twelve sampling boreholes was drilled to collect core samples for tracer analyses, as shown Figure 6.3.1-1. The core analyses delineated the extent of tracer-migration from an episodic liquid-release event as well as for all tracer and liquid-release tests.

Liquid-release tests were conducted prior to the niche excavation to evaluate how far a finite pulse of liquid would travel through unsaturated fractured rock (Section 6.2.1). Water containing colored dyes was used to mark the wetted area and flow paths resulting from each test. The niche was then excavated dry (using an Alpine Miner) to observe and photograph the distribution of fractures and dye within the welded tuff (Section 6.2.1 and Wang et al. 1999 [106146], pp. 329–332). After niche excavation, a series of short-duration seepage tests were performed to determine the amount of liquid that would seep into the mined opening (Section 6.2.2).

Along the three upper boreholes (UL, UM, UR), two Food, Drug & Cosmetics (FD&C) dyes were released before niche excavation: FD&C Blue No. 1 and FD&C Red No. 40. Blue and red bars in Figure 6.3.1-1a on the upper-left side of test-interval locations represent the pre-excavation liquid-release tests. Post-excavation liquid-injection tests, both with and without tracers, were conducted at various intervals along the boreholes to measure seepage into the niche. Post-excavation tracers included FD&C Blue No. 1, Sulpho Rhodamine B, Pyranine, FD&C Yellow No. 6, Acid Yellow 7, and Amino G Acid. The post-excavation seepage test sequences are summarized schematically on the lower right side of test-interval locations in Figure 6.3.1-1a.

6.3.1.2 Tracer-Migration Test

The tracer-migration test was conducted at Niche 3650 six months after the seepage tests. From September 16–18, 1998, water containing six tracers (4.60 g/l NaI, 4.60 g/l CaI_2, 4.60 g/l $CaBr_2$, 1.56 g/l FD&C Blue No.1, 1.76 g/l FD&C Yellow No. 5, 0.019 g/l 2,3-difluorobenzoic acid, and 0.018 g/l pentafluorobenzoic acid) was released into a highly permeable zone located in Borehole UM 4.88–5.18 m from the borehole collar. Iodide, bromide, and fluorinated benzoic acids were used as nonreactive tracers, while the others were applied as sorbing tracers. The release rate was 0.013 g/s, with a total released volume of about 1.52 liters. The wetting front

was observed to reach the niche ceiling in a large fracture/breakout, but water did not drip into the niche.

Between September 23 and October 1, 1998, twelve sampling boreholes, nominally 1.5 m long, were drilled into the niche ceiling around and below the liquid-release interval to determine the extent of the tracer-migration. Rock-core samples were collected during the drilling process for subsequent laboratory chemical analyses. (Refer to Wang 1999 [153449], p. 99–107, 123, and 124 for detailed description of this tracer-migration test.)

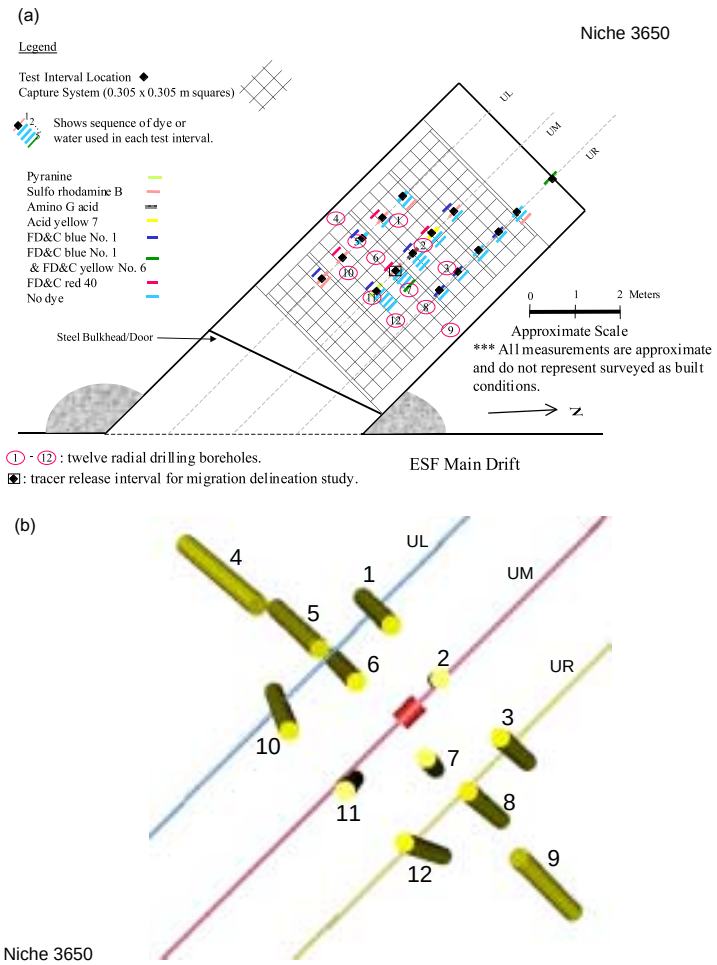

NOTE: The red-colored cylinder denotes the release interval of the tracer-migration test.

Figure 6.3.1-1. Schematic of Sampling Borehole Array: (a) Plan View with Liquid-Release/Dye-Application History, and (b) Three-Dimensional View from inside the Niche

Figure 6.3.1-1b shows a 3-D perspective view of the sampling borehole array. The cores from the boreholes were 4.47 cm in diameter and were divided into sections during coring, with each section separately wrapped in Saran wrap. Each wrapped sample was placed inside a Lexan liner (with tape wrapping sealing both ends of the liners) and sealed in a Protecore® packet. The interval for each section was noted on the packet, which was assigned a unique numeric identifier.

The tracer chemical information is shown in Hu 1999 ([156541], p. 154–155), and Hu 1999 ([155691], p. 151). Tracer analysis results and discussions are presented as concentration ratios (independent of chemical purity). Attachment V describes core sample processing and aqueous tracer measurement for the analyses of tracer distribution.

Iodide and FD&C Yellow No. 5 concentrations were not detected above background levels in the samples collected from the twelve boreholes drilled around the release interval. Iodide and FD&C Yellow No. 5 were applied only during the tracer-migration test and were not used in earlier seepage tests at Niche 3650. These results indicate that the sampling borehole array did not capture the tracer plume of the tracer-migration test. Liquid migration was most likely localized and very possibly confined within the 1.0 m × 1.6 m area directly below the liquid-release interval.

Several rock-chip samples were collected from the ceiling of Niche 3650 in March of 2001. These samples were obtained directly under the release interval of the tracer-migration test (within a radius of about 20 cm), and within the twelve sampling boreholes. Six samples have been processed for chemical concentration measurements as documented in Hu 1999 ([155691], pp. 143–144), and Hu 2000 ([156473]). Iodide was detected in all six of the analyzed samples, confirming the arrival of iodide from the wetting front observed at the niche ceiling during the tracer-migration test. FD&C Yellow No. 5 was not found among the samples, possibly because of its higher sorption compared to iodide.

6.3.2 Delineation of Tracer Distributions from Previous Liquid-Release Tests

Tests prior to the tracer-migration test were conducted at different borehole intervals at various flow rates to determine the seepage thresholds for each interval. A total of 40 liquid-release tests over 16 borehole intervals were conducted at Niche 3650 using both water with and without dye tracers as shown in Figure 6.3.1-1a. The distributions of these tracers were evaluated through the analyses of cores from the twelve sampling boreholes drilled into the flow domains. Examples of measured dye concentration versus borehole interval are shown in Figure 6.3.2-1 and Figure 6.3.2-2. The distribution of the tracers above the niche is used to assess the extent of tracer spreading and to provide data for the evaluation of seepage processes.

Tracer data are presented as dimensionless ratios of the detected tracer level to the background level. A higher ratio indicates the stronger presence of the tracer in the particular interval of a borehole. These detection ratios provide sufficient information about the spatial distributions of tracers, reconcile the difference in measurement techniques (i.e., ultraviolet/visible and fluorescence spectrophotometers), and eliminate the need to use and verify chemical purity information provided by the manufacturers. In Section 6.3.2.2 the measured dye distributions are illustrated in three dimensions based on as-built borehole survey coordinates using EARTHVISION-2 V4.0 software (STN: 30035–2 V4.0).

6.3.2.1 Detection of Tracers

Several dyes from previous applications of seepage tests (Section 6.2.1.3.1) were detected within the borehole samples, as summarized in Table 6.3.2-1. FD&C Blue No.1 was present in seven out of 12 boreholes, with some of the boreholes containing relatively high concentrations of the

tracer. Sulpho Rhodamine B was detected within four borehole samples. Overall, the dye distribution pattern was relatively spotty, reflecting the complex interplay of preferential flow paths and liquid application history. All of the previous liquid-release and seepage tests were conducted at least six months prior to the tracer-migration test (Section 6.3.1).

Table 6.3.2-1. Compilation of Tracer Detection Versus Borehole Location

Borehole ID	FD&C Blue No. 1	Sulpho Rhodamine B	FD&C Yellow No. 6	Pyranine	Acid Yellow 7	Amino G Acid
1	-	+++	-	-	-	-
2	+++	-	-	-	+++++	+
3	+++	-	-	-	-	-
4	-	-	-	-	-	-
5	-	-	-	-	-	-
6	-	-	-	-	-	-
7	+++++	+++++	+++	-	-	-
8	+++	-	-	-	-	-
9	+	-	-	-	-	-
10	+++	+++++	-	+	-	-
11	+++++	+	-	+++	-	-
12	-	-	-	-	-	-

DTN: LB990601233124.003 [106051]

NOTES: -: detection ratio < 3 (treated as absent).
+: the highest detection ratio is between 3 - 100 within this particular borehole.
+++: the highest detection ratio is between 100 - 1000 within this particular borehole.
+++++: the highest detection ratio is >1000 within this particular borehole.

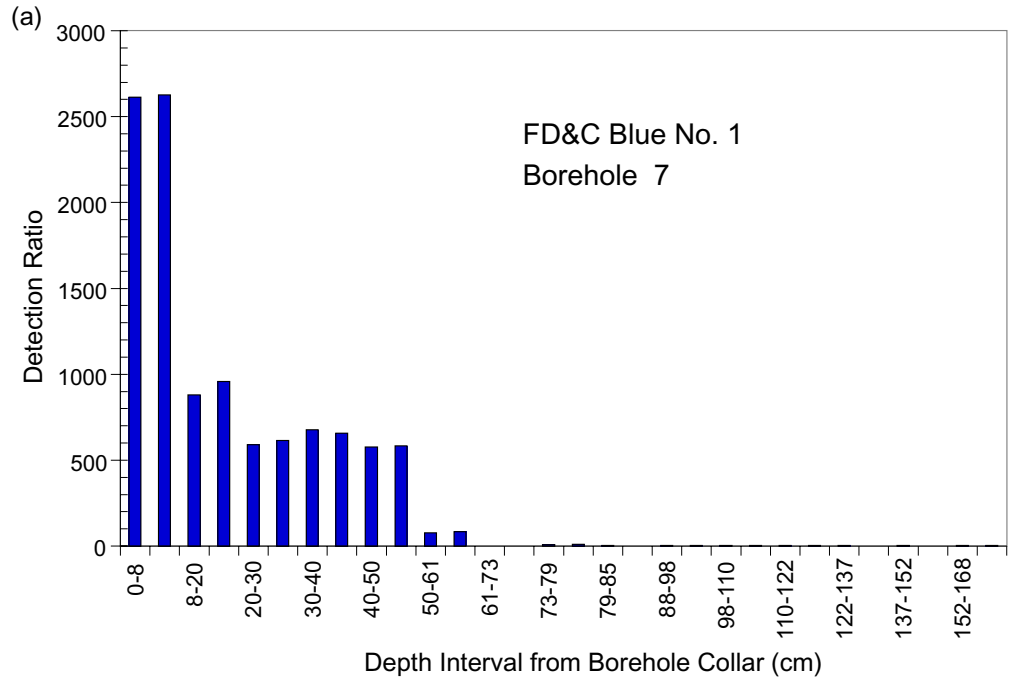

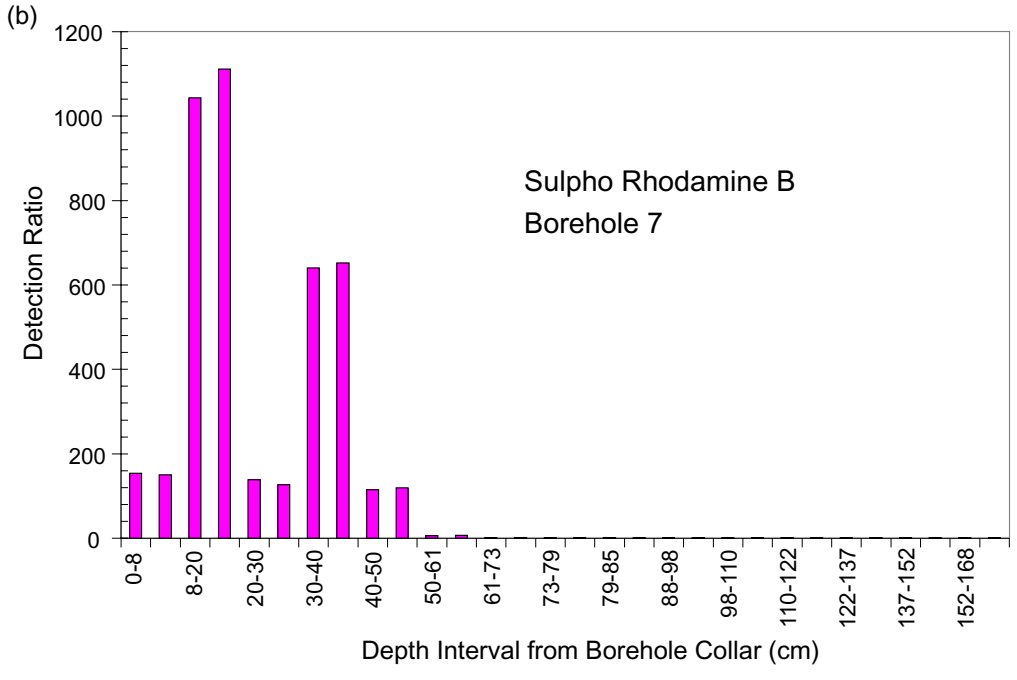

DTN: LB990601233124.003 [106051]

NOTE: Duplicate measurements were conducted in each specific interval.

Figure 6.3.2-1. Dye Detection along Borehole 7: (a) FD&C Blue No. 1, and (b) Sulpho Rhodamine B

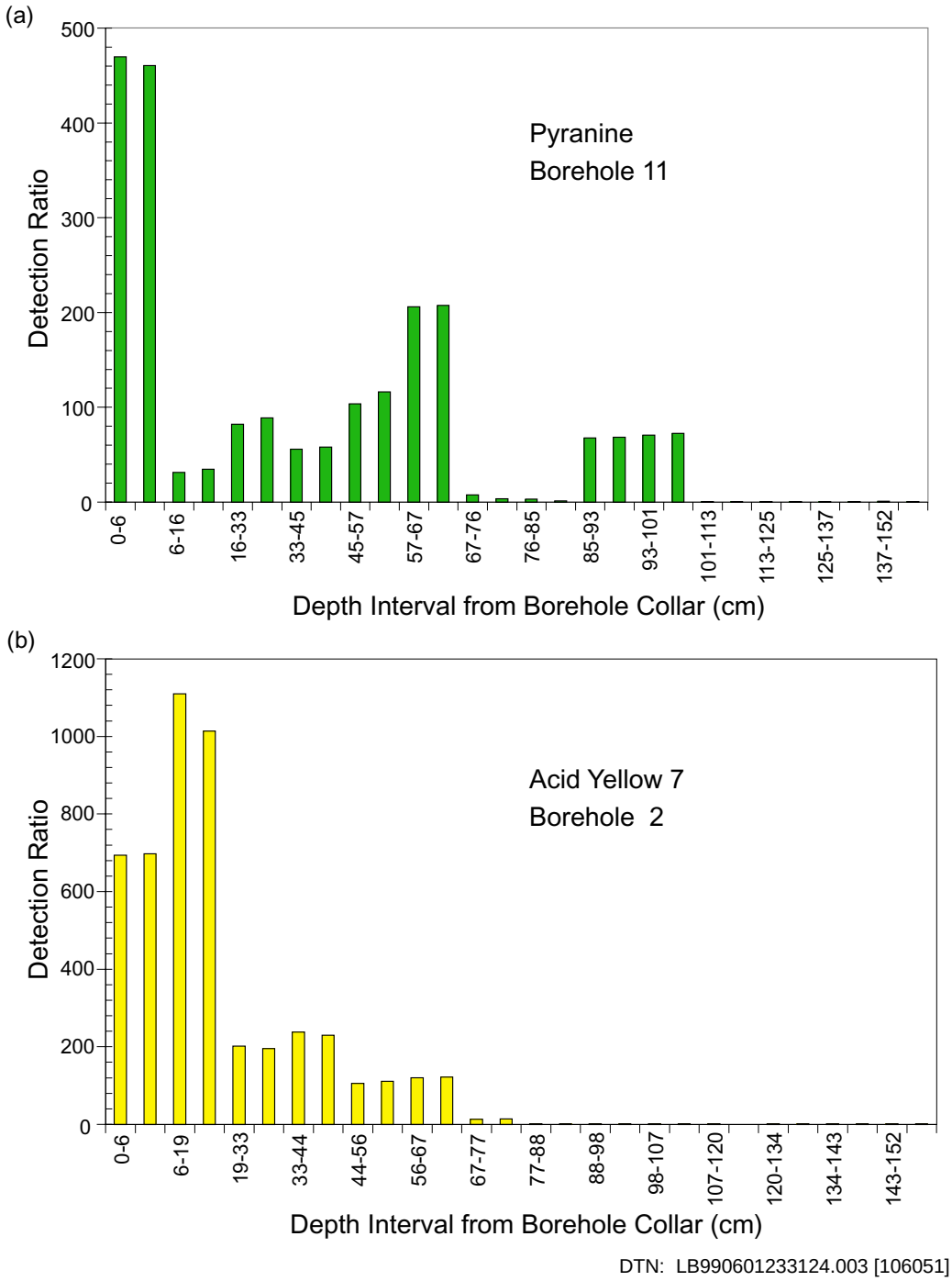

Figure 6.3.2-2. Dye Detection of: (a) Pyranine Along Borehole 11, and (b) Acid Yellow 7 along Borehole 2

6.3.2.2 Distribution of Dyes

FD&C Blue No. 1 was released in six intervals during pre-excavation liquid-release tests and in four intervals during post-excavation seepage tests (including one with a mixture of blue and yellow dyes). The blue dye distributions, together with release-interval locations, are illustrated in Figure 6.3.2-3. Boreholes where the tracer was not detected are represented by narrow lines. The multiple releases and dilutions introduced a complex application history. Overall results suggested that most regions containing blue dye were associated with tracer tests from nearby release intervals.

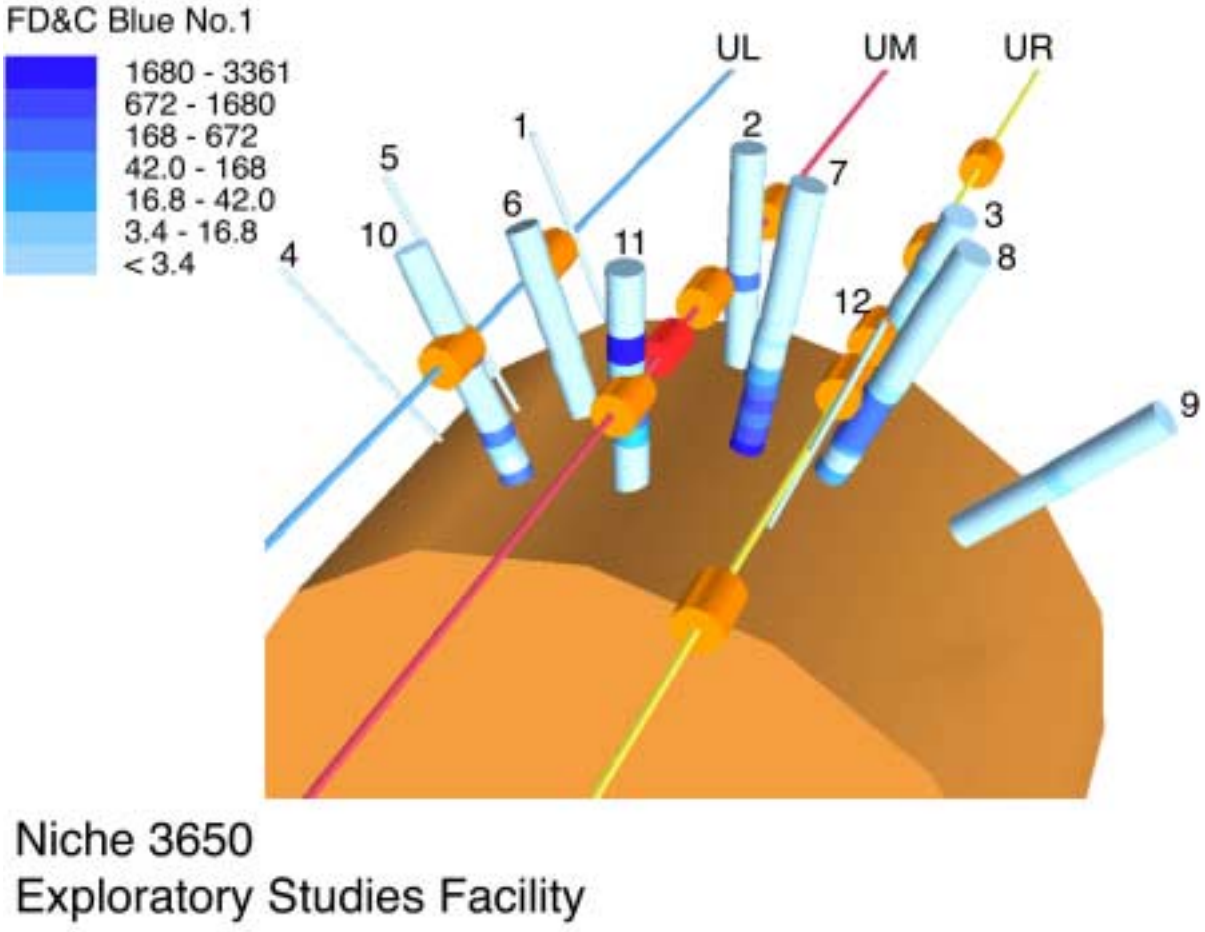

DTN: LB990601233124.003 [106051]

NOTE: The red cylinder denotes the tracer release interval of the tracer-migration test and the other orange cylinders for intervals of early-release events. The sampling boreholes are individually identified. Detection ratios (dimensionless) are presented in the legend.

Figure 6.3.2-3. Three-Dimensional View of FD&C Blue No. 1 Detection Related to the Release Intervals above the Niche

Sulpho Rhodamine B was used in eight seepage tests along seven borehole intervals. Figure 6.3.2-4 illustrates the results for Sulpho Rhodamine B. Near Borehole 7, Sulpho Rhodamine B was released once (in the interval UM 4.88–5.18 m), followed by three releases of water without dyes, and once with a mixture of FD&C Blue No. 1 and FD&C Yellow No. 6. The Sulpho Rhodamine B in Borehole 7, and near the niche ceiling in Borehole 8, most likely originated from this release episode. There was no Sulpho Rhodamine B detected in Boreholes 3, 9, and 12. This suggested that the Sulpho Rhodamine B was likely migrating downward, rather than spreading laterally.

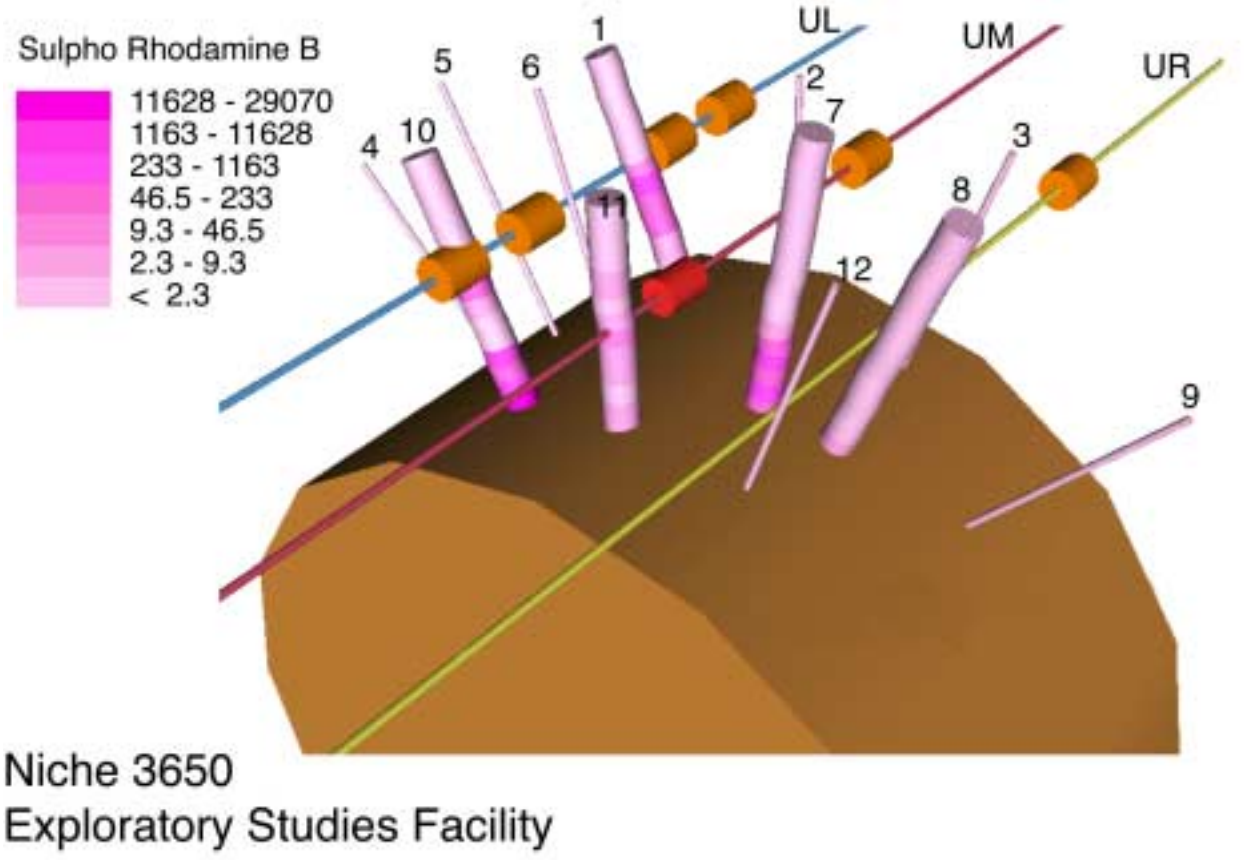

DTN: LB990601233124.003 [106051]

NOTE: The red cylinder denotes the tracer release interval of the tracer-migration test and the other orange cylinders for intervals of early-release events. The sampling boreholes are individually identified. Detection ratios (dimensionless) are presented in the legend.

Figure 6.3.2-4. Three-Dimensional View of Sulpho Rhodamine B Detection Related to the Release Intervals above the Niche

In Niche 3650, Pyranine, Acid Yellow 7, and Amino G Acid were used only once. Pyranine, Acid Yellow 7, and Amino G Acid are fluorescent dyes. The low detection limits achievable with the fluorescence spectrophotometer provide the confidence for the delineation of dye-stained flow paths within the sampling borehole array. Additionally, FD&C Yellow No. 6 was used once at UM 4.88–5.18 m within the sampling borehole array, and another time at Interval UL 7.62–7.92 m outside the borehole array (Figure 6.3.1-1a). The observations from these tracer

distribution also showed localized distributions of tracers, confirming downward migration (as opposed to lateral spreading as observed in the earlier tests).

Pyranine, for example, was detected at the nearby Boreholes 10 and 11, with its presence much lower at Borehole 10 than that at Borehole 11 (Table 6.3.2-1 and Figure 6.3.2-5). Borehole 11 is located almost exactly below the interval of UM 4.27–4.57 m where Pyranine was released. Four episodes of water-only seepage tests were conducted following this Pyranine application. These liquid releases did not seem to enhance extensive lateral spreading. Overall, the lateral spreading of Pyranine was observed to be about 0.75 m to the left (i.e., Borehole 10), resulting from these five release tests. However, its presence at Borehole 10 was only slightly above the background level.

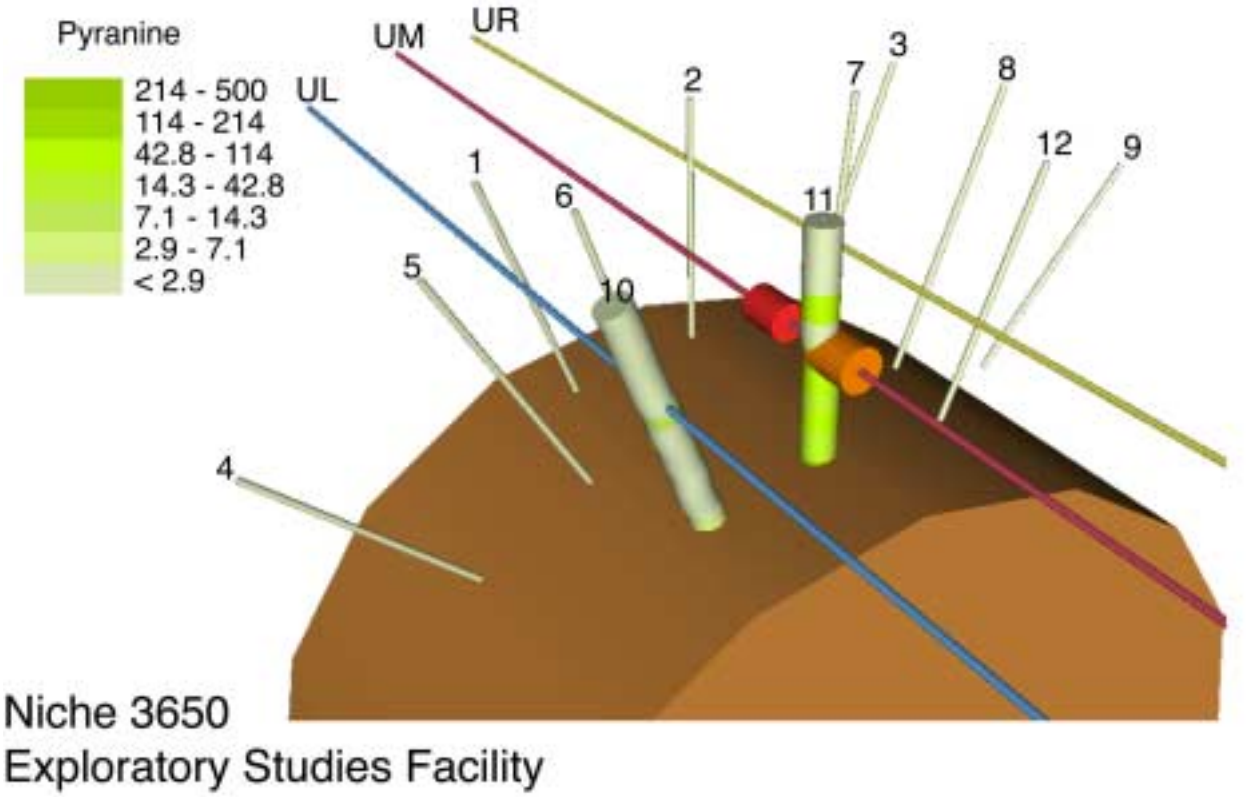

DTN: LB990601233124.003 [106051]

NOTE: The red cylinder denotes the tracer release interval of the tracer-migration test and the other orange cylinder for interval of an early-release event. The sampling boreholes are individually identified. Detection ratios (dimensionless) are presented in the legend.

Figure 6.3.2-5. Three-Dimensional View of Pyranine Detection Related to the Release Interval above the Niche

Acid Yellow 7 was detected only at Borehole 2, about 0.3 m from Interval UM 6.10–6.40 m where it was released (Figure 6.3.2-6). Amino G Acid was also detected near the detection limit at Borehole 2, about 0.3 m from Interval UM 5.49–5.79 m where it was released (Figure 6.3.2-7). Note that although the Interval UM 5.49–5.79 m was encompassed within the sampling borehole array, Amino G Acid was not detected in any other borehole.

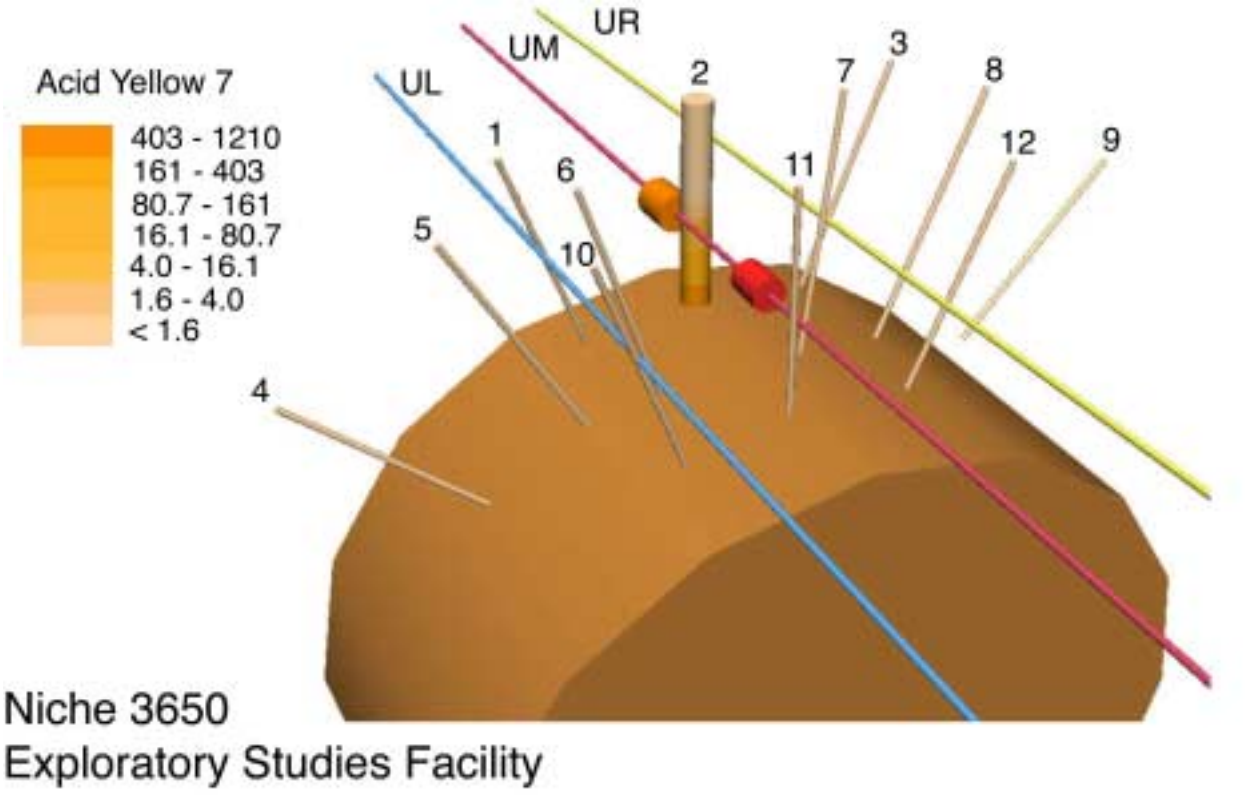

DTN: LB990601233124.003 [106051]

NOTE: The red cylinder denotes the tracer release interval of the tracer-migration test and the other orange cylinder for intervals of an early-release event. The sampling boreholes are individually identified. Detection ratios (dimensionless) are presented in the legend.

Figure 6.3.2-6. Three-Dimensional View of Acid Yellow 7 Detection Related to the Release Interval above the Niche

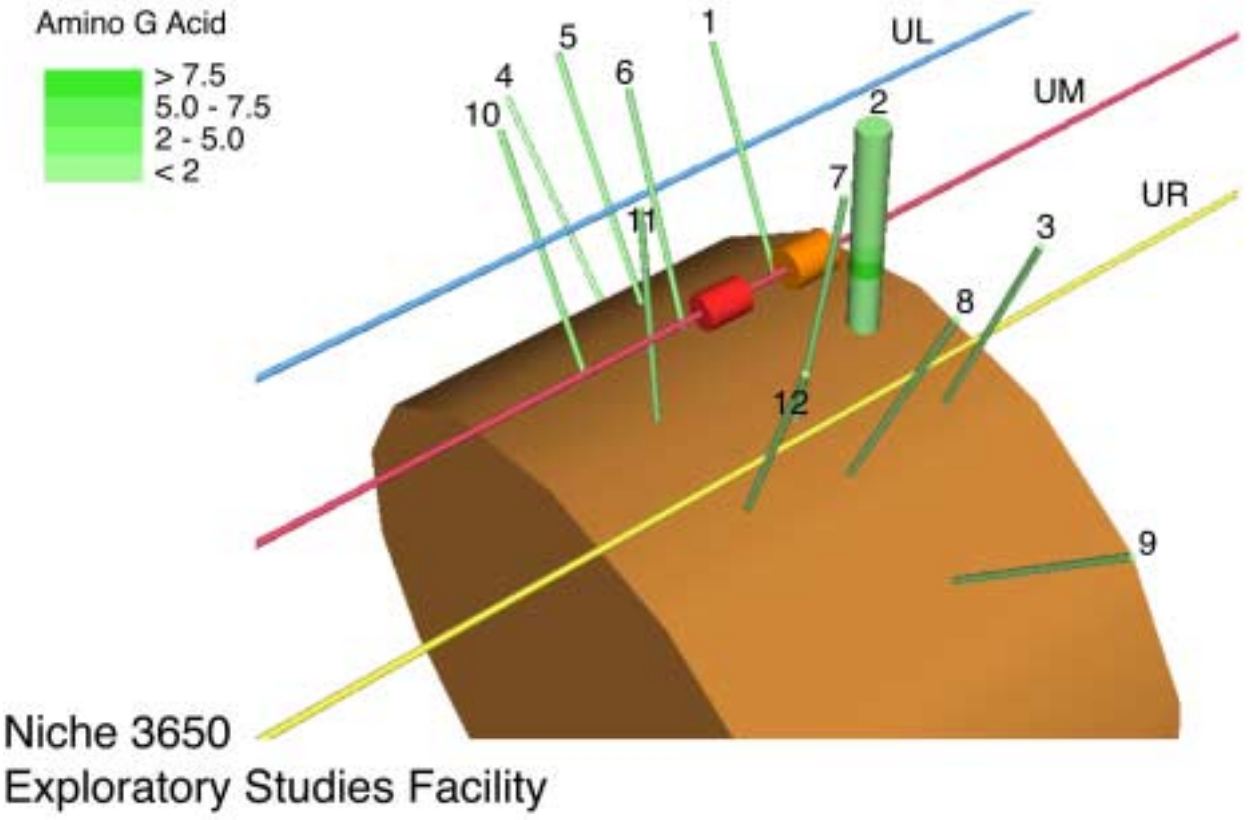

DTN: LB990601233124.003 [106051]

NOTE: The red cylinder denotes the tracer release interval of the tracer-migration test and the other orange cylinder for interval of an early-release event. The sampling boreholes are individually identified. Detection ratios (dimensionless) are presented in the legend.

Figure 6.3.2-7. Three-Dimensional View of Amino G Acid Detection Related to the Release Interval above the Niche

The last dye distribution shown is for FD&C Yellow No. 6 (Figure 6.3.2-8). The dye was present at Borehole 7. Borehole 7 was about 0.5 m from Interval UM 4.88–5.18 m where both FD&C Yellow No. 6 and FD&C Blue No. 1 were simultaneously released. This release episode had one of the lowest release rates (0.013 g/s) with one of the largest release volumes (5,597 g) among all the liquid-release tests conducted at Niche 3650 (see Section 6.2 of this report). Borehole 7 is located in the middle of the sampling borehole array. The observation that FD&C Yellow No. 6 was only present in Borehole 7 further demonstrated the localized characteristics of liquid flow with limited lateral spreading, even in this case with comparatively large release volume.

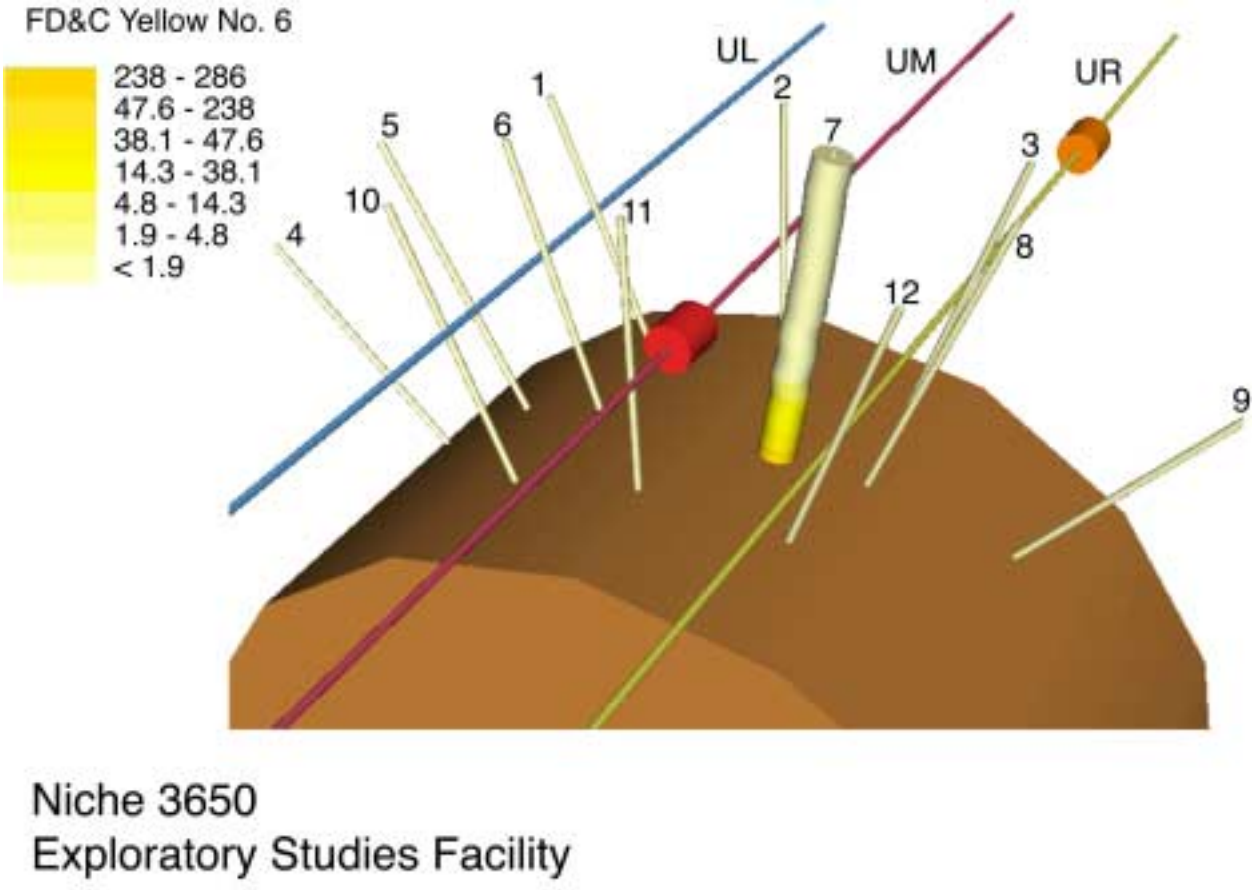

DTN: LB990601233124.003 [106051]

NOTE: The red cylinder denotes the tracer release interval of tracer-migration test and the other orange cylinders for intervals of early release events. (One of the two release intervals is the same as the last release event, represented by the red cylinder.) The sampling boreholes are individually identified. Detection ratios (dimensionless) are presented in the legend.

Figure 6.3.2-8. Three-Dimensional View of FD&C Yellow No. 6 Detection Related to the Release Intervals above the Niche

The dye distribution plots also indicated that some dyes have migrated above the injection intervals, as illustrated in Figure 6.3.2-3 for FD&C Blue No. 1, in Figure 6.3.2-5 for Pyranine, and to a lesser degree in Figure 6.3.2-4 for Sulpho Rhodamine B, in Figure 6.3.2-6 for Acid Yellow 7, and in Figure 6.3.2-7 for Amino G Acid. This is an interesting observation, indicating that fairly strong capillary forces may induce upward movements against gravity. Similar behavior was also observed in the Busted Butte test, as described in Section 6.13.3.1.1. However,

further verification would be needed to determine the exact spatial extents of upward suction and tracer distribution. The locations of subsamples were derived from sample packets, and the spatial resolutions were poor, especially for fragmented core samples. The tracer subsample locations could be further checked against borehole logs (digital version if available) and core logs to improve spatial resolution.

6.4 ANALYSES OF TRACER PENETRATION AND WATER IMBIBITION INTO WELDED TUFF MATRIX

The objectives of this study are to investigate water flow and tracer transport, focusing on the relative extents of fracture flow and fracture-matrix interaction in the unsaturated, fractured tuff through a combination of field and laboratory experiments. Fieldwork was conducted in the ESF niches with liquid-containing tracers released at specified borehole intervals. Tracer-stained rock samples were collected during niche excavation for subsequent laboratory analyses. Clean rock samples, collected from the same stratigraphic unit, were machined into cylinders for laboratory studies of tracer penetration into the rock matrix under different initial water-saturation levels. The use of laser-ablation inductively-coupled-plasma mass spectrometry (LA-ICP-MS) to investigate chemical transport and sorption in unsaturated tuff is also presented.

6.4.1 Penetration of Dyes into Rocks from the Niches

Samples for laboratory analyses were collected from Niche 3650 and Niche 4788. The niche test sites, borehole configurations, liquid-release tests, and tracers used in the field are described in Section 6.2 and Section 6.3. Laboratory tests under controlled conditions were conducted to compare the travel front behavior of moisture, nonreactive bromide, and sorbing dye tracers (FD&C Blue No. 1 and Sulpho Rhodamine B). Sample drilling and tracer profiling techniques were developed. The descriptions and evaluations of laboratory analyses are presented in Attachment V.

6.4.1.1 Field Observations

During the niche excavation, as described in Section 6.2.1.2, dye was observed along individual fractures and intersecting fractures to a maximum depth of 2.6 m below the liquid-release points at Niche 3650, and to a maximum depth of about 1.8 m at Niche 4788. In general, the dye remained relatively close to the release interval and did not spread laterally more than 0.5 m. Figure 6.4.1-1 is a photograph taken during the excavation of Niche 4788 showing the wall face with the fracture network stained by FD&C Blue No. 1. Results of post-excavation liquid-seepage tests at Niche 3650 also indicated fast fracture flow with limited lateral spreading, as seepage water was captured directly below in trays beneath or immediately adjacent to the test interval.

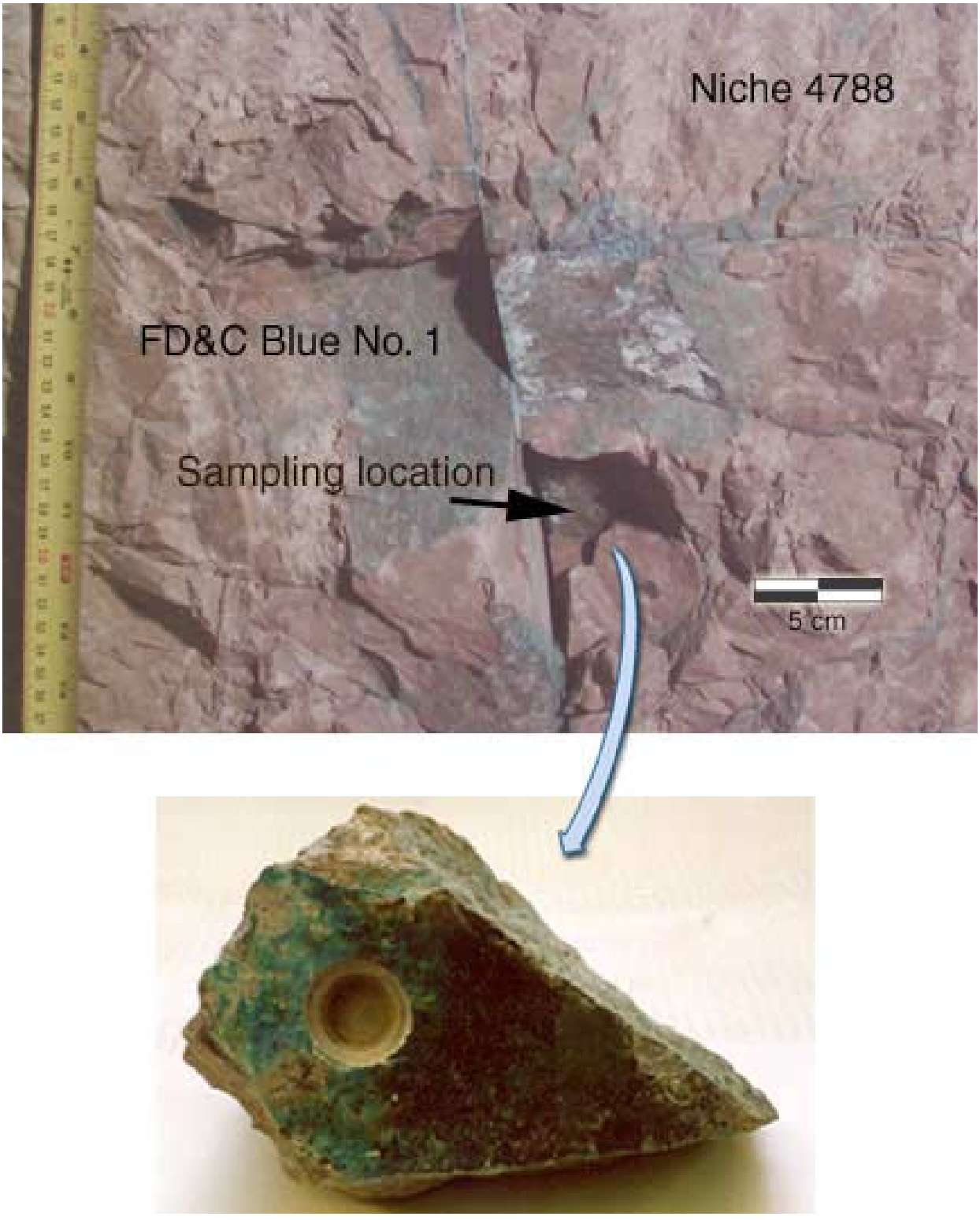

SOURCE: YMP-LBNL-JSW-6C (Wang 1999 [153449], pp. 69–71)

Figure 6.4.1-1. Photograph showing the wall face with fracture network and sampling location of rock. Stained by FD&C Blue No. 1 during Niche Excavation at Niche 4788

6.4.1.2 Dye Penetrations into Rocks

Visual inspection of dyed rocks collected from the field studies showed that the dye stained the fracture surfaces and the color decreased with the distance and disappeared within a few millimeters from the fracture surfaces (Figure 6.4.1-1). The plot of Sulpho Rhodamine B detection ratio versus depth from the fracture surface is shown in Figure 6.4.1-2. (The dimensionless detection ratio is the measured tracer level divided by the background level.) The depth on the x-axis denotes the mid-point of the drilling interval. For example, the measured tracer concentration from a 1–2 mm drilling interval is shown at the 1.5 mm location from the sample surface. For three rock samples stained with either FD&C Blue No.1 or Sulpho Rhodamine B, each dye concentration decreased from the highest concentration to the background level in less than 6–7 mm. These results quantify the noticeable tracer matrix imbibitions from liquid flowing through the fractures.

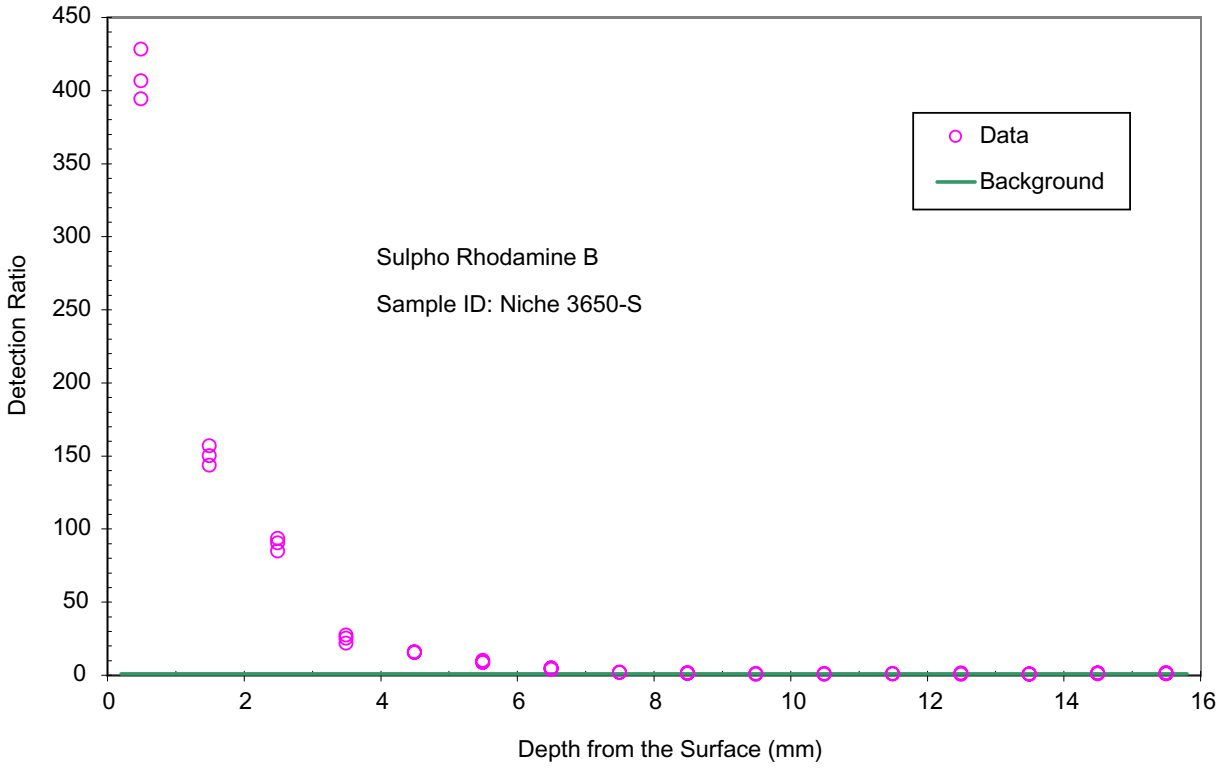

Figure 6.4.1-2. Sulpho Rhodamine B Penetration Profiles into Rock Matrix from the Fracture Surface

Table 6.4.1-1 provides relevant experimental conditions used during the liquid-release tests resulting in the three dyed rock samples collected during excavation. The samples were collected 7–13 days after the dye-spiked water was released into the formation. Water flow in post-excavation seepage tests was found to be very rapid, traversing 0.65 m in 4 minutes under the release rate of about 1.9 g/s (Table 6.4.1-2). It is therefore expected that the fluid-rock contact time is relatively short. Short travel times, together with high ratios of dye concentration in seepage water versus release water (in the far-right column of Table 6.4.1-2), indicated that the

contacts between flowing water in the fractures and the adjacent tuff matrix were highly transient. The exact duration of contacts on the fracture surfaces could not be measured.

Table 6.4.1-1. Liquid Release Tests and Experimental Conditions

Tracer	Test Date	Test Location [c]	Tracer Conc. (g/l)	Release Rate (g/s)	Release Duration (min)	Mass Released (g)	Sampling Date
Sulpho Rhodamine B [a]	8/8/97	ML 6.71–7.01 m	2.0	2.0	8.22	170.9	8/19/97
FD&C Blue No. 1 [a]	8/6/97	UM 6.71–7.01 m	7.7	1.9	8.20	438.7	8/19/97
FD&C Blue No. 1 [b]	7/2/98	UM 6.40–6.70 m	6.77	0.49	35.0	1019.7	7/9/98

DTN: LB980001233124.004 [136583], LB980901233124.003 [105592]

NOTES: [a]Tests conducted at Niche 3650 m location.

[b]Test conducted at Niche 4788 m location.

[c]UM: upper middle borehole; ML: middle left borehole. Depth measurement (in meters) is from the collar of the borehole to the test interval.

Table 6.4.1-2. Post-Excavation Tracer Release Tests at Niche 3650

Tracer	Test Location [a]	Release Rate (g/s)	Mass Released (g)	Mass of Seepage Recovered (g)	Wetting Front Arrives at (min:sec) [b]	Ratio of Seepage vs. Release Conc. (%)
Sulpho Rhodamine B	UL 7.01 – 7.32 m	1.949	1005.5	16.0	4:00	95.6
FD&C Blue No. 1	UR 4.27 – 4.57 m	0.198	995.7	4.0	56:08	77.0
FD&C Blue No. 1	UR 4.88 – 5.18 m	0.190	1016.4	4.0	29:50	103.9

DTN: LB980001233124.004 [136583]

NOTES: [a]UL: upper left borehole; UR: upper right borehole. Depth measurement (in meters) is from the collar of the borehole to the test interval.

[b]Time wetting front arrives at Niche ceiling following the start of water release to the formation.

Summary data are contained in DTN: LB990901233124.003 [155690]

6.4.1.3 Fast Fracture Flow

Fast fracture flow was demonstrated during the post-excavation seepage tests where dye-spiked water was released and collected, if possible, at the collection system below the niche ceiling. The last column of Table 6.4.1-2 shows the ratios of collected to released concentrations for FD&C Blue No. 1 and Sulpho Rhodamine B. Average seepage versus release-concentration ratio is 92.2 ± 13.8% over three tests with dyes. The seepage solution is a composite sample, which could be diluted from the resident water, if any, in the flowing fractures. Also, note that the release concentrations were obtained from the known dye mass dissolved in the known liquid, and no liquid sample was collected for the released solution during these tests. This uncertainty could contribute to the unphysical ratio of 103.9% for one of the FD&C Blue No. 1 tests. Significant dilutions (about 1,000 times), needed to bring down the sample concentration within

the linear standard curve needed for measurement, could also contribute to the uncertainty. More accurate ratios could be obtained if both the seepage and release solutions were measured simultaneously.

6.4.1.4 Concentration of Dye Tracer at Saturated Contact

For the dye-stained samples from the field, tracer concentrations were measured on rock powders collected from drilling intervals of the rock. Tracer concentrations on the solid mass basis (C_g, mg/kg) were transformed to the tracer concentration on the liquid basis (C_v, mg/l) using the following relationship:

$$C_v = C_g \times (\rho_b / \ \theta) \qquad \text{(Eq. 6.4.1-1)}$$

where ρ_b is the bulk density (g/cm^3) and θ is the volumetric water content (cm^3/cm^3). With this conversion, measured tracer concentrations can be compared directly with concentration of released water. Measured bulk density (2.238 ± 0.029) and porosity ϕ (0.0877 ± 0.009) for 15 core samples were used in the calculations (DTN: LB990901233124.003 [155690]).

The primary interest in the tracer concentration profiles is on the first several millimeters from the fracture surface. Table 6.4.1-3 presents the results of the first sampling interval (0–1 mm from the fracture surface) for different field samples, as well as laboratory core samples (discussed below). For the three dye-stained samples collected in the field, two samples were from seepage tests at Niche 3650 with FD&C Blue No.1 (sample Niche 3650-F) and with Sulpho Rhodamine B (sample Niche 3650-S). These tests results, based on low volumetric concentration ratios C/C_0 (e.g., measured C_v divided by the released concentration C_0) of 17.2% and 23.3% for the first sampling intervals (i.e., 0–1 mm), is associated with matrix imbibition from fast transient flows through open fractures. Noticeable water and tracer imbibition into the surrounding matrix was observed even though fracture flow can be fast. The average value over these two samples is 20.3 ± 4.3%. The concentration profile for FD&C Blue No. 1 dye is presented in Figure 6.4.1-3a.

Table 6.4.1-3. Compilation of C/C_0 Value for Rock Drilling Taken at the 0–1 mm Interval

Sample ID	Initial Saturation S_w (%)	Tracer	C/C_o (%) [a]
Niche 3650-F	Not known	FD&C Blue No. 1	17.2±0.5
Niche 3650-S	Not known	Sulpho Rhodamine B	23.3±0.1
Niche 4788	Not known	FD&C Blue No. 1	105.5±0.6
Core D	12.5	Bromide	138.1±3.6
Core E	12.2	Bromide	135.1±3.7
Core F	15.2	Bromide	108.7±2.8
Core J	83.0	Bromide	91.4±2.1
Core H	75.8	Bromide	104.9±2.9
Core D	12.5	FD&C Blue No. 1	281.6±1.8
Core H	75.8	FD&C Blue No. 1	220.3±1.9
Core D	12.5	Sulpho Rhodamine B	272.2 ± 0.1
Core H	75.8	Sulpho Rhodamine B	271.7±0.1

DTN: LB990901233124.003 [155690]

NOTE: [a] Average of data ± background (triplicate measurements)

The third data point of 105.5% ratio in Table 6.4.1-3 is associated with the sample shown in Figure 6.4.1-1. The sample was adjacent to a vertical fracture that apparently dead-ended near the sampling location. The full profile is illustrated in Figure 6.4.1-3b. For this sample, the fluid-rock contact time could have been longer, contributing to the higher concentration ratio at the first interval. The measured volumetric concentration ratio in the second (1–2 mm) interval drops drastically to 12.5%, which is similar to the other two rock samples. With longer contact time, stronger surface sorption of the dye might also have occurred in this rock sample.

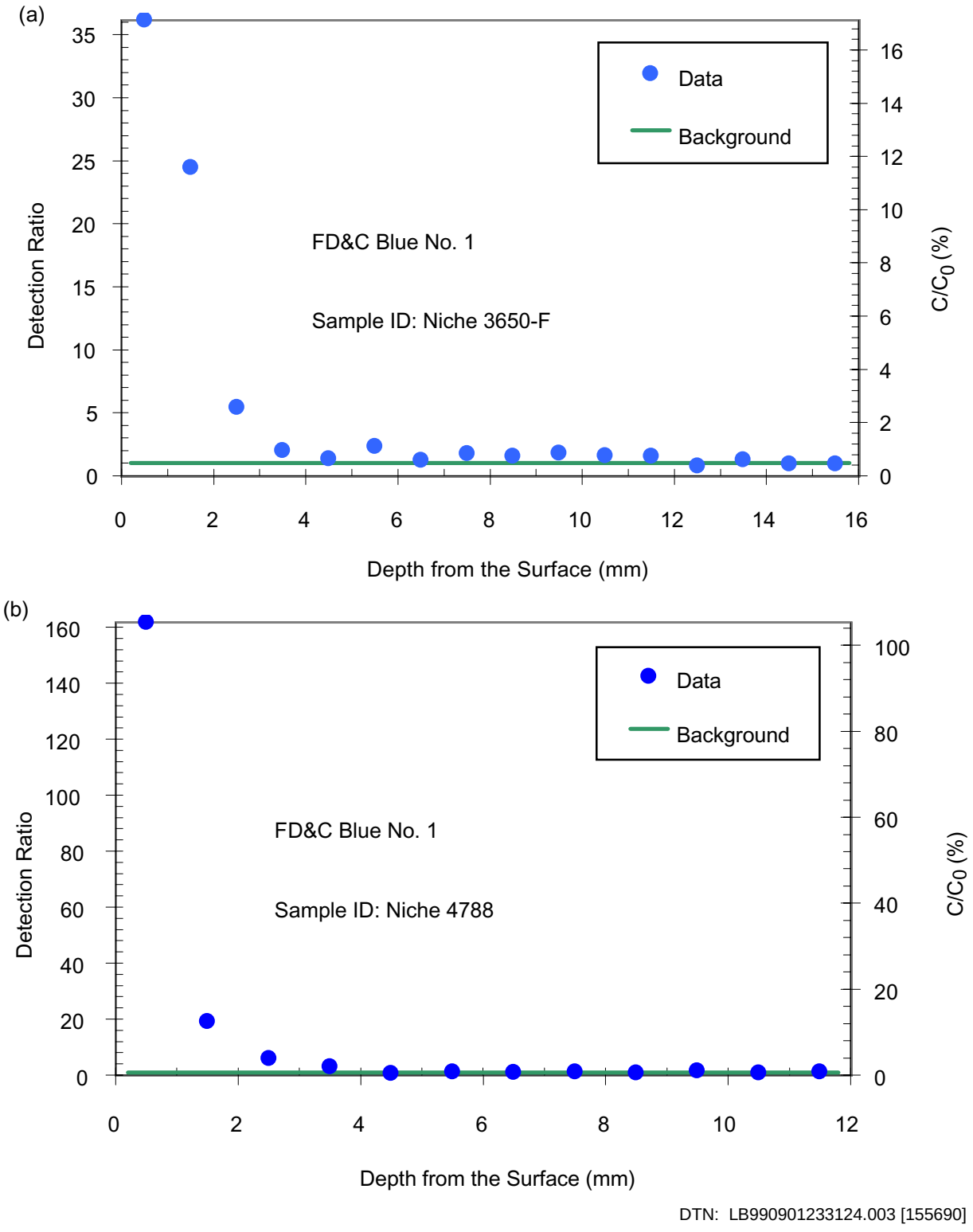

DTN: LB990901233124.003 [155690]

Figure 6.4.1-3. Tracer Penetration Profile into Rock Matrix from the Fracture Surface: (a) FD&C Blue No.1 at Niche 3650, (b) FD&C Blue No.1 at Niche 4788

6.4.2 Retardation and Tracer Front Movement

Laboratory tests were conducted to quantify the imbibition of water and the retardation of tracers into rock cores. In the laboratory, tests can be conducted under controlled conditions, with concentrations in rock samples and in the core reservoir measured simultaneously. The flow paths along cores are well defined compared to the flow paths in the field. The laboratory test results can assist in interpreting data collected on dye-stained samples from the field tests.

There are two approaches presented for measuring the retardation factor: front separation and local "saturated" measurements at the core-reservoir contact. The consistency between these two approaches lends credence to the quantification of retardation factors on core samples.

6.4.2.1 Dye Retardation Factor Determined by Front Separation

The descriptions and evaluations of laboratory tracer tests on core samples are presented in Attachment V. Figures 6.4.2-1 and 6.4.2-2 compare the concentration profile of nonreactive bromide with the concentration profiles of both FD&C Blue No. 1 and Sulpho Rhodamine B, relative to the moisture fronts obtained from visual inspection. The dyes lag behind the bromide front, indicating dye sorption to the rock. FD&C Blue No. 1 and Sulpho Rhodamine B were the most visible in the tuffs of the tested dyes. Sorption of these dyes on rock is not surprising considering their complex chemical structure with various functional groups, even though they are negatively charged under normal pH conditions.

From the tracer profiles, the retardation factor R can be derived as the ratio of travel distance of nonreactive tracer divided by the travel distance of sorbing tracer. Bromide is assumed to be a nonreactive tracer in tuff, as indicated by its nearly coincident front with the wetting front at low initial water saturation. In Figure 6.4.2-1 for Core D at low initial saturation, the bromide front is located at 17−18 mm from the core bottom ($d_{0.5}$ = 17.5 mm, where $d_{0.5}$ is the depth at which the concentration is half of the steady-state concentration in the profile). The first data point at the 0-1 mm interval was excluded for bromide front determination. The 0−1 mm interval measurement was systematically higher than deeper intervals and was consistently observed for bromide in all core measurements. Because the 0–1 m interval at the core-reservoir interface is in direct contact with the tracers, it is not included in the calculation of the travel distance used to determine the retardation factor R. This does not seem to affect the sorbing tracers (FD&C Blue No. 1 and Sulpho Rhodamine B), as evident in the steady-state concentration of the first three intervals in Core D (Figure 6.4.2-1). For the sorbing tracers, $d_{0.5}$ is located at 3.5 mm (Figure 6.4.2-1). The retardation factor for both dyes is estimated to have the value 5 (= 17.5 mm/3.5 mm). Similarly, R is estimated to be 2.33 (= 3.5 mm / 1.5 mm) for both dyes in Core H with high initial S_w (Figure 6.4.2-2).

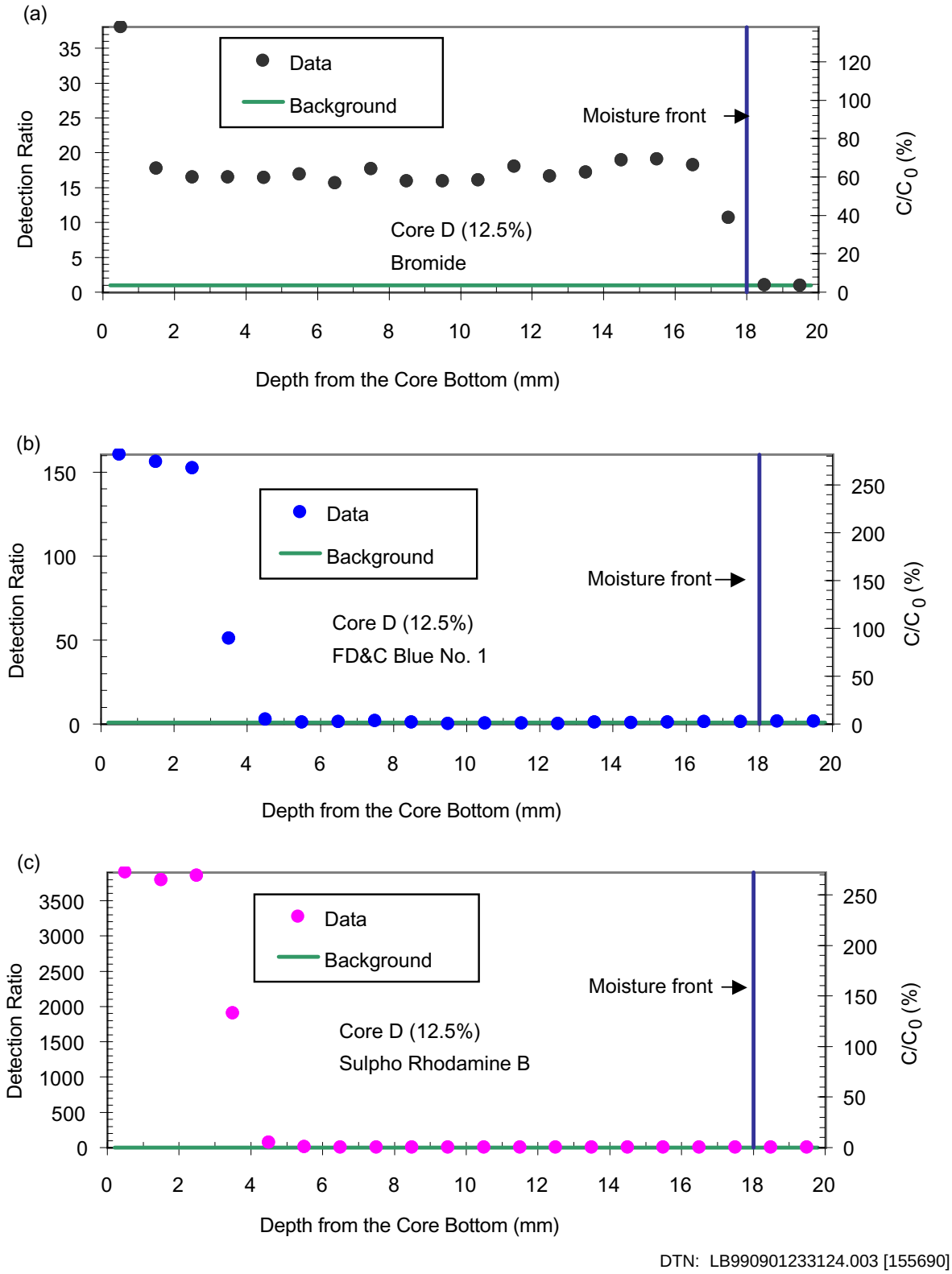

DTN: LB990901233124.003 [155690]

Figure 6.4.2-1. Comparison of Tracer Concentration Profiles in a Low-Initial-Saturation Core: (a) Bromide, (b) FD&C Blue No. 1, (c) Sulpho Rhodamine B. Core D had initial saturation of 12.5% and was in contact with saturated boundary for 19.5 hours

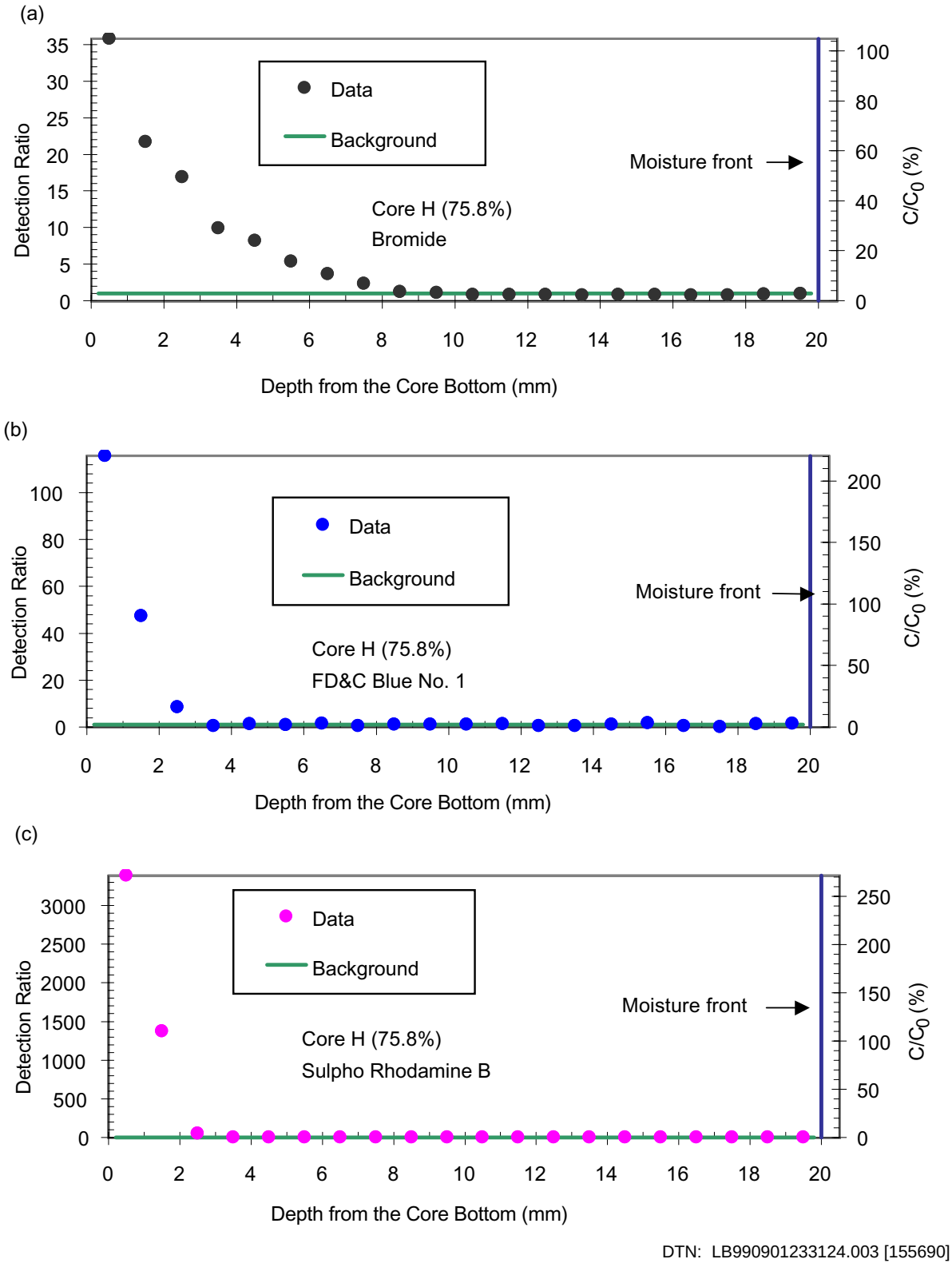

DTN: LB990901233124.003 [155690]

Figure 6.4.2-2. Comparison of Tracer Concentration Profiles in a High-Initial-Saturation Core: (a) Bromide, (b) FD&C Blue No. 1, (c) Sulpho Rhodamine B. Core H had initial saturation of 75.8% and was in contact with saturated boundary for 17.9 hours

The saturation dependence of the retardation factor is derived from the following functional relationship (Porro and Wierenga 1993 [134083], pp. 193–194):

$$R = 1 + \rho_b \times K_d / \theta \qquad \text{(Eq. 6.4.2-1)}$$

where K_d (mL/g) is the sorption distribution factor representing the distribution of solutes between aqueous and solid phase, ρ_b is the bulk density (g/mL), and θ is the water content. This equation explicitly shows that solute retardation is inversely related to water content. If the effective θ value is estimated as the average of the initial water content and the final water content (here assumed to be the measured porosity), the K_d value can be derived from the R-value. For the two core samples, the K_d value was calculated to be 0.089 mL/g for Core D and 0.047 mL/g for Core H. The bulk density and porosity values for each core were measured independently, with values listed in Table 6.4.2-1. These measured values in Table 6.4.2-1 were used in calculating K_d values from measured R values.

Table 6.4.2-1. Measured Properties for Core Samples

Sample ID	Porosity (cm^3/cm^3)	Bulk Density (g/cm^3)
Core D	0.0888	2.248
Core E	0.0849	2.251
Core F	0.0890	2.239
Core H	0.0896	2.245
Core J	0.0823	2.266

DTN: LB990901233124.003 [155690]

As an additional consistency check, the calculations can be inversed and the R values derived from the K_d values for a fully saturated condition (i.e., 100% saturation). The $R_{100\%}$ is 3.25 for Core D and 2.17 for Core H from the inverse calculations. The average $R_{100\%}$ is 2.71 ± 0.76 for both FD&C Blue No. 1 and Sulpho Rhodamine B. Both K_d value and $R_{100\%}$ are constants independent of saturation. The simple checking verifies the functional relationship of Equation 6.4.2-1. For comparison, Andreini and Steenhuis (1990 [106071], pp. 85, 98) found that the retardation factor for FD&C Blue No. 1 ranged from 1.5 to 7 in a fine, sandy loam soil.

6.4.2.2 Dye Retardation Factor Measured at Saturated Contact

Another way to evaluate the test data is to compare the saturated $R_{100\%}$ with the measured concentration ratios at the core contact boundary. The 0–1 mm interval of a core sample is placed in direct contact with water containing tracers in the laboratory tests and therefore is at nearly saturated conditions. The ratio C/C_0 is a direct measure of the retardation factor or the effects of sorbing-tracer accumulation. For the two tests with each dye in Table 6.4.1-3, the averaged values for C/C_0 are 2.51 for FD&C Blue No. 1, 2.72 for Sulpho Rhodamine B, and 2.61 ± 0.28 over both dyes. These values can be compared to the $R_{100\%}$ value of 2.71 ± 0.76. With the small number of samples (two cores, two tracers), the consistency with different approaches is

encouraging. For comparison, the average of five tests with bromide in Table 6.4.1-3 is 1.16 ± 0.20 for this presumably nonreactive tracer.

Note that the core measurements presented in this study can generate K_d values for intact rock under *in situ* partially saturated conditions. Most of the K_d values for sorbing solutes have been acquired by batch experiments using crushed rock, with the sizes chosen more or less arbitrarily and mainly for experimental convenience. The batch experiments were performed under saturated conditions with large water/rock ratios. There are concerns regarding the use of crushed-rock samples versus solid-rock samples in batch experiments on tuff rocks. The water/rock ratios used in the sorption experiments with crushed samples were large in comparison with the water/rock ratios likely to exist in the UZ. The laboratory approach with core analyses presented here could be adopted to generate more representative K_d values for radionuclide transport in the UZ.

6.4.2.3 Extent of Fracture-Matrix Interaction

The laboratory-tested core samples in contact with water containing sorbing dyes were shown to accumulate high concentrations in the first 1 mm interval, with the average concentration ratio C/C_0 (%) of 261 ± 28% from the last four entries in Table 6.4.1-3. The first two entries in the table, as discussed in Section 6.4.1.2 and Section 6.4.1.3, were associated with two field samples stained by relative fast flows activated by the pulsed releases used in seepage tests. The average concentration ratio of 20.3 ± 4.3% was much lower than the corresponding laboratory core values. The dilution factor of 7.7% (= 20.3%/261%) represents the percentage of tracer water imbibed into the 0–1 mm interval of the matrix adjacent to the flowing fracture relative to laboratory core samples. In other words, it quantifies the extent of fracture-matrix interaction (i.e., matrix imbibition for experimental conditions) for the fracture dominated flow in the field relative to the laboratory experiments.

6.4.2.4 Travel-Front Separation

As a nonreactive tracer, bromide is frequently used for flow tracking. The bromide front is comparable to the moisture front in the rock core at the initial water saturation of 12.5%, as illustrated in Figure 6.4.2-1a. The bromide front lags significantly behind the moisture front at the higher initial water saturation of 75.8%, as shown in Figure 6.4.2-2a. Note that the core top (20 mm) was wet when the experiment was ended, although the moisture front is shown at the 18 mm location in Figure 6.4.2-1b. This observation of nonreactive solute front lagging behind the moisture front agrees with the findings in moist soils (Warrick et al. 1971 [106150], pp. 1216, 1221; Ghuman and Prihar 1980 [106099], pp. 17, 19; Porro and Wierenga 1993 [134083], pp. 193, 196). Warrick et al. (1971 [106150]) first reported that the advance of a solute front was highly dependent on the soil moisture content during infiltration. During infiltration, no solute was found in the advancing wetting front where soil moisture contents were increasing, although the initially infiltrating water contained nonreactive tracer. The importance of this front separation, observed under a transient flow condition, might be more pronounced for low porosity materials under high moisture saturation, such as tuff at Yucca Mountain. Under these circumstances, a relatively small amount of invading solution can push the antecedent water further into the matrix.

For the imbibition experiment in Core D with low initial water saturation, the bromide front is sharp, with the strong capillary force driving the advection-controlled transport. Conversely, for the Core H with high initial water saturation, the bromide front is quite diffuse, since dispersion and dilution become important processes (on account of weaker capillarity) compared to advective flow. Sharp and diffused front separations between the bromide nonreactive tracer front and the moisture front, as well as between sorbing tracer front and bromide front, would provide the data for elucidating flow and transport in unsaturated, fractured tuff.

6.4.3 Application of LA-ICP-MS to Investigate Chemical Transport and Sorption

Laser ablation refers to the process in which an intense burst of energy delivered by a short laser pulse is used to vaporize a minute sample from a specific location. Chemical composition of the vaporized sample is then analyzed with inductively coupled plasma-mass spectrometry (ICP-MS). Laser ablation, coupled with ICP-MS (LA-ICP-MS), has recently evolved as a powerful analytical tool for solid samples (Russo et al. 2000 [155697]). LA-ICP-MS can determine simultaneously a large number of chemical elements with very low detection limits. The applications of LA-ICP-MS have been recently reported in studies of tree rings, airborne particulates, and geochemistry. However, we are not aware of any studies where transport, sorption, or diffusion of contaminants in rocks are investigated by LA-ICP-MS. The high spatial resolution achieved by a focused laser beam makes LA-ICP-MS a very attractive approach to such environmental-pollution studies.

This section describes the investigation of transport and sorption of chemicals that are of interest to the Yucca Mountain Project in unsaturated tuff. Laboratory tracer imbibition tests are similar to those presented in Attachment V, except that an initially dry tuff cube (1.5 cm in each side) was used in this LA-ICP-MS work, compared to core cylinders used in the drilling work as described in Section 6.4.1 and Section 6.4.2. Compared to the drilling technique presented in Attachment V, employment of LA-ICP-MS provides a quick way of profiling tracer chemical concentration with high spatial resolution. Surrogate compounds are chosen based on their chemical similarity to radionuclides of interest. The tracer solution used in this study contained a mixture of NaBr, $NaReO_4$, CsBr, and RbBr. Both Br^- and perrhenate (ReO_4^-) are used as nonsorbing tracers, with perrhenate serving as an analog to technetium, which exists in a form of pertechnetate ($^{99}TcO_4^-$). Cesium (Cs^+) and rubidium (Rb^+) were used as cationic tracers to examine the sorption effect on delayed transport of radionuclides in unsaturated tuff. Non-radioactive cesium is directly used for radioactive ^{137}Cs. Experimental conditions and analyses are recorded in Scientific Notebook YMP-LBNL-JSW-QH-1E (Hu 2000 [156473] pp. 130–136, 145–146).

Figure 6.4.3-1 shows the spatial-distribution results obtained from LA-ICP-MS profiling for the tuff cube face in contact with the tracer solution. Intensity in the Y-axis indicates the signal, measured by ICP-MS, from the laser-abated mass for both the applied tracers and elements (Al, K, Ce, Th) intrinsic to the tuff sample. Peterman and Cloke (2001 [155696]) reported a very uniform distribution of elemental compositions in tuff. Signals shown in Figure 6.4.3-1 are in direct relationship to the reported elemental compositions: percent weight level for Al and K, trace (parts per million) level for Ce and Th. As expected, the spatial distribution of all elements measured is fairly uniform, because this cube face was in contact with the tracer solution throughout the imbibition test duration.

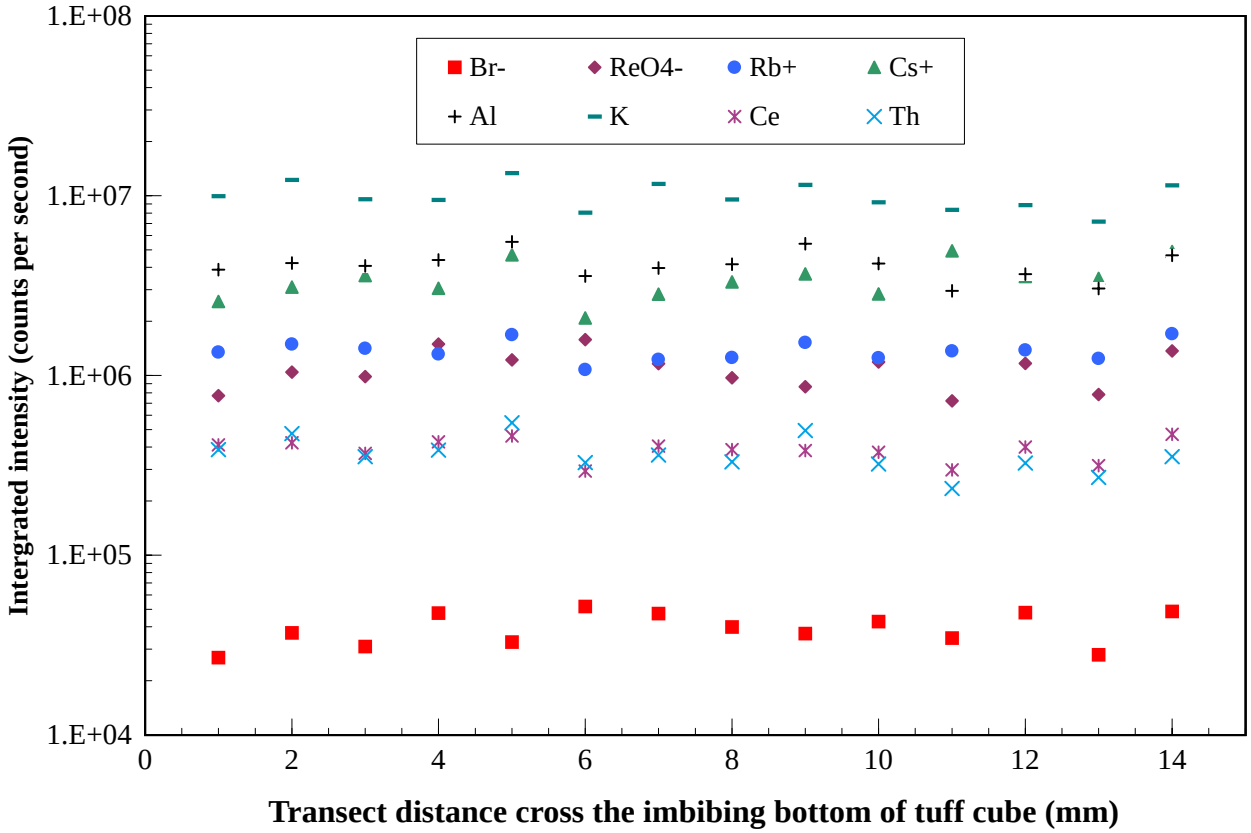

DTN: LB0110TUFTRACR.001 [156979]

Figure 6.4.3-1. Spatial Distribution along the Tracer Solution Contact Surface of Applied Tracers and the Distribution of Intrinsic Tuff Elements Profiled Using LA-ICP-MS

Figure 6.4.3-2, on the other hand, presents the spatial distributions of applied tracers, as well as uniform distribution of element K as it exists inherently in the tuff sample, for a side cube face parallel to the direction of imbibition. Anionic tracers, Br^- and ReO_4^-, travel much further than cationic tracers (Cs^+ and Rb^+) that sorb to the tuff. This is similar to those discussed in Section 6.4.2.1, where sorption of dyes is observed. By the same approach, $d_{0.5}$ is located at about 10.15 mm for both Br^- and ReO_4^-, and $d_{0.5}$ is located at about 2.95 mm and 3.50 mm for Cs^+ and Rb^+, respectively. The retardation factors for Cs^+ and Rb^+ are, therefore, estimated to have the value of 3.44 (= 10.15 mm/2.95 mm) and 2.90 (10.15 mm/3.50 mm), respectively. Similar behavior is observed from the measurements made on another side cube face parallel to the direction of imbibition. Overall, LA-ICP-MS provides a useful way of sampling and understanding tracer, and by extension radionuclide, imbibition and transport in the rock matrix at small spatial scales and reasonable sampling times.

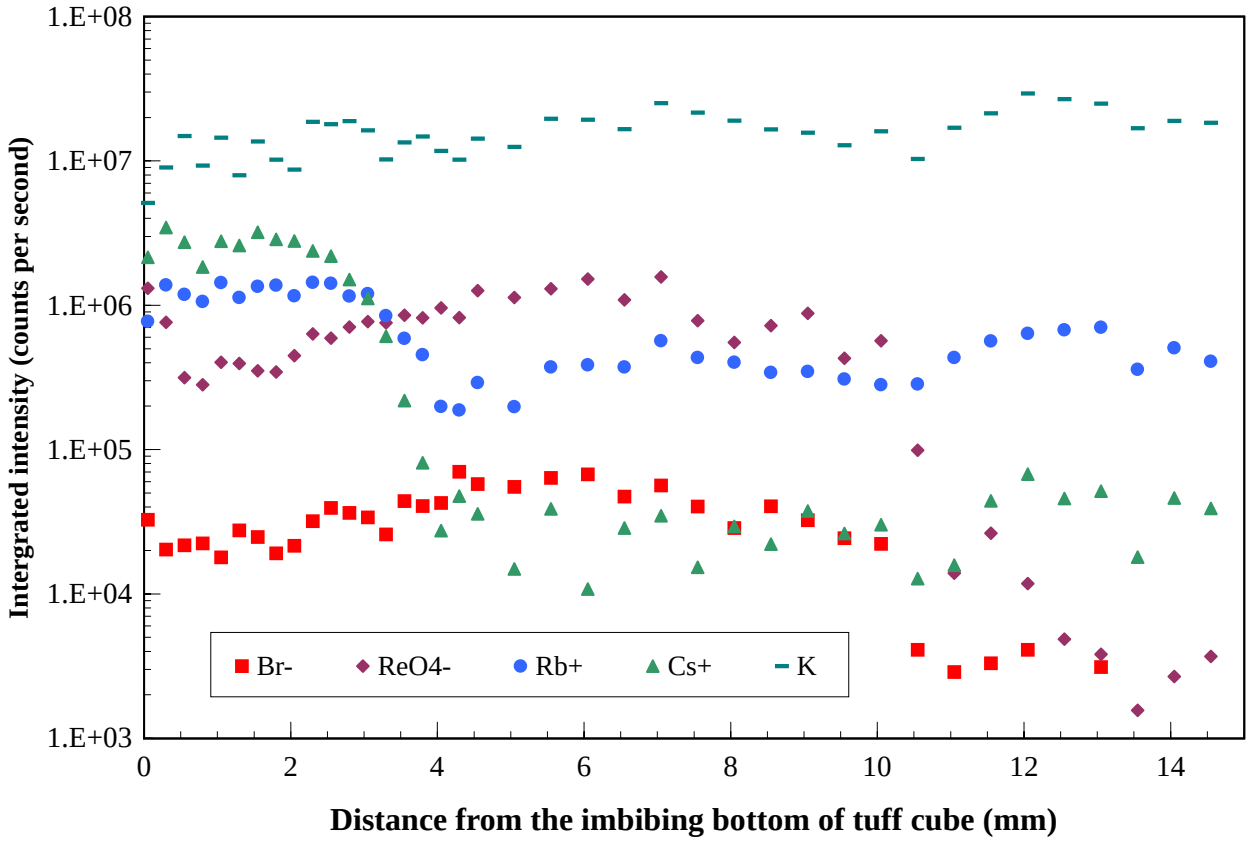

DTN: LB0110TUFTRACR.001 [156979]

Figure 6.4.3-2. Spatial Distribution Normal to the Tracer Solution Contact Surface (in the Direction of Liquid Imbibition) of Applied Tracers and Distribution of Intrinsic Tuff Elements Profiled Using LA-ICP-MS

6.5 CROSSHOLE ANALYSES OF AIR-INJECTION TESTS

This section continues the pneumatic air-permeability test analyses first presented in Section 6.1. Section 6.1 focuses on the air-permeability variations along boreholes in niches. The permeability profiles provide initial inputs to liquid-release-test interval selection, as described in Section 6.2. The permeability profiles were also used in a seepage-calibration study documented in the AMR on seepage calibration in defining the heterogeneity permeability structure used in modeling.

This section focuses on analyses of crosshole data for fracture-network connectivity. Fracture-network connectivity is one of the most important characteristics in evaluating flow paths from the inlets to the outlets of a given regime. The larger the system, the more elusive it is to determine the dominant flow paths. Air flow paths elucidated in this section are used to characterize test beds for liquid-flow test design and analysis, as described in Section 6.6 and Section 6.7 below for two slotted test beds in the ESF.

Crosshole tests used the same pneumatic testing equipment described in Attachment I. Up to seven identical packer strings were fabricated and installed in the boreholes to sample a rock

volume in the niches and in the test beds. The packer can isolate 0.3 m intervals along its length. Each interval can become either an observation zone used to monitor pressure or an injection zone where air is introduced under pressure during the test. The automation system controls the permutations through pre-assigned sequences of injection tests in all borehole intervals in the borehole cluster.

Crosshole data is acquired at the same time as single-borehole data, by logging the steady-state pressure response in all observation zones while performing an injection. As described in Section 5.5, the observation response pressure is divided by the injection pressure to provide a measure of how well a response zone is connected to an injection zone in relation to that response zone's connections to the rest of the site. The normalization with injection pressure enables all the observation responses from all injections at a site to be directly compared. The crosshole connections can all be viewed on a single 3-D diagram instead of individual diagrams for each tested injection zone.

The niches and Alcove 6 are located within the TSw unit in the potential repository horizon. The Alcove 4 test site is in the PTn unit along the North Ramp of the ESF. Both the fractured TSw and the predominately porous PTn were evaluated by the pneumatic air-permeability tests.

6.5.1 Crosshole Responses in Welded Tuff

In Section 6.1.2, the single-borehole permeability profiles were presented for niches as the bases for selecting liquid-release intervals for drift seepage testing. The first example of crosshole analysis in fractured rock is on Niche 4788, located in an intensely fractured zone. The crosshole analysis for Niche 4788 is illustrated in Figure 6.5.1-1. The single-borehole permeability values (presented in Section 6.1 as profile plots in Figure 6.1.2-7 and Figure 6.1.2-8) are represented by circles in the crosshole plot, with each circle centered along the test interval within each of the boreholes. The size of the circles scales with the single-borehole permeability at each interval. Grayscale pins are shown with their points at the centers of the circles of the injection zones and heads intersecting through the centers of other circles at the observation zones. Direction of flow is towards the pinhead, and the grayscale indicates the normalized response ratio (Resp. Ratio in the figure) from zero to one.

Figure 6.5.1-1 for Niche 4788 is fairly representative of a fractured site, showing discrete connections. It should be noted that very few of the connections have an opposite counterpart; the connections are predominantly one-way. This observation by no means indicates that flow is limited to one direction between points in the rock, but rather that the influence of local connections on the pressure response is strong. The pressure at a response zone discretely connected to the injection zone (and no other zone) will yield a large response. However, if the original injection zone in the reversed injection-observation combination is also well connected to the fracture network or a free surface, then it will not respond strongly to an injection in the original observation zone.

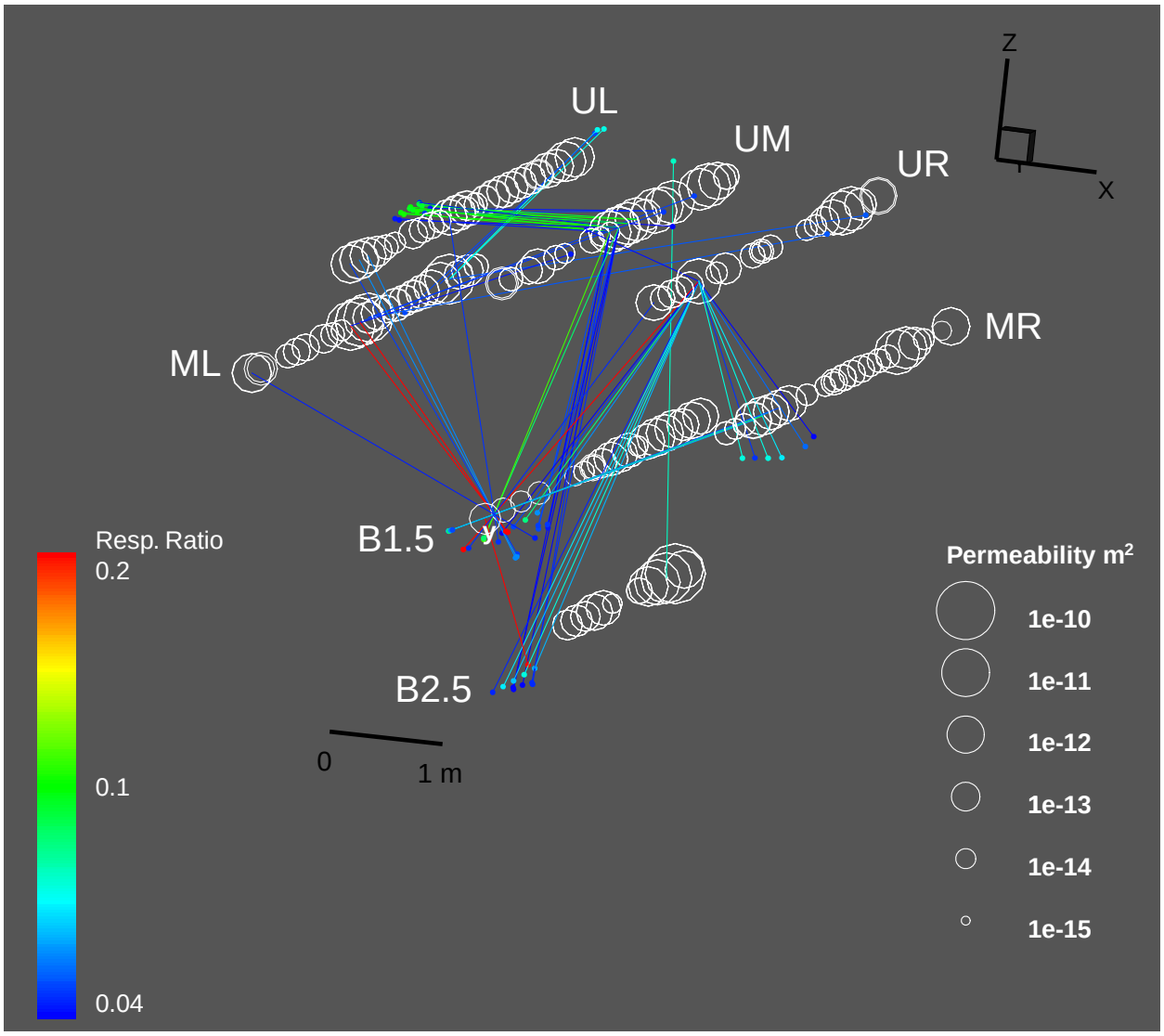

DTN: LB990901233124.004 [123273]

Figure 6.5.1-1. Cross-Hole Responses for the Borehole Cluster in Niche 4788

The fracture-matrix interaction test site in Alcove 6 of the ESF is in rock that is fractured, with discrete, subvertical fractures and relatively few subhorizontal fractures. The single-borehole permeability profiles for three boreholes tested in Alcove 6 are illustrated in Figure 6.5.1-2. Borehole A was used for a series of liquid-release tests, as described in Section 6.6. Boreholes C and D were used for wetting-front monitoring. Boreholes C and D are located 0.7 m and 0.6 m below Borehole A, respectively, and 0.7 m apart. The crosshole responses for this triangular cluster of boreholes are illustrated in Figure 6.5.1-3. Both Figure 6.5.1-2 and Figure 6.5.1-3 correspond to the first series of tests conducted in the region between 1.3 m and 5.3 m from the borehole collars. Another series of tests was conducted with a straddle packer system (two-packer string to isolate one zone for liquid releases) right before liquid-release tests along the injection borehole.

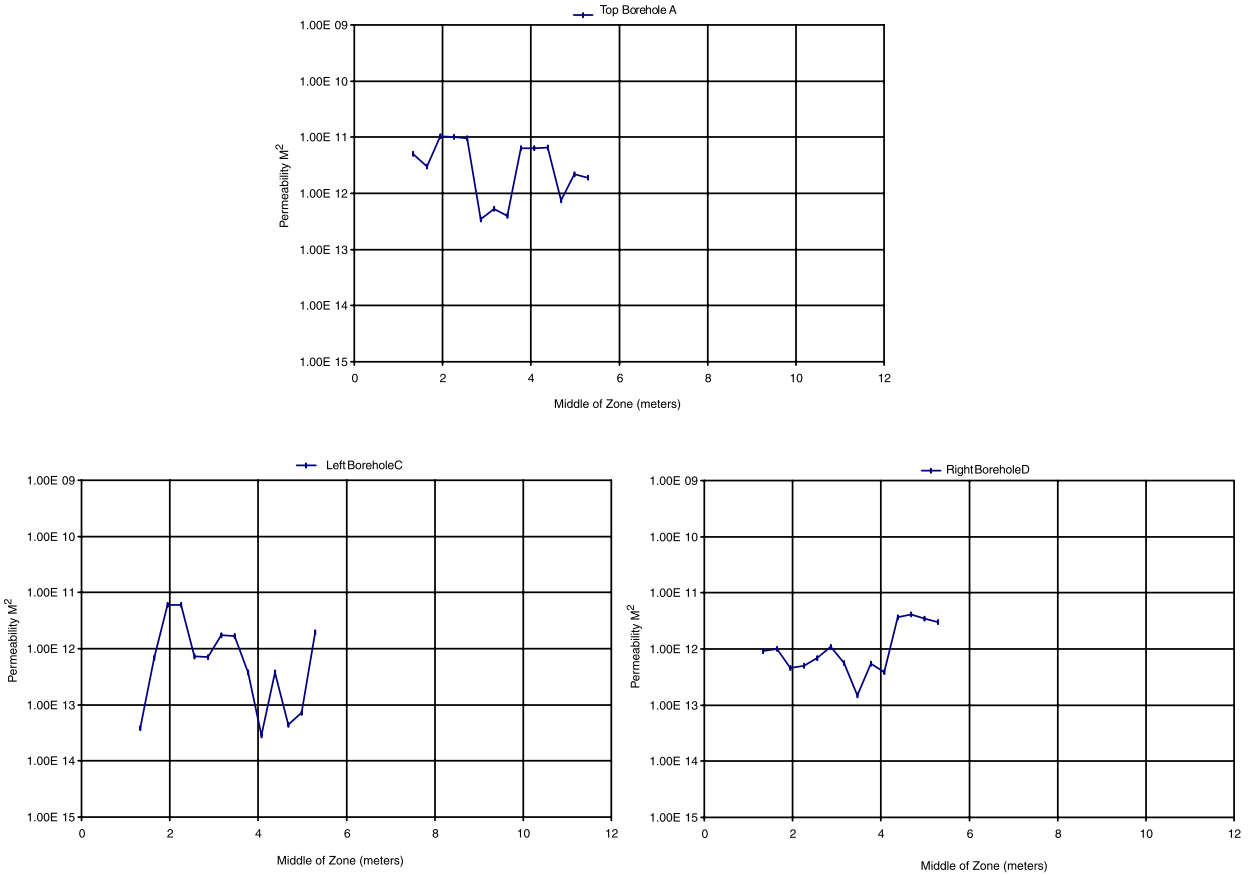

DTN: LB980901233124.004 [105855]

Figure 6.5.1-2. Air-Permeability Profiles along Boreholes in Alcove 6

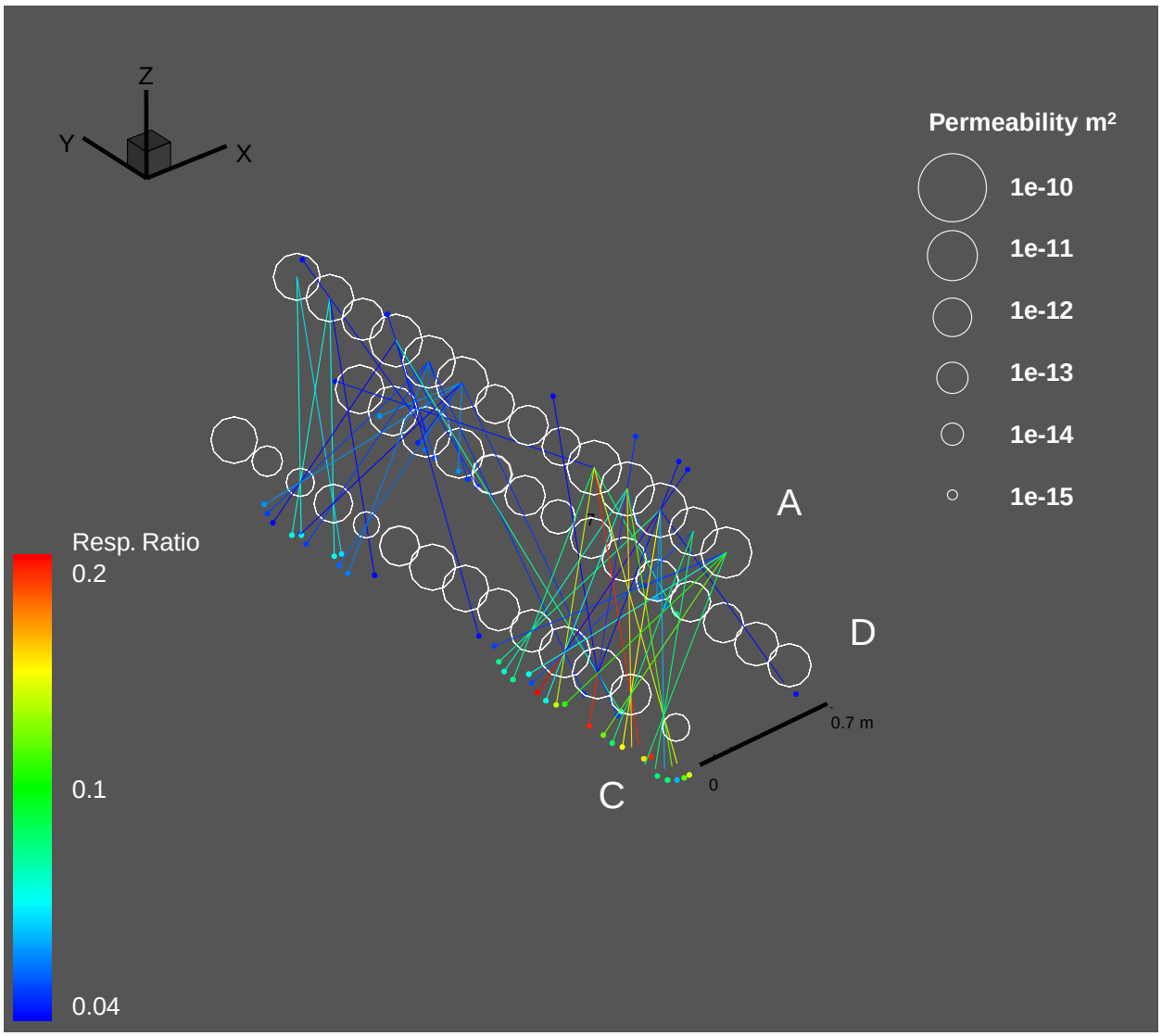

DTN: LB990901233124.004 [123273]

Figure 6.5.1-3. Crosshole Responses for the Borehole Cluster in Alcove 6

Both Figure 6.5.1-1 for Niche 4788 and Figure 6.5.1-3 for Alcove 6 represent crosshole responses in fractured rock. The ratios of pressure response in the observation borehole interval to pressure in the injection borehole interval ("Resp." in figure scales) were displayed in the figures for the maximum value of 0.2 (or 20%). Niche 4788, in an intensely fractured zone, has wider range (or larger standard deviation, as shown in Table 6.1.2-3) of distribution in permeability than the variations over a smaller scale at Alcove 6. Both fracture sites contain discrete and well-defined flow paths between boreholes.

During liquid-release tests in the welded tuff (Section 6.2 on niche seepage tests and Section 6.6 on fracture flow tests), it was observed, in some cases, that liquid flux at certain zones was not always commensurate with the air-permeability values at these zones (see Attachment III). Besides the capillary mechanism (that water will prefer smaller aperture fractures), another

possible explanation for this observation is that liquid tries to flow downward following gravity and is thus more sensitive to the directionality of permeability than is air. Directionality of flow is not available from single-borehole data and requires crosshole data analyses.

6.5.2 Permeability Distributions and Crosshole Responses in Nonwelded Tuff

The Alcove 4 test bed is located in the PTn unit. The test bed contains several nonwelded and bedded subunits, including a pinkish-colored argillic layer. The test bed contains a fault plane as illustrated in Figure 6.5.2-1. Section 6.7 below describes in more detail the borehole configuration and specifications. In this section, the focus is on the cluster of seven boreholes. Boreholes 1, 4 11, and 12 intersected the projected fault plane in the front part of the test block, while boreholes 2, 15, and 16 penetrated other features in the test block, with potential fault zone influences (if any) confined near the ends of the boreholes. If the fault is perfectly planar, the last three holes would not be intercepted by the fault.

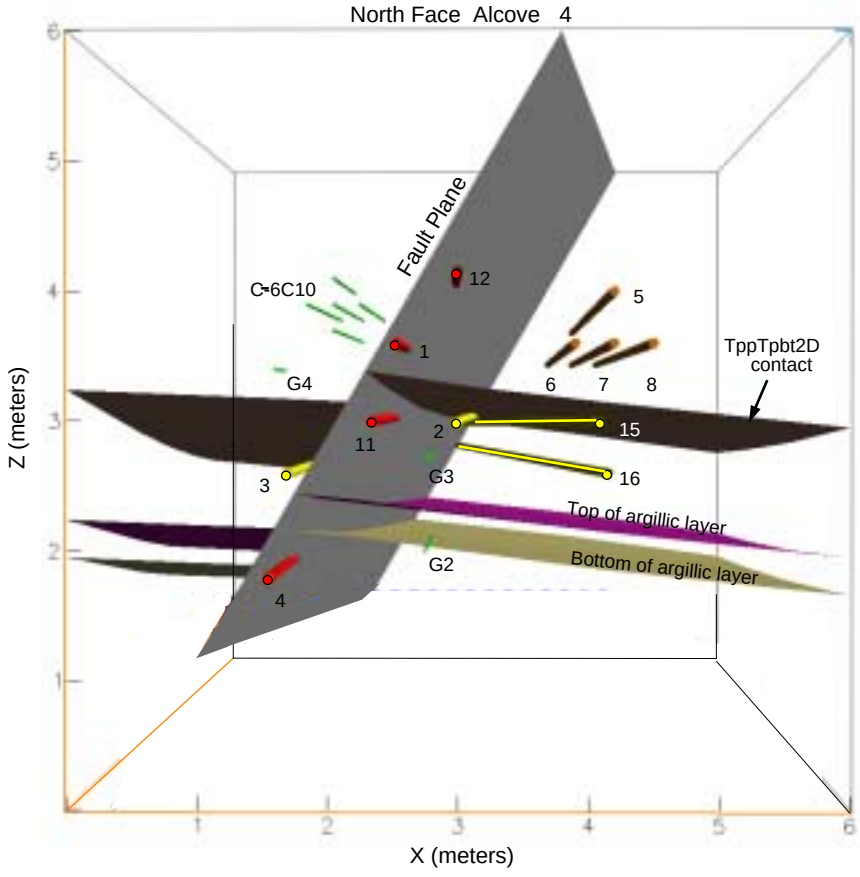

Figure 6.5.2-1. Perspective Illustration of Alcove 4 Test Bed

Figure 6.5.2-2 illustrates the single-borehole air-permeability profiles along the boreholes. Layer variations and the influence of faults could contribute to the widely distributed set of permeabilities over a broad range, both along individual boreholes and among different boreholes. With the exception of borehole 12, the other six boreholes penetrate a high-permeability zone near the end of the boreholes. Among all the borehole clusters tested in the ESF up to date, the Alcove 4 PTn cluster shows the largest standard deviation of any of the sites (see Table 6.1.2-3 in Section 6.1.2.3). Even the cluster at the intensely fractured site at Niche 4788 has lower standard deviation of log permeability (0.85) than the value at Alcove 4 (0.93). The mean permeabilities of these two distinctly different sites (in lithological, geological, and fracture characteristics) are incidentally nearly identical. In comparison, the standard deviation for Alcove 6 cluster was 0.67, and mean was nearly one order of magnitude higher.

Figure 6.5.2-3 shows the connections for Alcove 4 at the same shading scale used in welded tuff plots (Figure 6.5.1-1 and Figure 6.5.1-3). The number of connections is much higher for this nonwelded tuff site. To better display the stronger connections, Figure 6.5.2-4 portrays the data at Alcove 4 on a more appropriate scale legend and trims off the weaker connections. The salient features of the site now become apparent. Strong vertical connections are apparent between the upper and middle boreholes, but very little connectivity exists between the middle borehole and the lower-left borehole, despite similar flow rates and distances. The argillic layer exists between these locations, and the slot provides a nearly impermeable barrier. The single strong connection running from left to right is most likely associated with a high-permeability zone identified by the single-borehole profiles. The high-permeability zone could be associated with the fault intersecting the boreholes near the end. Interceptions were not identified in pre-test design in Figure 6.5.2-2. The connections were identified by crosshole analyses of pneumatic air-permeability test data.

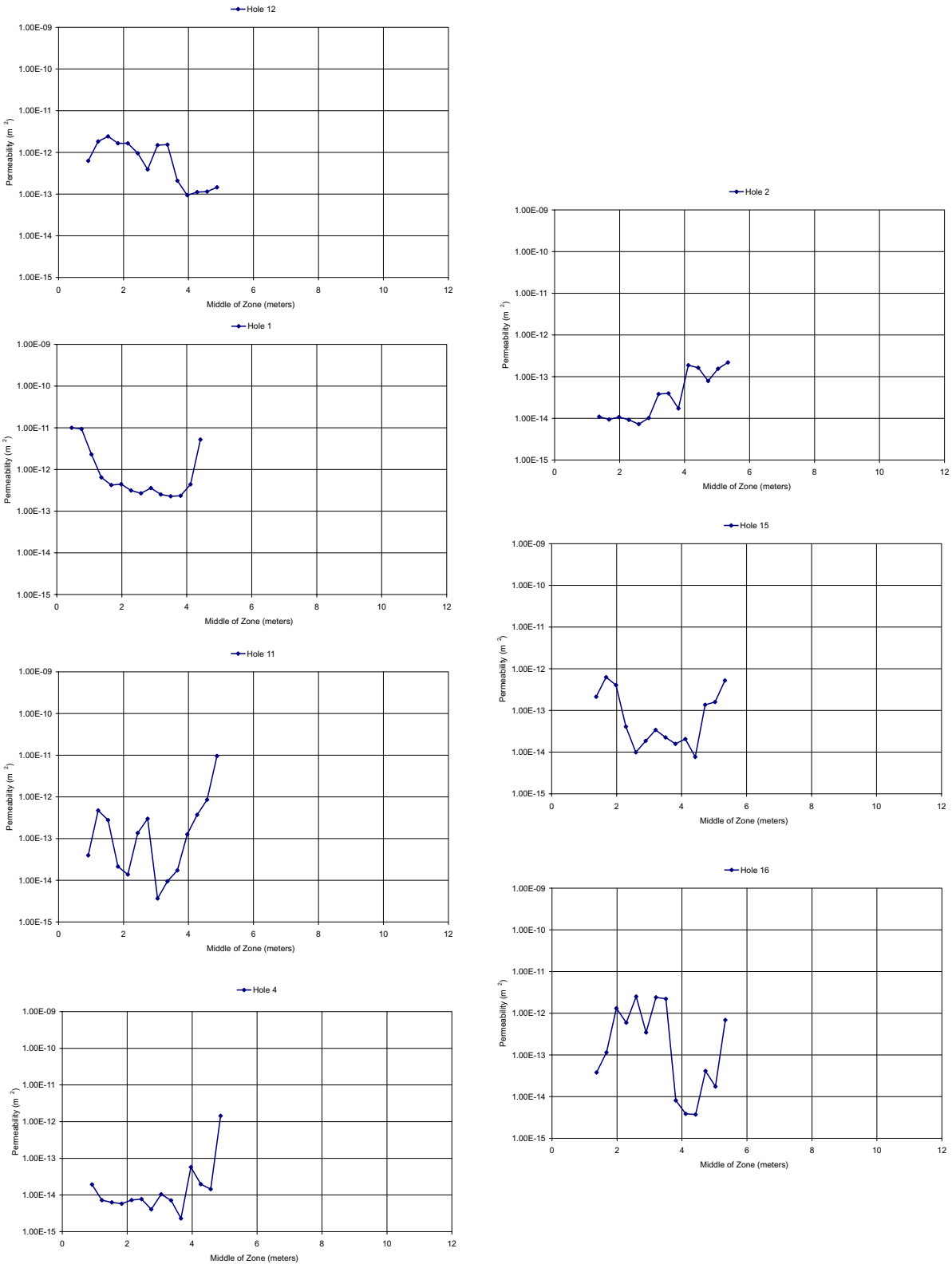

DTN: LB990901233124.004 [123273]

Figure 6.5.2-2. Air-Permeability Profiles along Boreholes in Alcove 4

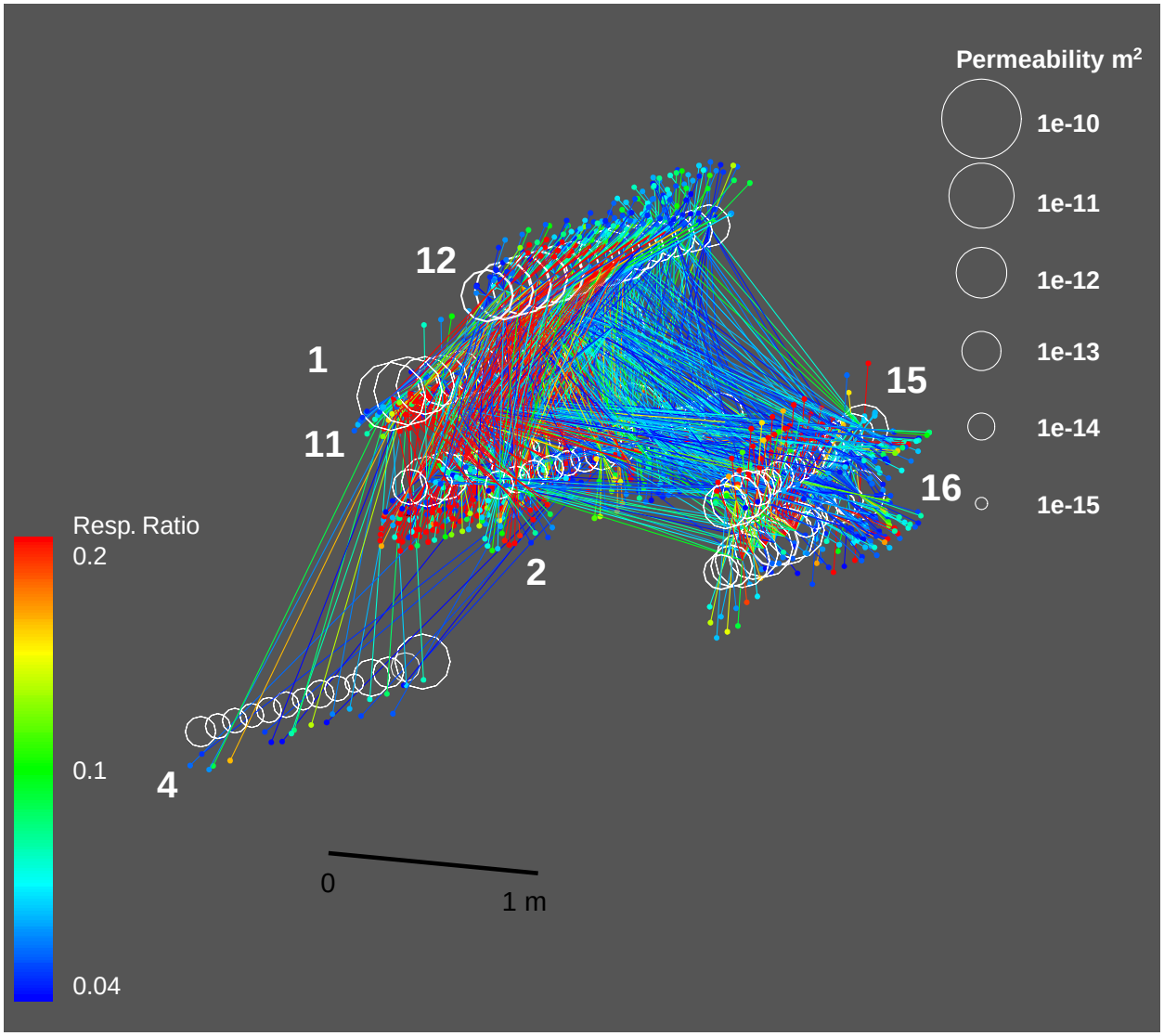

DTN: LB990901233124.004 [123273]

Figure 6.5.2-3. Crosshole Responses for Borehole Cluster at Alcove 4 PTn Test Bed with All Response Pressure (Resp.) Ratios below 0.2 Included

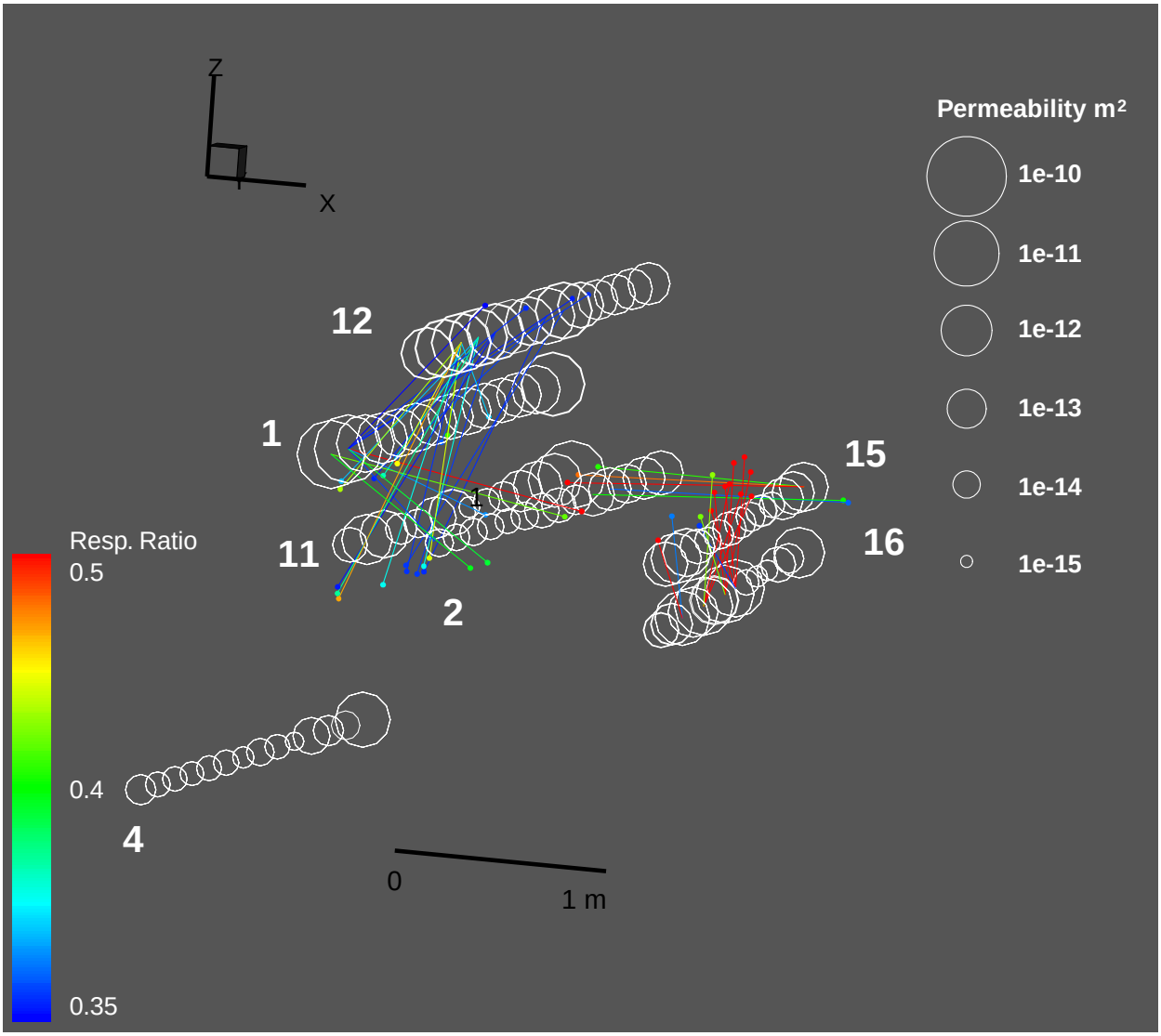

DTN: LB990901233124.004 [123273]

Figure 6.5.2-4. Crosshole Responses for Borehole Cluster at Alcove 4 PTn Test Bed with Small Response Pressure (Resp.) Ratios Filtered

6.6 ANALYSES OF FRACTURE FLOW IN FRACTURE-MATRIX TEST BED AT ALCOVE 6

Wetting-front movement, flow-field evolution, and drainage of fracture flow paths were evaluated in a test bed with a slot excavated below a cluster of boreholes. The slotted test bed is located within the Topopah Spring welded tuff (TSw) at Alcove 6 in the ESF at Yucca Mountain, Nevada. Hydraulic parameters such as formation intake rates, flow velocities, seepage rates, and fracture volumes were measured under controlled boundary conditions, using techniques developed specifically for *in situ* testing of flow in fractured rock. The test-bed configuration and field instrumentation are described before the results are presented.

6.6.1 Liquid-Release Tests in Low- and High-Permeability Zones

Field tests were conducted at Alcove 6 over a period of six weeks, starting in late July 1998. These included multiple releases of tracer-laced water in one high-permeability zone (HPZ) and one low-permeability zone (LPZ) along an injection borehole. The permeabilities of these zones were determined from air-permeability measurements conducted over 0.3 m sections along the borehole, using a straddle packer that also was used for liquid releases. The HPZ had an air-permeability value of 6.7×10^{-12} m^2, and the LPZ had an air-permeability value of 2.7×10^{-13} m^2 (Scientific Notebooks YMP-LBNL-JSW-RS-1 (Salve 1999 [155692], pp. 48–49) and YMP-LBNL-JSW-PJC-6.2 (Cook 2001 [156902], pp. 51–53)). During and following liquid-release events, changes in saturation and water potential in the fractured rock were measured in three monitoring boreholes, with changes continuously recorded by an automated data acquisition system. The water that seeped into the excavated slot below the injection zone was collected, quantified for volumes and rates, and analyzed for tracers.

6.6.1.1 The Test Bed

The test bed was located at Alcove 6 in the ESF (Figure 6.6.1-1a), lying within the middle nonlithophysal zone of the TSw. The rock was visibly fractured, with predominantly vertical fractures and a few subhorizontal fractures. The relatively wide fracture spacing (on the order of tens of centimeters) facilitated the choice of injection zones, allowing discrete fractures and well-characterized fracture networks to be isolated by packers for localized flow testing.

A horizontal slot and a series of horizontal boreholes are the distinct features of the test bed (Figure 6.6.1-1b). The slot, located below the test bed, was excavated by an over-coring method. The excavation sequence required (first) the drilling of parallel pilot holes, 0.10 m in diameter, over 4 m in length with a 0.22 m spacing, normal to the alcove wall. The pilot holes were then over-cored by a 0.3 m drill-bit to excavate the 2.0 m wide, 4.0 m deep and 0.3 m high slot located approximately 0.8 m above the alcove floor. Three I-beam supports were installed along the length of the slot for support. Four horizontal boreholes, 0.1 m in diameter and 6.0 m in length, were drilled perpendicular to the alcove wall above the slot. Boreholes A and B were located 1.6 m above the slot ceiling, while boreholes C and D were 0.9 m and 1.0 m above the slot ceiling, respectively, and 0.7 m apart (Figure 6.6.1-1b).

Borehole A was used for fluid injection, while boreholes B, C, and D were monitored for changes in moisture conditions. The slot was used to collect water seeping from the fractured rocks above. A flexible plastic curtain 3.0 m wide and 0.9 m high was installed to cover the slot face and to minimize air movement between the alcove and the slot.

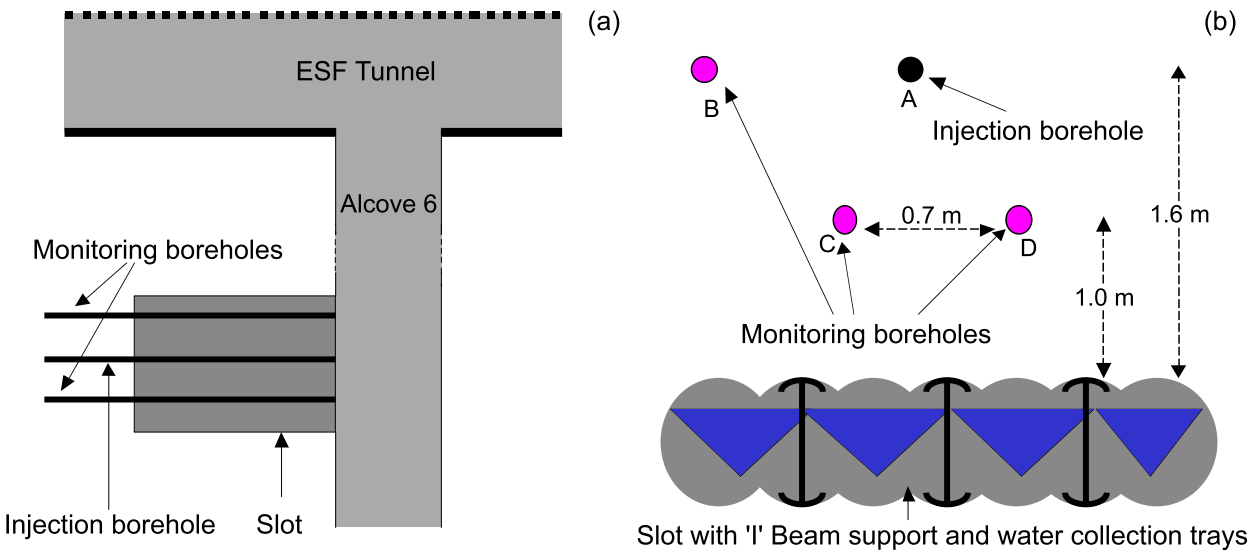

NOTE: Figures are not drawn to scale.

Figure 6.6.1-1. Schematic Illustration of (a) Plan view of Location and (b) Vertical View of Layout of Test Bed at Alcove 6 in the ESF at Yucca Mountain

6.6.1.2 Instrumentation

There were three distinct components to the flow investigation: (1) controlled release of water into isolated zones, (2) borehole monitoring for changes in saturation and water potential, and (3) collection of seepage from the slot ceiling. The key features of new instruments developed for this field investigation are presented in Attachment VI.

6.6.1.3 Liquid-Release Experiments

Air-permeability measurements were done along 0.3 m sections of the injection borehole as described in Section 6.1 and Section 6.5. The HPZ is located 2.3–2.6 m from the borehole collar, whereas the LPZ is 0.75–1.05 m from the collar. In both HPZ and LPZ, a series of constant-head tests were conducted to determine the temporal changes in the rate at which the formation could take in water. In the HPZ, a second series of tests was conducted with different injection rates. Tests conducted in this field investigation are summarized in Table 6.6.1-1. Seepage rates into the slot were monitored.

All the water used in the ESF was spiked with lithium bromide for mining-related activities and for most of the scientific investigations. Additional tracers were added to the water injected into the LPZ and during the first set of experiments in the HPZ (Table 6.6.1-1). During the tests, water that seeped into the slot was periodically sampled and analyzed for tracer concentrations.

Water was released into the LPZ three times over a period of two weeks, starting on July 23, 1998 (Table 6.6.1-1). For the first release, water was injected at a constant pump rate of approximately 56 mL/min. At 66 minutes, water was observed in the overflow line, indicating that water was being injected at a rate higher than the intake capacity of the zone. At this time, the flow rate on the pump was immediately reduced to approximately 6.0 mL/min. Within 22

minutes, return flow ceased, and water was injected continuously at this rate for the next 4 hours and 23 minutes. Based on the actual flow rate determined from transducers located at the bottom of the water reservoir (see Attachment VI.1), a total of 6.3 liters of water was injected into the zone, of which 0.7 liters was recovered as return flow. The other 5.6 liters was released into the formation. Average net release rate into the formation rate was approximately 17 mL/min.

For the second liquid release in the LPZ, the constant-head injection system was used. The constant-head chamber was located adjacent to the injection borehole such that the head of water was 0.07 meters in the injection zone. This constant head was maintained for 4 hours in the injection zone, while the water level in the reservoir was continuously monitored. At the end of this constant-head period, water supply to the injection zone was discontinued, resulting in a falling-head boundary condition inside the injection zone. A total of 1.4 liters of water was introduced into the LPZ from both the constant-head and falling-head periods.

The final release into the LPZ was initiated on July 29, 1998, when water was introduced into the formation under a constant head (of 0.07 m) maintained for 43 hours, after which the ponded water in the injection zone continued to percolate into the formation under a falling-head condition. During the test, 1.0 liters of water were released under the constant-head boundary, wheras 1.2 liters were released under the falling head.

Summing up all three tests in the LPZ, 9.2 liters of water were released to the formation under a combination of constant and falling-head boundary conditions at the point of injection.

Water was injected into the HPZ during two groups of tests over a period of two weeks (Table 6.6.1-1). The first group of four tests was conducted during August 4–6, 1998, and the second group of four tests were conducted during August 25–28, 1998. The first two tests (Test HPZ-1 and Test HPZ-2) in the first group were constant-head tests (of head 0.07 m) that served to establish the intake rates at which the injection zone could release water to the formation. The HPZ-1 constant-head test rate was ~119 mL/min. The HPZ-2 constant-head test rate was ~98 mL/min. After HPZ-2 test, tests were conducted at constant flow rates. During the third test (Test HPZ-3) conducted on the next day, water was injected at approximately half the intake rates observed with the constant-head system (i.e., ~ 53 mL/min). During the fourth test (Test HPZ-4) on August 6, 1998, water was injected at a constant rate of ~ 5 mL/min over 12 hours. During the second group of tests (Tests HPZ-5 through HPZ-8) over a period of four days starting on August 25, 1998, the injection rate was sequentially reduced from ~69, ~38, ~29 and finally to ~14 mL/min.

Table 6.6.1-1. Amount of Water and Types of Tracers Released into the Injection Borehole

Date	Test #	Injection type	Infiltration rate (mL/min)	Volume of water injected (l)	Additional Tracer *
7/23/98	LPZ-1	Constant rate	~16	5.6	Sodium Bromide 2,3,6 Trifluorobenzoic acid
7/24/98	LPZ-2	Constant head	~1.2	0.3	2,4,5 Trifluorobenzoic acid
7/24-25/98	LPZ-2	Falling head		1.1	2,4,5 Trifluorobenzoic acid
7/29-30/98	LPZ-3	Constant head	~0.5	0.4	3,5 Difluorobenzoic acid
7/30-31/98	LPZ-3	Constant head	~0.5	0.6	3,5 Difluorobenzoic acid
7/31-8/4/98	LPZ-3	Falling head		1.2	3,5 Difluorobenzoic acid
8/4/98	HPZ-1	Constant head	~119	16.3	Potassium Fluoride Pentafluorobenzoic acid
8/4/98	HPZ-2	Constant head	~98	17.3	2,3,4 Trifluorobenzoic acid
8/5/98	HPZ-3	Constant rate	~53	17.5	3,4 Difluorobenzoic acid
8/6/98	HPZ-4	Constant rate	~5	3.4	2,3,4,5 Tetrafluorobenzoic acid
8/25/98	HPZ-5	Constant rate	~69	18.4	
8/26/98	HPZ-6	Constant rate	~38	18.4	
8/27/98	HPZ-7	Constant rate	~29	18.2	
8/28/98	HPZ-8	Constant rate	~14	9.4	

DTN: LB990901233124.002 [146883]

NOTES: LPZ located 0.75-1.05 m from borehole collar
HPZ located 2.30-2.60 m from borehole collar
* All injected water was tagged with lithium bromide

6.6.2 Observations of Wetting Front Migration and Fracture Flow

Water released in the injection borehole flowed through the fractured rock and, in the case of the HPZ, some of the water seeped into the slot located 1.6 m below. Liquid-release rates in the injected zone were measured, saturation and water-potential changes were observed along monitoring boreholes, and seepage water into the slot was collected.

6.6.2.1 Liquid-Release Rates

Measurements of liquid-release rates in the LPZ in this test bed in fractured welded tuff exhibited a response similar to that observed for (unfractured) porous media. The initially high rates asymptotically approached low steady-state values of ~0.35 mL/min (Figure 6.6.2-1a). Near continuity was observed in the decreasing liquid-release rates, even with a five-day gap between liquid releases into the formation (Figure 6.6.2-1b).

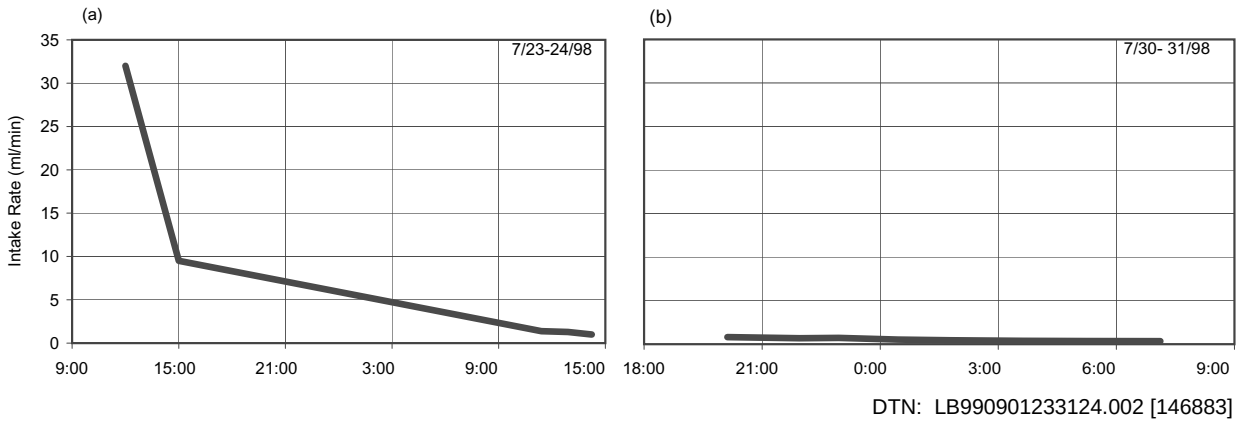

Figure 6.6.2-1. Water Intake Rates Observed in the Low Permeability Zone

For the first two constant-head tests conducted in the HPZ, the rates of liquid release varied significantly during and between tests (Figure 6.6.2-2). In the first test, the liquid-release rate continued to climb for the first sixty minutes and then remained steady for the next 15 minutes before briefly increasing sharply. For the remainder of the test it continued to fluctuate between 70 and 160 mL/min. In the second test, the liquid-release rate rapidly increased for the first 15 minutes. The rate then slowly decreased and steadied off to ~100 mL/min. Ninety minutes into the test, the liquid-release rate briefly fell to 35 mL/min, sharply increased to 130 mL/min, and slowly decreased to a quasi-steady rate of 90 mL/min in the next 80 minutes.

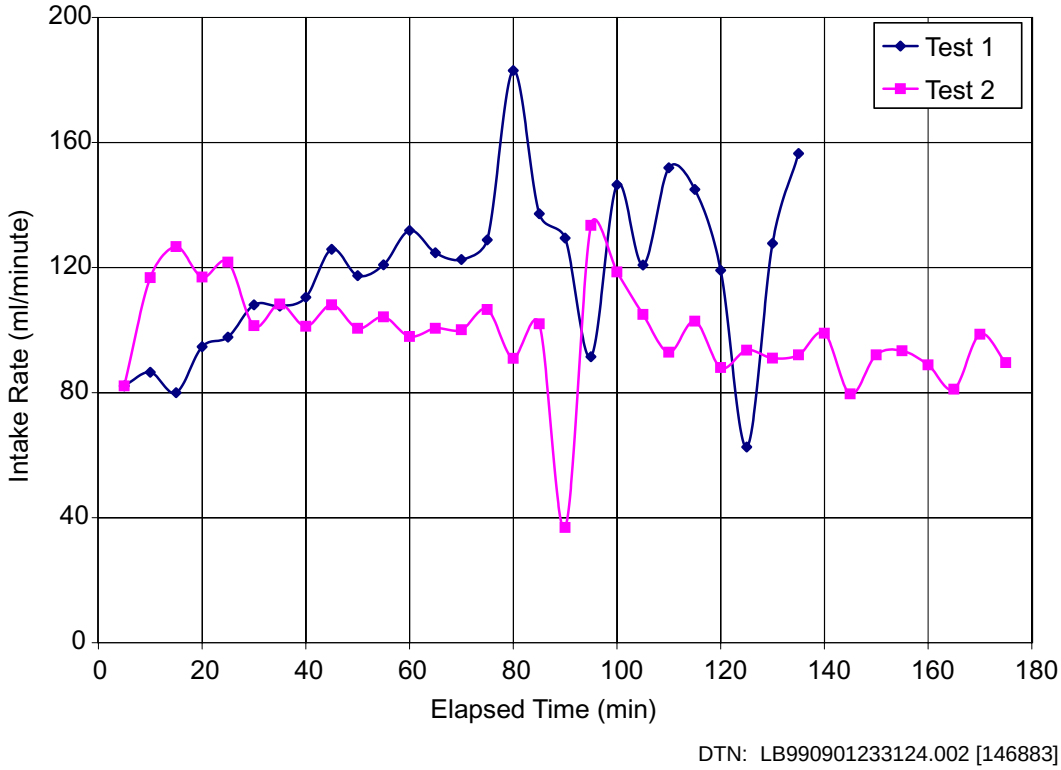

Figure 6.6.2-2. Water Intake Rates Observed in the High Permeability Zone

6.6.2.2 Formation Wetting and Drying

In the two monitoring boreholes (C and D, shown in Figure 6.6.1-1b) located below the injection borehole (A), changes in saturation were detected both by the electrical-resistivity probes (ERPs), as shown in Figure 6.6.2-3a and Figure 6.6.2-3c, and by the psychrometers, as shown in Figure 6.6.2-3b and Figure 6.6.2-3d. The ERPs consisted of two electrical leads sandwiched between pieces of filter paper. The results in Figure 6.6.2-3 are the responses to liquid release in the LPZ located 0.75–1.05 m from the borehole collar. In both boreholes, large changes in saturation were detected by either ERPs or psychrometers or both located between 0.9 and 1.9 m from the collar. At a distance of 2.15 m from the borehole collar, the changes were much smaller.

The wetting process reduces electrical resistance and increases the water potential (making it less negative). The drying process induces opposite changes. In borehole C, the first drying response was detected by the ERP 0.90 m from the borehole collar, as illustrated in Figure 6.6.2-3a. A step increase in resistance was observed 30 minutes after water had been released, suggesting some initial drying with dry air preceding a wetting front. Two hours later, an abrupt increase in wetting was indicated by a stepped decrease in resistance. ERPs located at 1.15, 1.40, and 1.65 m also detected the arrival of a wetting front within 2 to 4 hours of liquid release. In borehole D (Figure 6.6.2-3c), the ERPs located at 0.9 and 1.15 m from the collar were first to detect increases in saturation, 30 minutes after the first release of water. At distances of 1.40 and 1.65 m, the wetting front arrived 6 hours later.

In both boreholes, the probes that had the largest and quickest responses (i.e., probes located between 1.15 and 1.65 m) were also the ones that showed some drying between the two injection events. Probes located at a distance of 0.90–1.15 m detected a continuous drying trend after the initial period of injection.

The borehole C psychrometer data in Figure 6.6.2-3b supported the ERP data in Figure 6.6.2-3a with smoother and more systematic changes induced by wetting-front arrivals. The sensors closer to the release point had larger changes in water potential. At distances between 1.40 and 2.15 m from the collar, water potentials were between -140 and -75 m before the first injection. Immediately after water was introduced, water potentials began to rise steadily for the next four days, reaching values between -70 and -30 m. In response to the second injection period (i.e., July 29–August 4, 1998, in Table 6.6.1-1), the most noticeable increases in potentials were observed in the psychrometer located at 1.40 m, where water potentials increased from -40 to -15 m after the second injection period. In borehole D, illustrated in Figure 6.6.2-3d, changes in water potential were observed between 0.90 and 1.90 m following the first injection. However, the extent of drying as seen in the decrease in water potentials at 1.40 and 1.65 m was greater than observed in borehole C. During the second wetting event, water potentials in this zone were similar to those observed following the first event. Oscillatory responses could be related to variations of drift conditions for sensors near the borehole collars. This is a speculative interpretation, to be substantiated or refuted.

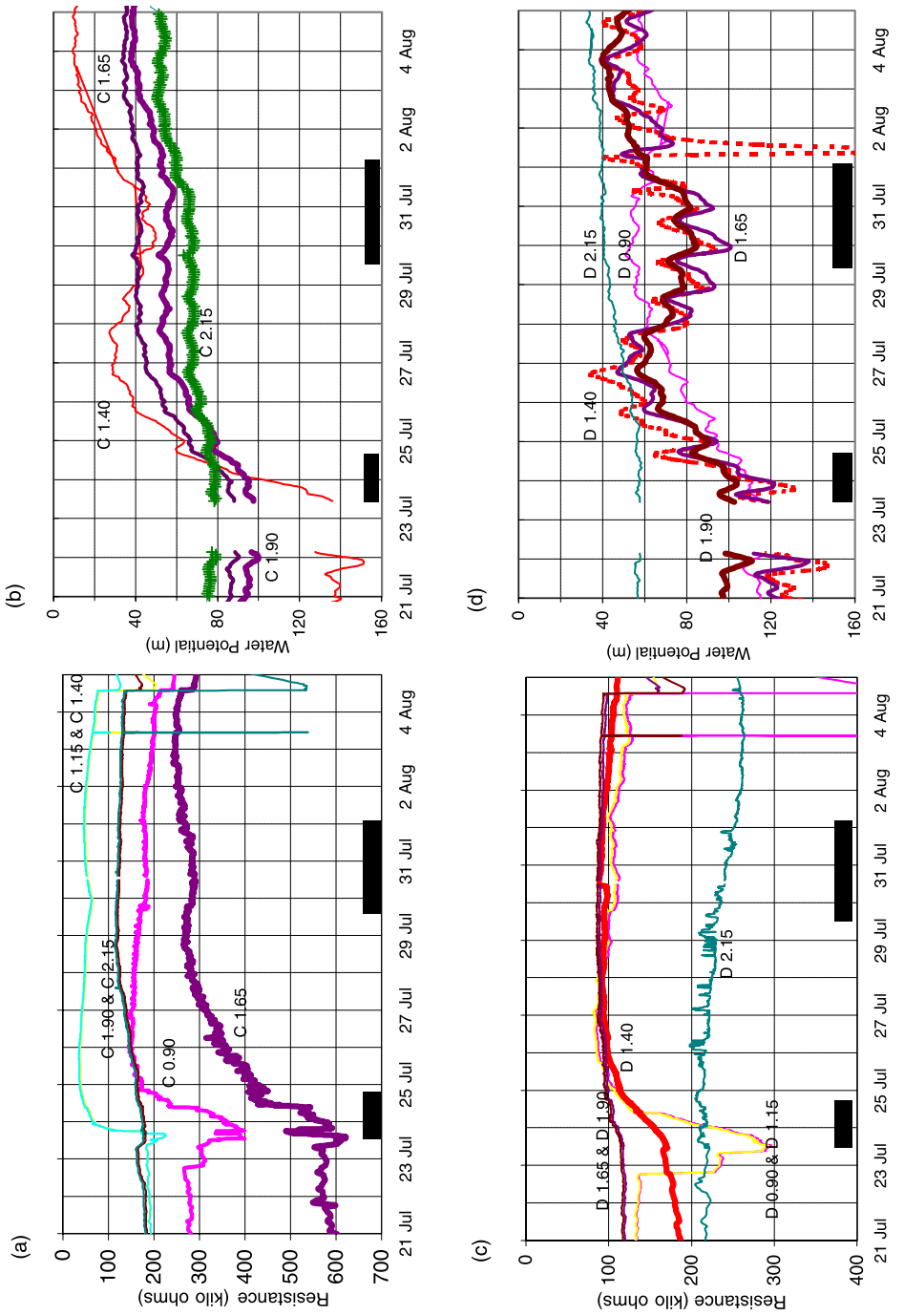

DTN: LB990901233124.002 [146883]

Figure 6.6.2-3. Changes in Electrical Resistance and Water Potential Detected during Liquid Release into the Low Permeability Zone. The legend identifies the sensor location in borehole (C & D) and distance of sensor from the borehole collar. Shaded zones indicate the duration of liquid-release events. Note resistance axis is inverted.

Similar to the injection response in the LPZ, changes in saturation were detected both by the ERPs and psychrometers in the monitoring boreholes (Figure 6.6.2-4) from liquid releases into the HPZ located 2.30–2.60 m from the borehole collar. In borehole C, changes in saturation were observed between 1.9 and 3.4 m from the borehole collar, with the largest changes observed between 2.15 and 3.15 m. Both the ERPs and the psychrometers detected the changes. The largest changes in water potentials were detected between 2.15 and 2.40 m from the borehole collar in borehole C, where pre-injection water potentials, which were between -70 to -60 m, climbed to between -20 and -10 m after the first set of releases. These values persisted after the second set of releases. In borehole D, saturation changes were observed over a slightly wider span along the borehole (i.e., 1.65 to 3.65 m from the borehole collar), with the noticeable changes observed between 1.90 and 3.40 m from the borehole collar. After the initial release of water in the HPZ, water potentials between locations 2.15 and 2.90 m increased over a period of a week. These were between -15 to -5 m for the duration of the remaining liquid releases.

In both boreholes, the psychrometer data suggest that after the first batch of water releases (i.e., August 4–6, 1998) water potentials were significantly increased (e.g., -60 to -20 m), which then persisted until the start of the second period of injection (August 25–28, 1998). During this second set of injections, more water was retained by the formation, resulting in further increases in water potentials. The ERP and psychrometer data indicate that the zones between 2.15 and 2.40 m in borehole C, and between 2.15 and 2.65 in borehole D, showed the largest changes during active testing.

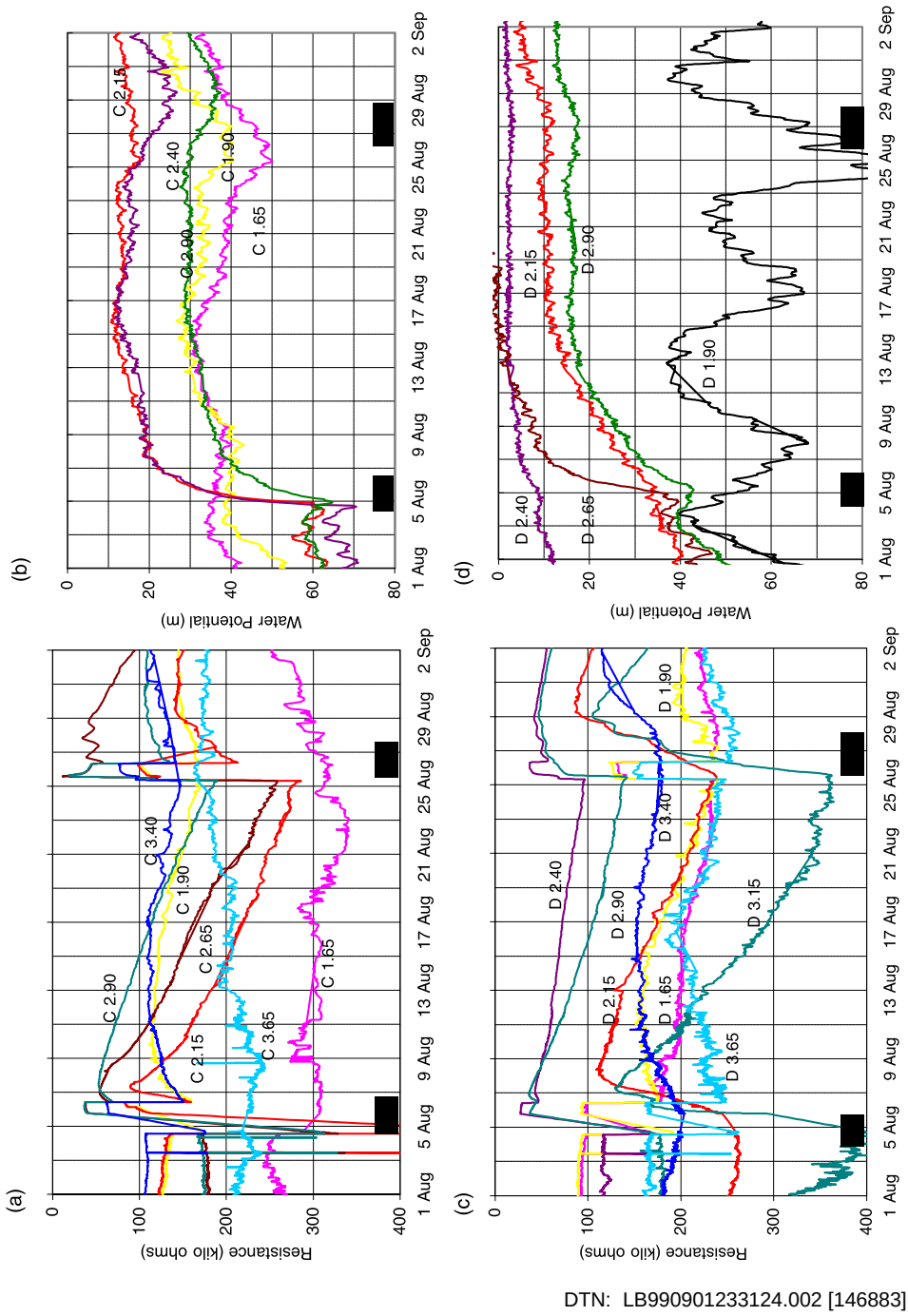

DTN: LB990901233124.002 [146883]

NOTE: The HPZ is located between 2.30 to 2.60 m from the borehole collar. The legend identifies the sensor location in borehole (C & D) and distance of sensor from the borehole collar. Shaded zones indicate the duration of two groups of liquid-release events. Note resistance axis is inverted.

Figure 6.6.2-4. Changes in Electrical Resistance and Water Potential Detected during Liquid Release into the High Permeability Zone

6.6.2.3 Seepage into the Slot

Seepage into the slot was observed during all eight tests in the HPZ (and none in the LPZ tests). The test results are summarized in Table 6.6.2-1. The eight tests were conducted in two groups (Table 6.6.1-1 and illustrated in Figure 6.6.2-3 and Figure 6.6.2-4 as two shaded test duration zones). During the first test in the first group (Test HPZ-1), water was first observed on the slot ceiling five minutes after the start with 0.41 liters of water released under constant-head conditions. In the HPZ-2 and HPZ-3 tests, water appeared in the slot within 3 minutes after 0.17 and 0.14 liters, respectively, had been released. In the HPZ-4 test, water appeared in the slot after five hours with 1.50 liters of water injected at a rate of 5 mL/min.

In the second group of tests, travel time for the first drop of water was 3 minutes after 0.14 liters was injected at a rate of ~ 69 mL/min (Test HPZ-5). In the HPZ-6 and HPZ-7 tests, the arrival time of the wetting front was 7 minutes after 0.26 and 0.20 liters of water were injected at a rate of 38 and 29 mL/min, respectively. In the final HPZ-8 test, water first appeared in the slot after 1:08 hr, with 0.90 liters injected into the formation at a rate of 14 mL/min.

Table 6.6.2-1. Summary of Liquid-Injection Tests in the High Permeability Zone.

Test Number	Injection Rate (mL/min)	Duration of Injection (hh:mm)	Volume Recovered (liters)	Travel Time of First Drop (hh:mm)	Volume of Water In Formation (liters)		Water Retained in Formation (%)
					At First Drop	At End of Injection	
HPZ-4	5	11:54	0.36	5:00	1.51	3.03	89
HPZ-8	14	11:19	4.56	1:08	0.90	4.82	51
HPZ-7	29	10:36	13.21	0:07	0.20	5.02	28
HPZ-6	38	8:00	14.73	0:07	0.26	3.71	20
HPZ-3	53	5:25	11.14	0:03	0.14	6.31	36
HPZ-5	69	4:26	11.47	0:03	0.14	6.90	38
HPZ-2	98	2:56	12.17	0:03	0.17	5.15	30
HPZ-1	119	2:17	11.61	0:05	0.41	4.67	29

DTN: LB990901233124.002 [146883]

The fraction of injected water recovered in the slot continued to increase as each test progressed. Significant variability was observed in the percentage of water recovered and the seepage rate during and between tests (Figure 6.6.2-5a and b). Seepage variability was related to both the amount of water injected and the rate at which water was released into the formation. Early in each test, the amount of water recovered sharply increased. The percentage of injected water recovered approached relatively constant values after approximately 10 liters of water had been injected. Intermittent seepage behavior (Figure 6.6.2-5b) was observed during all the tests.

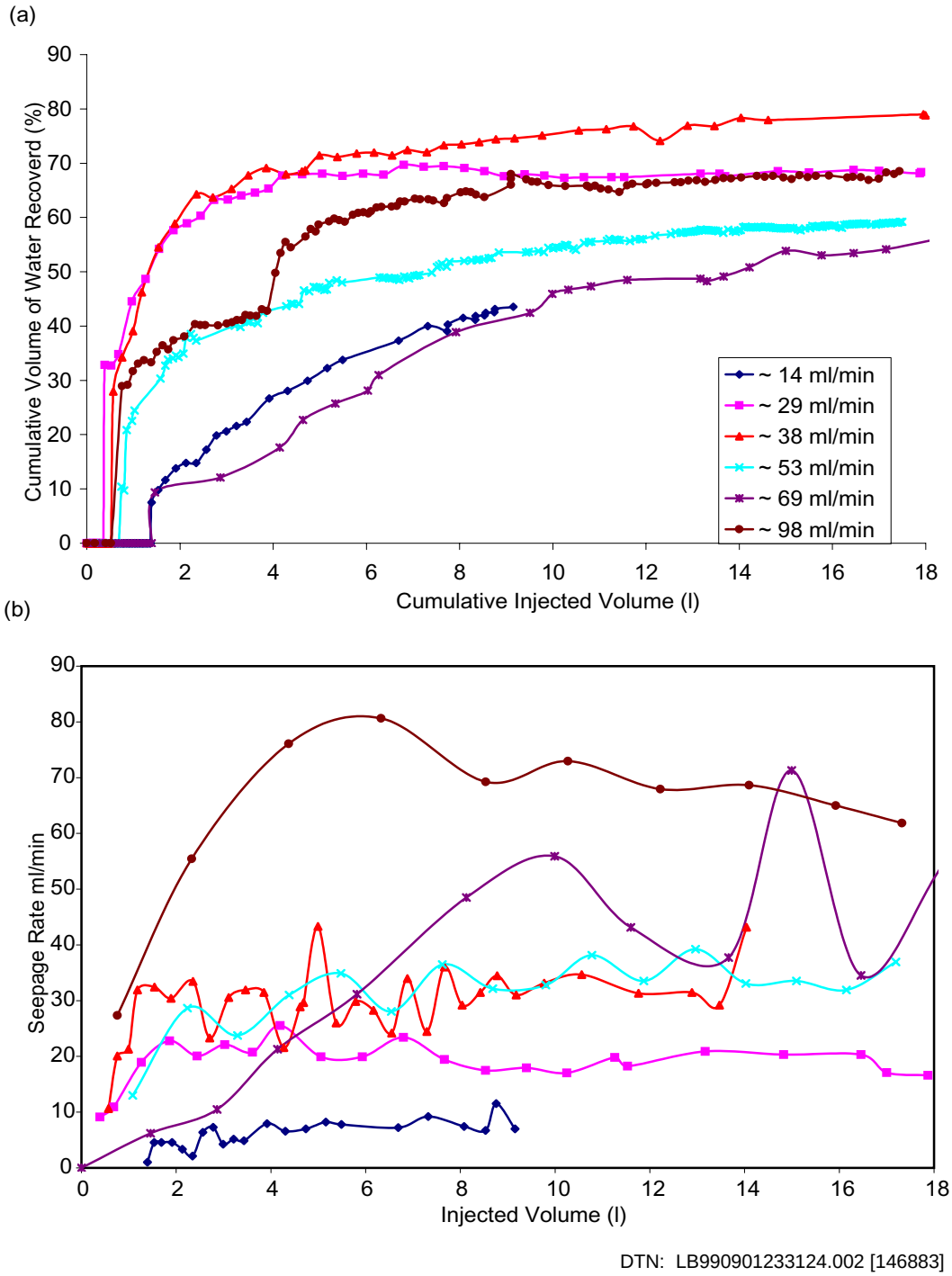

Figure 6.6.2-5. Seepage into Slot: (a) Percentage of Injected Water Recovered and (b) Seepage Rates for Various Release Rates

As illustrated in Figure 6.6.2-6, the percentage of the amount of injected water recovered at the release rate of 38 mL/min was higher than the percentages at other injection rates. The first maximum percentage could be associated with the dominant flow path connecting the injection zone with the outflow slot boundary. With increasing injection rate, additional flow paths, either through other fractures or through other areas in the same fracture, could contribute to the storage and flow of additional water.

Figure 6.6.2-6 also illustrates the distribution of seepage among the collection trays in the slot. As each test progressed, water initially appeared on the slot ceiling at one single point directly below the injection zone, and seepage water was collected from four trays located around the point of entry. During these tests, water seeping into the slot was largely concentrated in a single tray, with the three other trays collecting significantly smaller amounts of water. Slight increases at higher injection rates were noticeable in some of the secondary trays. The remaining 24 trays stayed dry during all the liquid-release tests.

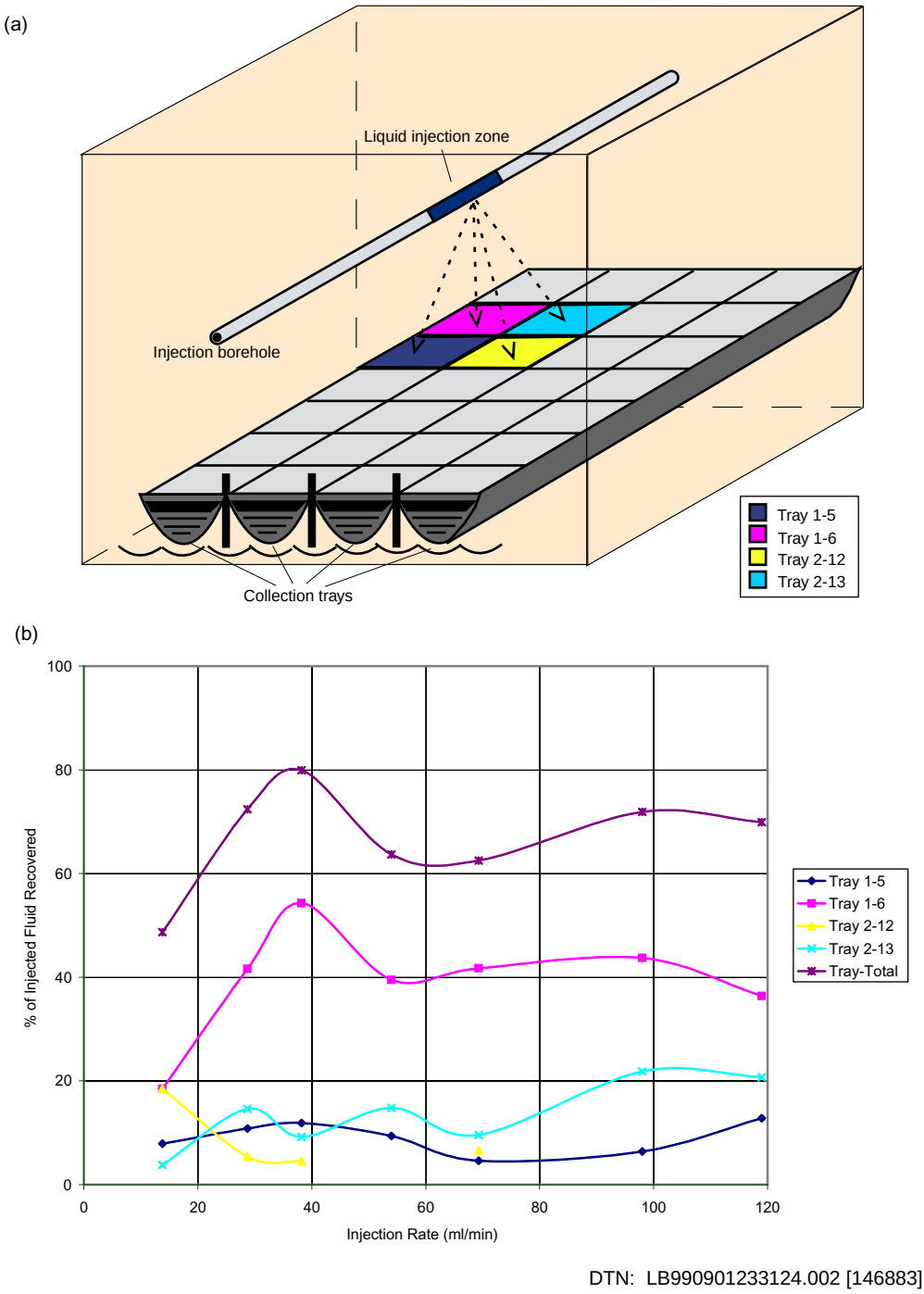

DTN: LB990901233124.002 [146883]

Figure 6.6.2-6. Seepage into Collection Trays in the Slot: (a) Tray Configuration and (b) Percentages of Injected Water Recovered for Different Trays

In all the tests during which there was seepage, 0.5 to 1.3 liters of water entered the slot after the water supply to the formation was switched off (Figure 6.6.2-7). Most of this water was collected within one hour, with recovery rates being largest immediately after the test. The constant-head test with ~98 mL/min release rate had a "stepped" nature to the post-injection recovery. During the first fifteen minutes, the 0.8 liters of collected water appeared in four bursts, each containing 0.10–3 liters of water. Changes of similar magnitudes were observed in the tests with injection rates of ~53 mL/min and ~14 mL/min (with one late burst each shown in Figure 6.6.2-7).

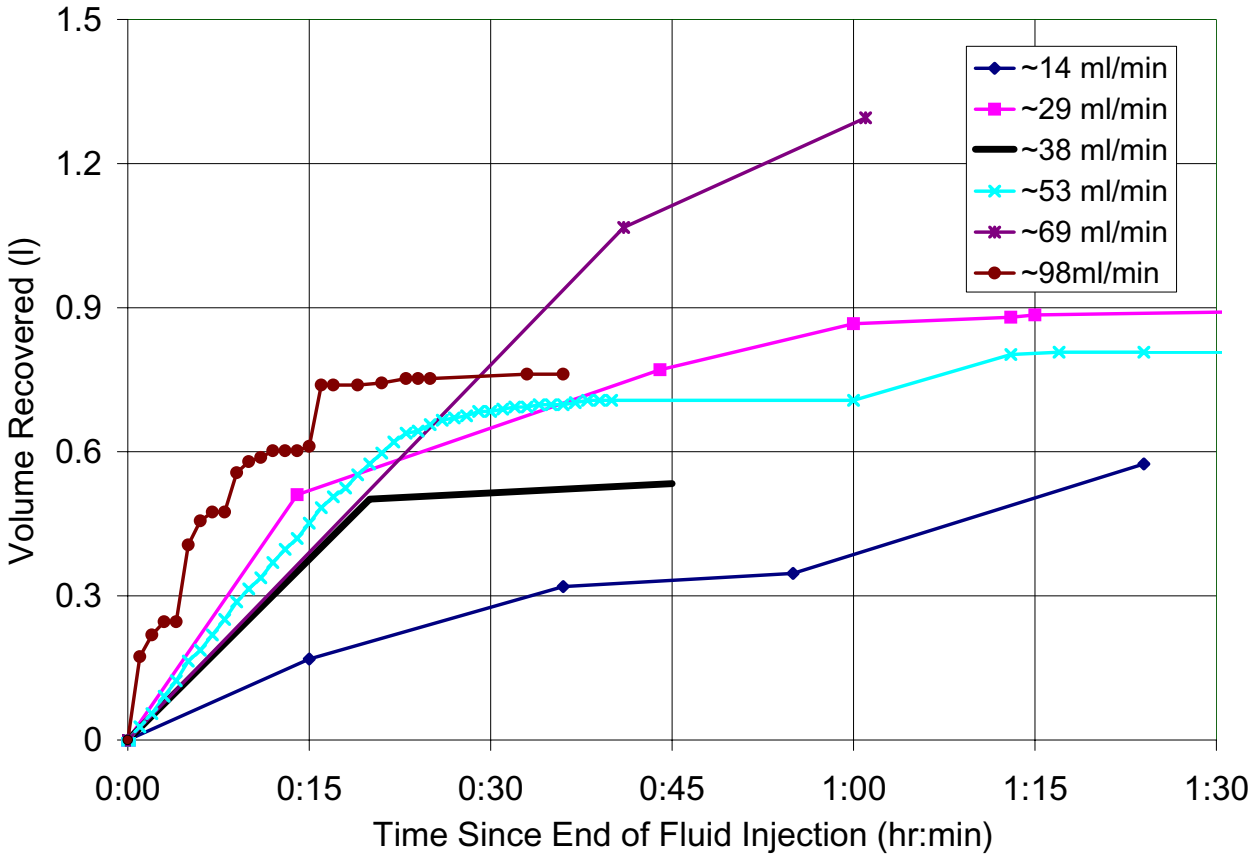

DTN: LB990901233124.002 [146883]

Figure 6.6.2-7. Volume of Water Recovered in the Slot after Liquid Injection at Various Rates into the High Permeability Zone was Stopped

6.6.2.4 Tracer Recovery

Tracers injected in the HPZ were detected in the water samples collected in the slot. (None of the traced water introduced in the LPZ was recovered.) Typically, tracers introduced in one test were rapidly flushed out of the system during the subsequent test (Figure 6.6.2-8). The pattern of recovered concentrations of tracers suggests that plug flow was the dominant process by which 'new' water replaced 'old' water from the previous test. Some recovery of tracers from the formation was observed during subsequent tests.

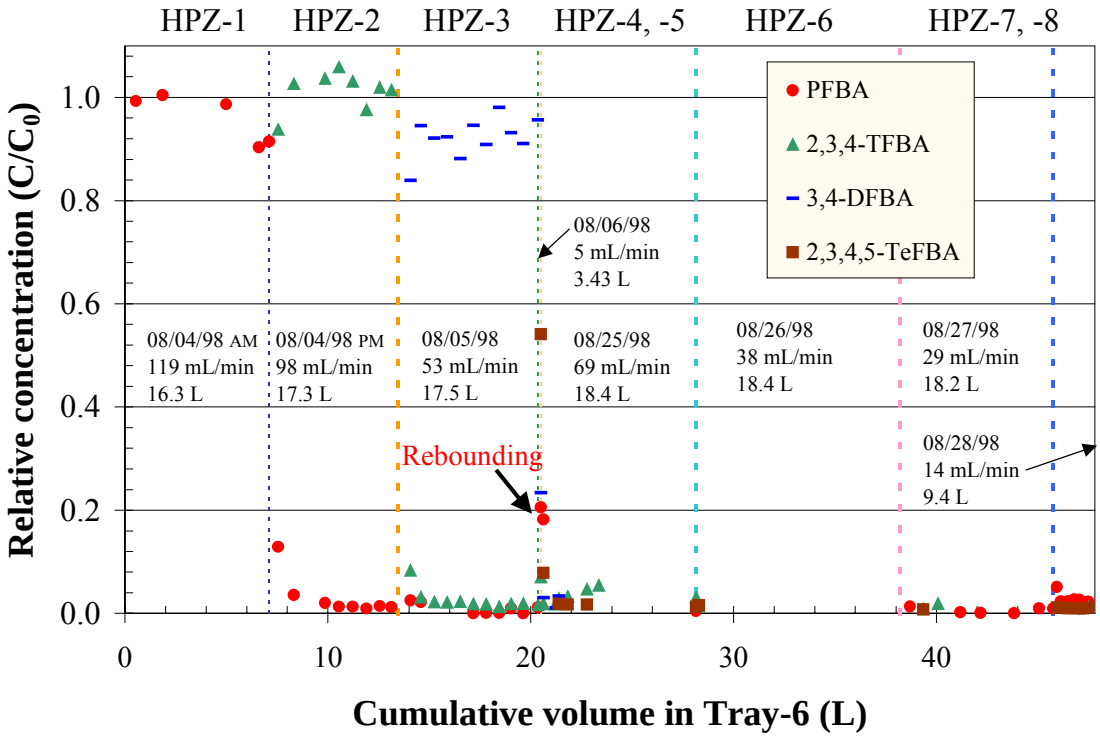

DTN: Flow Rate Data: LB99091233124.002 [146883] and Chemical Data: LB99091233124.001 [155694]

Figure 6.6.2-8. Tracer Concentrations in Seepage Water Following Injection into the High Permeability Zone

6.7 ANALYSES OF FLOW THROUGH THE FAULT AND MATRIX IN THE TEST BED AT ALCOVE 4

The evolution of a flow field and the migration of a wetting front following the release of liquid into a fault and matrix were evaluated in a test bed using a cluster of horizontal boreholes.

6.7.1 Flow Tests in Paintbrush Tuff Unit Layers and Fault

Field experiments were conducted in the PTn within the ESF at Yucca Mountain. These experiments included multiple releases of tracer-laced water in isolated zones along three horizontal boreholes. The zones into which water was released were selected based on air-permeability measurements conducted over 0.3 m sections of borehole (Section 6.5.2). The plumes that developed from these releases were monitored in six separate horizontal boreholes. During and following liquid-release events, changes in saturation and water potential along horizontal monitoring boreholes were continuously recorded by an automated data acquisition system.

6.7.1.1 The Test Bed

The test bed is located at Alcove 4 in the ESF. It is accessed through an alcove excavated (by an Alpine miner) at approximately 67 degrees to the central axis of the ESF North Ramp. Alcove 4 transects portions of the lower Pah Canyon Tuff (Tpp) and the upper pre-Pah Canyon bedded tuffs (Tpbt2) of the PTn (nomenclature of Buesch et al. 1996 [100106], p. 7). The central axis of the alcove has an azimuth of 6 degrees, which coincides with the approximate strike of the PTn units in the vicinity. The north face of the alcove, in which the test bed is located, is approximately 6 m wide and 5.3 m high (Figure 6.7.1-1).

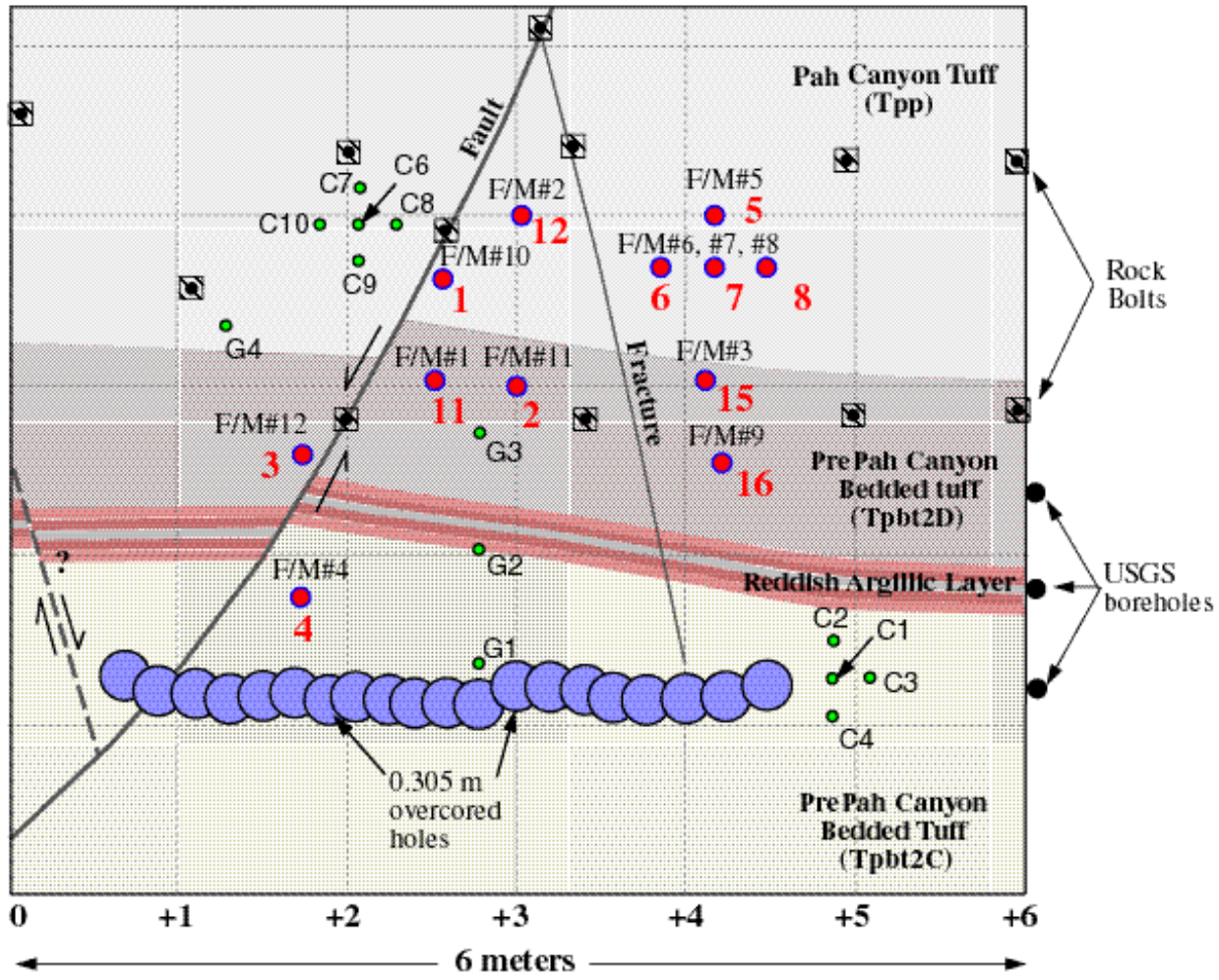

- 0.0762 m diameter (NQ) boreholes, approximate depth = 6 m
- 0.0254 m diameter boreholes, depth of "G" holes = 1 m, depth of "C" holes = 2 m

NOTE: Also included are location of boreholes and the slot.

Figure 6.7.1-1. Geological Sketch for the North Face of Alcove 4 in the ESF at Yucca Mountain

The lower Tpp and upper Tpbt2 units D and C (units from Moyer et al. 1996 [100162], pp. 46-50) are exposed along the north face of Alcove 4. Tpp is nonwelded and pumice-rich. It exhibits a chalky-white color and is apparently zeolitically altered (based on destruction of the texture of the matrix ash and destruction of the integrity of the glass shards, Moyer et al. 1996 [100162], p. 46). Zeolitic alteration in the North Ramp of the ESF commonly follows fractures and faults that cut through the Tpp and Tpbt2 units (Barr et al. 1996 [100029], p. 44). The contact between the lower Tpp and upper Tpbt2D is sharp in Alcove 4, marked by distinct color changes. Tpbt2D is also nonwelded, possibly reworked, and has variably abundant (while zeolitically altered) pumice within a fine- to coarse-grained, medium-brown matrix.

Below Tpbt2D, lying in the upper Tpbt2C, is a thin (0.20-0.30 m), light pink to red argillically altered layer that is almost completely offset by a small, westward-dipping normal fault.

Alteration within this layer can be traced from the end of Alcove 4 out into the North Ramp. It is uncertain whether the argillic alteration seen in Alcove 4 is laterally continuous, though reddish alteration is commonly observed in several boreholes and in outcrops across Yucca Mountain at the same stratigraphic horizon (Moyer et al. 1996 [100162], pp. 54-55). The remaining Tpbt2C exposed along the north face below the argillic layer is massive and nonwelded, has very pale tan coloring, and contains abundant, coarse pumice and lithic fragments.

Cutting the north face of Alcove 4 is a normal fault with a small offset (0.25 m). As mapped along the crown at the end of the alcove (Barr et al. 1996 [100029], full-periphery geologic map OA-46-289, DTN: GS960908314224.020 [106059] for the crown, but not for the end face), the fault has a strike of approximately 195 degrees and a westward dip of 58 degrees. The fault is open in the ceiling and is closed, with knife-edge thickness, near the invert on the north face. Intersecting the fault near the alcove crown along the north face is a high-angle fracture. The cause of the fracture is uncertain and could have been induced by drilling or drying, considering the location of rock bolts and the clay content of the rocks. The orientation of the fracture is unknown, though it has an apparent eastward dip of about 75 degrees. Similar to the fault, the fracture appears to have a large aperture near the ceiling and a much smaller aperture (eventually becoming undetectable) near the invert.

Two distinct features that were imposed on the formation define the layout of the field experiment, i.e., a horizontal slot and a series of horizontal boreholes. The slot, located immediately below the test bed, was designed to capture any seepage resulting from gravity drainage. It was excavated by a drilling sequence that required 0.10 m diameter pilot holes drilled parallel at 0.22 m spacing, perpendicular to the alcove wall. These pilot holes were then over-cored by a 0.3 m drill-bit to excavate a 6.0 m wide, 4.0 m deep and 0.3 m high cavity located approximately 1.5 m above the alcove floor. I-beam supports were installed along the length of the slot to prevent it from collapsing during the duration of the field tests.

Twelve 6.0 m long, 0.1 m diameter boreholes were drilled into the alcove face, as illustrated in Figure 6.7.1-1 and Figure 6.7.1-2. Borehole 1, borehole 4, borehole 11, and borehole 12 were positioned to intersect the fault for the purpose of conducting flow tests within the fault. Borehole 2 was located to detect moisture that could migrate through the matrix below borehole 12. Borehole 12 was the injection borehole for the fault flow tests conducted. The configuration of borehole 5, borehole 6, borehole 7, and borehole 8 was designed to investigate the nature of matrix flow in the Tpp, with borehole 5 serving as the injection borehole and borehole 6, borehole 7, and borehole 8 equipped with probes to detect changes in moisture conditions. Borehole 3 on the left side of the fault and borehole 15 and borehole 16 away from the injection boreholes were not instrumented for the tests conducted. (Borehole 9, borehole 10, borehole 13, and borehole 14 were planned but not drilled.)

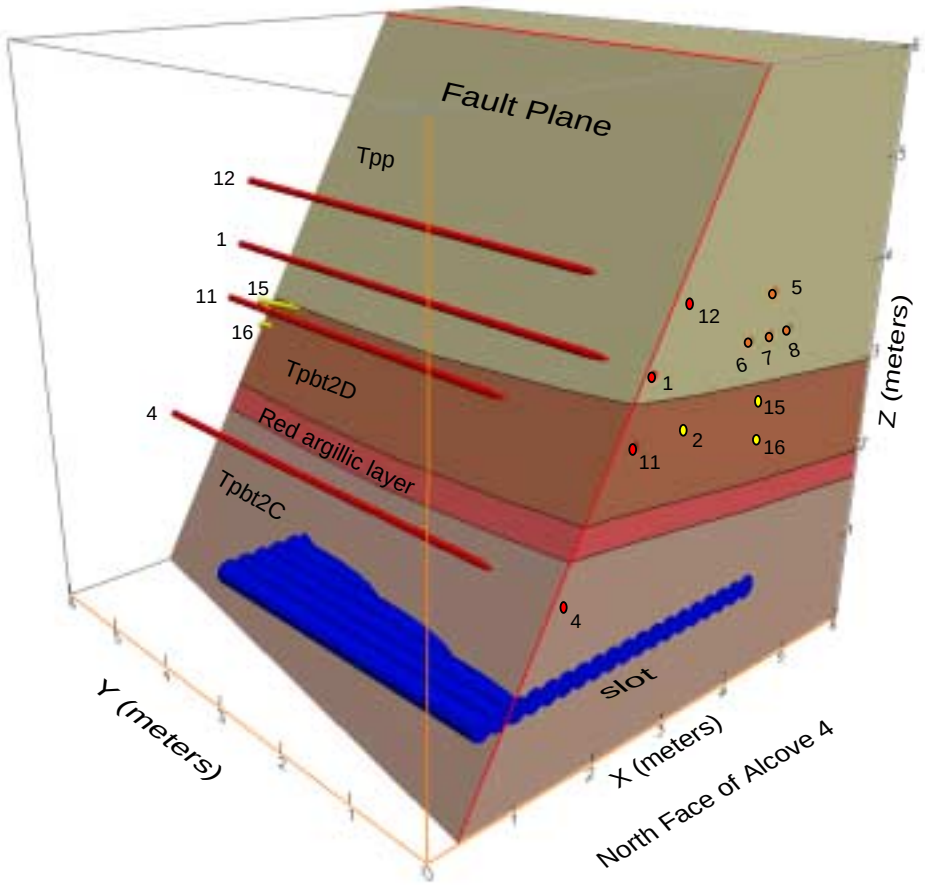

Figure 6.7.1-2. Perspective Illustration of Three-Dimensional View of the Boreholes, Slot, and Lithological Unit Contacts in the Alcove 4 Test Bed

6.7.1.2 Instrumentation

The flow investigation had three distinct components: (1) controlled release of water into isolated zones, (2) borehole monitoring for changes in saturation and water potential, and (3) the monitoring of seepage from the slot ceiling. For each component, new instruments were developed, details for which are described in Attachment VI. Because water did not seep into the slot, the seepage monitoring system was not used. Key features of the liquid-injection and borehole-monitoring system are presented in the following sections.

6.7.1.2.1 Fluid Injection

The liquid-release experiments required water to be injected into the formation over a 0.3 m section of borehole with a constant-head boundary condition to determine the maximum rates at which the zone could take in water. The main components of the fluid-release apparatus included an inflatable packer system used to isolate the injection zone, a pump to deliver water to a constant-head chamber from which water was introduced in to the injection zone, and a reservoir to provide a continuous supply of water. To capture the temporal variability in vertical flux of

water from the injection zone, we developed an automated liquid-release system to measure changing flow rates on a ponded surface. This system allowed for continuous measurement of local liquid-release rates during the entire experiment.

6.7.1.2.2 Borehole Monitoring

In six monitoring boreholes (Borehole 1, borehole 2, borehole 11, borehole 6, borehole 7, and borehole 8 in Figure 6.7.1-2) located above the slot, changes in saturation and water potential were continuously recorded during the entire investigation. Changes in saturation along boreholes were measured with ERPs located at 0.25 m intervals along a 6.0 m length of each borehole. Water potential measurements were made with psychrometers, as described in Attachment VI-2 for Alcove 6 testing. The psychrometers and ERPs were housed in special Borehole Sensor Trays (BSTs) installed along the length of each monitoring borehole.

6.7.1.3 Liquid-Release Experiments

Air-permeability measurements were made along 0.3 m sections of all nine boreholes to determine the exact location of the fault in borehole 4, borehole 11 and borehole 12, as discussed in Section 6.5.2. All water used in the ESF (for mining-related activities and scientific investigations) was spiked with the same concentration of lithium bromide. For the entire duration of the experiments, saturation and water-potential changes along the monitoring boreholes were continuously measured.

A total of 193 liters of water was released into borehole 12 during seven events, under constant-head conditions, between October 21 and November 5, 1998, as summarized in Table 6.7.1-1. In this borehole, as in all others, water was released over a 0.30 m interval. Here, the injection interval was centered at a distance 1.4 m from the borehole collar, determined from air-permeability measurements to be the location of the fault.

Table 6.7.1-1. Summary of Liquid Releases into the Fault Zone in Borehole 12

Test Number	Date (mm/dd/yy)	Volume Injected (l)	Duration (hh:mm)	Average Intake Rate (mL/min)
1	10/21/98	42.90	5:12	138
2	10/22/98	41.44	5:59	115
3	10/26/98	21.34	4:22	81
4	10/27/98	29.53	6:59	70
5	10/28/98	22.16	6:10	60
6	11/04/98	17.08	5:48	49
7	11/05/98	18.85	6:31	48

DTN: LB990901233124.005 [146884]

In borehole 5 away from the fault, water was released into two zones. In the first zone (located 1.50 to 1.80 m from the collar) 1.37 liters of water were released to the zone on October 19, 1998, and a similar volume was released on October 20, 1998. Because a problem was detected with the constant-head system, no more water was injected into this zone. On October 27, 1998, after the injection system was repaired, water was released into borehole 5 at a distance of 2.44–2.74 m from the borehole collar. In this zone, 6.5 liters of water were released under constant head conditions over a period of 23 days.

6.7.2 Observations of Fault Flow and Matrix Flow

During and following the release of water into the test bed, intake rates (rates of water moving into the formation during constant-head tests), travel times, and lateral dispersion of the plume (as seen along the length of horizontal boreholes) were continuously monitored. In the following section, the observed hydrologic responses to liquid releases in the three zones as detected by ERPs and psychrometers are presented.

6.7.2.1 Fault Responses

6.7.2.1.1 Intake Rates

Water was injected into the section of borehole 12 that intercepted the fault approximately 1.40 m from the collar. Here, 193 liters of water were released into the formation during seven events that extended over a period of two weeks as illustrated in Figure 6.7.2-1. Each event lasted between 4 and 7 hours, during which 20–43 liters of water entered the injection zone. Each release event began with water filling the 1.37-liter injection cavity in about 3 minutes, after which the liquid-release apparatus kept the injection zone filled by maintaining a constant-head boundary for the period of injection. After water was injected into the formation, the 1.37 liters of water occupying the injection zone were released to the formation under falling head conditions.

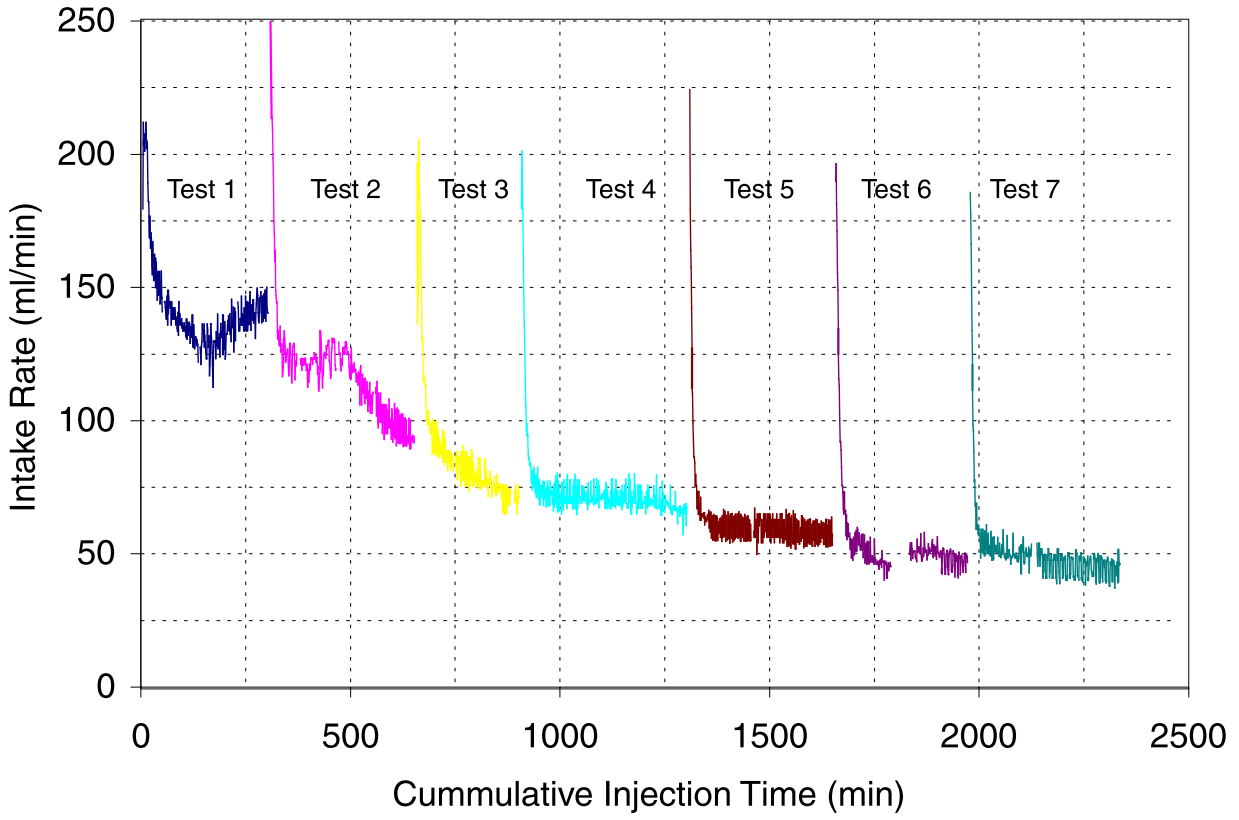

DTN: LB990901233124.005 [146884]

Figure 6.7.2-1. Intake Rates along the 0.3-m Zone Located on the Fault in Borehole 12

During Test 1 into the fault, the intake rate dropped from 200 mL/min to 120 mL/min over a period of 180 minutes before recovering to 145 mL/min in the next 120 minutes. In Test 2, conducted one day later, the intake rate dropped from 200 mL/min to 120 mL/min over a period of 80 minutes before remaining fairly constant for the next 100 minutes. Approximately 180 minutes after this release event started, the intake rates began to drop steadily, reaching a rate of 95 mL/min by the end of the test. In Test 3, which was initiated four days later, the intake rates rapidly dropped to 95 mL/min during the first 40 min and then continued to decrease at a more gradual rate for the next 200 minutes to a rate of 70 mL/min. During Test 4 and Test 5, conducted during the next two days, the pattern of rate change was similar, with an initially high intake rate quickly dropping to a near constant value (70 to 60 mL/min, respectively). In Test 4, this constant value persisted 300 min into the test, after which there was a gradual decrease in intake rates for the remainder of the test. During Test 6, which began after a six-day hiatus, water was injected during two intervals. During this test, water was introduced under constant-head conditions for 140 and 158 minutes periods with a gap of 22 minutes, during which water imbibed into the formation under a falling head. The intake rates rapidly dropped to 50 mL/min. In Test 7 into this zone, the intake rates again dropped to 50 mL/min after 100 minutes of release. The rates gradually decreased during the 200 minutes of injection, which approached 40 mL/min after 18 liters of water had been injected.

6.7.2.1.2 Travel Times in Fault

When water was introduced into borehole 12, the time taken for the wetting front to travel 1.07 m along the fault to borehole 11 varied among the seven tests (Figure 6.7.2-2). In the first test, water was detected in the lower borehole ~300 minutes after the first release, while in the second test, the travel time was reduced to ~200 minutes. For the third test, this travel time was ~250 min; in the fourth test, water appeared in the fault in borehole 11 within ~150 minutes. The fastest travel time was observed for the fifth test, when the front arrived within ~120 minutes in borehole 11. In the last two tests, the travel times were significantly slower, with increasing saturations observed 400 and 700 minutes after the initial release of water.

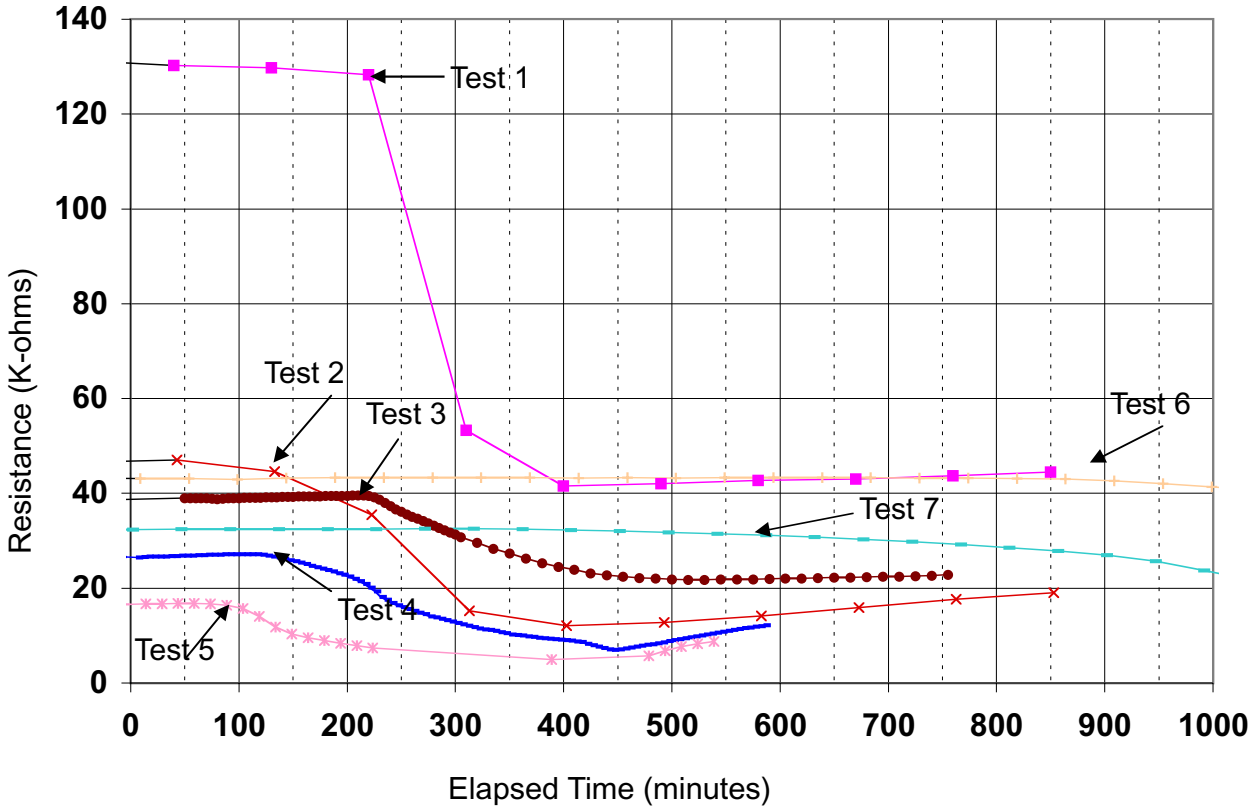

DTN: LB990901233124.005 [146884]

Figure 6.7.2-2. Wetting Front Arrival in Borehole 11 Following Liquid Released into the Fault in Borehole 12

6.7.2.1.3 Dispersion

Water injected into the fault in borehole 12 was detected along the length of borehole 11 by ERPs located between 0.65 and 2.40 m (Figure 6.7.2-3). Unlike the ERP located on the fault (1.40 m from the collar), which showed a stepped response to individual release events, these other ERPs showed a slow, gradual decrease in resistance measurements. The first response was seen in the ERPs located on either side of the fault, with the one at 1.65 m responding first. ERPs located between the alcove face and the fault appeared to be significantly drier at the start of the experiment than those located deeper in the test bed. These ERPs responded with larger decreases in resistance measurements following the start of the release water. The largest response to the injection events in borehole 12 was detected between 0.9 and 1.65 m from the collar in borehole 11.

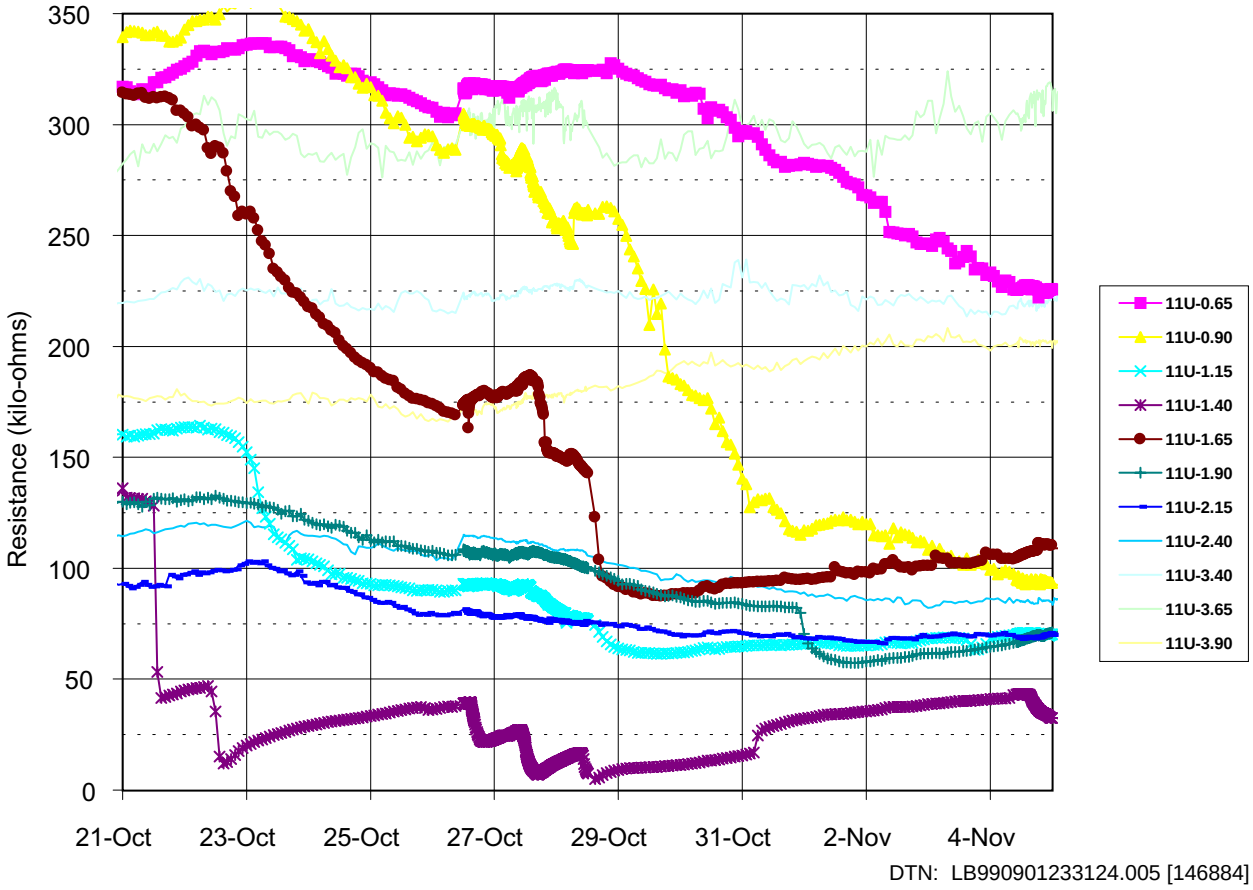

DTN: LB990901233124.005 [146884]

NOTE: The legend indicates the location of the measurement (in meters) from the collar. The 'U' indicates that these are measurements from the upper BSTs in the borehole.

Figure 6.7.2-3. Changes in Electrical Resistance in Borehole 11 in Response to Liquid Released into the Fault in Borehole 12

In borehole 2 located 0.97 m vertically below borehole 12, the first ERPs to detect the wetting front were centered immediately below the fault (Figure 6.7.2-4). Here, at a distance of 1.15 to 1.65 m from the borehole collar, changes in saturation were detected almost one week after the first injection event on October 21, 1998. Over the next three weeks, ERPs at 1.15 and 1.40 m continued to detect increasing saturations, while the ERP at 1.65 m wetted for four days before maintaining a relatively constant saturation level for the next 18 days. At depths between 1.90 and 2.40 m, the response was delayed very slightly.

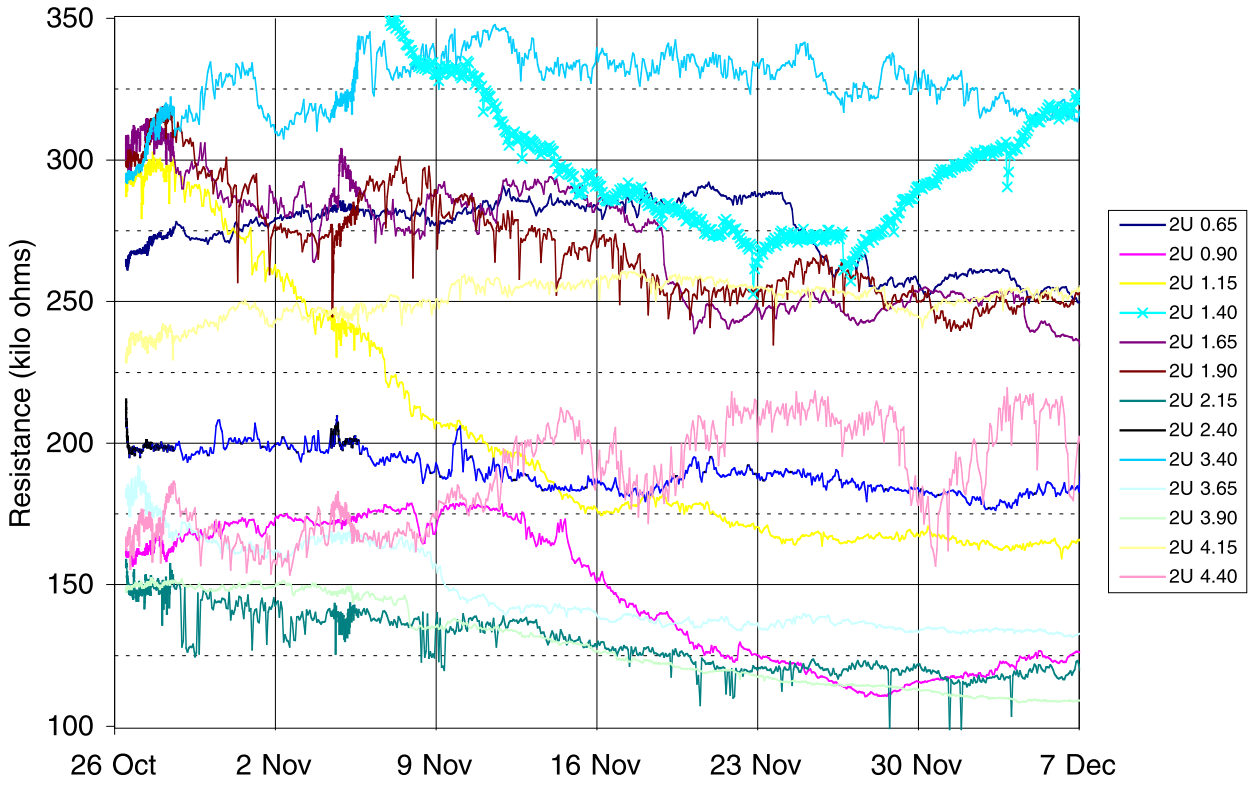

DTN: LB990901233124.005 [146884]

NOTE: The legend indicates the location of the measurement (in meters) from the collar. The 'U' indicates that these are measurements from the upper BSTs in the borehole.

Figure 6.7.2-4. Changes in Electrical Resistance in Borehole 2 in Response to Liquid Released into the Fault in Borehole 12

6.7.2.2 Matrix Responses

6.7.2.2.1 Intake Rates

When water was released into borehole 5, in the zone 2.44–2.74 m from the collar, the intake dropped steeply to 1 mL/min within 150 minutes (Figure 6.7.2-5). The intake rate then continued to gradually decrease over the next 2,000 minutes before reaching a constant rate of ~0.1 mL/min. This rate remained approximately constant for the entire duration of test.

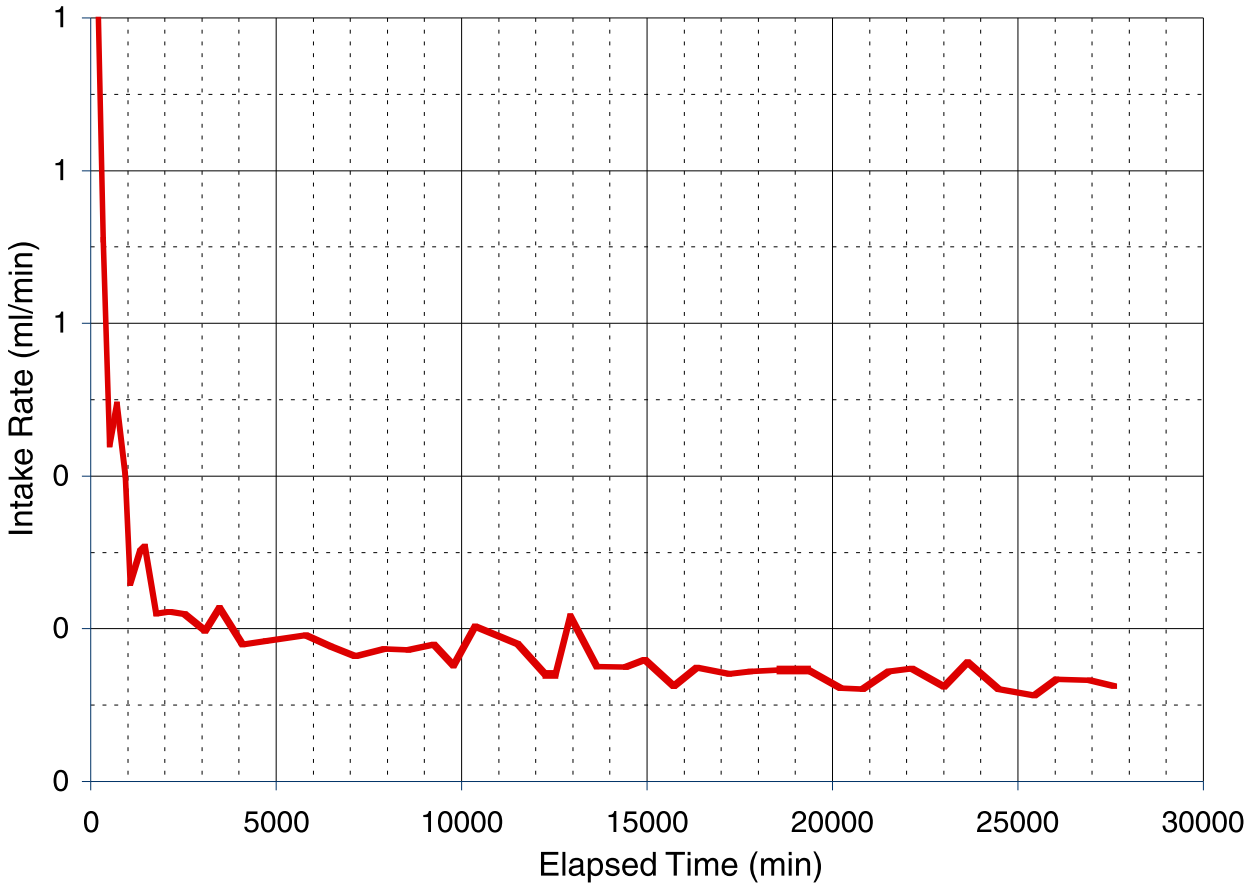

DTN: LB990901233124.005 [146884]

Figure 6.7.2-5. Intake Rates along a 0.3-m Zone in the Matrix Located 2.44–2.74 m from the Collar in Borehole 5

6.7.2.2.2 Wetting Front Migration

Following the first release of water in borehole 5 on October 27, 1998 (at 2.44–2.74 m from the collar), the wetting front was detected in the upper section of borehole 6 (located 0.45 from borehole 5) after a period of 14 days on November 10, 1998 at a distance of 2.90 m from the collar (Figure 6.7.2-6). Some of the sensors near the collar had high resistance values and fluctuating changes that might represent responses to additional drying and wetting processes near the borehole collar.

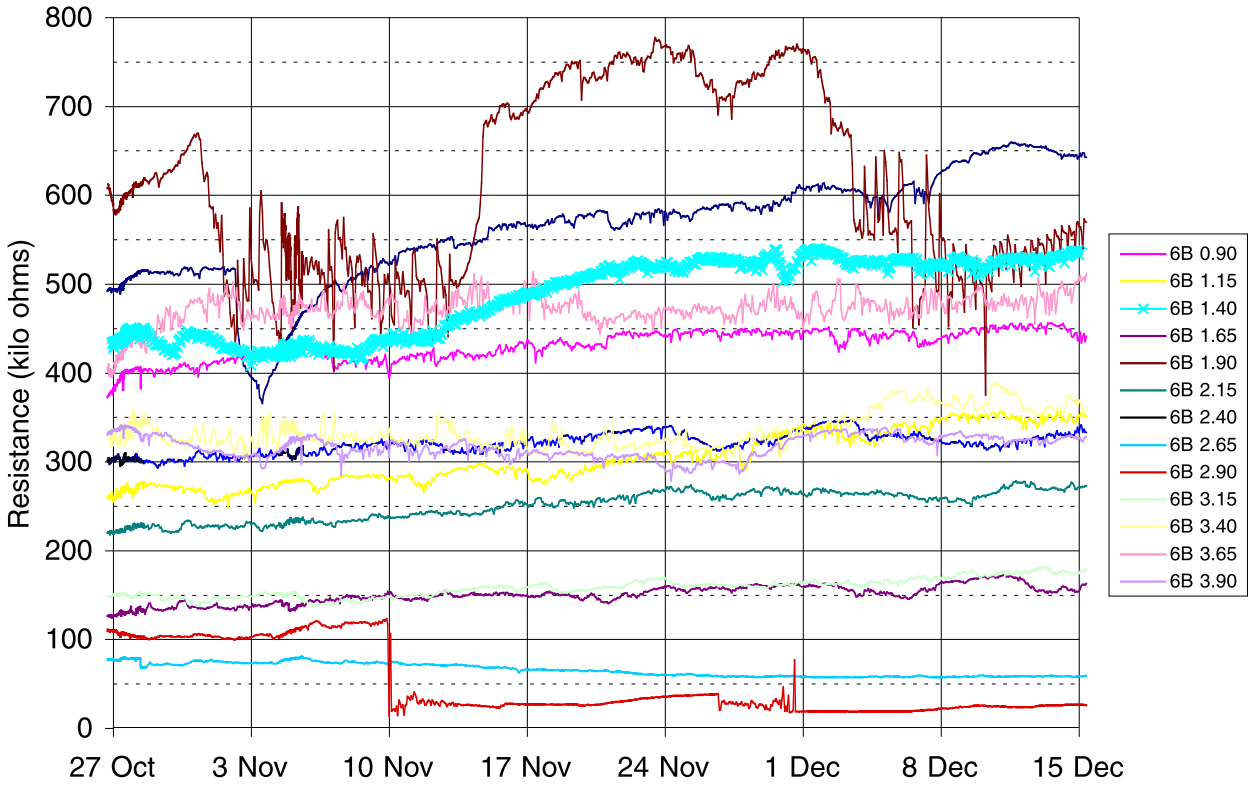

DTN: LB990901233124.005 [146884]

NOTE: The legend indicates the location of the measurement (in meters) from the collar. The 'B' indicates that these are measurements from the lower BSTs in the borehole.

Figure 6.7.2-6. Changes in Electrical Resistance in Borehole 6 in Response to Liquid Released in Borehole 5

6.8 COMPILATION OF WATER-POTENTIAL MEASUREMENTS IN NICHES

Measurements of water potentials from three niche sites in the ESF are presented. These sites are located on the west side of the ESF Main Drift at Niche 3566, Niche 3650, and Niche 3107. Two faults (the Ghost Dance fault and Sundance fault) lie within the immediate vicinity of the niches, with Niche 3566 lying between the Sundance fault and a cooling joint branching out from the fault.

The primary objective of this effort was to determine the water potential at various points within the three niche sites. To meet this objective, we adapted a common method to measure water potential, the use of psychrometers, for borehole application. The psychrometers were also used in wetting-front detection, as described in Section 6.6 for Alcove 6 and Section 6.7 for Alcove 4. The sensitivity of psychrometer performance is described in Attachment VII.

6.8.1 Location and Timing of Water-Potential Measurements at Niches

Water potentials were measured either along the length or at the ends of 0.0762 m diameter boreholes. Three different types of housing units were used to locate psychrometers in the boreholes. The main feature of the housings was the creation of a small air chamber that allowed for quick equilibration and measurements of humidity close to the borehole wall.

At Niche 3566, two separate sets of measurements were made: before and after niche excavation. Pre-excavation measurements were made during May 1997 in three holes (U, M, and B) at a distance of 10 m from the borehole collar (Figure 6.8.1-1a). Between July and September 1997, two sets of measurements were made along borehole U at distances between 3.5 and 8.0 m from the collar. Post-excavation measurements of water potential were made in October 1997 in five boreholes extending radially along a horizontal plain from the niche cavity (Figure 6.8.1-1b).

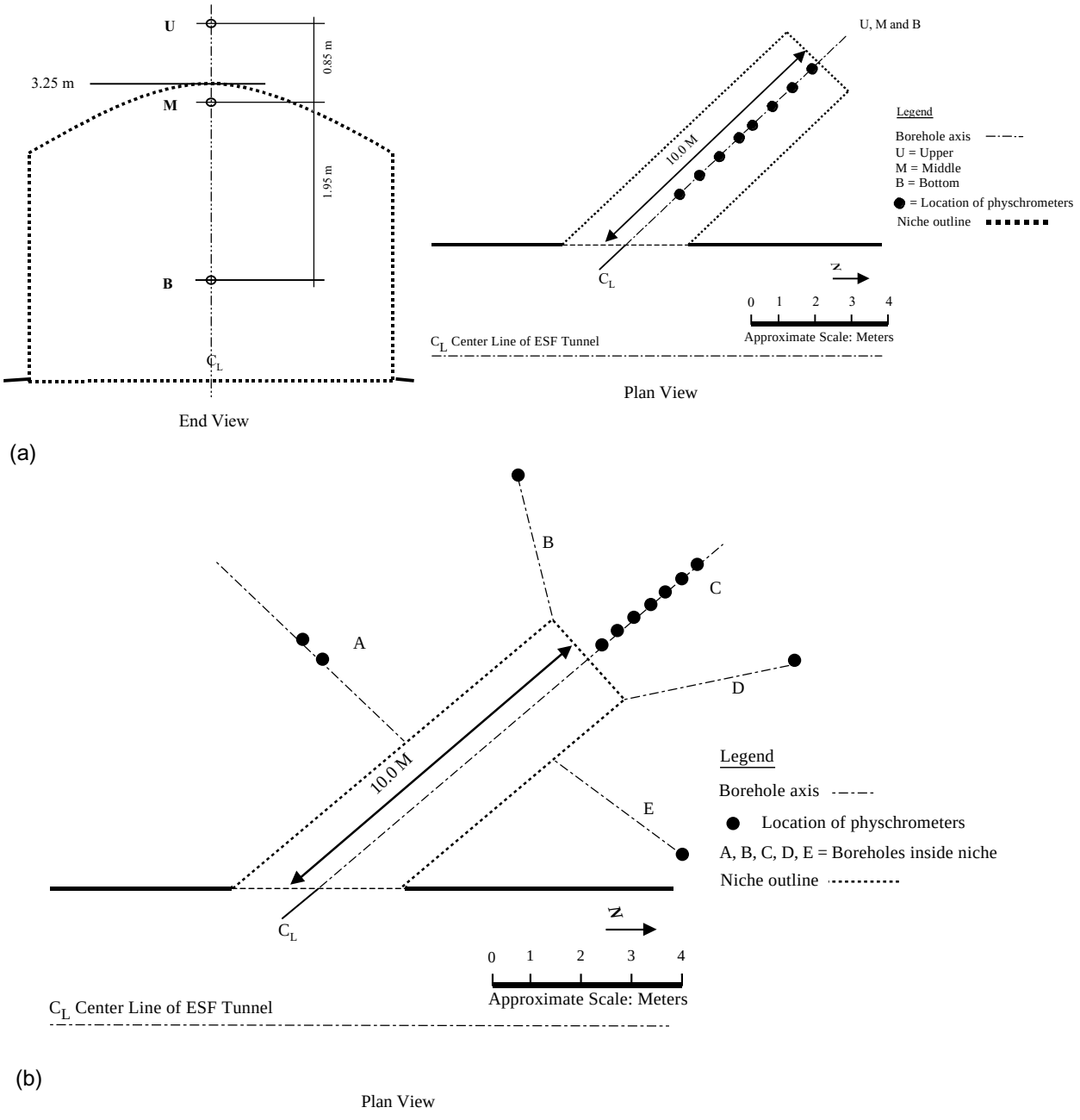

Figure 6.8.1-1. Schematic Illustration of the Location of Psychrometers in Niche 3566 (a) in Pre-Excavation and (b) in Post-Excavation Conditions

At Niche 3650, two separate sets of water-potential measurements were made in July 1997, before and after air-permeability tests were conducted in the boreholes. In three boreholes at this location (ML, BR, and BL), water potentials were measured at the end of the boreholes (10 m). In borehole UM, measurements were made close to the borehole collar, i.e., between 0.6 and 1.2 m (Figure 6.8.1-2).

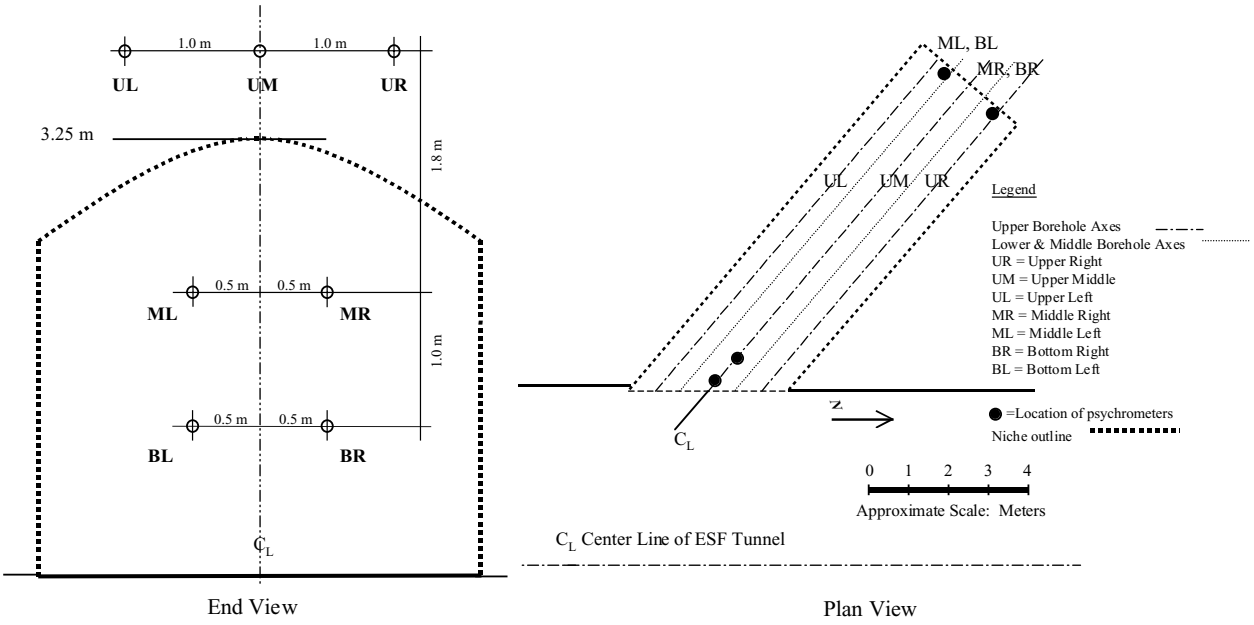

Figure 6.8.1-2. Schematic Illustration of Location of Psychrometers in Niche 3650

At Niche 3107, four boreholes were instrumented with psychrometers (Figure 6.8.1-3). One set of potential measurements were made in December 1997 and January 1998. In the upper middle (UM) borehole, multiple measurements were made along the first 3.0 m, while in the remaining three boreholes (ML, UL, UR), single measurements were made using different lengths of borehole cavity. In the upper-right borehole (UR), sensors were located at the back of the borehole and sealed off with inflation packers such that the borehole cavity was less than 0.04 m long. In the upper-left (UL) borehole, sensors were located 5 m from the borehole collar, with the cavity sealed off with inflation packers. In this case, the sensing cavity extended over 5 m of the borehole. In the middle-lower borehole (ML), sensors were located 0.3 m from the borehole collar, with an inflation packer installed to isolate the entire 10 m length of borehole from the ESF Main Drift.

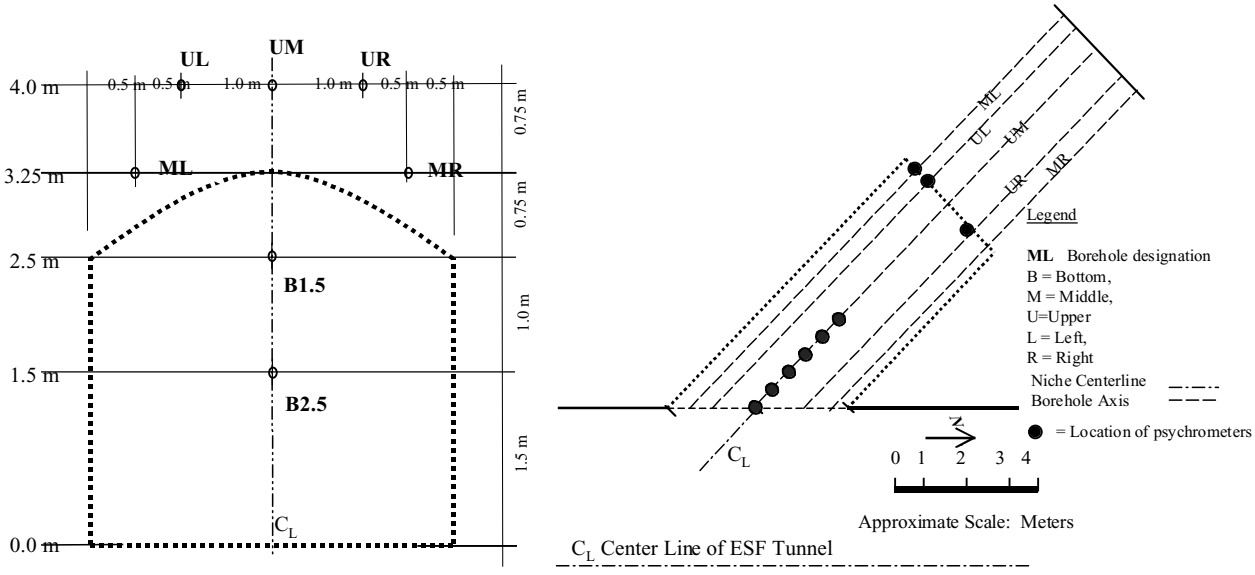

End View Plan View

Figure 6.8.1-3. Schematic Illustration of Location of Psychrometers in Niche 3107 (Pre-Excavation)

6.8.2 Observations of Dryout in Niche Boreholes

Water-potential measurements obtained from the three niches are summarized in Table 6.8.2-1 to Table 6.8.2-2. The time and duration of measurements are presented for each location.

Table 6.8.2-1. Water-Potential Measurements in Niche 3566

Borehole ID	Dist. from Collar (m)	Duration of Measurement	Psych #	Water Potential (m)
Pre-Excavation				
U	10.0	5/9-16/97	Psy -51	-13
U	10.0	5/9-16/97	Psy -52	-13
M	10.0	5/9-16/97	Psy -53	-7
M	10.0	5/9-16/97	Psy -54	0.4
B	10.0	5/9-16/97	Psy -55	-12
U	6.1	7/8-14/97	Psy -42	-49
U	5.5	7/8-14/97	Psy -43	-46
U	5.5	7/8-14/97	Psy -44	-34
U	4.9	7/8-14/97	Psy -45	-46
U	4.3	7/8-14/97	Psy -48	-68
U	3.7	7/8-14/97	Psy -50	-62
U	7.9	9/16-24/97	Psy -42	-49
U	7.3	9/16-24/97	Psy -60	-46
U	6.7	9/16-24/97	Psy -45	-71
U	6.1	9/16-24/97	Psy -48	-67
U	5.5	9/16-24/97	Psy -50	-36
Post-Excavation				
A	6.25	10/18-21/97	Psy-43a	-2
A	6.75	10/18-21/97	Psy-60	-30
B	6.00	10/18-21/97	Psy-51	-43
C	0.15	10/18-21/97	Psy-49	-132
C	0.76	10/18-21/97	Psy-42	-33
C	1.98	10/18-21/97	Psy-45	-22
C	1.98	10/18-21/97	Psy-47	-47
C	1.37	10/18-21/97	Psy-48	-40
C	2.60	10/18-21/97	Psy-43	-57
D	6.00	10/18-21/97	Psy-54	-22
D	6.00	10/18-21/97	Psy-56	-32
E	6.00	10/18-21/97	Psy-57	-75
E	6.00	10/18-21/97	Psy-59	-81

DTN: LB980001233124.001 [105800]

Table 6.8.2-2. Water-Potential Measurements in Niche 3650

Borehole ID	Dist. from Collar (m)	Duration of Measurement	Psych #	Water Potential (m)
Pre-Air-Injection Testing				
UM	1.2	7/1-8/97	Psy -48	-127
UM	0.6	7/1-8/97	Psy -49	-139
UM	0.6	7/1-8/97	Psy -50	-165
BR	10.0	7/1-8/97	Psy -51	-37
BR	10.0	7/1-8/97	Psy -52	-39
BR	10.0	7/1-8/97	Psy -53	-32
BL	10.0	7/1-8/97	Psy -54	-24
BL	10.0	7/1-8/97	Psy -55	-36
ML	10.0	7/1-8/97	Psy -57	-1
Post-Air-Injection Testing				
ML	10.0	7/24-28/97	Psy -51	-29
ML	10.0	7/24-28/97	Psy -52	-38
ML	10.0	7/24-28/97	Psy -53	-39
BR	10.0	7/24-28/97	Psy -54	-58
BR	10.0	7/24-28/97	Psy -55	-49
BR	10.0	7/24-28/97	Psy -56	-48
BL	10.0	7/24-28/97	Psy -57	-21
BL	10.0	7/24-28/97	Psy -58	-15
BL	10.0	7/24-28/97	Psy -59	-28

DTN: LB980001233124.001 [105800]

Table 6.8.2-3. Water-Potential Measurements in Niche 3107

Borehole ID	Dist. from Collar (m)	Duration of Measurement	Psych #	Water Potential (m)
UM	0.45	12/22/97-1/8/98	Psy-86	-273
UM	1.06	12/22/97-1/8/98	Psy-83	-154
UM	1.67	12/22/97-1/8/98	Psy-75	-83
UM	2.90	12/22/97-1/8/98	Psy-68	-28
UL	10.00	12/22/97-1/8/98	Psy-64	-15
ML	10.00	12/22/97-1/8/98	Psy-66	-84

DTN: LB980001233124.001 [105800]

6.8.2.1 Niche 3566 (Pre-Excavation)

Water potentials measured at the ends of the three pre-excavation boreholes (U, M, and B) in Niche 3566 were close to saturation values, indicating that approximately 10 m from the ESF,

the formation is relatively wet. Of the three, the end of the middle borehole appeared to be wettest, with water potentials between 0.4 and -7 m. Measurements made along the profile of borehole U (between 3.7 and 7.9 m from the collar) ranged between -34 and -71 m (Figure 6.8.2-1 and Table 6.8.2-1).

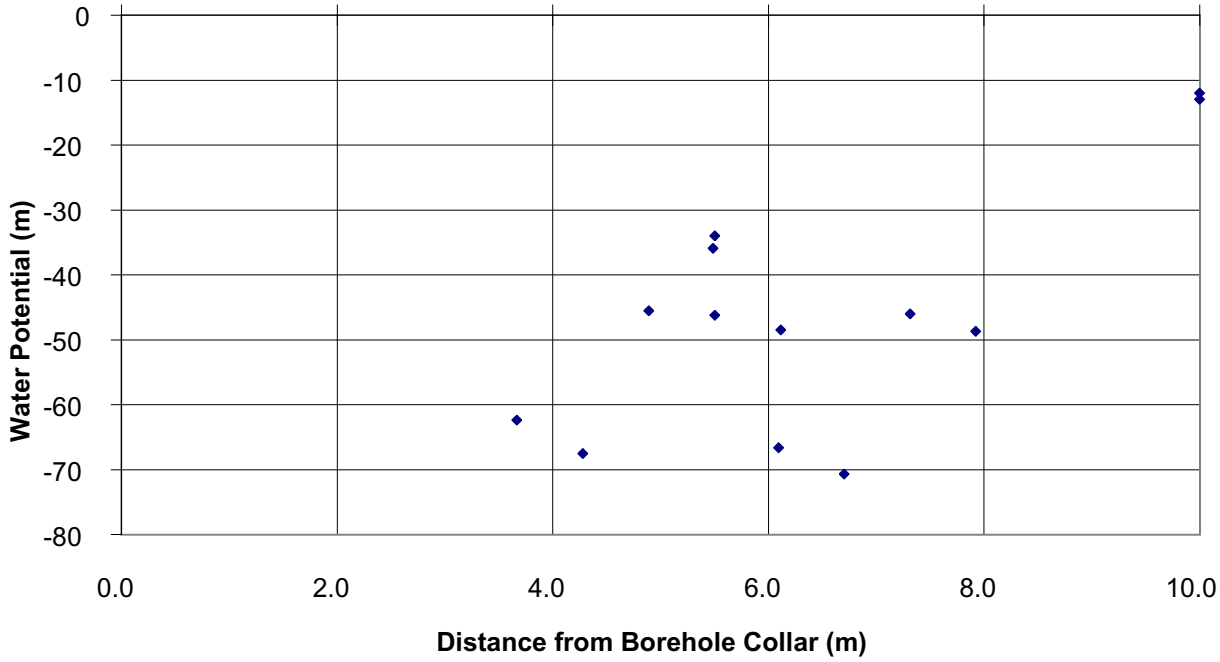

DTN: LB980001233124.001 [105800]

Figure 6.8.2-1. Pre-Excavation Water Potential Measured along Borehole U in Niche 3566

6.8.2.2 Niche 3566 (Post-Excavation)

In the excavated niche cavity, water potentials were monitored in five boreholes. The monitored locations in borehole A (Figure 6.8.1-1b) were at 6.25 and 6.75 m from the collar. High water potentials were measured at these points (-2 and -30 m respectively). In three of the remaining boreholes (B, D, and E) water potentials measured at depths of 6.0 m varied significantly between boreholes. Borehole D (-27 m) was wettest, followed by B (-43 m) and then E (-78 m). These observations appear to be consistent with those made in the pre-excavation boreholes, which indicated that the formation tended to get wetter with increasing distance from the Main Drift.

Measurements made close to the collar in borehole C suggest that there was significant dry-out in the rock surrounding the niches to a depth of at least 0.15 m, extending possibly to 2.6 m.

6.8.2.3 Niche 3650 (Pre-Excavation)

Measurements were made at the end of three boreholes BR, BL, and ML (Figure 6.8.1-2, Table 6.8.2-2), each 10 m long, before and after a series of air-permeability tests. Pre-test water-potential values ranged between -1 and -39 m. However, following the test, water potentials in one hole (BR) dropped to between -48 and -58 m, while in another hole (BL) the measurements did not show significant changes. Closer to the borehole collar of Borehole UM, readings made between 0.6 and 1.2 m indicate a relatively dry zone, with water potentials between -125 and -137 m.

6.8.2.4 Niche 3107

The observations made in Niche 3107 (Table 6.8.2-3) indicate significant variability among the boreholes in the niche. Measurements made at the ends of boreholes UL (-15 m) and ML (-84 m) indicate that at a depth of 10 m with a separation distance of 0.9 m (0.75 m vertically and 0.5 m horizontally, as illustrated in Figure 6.8.1-3), there is a steep potential gradient. Furthermore, from observations within borehole UM, it is clear that a prominent dry-out zone (Figure 6.8.2-2) is associated with the Main Drift of the ESF.

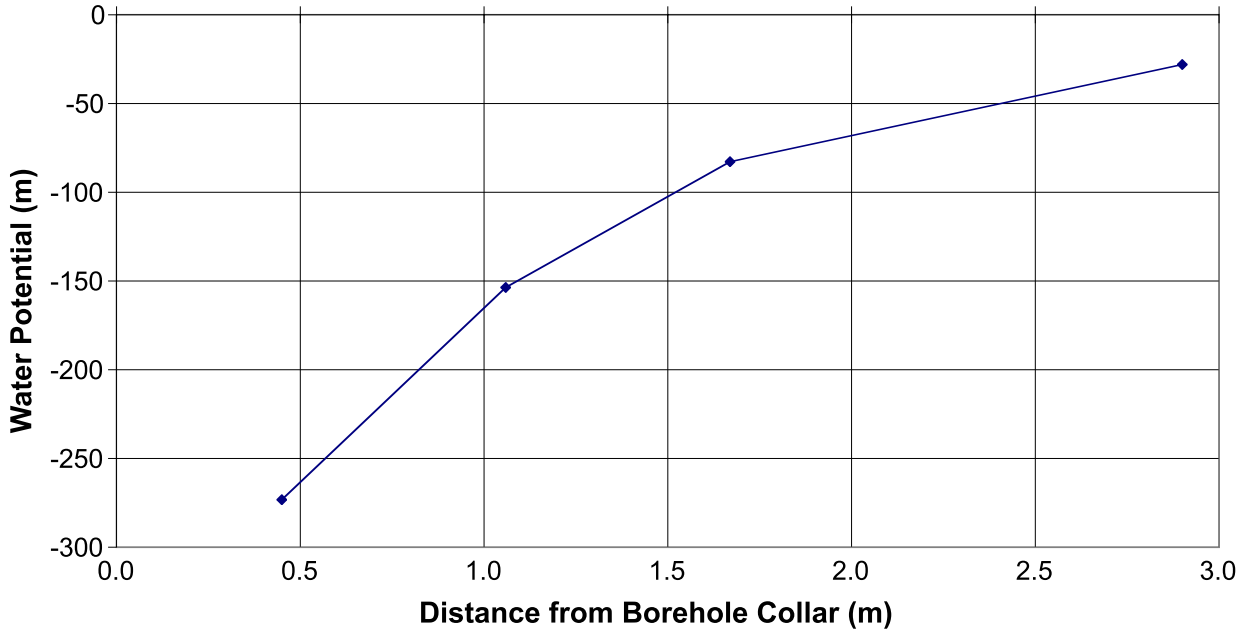

DTN: LB980001233124.001 [105800]

Figure 6.8.2-2. Water Potential Measured along Borehole UM in Niche 3107

6.9 OBSERVATIONS OF CONSTRUCTION-WATER MIGRATION

During the ECRB Cross Drift excavation, sensors and water-collection trays were placed in a borehole below the Starter Tunnel and along the ESF Main Drift at the cross-over point. This section summarizes the results of monitoring the migration of water plumes from tunneling activities. A secondary objective was to evaluate the performance of ERP as a tool to detect the migration of wetting fronts in the unsaturated zone of fractured tuffs. The time domain reflectometry (TDR) was also used to monitor construction-water arrivals in drift walls. The TDR is based on electric measurement of waveguide reflection signals from changes in dielectric constant associated with water content changes.

6.9.1 Equipment Set-Up for Construction-Water Monitoring

6.9.1.1 Starter Tunnel Borehole

To monitor the migration of a water plume resulting from construction of the ECRB Cross Drift, a 30 m long borehole (0.10 m ID) at an angle of 30 degrees (from the horizontal), along the proposed path of the ECRB Cross Drift tunnel (Figure 6.9.1-1). This borehole was in the Tptpul unit. The borehole originated at the end of a starter tunnel that was the launching pad for the Tunnel Boring Machine (TBM) used to excavate the ECRB Cross Drift. Changes in water saturation and potential were monitored along the entire length of borehole, using psychrometers and ERPs, as the TBM advanced through the formation above.

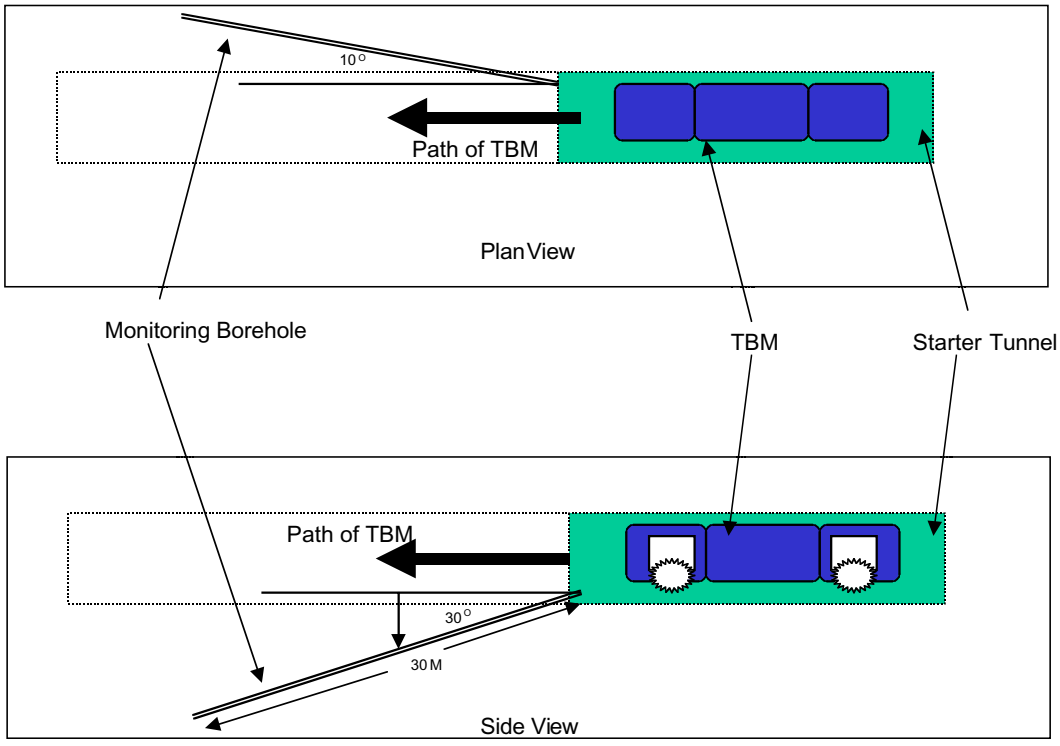

Figure 6.9.1-1. Schematic Illustration of the Location of Wetting Monitoring Borehole at the Starter Tunnel of the ECRB Cross Drift

6.9.1.2. Electrical Resistivity Probes and Psychrometers

The psychrometers and ERPs were housed in PVC trays. These trays were fabricated from PVC pipes (0.10 m OD) bisected along the lengths. On each tray, psychrometers were installed at a spacing of 1.0 m along the borehole, while ERPs were located at 0.5 m intervals. To locate the psychrometers, we glued squares of PVC (0.02 m) at the 1.0 m mark and drilled small diameter holes (~0.003 m ID) through the tray. Psychrometers were then installed in these holes (Figure 6.9.1-2). ERPs were attached to the outer surface of the PVC trays with strips of Velcro. This housing permitted close contact between the ERPs and borehole wall, while allowing the psychrometers to contact the borehole wall through a small cavity.

A steel spoon, 3.0 m long and having the same configuration as the trays, was used to locate each PVC tray along the borehole. Typically, each tray was placed on the steel spoon and carried to the desired location where the spoon was slipped out, allowing the tray to settle snugly against the borehole wall.

Twenty-seven psychrometers and 54 electrical resistivity probes located on nine PVC trays were installed in the borehole (Figure 6.9.1-2) on February 26, 1998. Psychrometer data were collected at 1.5-hour intervals starting on February 28, 1998 for a period of four months. ER data collection started on March 25, 1998, and was collected at the same frequency and for the same duration as the psychrometers.

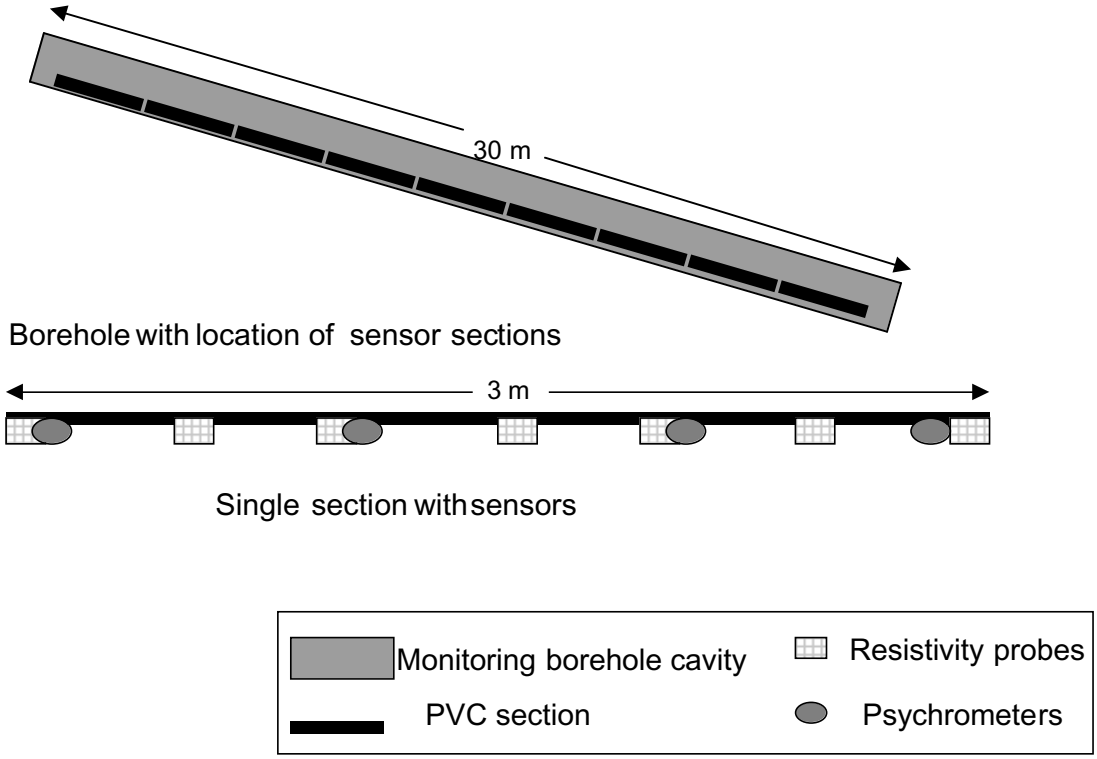

Figure 6.9.1-2. Schematic Illustration of the Borehole Wetting Front Monitoring System with Psychrometers and Electrical Resistivity Probes

6.9.1.3 Drift Monitoring at the Cross-Over Point

The schematics of the seepage detection system, with fluid collection trays hanging below the ceiling of the ESF Main Drift, are illustrated in Figure 6-2. The schematics of the associated sensor arrays are illustrated in Figure 6.9.1-3. The seepage monitoring system was used to detect the wetting front in the ESF Main Drift as the result of releases of traced water in the ECRB Cross Drift above.

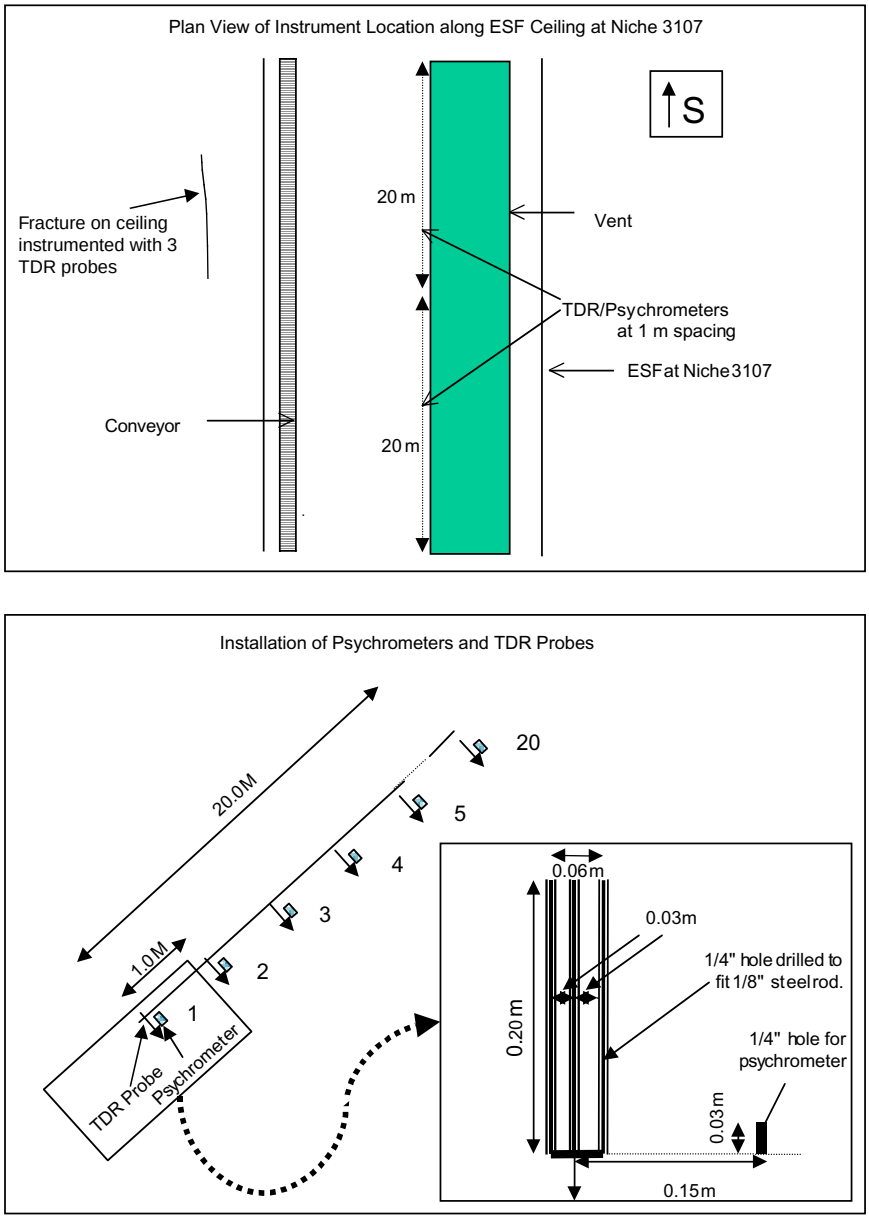

Figure 6.9.1-3. Schematic Illustration of Sensor Arrays for Wetting Front Monitoring

At the crossover monitoring station, we installed 132 collection trays, each 0.3 m wide and 1.23 m long, from station 30+40 to 30+80 m. The trays were hung below the tunnel ceiling next to the ventilation duct along the ESF Main Drift. On the drift walls above the spring line (3.18 m above

the floor), psychrometers and TDR probes were installed. A horizontal sensor array with 40 psychrometer-TDR pairs at 1 m spacing was installed along the west wall (right rib). At the crossover location, vertically along the west wall, between the spring line and the ventilation duct, three psychrometers were installed. On the east wall (left rib), three TDR probes were installed along the trace of a major fracture. In addition to the sensor on the walls, an infrared camera and a video camera periodically monitored the area around one TDR probe on the fracture trace. Infrared images are sensitive to temperature changes associated with evaporation processes.

6.9.2 Wetting Front Detection and Monitoring Below the ECRB Cross Drift

The following results are presented to show that the wetting front was detected up to 12.15 m below the ECRB Cross Drift Starter Tunnel and no seepage was observed at the crossover point in the Main Drift 17.5 m below the ECRB Cross Drift. The Starter Tunnel is located in the upper lithophysal TSw tuff unit and the crossover point is located in the middle nonlithophysal TSw tuff unit.

6.9.2.1 Wetting Front Detection at the Starter Tunnel

The responses of all psychrometers and ERPs used in this investigation are summarized in Table 6.9.2-1 and Table 6.9.2-2. The last columns of both tables, all working sensors with signals in response to construction-water usage are labeled “yes” and those not in response are labeled “no.” With the arrival of a wetting front, the water potential measured by psychrometers and the electrical resistance measured by ERPs change to near zero values.

Table 6.9.2-1. Psychrometers Response to Excavation at the Starter Tunnel of the ECRB Cross Drift

PSY_ID	Dist. Collar (m)	Vertical Depth (m)	Response to Tunneling
Psy_30.3	30.3	15.15	-
Psy_29.3	29.3	14.65	-
Psy_28.3	28.3	14.15	No
Psy_27.3	27.3	13.65	-
Psy_26.3	26.3	13.15	No
Psy_25.3	25.3	12.65	No
Psy_24.3	24.3	12.15	Yes
Psy_23.3	23.3	11.65	No
Psy_22.3	22.3	11.15	Yes
Psy_21.3	21.3	10.65	No
Psy_20.3	20.3	10.15	No
Psy_19.3	19.3	9.65	-
Psy_18.3	18.3	9.15	Yes
Psy_17.3	17.3	8.65	Yes
Psy_16.3	16.3	8.15	Yes
Psy_15.3	15.3	7.65	Yes
Psy_14.3	14.3	7.15	Yes
Psy_13.3	13.3	6.65	Yes
Psy_11.4	11.4	5.7	Yes
Psy_10.4	10.4	5.2	Yes
Psy_9.4	9.4	4.7	Yes
Psy_7.2	7.2	3.6	-
Psy_6.2	6.2	3.1	Yes
Psy_5.2	5.2	2.6	Yes
Psy_3.9	3.9	1.95	-
Psy_2.6	2.6	1.3	-
Psy_1.6	1.6	0.8	Yes

Table 6.9.2-2. Electrical Resistivity Probe Responses to Excavation at the Starter Tunnel of the ECRB Cross Drift

ER_ID	Dist. Collar (m)	Vertical Depth (m)	Response to Tunneling
ER_30.3 m	30.3	15.2	No
ER_29.8 m	29.8	14.9	No
ER_29.3 m	29.3	14.7	No
ER_28.8 m	28.8	14.4	No
ER_28.3 m	28.3	14.2	No
ER_27.8 m	27.8	13.9	No
ER_27.3 m	27.3	13.7	Yes
ER_26.8 m	26.8	13.4	Yes
ER_26.3 m	26.3	13.2	No
ER_25.8 m	25.8	12.9	No
ER_25.3 m	25.3	12.7	No
ER_24.8 m	24.8	12.4	No
ER_24.3 m	24.3	12.2	Yes
ER_23.8 m	23.8	11.9	No
ER_23.3 m	23.3	11.7	No
ER_22.8 m	22.8	11.4	No
ER_22.3 m	22.3	11.2	Yes
ER_21.8 m	21.8	10.9	Yes
ER_21.3 m	21.3	10.7	Yes
ER_20.8 m	20.8	10.4	No
ER_20.3 m	20.3	10.2	Yes
ER_19.8 m	19.8	9.9	Yes
ER_19.3 m	19.3	9.7	Yes
ER_18.8 m	18.8	9.4	Yes
ER_18.3 m	18.3	9.2	Yes
ER_17.8 m	17.8	8.9	Yes
ER_17.3 m	17.3	8.7	Yes
ER_16.8 m	16.8	8.4	Yes
ER_16.3 m	16.3	8.2	Yes
ER_15.8 m	15.8	7.9	Yes
ER_15.3 m	15.3	7.7	Yes
ER_14.8 m	14.8	7.4	Yes
ER_14.3 m	14.3	7.2	Yes
ER_13.8 m	13.8	6.9	Yes
ER_13.3 m	13.3	6.7	Yes

ER_ID	Dist. Collar (m)	Vertical Depth (m)	Response to Tunneling
ER_12.8 m	12.8	6.4	Yes
ER_11.4 m	11.4	5.7	Yes
ER_10.9 m	10.9	5.5	Yes
ER_10.4 m	10.4	5.2	Yes
ER_9.9 m	9.9	5.0	Yes
ER_9.4 m	9.4	4.7	Yes
ER_8.9 m	8.9	4.5	Yes
ER_7.2 m	7.2	3.6	Yes
ER_6.7 m	6.7	3.4	Yes
ER_6.2 m	6.2	3.1	Yes
ER_5.7 m	5.7	2.9	Yes
ER_5.2 m	5.2	2.6	Yes
ER_4.7 m	4.7	2.4	Yes
ER_3.9 m	3.9	2.0	Yes
ER_3.1 m	3.1	1.6	Yes
ER_2.6 m	2.6	1.3	Yes
ER_2.1 m	2.1	1.1	Yes
ER_1.6 m	1.6	0.8	Yes
ER_1.1 m	1.1	0.6	Yes

6.9.2.1.1 Psychrometers

The data from the psychrometers illustrated in Figure 6.9.2-1 show that along the entire length of the borehole, the walls were at water potentials approximately -500 m when the sensors were installed in late February 1998. A uniform, steep increase in water-potential values over the first two weeks in March suggests the recovery of the borehole wall from drying that occurred during the dry drilling of this borehole. The following four months of data show all psychrometers approaching equilibrium values, with water potentials ranging from -70 to 0 m (Figure 6.9.2-1).

Superimposed on this asymptotic trend in water-potential values are periodic deviations, with psychrometers nearer the borehole collar showing a larger number of such events. These events were restricted to the first two months of monitoring, and by the third week of April the last of these events had occurred. In three of the psychrometers (located at distances of 1.6, 6.2 and 9.4 m from the borehole collar), we found evidence of wetting events, which increased water potential to (near) zero. The psychrometer at 1.6 m had near-zero water potential for three distinct periods. The first extended from the start of monitoring until March 3, with the second extended for four days beginning on March 8. A final period, significantly shorter, lasted for almost 24 hours on March 22. The psychrometer located at 6.2 m measured water potential close to zero for a three-day period starting on March 8th. The psychrometer located at 9.4 m detected water-potential values close to zero for a single event on March 13, for nearly eleven hours.

One concern that could arise from the use of a slanting borehole to measure wetting-front migration is the possibility of the bore cavity short-circuiting flow paths. For this particular investigation, this short-circuiting does not appear to be happening, as indicated by the analysis of recovery responses observed at the depth of 5.2 m. Here, the response to a wetting event was negligible when compared with other psychrometers close to this location (above and below), suggesting that this zone was well isolated (hydraulically) from the adjacent zones and did not detect the wetting front. In the remaining eight psychrometers located between 9.4 m and 17.3 m from the borehole collar, we found evidence of small increases in water potential that extend beyond the projected recovery rate. Some of these increases coincided with periods when the psychrometers at distances of 1.6, 6.2, and 9.4 m along the borehole showed near-zero potentials; the rest of the psychrometer data remained uncorrelated until the end of April 1998. The psychrometers up to a distance of 10.4 meters maintained a sinusoidal response, which fluctuated around a trend of slow water-potential increase.

By early May 1998, the rates at which water potential was increasing had decreased significantly, and by mid-June all psychrometers readings appeared to have stabilized. In the case of two deep psychrometer (i.e., at 18.3 m and 22.3 m), there appears to have been individual events that for brief periods increased the rate at which water potentials were increasing. The deep psychrometers maintained nearly constant readings once they approached equilibrium, without the oscillations observed for shallow psychrometers.

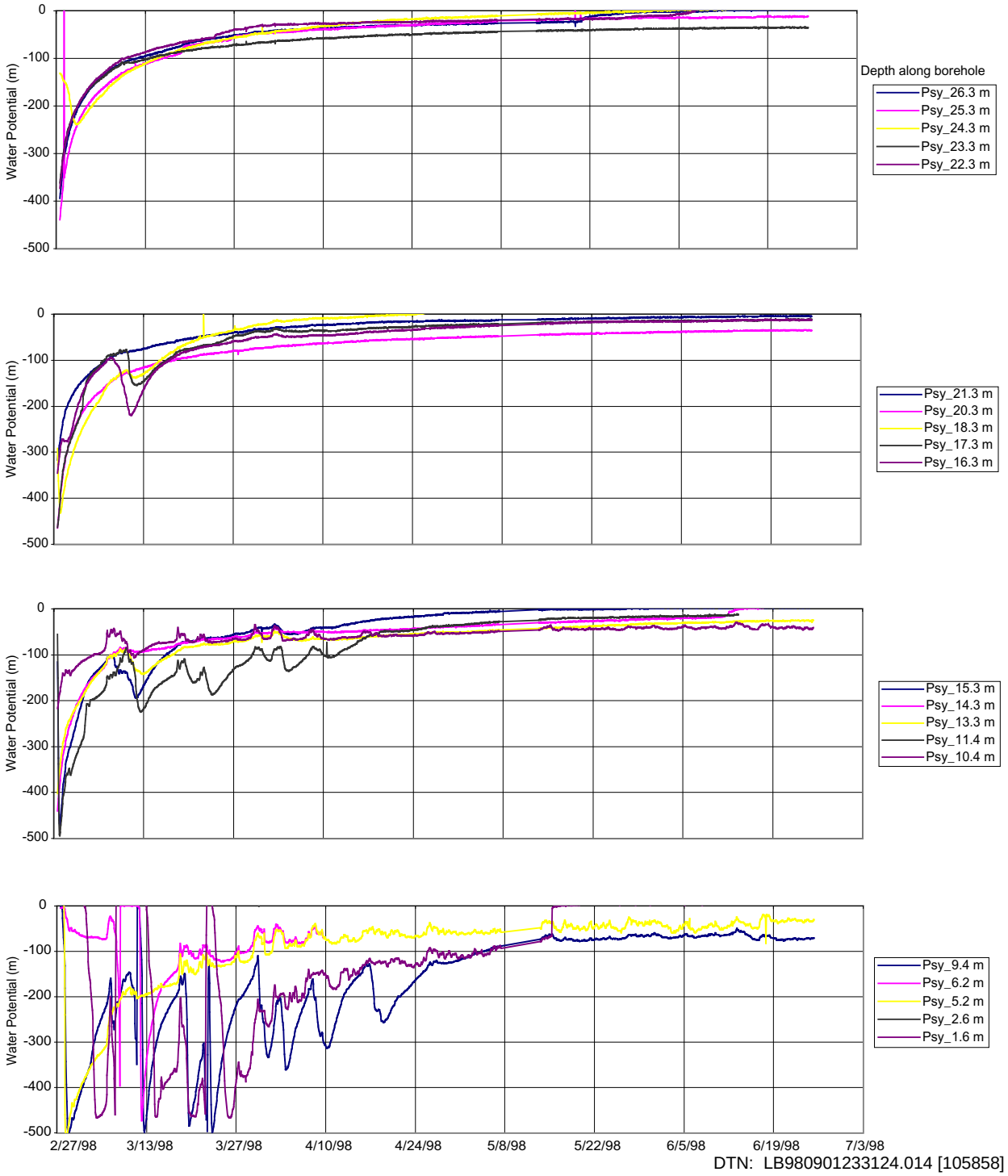

Figure 6.9.2-1. Changes in Water Potential Observed along the Wetting Front Monitoring Borehole at the Starter Tunnel of ECRB Cross Drift

6.9.2.1.2 Electrical Resistivity Probe

Measurements of electrical resistance were initiated in late March and continued until late June. Figure 6.9.2-2 summarizes the responses observed from probes located at 0.5 m intervals along the walls of the borehole between 17.3 and 29.8 m from the borehole collar.

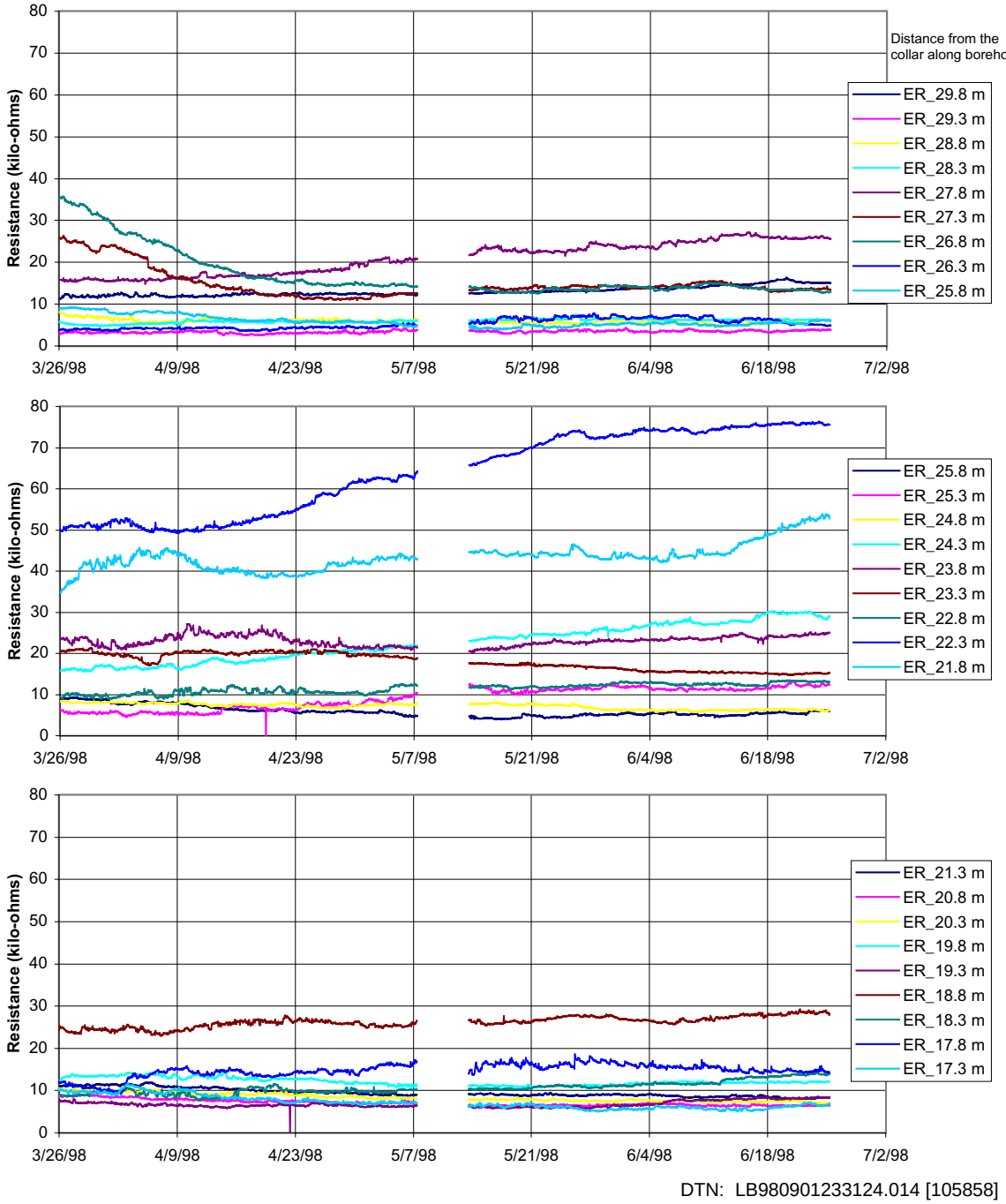

Figure 6.9.2-2. Changes in Electrical Resistance Observed along the Wetting-Front Monitoring Borehole at the Starter Tunnel of the ECRB Cross Drift

6.9.2.1.3 Potential Sensor Comparison

As part of an effort to evaluate the performance of ERPs as a sensor to monitor the arrival and movement of a wetting front, a series of probes were installed adjacent to psychrometers along the borehole length. The performance of the ERPs were compared with those of psychrometers.

From the psychrometer data collected between late March and June 1998, as illustrated in Figure 6.9.2-3, the events of interest were:

- Sinusoidal responses in the shallower psychrometers (e.g., psychrometer at distance of 5.2 m)
- The wetting and drying cycles observed in the shallower zones as the borehole walls approached equilibrium (e.g., psychrometer at distance of 9.4 m)
- Steady approaches to equilibrium as seen in the deeper psychrometers (i.e., at depths greater than 10.4 m).

Figure 6.9.2-3a to Figure 6.9.2-3c summarize examples of responses of both psychrometers and ERPs for the three response patterns observed in the psychrometer data. (The y-axes for resistance were presented in decreasing scales, so that wetter sensors have higher y-values.) In two of the three cases, the ERPs responded in a pattern similar to that of psychrometers located adjacent to the probes. With the exception of the sensor at 5.2 m, the sinusoidal response observed by the psychrometer was well tracked by the ERPs, with points of changing trends fairly well synchronized. However, the direction of the trends between small time intervals is not consistent, suggesting that the response times of the probes are significantly different. The ERPs at shallow depths might be sensitive to air flows through the fractures in addition to moisture conditions in the vicinity of the probes. The psychrometers measure the moisture conditions in the vicinity of the probes.

(a)

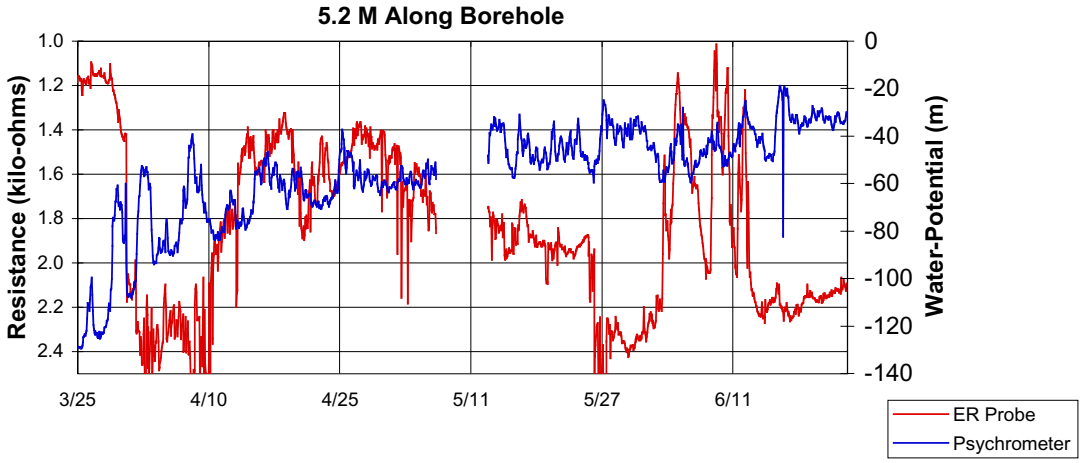

(b)

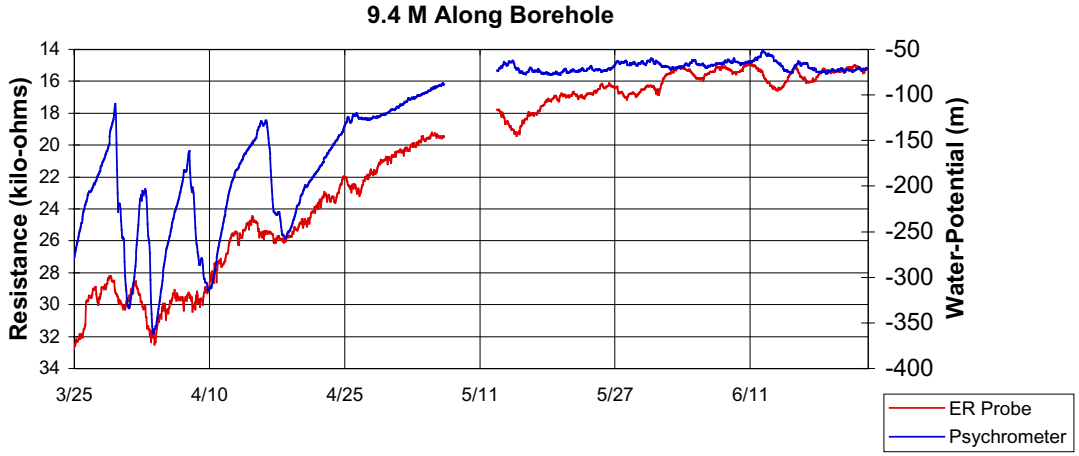

(c)

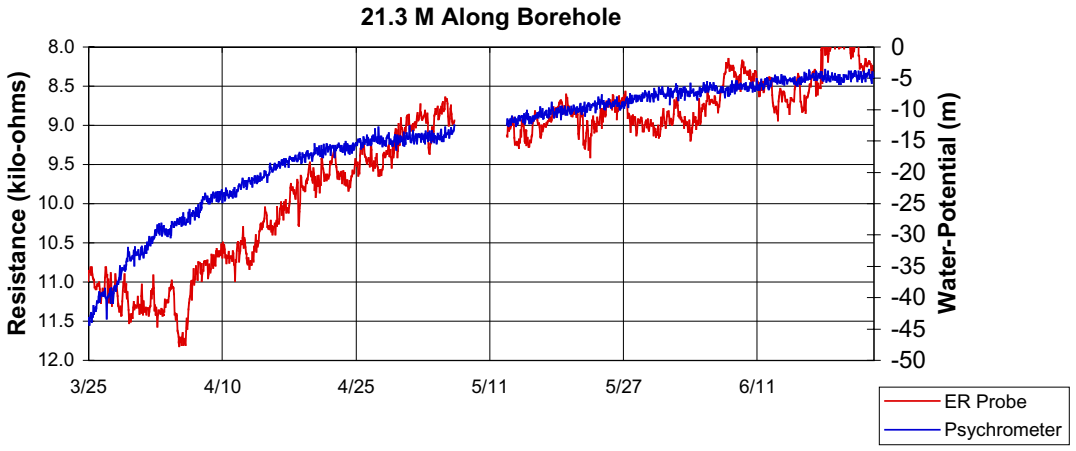

DTN: LB980901233124.014 [105858]

Figure 6.9.2-3. Comparison of Performance of Electrical Resistivity Probe and Psychrometer

At a distance of 9.4 m, the potential increased steadily from -400 m to -70 m between late March 1998 and June 1998, and the corresponding ERP measurements followed a similar pattern. Here, large fluctuations in water potentials in relatively short periods of time (-200 m in 4 days) were comparably detected by both types of probes. The slower, more gradual recovery observed by psychrometers deeper in the formation was generally well tracked by the ERPs (e.g., at 21.3 m).

6.9.2.2 Wetting Front Monitoring at the Cross-Over Point

Figure 6-2 illustrates the ECRB Cross Drift to the ESF Main Drift seepage collection system to study the migration of water and tracer flow from one drift to another. The seepage monitoring system was used to monitor the migration of construction water from the ECRB Cross Drift. Niche 3107, is currently part of the drift-to-drift study as a monitoring station. The existing horizontal boreholes at Niche 3107 are used for wetting-front monitoring for liquid released from a new alcove excavated horizontally from the ECRB Cross Drift and directly above the niche.

The ECRB Cross Drift passed over the ESF Main Drift on the second shift of July 1, 1998. No seepage was observed. The observers in the ESF Main Drift could hear rumbling noises from the TBM and feel vibrations on the railroad tracks and tunnel wall. However, no falling of loose rock was observed.

Figure 6.9.2-4 illustrates an example of the data collected by the TDR probes. No evident signals were associated with wetting-front arrivals. These null results from the sensors substantiated the field observations of no seepage associated with TBM passing over the ESF Main Drift. The confirmation of no seepage at the cross-over point establishes the lower limit for the drift-to-drift flow and drift seepage processes associated with localized construction-water usage. It also provides a guide to the design of controlled drift-to-drift experiments at this unique location, with one drift above another drift.

The underground water usage in the ECRB Cross Drift is being monitored by Science and Engineering Testing on a shift-by-shift basis; the tunnel-water use logs are being evaluated by the Testing Safety Assurance group.

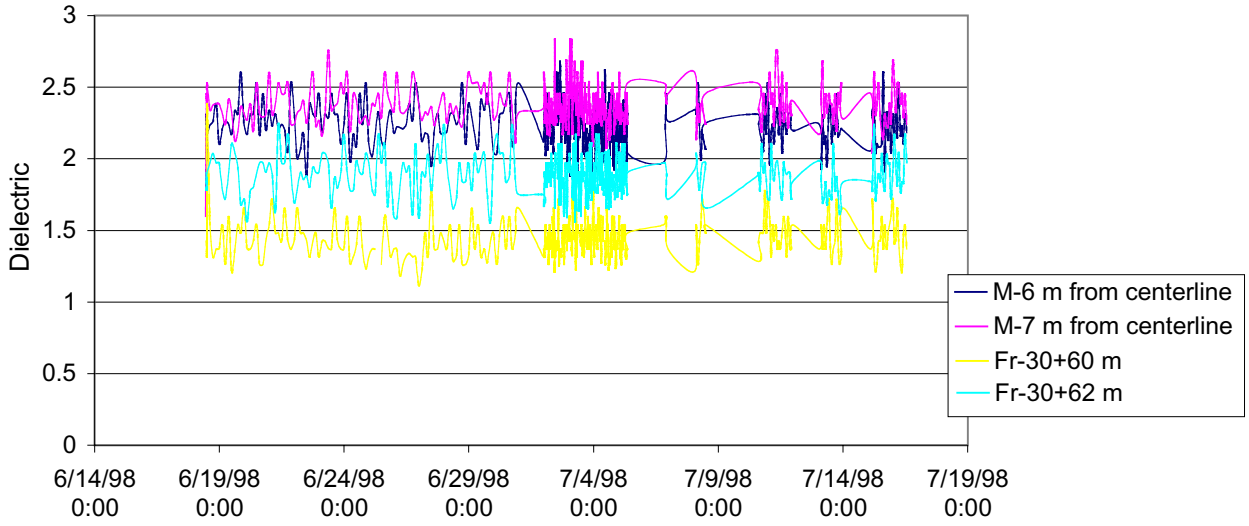

Measurement of Dielectric in Formation Matrix (M-6, M-7) and Fracture (Fr) at Crossover Point

DTN: LB980901233124.014 [105858]

Figure 6.9.2-4. Example of Time Domain Reflectometry Probe Data at the Cross-Over Point in the ESF Main Drift

6.10 MOISTURE MONITORING AND WATER ANALYSIS IN UNDERGROUND DRIFTS

In ventilated drift sections, no continuous dripping (or seepage) was observed in either the ESF Loop or in the ECRB Cross Drift. The lack of seepage may be explained by the capillary barrier mechanism, as described in Section 6.2, with capillary forces holding water within the rock mass. The other explanation is related to ventilation. Ventilation can remove a large amount of moisture, dry the rock behind the drift walls, and suppress seepage. To determine if seepage returns if there is no ventilation, the last one-third of the ECRB Cross Drift was sealed with multiple bulkheads. Section 6.10.1 summarizes the moisture conditions and construction migration associated with drift excavation. Section 6.10.2 described the preliminary results from the ongoing moisture monitoring in ECRB Cross Drift. Together with Section 6.8 on wall drying and Section 6.9 on wetting front detection, Section 6.10 summarize the current information on both the moisture conditions during drift operation and the post-emplacement environment in sealed drifts.

6.10.1 Construction Induced Effects from Drift Excavation

6.10.1.1 Status of the ESF Moisture-Monitoring Study

The moisture conditions in the ESF tunnels were monitored at 17 stations in the ESF main tunnel (from station 7+20 to station 73+50) and 10 stations in the ECRB Cross Drift (from station 0+25 to station 25+55), as summarized in Table 6.10.1-1. Relative humidity, temperature, barometric pressure, and air velocity were measured at various stations. The moisture-monitoring stations were supplemented by measurements from sensors with humidity/temperature probes and barometers mounted on the TBM during excavations. Additionally, periodic surveys were

conducted along the tunnels with these sensors, mounted on a mobile cart. An infrared camera was used in mobile surveys to measure the temperature changes on the tunnel walls.

Table 6.10.1-1. Moisture-Monitoring Stations in the Exploratory Studies Facility

Moisture-Monitoring Station Location/ ID*	Description**	DTN
21+00/LB20, 28+30/LB50, 35+00/LB40, 42+50/LB60, 47+00/LB70, 51+73/LB80, 57+50/LB90, 64+59, 67+00, 73+50, AOD5, BKH5	Relative Humidity, Temperature, and Pressure in ESF Monitoring Stations in Report "Evaluation of Moisture Evolution in the Exploratory Studies Facility." VA Supporting Data	LB960800831224.001 [105793]
	Moisture Data Report from October, 1996 to January, 1997	LB970300831224.001 [105794]
	Moisture-Monitoring Data Collected at ESF Sensor Stations, Moisture Monitoring Before and After the Completion of the ESF	LB970801233124.001 [105796]
	Moisture-Monitoring Data Collected at Stationary Moisture Stations	LB970901233124.002 [105798]
7+20/GS#3, 10+93/GS#4, 28+93, 51+64, 67+20, Operator-Shack/GS#1 (on TBM), Vent-Line-Intake/GS#2 (on TBM)	Moisture Monitoring in the ESF, Oct. 1, 1996 through Jan. 31, 1997	GS970208312242.001 [135119]
	Moisture Monitoring in the ESF, Feb. 1, 1997 through July. 31, 1997	GS970708312242.002 [135123]
	Moisture Monitoring in the ESF, August 1, 1997 through July. 31, 1998	GS980908312242.024 [135132]
ECRB Cross Drift GS: 0+25, 2+37, 2+88, 3+38, 10+03, 21+07, 24+75; LB: 14+35, 21+40, 25+55	Moisture Monitoring in the ECRB CROSS DRIFT, 04/08/98 to 7/31/98	GS980908312242.035 [135133] LB990901233124.006 [135137] (This AMR/Section 6.10.2.2)

NOTES: * LB for stations maintained by LBNL, and GS for stations maintained by USGS in this cooperative moisture-monitoring study.

** From ATDT or equivalent description.

The moisture data in the drifts, together with ventilation data and construction-water usage data, can be used to evaluate the amounts of moisture removed from the ESF drifts and the net quantities of construction water drained into the surrounding tuff formations. In this AMR, examples of moisture-monitoring data collected right after excavation of the ECRB Cross Drift are presented. Simple observations are qualitatively discussed to highlight the importance of excavation and operation data for determining site perturbations. Potential sources for corroborative evidence of the induced effects are presented in Table 6.10.1-1 through Table 6.10.1-3.

Table 6.10.1-1 summarizes the data collected in moisture-monitoring stations during and after drift excavations. Moisture removals in the drift dry up the surrounding tuffs. Water-potential measurements are listed in Table 6.10.1-2. Use of construction water changes the saturation of

the tuffs along flow paths. Table 6.10.1-3 summarizes the saturation measurements for both perturbed conditions and for ambient conditions.

Table 6.10.1-2. Water-Potential Measurements in the Exploratory Studies Facility

Potential Measurement	Description*	DTN
Niche 3566—psychrometer Niche 3650—psychrometer	3 main boreholes, 5 lateral boreholes in Niche 3566, 5/9/97—10/21/97; 6 main boreholes in Niche 3650, 7/1/97—7/28/97	LB980001233124.001 [105800]/ This AMR/Section 6.8.2
Niche 3566—heat dissipation probe	21 heat dissipation probe drill holes, 11/4/97—7/31/98	GS980908312242.022 [135157]
Niche 3107—psychrometer	3 main boreholes, 12/22/97—1/8/98	LB980001233124.001 [105800]/ This AMR/Section 6.8.2.4
Alcove 7—heat dissipation probe	heat dissipation probe drill holes, 12/9/97—1/31/98	GS980908312242.022 [135157]
Alcove 3—filter paper Alcove 4—filter paper	1 core hole in Alcove 3, 2 core holes in Alcove 4	GS980908312242.033 [107168], GS980908312242.032 [107177]
North Ramp 7+27 to 10+70 South Ramp 69+65 to 76+33—filter paper	18 North Ramp boreholes, 3 Alcove 4 boreholes, and 46 South Ramp boreholes, HQ, 2-m length	GS980308312242.004 [107172]
South Ramp—heat dissipation probe	heat dissipation probe drill holes, 8/1/97—1/4/98	GS980308312242.002 [135163]
Cross-Over Point 30+62 in the ESF Main Drift Below the ECRB Cross Drift—psychrometer	43 psychrometers on ESF drift walls, 6/19/98—7/16/98	LB980901233124.014 [105858]/ This AMR/Section 6.9.2.2
ECRB Cross Drift Starter Tunnel—psychrometer & electrical resistivity probe	1 slant borehole below the invert	LB980901233124.014 [105858]/ This AMR/Section 6.9.2.1
ECRB Cross Drift 0+50 to 7+75—heat dissipation probe	6 heat dissipation probe drill holes, 4/23/98—7/31/98	GS980908312242.036 [119820]
Surface Based Boreholes—psychrometer	USW NRG-7a, UE-25 UZ#4, UE-25 UZ#5, USW UZ-7a and USW SD-12; 1/1/97—6/30/97; 7/1/97—9/30/97; 10/1/98—3/31/98; 4/1/98—9/30/98	GS970808312232.005 [105978] GS971108312232.007 [105980] GS980408312232.001 [105982] GS981208312232.002 [156505]

NOTE: * ATDT or equivalent description.

Table 6.10.1-3. Saturation Measurements in the Exploratory Studies Facility

Saturation Measurement	Description*	DTN
Niche 3566 (#1) - core Niche 3650 (#2) - core	3 main boreholes, 6 lateral boreholes in Niche 3566 (#1) and 7 main boreholes in Niche 3650 (#2)	GS980908312242.018 [135170], GS980908312242.020 [135172]
Alcove 6 - core Alcove 7 - core	3 boreholes in Alcove 6, 1 borehole in Alcove 7	GS980908312242.029 [135175], GS980908312242.028 [135176]
Alcove 3 - core Alcove 4 - core	1 core hole in Alcove 3, 2 core holes in Alcove 4	GS980908312242.033 [107168], GS980908312242.032 [107177]
North Ramp 7+27 to 10+70 South Ramp 59+65 to 76+33 - core	Borehole samples	GS980308312242.005 [107165], GS980308312242.003 [135180]
South Ramp - time domain reflectometry	TDR measurements, 8/1/97 - 1/4/98	GS980308312242.001 [135181]
ECRB Cross Drift Starter Tunnel - core	1 slant borehole core	GS980908312242.030 [135224]
Cross-Over Point 30+62 in the ESF Main Drift Below the ECRB Cross Drift - time domain reflectometry	43 TDR probes on ESF drift walls, 6/19/98 - 7/16/98	LB980901233124.014 [105858]/ This AMR/Section 6.9.2.2

NOTE: * From ATDT or equivalent description.

6.10.1.2 Moisture Conditions and Perturbations Observed in Drifts

6.10.1.2.1 ESF Main Drift Observations

Preliminary evaluation of the moisture data during ESF excavation showed that the moisture conditions were sensitive to construction activities. The daily usage of water for excavation, muck transport, dust-control, and other operations introduced rapid changes in moisture conditions throughout the tunnel atmosphere and in the wall rock. During weekends in 1996 when construction activities were absent, the tunnel atmosphere generally stabilized to either high-humidity conditions if the ventilation was turned off, or to low-humidity conditions if the ventilation was left on (DTN: LB960800831224.001 [105793]). After completion of the ESF main tunnel with two portals for entrance and exit, high-humidity conditions were suppressed by natural ventilation through the portals (DTN: LB970801233124.001 [105796]).

The following order-of-magnitude estimate of moisture removal capacity represents the ESF system in 1996 conditions. (The ESF was excavated from 1994 to 1997.) For a 6250 m long tunnel with cross-sectional area of 40 m^2 (circular cross-sectional area with invert, vent line, and conveyor blockage areas subtracted), the humid tunnel air can contain 2,500 kilograms of excess water mass if we estimate that the tunnel is on average 50% higher in relative humidity than the outside air, with the corresponding vapor density difference on the order of 0.01 kg/m^3. If the tunnel air is ventilated with a flow rate of 47 m^3/s or 100,000 ft^3/min (cubic feet per minute, or cfm), it will take 5,300 seconds or 1.5 hours to remove and replace the tunnel air. The water-

removal rate of 2,500 kg over 1.5 hr corresponds to 285 m^3/week (285 kiloliter/week or 75,000 gallon/week). Approximating that all the moisture in the tunnel air is from evaporation, the equivalent evaporation rate from the tunnel walls and inverts (with area 6250 m × 23.7 m) is on the order of 100 mm/yr (Wang et al. 1996 [101309]).

More specific estimates were made for sections in different tuff units, using measured relative humidity changes. Vapor-density differences between different locations, together with a simple approximation of air flow in the tunnel, were used to estimate the moisture-removal rate and the equivalent evaporation rate. Weekly rates of amount of water removed by ventilation were a substantial fraction of water used in the tunnel. Estimated equivalent evaporation rates were on the order of 200 mm/yr, with standard deviation over 90 mm/yr, for both the Topopah Spring welded tuff units in a 1400 m section centered at Alcove 5 (the thermal test alcove) and the Paintbrush nonwelded units in a 380 m section between Alcove 3 and Alcove 4. The uncertainties were related to fluctuations in the moisture conditions introduced by construction activities, including air ventilation and water usage.

The equivalent evaporation rate over 100 mm/yr is an order of magnitude larger than the ambient percolation flux. The large evaporation rate could suppress the observations of active seeps and contribute to the apparent dry tunnel conditions. Rock temperatures near the TBM were observed to change spatially and temporally and could be related to evaporation from rock surfaces. Water potentials near the rock surfaces were measured with heat dissipation probes, and water potential profiles along boreholes were measured by psychrometers in niches and alcoves along the ESF Main Drift and along the ECRB Cross Drift, as summarized in Table 6.10.1-2. Field measurements in boreholes and laboratory measurements of physical and hydrologic properties of cores were conducted to measure saturation distributions, as summarized in Table 6.10.1-3 and Section 6.8. The dry-out zones could extend nominally 1 to 3 m into the walls, with fractures and faults likely extending the depths of drying influence.

The advances of the ESF tunnel excavations were detected pneumatically by sensors in 10 surface-based boreholes within 200 m of the ESF. In comparison to the damping of barometric signals from the ground surface, less attenuation and phase lag were observed for signals from the ESF. For the borehole NRG-7a, within 30 m in horizontal distance from the ESF tunnel, the changes of water potential could also be related to the ESF dry-out (see last entry of Table 6.10.1-2 for DTNs of surface-based boreholes.)

The main effects of ESF ventilation are the drying of rocks around the tunnel, the suppression of potential seepage into tunnels, and the perturbation of the gas flow field around the tunnel. Niche 3566, Alcove 7, and the last section of the ECRB Cross Drift, have been closed for long time periods to gain additional information on the rewetting processes and potential seepage events. Both the data collected during active ventilation phases and passive nonventilation phases will contribute to the assessment of UZ responses to large-scale perturbations at Yucca Mountain.

6.10.1.2.2 ECRB Cross Drift Observations

The drift conditions at the ECRB Cross Drift in 1998 were similar to the conditions of the ESF Main Drift in 1996. High-humidity conditions existed in the new sections just excavated.

Relative humidity data from three moisture stations in the ECRB Cross Drift are illustrated in Figure 6.10.1-1 and Figure 6.10.1-2 for the month of November, 1998, right after the completion of the excavation by the TBM. The moisture sensor assembly at ECRB Cross Drift Construction Station CD 25+55 (2,555 meters from the ECRB Cross Drift entrance) are located near the Solitario Canyon fault on the western boundary of the potential repository block. The other two stations, at CD 14+43 and CD 21+40, measured the moisture conditions in the middle part of the ECRB Cross Drift within the potential repository block.

The figures illustrate the temporal fluctuations and the spatial distributions of moisture conditions along the ECRB Cross Drift. The data were collected every 15 minutes. CD 25+55 was much more humid than the other two stations under the control of the same ventilation system. The day shifts had more activities than the other two shifts. During the week of Thanksgiving holiday (November 26, 1998), there were increases in moisture conditions that might be correlated with ventilation shut down. The monthly averaged relative-humidity values are 15 ± 3% for CD 14+43, 18±4% for CD 21+40, and 28±5% for CD 25+55.

The spatial variations illustrated in Figure 6.10.1-2 are based on weekly averaging over the day shifts. The differences in relative humidity are more clearly shown with the spatial distribution plot. While the magnitude varies from week to week, the spatial gradients were relatively constant. The average gradients for the two sections were 3.4% per kilometer between CD 14+35 and CD 21+40, and 25.2% per kilometer between CD 21+40 and CD 25+55. The section near the end of the tunnel apparently had more moisture removed than the section near the entrance.

The temporal and spatial distributions in Figure 6.10.1-1 and Figure 6.10.1-2 are presented to illustrate the characteristics of the moisture evolution in a newly excavated tunnel. Moisture gradients, together with the ventilation rates, are needed to calculate the moisture removal rates. The ECRB Cross Drift is a simple tunnel system compared to the ESF Main Drift. There is only one ventilation line operating along the ECRB Cross Drift, without any secondary branches separating the air flows into side alcoves and niches.

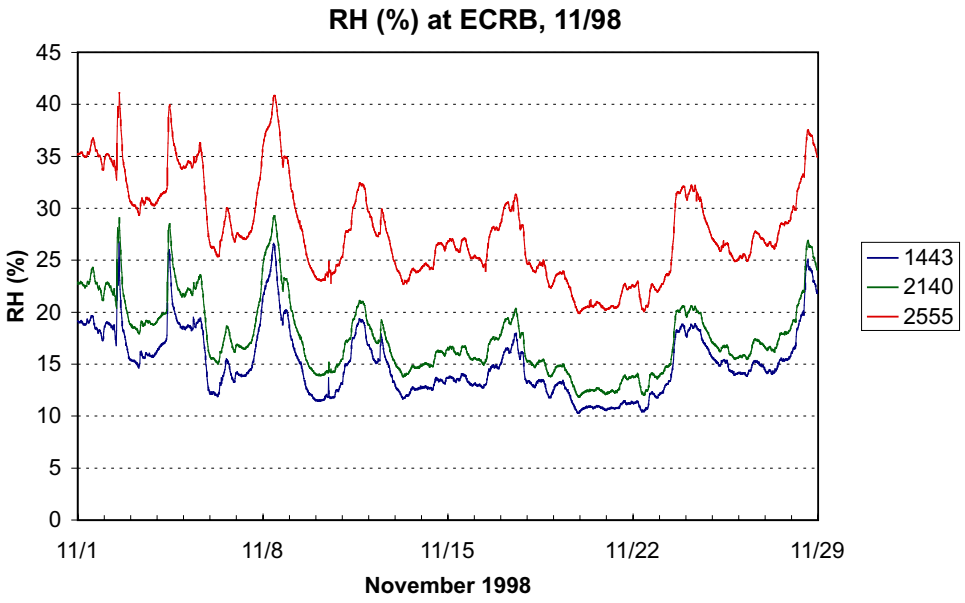

DTN: LB990901233124.006 [135137]

NOTE: The data were collected in November 1998 after completion of excavation. The legends are the distances in meters from the moisture station to the ECRB Cross Drift entrance.

Figure 6.10.1-1. Relative Humidity Temporal Variations in the ECRB Cross Drift

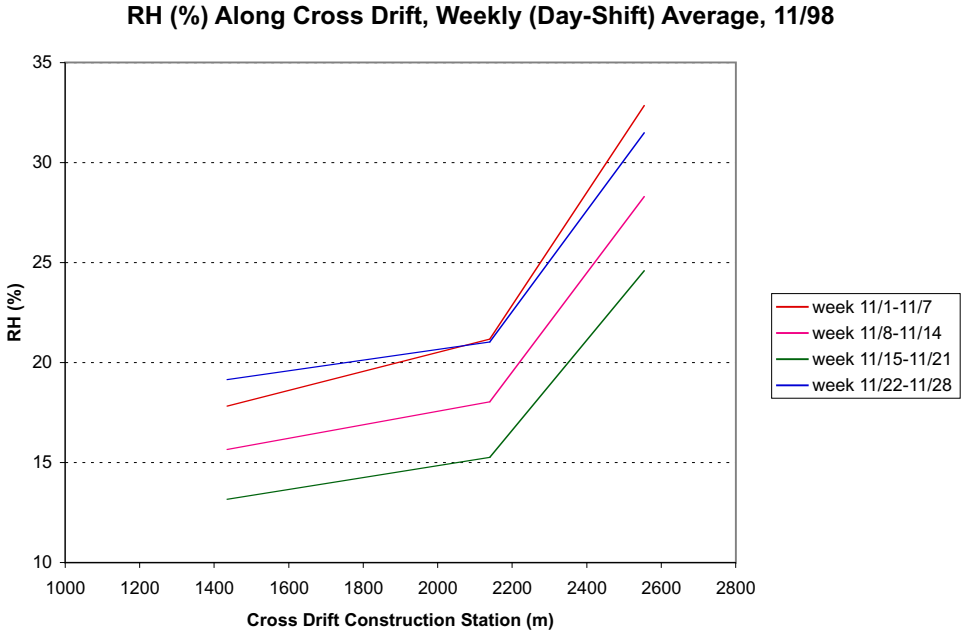

DTN: LB990901233124.006 [135137]

NOTE: The weekly averages of day shift data are presented for November 1998 after completion of excavation.

Figure 6.10.1-2. Relative Humidity Spatial Variations along the ECRB Cross Drift

6.10.1.3 Construction Water Migration Below Invert from Excavation

Construction water used in the excavation of the ESF contained lithium bromide as a tracer. The presence of the tracer (measured as bromide to chloride ratio, Br/Cl, leached out of crushed borehole samples) is illustrated in Figure 6.10.1-3 along three construction-water (CWAT) boreholes drilled in the ESF. The deepest tracer penetration was at borehole CWAT#2, in which construction water had reached the bottom of the borehole (30 m). CWAT#2 is located in an intensely fractured zone of the middle nonlithophysal zone of the TSw. In CWAT#1, the construction water was detected in all samples to a depth of 2.4 m, with two isolated peaks at greater depths. In CWAT#3, located in the upper lithophysal zone, the construction water was detected only in the top 2 m. Figure 6.10.1-3 also illustrates the areal distributions of three tuff units in the potential repository horizon: the middle nonlithophysal zone, the lower lithophysal zone, and the lower nonlithophysal zone, all of the Topopah Spring welded hydrogeologic unit. Both the variations in hydrological properties of different tuff units and in the construction usage rates could have affected the construction-water penetrations.

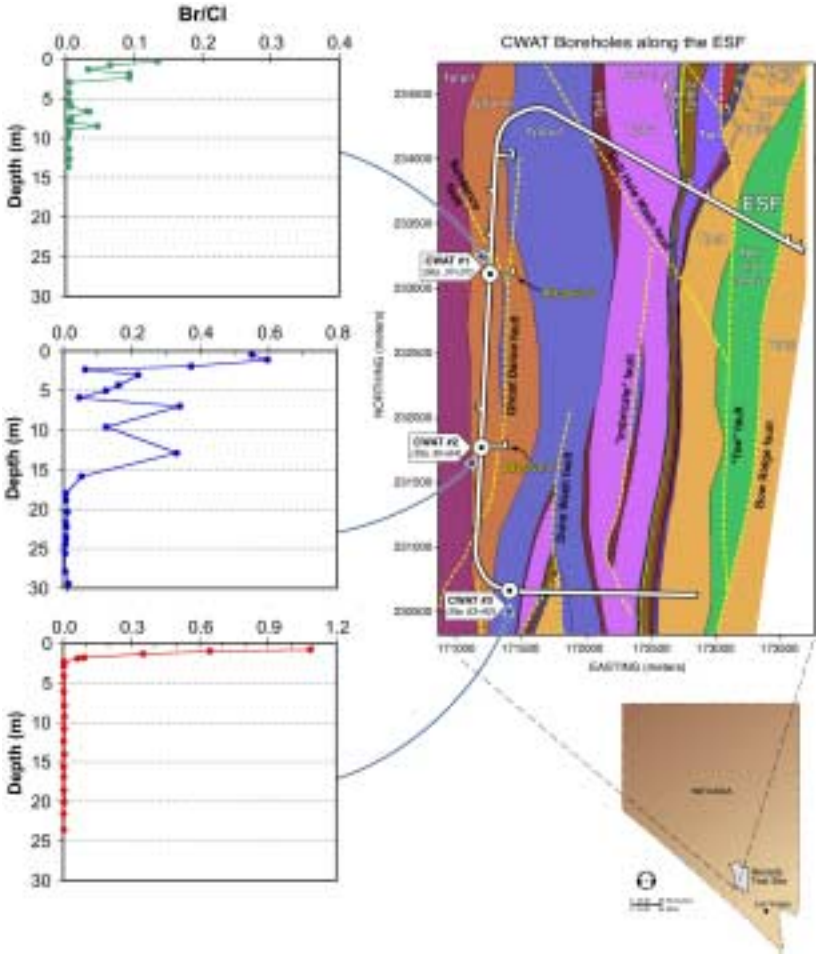

DTN: LAJF831222AQ98.007 [122730]

Source: Geological framework model GFM3.1 (BSC 2001 [154622]).

Figure 6.10.1-3. Construction Water Distribution below Exploratory Studies Facility Drift

6.10.2 Analysis and Observation of Non-Ventilated ECRB Cross Drift

The moisture monitoring study conducted in the ECRB Cross Drift is designed to detect drips in sealed drift sections. To observe potential seepage, ventilation effects to the terminal section of the ECRB Cross Drift were minimized with the construction of three bulkheads (Figure 6.10.2-1). The non-ventilated sections include the area below the Solitario Canyon wall and intercept the Solitario Canyon fault.

Along three boreholes in the ECRB Cross Drift, psychrometer measurements of water potential are being made. Within the drift opening, humidity, temperature, and barometric pressure are being measured at various stations to provide information on moisture dynamic along ECRB Cross Drift.

Section 6.10.2.1 summarizes the water potential and moisture monitoring data. Periodically, the bulkheads sealing the nonventilated sections are opened for observations. Section 6.10.2.2 presents the observations in periodic entries behind the bulkheads to observe wet zones. Section 6.10.2.3 presents the preliminary data of water samples collected during early entries.

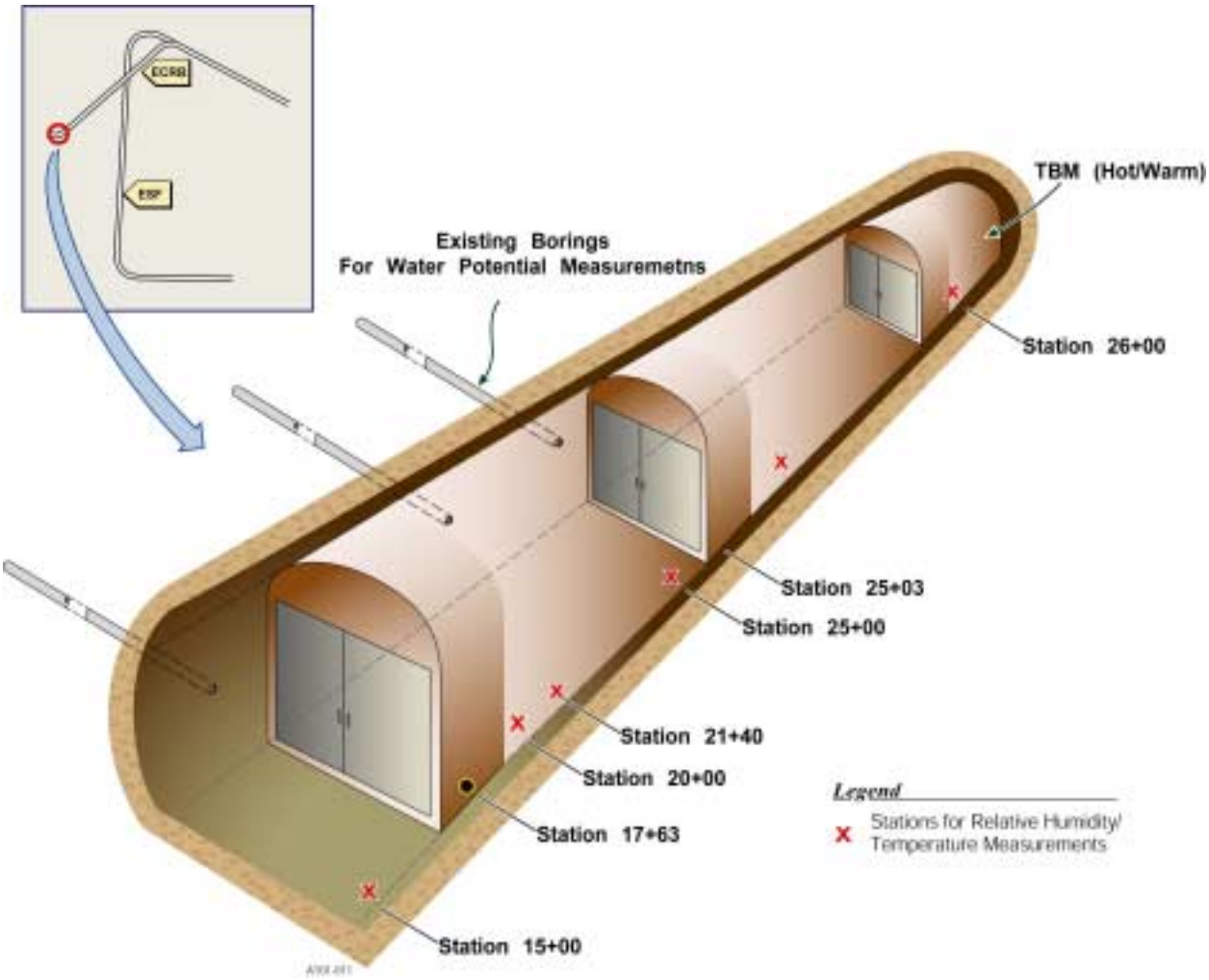

Figure 6.10.2-1. Schematic Illustration of Moisture Monitoring Stations in the ECRB Cross Drift

6.10.2.1 Water-Potential Measurements and Drift Relative Humidity and Temperature Variations

The monitoring effort behind the bulkheads is an integrated part of the field seepage testing and moisture-monitoring program that began with Niche 3566, Niche 3650, Niche 3107, and Niche 4788 in the ESF and continues with Alcove 1, Alcove 7, Niche CD 1620, and Alcove 8/Niche 3107 tests. The seepage studies, together with hydrological measurements in boreholes and benches, provide field measurements and data used for understanding flow and seepage.

Past observations have shown that, in an open tunnel, the evaporation potential of ventilation is much greater than any expected seepage. Observations from boreholes installed perpendicular to the tunnel wall suggest a clear dry-out zone associated with ventilation of the tunnel. General conclusions from our understanding of the unsaturated zone suggest that, if seepage were to occur into drifts, it would be most likely in the western portion of the potential repository block where geologic conditions are most conducive to infiltration, percolation, and seepage. The characteristics in this portion of the tunnel that make it suitable for such a test are the absence of overlying PTn past about 23+50 and the relatively high percolation rates due to high infiltration from shallow soils and higher elevation at the surface.

The 918 m long drift section is located in the Topopah Spring lower lithophysal (Tptpll) and the lower nonlithophysal (Tptpln) tuff units, and includes the Solitario Canyon fault (the western boundary of the primary potential repository block) (Figure 6.10.2-1). To observe potential seepage, the first two bulkheads (17+63 and 25+03) were installed in the ECRB Cross Drift in June of 1999. In July of 2000, a third bulkhead (25+99) was installed to isolate the influence of the TBM (which acts as a heat source) on tunnel conditions (Figure 6.10.2-1).

6.10.2.2 Observations

Data collected from terminal 918 m of the ECRB Cross Drift includes measurements of water potential along the lengths of horizontal boreholes, barometric pressure, relative humidity, and temperature that have been made along the tunnel, before the first bulkhead and in the three sections defined by the bulkheads.

Water-Potential Measurements

Water-potential measurements along three horizontal boreholes in the ECRB Cross Drift are summarized in Figure 6.10.2-2. These three boreholes are located at CD 15+00, CD 20+00 and CD 25+00, and are 6 m long. The borehole at CD 15+00 is located before the first bulkhead, while the boreholes at CD 20+00 and CD 25+00 are located between the first and second bulkhead.

There are three aspects to the water-potential measurements in the ECRB Cross Drift, i.e., spatial variability within boreholes, spatial variability between boreholes, and the temporal variability within boreholes located between the first and second borehole. Spatial variability within boreholes begins with low water potentials close to the drift, increases rapidly over a distance of 1-2 m, and then remains close to saturation values along the deeper profile. Among the three monitored boreholes, the one located at CD 15+00 has its lowest water potential (i.e., driest) close to the drift wall. The borehole at CD 20+00 also has lower water potentials up to a distance

of ~1.5 m from the borehole collar in September 1999 (prior to the location of the bulkhead doors), which have since increased over a period of 1.5 years. The borehole located furthest into the ECRB Cross Drift at CD 25+00 did not show large drops in water potential closer to the collar, nor did the borehole show any increases in water potentials following the installation of the bulkhead doors.

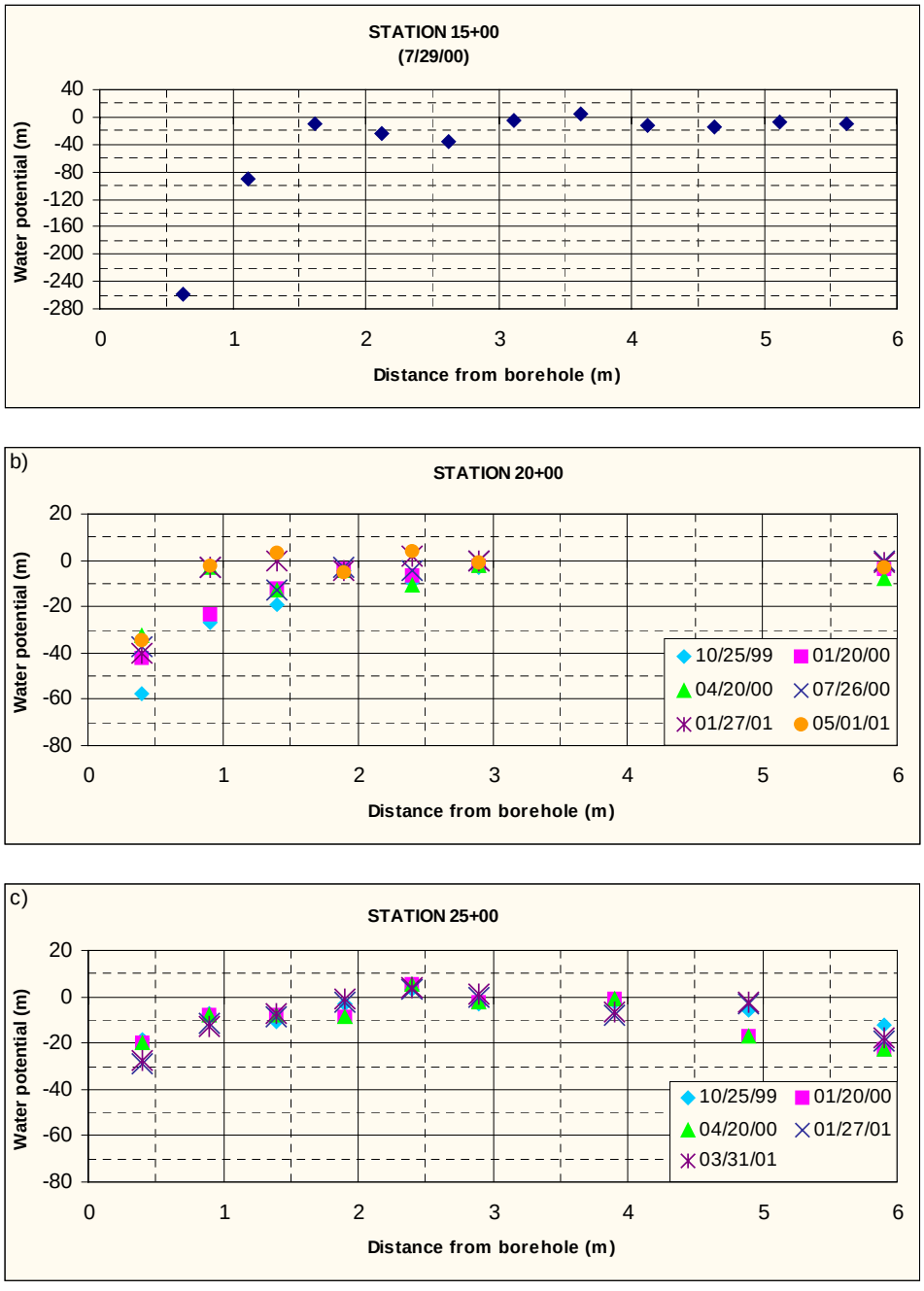

DTN: LB0110ECRBH2OP.001 [156883]

Figure 6.10.2-2. Water potential measurements along the ECRB Cross Drift: a) Station 15+00; b) Station 20+00; c) Station 25+00

Barometric-Pressure Variations

Barometric-pressure measured along four locations in the ECRB Cross Drift did not show any spatial variability but had a pronounced change over time (Figure 6.10.2-3). The range of the temporal variability was between ~870 and ~905 millibars (mbars). From May to September 2000, the barometric pressure along the ECRB Cross Drift was restricted between ~880 and ~895 mbars. Larger fluctuations in the barometric pressure were observed between October 2000 and May 2001.

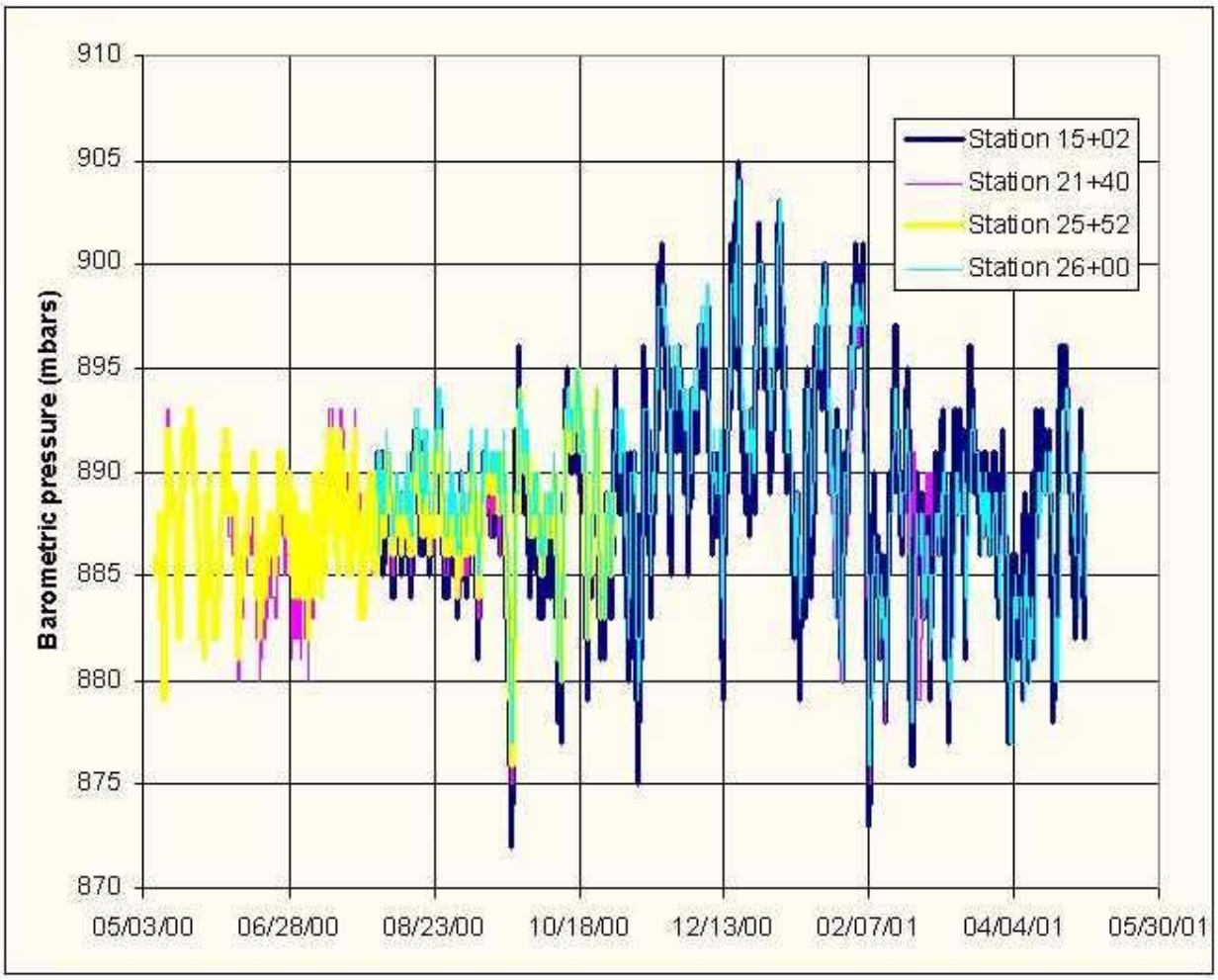

DTN: LB0110ECRBRHTB.001 [156885]

Figure 6.10.2-3. Barometric-Pressure Measured along the ECRB Cross Drift

Temperature Variations

Temperature measurements along the ECRB Cross Drift made over a period of nine months, starting in early August 2000, show a clear temperature gradient extending through the section of the ECRB Cross Drift behind the bulkhead doors (Figure 6.10.2-4).

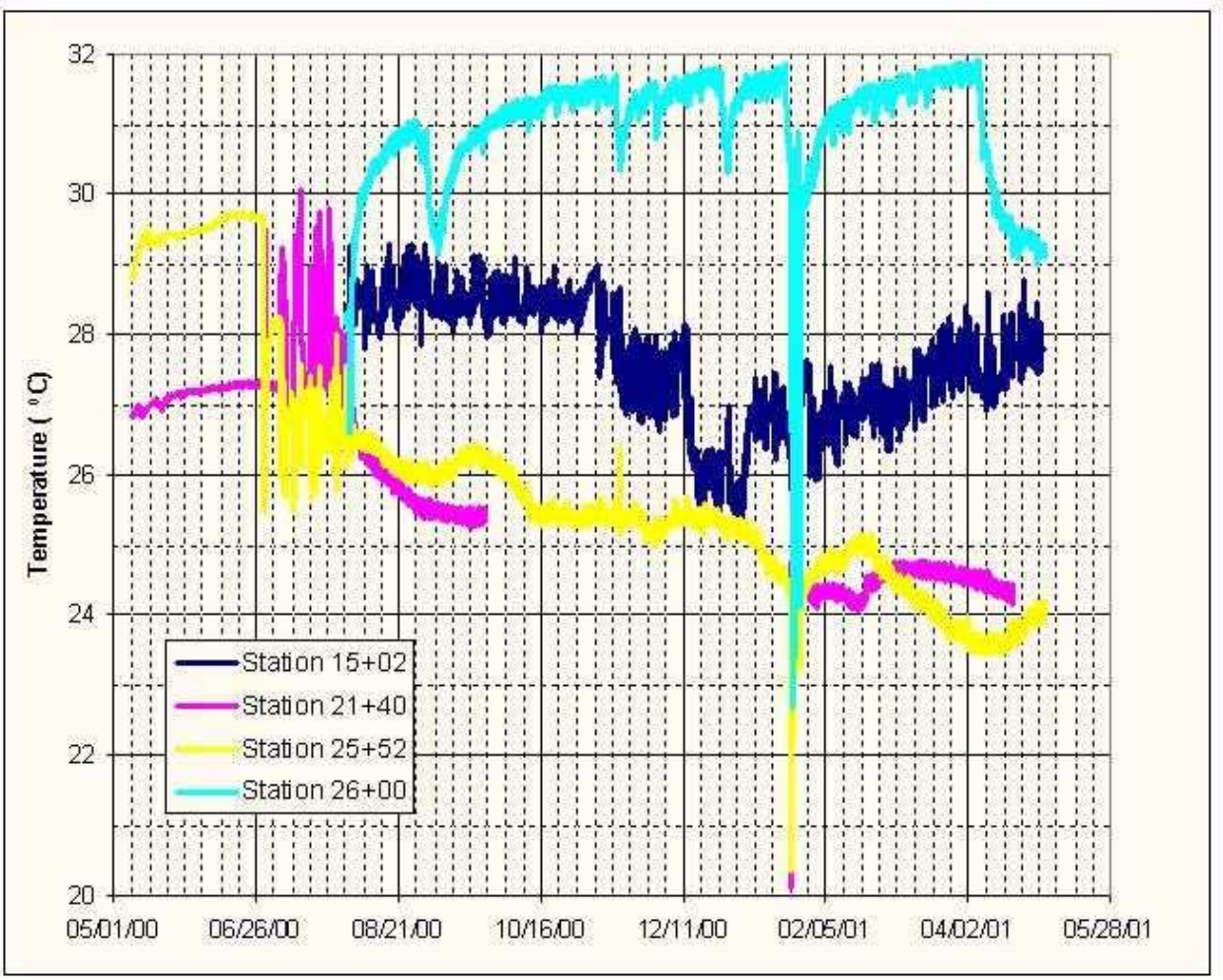

DTN: LB0110ECRBRHTB.001 [156885]

Figure 6.10.2-4. Temperature Measured in the Four ECRB Cross Drift Stations

The highest temperatures were recorded in the zone behind the third bulkhead, which houses the TBM. In this zone the temperature fluctuated between 30˚ and 32˚C during most of the monitoring periods. However, there were three distinct periods when the temperature in this zone dropped below 30˚C. The first occurred in early September 2000 and was likely caused by power interruptions, which in turn caused the TBM to cool. The second temperature drop was in late January 2001, when all the bulkhead doors were opened. During this brief period, the temperature in the vicinity of the TBM dropped to ~22.5˚C. The temperature in this zone again dropped to below 30˚C in early April 2000, likely because of the powering-off of the TBM.

In the zone between the second and third bulkheads, the temperature tended to continuously drop from ~26.5˚C to ~ 24˚C between August 2000 and May 2001. Significant deviations from trend were observed in early September 2000, when the temperature increased briefly. These deviations coincide with the temperature decreases in the zone housing the TBM. Because similar observations were not recorded before the first bulkhead, it is likely this perturbation was caused when the third bulkhead door was left open for a few days.

The temperature data collected between the first and second bulkhead shows the region steadily cooling immediately following the closure of the bulkhead doors in July 2000. (Because of the lack of temperature data from this location between late September 2000 and February 2001, temperature dynamics in this zone cannot be compared with the other two zones during this time.) Following the closure of the bulkhead doors in late January 2000, the temperature in this zone immediately dropped to ~24˚C and remained close to that value over the next two months.

Temperature in the ECRB Cross Drift measured immediately before the first bulkhead shows diurnal and seasonal fluctuations. While the diurnal fluctuations appear to be restricted to within 3˚C, the seasonal temperature changes from ~29˚C in late August 2000, to ~25˚C in late December 2000.

In summary, the three zones defined by the bulkhead in the ECRB Cross Drift appear to be partially thermally isolated from each other and also the area before the bulkhead *when the doors are closed*. The zone housing the TBM was warmer than the area before the first bulkhead while the other two zones were consistently cooler when the doors were closed. During the period when the bulkhead doors were opened the temperature in each of the zones rapidly approached that of the zone outside the bulkheads.

Relative Humidity Variations

The relative humidity in the three zones defined by the bulkheads shows spatial variability similar to the temperature data (Figure 6.10.2-5). The lowest humidity was observed in the area before the first bulkhead, where it fluctuated between ~10 and 40%, with a few instances where the humidity was greater than 60%. When the bulkheads were closed, the zone behind the third bulkhead maintained a relative humidity of ~90% until late January when the bulkhead doors were briefly opened. Between January and May 2001, the relative humidity in this region fell closer to 80%. In the two zones between the first and third bulkhead, the relative humidity remained close to ~95%, with some changes observed in March 2001, when the humidity in the second zone gradually fell closer to ~90%.

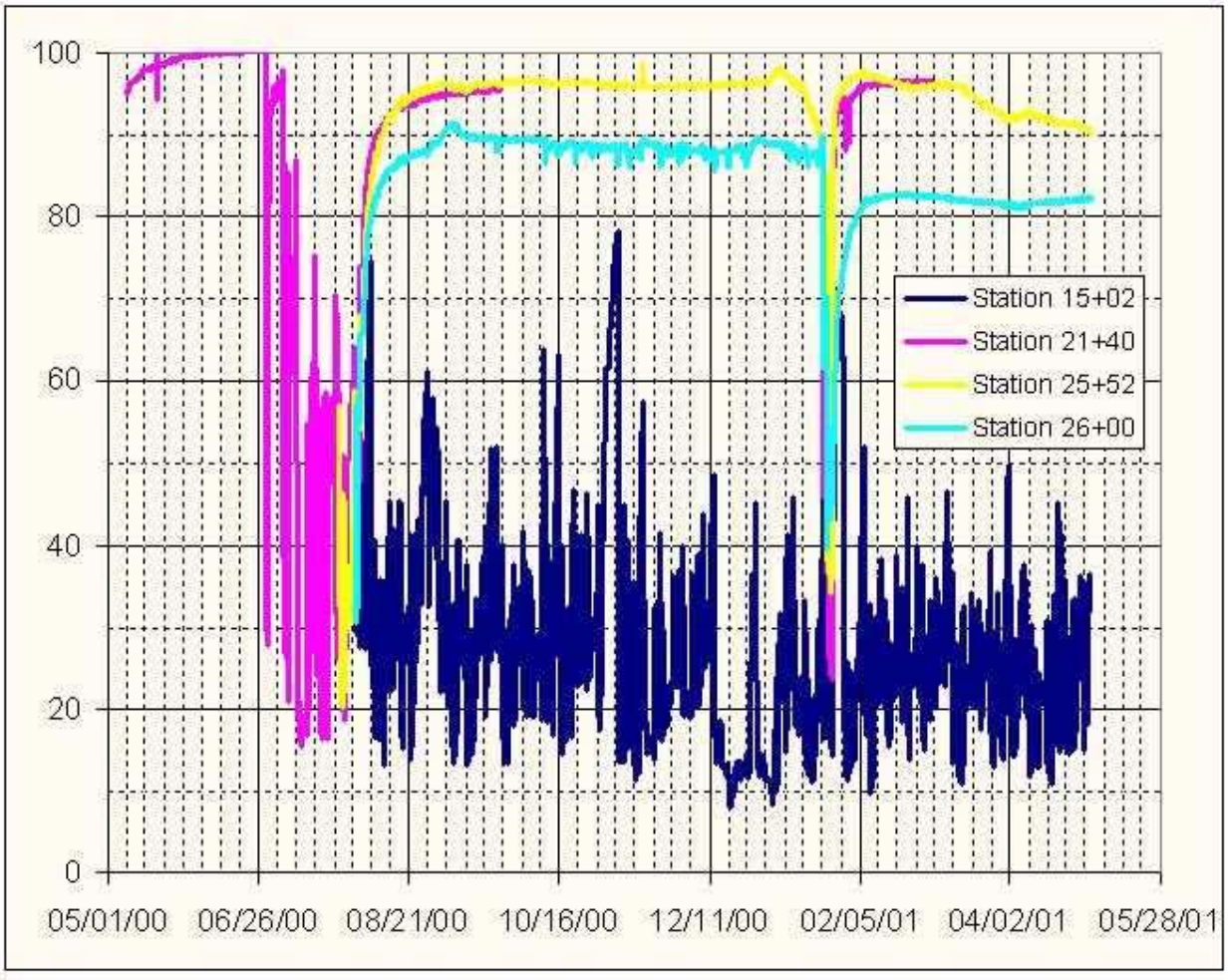

DTN: LB0110ECRBRHTB.001 [156885]

Figure 6.10.2-5. Relative Humidity Measured in the Four ECRB Cross Drift Stations

6.10.2.3 Observations of Wet Zones During Bulkhead Entries

Additional information on the moisture conditions within the nonventilated zone has been gleaned during several periods when the bulkhead doors were opened: (1) January 12–13, 2000; (2) May, June, and July 2000 to install the third bulkhead, (3) January 22–25, 2001, (4) May 22, 2001, to repair electrical power, and (5) October 1–December, 2001. During these entries, the entire ECRB Cross Drift was accessible for visual inspection. Wet spots were observed and water samples were manually collected. Observations have been made in the nonventilated sections that show the existence of liquid water, as well as rust spots and organic growths (i.e., indicators of the prolonged presence of water). To date, no continuous seepage from the rock into the closed sections of the ECRB Cross Drift has been observed.

Early Bulkhead Entries

The moisture-monitoring study conducted behind the bulkheads in the ECRB Cross Drift is designed to detect seepage in sealed drift sections. Figure 6.10.2-6 provides a geologic cross section at the terminal end of the ECRB Cross Drift, showing the locations of the second bulkhead, third bulkhead, and the TBM. These sections have higher potential for seepage due to higher surface net-infiltration rates and higher percolation flux distributions in the potential repository level. The high flux region could be located especially in areas with no overlying nonwelded tuff. The section between second and third bulkhead also intersects the Solitario Canyon fault at CD 25+84. The section behind the third bulkhead contains the TBM used for ECRB Cross Drift excavation. The TBM is a heat source due to power being supplied to the TBM. Table 6.10.2-1 provides rock unit contacts intersected by the tunnel sections behind the bulkheads.

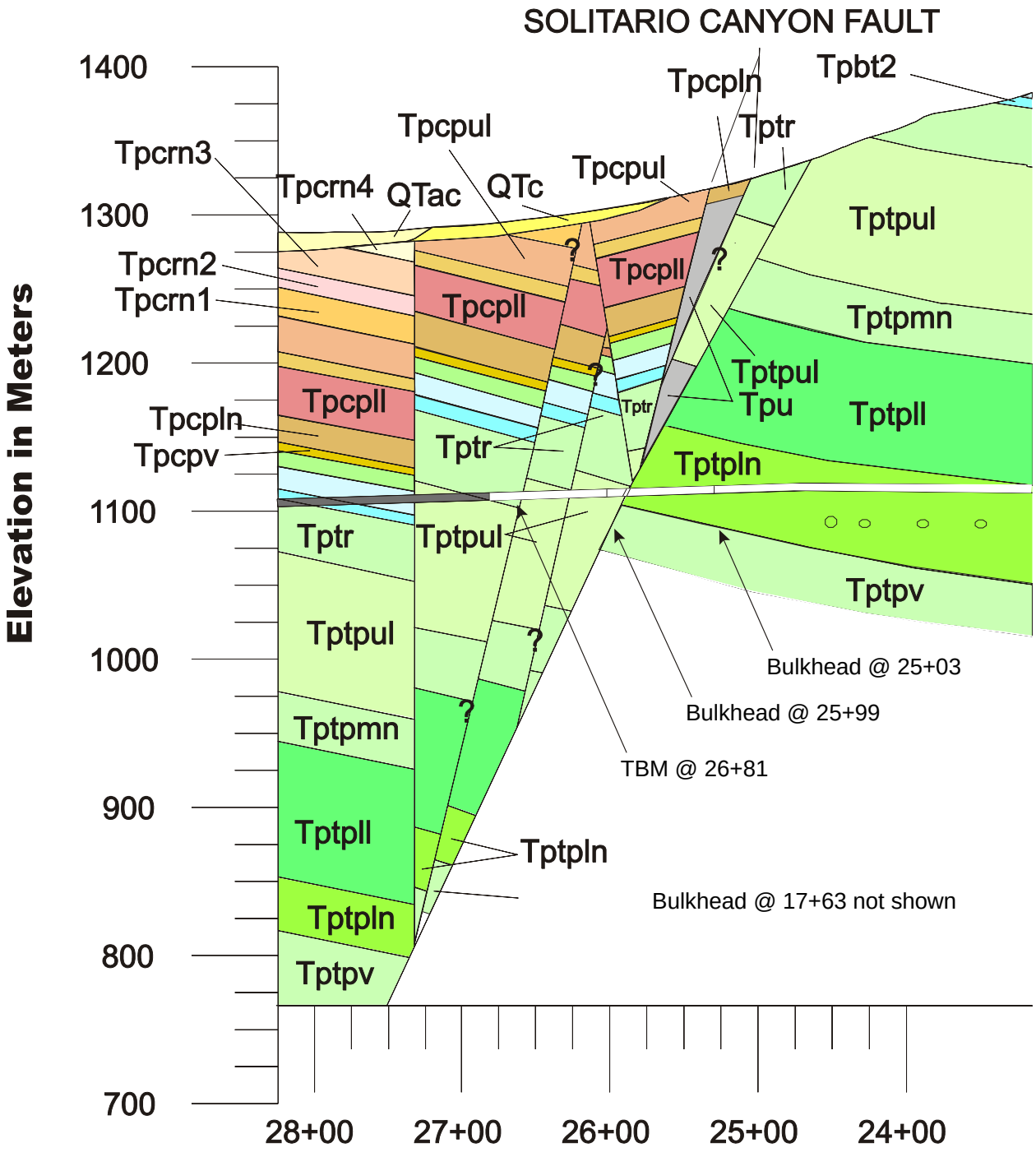

DTN: GS990908314224.010 [152631]

NOTE: For stratigraphic abbreviations, refer to Drawing OA-46-345 “Comparative Geologic Cross Section along the Cross Drift”.

Figure 6.10.2-6 As-Built Cross Section of the Terminal End of the ECRB Cross Drift (23+00 m to 26+81 m) Showing the Bulkhead Locations

Table 6.10.2-1 Rock Unit Contacts Intersected by the Bulkhead Sections (All within the Topopah Spring Tuff)

Station	Mapped Contact
23+26	Tptpll / Tptpln (Topopah Spring Tuff lower lithophysal / lower non-lithophysal Contact)
25+84	Tptpln / Tptpul (Topopah Spring Tuff lower non-lithophysal / upper lithophysal Solitario Canyon Fault Zone)
26+64	Tptpul / Tptr (Topopah Spring Tuff upper lithophysal / crystal rich lithophysal Solitario Canyon Fault Zone)

DTN: GS990408314224.006 [108409]

The first two bulkheads (at CD 17+63 and at CD 25+03) were installed in the ECRB Cross Drift in June of 1999. Visual inspection was conducted during the first entry (January 12-13, 2000) for elevated moisture on the vent line, cables, and pipes along the ECRB Cross Drift behind bulkheads. Additional investigations were conducted to evaluate possible sources of the observed moisture. Part of the analysis focused on the TBM and tunnel lighting as heat sources.

In July of 2000, to ameliorate (but not eliminate) the influence of heat sources on the tunnel conditions, a third bulkhead was installed to further reduce heat flow from the TBM. The lights were turned off. These modifications had some positive impact but did not eliminate the effects. To assist in determining the location of drips, drip detection sheets were installed. Recent observations indicate that these were overwhelmed by condensation. Low wind speed sensor and surface thermocouples were also installed in July of 2000.

The bulkheads were opened from January 22, 2001 to January 25, 2001. The ECRB Cross Drift was dry from the first bulkhead at CD 17+63 to about CD 19+00. Photographs from the initial entry show evidence of condensation on the metallic surfaces of the vent line, utility lines, and conveyor belt. Most of the glistening on metallic surfaces that was evident in the initial photographs evaporated rapidly. There was some evidence of rust on metallic surfaces, indicating prolonged presence of water. Canvas sheets located between CD 24+75 to CD 24+95 m were mottled blue, and drip marks covered the entire sheets. Most of the water was observed in the middle nonventilated section between the second and third bulkheads from CD 25+03 to CD 25+99. All drip detection sheets hung in this section were wet, with some areas noticeably wetter. The back nonventilated section behind the third bulkhead to the terminal end of the ECRB Cross Drift (CD 25+99 to CD 26+81) was dry.

Observations During Nonventilated Entries

To avoid loss of data, an unventilated entry behind the bulkheads was done on May 22, 2001, to restore power to the dataloggers and to the TBM. The first bulkhead at CD 17+63 was opened at 11:10 am on May 22, 2001. No ventilation was established, and entry was permitted at 11:20 am. This entry was restricted to the same day, with bulkheads closed after the entry.

There was initial observation of the existence of water (glistening) on the utility and vent lines in the first 250 m. The water appeared to be present only on the surface. Within two hours the moisture had evaporated. At CD 21+00 everything was dry. Moisture began reappearing on the utility and vent lines at about CD 23+50. There were rust spots on the steel channels and on the tracks. There was moisture at about a meter interval on the conveyor belt, but the water had not accumulated into puddles. A canvas sheet that was hung on January 25, 2001 at CD 24+10 was mottled blue with drip marks covering the entire sheets. This sheet was further up the tunnel then the other sheets. The sheets between CD 24+75 and CD 24+95 were moist, and there was moisture on the utility and vent lines and on the second bulkhead. The second bulkhead was opened at 12:06 pm. Between the second and third bulkhead, the canvas sheets were moist, but there was much less puddled water than during the January 22–25, 2001 entry. Moisture was evident on the canvas sheets, conveyor belt, and metal surfaces. There were some small rocks on the conveyor belt. The third bulkhead was opened at 12:17 pm. There was moisture on utility lines and instruments cables to about 10 m behind the bulkhead. Beyond 10 m behind the third bulkhead, everything was dry.

Less moisture was observed during the May 22, 2001 entry than had been observed during the January 22–25, 2001 entry. The moisture had not accumulated into puddles. The canvas drip detection sheet at CD 24+10 and the observed rust spots at CD 23+50 indicate that liquid moisture had been present at least this far up the tunnel. The continued power loss to the TBM resulted in a decreased temperature gradient within the tunnel. Moisture behind the third bulkhead and the smaller amount of moisture between the second and third bulkhead indicate that as the temperature gradient decreases, observable moisture tends to move toward the TBM.

An entry occurred on October 1 and a follow-up entry occurred on October 2, 2001. Four sections of alternating dry and wet conditions were observed between the first and second bulkhead on the first day, October 1, 2001 (12:03 pm to 13:37 pm). The first dry section was from CD 17+63 (first bulkhead) to ~CD 18+00, with dry stalactites observed on the vent tube. The drift was wet from ~CD 18+00 to ~CD 19+00. In the wet sections, the dampness was more pronounced on the upper part of the drift walls. The conveyer had clear water droplets spaced approximately evenly on rubber surfaces, and had puddles at local depression points in the belt (large puddle at CD 18+25).

The drift was dry from ~CD 19+00 to ~CD 21+50 and was very wet from ~CD 21+50 to CD 25+03 (second bulkhead). There is visual evidence of moisture retention in calcite in-fill in the fractures but not in the matrix. Condensate is prevalent on the shotcrete after the second bulkhead and behind the third bulkhead. The fault between the second and third bulkhead was dry. A cloth tarp hanging before the third bulkhead showed a bluish discoloration for about 6 m right before the bulkhead. The last section behind the third bulkhead was also dry, with no rust observed (implying that the section was not wet during the closure period).

On the next day October 2, 2001, most of water droplets were evaporated, with some of the rock and especially the in-filled fractures remains damp. The wire mesh on the crown was wet, with clear condensate and new rust observed on the mesh at evaporated droplet locations. A patch of paint was observed to have beads of water drops on its surface, while no similar beads were observed on the surrounding rock surfaces. Since the paint is impermeable, the observed beads are likely the results of condensation, not from seepage through the rocks below the painted batch. This is a new observation to substantiate the hypothesis that the observed water originated from condensation as the result of local temperature variations. The hypothesis is based on observations of early bulkhead entries and on chemical analyses from limited water samples collected.

6.10.2.4 Chemical and Isotopic Analysis of Water Samples Collected During Bulkhead Entries

The nonventilated sections of the ECRB Cross Drift were opened four times from January 2000 to January 2001, and water samples were collected. Both chemical analysis and isotopic measurements were conducted on the samples. The chemical analyses were on major anionic and cationic constituents (including bromide, chloride, and lithium) in the liquid samples. The hydrogen (δD) and oxygen ($\delta^{18}O$) isotope compositions were also analyzed.

Most of the initial samples were collected directly from pools that had formed on the conveyor belt, and these samples were of brownish to dark brown color, with some examples shown in Figure 6.10.2-7. Their chemical compositions show high and spurious concentrations of many constituents, as shown in Table 6.10.2-2. These samples are likely contaminated from the conveyor belt resulting from the belt usage/operation before ECRB Cross Drift closure, with the degree of contamination unknown and unable to be quantified. Contamination of the conveyor belt may include salt accumulated from water evaporation following transportation of the tuff debris, as well as other miscellaneous contamination. Therefore, these samples may not yield useful information about the origin of the water (condensate or seepage) observed in the ECRB Cross Drift behind bulkheads.

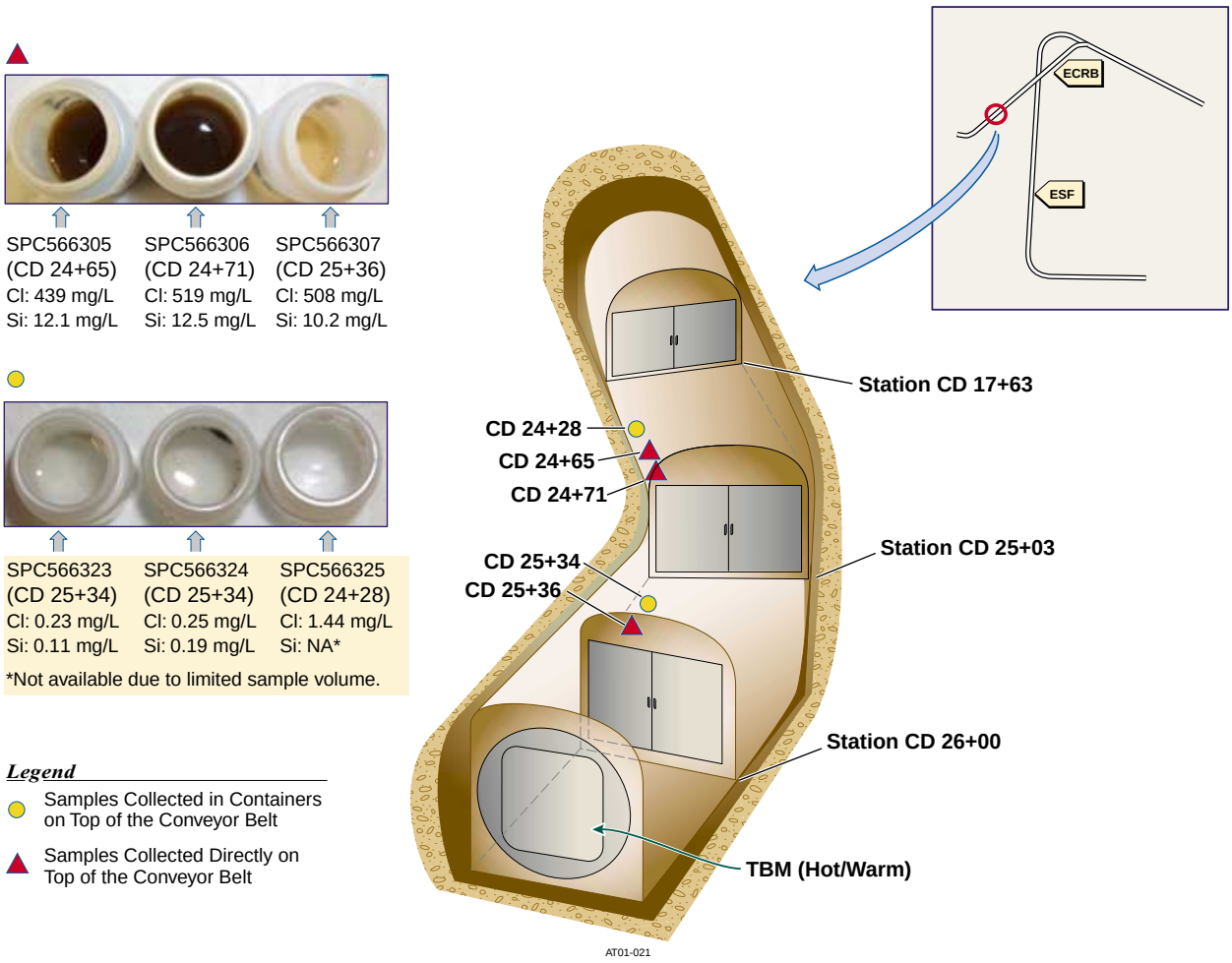

DTN: LB0110ECRBH2OA.001 [156886]

Figure 6.10.2-7. Chemical Analyses of Liquid Samples Collected during Bulkhead Entries

Subsequently, three samples were collected from collection containers placed on the top of the conveyor belt. These samples are clear (Figure 6.10.2-7). Their chemistry, particularly low chloride and silica contents, indicates that this water is condensate (Figure 6.10.2-8). The water does not have the chemical signature of the construction water that contains about 20 mg/L of lithium bromide added to J-13 well water. Condensate, and subsequent dripping down, could occur as a result of vapor-to-liquid transition associated with local temperature variations in a humid environment. The moisture conditions measured by humidity and temperature probes support the presence of drift moisture variations (Section 6.10.2.2). These clear samples also show a relatively high amount of calcium and a high sulfate/chloride ratio, suggesting some minor contamination from either rock grout or rock dust (Figure 6.10.2-8). Some grout or dust present along the drift crown above the sampling containers may have dissolved in the condensate prior to collection. Samples collected on the drift wall (using a needle syringe for SPC566308 in Table 6.10.2-2, and absorbent pad attached to the wall) show an even higher concentration of calcium and a larger sulfate/chloride ratio, resulting from the direct contact of the sample with the rock.

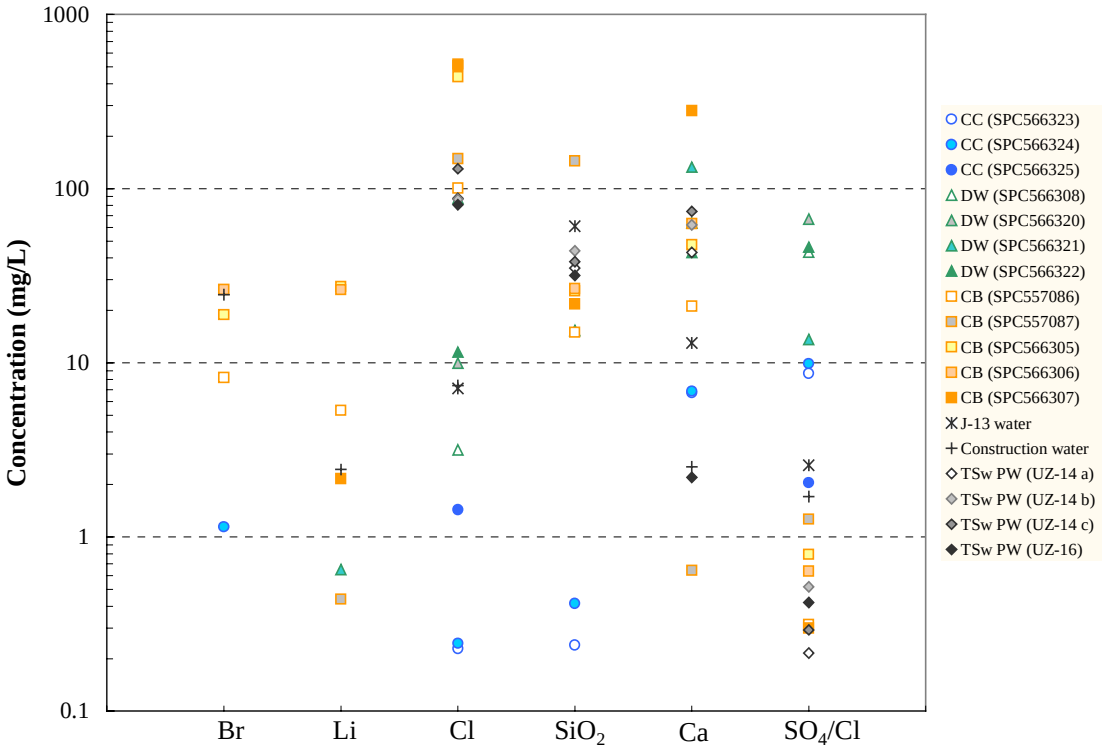

SOURCE: J-13 well water composition from DTN: MO0006J13WTRCM.000 [151029].
TSw porewater data from BSC 2001 [154874], Table 6.
ECRB water data from DTN: LB0110ECRBH2OA.001 [156886]

NOTE: Unit of the Y-axis is in mg/L, except for the ratio of sulfate to chloride (dimensionless).
ECRB Samples are grouped as follows: CC in collection container, DW on drift wall, and CB on conveyor belt.
Construction water data presented here are an average value from seven samples.
TSw PW: pore water in Topopah Spring welded tuff unit.

Figure 6.10.2-8. Comparison of Chemical Signatures

Table 6.10.2-2. Chemical and Isotopic Data for Liquid Samples Collected in the ECRB Cross Drift

Specimen ID#	Sample Location	Collection Date	Br^-	Cl^-	F^-	NO_3^-	SO_4^{2-}	Ca^{2+}	Li^+	Mg^{2+}	K^+	Na^+	SiO_2	δD	$\delta^{18}O$
			(mg/L)[1]											(%)[2]	
SPC557086	Conveyor belt - Station CD 24+83	1/31/00	8.23	101	ND	ND	31.7	21.2	5.33	3.10	19.0	88.6	15.0	-59	-7.1
SPC557087	Conveyor belt - Station CD 25+17	1/31/00	ND	149	29	ND	188	0.64	0.44	0.10	160	139733	144	-80	-9.3
SPC566305	Conveyor belt - Station CD 24+65	5/03/00	18.9	439	ND	ND	349	47.6	27.5	9.00	27.9	195	25.9	-79	-9.3
SPC566306	Conveyor belt - Station CD 24+71	5/03/00	26.3	519	9.19	ND	330	62.9	26.3	12.0	35.3	230	26.7	-80	-8.9
SPC566307	Conveyor belt - Station CD 25+36	5/03/00	ND	508	6.41	24.1	152	280	2.16	34.0	36.3	191	21.8	-79	-8.7
SPC566308	Shotcrete- Station CD 25+50	5/03/00	ND	3.16	ND	4.29	136	---	---	---	---	---	---	---	---
SPC566300	Construction Water	5/31/00	25.1	6.82	---	ND	13.4	6.64	2.02	---	5.94	59.1	---	---	---
SPC566320	Absorbent pad - Station CD 25+62	6/28/00	ND	9.95	7.05	3.99	665	63.5	ND	11.5	172	105	<1.0	---	---
SPC566321	Absorbent pad - Station CD 25+62	6/28/00	ND	88.0	15.8	5.79	1197	133	0.65	18.1	163	233	15.4	-69	-6.9
SPC566322	Absorbent pad - Station CD 25+62	6/28/00	ND	11.5	8.02	2.20	531	43.0	ND	6.50	141	78.6	<1.0	-71	-7.8
SPC566323	Collection container - Station CD 25+34	6/28/00	ND	0.23	ND	1.63	1.99	6.73	ND	0.40	0.84	1.56	0.24	-83	-9.4
SPC566324	Collection container - Station CD 25+34	6/28/00	1.14	0.25	ND	ND	2.42	6.87	ND	0.40	0.90	1.65	0.42	-84	-9.4
SPC566325	Collection container - Station CD 24+28	6/28/00	ND	1.44	ND	2.34	2.95	---	---	---	---	---	---	-67	-8.1

Table 6.10.2-2. Chemical and Isotopic Data for Liquid Samples Collected in the ECRB Cross Drift (Continued).

Specimen ID#	Sample Location	Collection Date	Br^-	Cl^-	F^-	NO_3^-	SO_4^{2-}	Ca^{2+}	Li^+	Mg^{2+}	K^+	Na^+	SiO_2	δD	$\delta^{18}O$
			(mg/L)[1]											(%)[2]	
SPC573600	Conveyor belt - ~5 m from 2nd bulkhead	1/22/01	45.4	---	---	---	---	---	0.11	---	---	---	---	-90	-10.6
SPC573602	Conveyor belt - Station CD 25+37	1/22/01	79.7	---	---	---	---	---	0.17	---	---	---	---	-74	---
SPC573604	Conveyor belt - ~7 m from 2nd bulkhead	1/22/01	56.3	---	---	---	---	---	12.31	---	---	---	---	-89	-10.7
SPC573605	Conveyor belt - Station CD 25+42	1/22/01	ND	---	---	---	---	---	0.22	---	---	---	---	-55	-3.7
SPC573601	Conveyor belt - Station CD 25+10	1/23/01	72.5	---	---	---	---	---	14.8	---	---	---	---	-48	-5.0
SPC573603	Conveyor belt - Station CD 25+21	1/23/01	52.5	---	---	---	---	---	0.13	---	---	---	---	-55	-4.9

DTN: LB0110ECRBH2OA.001 [156886]; LB0110ECRBH2OI.001 [156887]

NOTE: Liquid samples were filtered through 0.45 µm filters prior to chemical analyses. Phosphate was not detected in any of the liquid samples.
ND: not detected, e.g., below the analytical detection limit (about 0.1 mg/L).
---: Data not available.

Water samples collected were also used for isotopic analyses, with the results presented in Table 6.10.2-2 and illustrated in Figure 6.10.2-9. The δD values of the ECRB Cross Drift water range from -48‰ to -9‰ and the $\delta^{18}O$ values range from -3‰ to -10.7‰. These values are higher than those found in the construction water. The lag time between opening of bulkheads and allowing sample collection (3-4 hours) is sufficient to result in a significant degree of evaporation of the samples. In Figure 6.10.2-9, all samples from the ECRB Cross Drift are shifted from the global meteoric water line, similar to samples from Alcove 5. The offset is characteristic of waters that have undergone some degree of vapor loss. The same degree of shifts for both the contaminated samples and the relatively clean samples may indicate that approximately the same degree of evaporation occurred for water collected in the ECRB Cross Drift.

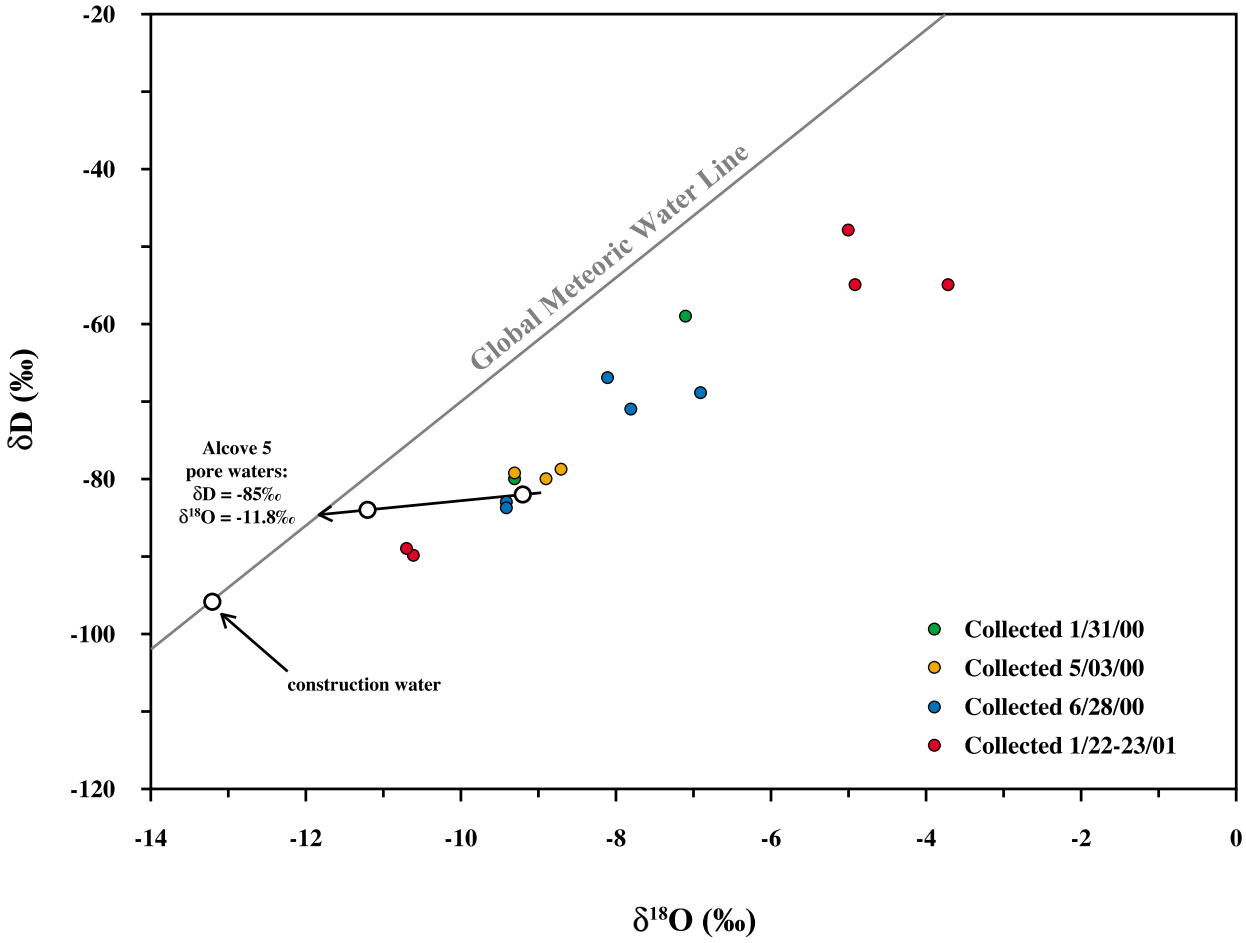

DTNs: LB0110ECRBH2OI.001 [156887], LB0108CO2DST05.001 [156888], LB0011CO2DST08.001 [153460]

NOTE: Also plotted is the isotopic composition of construction water, two pore water samples extracted from core samples from Alcove 5 and the location of the Global Meteoric Water Line.

Figure 6.10.2-9. Plot of the Hydrogen and Oxygen Isotope Compositions of Water Samples Collected from the ECRB Cross Drift

6.11 ANALYSES AND INTERPRETATIONS OF SYSTEMATIC HYDROLOGICAL CHARACTERIZATION

A systematic approach—testing at regular intervals regardless of specific features arising from spatial heterogeneity—has been chosen to perform hydrological characterization tests in boreholes drilled at regular intervals along the ECRB Cross Drift within the lower lithophysal zone of the TSw. The lower lithophysal welded tuff unit is intersected by many small fractures (less than 1 m long) and interspersed with many lithophysal cavities (ranging in size from 15 to 100 cm). The size and spacing of both the fractures and lithophysal cavities vary appreciably along the drift walls (the drift is 5 m in diameter) over an 800 m stretch. This indicates that hydrological characteristics at one particular location may not be representative of the entire unit. Therefore, a systematic approach of testing at regular intervals is adopted to acquire knowledge of the heterogeneous hydrological characteristics of this unit, in which over 80% of the potential repository will reside. The systematic approach is to complement other hydrological testing in the ambient testing program, in which test locations are selected either by avoiding or focusing on specific features (such as large fractures or extra abundance of fractures or cavities). Systematic hydrological characterization investigates the hydrological properties that are important to repository performance. Field measurements include:

1. Air-injection tests that give a measure of fracture permeability

2. Liquid-release tests that determine the ability of the open drift to act as a capillary barrier (diverting water around itself) as well as the potential of the water to seep into the drift

3. Crosshole gas-tracer tests to measure the effective porosity of the rock mass.

6.11.1 Systematic Borehole Testing Setup

6.11.1.1 Systematic Borehole Configuration

Figure 6.11.1-1 shows a schematic of the arrays of boreholes (all 20 m in length) drilled at regular intervals along the ECRB Cross Drift. The borehole arrays are divided into three groups. Group I consists of low-angled boreholes drilled from the crown of the 5 m diameter ECRB Cross Drift, inclined at 15^{o} from the drift-axis. These boreholes are intended for both air-injection and liquid-release tests, with the spacing of adjacent boreholes from collar to collar at 30 m. Group II consists of near-vertical boreholes drilled from the crown of the drift. Group III consists of pairs of parallel horizontal boreholes, spaced 3 m apart and drilled from the side of the drift. The former are intended for air-injection tests to determine the effect of drift excavation on fracture properties, and the latter are for gas-tracer tests to determine the effective porosity. Group II and III boreholes are in groups of three spaced 90 m apart as shown in Figure 6.11.1-1.

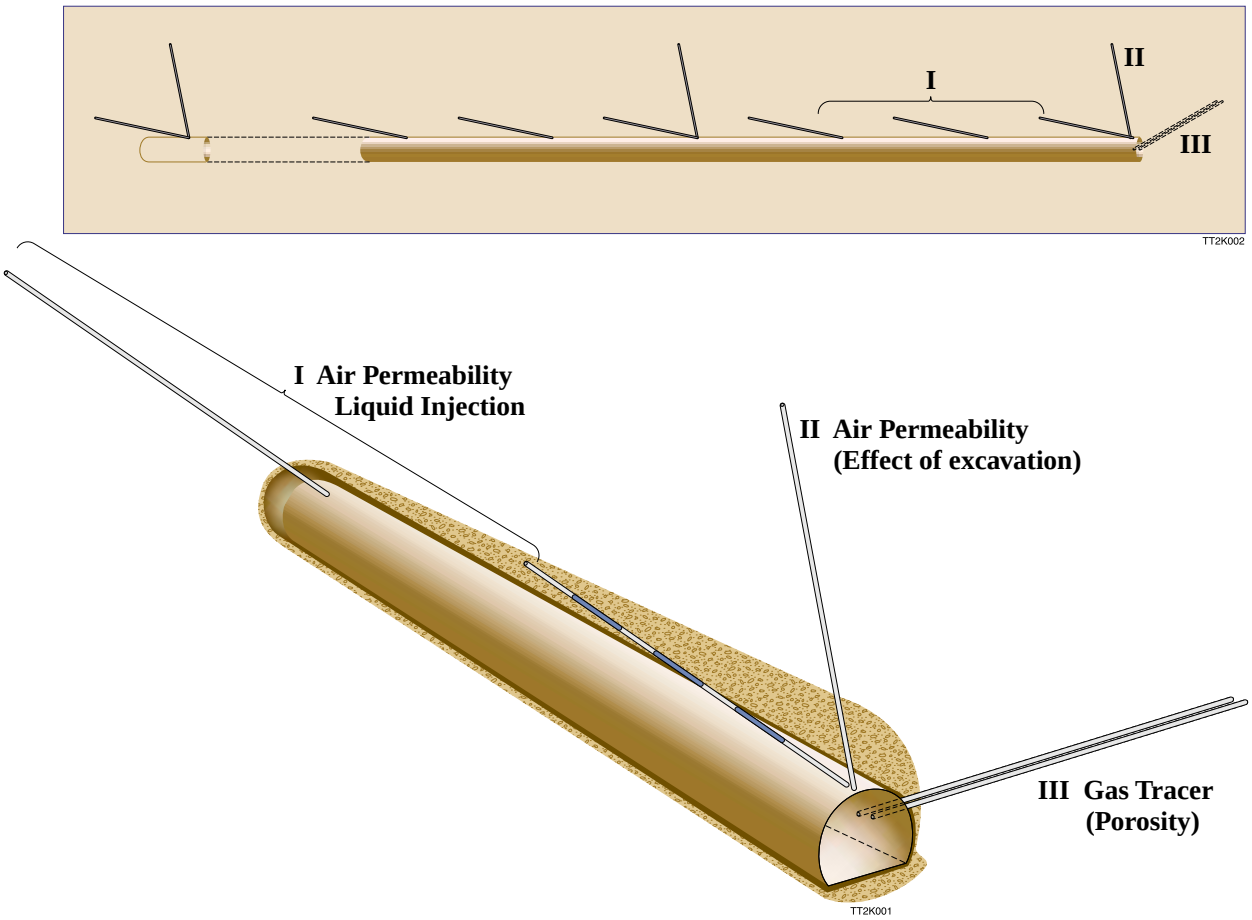

Figure 6.11.1-1. Schematic of Borehole Configuration in the ECRB Cross Drift for Systematic Characterization of the Lower Lithophysal Unit

6.11.1.2 Equipment

The equipment system has been custom-designed for the systematic characterization study based on two criteria: automation and mobility. Field-scale measurements involving liquid flow in unsaturated rock require continuous testing, lasting for weeks to months, whereas the ECRB Cross Drift is open only for eight hours, four days every week. Therefore, the control of test equipment has been fully automated, allowing remote manipulation via computer network when there is no human presence at the field site. The second criterion of mobility is achieved by designing all equipment needed for the systematic characterization as a complete unit to fit on flatbed rail cars. This enables investigators to efficiently transport equipment from one test station to another along the ECRB Cross Drift.

A schematic of the testing equipment for air injection and liquid release is shown in Figure 6.11.1-2. The main function of the equipment is to distribute water at a specified rate along a specified length of borehole and to capture any water that makes its way from the borehole through the rock formation as seepage into the drift. The key components of the system are the packer assembly, water supply hardware, and seepage-capture system.

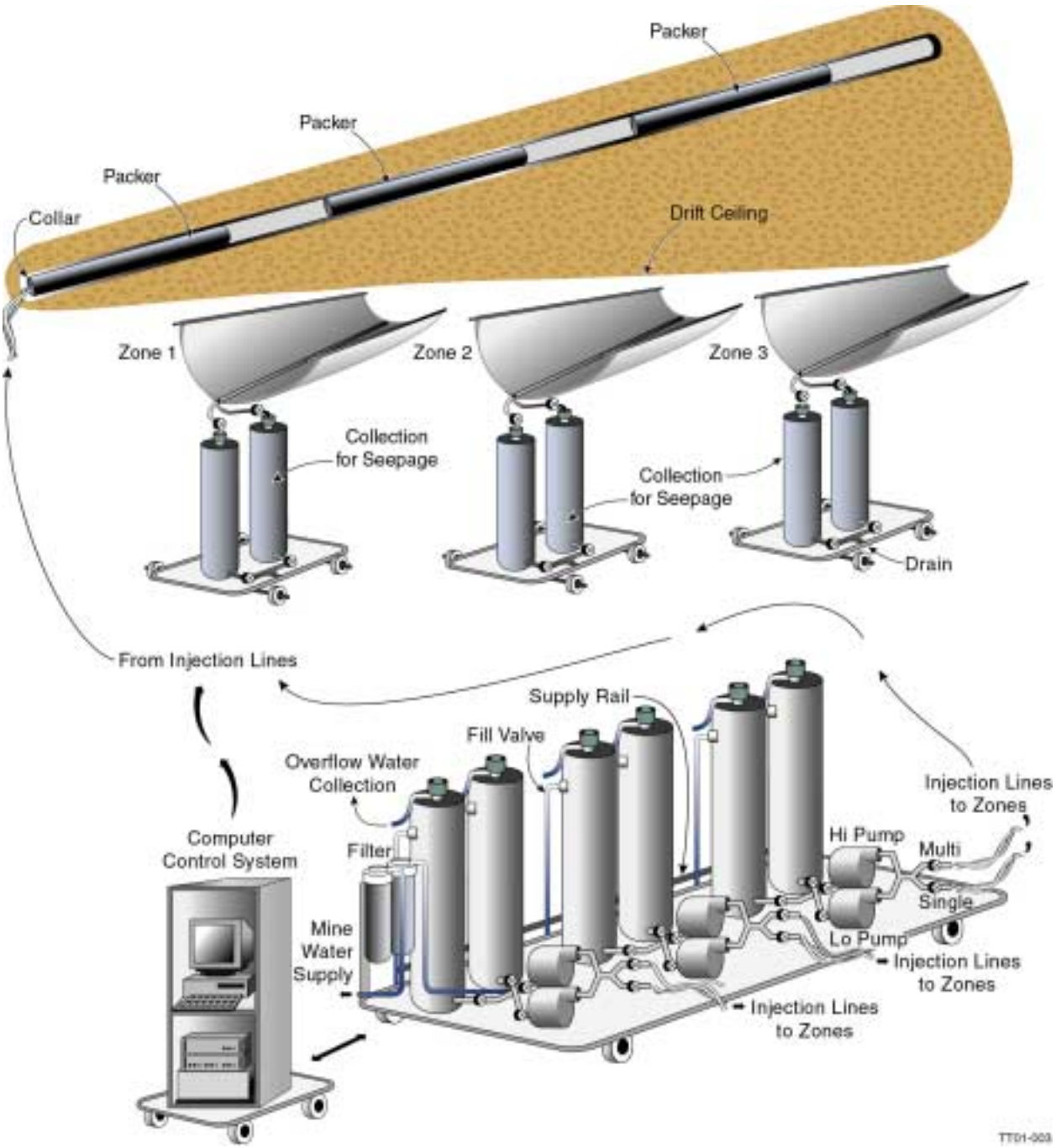

Figure 6.11.1-2 A Schematic of the Equipment System: Packer Assembly, Water Supply and Air-Injection Component, Seepage Collection Component, and Data Acquisition and Control

6.11.1.2.1 Packer Assembly

The packer assembly uses inflatable-rubber-packer units to seal off sections of borehole (so that released water cannot reach these sections) and isolates each borehole into three nonsealed 1.83 m water-release sections. The three sealing sections of the packer assembly use 3 m, 0.64 cm

wall, soft inflatable rubber tubing supported by and clamped at each end onto a 5 cm stainless-steel core, for an overall diameter of 6.3 cm. The relatively long packers (3 m) are intended to provide effective sealing in a lithophysal unit, where the size of cavities can reach to 1 m. Cores of these rubberized sections contain internal tubing to inflate the rubber up to the borehole diameter (7.6 cm) using compressed air.

Of the three water-delivery sections, also made of 5 cm diameter stainless tubing, two lie between the three rubberized sections in the borehole, and the third lies beyond the farthest rubber section into the borehole. Because of the small-angle incline of the borehole, the vertical distance from the outermost unsealed section to the drift crown is about 1 m, whereas the vertical distance between the second and innermost sections and the crown are on the order of 2.5 and 5 m respectively. Water is released into these unsealed sections or zones by one of two means. One method uses a single release point close to the rubber sealing section at the far (upper) end of the unsealed zone. The other method uses multiple orifices along an unsealed section to enable water to be released at six evenly spaced locations along the entire unsealed section. Tubing resides inside each of the delivery sections for single-point injection, for multipoint injection at six evenly spaced locations, and for drainage of overflow should the delivery rate prove to be too high for all the water to completely enter the formation. One additional tube from each delivery section connects it to a pressure transducer located outside the hole, to measure air pressure in each zone.

In keeping with the design requirements of the testing site, the sections of packer assembly are shipped as separate parts and assembled at the site. O-rings at the connections between sections assure that the annuli left around the water-delivery sections are sealed from atmospheric conditions inside the hollow, open-packer core. The packer inflation, water supply, and water drain tubing from all sections run through the core of the packer assembly to the outside of the borehole, where it is connected to the water supply system.

6.11.1.2.2 Water Supply System

Each delivery section in the borehole has its own water supply system. The triplicate design allows testing in all three zones of the same borehole simultaneously. The water supply hardware controls the amount of water delivered to a section and also measures the total quantity of water supplied to that section over time. In addition, the supply hardware also measures, over time, the quantity of any return flow through the drain port from the delivery section. Each supply system makes use of twin vertical, cylindrical bottles to supply and measure the water that is delivered. The bottles are 1.5 m tall and 20 cm in diameter, a size that enables mobility of the units between test locations without sacrificing volume resolution or supply volume. One bottle can fill from the tunnel water supply, while the other is pumped, so that the supply and measurement system can run without interruption. Located at the base of each bottle, differential-pressure transducers (which cancel atmospheric changes) measure the head of water in each bottle. These transducers, when multiplied by the known area of a bottle, yield the current water quantity residing in the bottle. One of two sizes of electronically controlled gear pumps pushes water from the bottom of the active supply bottle up to the packer assembly for water delivery. The two different-sized pumps are used to provide a range of 10 mL/min to 2,000 mL/min supply rate. The crossover from the small pump to the large pump is about 300 mL/min. Valves enable either bottle to supply either pump with the single-point delivery tube or the multipoint delivery tube. Another

valve to each bottle directs any return flow to run back into the inactive bottle, so that this flow can be measured. One more valve at each bottle supplies each with refill water from the tunnel supply when needed. All the valves are pneumatically actuated via air lines controlled by solenoids. Electronic relays under computer control operate the solenoids. Voltage signals delivered by digital-to-analog converters under computer control govern the pumps, and an analog-to-digital converter with multiplexor converts the transducers' current-loop output to digital format, which is recorded by the same computer used for valve and pump control.

6.11.1.2.3 Seepage-Capture System

Hardware for seepage capture at each zone consists of a horizontally mounted U-shaped PVC curtain, which captures seepage from the rock under the release zone and funnels it into twin collection bottles designed similarly to the supply bottles. Figure 6.11.1-2 shows the arrangement of the capture curtains relative to the packer system. The length of the capture curtain is four meters, twice over that of the release zone (1.83 m in length). A valve at the bottom of each bottle allows drainage into a continuous drain, while another valve at the top of each determines whether collected water can enter. This configuration allows drainage of one bottle without interruption of seepage collection and measurement in the other. The collection system also utilizes differential-pressure transducers to obtain head (and therefore quantity of water) in the bottles. The diameter of 20 cm for the collection system implies that a volume of 0.03 liters of seepage water needs to be accumulated for every mm rise of water level. As with the supply system, the collection system is serviced by computer recording and control system.

6.11.1.2.4 Air-Injection System

The water supply system supports an air-injection system for determining the air permeability of each delivery zone. Incorporated into the single-point delivery tubes are valves that allow water to drain from these tubes and that allow introduction of air into each zone. Mass-flow controllers deliver air at constant-mass flux through the single-point injection line. Dedicated absolute-pressure transducers for each zone enable air-pressure measurements during air injection and thus allow calculation of air permeability. The mass-flow controllers are computer-controlled, and air-flow rates are recorded by the data acquisition system.

6.11.1.2.5 Control and Recording System

In addition to continuous recording of all transducer outputs, the computer interface for the supply and collection systems enables the processes to be manually or automatically controlled. The computer incorporates remote-control capability so that the systems can be started and controlled through computer networks.

Figure 6.11.1-3 shows the front panel from the user interface on the computer control. Depicted are the supply bottles at the top and the collection bottles at the bottom. There are three completely independent systems, one for each zone. The zone 1 system is shown operating on automatic control, using the low flow pump at 50% flow capacity from Bottle A. Return flow is being collected in Bottle B. Seepage is being collected in Bottle B while Bottle A is draining. Other zones are not operating. Paths for water highlight themselves with thicker lines when operational. The toggle switch on the zone 1 control panel is on to enable automatic operation.

When this switch is enabled, manual operation of the valve and pump controls is disabled, and they merely function as indicators from which to monitor the automatic operation. A separate automation program then operates the controls much as an operator would.

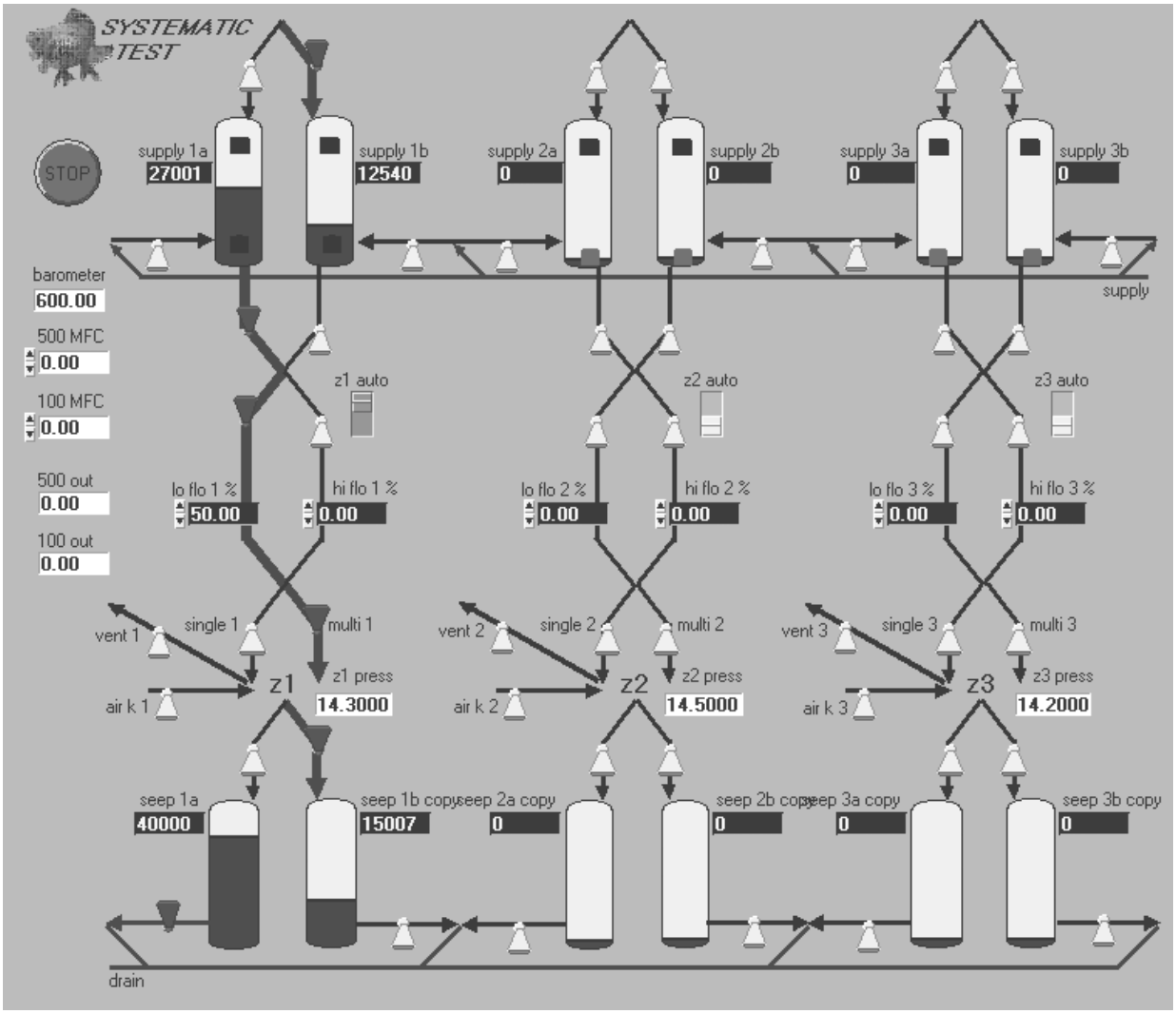

Figure 6.11.1-3. Front Panel for Control Interface on Computer

6.11.1.2.6 Automation Program

The automation program takes two basic parameters from the operator, that of pump rate and that of water-delivery zone selection. All other aspects of control are performed automatically. Pumping starts in Bottle A, while Bottle B collects return water, until the water content read by the Bottle A transducer indicates that this bottle is nearly empty. At this point, Bottle B is filled to a preset limit (as read by the transducer) if it is not at this limit already. When Bottle B is filled, pumping is switched from Bottle A to Bottle B. Bottle A is now able to collect any return flow. While filling from the main water supply, bottles are not able to collect return flow. Because filling is a rapid event, this pause in collection does not affect data collection. If filling does not occur rapidly enough to prepare the second bottle before the first one runs dry, the

pump is switched to the second bottle even before it is completely full when a lower limit is passed (as read by the transducer of the first bottle). To obtain a smooth record of all the water delivered to a zone, the water content of a bottle being filled is subtracted from the water content at the start of that bottle's filling. This value is in turn added to the total recorded when the last bottle switch occurred. A similar arrangement works for the return-water record.

6.11.1.2.7 System Fail-Safes

To avoid overfilling of the bottles or the pumps running dry in the event of a failure in the automatic control system or inadvertent use of the controls on manual setting, the system employs float switches at the top and bottom of the bottles as a backup to the automation. The bottom float switches when triggered (depicted in light gray in Figure 6.11.1-3) for the zone 2 and zone 3 systems, forcing the pumps on these to stay off even if requested by a user or automation system to operate. The top float switches interrupt the electrical current to the fill valves when triggered. In the event of a computer shutdown such as during a power failure, all the relays and pump controls are turned off, causing the system to default to a stand-by mode.

6.11.2 Systematic Testing Results and Observations

Sets of completed tests in two low-angle boreholes (belonging to Group I according to the nomenclature in Figure 6.11.1-1, ECRB-SYBT-LA#1 and ECRB-SYBT-LA#2, will be described below in the order in which they were performed.

6.11.2.1 Air-Injection Tests and Liquid-Release Tests in LA2, Initiated on May 11, 2000

ECRB-SYBT-LA#2 (hereafter referred to as LA2) is collared at ECRB Cross Drift CS 17+26. Three packers isolated the borehole into three zones so that the distance from the middle of the 1.83 m liquid-release zone to drift crown is respectively 1.58 m, 2.84 m and 4.10 m for zone 1, zone 2 and zone 3.

Air-permeability estimates for the three zones from the steady-state pressure response to constant-flow-rate air-injection tests is tabulated in Table 6.11.2-1 (DTN: LB00090012213U.001 [153141]).

Table 6.11.2-1. Air-Permeability Estimates for the Three Zones in Borehole LA2

Zone ID	Zone Length (m)	Air Permeability k(m^2), for Packer Inflation at 27.5 PSI	Air Permeability k(m^2), for Packer Inflation at 32.5 PSI
LA2 zone 1	1.83	2.5×10^{-11}	2.3×10^{-11}
LA2 zone 2	1.83	2.7×10^{-11}	2.5×10^{-11}
LA2 zone 3	5.18	1.1×10^{-11}	0.95×10^{-11}

DTN: LB00090012213U.001 [153141]

Pressure response and injection flow rates are shown in Figure 6.11.2-1. The fast rise and decay of the pressure in response to initiation and termination of air injection indicate very little storage effect. Zone 3 is longer than the designed 1.83 m liquid-injection section because the last zone for air injection begins at the end of the third packer and extends to the end of the borehole. The air-permeability measurements were repeated for a lower and higher inflation pressure. The repeatability of the two measurements for different packer inflation pressure indicates that there was little leakage between zones from possible improper sealing of the packers.

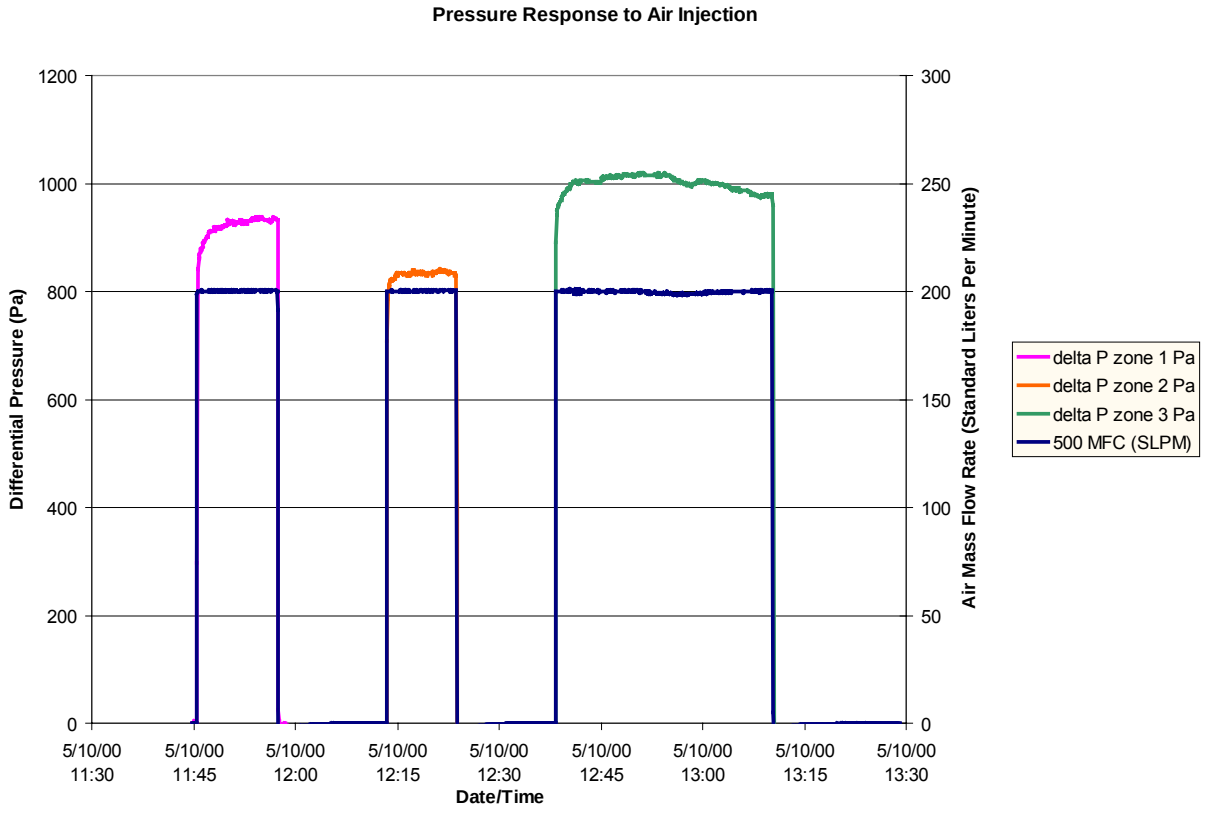

DTN: LB00090012213U.001 [153141]; LB0110SYST0015.001 [OUTPUT]

Figure 6.11.2-1. Pressure Responses (Red, Orange, and Green) to Constant Mass Flow of Air-Injection (Blue) for Estimation of Fracture Permeability in ECRB-SYBT LA#2

Following the air-injection tests in all three zones, a liquid-release test was conducted in zone 1 only. A large liquid release rate of ~450 mL/min was initiated in zone 1 through one single release point in the 1.83 m injection zone. No return flow was detected, indicating that all released water was able to enter the rock formation through the injection section. Figure 6.11.2-2 gives the cumulative volume of water supplied to zone 1 (left axis) and the cumulative volume of water collected in the seepage-collection system (right axis) as a function of time. Figure 6.11.2-2 indicates that the initiation of water release was at 9:31 and the start of seepage collection was at 12:00 (although a wet spot made its first appearance at the drift ceiling at 11:10, and water began to seep shortly after). Understandably, a time lapse existed between the first wetting of the drift ceiling and the time when enough water was collected in the seepage-collection cylinder to cause a measurable change in the water level (nominally, 3 mm change in water level for every 100 mL of water). The wetting of the drift ceiling expanded with time, and by 15:15, the wetted area was on the order of 0.8 m^2. The following morning (May 12, 2000), it was noted that in addition to the seepage from the wetted drift ceiling directly below the injection zone, water was also seeping through a rock-bolt borehole beyond the edge of the capture curtain. The capture curtain was 4 m in length and was centered approximately below the 1.83 m liquid injection zone. Seeped water from the rock-bolt borehole was missed by the seepage collection data acquisition and may be related to the recorded decrease in seepage rate after ~20:00 on May 11 (as shown in Figure 6.11.2-2). The water release into zone 1 was terminated at 8:36 on May 12, 2000.

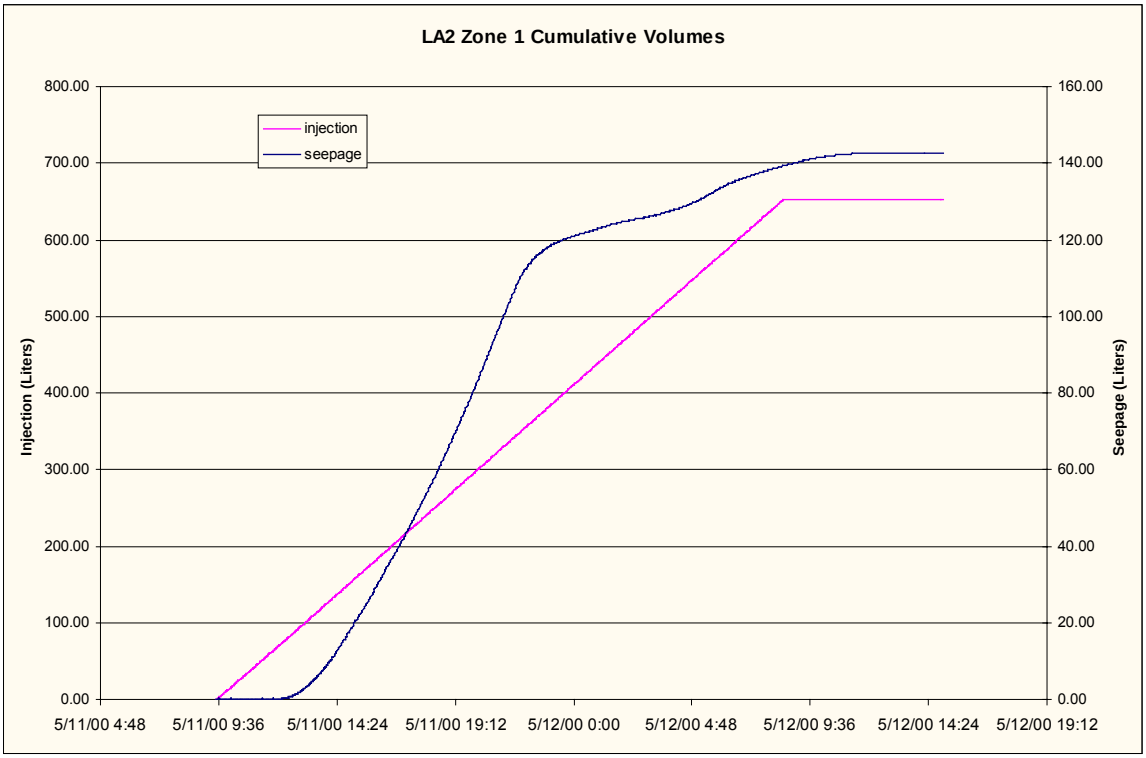

DTN: LB00090012213U.002 [153154]; LB0110SYST0015.001 [OUTPUT]

Figure 6.11.2-2 Cumulative Water Supplied to ECRB-SYBT-LA#2 Zone 1 and Cumulative Seeped Water into the ECRB Cross Drift for Test Performed on May 11–May 12, 2000

6.11.2.2 Liquid-Release Test in Zone 1, Zone 2, and Zone 3 in LA2, Initiated on May 17, 2000

Between 11:45 and 11:49 on May 17, 2000, liquid release into zone 1, zone 2, and zone 3 was initiated (Figure 6.11.2-3). The multipoint mode of injection was used so that water was evenly spread along each 1.83 m zone. A liquid release rate of 30 mL/min was intended for every zone. However, for the same specified water-release pump rate, the actual release rate to each zone would differ because of the difference in zone height. Subsequent adjustments to the pump rate may be made as guided by the actual release rate recorded by the data acquisition. Figure 6.11.2-3 shows the cumulative volume of water supplied to zone 1, zone 2, and zone 3 (left axis) and the cumulative volume of water seeped (right axis). Note that seepage from zone 1 was recorded beginning at 3:11 of May 18, 2000 (none from zone 2 or zone 3). On our return to the test site the next morning (May 18, 2000), it was found that the software control of the filling function to supply Bottle B was not functioning properly. We therefore terminated delivery of water to all three zones at 9:08, May 18, 2000. Note that data in Figure 6.11.2-3 as recorded by the data acquisition system show that cumulative volume of supply water ceases to increase after 5/17/00 (21:23), 5/18/00 (0:39), and 5/18/00 (7:13) respectively for zone 1, zone 2, and zone 3. These were the times at which Bottle A was "emptied," and water supply to the rock was switched to Bottle B. However, field observations showed that refill in Bottle B was being mechanically controlled by the float switches, so that that bottle stayed at the full level and water was continually being released into the rock formation, presumably at the prevailing pumping rate prior to the fill problem. Therefore, although Figure 6.11.2-3 gives the false impression of no cumulative increase in supply water, in fact water was being supplied to the rock formation from Bottle B, possibly at the prevailing rate (as supplied by Bottle A), until May 18 at 9:08.

The noisy "swings" in the cumulative seepage data in Figure 6.11.2-3, and in later figures, may be attributed to the slow response time in differential-pressure transducers to the atmospheric fluctuations. While the water level in the seepage-collection cylinders responded instantaneously to the atmospheric fluctuations, filters placed in the differential-pressure-transducer ports caused a delay response. The filters were originally put in place to keep the ports "clean"; they were removed from use in May 2001.

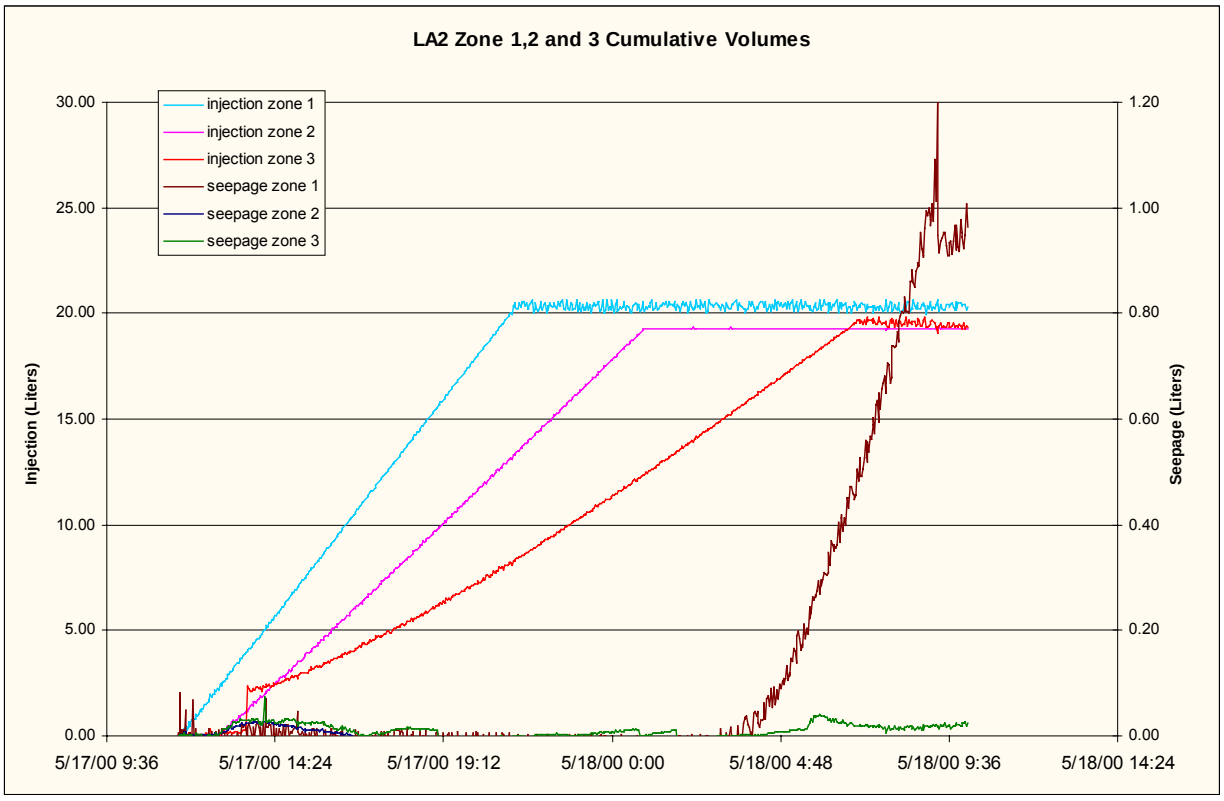

DTN: LB00090012213U.002 [153154]; LB0110SYST0015.001 [OUTPUT]

Figure 6.11.2-3. Cumulative Water Supplied to ECRB-SYBT-LA#2 Zone 1, Zone 2, and Zone 3 and Cumulative Seeped Water into the ECRB Cross Drift for Tests Performed on May 17–May 18, 2000

6.11.2.3 Liquid-Release Test in Zone 1, Zone 2, and Zone 3 in LA2, Initiated on May 23, 2000

Faulty software control of the filling function in May 17 tests was resolved. Liquid-release tests from six multiple points in zone 1, zone 2, and zone 3 were resumed at 14:25 on May 23, at the intended rate of 30 mL/min. Data for the three zones will be discussed separately.

6.11.2.3.1 Zone 1

Figure 6.11.2-4 shows cumulative supply (left axis) and cumulative seepage volume (right axis) as a function of time from May 23, 2000, to June 1, 2000, 11:14, when water release was terminated. Data show that seepage collection initiated on May 24, 2000, 13:19, although a wetted spot ~0.5 m in diameter was observed as early as 8:40. The rate of supply water was on the order of 28 mL/min, and the rate of seepage stabilized to ~4 to 5 mL/min within a week. Water release was terminated on June 1, 2000.

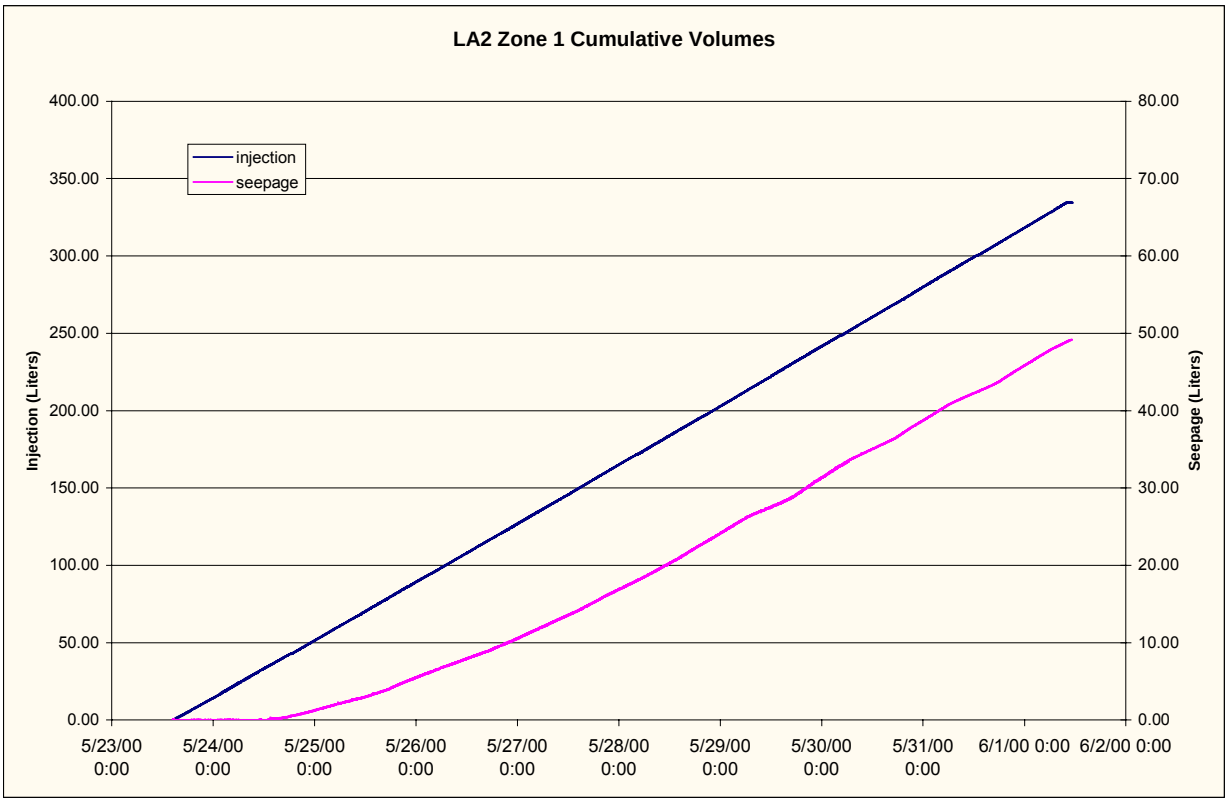

DTN: LB00090012213U.002 [153154]; LB0110SYST0015.001 [OUTPUT]

Figure 6.11.2-4. Cumulative Water Supplied to ECRB-SYBT-LA#2 Zone 1 and Cumulative Seeped Water into the ECRB Cross Drift for Tests Performed on May 23–June 1, 2000

6.11.2.3.2 Zone 2

Water release continued from May 23, 2000, through June 8, 2000. To keep data files at a manageable size, multiweek liquid-release tests were stopped and restarted periodically. Every time the software control routine was restarted, new data files with date/time stamp were generated, and cumulative supply and seepage reference was restarted at zero. Figure 6.11.2-5 shows cumulative supply (left axis) and cumulative seepage volume (right axis) in two graphs: (a) from May 23 to June 1 and (b) from June 1 to June 8, since the test was stopped on June 1, 2000, 11:14 and restarted at June 1, 11:23. Figure 6.11.2-5a shows that seepage from zone 2 initiates at 20:26, May 29, 2000. Step-like structures are very prominent in the cumulative volume of seepage water data in Figure 6.11.2-5b, indicating two different slopes and therefore different rates of seepage. The periods of larger slope (higher seepage rate of ~2-3 mL/min) in Figure 6.11.2-5b can be correlated to evenings and weekends when the underground tunnels were closed for access and the ventilation system was not in operation. Data in Figure 6.11.2-4 for zone 1 also give different slopes for seepage-water volume versus time, depending on whether ventilation is on or off. The step-like signature in Figure 6.11.2-4 is subtler than that in Figure 6.11.2-5b because of the higher seepage rate there. That water seeping into the drift has partly evaporated places uncertainty on the seepage data, because even when the ventilation is not in operation in the evenings and on weekends, the relative humidity in the underground tunnels is still far below 100%. As a result, while data in Figure 6.11.2-4 and Figure 6.11.2-5

give a measure of the amount of water lost to evaporation resulting from active ventilation, they do not provide information on the amount of water lost to evaporation in the absence of active ventilation. In response to these initial results, we have (for subsequent tests) modified the systematic measuring system to incorporate measurements of relative humidity and evaporation rate (from an open pan) in the tunnel space between the drift crown and the seepage-collection PVC curtain enclosure. No direct measurement system exists to ascertain the evaporation rate from within the fracture system.

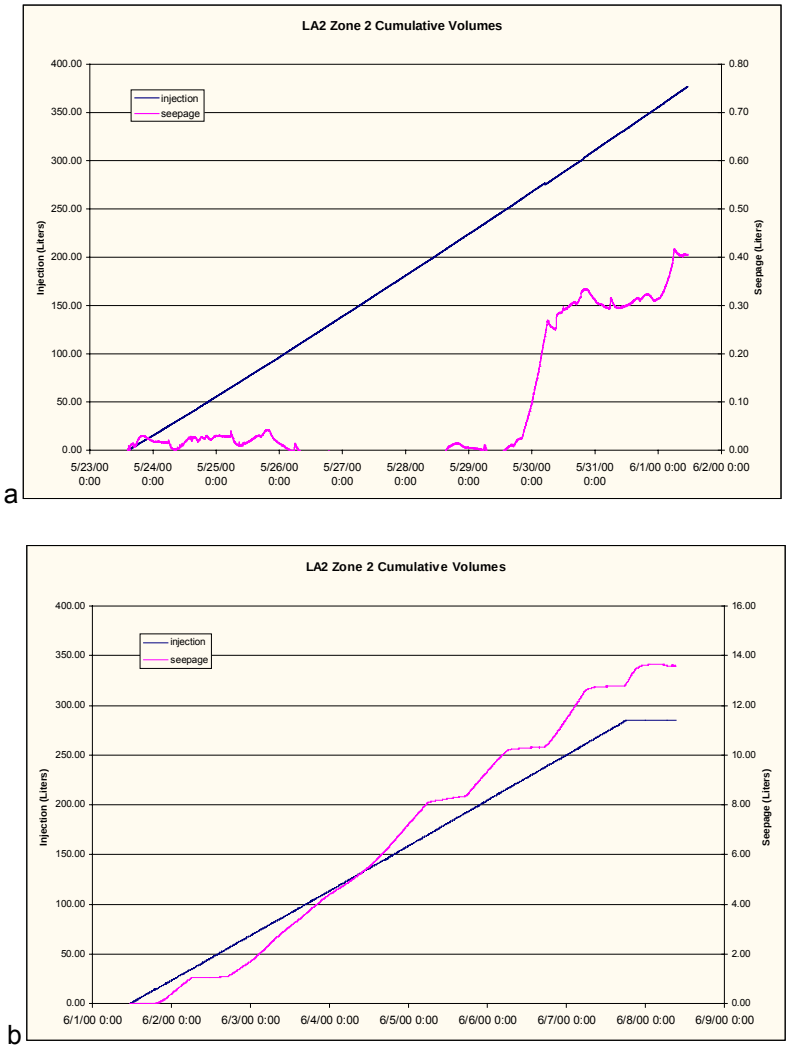

DTN: LB00090012213U.002 [153154]; LB0110SYST0015.001 [OUTPUT]

Figure 6.11.2-5. Cumulative Water Supplied to ECRB-SYBT-LA#2 Zone 2 and Cumulative Seeped Water into ECRB Cross Drift for Tests Performed on May 23-June 8, 2000. (a) May 23-June 1, 2000 (b) June 1–June 8, 2000.

6.11.2.3.3 Zone 3

Cumulative supply and cumulative seepage data for zone 3 between May 23, 2000 and June 27, 2000, are presented in Figure 6.11.2-6a through Figure 6.11.2-6d. Because of unanticipated

experimental problems of interface between the software control and the valves controlling the water supply system for this zone, the release of water was interrupted for two periods over a total duration of 34 days of testing. The periods where no water was supplied were (1) two days between May 30 and June 1, and (2) 11 days between June 3 and June 14. The problem was fully corrected from June 14 onwards, and the first indication of seepage water being collected in the seepage bottles for zone 3 was recorded by the data acquisition system at midnight June 26, 2000. Unfortunately, other testing activities in the underground tunnel necessitated the termination of water release in zone 3 (as well as monitoring of data) only about 8 hours after the first onset of seepage.

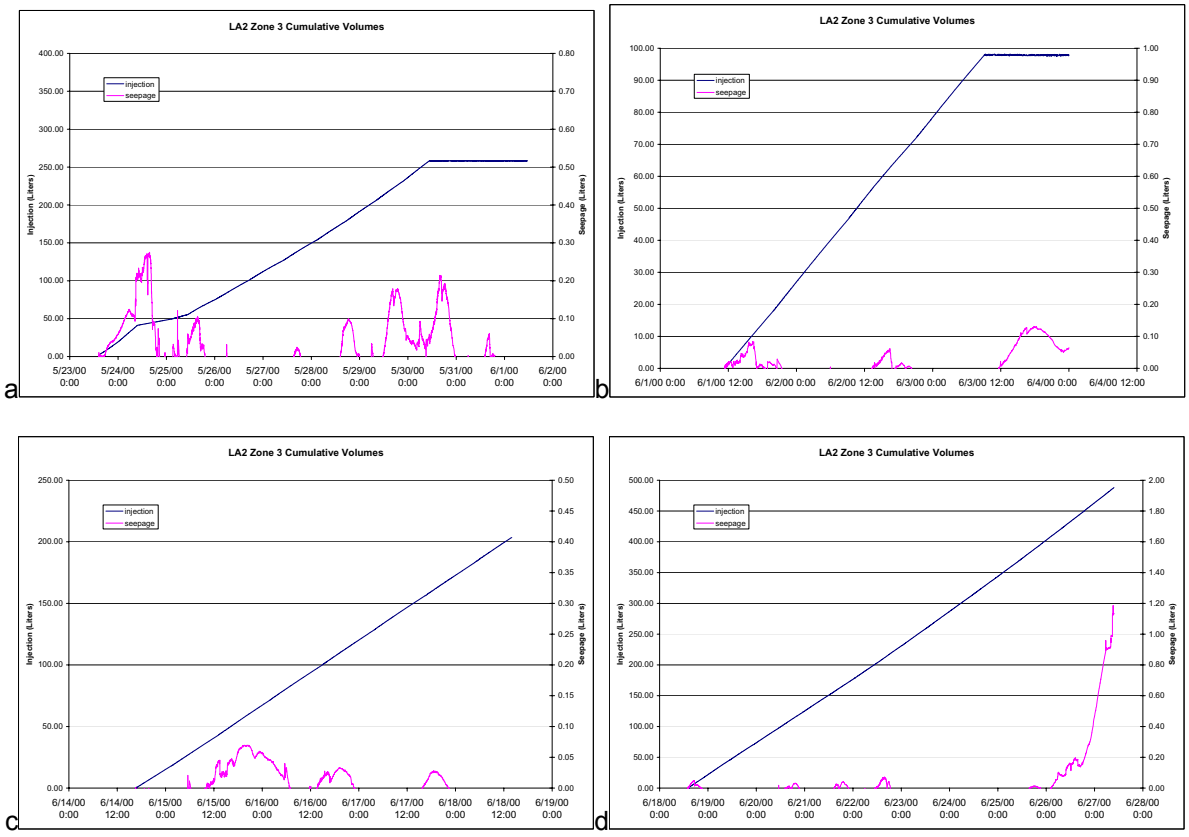

DTN: LB00090012213U.002 [153154]; LB0110SYST0015.001 [OUTPUT]

Figure 6.11.2-6. Cumulative Water Supplied to ECRB-SYBT-LA#2 Zone 3 and Cumulative Seeped Water into ECRB Cross Drift for Tests Performed on May 23-June 27, 2000. (a) May 23-June 1 (b) June 1 to June 3 (c) June 14-June 18 (d) June 18–June 27.

6.11.2.4 Liquid-Release Test in Zone 2 and Zone 3 in LA2: October 23–December 1, 2000

Other activities in the ECRB Cross Drift prevented the redeployment of systematic testing equipment for four months after the tests described in the previous section 6.11.2.3. In this current set of testing, liquid-release tests were repeated in zone 2 and zone 3 of LA2, specifically to evaluate the impact of evaporation from active ventilation and less-than-100% relative humidity on seepage data. The following modifications to the test design and measuring system were made since the completion of the previous test in June 2000. First, additional curtains were installed on the two ends of the V-shaped seepage capture PVC curtains shown in Figure 6.11.1-2 to mitigate drying of the wetted drift crown from ventilation. Second, humidity and temperature sensors were placed within the curtain enclosures of zone 2 and zone 3 to investigate the correlation of humidity conditions to seepage data. Also, a camera was installed to take photographs of the drift ceiling below the injection section of zone 2 to monitor the evolution of wetting.

Cumulative water supply and cumulative seepage data for zone 2 and zone 3 are shown in Figure 6.11.2-7. Data show that the first recorded seepage (as indicated by a rise in water level in the seepage collection cylinder) occurred on October 31 at ~20:00, for both zone 2 and zone 3. Photographs taken periodically of the drift ceiling below zone 2 indicate that a wetted area first appeared on October 27 around 8:00 and expanded with time. The wetted area on the drift ceiling could be estimated by counting the number of ground-support wire-mesh grids it covered. Photographs indicate that by November 7, 2000, the wetted area had stopped expanding and become stabilized at 6.8 m^2. Derivatives of the cumulative supply and cumulative seepage from Figure 6.11.2-7 give the rates of supply and seepage. Supply rate, seepage rate, and relative humidity and temperature within the capture curtain enclosure for zone 2 and zone 3 are respectively shown in Figure 6.11.2-8 and Figure 6.11.2-9. Note that the relative humidity was on the order of 35% prior to initiation of seepage on October 31, 2000. Coincidentally, the vent line in the ECRB Cross Drift collapsed on October 31, 2000, cutting off the ventilation. Note that the humidity within the capture curtain enclosures of zone 2 and zone 3 rose to almost 90% by November 7, 2000. Since the collapse of the vent line, ventilation was restored in the ECRB Cross Drift only partially on and off throughout the current set of tests, and the humidity reading varied with time between the preseepage value of 35% to the high of 90%.

Figure 6.11.2-8 and Figure 6.11.2-9 show that the seepage rates in both zone 2 and zone 3 track the relative humidity; that is, seepage rates increase and decrease with the rise and fall of relative humidity values. The seepage rate in zone 3 is higher than that in zone 2, reaching a high of about 6 mL/min. This may result from the higher water-release rate in zone 3 (~38 mL/min, as compared to ~34 mL/min in zone 2). It is not known whether the smaller evaporation component (from a smaller wetted area on the drift ceiling than that in zone 2) that existed for zone 3 possibly led to the higher seepage in zone 3. This is because our measuring system had only one camera positioned to monitor zone 2, and the vent line collapse and subsequent delay in repair has prevented access to the LA2 test site for direct observation of the drift ceiling. Note also that there were several brief periods of interruption of liquid release on November 26, 29, and 30 (these show up as data gaps in Figure 6.11.2-7) results from problems with network-connection power outages and the equipment-computer interface. These control-program shutdowns required a few restarts of liquid injection. Liquid release to zone 2 and zone 3 was terminated on

December 1, 2001. Data in Figure 6.11.2-7 and Figure 6.11.2-8 indicate that recorded seepage ceased within 11 hours of liquid-release termination.

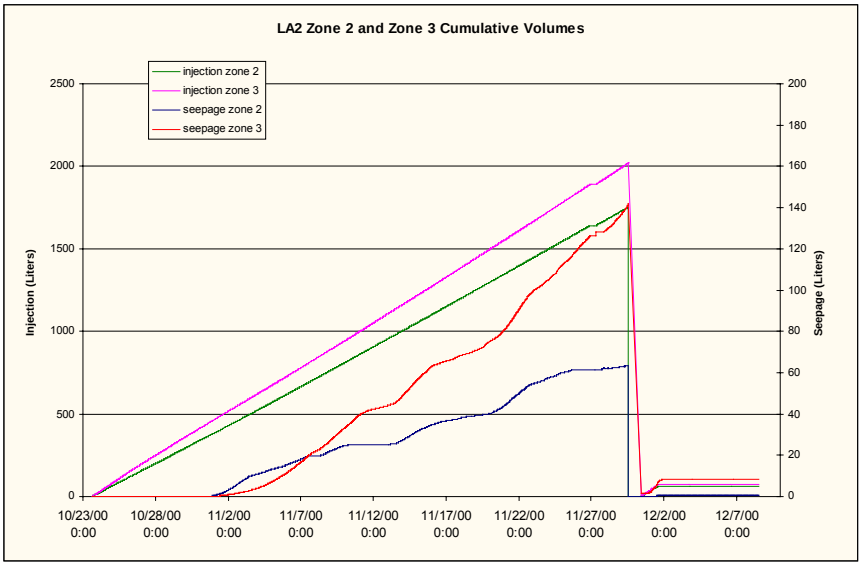

DTN: LB0110ECRBLIQR.003 [156877]; LB0110SYST0015.001 [OUTPUT]

Figure 6.11.2-7. Cumulative Water Supplied to ECRB-SYBT-LA#2 Zone 2 and Zone 3 and Cumulative Seeped Water into ECRB Cross Drift for Test Performed on October 23, 2000 to December 1, 2000

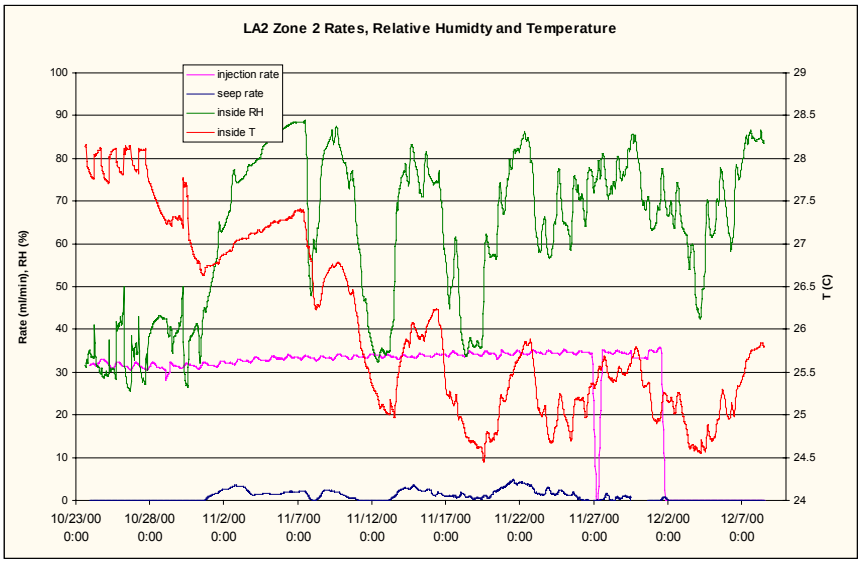

DTN: LB0110ECRBLIQR.003 [156877]; LB0110SYST0015.001 [OUTPUT]

Figure 6.11.2-8. Supply Rate, Seepage Rate and Relative Humidity and Temperature for Liquid-Release Test Performed in ECRB-SYBT-LA#2 Zone 2 on October 23, 2000 to December 1, 2000

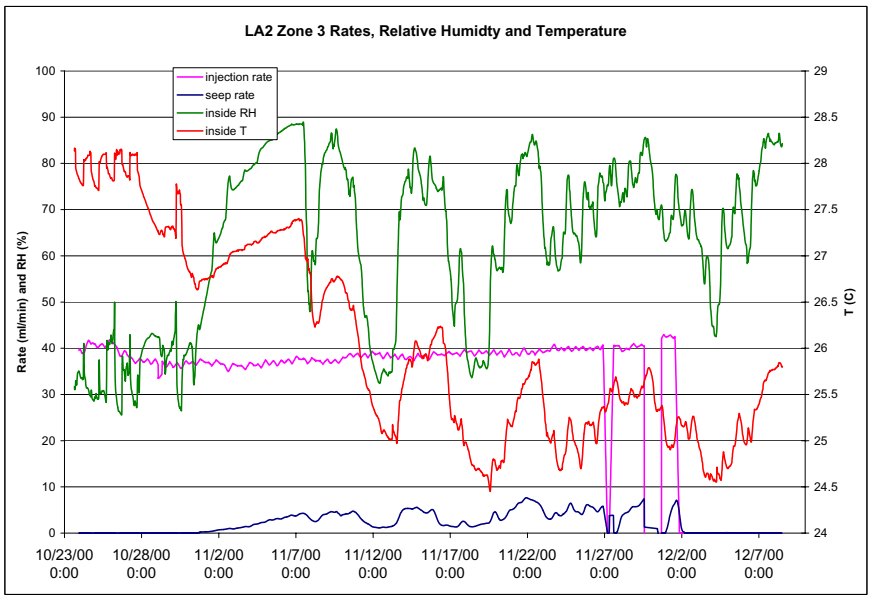

DTN: LB0110ECRBLIQR.003 [156877]; LB0110SYST0015.001 [OUTPUT]

Figure 6.11.2-9. Supply Rate, Seepage Rate, and Relative Humidity and Temperature for Liquid-Release Test Performed in ECRB-SYBT-LA#2 Zone 3 on October 23, 2000 to December 1, 2000

6.11.2.5 Liquid-Release Test in Zone 2 of LA1: December 20, 2000 – January 2, 2001

Similar to ECRB-SYBT-LA#2, LA#1 is a low-angle near-horizontal borehole (inclination of 15^{o} from the Cross Drift axis), drilled from the ECRB Cross Drift crown. It is collared at ECRB Cross Drift CS 17+49 m, immediately outside of the first bulkhead. Rock fragments that fell into the borehole (post-drilling) caused the borehole to be totally obstructed from 8.2 m from the collar to the end of the 20 m long hole. Therefore, only one zone instead of the intended three (as in LA2) was accessible for fluid testing.

Zone 2 was isolated by two inflated packers and nominally at 3–4.9 m from the collar. Therefore, height of mid-zone from drift crown was 1.03 m. Liquid release carried out in this zone (denoted as zone 2 in the data acquisition system) took place through the six equally spaced outlet nozzles. To better evaluate the impact of evaporation on the seepage data, an evaporation pan was installed within the space enclosed by the seepage capture and end curtains. A differential-pressure transducer monitored the drop in water level from evaporation. Liquid release into zone 2 started on December 20, 2000, 14:56, with a requested pump rate of 30 mL/min. Data (Figure 6.11.2-10) show that the actual water-release rate was 15 mL/min. ECRB Cross Drift was closed and not ventilated during the Christmas break, so the test was run and monitored remotely. A power outage shortly after midnight of Christmas terminated the liquid injection and data acquisition at 0:22, December 26, 2000. Power was restored on December 28, 2000, and the data acquisition system was restarted remotely. Unfortunately, the pumps that deliver water could not be restarted properly. Also, photographs taken periodically of the drift ceiling show the beginning of a wet spot the morning of Christmas prior to the power outage, indicating the first arrival of water to the drift ceiling. Figure 6.11.2-10a shows that ~103 liters of water has been released into zone 2 at the time of the sign of this first arrival of water at the drift ceiling. Since

water release stopped about 15 hours later and could not be resumed, the test did not run long enough to witness seepage. Figure 6.11.2-10a and Figure 6.11.2-10b also show respectively that the relative humidity and temperature within the curtain enclosure remained at about 12% and 26°C throughout the data acquisition period. Figure 6.11.2-10b shows that the data from the evaporation pan indicate the evaporation rate was on the order of 3 mm/day.

The ECRB Cross Drift was reopened January 2, 2001, after the Christmas break, but other field activities (such as opening of the bulkhead) required the removal of systematic test equipment from the ECRB Cross Drift and prevented resumption of the liquid release test in LA1. Data acquisition in LA1 was terminated on January 2, 2001.

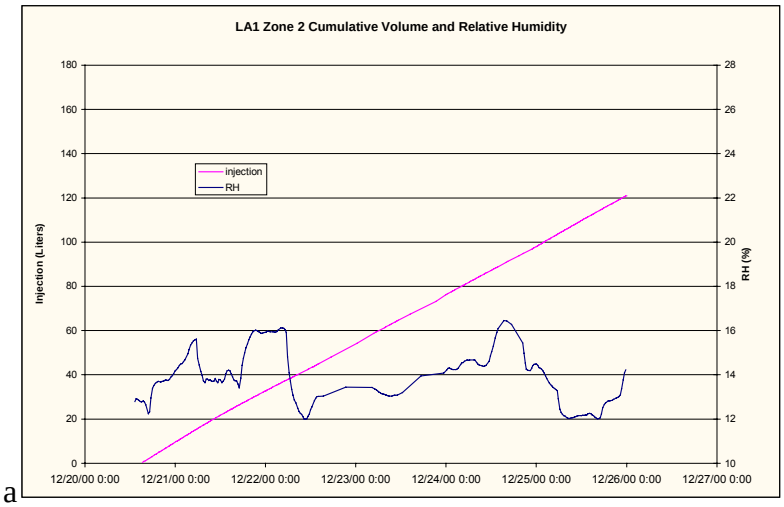

a

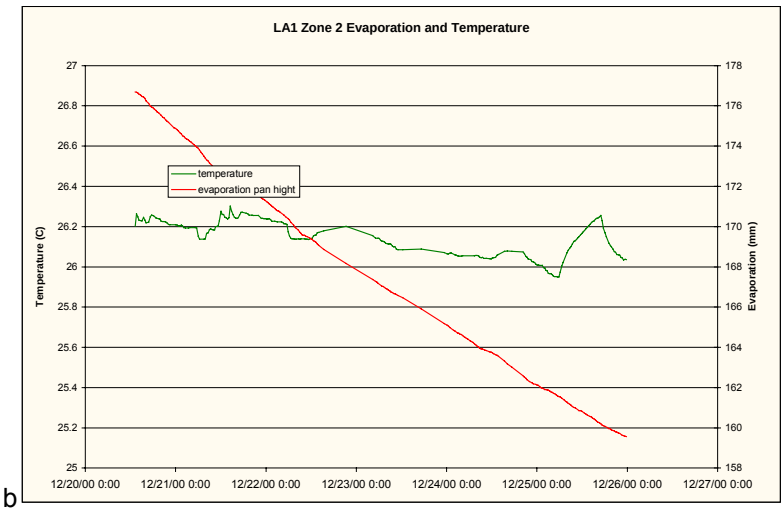

b

DTN: LB0110ECRBLIQR.001 [156878]; LB0110SYST0015.001 [OUTPUT]

Figure 6.11.2-10. (a) Cumulative Water Supplied to ECRB-SYBT-LA#1 Zone 2 for Test Performed on December 20, 2000 to January 2, 2001. Also shown are humidity and (b) temperature, and the water level in the evaporation pan.

6.11.2.6 Liquid-Release Test in Zone 2 of LA1: February 28 – April 30, 2001

This test, initiated on February 28, 2001, was a resumption of the test conducted in December 2000. Line release of water over a 1.83 m zone was initially set at the same rate as that of the December tests, ~15 mL/min, actual. Photographs show that the first appearance of a wet spot (water arriving at the drift ceiling) was on March 3, 2001, 16:23; that is, about 75 hours after initiation of water release. Figure 6.11.2-11a, which shows the cumulative supply and seepage of water, indicates that about 60 liters of water has been introduced into the formation at this time. The seepage collection system (rise in water level in the seepage collection cylinder) registered the initiation of seepage at ~22:00 on March 15, 12 days since the observation of the first wetting on the drift ceiling. Furthermore, in this period, the actual water-release rate had increased from 14 mL/min to above 20 mL/min. Following March 15, a Thursday, was a three-day weekend when ventilation was turned off, during which time the average injection remained at ~20 mL/min and average seepage was on the order of 1 mL/min. Figure 6.11.2-11b shows that on Monday, March 19 (when ventilation was resumed) the seepage rate decreased dramatically to almost zero. This was true even during the next three-day weekend (March 23 to March 25). Recorded seepage continued to be about zero through the following week. Photographs also show that the wetted area on the drift ceiling had shrunk. A study of the plotted data (Figure 6.11.2-11b) indicates that the average release rate during this period has fallen below 20 mL/min to around 18 mL/min. That is, though the request pump rate was constant (at 30 mL/min), the actual injection rate went above 20 mL/min on the weekend of March 16 to 18, and then fell back to ~18 mL/min afterwards. Data therefore indicate that, in general, the actual water-release rate needed to be above 20 mL/min for recorded seepage.

An unplanned interruption of water release occurred on Thursday, March 29, 2001, 4:43, because of an air-compressor problem. Water release was resumed on Tuesday 4/3/2001 9:50, at a higher requested pump rate. Data (Figure 6.11.2-11b) show that the actual injection rate was on the order of 42 mL/min, and seepage-collection data acquisition began to record non-zero seepage at ~20 hours after resumption of water release.

A planned power outage caused another interruption of water release on April 5, 2001, 17:48. The negative slope on the cumulative volume plot indicates no data recorded during this period. (What appears as a positive rate on Figure 6.11.2-11b just before April 9, 2001, 12:08 has no data.) Water release to LA#1 resumed on April 9, 2001, 12:08 (Friday), at an actual rate of ~42 mL/min. Data indicate onset of seepage at ~20 hours after resumption of water release. The seepage rate increases from ~7 mL/min to ~10 mL/min on April 16, 2001 (Monday). We carried out two planned, deliberate interruptions of water release for duration of less than a day. The first pause of water release occurred on 4/16/01 (Monday), 15:22. After a pause of 18 hours and 20 minutes, water release was resumed, and seepage was observed ~16 hours afterwards. Then for a second time on April 24, 2001, (Tuesday) at 16:54, water release was interrupted, then restarted on April 25, 2001, 11:39. Seepage began at ~16 hours afterwards. Following both these planned water-release pauses, the water-release rate was on the order of 42 mL/min, and seepage was on the order of ~ 10 mL/min.

Fall of water level in the evaporation pan indicated that the evaporation rate is on the order of 3 mm/day. Coupling this information with the largest (stable) wetted area estimated from

photographs of the drift ceiling (~4.5 m^2) would give an upper bound of the evaporation from the wetted drift surface a rate of 9.5 mL/min. Testing in LA1 was concluded on April 30, 2001.

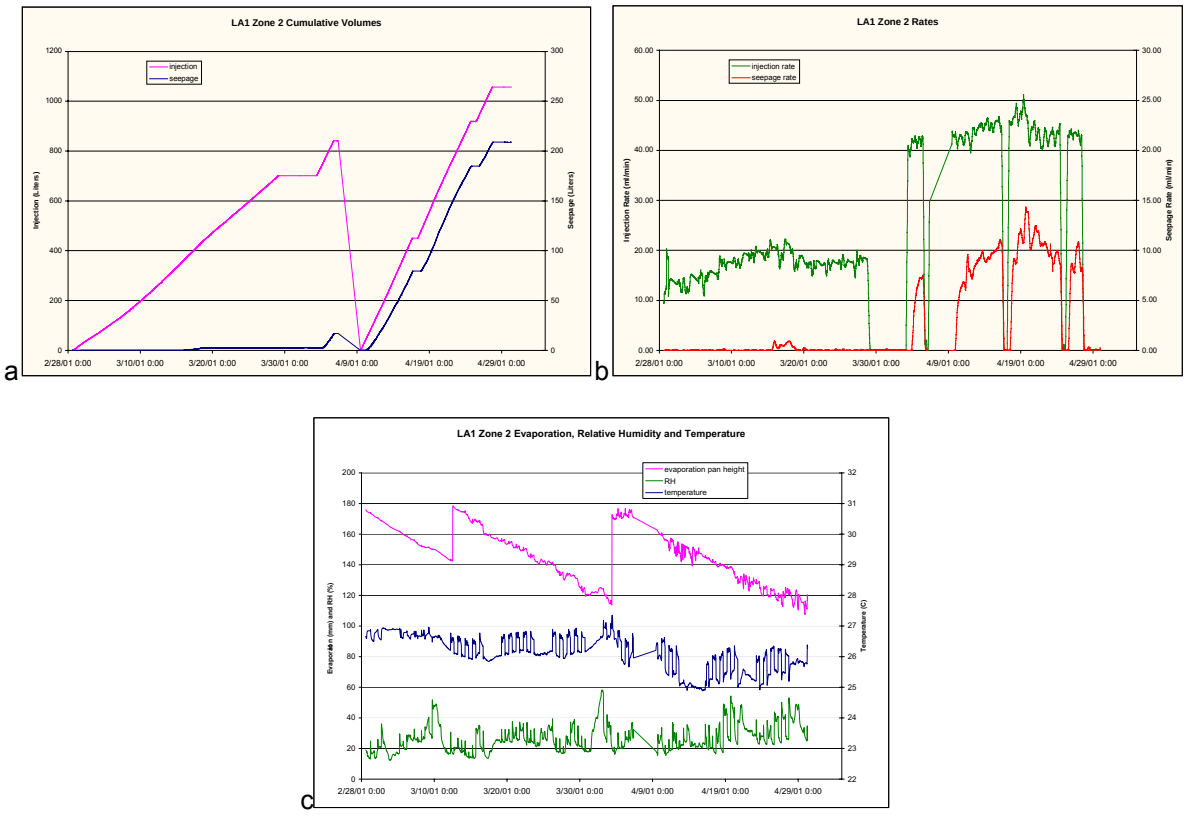

DTN: LB0110ECRBLIQR.002 [156879]

Figure 6.11.2-11. (a) Cumulative Water Supplied to and Seeped from ECRB-SYBT-LA#1 Zone 2 for Test Performed on February 28 to April 30, 2001, (b) Water Supply Rate and Seeped Rate, (c) Humidity, Temperature and the Water Level in the Evaporation Pan.

6.11.3 Systematic Testing Discussion and Interpretation

Several important results become apparent when examining the data presented above. One result is the further insight into the role of fractures, matrix, and lithophysal cavities in liquid flow through the partially saturated lower lithophysal unit. Another is the assessment of the nonintersecting flow (a combination of diversion by capillary barrier and of alternate flow paths) around the drift excavation. A third important result is the estimation of a threshold flux at the water-release borehole below which seepage into the drift does not occur. Though only a small number of locations have been tested, the data have allowed us to make significant progress in understanding the hydrological characteristics of the lower lithophysal unit. It is anticipated that as systematic testing continues in more locations at regularly spaced intervals, investigators will accumulate more valuable insight into fluid flow in the highly spatially heterogeneous fractured-porous lithophysal unit. Direct comparisons of the same type of data from location to location can provide knowledge applicable to a large portion of the ECRB Cross Drift.

6.11.3.1 Participation of Lithophysal Cavities in Storage and Flow Paths

Lithophysal cavities, fractures, and matrix contribute to the overall porosity of the lower lithophysal rock. Drift-wall mapping along the ECRB Cross Drift indicate a mean lithophysal cavity porosity of 0.125 in the lower lithophysal unit (Mongano et al. 1999 [149850]). Gas-tracer measurements of the effective porosity in the middle nonlithophysal units indicate that fracture porosity is on the order of 0.01 (DTN: LB980912332245.002 [105593]). Both cavities and fractures are expected to be essentially dry at ambient conditions. Laboratory measurements from 453 samples of surface-based boreholes give the mean matrix porosity of 0.13 and a mean saturation of 0.78 for the lower lithophysal unit (Flint 1998 [100033]). Fourteen measurements on cores from boreholes drilled for systematic testing at ECRB Cross Drift CS 17+49 (DTN: LB0110COREPROP.001 [157169]) give results similar to that of Flint: mean values of 0.12 for matrix porosity and 0.72 for liquid saturation. Because of the high ambient liquid saturation, matrix contributes to only about 0.03 in porosity that is available for liquid storage from systematic testing.

In liquid-release tests such as those conducted for the systematic testing, it is anticipated that fractures and possibly very open cavities will ultimately be responsible for the steady-state flow behavior of the fractures-matrix-lithophysal cavity system, while slow-draining cavities and matrix will contribute to the first-time storage. Of the first-time test storage features, slow-draining cavities and matrix will contribute to one-time storage, while only fractures and open cavities contribute to subsequent "steady-state" storage. Thus, in a flow test at a new borehole where no water has yet been introduced, all the storage components should be in full effect. The water released into the formation will partition into storage and steady flow paths. If the fast paths themselves contain a significant storage component, this should lengthen the first arrival time for water (from the delivery point in the borehole to the exit point in the drift) and also increase the amount of water needed to do so.

Data from niche liquid release tests (Section 6.2 in this AMR) with dye observations during excavation of Niche 1620 at ECRB Cross Drift CS 16+20 suggest that the shape of the flow plume in close vicinity to the release is roughly circular. During a liquid-release test, as soon as water is observed at the crown of the drift, the maximum distance of any flow can be interpreted to have reached (along fast paths) the surface of a cylinder (the diameter of the cylinder is the distance between the middle of the release zone and the crown). The cylinder length would be roughly that of the release zone. This cylindrical volume concept is applied during the first-time test period when the connected paths are being developed, as a bound to contain the fast, connected paths. At later times in the test during the steady-state phase, water may have moved well beyond the bounds of this cylinder. The volume of water injected up to the point of first wetting at the drift ceiling, divided by the volume of this cylinder, gives the effective porosity for establishing fast paths. Note that the effective porosity measured this way is very much injection-rate-dependent, because the degree to which different components of actual porosity participate in the flow path varies according to their time of exposure to the flow (and in this case this is the time needed for water to reach the edge of the cylinder).

For the test in LA2 zone 1 (Section 6.11.2.1), Figure 6.11.2-2 shows that 46 liters (0.046 m^3) of water has been introduced at the first wetting of the drift crown. The volume of the cylindrical plume (diameter 1.58 m and length 1.83 m) is estimated to be 3.6 m^3. Hence, the estimated

effective porosity for establishing fast paths is .046 m^3/3.6 m^3 =.013. Water was released into LA2 zone 1 at a relatively high rate of 450 mL/min.

For the test in LA1 (Section 6.11.2.5) the diameter of the cylinder is 1.03 m, and the length is 1.83 m, for a volume of 1.53 m^3. Flow volume for the initial wetting of LA1 was 103 liters (0.103 m^3), which gives an effective porosity of 0.067. In this case, the water was released at a much slower rate of 15 mL/min.

The two estimated effective-porosity values of 0.013 and 0.067 prior to the establishment of fast paths lead to the following interpretation. In the case of LA2 zone 1 when the release rate was as high as 450 mL/min, the fracture porosity was accessed with little imbibition into the matrix at the time of intersection with the drift. Also, for the lithophysal cavities that act as a capillary barrier with the very high release rate, little water would be expected to seep into these cavities. For LA1 when the release rate was about 30 times slower at 15 mL/min, the flowing water would have time to access the matrix porosity, and less would be diverted around the lithophysal cavities. The difference in effective-porosity results from these two tests could thus be a measure of the component of storage due to matrix and slow-filling cavities. Because cavities are the primary contributor of actual porosity in the system, even a little participation in the flow path would raise the effective porosity. In the case of LA1, they seem to contribute up to a maximum of about 0.057 (effective minus fracture porosity, not accounting for matrix participation) and a minimum of 0.027 (if all the available matrix porosity participates). These values indicate that only a quarter to one half of the lithophysal cavity volume (porosity of 0.125) participates in the liquid storage.

A refinement in the evaluation of effective porosity is to study the process of restarting a water-release test after some pauses in activity. For LA1, after slightly more than two months, a new release was made (Section 6.11.2.6). The first arrival was observed after only 60 liters, giving a new effective porosity of 0.039. Therefore it appears that the liquid storage from the matrix and cavities filled in the initial test (Section 6.11.2.5) has not completely drained in this two-month lapse. The difference between the new value and that of 0.067 from the previous test in the same location could be a measure of the capacity of the matrix and the slow-draining lithophsyal cavities. Lastly, the difference between the storage measured from the difference in the initially dry high and low-rate tests (= 0.067 – 0.013)and the storage obtained from low rate and repeated low-rate tests (= 0.067 – 0.039) can be viewed as a measure of storage due to fast-filling, slow-draining cavities. This difference is 0.026 (= 0.039 – 0.013), or just less than a quarter of the cavity estimated porosity.

6.11.3.2 Estimation of the Steady-State Nonintersecting Flow around the Drift

One of the key outcomes of testing to investigate seepage into drifts is an estimation of the component of introduced water diverted around the mined opening during steady-state flow, following the establishment of connected paths between borehole and drift ceiling, as discussed in the previous section. A fraction of the water will miss the drift opening because of the nonuniform flow from heterogeneity. At the drift crown, additional lateral flow will be diverted around the drift resulting from the drift acting as a capillary barrier. The total component of non-intersecting water (from flow channeling and capillary effects) can roughly be thought of as the difference between the rate of injection and the rate of seepage into the drift when the test has

reached steady-state conditions, provided that there are no other losses. However, the systematic data (Section 6.11.2.3, Section 6.11.2.4 and Section 6.11.2.6) show clearly that evaporation contributes to the difference in the recorded injected and seeped volume of water. It is thus essential that evaporation be taken into account in any attempt to estimate the nonintersecting component.

The evaporation contribution to the wetted-drift ceiling can be estimated by multiplying the flux from an evaporation pan mounted just below the seep (to get accurate conditions) by the wetted area associated with the seep. All monitoring data for the water-level drop in the evaporation pan show that the evaporation flux is on the order of 3 mm/day, for the wide range (15 to 90%) of relative humidity encountered. The largest wetted area for all the systematic tests to date was 6.8 square meters, corresponding to the test in LA2 described in Section 6.11.2.4. An upperbound of evaporation rate from systematic testing may be obtained by multiplying the evaporation flux of 3 mm/day by the largest wetted area recorded by half-hourly observations (photographs) at LA2, 6.8 m^2. The resultant evaporation rate is about 14.4 mL/min. Clearly, uncertainty in this number remains, since potential for injected water to leave the test system from barometric pumping and from vapor transport in a drying front behind the drift wall has not been included.

During the period from February 28, 2001 to March 30, 2001 (Section 6.11.2.6), injection proceeded at an approximate rate of 17.5 mL/min at LA1. Observational evidence showed that the crown underneath the injected zone was wet, but no seepage was collected during this period. The exception was for the period from the afternoon of March 15, 2001, to the morning of March 19, 2001, corresponding to a weekend shutdown of the ventilation, during which collection occurred at a rate of 0.6 mL/min. The next weekend shutdown did not cause any seepage collection to occur. That slight variations in ventilation conditions determined whether seepage collection occurred at a very low rate or none at all indicates that the system was just on the verge of collecting or virtually seeping. The evaporation rate from the largest wetted area at LA1 (4.6 m^2) of 9.5 mL/min left 8 mL/min of flow from the injection unaccounted for; this can be interpreted to be the flow that has missed the drift. A conclusion can be drawn from testing during this period that at injection rates just high enough to cause active seeping at this location, about 46% of steady-state flow is diverted.

Section 6.11.2.6 (Figure 6.11.2-11b) also shows that a seepage collection rate of 8.5 mL/min was obtained at LA1 for a higher injection rate of about 40 mL/min during the period from 4/10/01 to 4/16/01. The nonintersecting flow is the evaporation rate and the seepage-collection rate subtracted from injection rate to give 22.0 mL/min. The nonintersecting flow estimated from this testing is therefore about 55%. Nonintersecting flow arises from both flow channeling and capillary barrier, but at those rates where seeps occur, the capillary barrier is likely overcome and no longer plays a significant role. Because the geometry of the channeled flow during “steady state” is likely independent of the water-release rate, the conceptual model of non-intersecting flow would seem to support the notion that at a given test location, diverted flow is a fixed percentage of the injected flow. The flow paths for diverting flow are probably similar in structure to those that are responsible for total seepage (including evaporation) and so respond linearly to an increase in injection rate. Because of the evaporation component, seepage collection rate (as opposed to total seepage rate) is not necessarily proportional to injection rate.

For another estimate of the lateral nonintersecting component, consider the seepage volume drained following the injection turn-off during "steady-state" testing and compare this volume to that required to initiate seepage after water release has been restarted. Water will drain out of the fast paths and be collected as seepage for some time after injection is terminated. (For all the systematic tests to date, the drainage period lasted less than 24 hours.) This is the storage volume of fast-path water connecting directly to the drift. Upon resumption of water release, the volume required to initiate seeping into the drift, the refill volume, is that which has to supply both the seepage fast path and the nonintersecting fast paths. The difference between the drainage seep volume and the refill volume suggests the volume of the nonintersecting fast paths.

Several pause studies were performed at LA1 to obtain this volume of nonintersecting fast paths that missed the drift opening. Correction for effects of rock-surface evaporation to both the drainage value and the volume to reinitiate seep is incorporated in this estimate. Evaporation increases the actual drainage value over that collected as seepage and decreases the refill volume from that recorded from the injection. During one test pause in LA1 on April 16, 2001, the seep drainage was 1.1 liters, but an additional 10.3 liters can be attributed to evaporation for the whole period that the injection is turned off. Evaporation is interpreted to be at its maximum of 9.5 mL/min for the duration of 18 hours. This interpretation is conservative, since photographs of the drift ceiling indicate that drying of the wetted surface commences with the termination of water release, and evaporation would decrease and cease within this period. Consequently longer duration pauses would undergo about the same amount of surface evaporation. When injection is restarted on April 17, 2001, at the same rate as on April 10, 2001, it takes 16 hours to refill using a volume of 40 injection liters before the resumption of seepage. This volume is partly evaporated at a rate of 9.5 mL/min, so that the real refill volume is 34 liters. It might be argued that there is a volume component associated with the water hanging on the ceiling contained in the wet spot and contributing to drainage collection. There may well be such a component, but it should be fairly well cancelled out by a converse contribution to the wet spot during refill. It appears that, even when accounting for a very large estimate of evaporation, the refill volume is just over twice the drainage volume, meaning that more than half the flow is nonintersecting. This number agrees favorably with the rate method of obtaining nonintersection steady-state flow for the period of injection just before the 4/16/01 pause and also for the earlier lower-rate test. Note that this method of calculating the nonintersecting component of flow, even though transient, will nevertheless be independent of injection rate because the time-dependent features (slow-filling cavities and matrix) no longer participate in a refill test.

6.11.3.3 Minimum Injection Rate Needed to Induce Seepage

At the scale of the drift, flow is more likely to progress in concentrated regions than as a uniformly spread front. A borehole line release occurs locally over the area projection of the borehole zone. This area emulates one of these concentrated regions at a given distance above the drift. During the testing at LA1 (Section 6.11.2.5) for the period from December 20, 2001, to December 26, 2001, observations (photographs) every half-hour confirmed that at the flow rate of 15 mL/min, with no ventilation, seepage on the ceiling was just observable as a tiny spot on the morning of December 25, 2001. It is postulated that there was little evaporation from the surface because there was no significant area to the spot. The spot stayed small for the remainder of the test, indicating that the system as a whole was approaching steady state. The 15 mL/min of

injected flow in this case appear to just barely reach the crown, thus the threshold below which seepage into the drift does not occur is 15 mL/min.

6.11.3.4 Estimation of Evaporation from within the Fracture System

The observation of seepage was made within a day of water-injection resumption on April 3, 2001, and April 9, 2001, following a pause of 4 to 5 days; and also on April 17, 2001, following a pause of 18 hours. These observations indicated that "fast paths," connected paths comprised of flowing higher-permeability features, had been established. This delay in the onset of seepage enabled us to measure the capacity of water needed to refill the transient storage (that is, the storage volume needed before seepage occurs) of these fast paths upon resumption of injection. This volume exists because flow through fractures takes a finite amount of time to travel and needs to refill its paths before seepage again takes place. Because of the nature of fracture flow, once seepage occurs, the paths are essentially full and the system is again at steady state. This volume is the same as that of the water lost from all the paths during the pauses. After the 5-day pause, refill took 20 hours at a rate of 42 mL/min. The refill volume in this case was approximately 50 liters. For a pause of 18 hours, the refill volume was about 40 liters. The refill volume is thus seen as not very sensitive to the pause time. Drainage during each pause was the same and was complete long before the end of each of these pauses, so that any further loss was a result of longer-lasting processes (such as evaporation from within the fracture system from hanging water, which would then require more refill volume). The small difference in refill volumes provides a measure of the rate of water moving out of the system by evaporation after drainage. An estimate of this rate during the portion of pause time between 18 hours and 5 days can be made in dividing the difference in refill volumes by the difference in pause length revision. The result for this rate is 2.0 mL/min. If the surface area of the hanging water is not greatly different from that of the moving water, then this number also gives an indication of the rate of evaporation from the fracture system at other times during the testing phase.

6.12 PRELIMINARY OBSERVATIONS FROM THE FAULT TEST AT ALCOVE 8-NICHE 3107

This test is aimed at evaluating unsaturated zone (UZ) flow, seepage response, and matrix diffusion processes between two drifts. Alcove 8 (located in the ECRB Cross Drift) has been excavated for liquid releases through a fault and a network of fractures. Niche 3107 (located at station 31+07 in the Main Drift of the ESF, ~20 m below Alcove 8) serves as the site for monitoring the wetting-front migration and for collection of seepage originating at Alcove 8. A series of boreholes surrounding Niche 3107 have been instrumented with sensors to detect the arrival of a wetting front. The interior of the niche has been instrumented with water-collection trays. Additional boreholes have been drilled in Alcove 8 and Niche 3107 for geophysical measurements and other tests to characterize the plume migration.

The near-vertical fault that intercepts the formation between Alcove 8 and Niche 3107 provides a unique opportunity to evaluate important hydrological parameters associated with fault flows and fracture-matrix interactions. This section serves as an introduction to the fault tests and provides preliminary observations from the early stages of the liquid-release tests. The liquid-release tests are followed by tracer tests using mixtures of tracers with both large and small molecular diffusion coefficients to evaluate the importance of matrix diffusion from observations of breakthrough times, and the effective fracture-matrix interfacial area. The baseline geophysical images are also presented.

The major test objectives are:

- Quantification of large-scale (~20 m) infiltration and seepage processes along a fault in the potential repository horizon
- Estimation of relations between relative permeability and water potential for unsaturated flow in faults and through fracture networks
- Evaluation of the importance of matrix diffusion in the UZ transport processes.

6.12.1 Drift-to-Drift Fault Test Setup

6.12.1.1 Test Sequence of Liquid and Tracer Releases

A series of tests broadly outlined in Figure 6.12.1-1 has been initiated in the Alcove 8-Niche 3107 fault test bed. Broadly, this sequence of tests is to be conducted in two phases. During the first phase, water is introduced along the fault under ponded conditions (i.e., with 2 cm of water head) until steady seepage is observed in Niche 3107. The flow test is followed by the introduction of a finite volume of water containing two tracers with different molecular diffusion coefficients (Br and PFBA) into the fault. Once the tracer-laced water has been released into the fault, more tracer-free water will be released. Both tracer-laced and tracer-free releases occur under the same ponded condition. This release of tracer-free water will continue until breakthrough of the two tracers (Br and PFBA) is observed in the seepage collected in Niche 3107.

The second phase of the test series involves the release water (laced with single and double tracers) under nonponded conditions. During this phase, water will be released into the fault under controlled rates. Here, the first release rate will be set at ~75 % of the intake rates observed under ponded conditions. Following the observation of steady seepage in Niche 3107, the release rate will be stepped down to 50% and then 25% of the ponded intake rates.

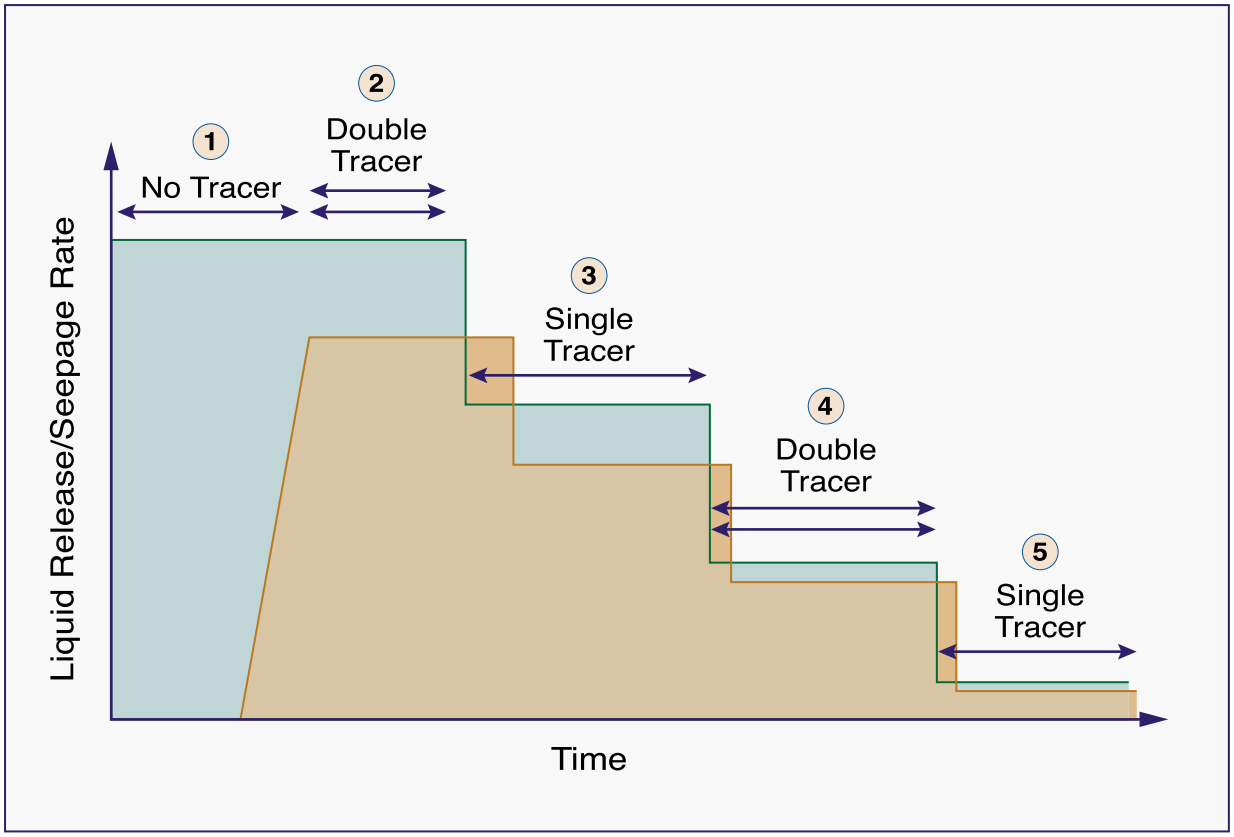

NOTE: Phase numbers in circles.
Blue = Introduced water.
Orange = Seepage

Figure 6.12.1-1. Schematic Illustration of Liquid Release and Seepage Collection Test Sequence

6.12.1.2 The Test Bed

Figure 6.12.1-2a shows the location of the test site within the ESF Main Drift and the ECRB Cross Drift. Figure 6.12.1-2b shows a three-dimensional representation of the test area, including several slanted (near-vertical) boreholes. Alcove 8 is located within the upper lithophysal zone of the TSw (Tplpul). Alcove 8 begins at Cross Drift Station (CS) 7+98.236 (CRWMS M&O 1999 [156876]). An elevation of 1093.973 masl is calculated for CS 7+98.236 using the software ECRB-XYZ V.03 (STN: 30093-V.03). The elevation at STA 0+00 of Alcove 8 is approximately 0.510 m above CS 7+98.236 or 1094.483 (± 0.15 m) based on Alcove 8 design drawings (CRWMS M&O 1999 [156876]). Niche 3107 is located in the middle nonlithophysal zone of the TSw (Tptpmn). The crown of Niche 3107 is ~2–3 m lower than the 1076.7 masl crown elevation of the ESF at CS 31+07. The location of the Tptpul-Tptpmn contact is ~1080 masl, based on GFM3.1 data (DTN: MO9901MWDGFM31.000 [103769]).

The distinctive feature of the test bed in Alcove 8 is a near-vertical fault that cuts across the floor (Figure 6.12.1-3). It is open on the ceiling, and appears to be closed along the floor of the alcove. To facilitate ponded releases of water, a trench ~5 cm wide and ~5 cm deep was etched along this fault.

Niche 3107 is approximately 4 m wide and extends to ~14 m from the centerline in the ESF Main Drift. The ceiling of the niche gradually drops from 3.25 m at the opening to 2.5 m towards the mid-point of the niche. Three 9.0 m long, 0.0762 m in diameter horizontal boreholes were drilled ~0.5 m above the ceiling. Additionally there are seven 6.0 m long, 0.0762 m in diameter boreholes drilled inside the niche (Figure 6.12.1-4). The fault is visible along the ceiling of Niche 3107 vertically below the trace along the floor in Alcove 8.

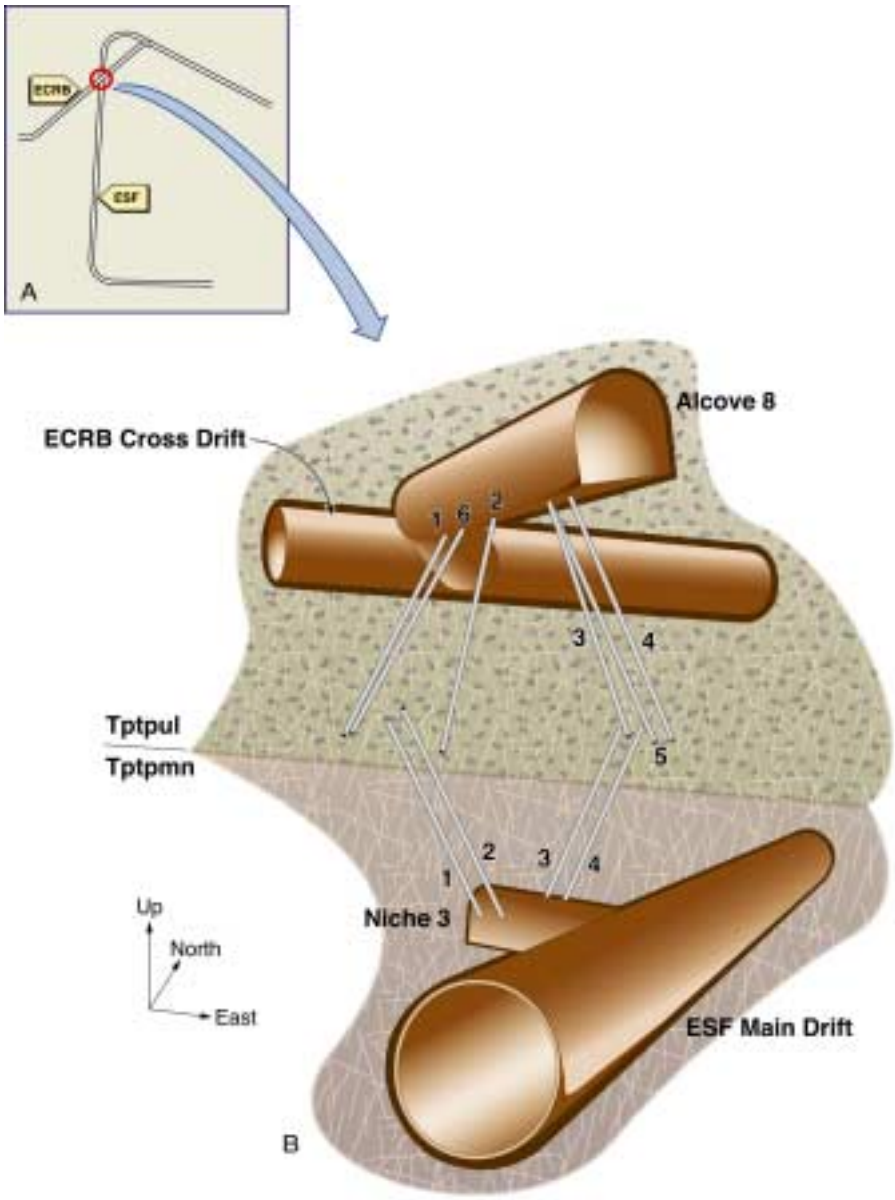

Figure 6.12.1-2. Schematic Illustration of the Test Bed for the Alcove 8-Niche 3107 Tests

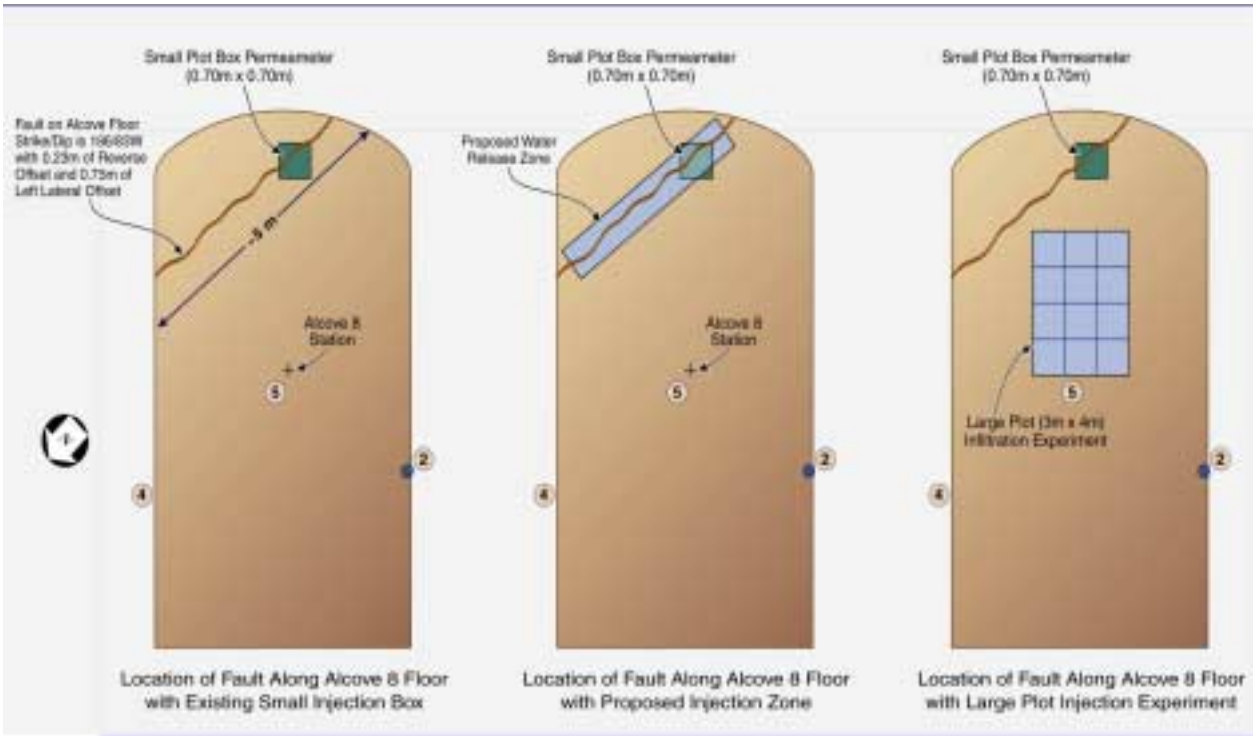

Figure 6.12.1-3. Schematic Illustration of the Infiltration Zones along the Floor of Alcove 8

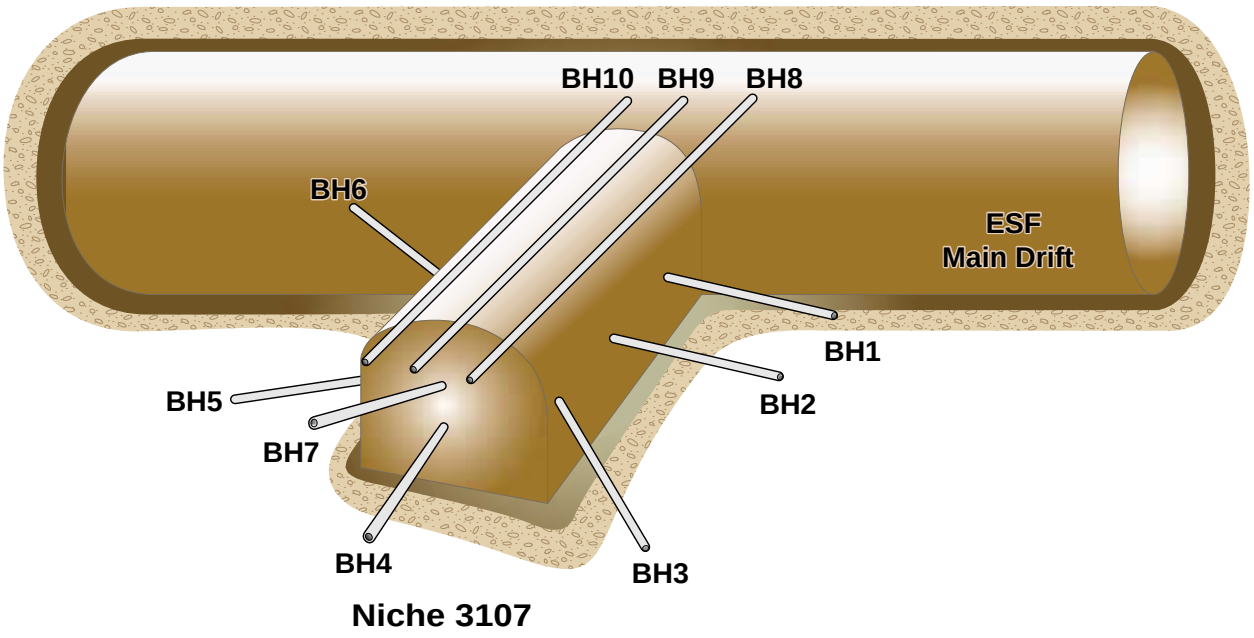

Figure 6.12.1-4. Schematic Illustration of the Monitoring Boreholes in Niche 3107

6.12.1.3 Instrumentation

There are three distinct components to the flow investigation: (1) controlled release of water into isolated zones along the fault in Alcove 8, (2) borehole monitoring for changes in saturation and water potential, and (3) collection of seepage from the ceiling of Niche 3107. The key features of techniques used in this field investigation are presented below.

6.12.1.3.1 Fluid Injection

Water was applied along the fault in Alcove 8 at three different times. Initially the application area was over a small section of the fault. This was increased to 1.0 m and then to 5.15 m. In the small injection zone water was first released with an infiltrometer, which is a cylinder 30 cm in diameter. During the second release, the infiltrometer cylinder was replaced with a box that measured 70 cm by 70 cm. For the third set of water releases (along 5.15 m), the fault was divided into four sections with each section serving as a separate release point. In each of these applications, water along the release zone was ponded to a head of ~0.02 m.

6.12.1.3.2 Borehole Monitoring

In nine monitoring boreholes (i.e., 1-7, 9, and 10 in Figure 6.12.1-4), changes in saturation are measured continuously with electrical resistivity probes (ERPs) during the entire field investigation located at 0.25 m intervals along the length of each borehole. Water-potential measurements were made with psychrometers along the single borehole (i.e., 8 in Figure 6.12.1-4)

The psychrometers and ERPs were housed in Borehole Sensor Trays (BSTs) installed along the length of each monitoring borehole. The BSTs were fabricated from 0.10 m OD PVC pipes, 3.0 m in section length. Each pipe section was cut lengthwise to produce a 0.075 m wide curved tray. The BST housing permitted immediate contact between ERPs and the borehole wall. The psychrometers were installed inside small cavities (0.005 m in diameter) perforated through the BST wall to measure water potentials of the rock.

6.12.1.3.3 Seepage Collection

An automated water-collection system was designed to capture seepage from the niche ceiling. With this system, water dripping from the niche ceiling is collected in plastic trays and diverted to PVC collection bottles. These bottles have been installed with pressure transducers to periodically measure the collected amount of seepage water.

6.12.2 Fault Liquid Test Observations

Water was applied in the small plot from August 9, 2000 to August 21, 2000 during which 18.8 liters of water were released. Liquid release into the small plot with the box permeameter began on August 22, 2000 and was stopped December 14, 2000. The box permeameter was removed in preparation for the whole fault trace to be trenched. The last data collected show that the infiltration rate was 1.8 cm/day and appeared to have stabilized. A total of 773 liters of water were applied in 120 days.

Liquid release to the extended fault section began along four sections on March 6, 2001 at 9:20 A.M. Each section has a permeameter for water application measurement; all four permeameters are supplied by a single water tank. (Note that Trench section #4 includes the area previously infiltrated during the Small Plot test.) As of May 31, 2001, 15,404 liters had been applied to the entire trench in 2102 hours of infiltration (87.5 days). Twice, the infiltration system in Alcove 8 failed, causing 233 liters to be applied in 90 minutes on March 7, 2001, and again on April 13, 2001, when about 755 liters were applied over 12 hours.

Water was first detected within the monitoring boreholes located immediately above the niche and then observed as seeps in Niche 3107. As cumulative seepage to the niche increased, measurements of seepage rates at localized zones suggest steady-state conditions.

6.12.2.1 Fault Intake Rates

The data from the four trences along the fault suggest that until ~April 20, 2001, the intake rates fluctuated significantly along the fault. When the rates reached quasi-steady state conditions, the intake rates ranged from ~25 liters/day to ~80 liters/day (Figure 6.12.2-1)

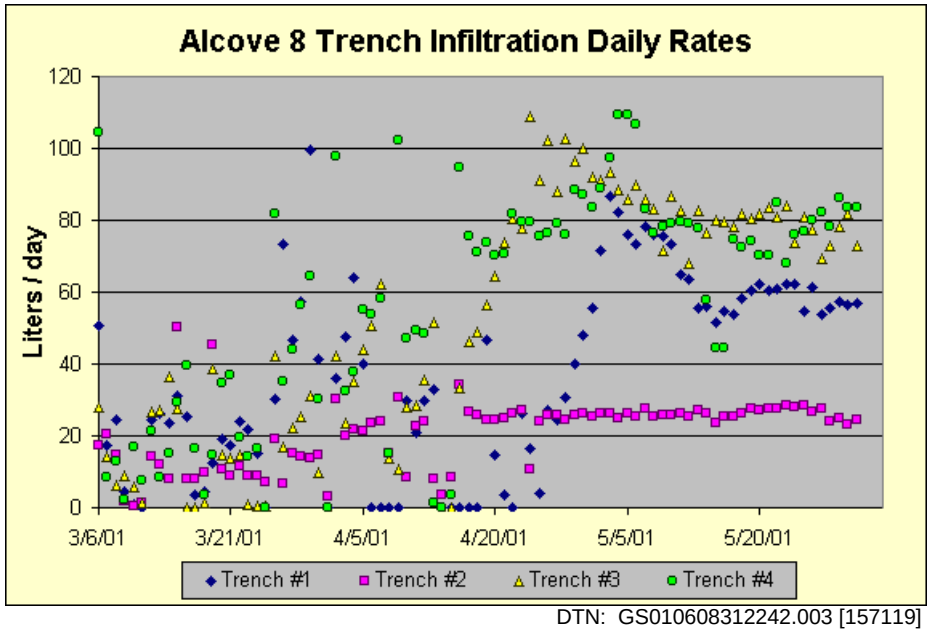

DTN: GS010608312242.003 [157119]

Figure 6.12.2-1. Infiltration Rates along Fault in Alcove 8

6.12.2.2 Wetting-Front Migration

The advancing edge of the wetting front was detected 1.9 m from the collar of borehole 10 on April 9, 2001, 34 days after the start of liquid releases along the fault in Alcove 8 (Figure 6.12.3-2). This plume was observed to extend between 1.65 and 2.40 m from the collar in borehole 10 over the next seven days.

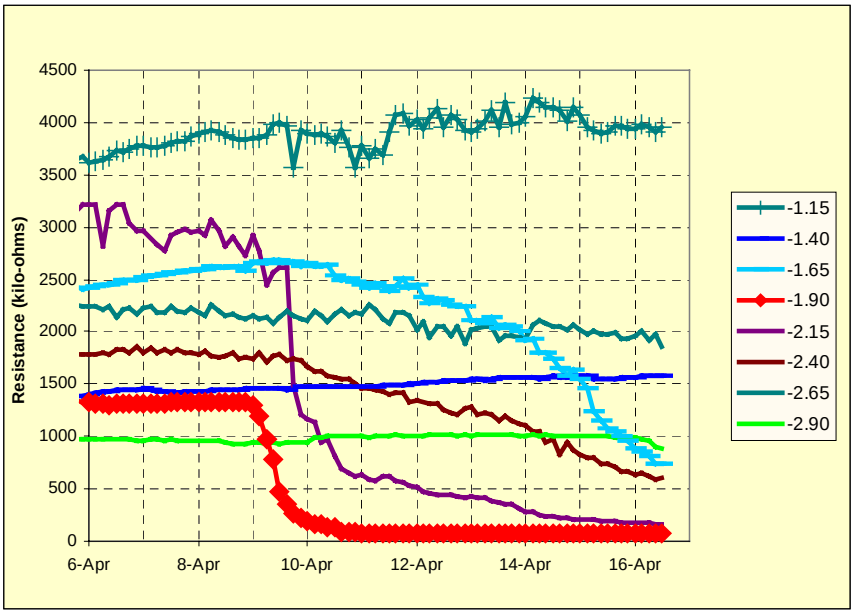

DTN: LB0110A8N3LIQR.001 [157001]

NOTE: Legend indicates the location of measurement (in meters) from borehole collar.

Figure 6.12.2-2. Wetting Front Arrival Detected in Borehole 10 in Niche 3107

6.12.2.3 Seepage in Niche 3107

Water was first observed along the fault at Niche 3107 on April 10, 2001. Over the next few weeks, the number of seeps along the fault exposed in Niche 3107 gradually increased. By June 18, 2001, approximately 1,100 liters of water had been collected from seeps into Niche 3107 (Figure 6.12.2-3). The seepage rate from a single seep location suggests that following the first measurable seepage, which occurred by the middle of April 2001, seepage rates climbed to near-steady values in the next four weeks (Figure 6.12.2-3).

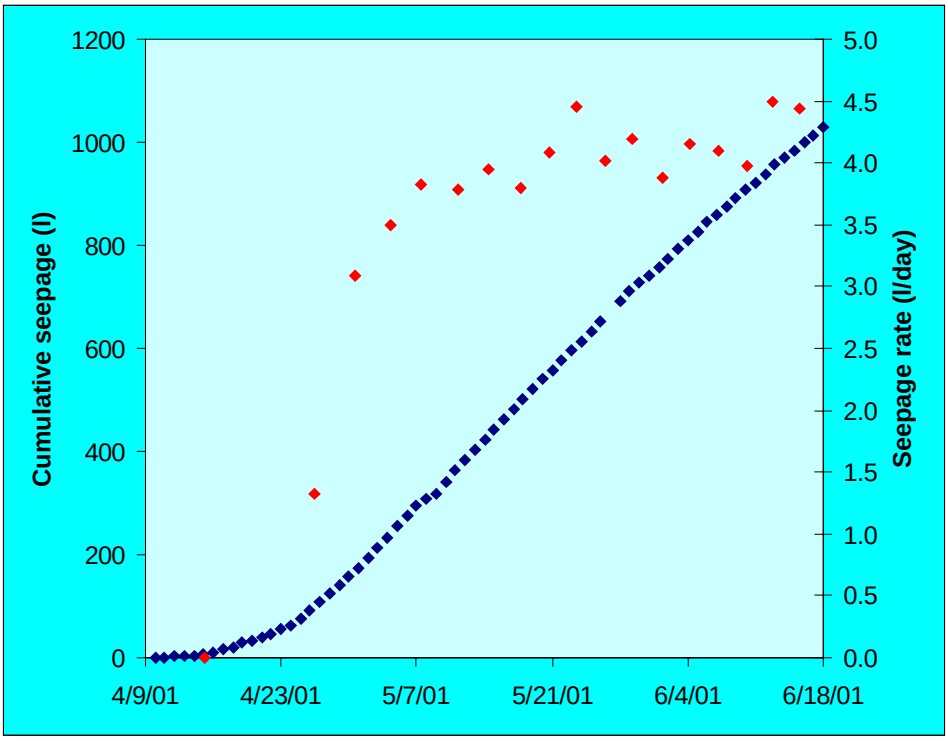

DTN: LB0110A8N3LIQR.001 [157001]

Figure 6.12.2-3. Cumulative Seepage (Blue) from All Collection Trays in Niche 3107 and the Seepage Rate Observed (Red) along a Section of Fault in Niche 3107 (as Measured in Tray U3-B4)

6.12.3 Geophysical Imaging of the Drift-to-Drift Test Block

Preliminary baseline images for the test block between Alcove 8 and Niche 3107 have been collected with two different techniques: seismic tomography and ground-penetrating radar (GPR) tomography. The objective of seismic tomography data acquisition was to acquire baseline data to help monitor the fluid infiltration tests. The GPR data are presented in details in this AMR and compared with documented seismic tomography data. The comparison helps to constrain the interpretation of the local lithology. Both geophysical tomography studies used the slant (near-vertical) boreholes drilled around the test block, as illustrated in Figure 6.12.1-2 and Figure 6.12.1-3, around a large plot prepared for planar infiltration tests.

6.12.3.1 Background and Ground-Penetrating-Radar Experimental Approach

In the borehole radar method, modified surface radar antennas are emplaced into a rock formation, and high-frequency electromagnetic signals are transmitted through the formation to a receiving antenna. Electrical properties of the subsurface material greatly influence the transmitted electromagnetic signal. In particular, the dielectric permittivity (K) of the rock has a strong influence on the propagation of the signal and on whether it travels at a high or low velocity. Furthermore, moisture content also affects dielectric permittivity. The high dielectric permittivity of water (K ~ 80) or wet rock (K ~20–30) in contrast to drier rock (K ~3-6) typically results in greatly reduced signal velocities. Changing chemical compositions (i.e., tracers) may

also alter the bulk dielectric permittivity of the rock and hence the propagation velocity of the radar wave. Any changes in signal character shall be measured over the course of the Alcove 8-Niche 3107 infiltration experiment, and any increase (or decrease) in the background moisture content or chemical composition resulting from the fluid infiltration (or rock dry-out) will result in changes in the received radar velocity.

The transmitted signals are represented as multiple ray paths crossing through a zone within the block. If sufficient ray paths are recorded, a tomographic image is obtained through computer processing. The information extracted from such data consists of the radar wave travel time, which depends on the wave velocity. This information, in the form of a processed radar velocity tomogram, offers a high-resolution approach to monitoring the changes occurring in the rock over the duration of the tracer-injection experiment. Previous experiments at Yucca Mountain indicate that the radar method should provide relatively high-resolution imaging of the zone of interest. The peculiar orientation of the boreholes between Alcove 8 and Niche 3107, however, may provide decreased image resolution relative to previous radar experiments (e.g., Busted Butte, Drift Scale Test, Single Heater Test).

A detailed description of the equipment used, the component specifications, the operating principles, and the GPR survey methodology can be found in the Technical Implementing Procedure, YMP-LBNL-TIP/GP 5.0, *Ground Penetrating Radar Data Acquisition*, governing all GPR data acquisition done in support of the Yucca Mountain site characterization effort.

6.12.3.2 Results of the Radar Data Acquisition

The radar data were acquired in all six of the boreholes located within Alcove 8. Additionally, two of the boreholes in Niche 3107 were used in combination with two of the holes in Alcove 8. The eight boreholes include the following: 1–6 (Alcove 8) and 1–2 (Niche 3107). The configuration of and layout of the boreholes used are illustrated in Figure 6.12.1-2.

The radar data were acquired in the two-dimensional planes defined by the two boreholes, more commonly referred to as well pairs. The well pairs acquired in Alcove 8 include the following: 1-2, 3-4, 1-3, 2-4, and 5-6. The well pairs acquired between Alcove 8 and Niche 3107 include the following: 1(Alcove 8)—3(Niche 3107) and 4(Alcove 8)—2(Niche 3107). The decision to acquire data between Alcove 8 and Niche 3107 stemmed from the fact that an image of the boundary between the two lithologic units in this region was desired. By working only in the boreholes located in Alcove 8, this boundary was not penetrated and hence was not able to be imaged by using these boreholes alone.

Thus far, the data have been processed for travel times, with the result being radar velocity tomograms. Differencing or subtraction of the velocity tomograms will be conducted over the course of infiltration tests. Such differencing or subtraction allows for the highlighting of the moisture front as it changes spatially and temporally. In essence, the background formation remains static in those areas not affected by the changing moisture front. By subtracting one velocity tomogram from another, we will be able to discount those areas remaining static while emphasizing those areas where change (i.e., flow or wetting) is occurring.

The well pairs between Alcove 8 and Niche 3107 differ slightly from the well pairs in Alcove 8 in their acquisition method. Because of the large distances between the well pairs (~20 meters), the 100 MHz antenna frequency used for the Alcove 8 well pairs was found to be too high (i.e., too prone to signal attenuation), and so the well pairs were collected using the 50 MHz antennas. Higher frequencies generally result in data of higher resolution (approximately 25.0 cm for 100 MHz), so the highest frequency antennas should be used if at all possible. Unfortunately, higher frequencies also result in greater attenuation of radar energy with increasing distance, so a balance must be struck between resolution and well-pair distance. The 50 MHz data collected between Alcove 8 and Niche 3107 resulted in very usable data, and for the purposes of this experiment, it is deemed perfectly acceptable.

6.12.3.2.1 Alcove 8 Well Pairs 1-2, 3-4, 1-3, 2-4, and 5-6

All of the radar data processed thus far between the boreholes in Alcove 8 show similar results and as such are considered together in this section (Figure 6.12.3-1a through Figure 6.12.3-1e). The radar velocity images all appear to suggest that the lithologic formation directly underlying Alcove 8 varies little in regards to its dielectric properties. This is as expected, because none of the boreholes penetrate the lithologic contact between Alcove 8 and Niche 3107 . As far as smaller structures are concerned (e.g., lithophysal cavities), they may be of too small a size or of insignificant-enough dielectric contrast to be imaged. Close inspection of the images, however, reveal some zones of anomalous velocity that may or may not correspond to such small structures. What the data do suggest is that any changes resulting from wetting or fluid flow upon commencement of the infiltration experiment are not expected to follow any particular path. In previous experiments using this method, potential flow paths had been defined by the baseline radar velocity images prior to infiltration, and velocity changes results from wetting were subsequently observed in these regions. Again, this is not observed for the baseline images acquired between the Alcove 8 boreholes.

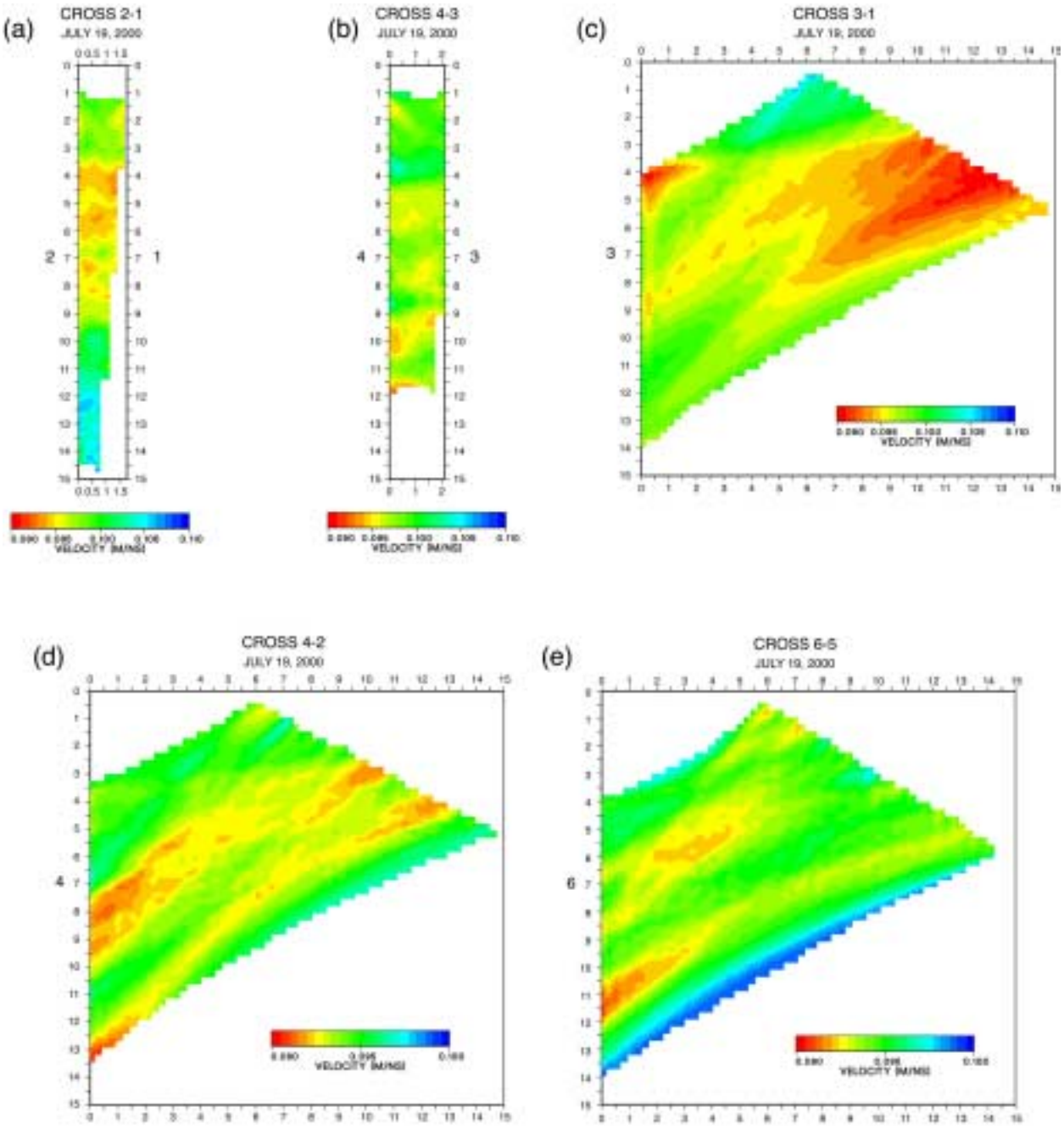

DTN: LB0110A8N3GPRB.001 [156912]

Figure 6.12.3-1. Radar Velocity Tomograms between Alcove 8 Well Pairs

6.12.3.3.2 Well Pairs 1(Alcove 8)—3(Niche 3107) and 4(Alcove 8)—2(Niche 3107)

After acquiring the radar data between the boreholes in Alcove 8, additional data were acquired in boreholes between Alcove 8 and Niche 3107. The drift-to-drift tests imaged the lithologic contact occurring between the two locations and allowed for monitoring of this contact during the infiltration. Figure 6.12.3-2a and Figure 6.12.3-2b are the baseline radar velocity data for the two well pairs. Immediately obvious is the higher velocity subhorizontal interface near the upper

portions of the Niche 3107 boreholes. This region is inferred to be the lithologic contact between the two locations. Comparing the two radar velocity images, this contact is quite similar, although it appears to be dipping at slightly different angles from one image to the other. The imaged contact will be a point of focus in infiltration tests.

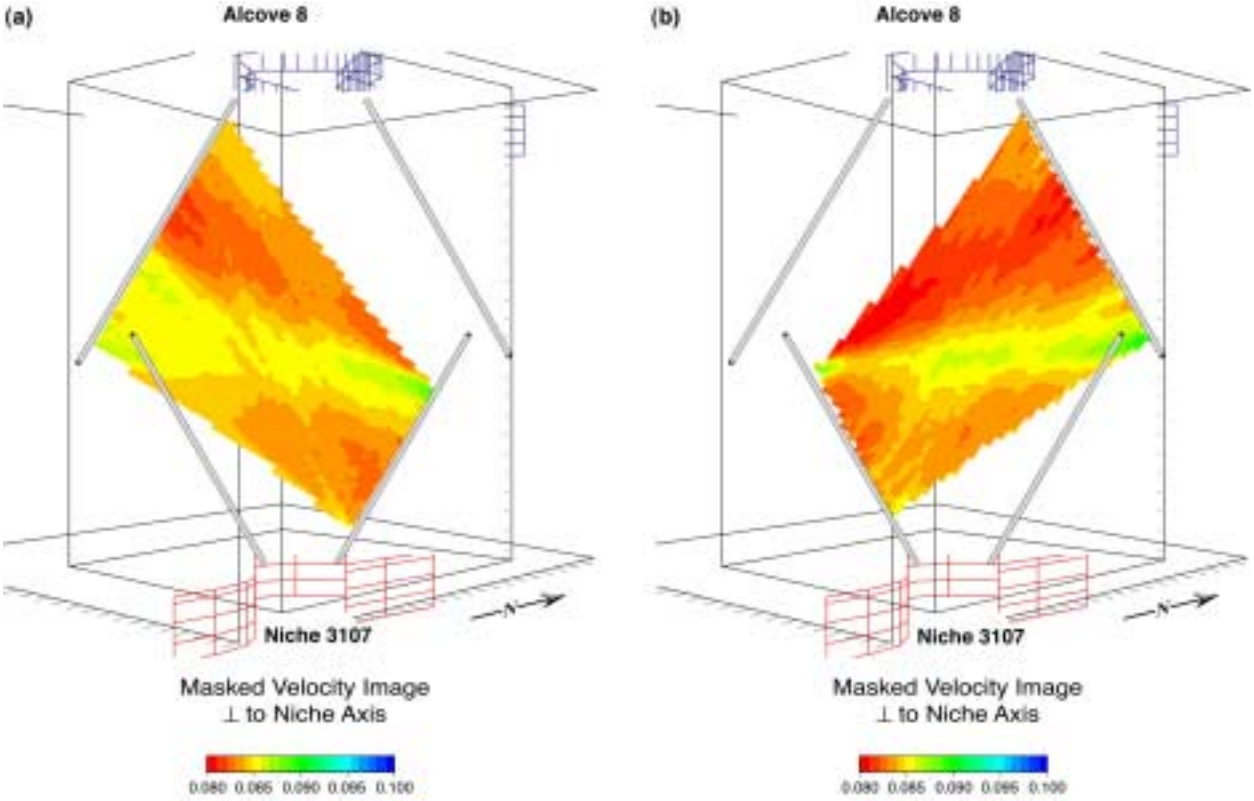

DTN: LB0110A8N3GPRB.001 [156912]

Figure 6.12.3-2. Radar Velocity Tomograms between Alcove 8 and Niche 3107 Well Pairs

6.12.3.3 Comparison with Seismic Tomography

Seismic tomography is another geophysical technique that is sensitive to structure heterogeneity. The seismic method relies on differences in the mechanical properties of the rock to produce a tomographic image. Results of the seismic tomographic images are presented by Descour et al. (2001 [156869]). Two representative images are illustrated in Figure 6.12.3-3. The seismic images also show a region approximating a lithologic contact between Alcove 8 and Niche 3107. The location of the contact closely mirrors that imaged by the radar method. Both geophysical tomographic techniques provide confirming evidence for the existence of the lithologic Tptpul-Tptpmn contact.

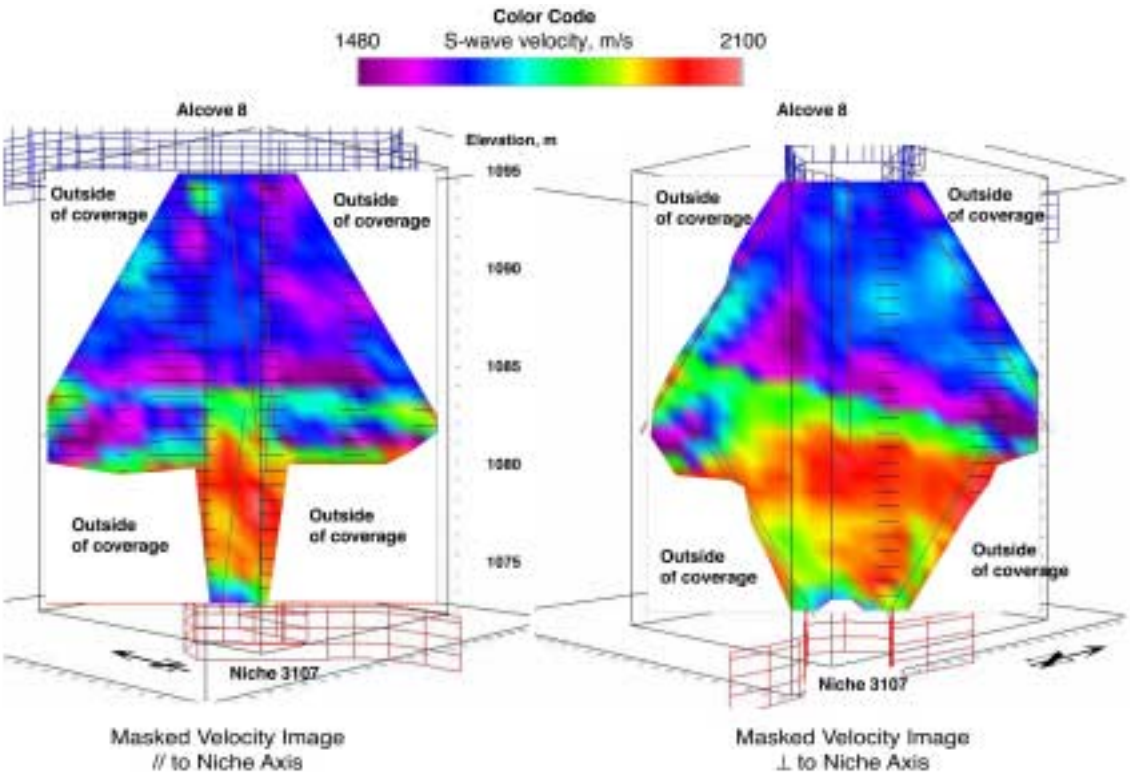

DTN: LB0110A8N3GPRB.001 [156912]

Figure 6.12.3-3. Seismic Tomograms between Alcove 8 and Niche 3107

6.13 BUSTED BUTTE UNSATURATED ZONE TRANSPORT TEST

This section presents the field data collected at the Unsaturated Zone Transport Test (UZTT) at Busted Butte in a distal extension of the Calico Hills formation below Yucca Mountain. The UZTT was described in the AMR *Unsaturated Zone and Saturated Zone Transport Properties (U0100)* (CRWMS M&O 2001 [154024]). Some of the early results are presented in this section for completeness. The overview in Section 6.13.1 in this AMR is equivalent to Section 6.8.1 and to test-related information in Section 6.8.2 of CRWMS M&O 2001 [154024]. The UZTT was conducted in two phases. The Phase 1 results in Section 6.13.2 in this AMR are equivalent to Section 6.8.5 of CRWMS M&O 2001 [154024]. Update of Phase 2 tracer test results is presented in Section 6.13.3 of this AMR. Early geophysical imaging results (CRWMS M&O 2001 [154024], Section 6.8.4) and update of the ground penetrating radar tomograph results of the Phase 2 test block are presented in Section 6.13.4 of this AMR. Because of the focus on the flow-and-transport-related results, the mineral evaluation of the Busted Butte samples and the geological implication on the applicability of Busted Butte results for Yucca Mountain study are presented in Attachment 6.13 (update of Section 6.8.3 of CRWMS M&O 2001 [154024]).

6.13.1 Overview of Unsaturated Zone Transport Test

6.13.1.1 Unsaturated Zone Transport Test Location

The Busted Butte test facility is located in Area 25 of the Nevada Test Site (NTS) approximately 160 km northwest of Las Vegas, Nevada, and 8 km southeast of the potential Yucca Mountain repository area. The site was chosen based on the presence of a readily accessible exposure of the Topopah Spring Tuff (Tpt) and the Calico Hills formation (Tac) and the similarity of these units to those beneath the potential repository horizon. The test facility consists of an underground excavation along a geologic contact between Tpt and Tac. The corresponding hydrogeologic contact between the Topopah Spring welded (TSw) unit and the Calico Hills nonwelded (CHn) unit, is comprised of the nonwelded portion of the basal vitrophyre of Tac (Tptpv1) and of Tpt (Tptpv2).

6.13.1.2 Unsaturated Zone Transport Test Objectives

The principal objectives of the test are to address uncertainties associated with flow and transport in the UZ site-process models for Yucca Mountain. These include but are not restricted to:

- The effect of heterogeneities on flow and transport in unsaturated and partially saturated conditions near the TSw-CHn contact; in particular, issues relevant to fracture-matrix interactions and permeability contrast boundaries
- The validation through field testing of laboratory sorption experiments in unsaturated Calico Hills rocks
- The effect of scaling from lab scale to field scale and site scale
- The inputs to the evaluation of the 3-D site-scale flow and transport process model used in the performance assessment (PA) abstractions for licensing application (LA)
- The migration behavior of colloids in fractured and unfractured Calico Hills rocks.

6.13.1.3 Unsaturated Zone Transport Test Concept

The Unsaturated Zone Transport Test (UZTT) is comprised of three integrated efforts: the field test, a parallel laboratory-scale testing program, and validation and assessment of models used for PA. The field test involves design of the test, analysis of the geology, identification of tracer breakthrough using chemical analyses, *in situ* imaging of liquid and tracer migration through geophysical techniques, and ultimately, destructive testing to quantify tracer migration. Only the field test results are described in this AMR. The laboratory and modeling efforts are summarized in the next two paragraphs and reported in CRWMS M&O (2001 [154024]).

In addition to field testing, parallel laboratory analytical and testing programs in geochemistry, tracer evaluation, hydrology, and mineralogy are designed to help interpret the field results. The geochemistry program includes measurement of *in situ* pore-water chemistry and development of a synthetic injection matrix. The tracer evaluation program includes batch-sorption studies on Busted Butte rock samples using nonreactive and reactive surrogate tracers and radionuclides.

The lab program also includes modeling of the geochemical behavior of those tracers in the ambient water chemistry, and tracer stability in the rock environments. The hydrology program involves the measurement of the matric potentials and conductivities as a function of saturation for core samples from Busted Butte with the porosity of each sample also characterized. Mineralogy/petrology (Min/Pet) activities involve the mineralogic characterization of the Busted Butte samples from cores.

The laboratory investigations undertaken are listed below for information purposes.

- Unsaturated hydraulic characterization of Busted Butte rocks (done by the USGS)
- Detailed mineralogic and oxide-coating characterization of Busted Butte rocks
- Batch measurements of radionuclide sorption to Busted Butte rocks
- Batch measurements of tracer sorption to Busted Butte rocks
- Short-term and long-term stability measurements of tracer solutions
- Short-term and long-term stability measurements of tracer-affected collection pads
- Short-term and long-term stability measurements of tracer-affected rock samples.

The geologic, mineralogic, and hydrologic properties form the basis for assessing the applicability of Busted Butte UZTT for the Calico Hills formation below the potential nuclear waste repository at Yucca Mountain, as depicted in detail in Attachment VIII.

The flow and transport modeling study is the third aspect of UZTT. The principal objective of the test is to evaluate the validity of the flow and transport site-scale process models used in PA abstractions. This effort makes it possible to improve or enhance the site-scale flow and transport model by simulating and predicting experimental field results and by addressing the effects of scaling from laboratory to field scales.

6.13.1.4 Test Design

The UZTT is comprised of the main adit, which is 75 m in length, and a test alcove, which is 19 m in length. The configuration of the UZTT site is shown in Figure 6.13.1-1. Details of the design and construction criteria can be found elsewhere (SubTerra 1998 [147703], pp. 9–21, 33–44).

The UZTT was designed as two test phases. The first phase, including test Phases 1A and 1B, was designed as a scoping study to assist in design and analysis of Phase 2, and as a short-term experiment aimed at providing initial transport data on fracture near an interface. The second phase incorporated a larger region than Phase 1, with a broader, more complex scope of tracer injection, monitoring, and collection.

Test Phase 1—Test Phase 1 was comprised of two small scale scoping tests, Phase 1A and Phase 1B. Phase 1A was in Tac and Tptpv1, and Phase 1B in Tptpv2. Phase 1A was a "blind" single-point injection test using four boreholes, at either 1mL/hr or 10 mL/hr rates. Following the injection period, a “mini-mineback” was done to expose the distribution of the tracer in the rock mass.

Phase 1B involved two pairs of injection and collection boreholes in Tptpv2. Phase 1B also used two injection rates (1 mL/hr and 10 mL/hr). Because of the paucity of data on fracture-matrix interactions in these lithologies, this test was designed as a "calibration" test for fracture-matrix interactions to be used in Phase 2 simulations. The 2 m long Phase 1B collection boreholes, immediately below the injection boreholes, were used to capture arrival of tracers. At the culmination of injection, overcoring was done to collect rock samples for tracer analysis.

Test Phase 2—The Phase 2 involved a large (7 m x 10 m x 10 m) block comprising all of the lithologies of Phase 1. Unlike the single-point injection geometries in Phase 1, the injection systems in Phase 2 were designed to activate large surfaces of the block. Phase 2 included 8 injection boreholes drilled from the test alcove, and distributed in two horizontal, parallel planes. Injection boreholes were placed to test the properties of the lower Topopah Spring Tuff (Tptpv2) and the hydrologic Calico Hills (Tptpv1 and Tac). In addition, there were 12 collection boreholes, drilled from the main adit. Collection holes were perpendicular in plan view to the injection holes and distributed at various distances from the injectors.

6.13.1.5 Site Characterization

The site characterization of the potential test block included core sampling from boreholes and grab samples from outcrops. Core samples were collected from the dry drilling of the boreholes from the main adit and the test adit for geologic, hydrologic, and geochemical laboratory investigations and scoping calculations. The boreholes were then surveyed and instrumented for the injection tests.

Design, construction, and scientific teams were all involved in ensuring that the test block itself remained undisturbed by construction activities. Minimal disturbance of the *in situ* test block in the initial stages of UZTT was the foremost objective. Sodium silicate was applied to the wall of the test block to minimize evaporation.

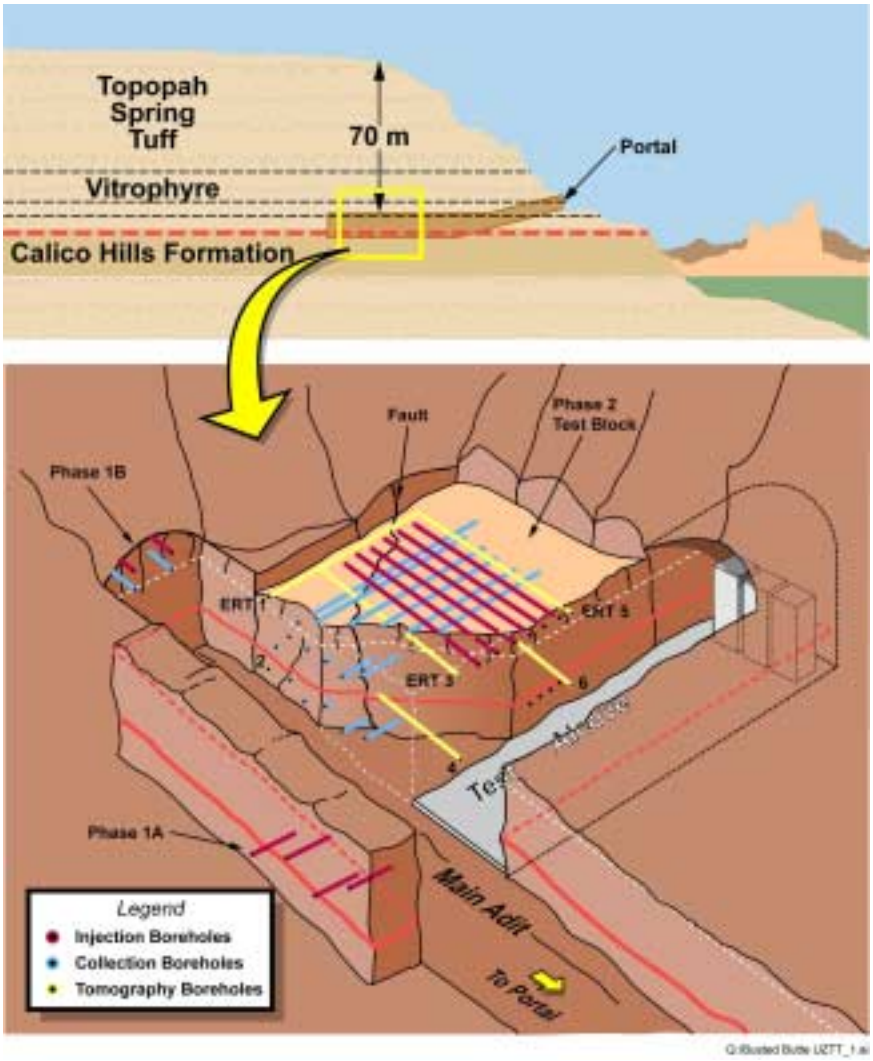

SOURCE: Derived from CRWMS M&O 2001 [154024], Figure 34 (For illustration purposes only).

NOTE: This schematic of the Busted Butte UZTT shows the relative locations of the different experiment phases and borehole locations.

Figure 6.13.1-1. Busted Butte Unsaturated Zone Transport Test

6.13.1.6 Borehole Injection and Sampling Systems

Injection and sampling of the liquid tracers was accomplished by two pneumatically inflated borehole sealing and measurement systems (Figure 6.13.1-2). To allow visual inspection of the injection points under both standard and ultraviolet (UV) illumination, a transparent packer system was developed for the tracer-injection systems. Moisture sensing and sampling were accomplished using pneumatically emplaced inverting membranes, which were fabricated with mesh pockets to retain absorbent sample pads. The inverting membranes are removed from the boreholes regularly (at interval ranging from daily to biweekly) for sample-pad removal and replacement, whereas the injection packers remain in the holes for the duration of the test program. Each system was maintained at slight overpressure (1.7 to 3.5 kPa) to maintain contact

between the sampling/injection pads and the tuff and to prevent circulation of air within the borehole.

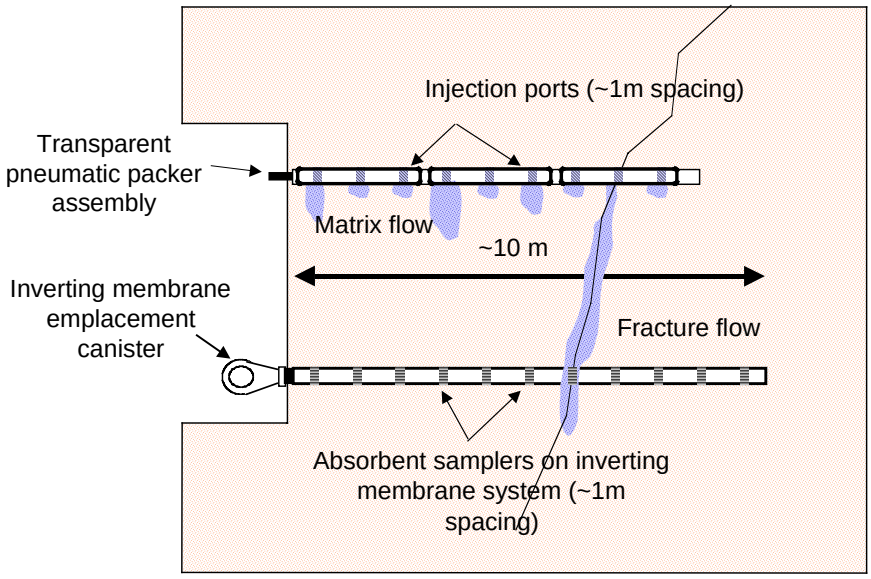

NOTE: Injection and collection boreholes are actually perpendicular in plan view.
SOURCE: CRWMS M&O 2001 [154024], Figure 35 (For illustration purposes only).

Figure 6.13.1-2. Vertical Cross-Section of Injection and Collection System Configuration

6.13.1.7 Electrical-Resistance Moisture Sensors

Simple electrical-resistance moisture sensors were installed to monitor the relative moisture state of the injection pads and the arrival of liquid tracer at the sampling-pad data collection. Two Campbell Scientific dataloggers were used to collect measurement data from sensors and instrumentation.

Phase 1—For the Phase 1A test, the dataloggers measured the pressure in the injection/sampling manifold, 12 to 14 moisture sensors, the datalogger panel temperature and battery voltage, the number of times the syringe pumps cycled in a given period of time, and the relative humidity, air temperature, and atmospheric pressure in the experimental area. For the Phase 1B test, the same data was collected, except a total of 32 moisture sensors were logged, as well as an anemometer in the ventilation shaft.

Phase 2—For the Phase-2 experiment, over 200 different sensors were measured. The data that are (or can be) collected include:

- Environmental information, such as ambient pressure, temperature, and relative humidity and wind speed in the ventilation system

- Experimental control information, such as injection pressure, the number of times pumps are activated, and relative saturation at injection points, at the face of boreholes or along sampling membranes.

6.13.1.8 Nonreactive and Reactive Tracers and Microspheres

Measurements on a small scale can be conducted in the laboratory, but validating the extrapolation of these data in the presence of larger-scale heterogeneities requires field-tracer tests. The behavior of actual radionuclides of concern has been extensively studied in the laboratory, but regulatory and environmental concerns prevent the use of these materials in the field. For the Busted Butte field tests, nonreactive and reactive tracers are used as surrogates for radionuclides. The tracers were chosen so that nonreactive, reactive, and colloidal behaviors could be monitored in a single continuous injection scenario. They were mixed together to normalize the hydrologic conditions of the injection. The tracer matrix was synthetic pore water, which is based on the measured composition of Busted Butte pore waters.

6.13.1.9 Phase 1 Tracers

Phase 1 tracers were chosen based on the list of tracers permitted for use in the C-wells tests. Surrogate nonreactive and reactive tracers and colloids are mixed together so as to normalize the hydrologic conditions they experience and provide for higher accuracy of the results. The tracers used in the Busted Butte experiments of Phase 1 include the following:

- Lithium bromide
- Fluorescent polystyrene latex microspheres
- Sodium fluorescein
- "Pyridone" (3-carbomoyl-2(1H)-pyridone)
- 2,6-difluorobenzoic acid (2,6-DFBA)
- Pentafluorobenzoic acid (PFBA).

The reactive sorbing tracer used is lithium, and the colloid analogs are fluorescent polystyrene latex microspheres of two sizes: 0.3 and 1 μm diameter. The 2,6-DFBA and PFBA are nonreactive tracers used to tag the various injection boreholes according to injection rates (i.e., 1 and 10 mL/hr rates). Sodium fluorescein and pyridone are UV fluorescent and are used as nonreactive tracer markers that can be detected in the field at a concentration level of approximately 10 ppm using UV illumination. Borehole numbers are shown in Figure 6.13.1-3 for Phase 1A and Figure 6.13.1-4 for Phase 1B and Phase 2.

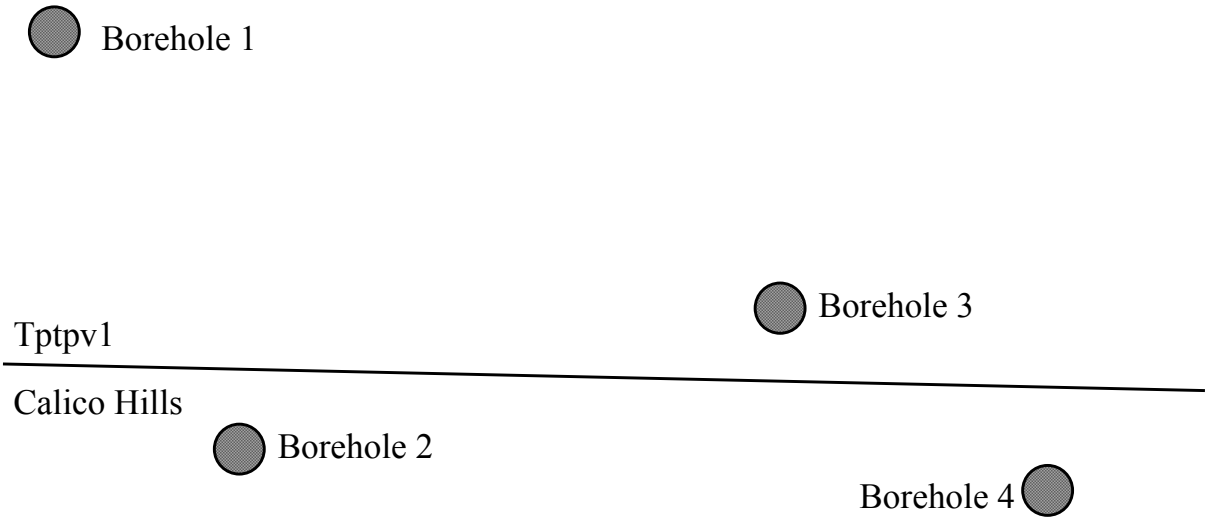

SOURCE: CRWMS M&O 2001 [154024], Figure 37 (for illustration purposes only).

Figure 6.13.1-3. Schematic of Phase-1A Borehole Numbers and Relative Locations

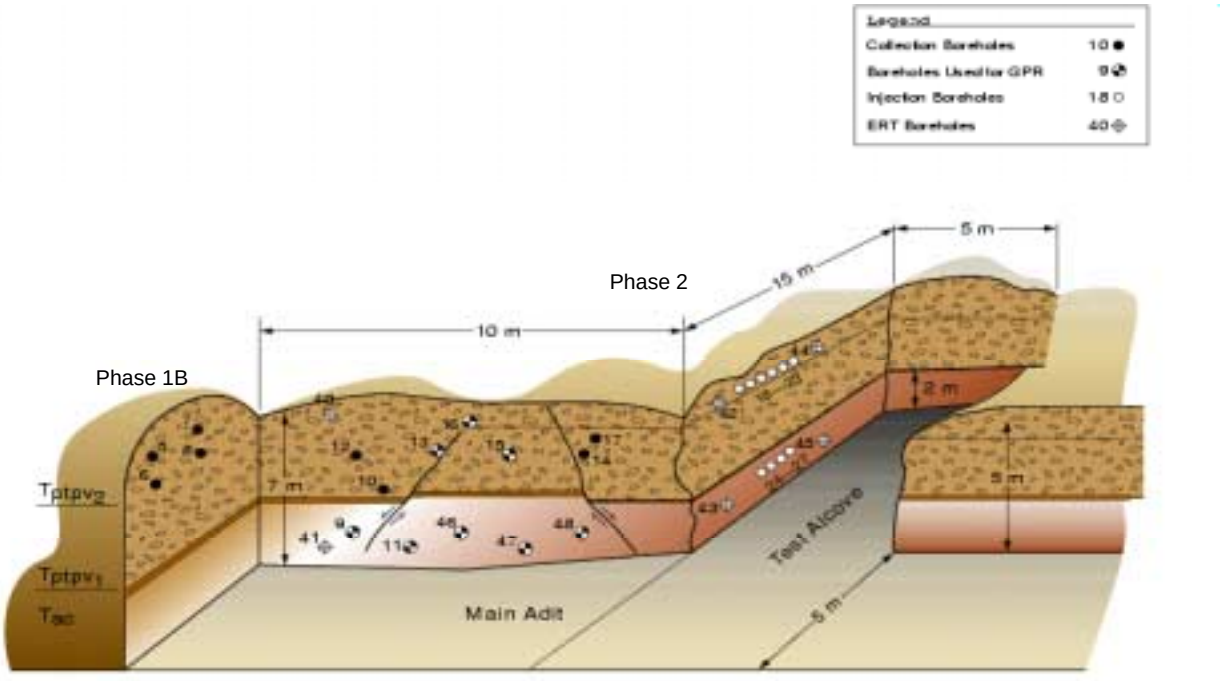

SOURCE: CRWMS M&O 2001 [154024], Figure 38 (for illustration purposes only).

Figure 6.13.1-4. Phase-1B and Phase-2 Borehole Numbers and Relative Locations

Table 6.13.1-1 summarizes the initial concentrations of Phase 1B injection with the lithium and bromide elemental concentrations derived from the 500 mg/kg lithium bromide value, based on

the elemental atomic weights of lithium and bromide. Table 6.13.1-2 summarizes the concentrations used for Phase 1B injections.

Table 6.13.1-1. Tracer C_0 Values for Phase 1B Injection

Tracer	C_0 (mg/kg)
Lithium	40
Bromide	460
2,6-DFBA (Borehole 5 only)	100
Pyridone	100
Sodium fluorescein	500

SOURCE: (CRWMS M&O 2001 [154024], Table 30)

Table 6.13.1-2. Summary of Concentrations Used for Phase 1 Injections

Phase 1A—10 mL/hr Injection Rate; Boreholes 1 and 3:
500 mg kg^{-1} lithium bromide
500 mg kg^{-1} sodium fluorescein
100 mg kg^{-1} 2,6-DFBA
1 mL kg^{-1} fluorescent polystyrene microspheres
Phase 1A—1 mL/hr Injection Rate; Boreholes 2 and 4:
500 mg kg^{-1} lithium bromide
500 mg kg^{-1} sodium fluorescein
100 mg kg^{-1} PFBA
1 mL kg^{-1} fluorescent polystyrene microspheres
Phase 1B—10 mL/hr Injection Rate; Borehole 5:
500 mg kg^{-1} lithium bromide
500 mg kg^{-1} sodium fluorescein
100 mg kg^{-1} 2,6-DFBA
100 mg kg^{-1} pyridone
1 mL kg^{-1} fluorescent polystyrene microspheres
Phase 1B—1 mL/hr Injection Rate; Borehole 7:
500 mg kg^{-1} lithium bromide
500 mg kg^{-1} sodium fluorescein
100 mg kg^{-1} PFBA
100 mg kg^{-1} pyridone
1 mL kg^{-1} fluorescent polystyrene microspheres

SOURCE: CRWMS M&O 2001 [154024], Section 6.8.2.4

6.13.1.10 Phase 2 Tracers

Phase 2 tracers include those used in Phase 1 but with three additional Fluorinated Benzoic Acids (FBAs) (2,4-DFBA, 2,4,5-triFBA, 2,3,4,5-tetraFBA), iodide, a fluorescent reactive tracer (Rhodamine WT), and additional reactive ions that serve as analogs for neptunium, plutonium, and americium. (See Figure 6.13.1-4 for Phase-2 borehole locations.)

- Neptunium Analogs (NpO_2^+, Np(V)):

  Nickel (Ni^{2+})
  Cobalt (Co^{2+})
  Manganese (Mn^{2+})

- Plutonium Analog (Pu3+):

  Samarium (Sm^{3+})

- Plutonium Analogs (colloidal form):

  Polystyrene microspheres

- Americium Analog (Am^{3+}):

  Cerium (Ce^{3+}).

The Phase 2 tracer recipes are presented in the following Table 6.13.1-3, Table 6.13.1-4, and Table 6.13.1-5.

Table 6.13.1-3. Summary of Concentrations Used for Phase 2A Injections

Phase 2A–1 mL/hr Injection Rate; Borehole 23:
1000 mg/kg lithium bromide
10 mg/kg sodium fluorescein
100 mg/kg 2,4,5-TriFBA
10 mg/kg pyridone
1 mL/kg microspheres
Starting October 7, 1998:
10 mg/L rhodamine WT
10 mg/kg $NiCl_2 \cdot 6H_2O$ (2.47 mg/kg of Ni^{2+})
10 mg/kg $MnCl_2 \cdot 4H_2O$ (2.78 mg/kg of Mn^{2+})
10 mg/kg $CoCl_2 \cdot 6H_2O$ (2.48 mg/kg of Co^{2+})
5 mg/kg $SmCl_3 \cdot 6H_2O$ (2.06 mg/kg of Sm^{3+})
5 mg/kg $CeCl_3 \cdot 7H_2O$ (1.88 mg/kg of Ce^{3+})

SOURCE: CRWMS M&O 2001 [154024], Section 6.8.2.4

On September 30, 1999, the Phase-2A recipe was changed with the elimination of the microspheres and the addition of 500 mg kg^{-1} potassium iodide.

Table 6.13.1-4. Summary of Concentrations Used for Phase 2B Injections

Phase 2B–10 mL/hr Injection Rate; Boreholes 24, 25, 26, 27
1000 mg/kg lithium bromide
10 mg/kg sodium fluorescein
100 mg/kg 2,6-DFBA (Borehole 26, Borehole 27)
100 mg/kg 2,3,4,5-TetraFBA (Borehole 24, Borehole 25)
10 mg/kg pyridone
10 mg/kg rhodamine WT
1 mL/kg microspheres
Starting September 2, 1998:
10 mg/kg $NiCl_2 \cdot 6H_2O$ (2.47 mg/kg of Ni^{2+})
10 mg/kg $MnCl_2 \cdot 4H_2O$ (2.78 mg/kg of Mn^{2+})
10 mg/kg $CoCl_2 \cdot 6H_2O$ (2.48 mg/kg of Co^{2+})
5 mg/kg $SmCl_3 \cdot 6H_2O$ (2.06 mg/kg of Sm^{3+})
5 mg/kg $CeCl_3 \cdot 7H_2O$ (1.88 mg/kg of Ce^{3+})

SOURCE: CRWMS M&O 2001 [154024], Section 6.8.2.4

On August 18, 1999, the Phase-2B recipe was changed with the elimination of the microspheres and the addition of 500 mg/kg potassium iodide.

Table 6.13.1-5. Summary of Concentrations Used for Phase 2C Injections

Phase 2C–50 mL/hr Injection Rate; Boreholes 18, 20, 21:
1000 mg/kg lithium bromide
10 mg/kg sodium fluorescein
100 mg/kg 2,6-DFBA (Borehole 18)
100 mg/kg PFBA (Borehole 20)
100 mg/kg 2,4-DFBA (Borehole 21)
10 mg/kg pyridone
10 mg/kg rhodamine WT
1 mL/kg microspheres
Starting September 2, 1998:
10 mg/kg $NiCl_2 \cdot 6H_2O$ (2.47 mg/kg of Ni^{2+})
10 mg/kg $MnCl_2 \cdot 4H_2O$ (2.78 mg/kg of Mn^{2+})
10 mg/kg $CoCl_2 \cdot 6H_2O$ (2.48 mg/kg of Co^{2+})
5 mg/kg $SmCl_3 \cdot 6H_2O$ (2.06 mg/kg of Sm^{3+})
5 mg/kg $CeCl_3 \cdot 7H_2O$ (1.88 mg/kg of Ce^{3+})

SOURCE: CRWMS M&O 2001 [154024], Section 6.8.2.4

On August 18, 1999, the Phase-2C recipe was changed with the elimination of the microspheres and the addition of 500 mg/kg potassium iodide.

6.13.1.11 Synthetic Pore-Water Recipe

Composition of the UZTT pore water is found in DTNs: LA9909WS831372.015 [140089], LA9909WS831372.016[140093], LA9909WS831372.017[140097], and LA9909WS831372.018 [140101] and composition of the synthetic pore water used in the UZTT is found in Table 29 in Section 6.8.5.2 of CRWMS M&O 2001 [154024].

6.13.2 Field-Scale Tracer Transport—Phase 1

6.13.2.1 Test Phase 1A

Phase 1A was located in the nonwelded Calico Hills (CHn) hydrogeologic unit spanning both the geologic Calico Hills formation (Tac) and the nonwelded subzone of the lowermost Topopah Spring Tuff (Tptpv1). It was a noninstrumented or "blind" test consisting of four single-point injection boreholes. All Phase 1 boreholes were 2 m in length and 10 cm in diameter. The injection point was located 90 cm in from the borehole collar. Continuous injection started on April 2, 1998 and ended on January 12, 1999. Injection rates were 1 mL/hr (Boreholes 2 and 4) and 10 mL/hr (Boreholes 1 and 3). A mixture of nonreactive tracers (bromide, fluorescein, pyridone, and fluorinated benzoic acids (FBAs)), a reactive tracer (lithium), and fluorescent polystyrene microspheres were used to track nonreactive transport, reactive transport, and colloid migration, respectively.

The field test was completed through excavation by "mineback" and auger sampling. Mineback of the Phase 1A test block began on January 15, 1999 and ended on March 3, 1999. During mineback, as successive layers of the adit wall were removed, digital photographs under visible and UV illumination were taken, and the exposed face was surveyed. In addition, rock samples were collected by augering for laboratory analysis of tracer and moisture content.

Results

Observations from the Phase 1A test demonstrate strong capillary-dominated flow for both the 1 and 10 mL/hr injection rates. The plumes are relatively uniformly distributed around the injection sites. Lithologic contacts were shown to influence the flow. Fractures have a relatively minor effect on the flow in Tac and Tptpv1 units. The fracture is acting as a permeability barrier rather than as a fast path.

A small number of augered rock samples have been analyzed for bromide and moisture content (DTN: LA9910WS831372.008 [147156]). Table 6.13.2-1 reports measured data from these samples. Samples 1–4 are taken at increasing distance below borehole 3. Samples 1 and 2 are above the ash layer, while Samples 3 and 4 are located vertically beneath the injector. Samples 5 to 12 are taken at increasing lateral distance from the injection point.

Table 6.13.2-1. Phase 1A Samples Taken from the 90-cm Mineback Face at Borehole 3

Sample Name	Gravimetric Moisture Content (g/g)	Bromide C/Co
BBR-990204-3-1-B	0.078	0.74
BBR-990204-3-2-B	0.112	0.49
BBR-990204-3-3-B	0.115	0.00
BBR-990204-3-4-B	0.122	0.00
BBR-990205-3-5-HS	0.064	2.77
BBR-990204-3-6-B	0.081	0.87
BBR-990204-3-7-B	0.077	0.75
BBR-990204-3-8-B	0.074	0.75
BBR-990204-3-9-B	0.077	0.81
BBR-990204-3-10-B	0.078	0.79
BBR-990204-3-11-B	0.074	0.32
BBR-990204-3-12-B	0.077	0.01

DTN: LA9910WS831372.008 [147156]

NOTE: Samples were analyzed for moisture content and bromide concentration. Sample BBR-990205-3-5-HS was a hand sample and is suspected to have been concentrated by evaporation.

6.13.2.2 Test Phase 1B

Phase 1B involved both injection of a tracer mixture and collection of pore-water/tracer samples in the lower section of the Topopah Spring Tuff (Tptpv2). Because of the paucity of data on fracture-matrix interactions in these lithologies, this test was designed to provide data on fracture-matrix interactions in the TSw. The results are being used to calibrate fracture properties for Phase 2 analysis.

Phase 1B consisted of two 2 m injection boreholes (5 and 7) and two 2 m collection boreholes (6 and 8). The tracer mixture was injected at 10 mL/hr in borehole 5 and at 1 mL/hr in borehole 7. Phase 1B injection began on May 12, 1998. Borehole 7 injection was terminated on November 9, 1998, and borehole 5 injection was terminated on November 18, 1998. Throughout the experiment, rock pore-water samples were collected at regular intervals using collection pads installed in boreholes 6 and 8.

At the conclusion of the experiment, overcoring of the Phase-1B boreholes was conducted. Moisture pad collection was conducted on collection borehole 8 directly below injection hole 7 until injection shut down of borehole 7 on November 9, 1998. Tracer injection and moisture pad collection was continued in boreholes 5 and 6 while two 10-inch-diameter overcores were drilled approximately tangential to one another, with their centerlines in a vertical plane and contained in the area between the top of injection borehole 7 and the bottom of collection borehole 8. When injection hole 5 was shut down, three 10-inch-diameter overcores were drilled approximately tangential to one another with their centerlines in a vertical plane and contained in the area

between the top of injection borehole 5 and 10 inches below the bottom of collection borehole 6. As soon as each of the injection holes was turned off, the injection and collection holes were surveyed, as well as video and neutron logged.

Results

There were 176 selected pads extracted for tracers, and the extracts were analyzed by ion chromatograph (IC), inductively coupled plasma/mass spectroscopy (ICP/MS), high pressure liquid chromatograph (HPLC), spectrofluorimetry, and epifluorescent microscopy. The extraction/analysis procedure is shown schematically in Figure 6.13.2-1. Altogether, 883 individual analyses were conducted, and full results were submitted (DTNs: LA9909WS831372.001 [122739] and LA9909WS831372.002 [122741]). Breakthrough of all 5 solute tracers was detected in borehole 6, directly below the 10 mL/hr injection site in borehole 5. No breakthrough was detected in borehole 8 below the 1 mL/hr injection site in borehole 7. No clear evidence of microsphere breakthrough was detected in either borehole, but this may be result from analytical difficulties, discussed below. The borehole 6 breakthrough results are summarized in Figure 6.13.2-2 (a through e), which shows tracer concentration in pad (C) normalized by the input tracer concentration (C_0) listed in Table 6.13.1-1 (see Section 6.13.1.9).

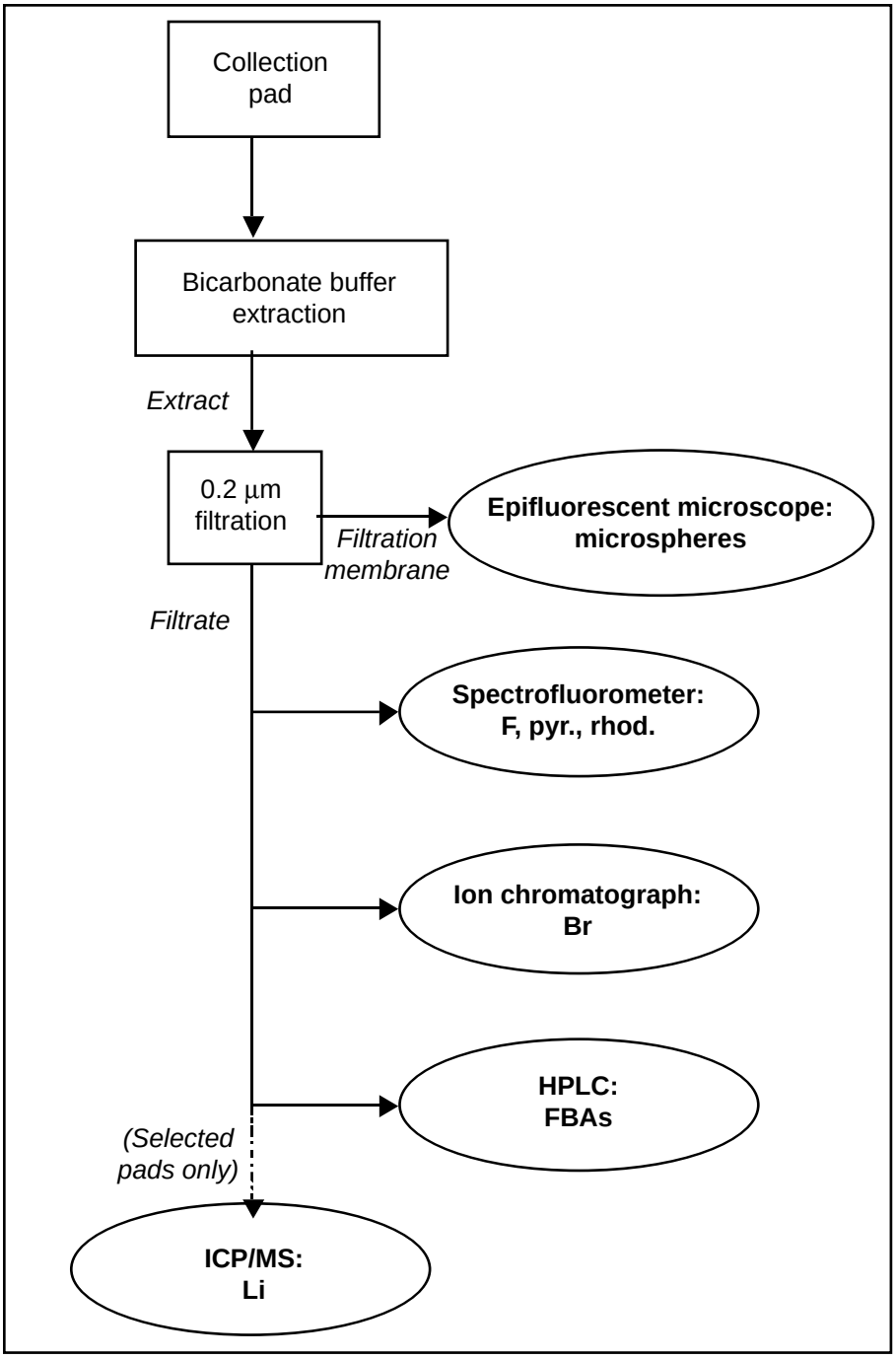

SOURCE: CRWMS M&O 2001 [154024], Figure 57 (For illustration purposes only).

Figure 6.13.2-1. Phase-1B Pad Extraction/Analysis Scheme

All five tracers shown in Figure 6.13.2-2 give clear evidence of breakthrough by the end of the experiment. All of the figures show peak concentrations at a (horizontal) depth of approximately 130 cm, directly below the injection port in borehole 5; but maximum recovery varies greatly. Bromide and 2,6-DFBA, both nonreactive anionic tracers, show similar and reasonable breakthrough patterns, with initial breakthrough detected in mid-late June 1998, after approximately 1 month of injection. Both bromide and 2,6-DFBA reached 50% injection concentrations in mid-July, after 2 months of injection. The fluorescein breakthrough pattern is more erratic. In particular, the peak concentration measured is over twice the injected concentration, which is clearly not reasonable. These anomalies probably reflect analytical difficulties associated with the extremely high concentration of fluorescein injected. The high concentration succeeded in improving field visualization of the plumes during mineback and overcore, even though it hurt the laboratory quantification. This analytical problem will be less severe for Phase 2, in which injected fluorescein concentrations are just 1/50 of that used in Phase 1. The later breakthrough and lower detected concentrations of pyridone may also reflect analytical difficulties; if real, they may indicate either sorption or degradation of this supposedly nonreactive tracer. Finally, although detected lithium concentrations are quite low, their contrast with background levels and their consistent location both in time and space indicate that true lithium breakthrough was observed in the field. The low and late breakthrough indicate that lithium was sorbed quite significantly.

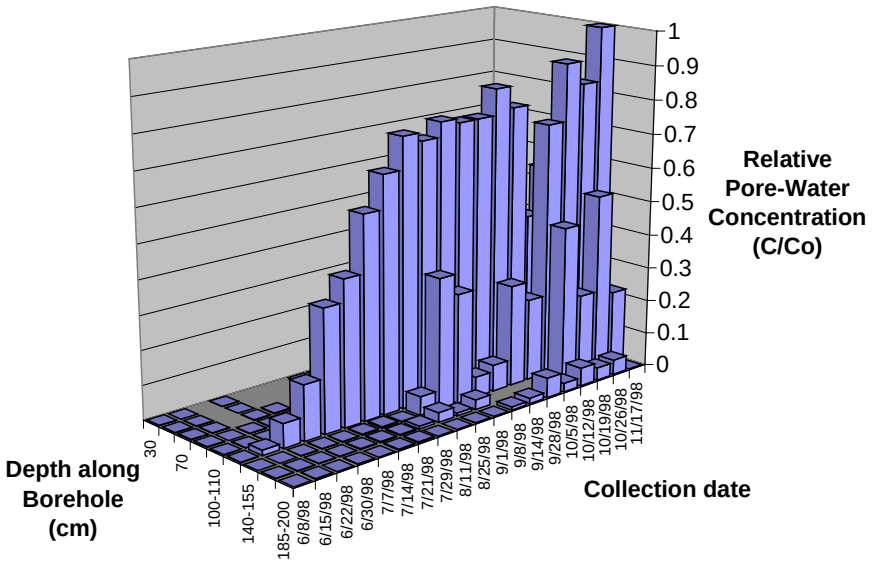

SOURCE: CRWMS M&O 2001 [154024], Figure 58a.

Figure 6.13.2-2a. Bromide Concentrations in Borehole 6 for Phase 1B

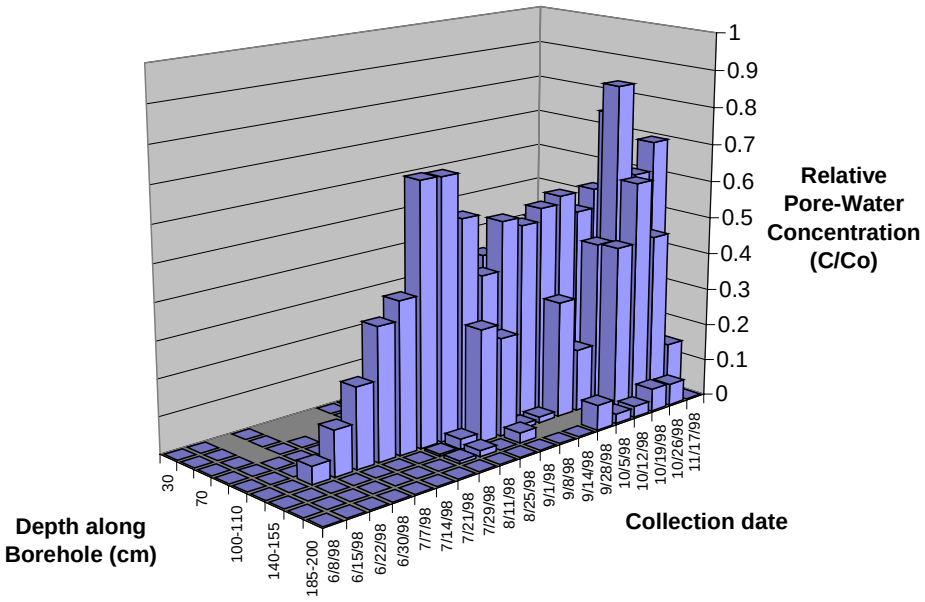

DTN: LA9909WS831372.001 [122739]; LA9909WS831372.002 [122741]

SOURCE: CRWMS M&O 2001 [154024], Figure 58

Figure 6.13.2-2b. 2,6-DFBA Concentrations in Borehole 6 for Phase 1B

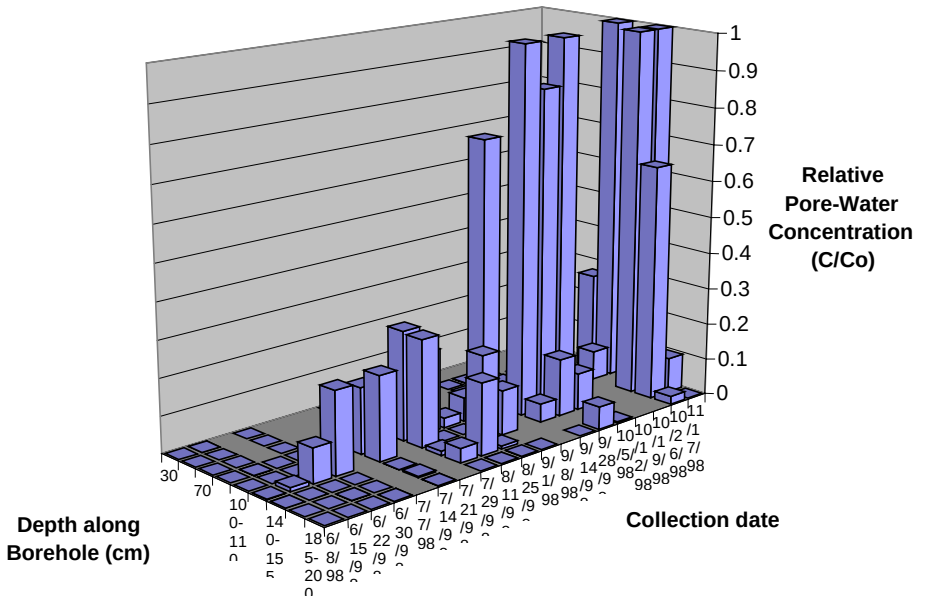

DTN: LA9909WS831372.001 [122739]; LA9909WS831372.002 [122741]

SOURCE: CRWMS M&O 2001 [154024], Figure 58c

Figure 6.13.2-2c. Fluorescein Concentrations in Borehole 6 for Phase 1B

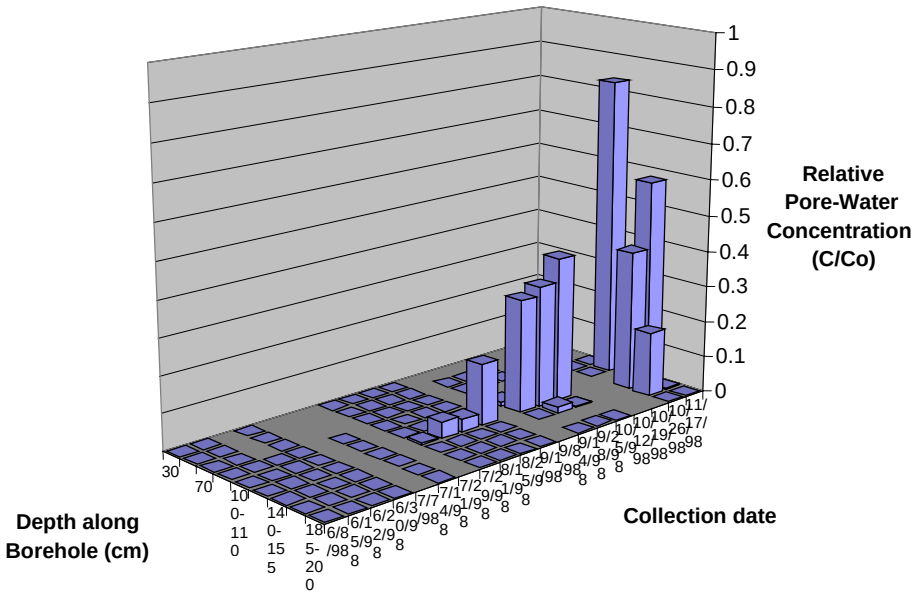

DTN: LA9909WS831372.001 [122739]; LA9909WS831372.002 [122741]

SOURCE: CRWMS M&O 2001 [154024], Figure 58d

Figure 6.13.2-2d. Pyridone Concentrations in Borehole 6 for Phase 1B

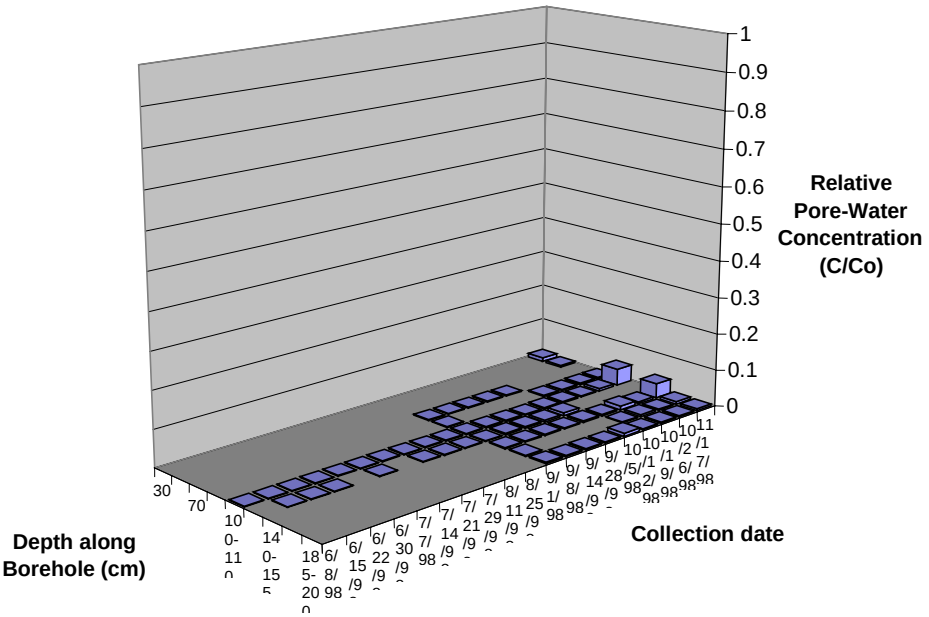

DTN: LA9909WS831372.001 [122739]; LA9909WS831372.002 [122741]

SOURCE: CRWMS M&O 2001 [154024], Figure 58e

Figure 6.13.2-2e. Lithium Concentrations in Borehole 6 for Phase 1B

6.13.3 Field-Scale Tracer Transport – Phase 2

6.13.3.1 Test Configuration

Phase 2 testing involved a 7 m high, 10 m wide, and 10 m deep block comprising all of the lithologies of Phase 1 (Figure 6.13.1-4). The injection systems in Phase 2 were designed to activate large surfaces of the block. The injection points for this phase are distributed in two horizontal, parallel planes arranged to test the properties of the lower Topopah Spring Tuff (Tptpv2) and the hydrologic Calico Hills (Tptpv1 and Tac). There were 6 upper injection boreholes drilled (4 used for injection) and 4 lower injection boreholes drilled from the test alcove. The upper injection plane consists of fractured Topopah Spring Tuff Tptpv2. As in Phase 1B, this unit represents the base of the TSw basal vitrophyre and is characterized by subvertical fractured surfaces representing columnar joints. Thirty-seven injection points distributed along 4 injection holes approximately 8 m deep each were used for tracer injection along a horizontal surface. The natural fracture pattern present in this unit serves as the conduit for tracer migration into the non-welded Calico Hills. The lower horizontal injection plane was located in the Calico Hills formation (Tac). There were 40 injection points distributed in four horizontal and parallel boreholes. These boreholes were designed to activate the lower part of the block in the event that the top injection system did not activate the entire block during the testing program.

Phase 2 included 15 collection boreholes drilled from the Main Adit, perpendicular to the injection boreholes. Twelve of the collection boreholes were drilled prior to the initiation of Phase 2 injection; 3 additional collection boreholes were drilled during injection. These boreholes were 8.5 to 10.0 m in length, and each contained 15 to 20 collection pads evenly distributed on inverted membranes.

Figure 6.13.3-1 is a view of the collection face, showing the positions of all the boreholes (to scale). It also shows the locations of the injection holes as horizontal lines. In describing the results of the field test, refer to Figure 6.13.3-1 to visualize the relative locations.

Phase 2 was subdivided into three subphases (2A, 2B, and 2C) according to location and injection rates used. Phase 2A consisted of a single borehole in the upper injection plane instrumented with 10 injection points and 10 moisture sensors, one at each injection point. The injection rate was 1 mL/hr per injection point. This borehole is restricted to the Tptpv2 lithology, which consists of fractured, moderately welded tuff from the basal vitrophyre. Phase 2A injection began on July 23, 1998, and was terminated on October 30, 2000.

Phase 2B consisted of four injection boreholes in the lower-injection plane, each instrumented with 10 injection points and 10 moisture sensors, one at each injection point. The injection rate was 10 mL/hr per injection point. This injection plane is restricted to the Calico Hills formation (Tac) and was planned to activate the lower section of the test block simultaneously with the upper section (Phases 2A and 2C). Phase 2B injection began on July 30, 1998, and was terminated on October 30, 2000.

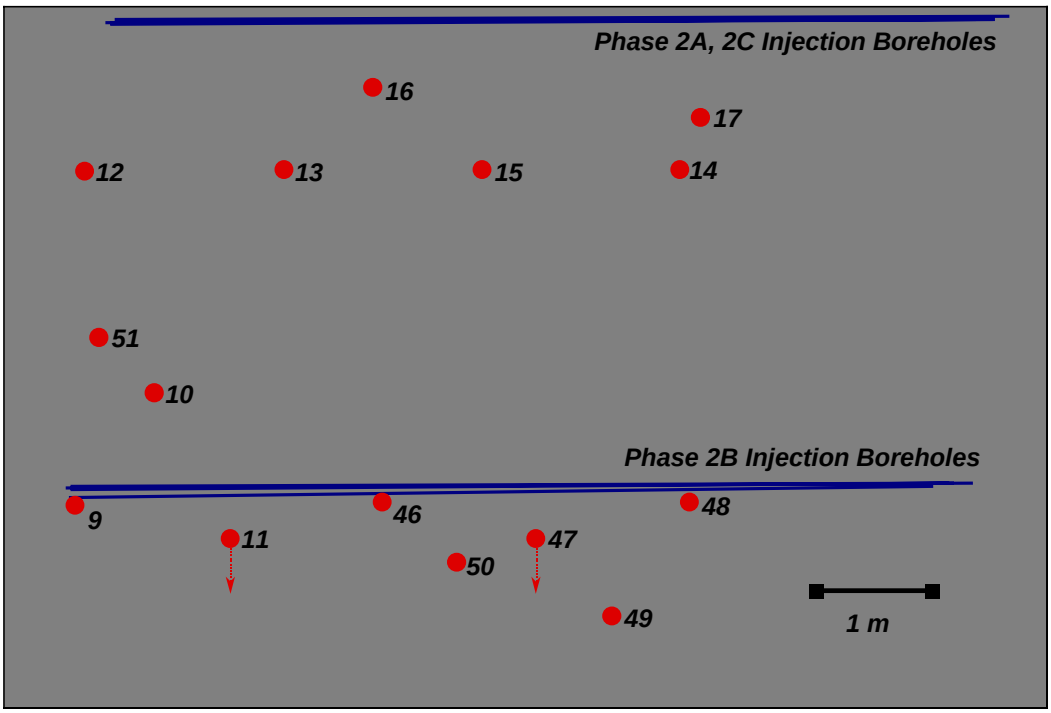

SOURCE: CRWMS M&O 2001 [154024], Figure 59 (For illustration purposes only).

Figure 6.13.3-1. Borehole Configuration on the Collection Face

Phase 2C consisted of three upper injection boreholes, each instrumented with nine injection points and 12 moisture sensors, one at each injection point, and two additional sensors located toward the borehole collar to detect tracer movement towards the front of the borehole. The injection rate was 50 mL/hr per injection point. This injection system was restricted to a horizontal plane in the Tptpv2 lithology. Phase 2C injection was initiated on August 5, 1998, and was terminated on October 30, 2000.

As discussed in Section 6.13.1.10, Phase 2 injected a mixed tracer solution that included those tracers used in Phase 1 plus three additional fluorinated benzoic acids (FBAs), a mixture of new reactive tracers (Ni^{2+}, Co^{2+}, Mn^{2+}, Sm^{3+}, Ce^{3+}, and Rhodamine WT). Beginning in August 1999, an additional nonreactive tracer (I^-) was added to the solution to study flow and transport response at higher system saturations.

Natural infiltration rates at Yucca Mountain vary between 0.01 and 250 mm yr^{-1}, with an average of 5 mm yr^{-1} (Flint et al. 1996 [100147]). Phase 2A falls within the range of natural present-day infiltration rates at Yucca Mountain, whereas Phase 2B lies at the high end of predicted values for a pluvial-climate scenario. Phase 2C infiltration rates are artificially higher than expected natural-infiltration rates for the region, but provide for the longest travel distances given the short duration of the experiment. Further, these high injection rates may provide insight into system behavior during unnaturally high flow potentially caused by repository heating.

In addition to the tracer collection system, two geophysical imaging techniques [electrical resistance tomography (ERT) and ground-penetrating radar tomography (GPR-T)] were used to image the *in situ* 2- and 3-D saturation state of the block at approximately bimonthly intervals.

6.13.3.2 Additional Coring

During February–March 2000, three additional cores were extracted from the Phase 2 collection face (boreholes 49 to 51, Figure 6.13.3-1). These boreholes were located to sample volumes of the block that were not being captured by existing boreholes. The core from these boreholes was analyzed in the laboratory for tracers. The boreholes were also instrumented for pad collection, and these additional pads/locations were also analyzed. Results are presented later in this section.

Following termination of tracer injection, 5 overcores were taken around and below injection holes (Figure 6.13.3-2) to analyze the rock for tracers. These overcores were located to obtain the broadest spectrum of information on metals and microspheres, which had not been observed on any collection pads.

6.13.3.3 Mineback

A partial mineback of the Phase 2 block is currently underway. The purpose of the mineback is (1) to collect additional information about the geology of the block, particularly faults and permeability contrasts, and (2) to obtain rock samples for tracer analysis that cover a larger portion of the test block volume than the collection boreholes.

Observations of block geology at this point have identified at least one fault. An ash layer was observed in the lower Tptpv1 unit. At least one of the injection boreholes was fully contained within this layer. Observations of *in situ* fluorescing tracer indicate that this layer strongly affected flow by impeding movement of injected tracer mix into the remainder of the block.

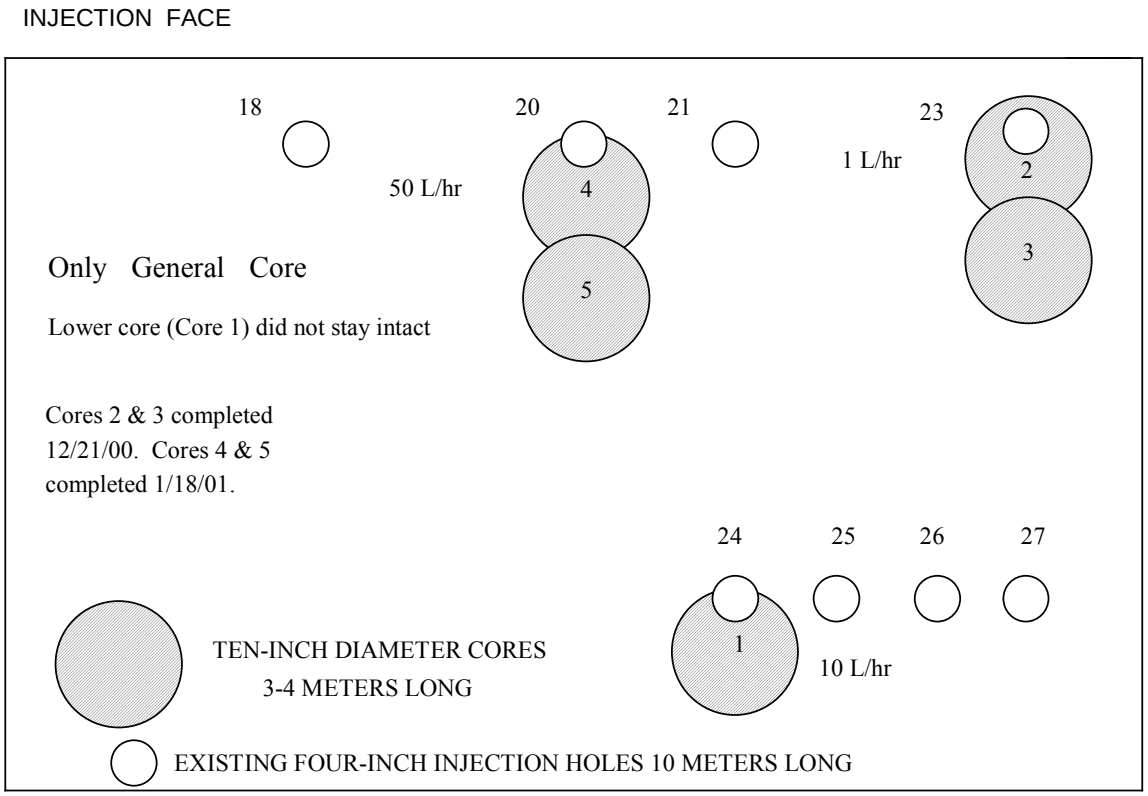

Figure 6.13.3-2. Locations of Phase 2 Post-Test Overcores

6.13.3.4 Pad Analyses

Phase 2 injection began in July 1998 and was terminated on October 30, 2000. Almost 19,000 Phase 2 sampling pads were collected. Selected pads were analyzed via the tracer extraction process. Over 5,000 pads have been extracted, and over 32,000 individual analyses have been completed.

Pad analyses run thus far confirm breakthrough of nonreactive tracers in 14 of the 15 collection boreholes (all except borehole 10). Lithium breakthrough has been confirmed in 10 of the 15 collection boreholes (all except boreholes 10, 11, 47, 49, and 51). No other sorbing tracers have yet been unequivocally detected, but pad extract analysis in continuing.

Breakthrough information is presented in the following figures. These figures show distance in from the collection face on the horizontal axis, and time on the vertical axis, increasing from the top of the figure down. The location of injection boreholes is shown by vertical lines. Note that the location of the injection boreholes varies slightly at the different collection holes because the starting location of the collection boreholes varies: the collection face is not precisely perpendicular nor flat with respect to the injection face.

6.13.3.5 Moisture Movement

Figure 6.13.3-3 presents the moisture data at collection boreholes 10 and 15 compared with the bromide tracer breakthrough. As expected, the breakthrough of moisture onto the collection pads precedes the breakthrough of tracer. Initial saturation of the UZTT Phase 2 block was estimated at approximately 16%. Because the block was not totally dry, tracer displaced existing water ahead of it as it was injected.

6.13.3.6 Scaling/Travel Distance

The configuration of the injection and collection boreholes was designed to allow analysis of a variety of different processes. Collection boreholes were placed at different distances from the injection boreholes to assess the influence of travel distance. Differing travel distances also provide a range of scales for studying transport, from tens of centimeters to meters.

The effect of travel distance on tracer transport is shown in Figure 6.13.3-4. Collection boreholes 16, 17, 15, and 10 are all parallel and at increasing distance from the upper injection holes. All of the collection holes reside in unit Tptpv1 (hydrologic Calico Hills).

Breakthrough times at the different distances scale approximately linearly with travel distance. Fifty percent breakthrough of bromide in borehole 16 occurs at just under 125 days, whereas at borehole 15, almost twice as far from the injection boreholes, breakthrough occurs at approximately 250 days. Based on this, breakthrough at borehole 10 is expected at approximately 570 days. Pad analyses for borehole 10 at those dates are not yet available.

6.13.3.7 Heterogeneity

Boreholes 12, 13, 15, and 14 are all equidistant from the upper injection boreholes and parallel. They are all in the same unit. Differences in breakthrough pattern between these boreholes is thus a result of heterogeneities in the test block. Figure 6.13.3-5 demonstrates noticeable variability in both breakthrough times and concentrations for bromide in these boreholes.

The significant delay between breakthrough in borehole 12 versus boreholes 13 and 15 is possibly a result of the presence of a fault that runs through the back of the block. This fault appears to cut between the injection boreholes and borehole 12.

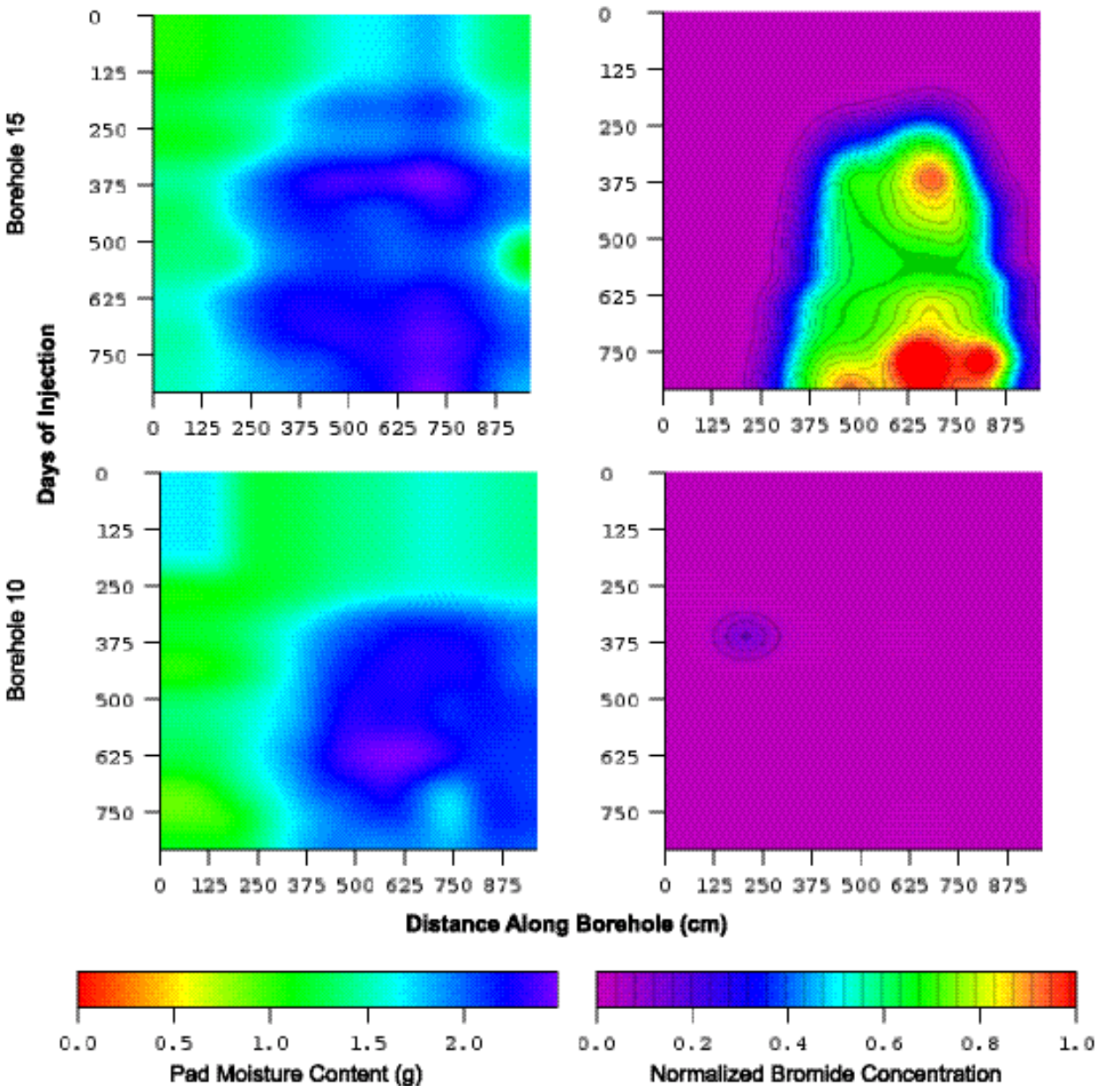

DTN: LA0112WS831372.001 [157100], LA0112WS831372.002 [157115], LA0112WS831372.003 [157106]

Figure 6.13.3-3. Moisture Front Precedes Tracer Front

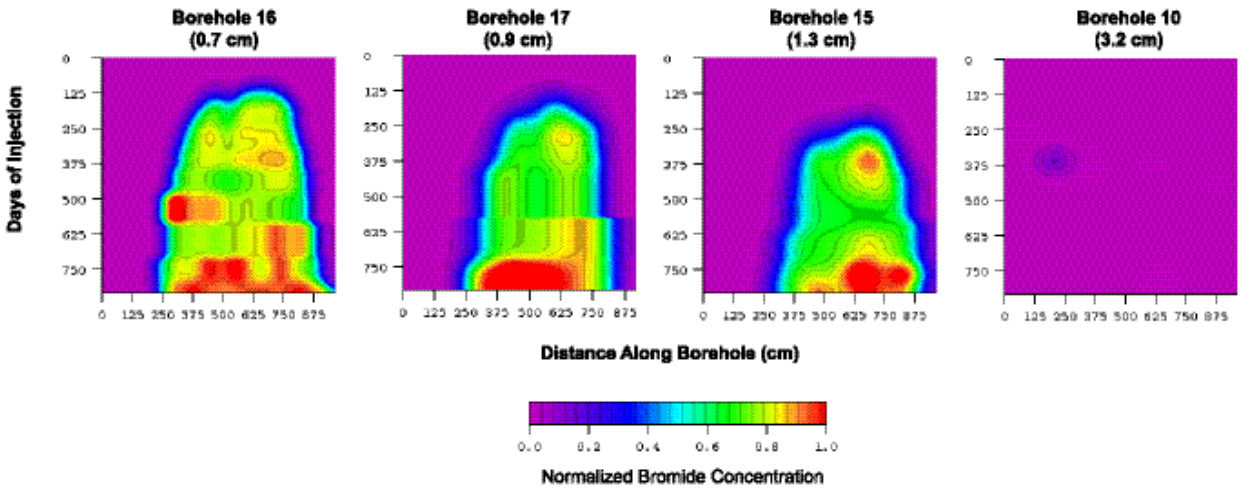

DTN: LA0112WS831372.001 [157100], LA0112WS831372.002 [157115], LA0112WS831372.003 [157106]

Figure 6.13.3-4. Influence of Scaling/Travel Distance on Tracer Transport in UZTT Phase 2

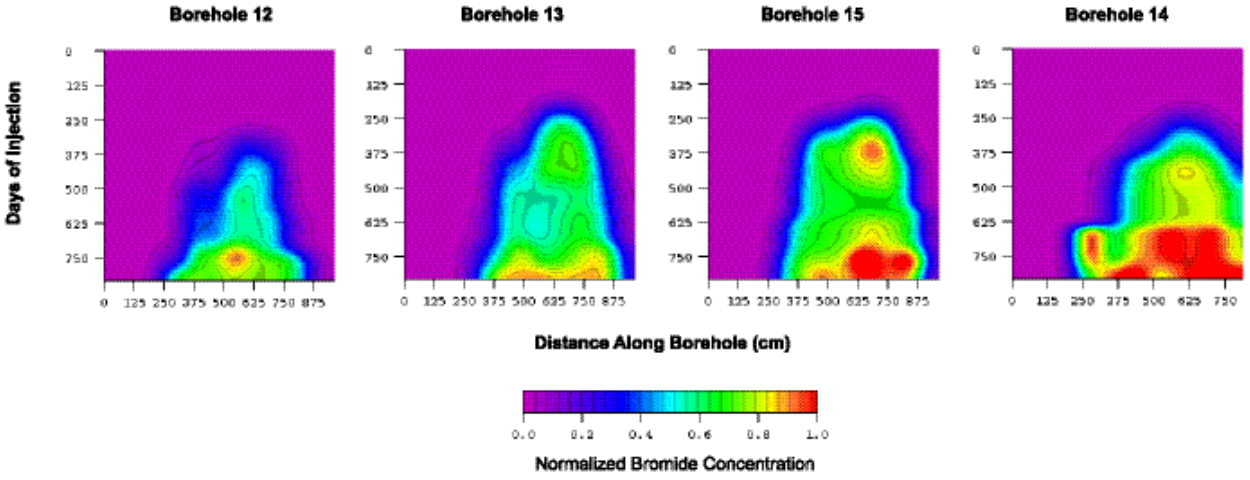

DTN: LA0112WS831372.001 [157100], LA0112WS831372.002 [157115], LA0112WS831372.003 [157106]

Figure 6.13.3-5. Influence of Rock Heterogeneity on Tracer Transport in UZTT Phase 2

6.13.3.8 Transverse Dispersion

In each of the injection holes, a mix of a number of tracers is introduced. The tracer mix is the same for all boreholes except with regard to the FBAs. Each injection borehole injects a different FBA to allow identification of the source of the tracer when collection pads are analyzed. Thus, by looking at tracer breakthrough patterns in a single collection borehole, the extent of lateral dispersion can be assessed.

Tracer breakthrough in borehole 16 is shown in Figure 6.13.3-6. Borehole 16 is 0.7 m below the injection boreholes. The vertical marks on Figure 6.13.3-6 show the location of the borehole that is injecting the particular FBA being plotted. Bromide is injected in all holes, so the bromide plot shows overall breakthrough in borehole 16.

The breakthrough pattern in borehole 16 indicates that there is little transverse dispersion or mixing of the tracer being injected at the various injection boreholes.

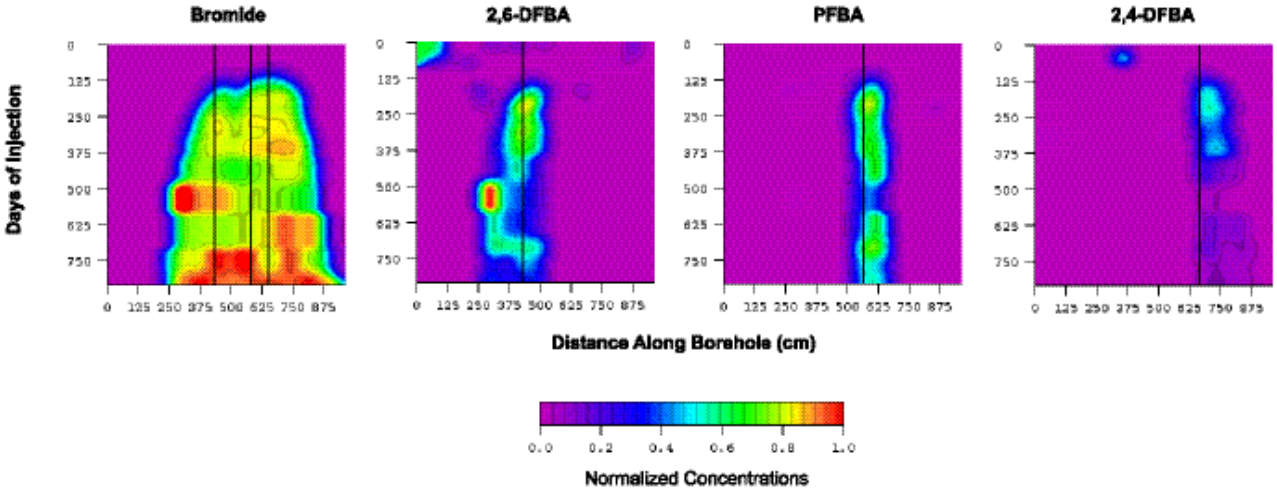

DTN: LA0112WS831372.001 [157100], LA0112WS831372.002 [157115], LA0112WS831372.003 [157106]

Figure 6.13.3-6. Extent of Transverse Dispersion on Tracer Transport Measured in Borehole 16 of the UZTT Phase 2

6.13.3.9 Sorption/Retardation

The influence of sorption/retardation is analyzed by comparing breakthrough curves for bromide versus lithium at various boreholes. Figure 6.13.3-7 shows breakthrough curves for the two tracers at three different boreholes. Borehole 16 and borehole 15 are below the upper injection boreholes (50 mL/hr), in Tptpv1, 0.7 m and 1.3 m, respectively. Borehole 48 is below the lower injection boreholes (10 mL/hr), located in the Tac.

As expected, lithium breakthrough is retarded with respect to bromide. Laboratory sorption measurements calculate lithium K_d values between 0.4 and 1.1 (DTN: LA9912WS831372.001 [156586]).

All of the other reactive tracers being used have significantly higher K_d values and were not expected to break through at any of the boreholes yet.

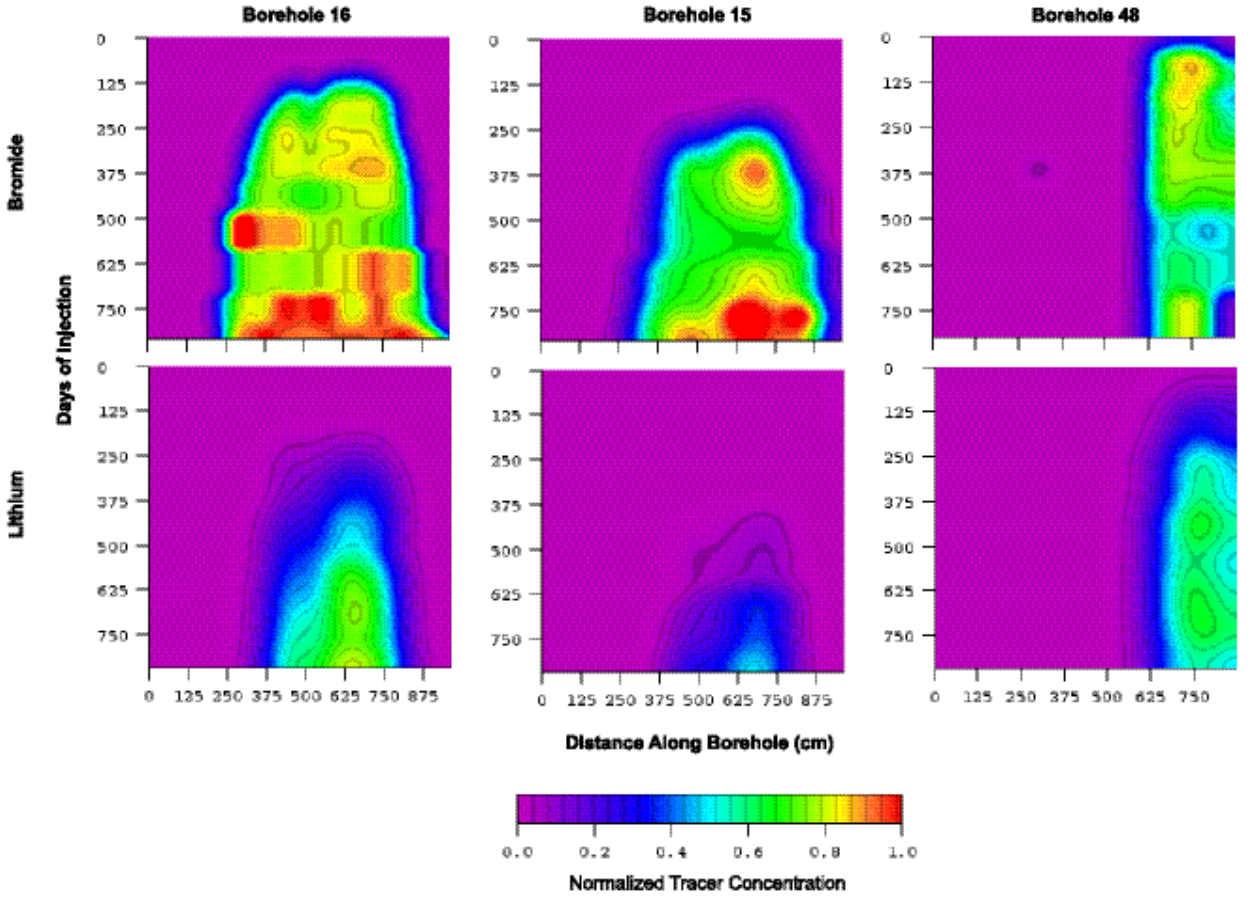

DTN: LA0112WS831372.001 [157100], LA0112WS831372.002 [157115], LA0112WS831372.003 [157106]

Figure 6.13.3-7. Effect of Sorption/Retardation on Tracer Transport in UZTT Phase 2

6.13.4 Tomographic Studies: Geophysical Techniques at the Busted Butte Unsaturated Zone Test Facility

Real-time geophysical monitoring techniques were used to provide real-time data on the advance of fluid fronts and tracer fronts through the block. Combining two geophysical techniques enables the collection of detailed, high-resolution, 3-D, calibrated, real-time monitoring of moisture and tracer movement through the unsaturated fractured medium. Specifically, electrical resistance tomography (ERT) provides 3-D global coverage, and ground-penetrating radar tomography (GPR-T) provides high spatial resolution.

6.13.4.1 Busted Butte Ground Penetrating Radar Tomography

The GPR data acquisition was conducted in the Phase 2 test block to monitor the tracer injection, both spatially and temporally, and to investigate the nature of fluid migration through the Calico Hills formation. The data collected, analyzed, and submitted to the Technical Data Management System (TDMS) thus far include the pre-injection/baseline radar velocity measurements as well as the subsequent velocity measurements made after the start of tracer injection (nine data collection visits though November 2000). All analyzed data were periodically compared to the

other available geophysical data (as well as to the tracer breakthrough data) to constrain the interpretation of the fluid/tracer migration within the block.

6.13.4.1.1 Background and Experimental Approach

In the borehole radar method, modified surface radar antennas are emplaced into a rock formation, and high-frequency electromagnetic signals are transmitted through the formation to a receiving antenna. The electrical properties of the subsurface material greatly influence the transmitted electromagnetic signal. In particular, the dielectric permittivity (K) of the rock has a strong influence on the propagation of the signal and whether it travels at a high or low velocity. Moisture content effects dielectric permittivity and hence has such an effect. The high dielectric permittivity of water (K ~80) or wet rock (K ~20-30) in contrast to drier rock (K ~3-6) typically results in greatly reduced signal velocities. Changing chemical compositions (i.e., tracers) may also alter the bulk dielectric permittivity of the rock and hence the propagation velocity of the radar waves. Because such changes in signal character are what are measured over the course of the Busted Butte UZTT, any increase (or decrease) in background moisture content or chemical composition resulting from the tracer injection (or rock dry-out) should result in changes in the received radar velocity.

The transmitted signals may be represented as multiple ray paths crossing through a zone of interest within the block. If sufficient ray paths are recorded, a tomographic image may be obtained through computer processing. The information extracted from such data consists of the transit time, which depends on the wave velocity. This information, in the form of a processed radar velocity tomogram, offers a high-resolution approach to monitoring the changes occurring in the rock over the duration of the tracer-injection experiment.

6.13.4.1.2 Equipment Description, Component Specifications, Operating Principles, and Survey Methodology

A detailed description of the equipment used, the component specifications, the operating principles, and the GPR survey methodology can be found in Bussod et al. (1998 [131513], Section 5.1.6). Additional information can be found in the Technical Implementing Procedure governing all GPR data acquisition done in support of the Yucca Mountain site-characterization effort (YMP-LBNL-TIP/GP 5.0).

6.13.4.1.3 Results of the Busted Butte Unsaturated Zone Transport Test Radar Data Acquisition

The radar data were acquired in eight of the Phase 2 collection boreholes orthogonal to the direction of the Phase 2 injection boreholes. Additionally, two of the Phase 2 injection boreholes were used to acquire data one time only after they were apparently affected by grout infiltration resulting from nearby ERT borehole grouting. The ten boreholes include the following: 9, 11, 13, 15, 16, 46, 47, and 48 (Phase 2 collection); 19 and 22 (Phase 2 injection). The configuration of and layout of the boreholes used are illustrated in Figure 6.13.3-1.

The radar data were acquired in the two-dimensional planes defined by the two boreholes, more commonly referred to as well pairs. The well pairs acquired include the following: 15-13, 48-46, 47-11, 46-9, 46-16, and 22-19 (one time only). The decision to acquire data in thee particular

well pairs was made based on the relative proximity to the injection boreholes. Data from both the upper horizontal well pair 15-13 and the vertical well pair 46-16 was acquired to monitor tracer injection associated with the upper injection boreholes 18, 20, 21, and 23. Data from the lower horizontal well pairs 46-9, 47-11, and 48-46 were acquired to monitor tracer injection associated with the lower injection boreholes 24, 25, 26, and 27. The vertical well pair 46-16 may also be used to image any tracer injection associated with the lower injection boreholes and the progress of the tracer beneath the horizontal well pair 15-13.

Thus far, the data have been processed for travel times, with the result being radar velocity tomograms. Differencing or subtraction of the velocity tomograms over time has also been completed for each of the well pairs. Such differencing or subtraction allows for the highlighting of the tracer or moisture front as it changes spatially and temporally. In essence, the background formation remains static in those areas not affected by the changing tracer or moisture front. By subtracting one velocity tomogram from another, we have been able to discount those areas remaining static, while emphasizing those areas where change is occurring.

Two of the well pairs differ slightly in the acquisition method used between the baseline and the post-injection surveys. These well pairs are 46-16 and 46-9. Data for well pair 46-16 was collected at a higher frequency (200 MHz) during the post-injection surveys to better match the data collected in all of the other well pairs. Higher frequencies generally result in data of higher resolution (approximately 10.0 cm for 200 MHz), so the highest-frequency antennas should be used if at all possible. Data were not originally acquired in well pair 46-9 because it was believed that well pair 48-46 provided sufficient coverage in the area of the lower injection boreholes. A decision was subsequently made after tracer injection began to gather more spatial information below the lower injection boreholes and, therefore, well pair 46-9 was added to the GPR acquisition list. Also, it should be noted that the pre-injection baseline data for several of the well pairs differs significantly from data acquired just one month after tracer injection began. The differences were likely the result of changes in the overall block assemblies (e.g., grouting of the ERT boreholes, addition of the injection apparatus) rather than the immediate consequence of the tracer injection. To enhance the subsequent differencing tomography, the “baseline” set of radar velocity tomograms chosen were those collected in August-September 1998, approximately one month after tracer injection began. Comparison with tracer breakthrough data on the collection pads indicated that tracer had not yet significantly entered those regions imaged by the GPR tomograms. Therefore, it was determined that the August–September 1998 data would provide an adequate starting point from which to evaluate the changes in the block over time.

Each of the well pairs witnessed some degree of velocity change over the course of the experiment. For the purposes of this AMR, however, only four of the well pairs will be discussed in detail: 46-16, 46-9, 11-47, and 15-13. Interpretation of the data suggested that the results for all of the well pairs are similar. Again, all data from each of the well pairs have been submitted to the TDMS and are available for review.

Well Pair 46-16

This well pair represents the only vertical slice through the block (approximately 9.5 m long and 3.5 m wide). It images tracer and moisture contributions from both the upper and the lower injection boreholes. When evaluating changes in velocity over time, one would expect such changes to occur in the regions directly surrounding the injection boreholes with decreased velocities representing areas of increased moisture content. This is exactly what is seen in the differenced tomograms. Figures 6.13.4-1 represent several time steps throughout the course of the experiment (dates of data acquisition are noted above each tomogram). As can be seen, decreases in the velocity relative to the baseline (Aug.-Sept. 1998) data are immediately obvious surrounding the high and low injections boreholes (these locations are marked on the tomograms as small white dots). Furthermore, the zones of decreased velocity can be seen to expand away from the injection boreholes over time, both in a vertical as well as a horizontal direction. Such vertical and horizontal spreading is to be expected as a result of the matrix or capillary-driven flow and was, in fact, confirmed in the Phase 1A excavation. Until the results of a similar excavation in the Phase 2 block are analyzed, the GPR data would seem to indicate a similar mechanism of flow for this area.

Also of note is the seemingly large extent of decreased velocity. It should be restated that low velocities are indicative of zones of higher dielectric permittivity, which indicate zones of elevated moisture content. That being the case, those zones of decreased velocity may represent regions of elevated moisture content and simply the presence of tracer. This subtlety is borne out when comparing the tracer breakthrough data with the tomography results. The zones of increased moisture content (i.e. decreased velocity) do not directly overlay the tracer breakthrough within boreholes 46 or 16. In fact, the locations of tracer breakthrough are contained within the zones of decreased velocity. This implies that as the fluid front containing the tracer spreads away from the injection boreholes, some of the tracer may be retarded relative to the spread of the moisture front. In effect, the tracer may be moving more slowly through the block than its associated fluid or water component.

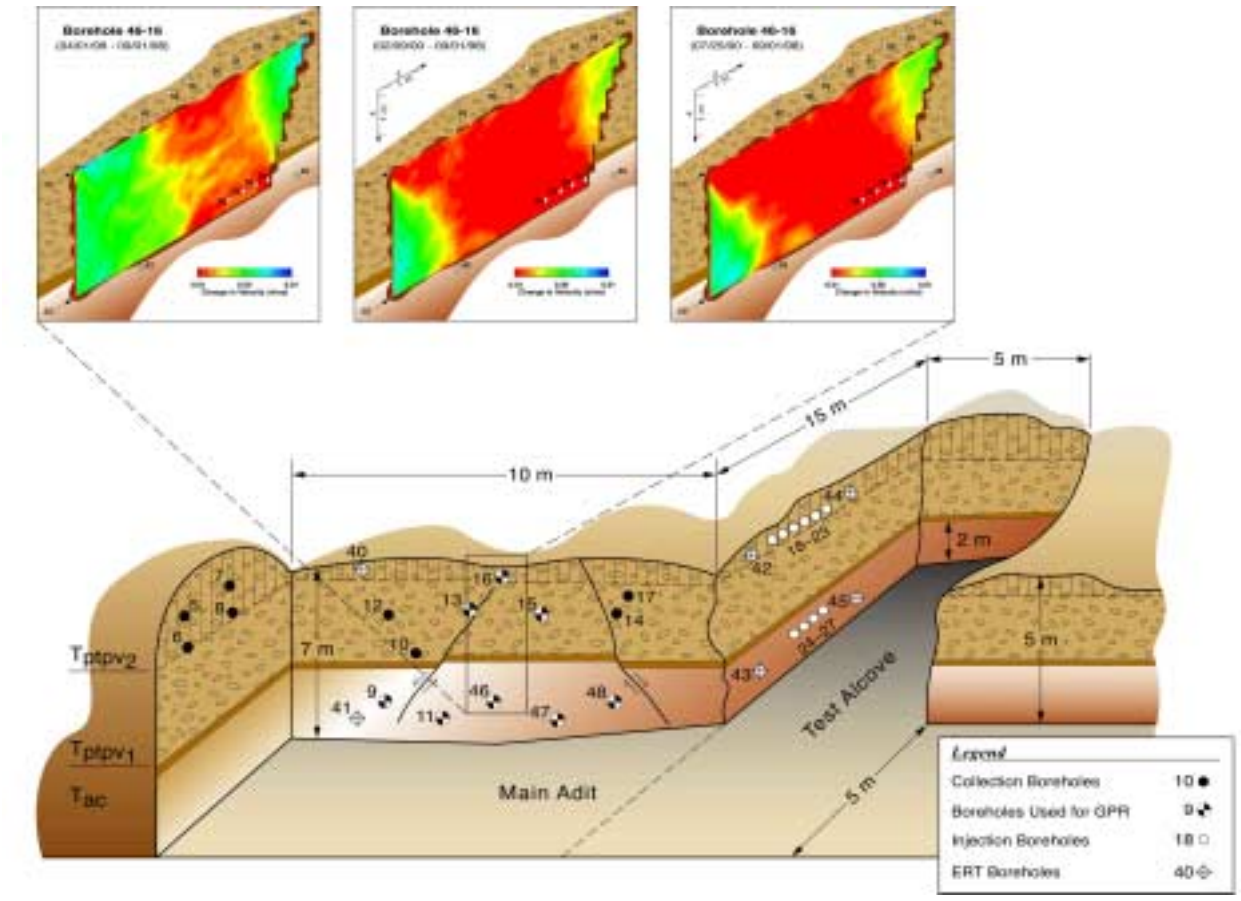

DTN: LB00032412213U.001 [149214]; MO0004GSC00167.000 [150300] (for location)

Figure 6.13.4-1. Tomography (GPR-T) Results for Well Pair 46-16 from December 1998; March 1999; and April 1999

Conversely, the fluid front leaving the injection boreholes may be simply displacing existing pore fluid and mobilizing it within the block. The radar velocities are insensitive to this effect and thus are incapable of distinguishing between existing pore fluid, introduced pore fluid, and tracer. Given the extent to which the velocities are decreasing, it seems unlikely at this time that sufficient natural pore water existed within the block prior to the experiment to account for all of the change observed. Again, comparing the tomography results with those recorded in the tracer breakthrough logs, it appears that some form of fluid breakthrough is occurring in the collection boreholes which is not comprised of tracer (so-called "contamination of pads" in the breakthrough logs). This is evidently what is being imaged by the differenced radar tomograms, and it is not an inconsequential finding.

Additionally, when compared to the radar results, the neutron probe data collected in these two boreholes imply a similar pattern of increased moisture content. Those zones that appear to be wetting as well as those that remain dry agree nicely with the same regions on the tomograms.

Well Pair 46-9

This well pair represents a horizontal slice (approximately 8.0 m long and 2.6 m wide) through the block and images the tracer/moisture front associated with the lower injection boreholes. Figures 6.13.4-2 represent several time steps throughout the course of the injection (dates of acquisition are noted above each tomogram). Decreases in velocity relative to the baseline (August–September 1998) data are immediately obvious surrounding the lower injection boreholes (these locations are marked on the tomograms as orthogonal tubes). Furthermore, the zones of decreased velocity expand away from the injection boreholes over time in a horizontal direction. Because a horizontal well pair cannot capture the vertical flow of moisture away from the boreholes, only the extent of the horizontal flow can be imaged. The decrease in velocity (i.e. the increase in moisture content) moves rapidly away from the injection boreholes early on in the experiment and then remains relatively constant (aside from localized changes). This would imply that much of the moisture front moves away from the injection apparatus to its greatest possible extent at which time it can no longer spread in such a direction. Presumably, the majority of fluid flow from the lower injection boreholes continues on in a vertical direction. Later in the course of the experiment, however, decreases in velocity (i.e., increases in moisture content) begin to show up at distances farther removed from the lower injection boreholes. This contribution possibly results from the upper injection boreholes. As the fluid/tracer front moves away from the upper injection boreholes in the downward direction, it ultimately comes into contact with the lower horizontal well pairs (e.g. 48-46, 46-9, 11-47). That this occurs is seen in the vertically oriented tomograms described for well pair 46-16.

The results implied by the radar tomograms support the tracer breakthrough logs for boreholes 48 and 9. Again, those zones of decreased velocity overlay those locations in the boreholes where tracer has been seen to break through onto the collection pads. The additional contribution of the moisture front relative to the tracer (as described above for well pair 46-16) does not appear to be as significant for this well pair. It is not yet clear whether this is because the region imaged is smaller or spatially close to the injection boreholes. Additionally, the neutron probe data collected in these two boreholes implies a very similar pattern of increased moisture content. Those zones that appear to be wetting as well as those that remain dry agree well with the same regions on the tomograms.

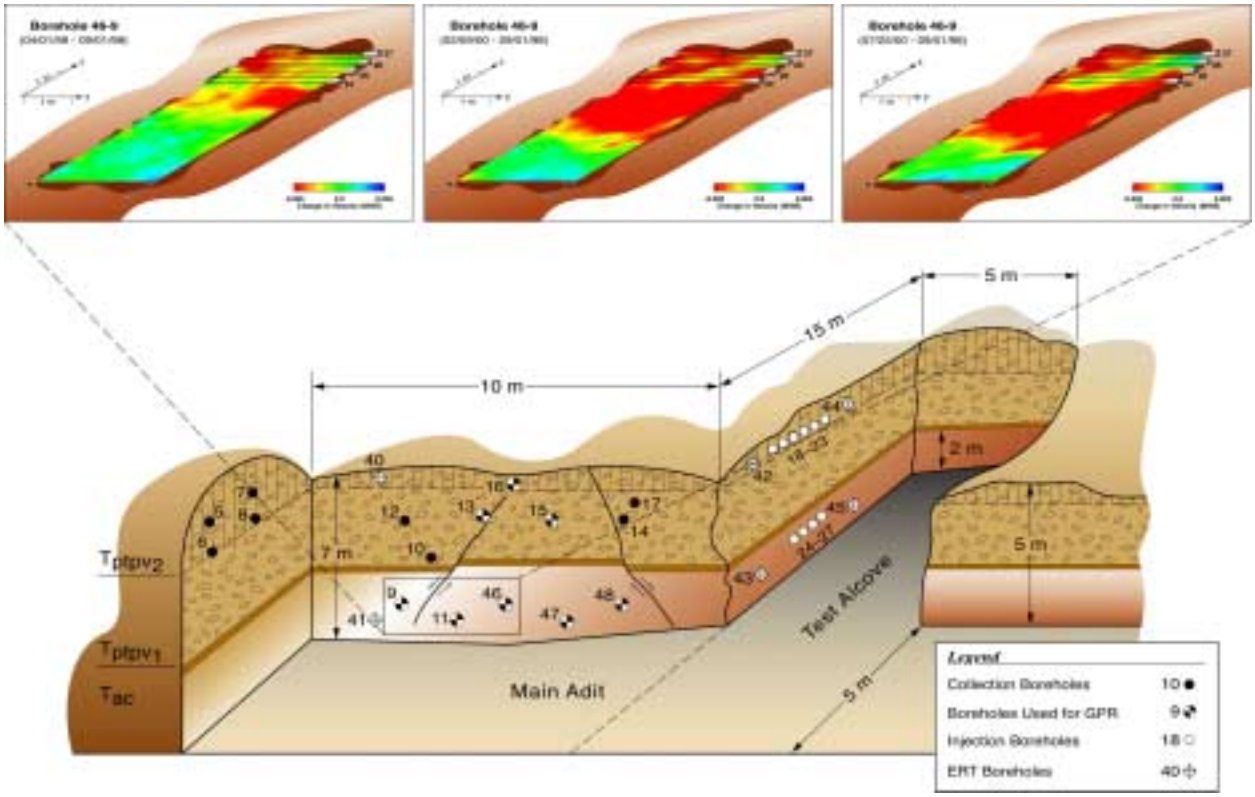

DTN: LB00032412213U.001 [149214]; MO0004GSC00167.000 [150300] (for location)

Figure 6.13.4-2. Tomography (GPR-T) Results for Well Pair 46-9 from April 1999; February 2000; and July 2000

Well Pair 11-47

This well pair represents a subhorizontal slice (approximately 10.0 m long and 2.6 m wide) through the block and images the tracer/moisture front associated with the lower injection boreholes. This well pair is of interest because of its component of dip, which allows the collection boreholes to get progressively farther away from the injection boreholes as a function of depth. Figure 6.13.4-3 represents several time steps throughout the course of the injection (dates of acquisition are noted above each tomogram. Decreases in velocity relative to the baseline (June 1998) data are immediately obvious surrounding the lower injection boreholes (these locations are marked on the tomograms as orthogonal tubes). The zones of decreased velocity expand away from the injection boreholes over time in a horizontal direction. Again, the dip of these two boreholes was designed to provide a means to measure sequential breakthrough down the length of the boreholes. The radar data does not appear to show such an effect. Due to either the time step chosen or to smearing inherent in the tomographic processing, there is no obvious "staggering" in the moisture/tracer breakthrough locations. The region of decreased velocity (i.e., the area of increased moisture content) moves away from the injection boreholes early on in the experiment and then continues in a similar fashion up to a point at which moisture spreading seems to cease. As for the other horizontal well pairs, this would imply that much of the moisture front moves away from the injection apparatus to its greatest possible extent at

which time it can no longer spread in such a direction. Presumably, the majority of fluid flow from the lower injection boreholes continues on in a vertical direction.

The results implied by the radar tomograms support the tracer breakthrough logs for boreholes 11 and 47. Again, those zones of decreased velocity overlay those locations in the boreholes where tracer has been seen to break through onto the collection pads. Additionally, the neutron probe data collected in these two boreholes implies a very similar pattern of increased moisture content. Those zones that appear to be wetting as well as those that remain dry agree well with the same regions on the tomograms.

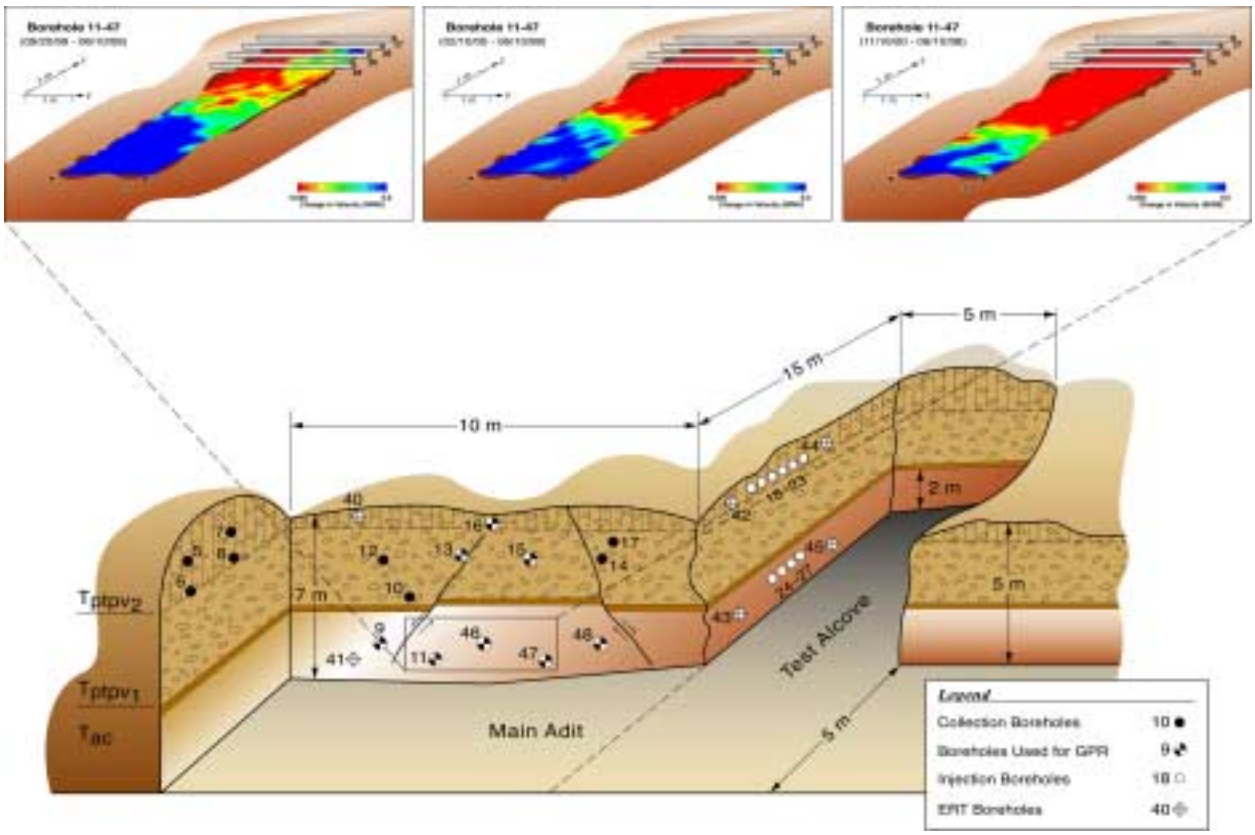

DTN: LB00032412213U.001 [149214]; LB0110BSTBTGPR.001 [156913]

Figure 6.13.4-3. Tomography (GPR-T) Results for Well Pair 11-47 from September 1999; February 2000; and November 2000

Well Pair 13-15

This well pair represents a horizontal slice (approximately 9.5 m long and 2.0 m wide) through the upper part of the block. Figure 6.13.4-4 represents several time steps throughout the course of the experiment (dates of data acquisition are noted above each tomogram). Decreases in the velocity relative to the baseline data (August–September 1998) are immediately obvious surrounding the upper injection boreholes (these locations are marked on the tomogram as orthogonal tubes). Furthermore, the zones of decreased velocity expand away from the injection boreholes over time in a horizontal direction. The decrease in velocity (i.e., the increase in moisture content) moves steadily away from the injection boreholes throughout the course of the

experiment. This varies a bit from the analogous well pair 48-46. Rather than reaching a maximum extent, the moisture front appears to be continually expanding away from the boreholes. This is probably the result of the well pair's increased distance beneath the injection boreholes and the much larger volume of fluid being introduced by the upper injection boreholes (50mL/hr as compared to 10mL/hr).

The results implied by the radar tomograms are in concurrence with the tracer breakthrough logs for boreholes 13 and 15. Again, those zones of decreased velocity overlay those locations in the boreholes where tracer has been seen to break through onto the collection pads. The additional input of the moisture front relative to the tracer (as described for well pair 46-16) does not appear to be as significant for this well pair. As for well pair 48-46, it is not yet clear whether this is because the region imaged is smaller or spatially closer to the injection boreholes. Also, the much larger volume of tracer injected into the region of this well pair may account for the lack of a discrepancy (i.e., there is simply more tracer in the area of the collection boreholes). Additionally, the neutron-probe data collected in these two boreholes imply a very similar pattern of elevated moisture content. Those zones that appear to be wetting as well as those that remain dry agree nicely with the same regions on the tomograms.

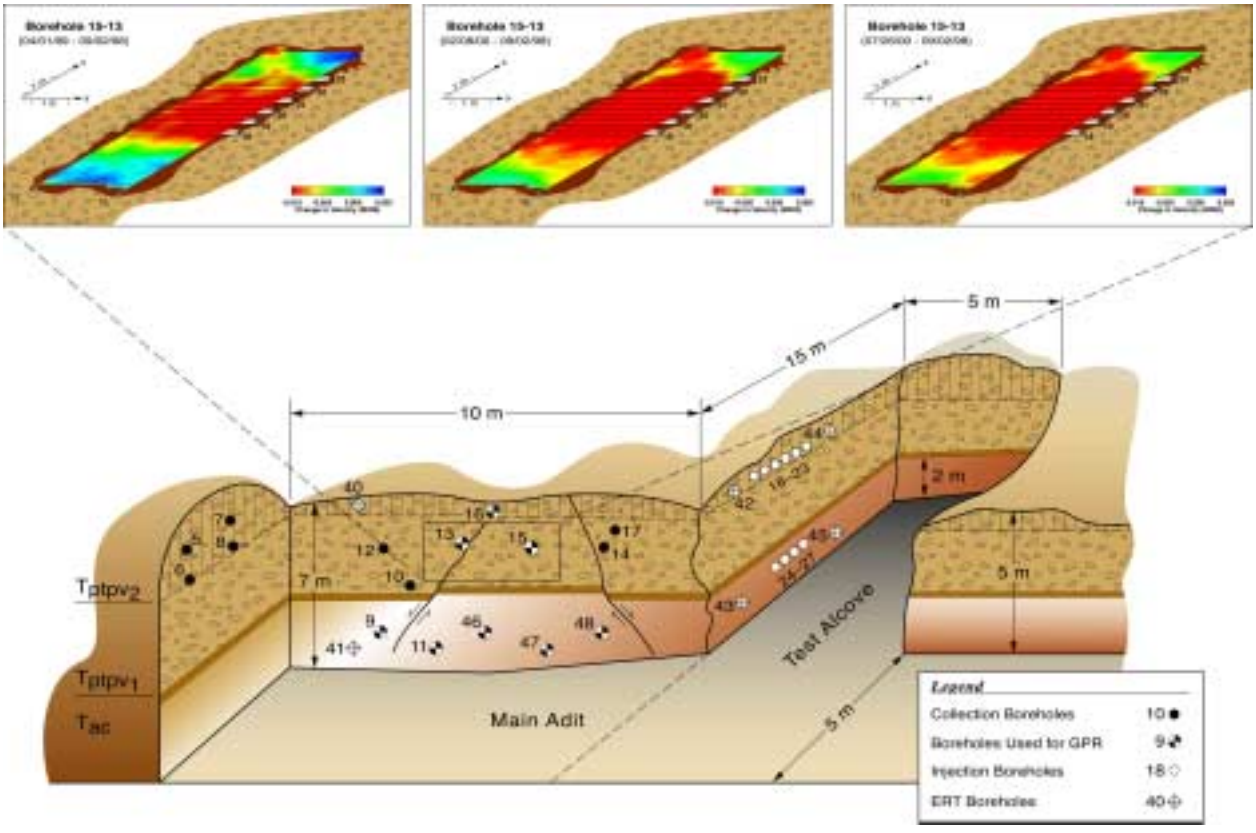

DTN: LB00032412213U.001 [149214]; LB0110BSTBTGPR.001 [156913]

Figure 6.13.4-4. Tomography (GPR-T) Results for Well Pair 13-15 from April 1999; February 2000; and July 2000

6.13.4.1.4 Summary of Ground-Penetrating Radar Tomography

The radar data collected thus far in support of the Busted Butte UZTT suggest that this method is appropriate for investigating subsurface velocity anomalies that may be related to tracer injection and moisture migration. Such anomalies are the result of changes in the dielectric permittivity of the rock mass. As noted above, such changes are most likely the result of some combination of the injected tracer and its associated fluid component. The regions of low velocity (i.e., elevated moisture content) appear to be in very close agreement with the other complementary evidence, including the tracer breakthrough logs and the neutron logging results. At this time, it appears likely that the differenced radar tomograms are defining the total extent of elevated moisture content within those zones defined by the radar well pairs. By defining the extent of this front, the radar tomography should provide an excellent control mechanism for the interpretation of the excavated Phase 2 block or any of the hydrologic flow modeling done to date.

6.13.4.2 Electrical-Resistance Tomography

The objective of this work is to provide 3-D electrical-resistance tomography (ERT) images of the movement of a tracer through the test block at the UZTT at Busted Butte. This report describes the results obtained during four separate data collections starting in July and ending in early September 1998.

Electrical-resistance tomography (ERT) is a new geophysical imaging technique that can be used to map subsurface liquids as flow occurs and to map geologic structure. ERT is a technique for reconstruction of subsurface electrical resistivity. The result of such a reconstruction is a 2- or 3-D map of the electrical resistivity distribution underground made from a series of voltage and current measurements from buried electrodes. The ERT approach followed here relies on detection and mapping of the changes in electrical resistivity associated with the movement of a tracer through the test block at the UZTT site.

6.13.4.2.1 Results of Data Collections—July to Early September 1998

ERT data were collected four times: July 2, July 14, August 19, and September 9, 1998. The intent was to make comparisons between the baseline condition on July 2 and data collected at later times. Comparisons between July 2 and August 19 and between July 2 and September 9 are presented because the data from July 14 were of questionable quality. These data have been submitted to the YMP Technical Data Management System (DTN: LL990612704244.098 [147168]).

Sixty ERT electrodes were installed in the test block as shown in Figure 6.13.4-5. The electrodes were placed in six drilled holes, ERT-1 though ERT-6, and two surface arrays (upper and lower). Holes ERT-3, 4, 5, and 6 and the surface arrays were drilled perpendicular to and from the instrumentation alcove. Holes ERT-1 and 2 were drilled from the main adit. The electrodes were grouped into boreholes 1 through 4 as shown in Figure 6.13.5-8. As is evident, each borehole is L-shaped and contains 15 electrodes. For example, borehole 1 is composed of the 8 electrodes in hole ERT-3 along with the 7 electrodes in the upper-surface array.

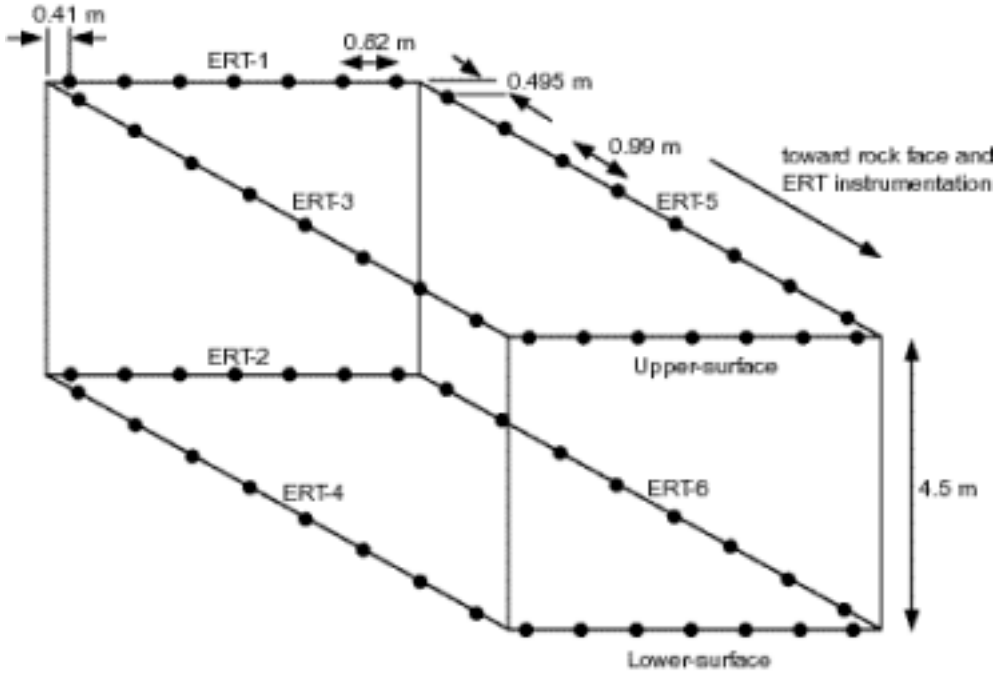

SOURCE: CRWMS M&O 2000 [154024], Figure 53
NOTE: This diagram gives the layout of drilled holes, ERT electrode locations, and spacing in the UZTT test block at Busted Butte.

Figure 6.13.4-5. Electrical-Resistance Tomography Layout

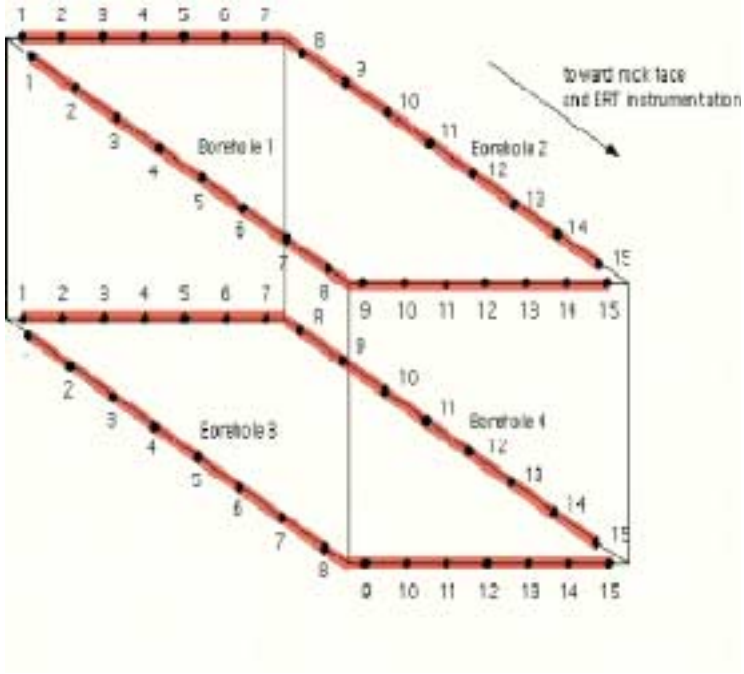

NOTE: This diagram gives the layout of the ERT boreholes and electrode assignments in the UZTT test block at Busted Butte.
SOURCE: CRWMS M&O 2000 [154024], Figure 54

Figure 6.13.4-6. Electrical-Resistance Tomography Electrode Assignments

The ERT data were collected between borehole pairs: boreholes 1 and 2 (upper horizontal plane), 3 and 4 (lower horizontal plane), 1 and 3 (left vertical plane), 2 and 4 (right vertical plane), 1 and 4 (diagonal), and finally 2 and 3 (diagonal) for a total of six data sets. The total number of data values collected was 2,430. These values provided the 3-D sampling of the test block resistivity, and the 3-D inversion algorithm operated on these data to produce a 3-D ERT image of the block.

It is most useful to look at comparison images when changes are taking place over time. The results presented here consider difference images that compare the resistivity of the block on August 19 and September 9 to July 2. Because the tracer mixture injected during Phase 2 of the UZTT experiment was approximately eight times more conductive than the pore water, resistivity decreases in the images are of interest.

6.13.4.2.2 Absolute Electrical-Resistance Tomography Images of the Block

Figure 6.13.5-9 shows an absolute image of the baseline condition of July 2 (top) and the difference between August 19 and July 2 (bottom). The baseline image shows a layered structure consistent with the lithology in the rear half of the block-that is, a high-resistivity layer over most of the middle of the block, Tptpv1, with a lower-resistivity region, Tptpv2, at the top, and a low-resistivity region, Tac, at the bottom. The image also shows an anomalously low resistivity region in the front half of the block, particularly near the bottom. This is not well understood and should be confirmed, if possible, by other means.

6.13.4.2.3 Difference Electrical-Resistance Tomography Images of the Block

The difference image of Figure 6.13.4-7 shows regions of resistivity decrease near injection holes 18, 20, and 21, as one would expect from the injection of conductive tracer mixture. It is apparent that a pronounced resistivity decrease exists in the slice 2.66 m from the front of the block, which could be associated with water moving downward in the block. The region of the block between 1.33 and 4.0 m, which contains this slice, also appears to be a low-resistivity region in the absolute image.

The September 9 to July 2 difference (Figure 6.13.4-8) also shows regions of resistivity decrease near injection boreholes 18, 20, and 21. The effect is even stronger in the 5.33 m slice. Moreover, the effect of water moving down into the block seems to be more pronounced in the 4.0 m slice compared to August 19.

The difference images from August 19 and September 9 show clear and consistent resistivity decreases in the region near boreholes 18, 20, and 21 that can be associated with the injection of conductive water. This effect appears to be stronger on September 9 in the 5.33 m slice. The images show very little effect in the region around the other injection boreholes, 23 and 24 through 27, where far less water was injected.

In addition, the difference images from August 19 and September 9 show resistivity decreases that could be interpreted as water moving down into the block between the 1.33 m and 4.0 m slices. This is the same region that has an anomalously low resistivity in the baseline image.

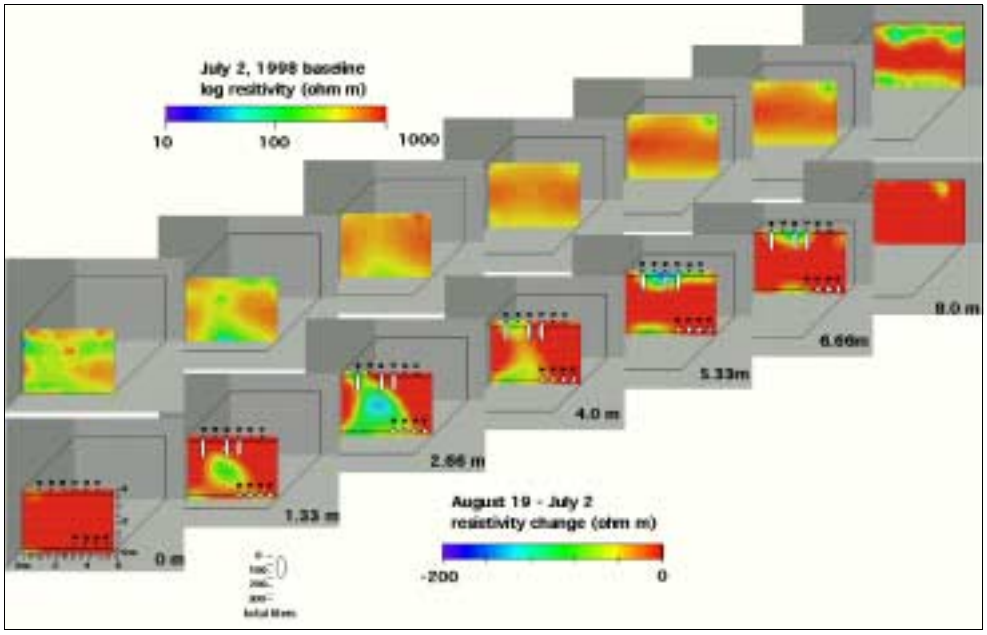

DTN: LL990612704244.098 [147168]

NOTE: The diagram shows vertical slices through block at 0, 1.33, 2.66, 4.0, 5.33, 6.66, and 8.0 m. The top series is an absolute image (baseline, July 2), and the bottom series is the August 19–July 2 difference images.

SOURCE: CRWMS M&O 2000 [154024], Figure 55

Figure 6.13.4-7. Electrical-Resistance Tomography Images of the Test Block Viewed from Test Alcove: Baseline and August Differences

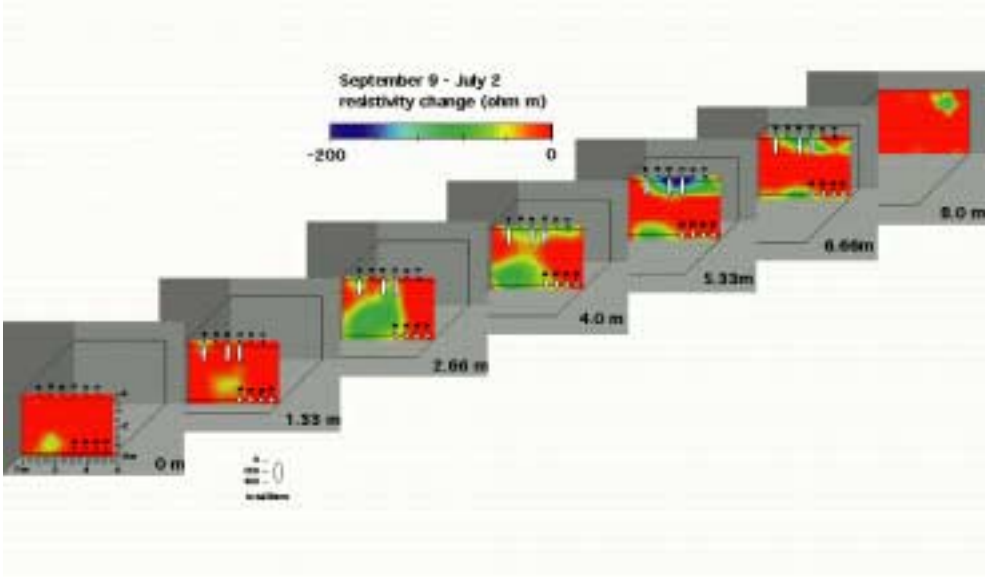

DTN: LL990612704244.098 [147168]

NOTE: The diagram shows vertical slices through the block at 0, 1.33, 2.66, 4.0, 5.33, 6.66, and 8.0 m that represent September 9–July 2 difference images.

SOURCE: CRWMS M&O 2000 [154024], Figure 56

Figure 6.13.4-8. Electrical-Resistance Tomography Images of the Test Block Viewed from Test Alcove: September Differences

7. CONCLUSIONS

Since the inception of the ambient field testing program in 1995 during the excavation of the ESF, progress was made in drift seepage studies in niches, systematic hydrologic characterization, fracture/fault flow tests in alcoves, wetting-front and moisture monitoring along ESF drifts, drift scale infiltration tracer testing, and tracer transport testing at Busted Butte. This AMR focuses on *in situ* field testing of processes. The technical summary and conclusions for analyses in Sections 6.1 through 6.13 are given in Sections 7.1 through 7.13. In brief, the key findings include:

- Seepage thresholds were established for the middle nonlithophysal zone of the TSw, with measured values at Niche 3650 ranging from the borehole flux of 200 mm/yr to 136,000 mm/yr for flow paths through fractures and fracture network. Fracture characteristic curves were derived from the seepage threshold data, with the effective fracture porosity as high as 2.4%. The fracture characteristic curves and effective fracture porosity, derived from seepage thresholds, are applicable for seepage-relevant processes within the test region between the air injection/liquid release point and the niche ceiling (this difference is less than 1 m). The tests were conducted through releases in 0.3 m borehole intervals, representing approximately the width of a flow path observed in the same tuff unit (Figure 6.2.1-1), to quantify seepage processes near the drift ceiling.

- Long-term seepage tests behind sealed bulkheads at Niche 4788 confirmed the seepage results of early short-term transient tests at Niche 3650.

- ECRB Cross Drift Niche 1620 in the lower lithophysal zone of TSw has the characteristics of larger permeability and stronger capillary, as indicated by air-permeability tests and flow-path patterns observed during niche excavation, and to be confirmed by ongoing tests.

- Systematic hydrological characterization along the ECRB Cross Drift through the lower lithophysal zone of TSw quantified the ventilation effects on measured seepage in this heterogeneous unit. The lithophysal cavities are shown to have minor effects on fast flow processes, based on available observations.

- Heterogeneity was systematically evaluated with air-injection tests, with borehole-scale and drift-scale distributions and excavation-induced enhancements of permeability variations orders of magnitude larger than the site-to-site variations of average values along the main drift. In additional to mechanical effects, some of the permeability increases could be related to the intersection of previously dead-ended fractures with the excavated free surface.

- Dyes and nonreactive tracers were confined locally (within 1.0 m × 1.6 m area for the last test in Niche 3650) near the liquid-release points above the niche ceiling from multiple sequences of short-term seepage tests.

- Flow partitioning data with 92% fracture flow and 8% matrix flow were derived from independent analyses of seepage water and dye-stained rock samples. The water front

moved much deeper into tuff matrix than inferred from measurements with nonreactive bromide tracer and sorbing dye tracers.

- Fracture flow paths were spatially heterogeneous and discrete in TSw. Fault zone flow paths and nonwelded tuff layers contributed to the complexity of pneumatic responses in PTn, with an argillic layer dampening the pneumatic responses effectively.

- Fracture flows in TSw were intermittent in nature even when the flow boundary conditions were stable.

- Fault and matrix flows in PTn had large capacities to accommodate damping of infiltration pulses.

- Rock dry-out zones were shown to extend approximately 3 m into the tunnel wall, construction water was detected nearly 10 m below the invert, and large changes in relative humidity conditions could be related to moisture removal by ventilation.

- After over two years of nearly continuous sealing of the last one-third of the ECRB Cross Drift, the rocks have not completely rewetted, based on water-potential measurements in boreholes.

- Wet spots were observed and liquid samples of condensate were collected during entries into sealed sections of the ECRB Cross Drift. The origin of water is attributed to the condensation process, based on limited chemical analyses of relatively clean water collected. The temperature and relative humidity differences needed for condensation and moisture redistribution processes were observed by variations in the in-drift moisture sensors.

- Preliminary infiltration, wetting front detection, and seepage collection data are being collected at the drift-to-drift fault test between Alcove 8 in the ECRB Cross Drift and Niche 3107 in the ESF Main Drift. The tuff interface between the test sites has been confirmed by baseline seismic and ground-penetrating-radar tomographies.

- The unsaturated zone transport test at Busted Butte provided field-scale data of transport properties of the vitric Calico Hills hydrogeological unit and the basal vitrophyre at the tuff interface between Topopah Spring and Calico Hills units. Capillarity was shown to be strong in the vitric Calico Hills, and spatial heterogeneity was shown to affect the transport through the vitrophyre. Sorbing tracers have been shown to move little, based on ongoing data analysis. The plume migration has been evaluated by ongoing mine-back sample analyses and by periodic ground-penetrating-radar tomography.

These findings are inputs to other AMRs and to the UZ Flow and Transport PMR. The AMRs are identified in the following list on the current field status of testing and monitoring activities at different sites in the ESF. The list includes many other laboratory studies on samples collected in the ESF and field studies analyzed in other AMRs.

- Extensive pneumatic air-permeability tests were conducted in borehole clusters before and after niche excavation, and in alcove test beds before liquid releases. The test results

are inputs to CRWMS M&O (2001 [153045]), CRWMS M&O (2000 [145771]), and CRWMS M&O (2001 [154291]).

- Niche 3566, in the vicinity of the Sundance fault, was sealed for over two years. The first damp feature in the potential repository horizon was observed in this niche.

- Niche 3650, in a fractured setting away from faults, had over 40 liquid-release tests conducted to quantify seepage thresholds. The core samples from the latest test were analyzed for tracer distribution. The test results are inputs to CRWMS M&O (2001 [153045]), CRWMS M&O (2000 [145771]), and CRWMS M&O (2000 [122797]).

- Niche 3107 in a relatively uniform rock mass, below the cross-over point between the ESF Main Drift and Cross Drift, is the site of ongoing drift-to-drift fault tests for matrix diffusion and active fracture model calibration and validation.

- Niche 4788, in an intensely fractured zone, has phases of pre- and post-excavation characterization and several long-term seepage testing sequences completed.

- Systematic hydrological characterization along the ECRB Cross Drift provided the first data set for the seepage calibration model (CRWMS M&O 2001 [153045]) in the lower lithophysal zone of TSw, quantified the ventilation effects along the open drift, and provided observations of heterogeneity controls by fractures and lithophysal cavities.

- Alcove 6, in a fractured zone with relatively competent matrix blocks, has been used for a preliminary series of tests, with water dripped into a slot below the test bed collected. The test results can be used to compare with the fracture flow fractions predicted by CRWMS M&O (2000 [122797]).

- Alcove 4, in a layered zone with a fault bounded by porous PTn, has been used for a preliminary series of tests, with a new series of tests planned to evaluate the migration of injected water. The test results can be used to evaluate the lateral diversion at the PTn addressed by CRWMS M&O (2000 [122797]).

- Alcove 1, 30 m below the ground surface near the North Portal in the Tiva Canyon welded tuff unit, is the site for the largest liquid-release tests at the ESF. The test results from two series of flow and tracer tests are analyzed in CRWMS M&O (2000 [122797], Section 6.8.1). Matrix diffusion is shown to be important in diluting the tracer concentration and reducing the tracer breakthrough at the Alcove 1 test site.

- Water-potential measurements with heat dissipation probes, with psychrometers, and with tensiometer are conducted in ESF boreholes at alcoves, at niches, and systematically along the ECRB Cross Drift. The results of potential data from ECRB are inputs to CRWMS M&O (2000 [144426]).

- Construction-water migration was monitored at the starter tunnel of the Cross Drift and below the cross-over point. Data on the distributions of lithium bromide tracers from

boreholes drilled into the drift floor (invert) are inputs to the Yucca Mountain site description document.

- Chloride-36, chloride, calcite, strontium, and other geochemical analyses are reported in CRWMS M&O (2001 [154874]) and CRWMS M&O (2001 [154024]). The uses of geochemistry and transport properties data for model calibration and validation are reported in CRWMS M&O (2000 [122797]) and CRWMS M&O (2000 [144331]).

- Moisture-monitoring stations continue to collect data to evaluate the impact of tunnel ventilation and moisture removal.

- Condensation observed in the sealed sections of the ECRB Cross Drift provides additional insights for in-drift redistribution of moisture under thermal and relative humidity variations.

- Busted Butte transport test data were reported in CRWMS M&O (2001 [154024]) with updates of Phase 2 results of plume migration from direct mineback and periodic ground-penetrating-radar tomography included in this AMR.

The ambient testing program has evolved from an initial focus on the middle nonlithophysal zone of TSw to the lower lithophysal zone of TSw, and to both the PTn above the repository horizon and CHn below the potential repository horizon. The tests confirm, validate, refine, or refute existing and alternative conceptual models for seepage into drifts, fracture flow, fracture-matrix interaction, and drainage and migration below the potential repository. With most of the potential repository horizon in the lower lithophysal unit of the TSw, it is critical to characterize this unit to determine if the presence of lithophysal cavities and friable tuff media change the seepage distributions and percolation characteristics. The seepage-threshold quantification is being confirmed with long-term tests to address the concerns about the capillary-barrier concept under steady-state conditions, the effects of evaporation, and the effects of moisture storage and flow-diversion capacities. Quantification of spatial distribution of fast flow paths and assessment of temporal variations of episodic percolation events require testing and monitoring refinements for *in situ* conditions.

The emphasis of this AMR is on active-flow testing in niches and alcoves. These activities, together with many other laboratory and field activities analyzed in other AMRs, provide data for inputs to other modeling AMRs and to the UZ flow and transport model for process evaluation, calibration, and validation. Since different activities and analyses for *in situ* field testing in processes are in different stages of progress, the summaries of test analyses presented in the following ten sections are in different degrees of maturity. Section 7.n is the summary of data analyses in Section 6.n, with n = 1, ..., 13. The data are summarized with minimal speculative interpretations. Credible interpretations can be achieved with close interactions between testing and modeling, as documented in the AMRs cited, and on an activity-by-activity basis.

This AMR may be affected by technical product input information that requires confirmation. Any changes to this AMR that may occur as a result of completing the confirmation activities

will be reflected in subsequent revisions. The status of the technical product input information quality may be confirmed by review of the DIRS database.

7.1 SUMMARY AND CONCLUSIONS OF AIR-PERMEABILITY DISTRIBUTION AND EXCAVATION-INDUCED ENHANCEMENT IN NICHES

Using the pneumatic packer system developed with automated controls and data acquisition, extensive series of air-permeability tests were systematically conducted in borehole clusters at four niches. Single-hole permeability data has proven its use in detecting changes in permeability (and boundary conditions) as a result of nearby excavation and in characterizing sites. Pre-excavation and post-excavation permeability profiles with 0.3 m spatial resolution are presented for boreholes used for drift-seepage and liquid-release tests. Air-permeability distributions are used as inputs for the seepage calibration model (CRWMS M&O 2001 [153045]) to assess the capillary-barrier and seepage-threshold mechanisms. Fractures immediately above the niches are important to the evaluation of seepage into drifts. The main results from air-permeability profile and distribution analyses are:

- The excavation-induced permeability enhancements in borehole intervals are large, with an average enhancement for boreholes of one to two orders of magnitude.

- Drift-scale variation of permeability values and permeability enhancement along boreholes and among different boreholes within the niches are larger than differences among different niche sites.

It is important in drift-scale assessment to characterize the permeability distributions controlling local flow path and seepage spatial variation. The results quantify the spatial variability associated with formation heterogeneity in fractured tuff. The relatively small difference in mean permeability values for different niches is encouraging in the reduction of uncertainties associated with site-scale spatial heterogeneity. If subsequent liquid-seepage tests in locally distinct niches result in seepage-threshold values within a relatively narrow range, the uncertainties for seepage into drifts could be greatly reduced for the middle nonlithophysal unit of TSw, where all existing niches were located. The characterization effort is planned for the lower tuff units to acquire the necessary data for the majority of the potential repository horizon area.

DTN: LB0110AIRK0015.001 is technical product output from the analysis presented in Section 6.1 of this AMR.

7.2 SUMMARY AND CONCLUSIONS OF LIQUID-RELEASE AND SEEPAGE TESTS IN NICHES

7.2.1 Pre-Excavation Liquid-Release Testing and Niche Excavation Activities

Numerous liquid-release tests were conducted prior to the excavation of each niche to evaluate how far a finite pulse of water would travel through relatively undisturbed fractures located in the middle nonlithophysal zone of the TSw. Similar tests were conducted in the lower

lithophysal zone of the TSw to identify the difference in capillary strengths between these two major potential repository host rocks.

The maximum depth that the wetting front moves, increases with increasing mass of fluid injected. It appears that maximum-depth data cannot discriminate the type of flow (i.e., high-angle fracture versus network flow) observed during the test. Lateral spreading and the aspect ratio (i.e., ratio of depth to lateral spreading) may be stronger measures of the type of flow that predominates. Increased lateral spreading of the wetting front appears to be typical of well-connected fracture networks containing both high- and low-angle fractures, whereas large aspect ratios appear to be typical of flow in individual vertical fractures.

- The middle nonlithophysal zone is dominated by gravity, with large aspect ratios observed in most flow paths.

- The lower lithophysal zone has some flow paths with symmetric patterns, indicating potential strong capillarity in spreading the plumes.

DTN: LB0110LIQR0015.001 and LB0110NICH4LIQ.001 are technical product outputs from the analyses presented in Section 6.2.1 of this AMR.

7.2.2 Post-Excavation Seepage Tests at Niche 3650 and Niche 4788

The purpose of the seepage tests was to investigate the amount of water that would drip into a mined opening from a transient liquid-release event of short duration.

- Forty post-excavation liquid-release tests were conducted on 16 different test intervals located above Niche 3650 within the middle nonlithophysal zone of the Topopah Spring welded unit.

- Of the 16 zones tested, water seeped into the capture system from 10 intervals, water appeared at the niche ceiling but did not drip in 3 cases, and water did not appear at all when introduced into the three remaining zones.

- The seepage percentage, defined as the amount of water captured in the niche divided by the amount released into the rock, ranged from 0 to 56.2%.

It was determined during the early stages of testing that the memory effect, or wetting history, had a profound impact on seepage. If the liquid-release tests were performed too close together in time, then it was found that the seepage percentage increased dramatically, as one would expect. This is because the fractures contained residual moisture, and their unsaturated conductivity was higher during subsequent tests. The test with seepage percentage of 56.2%, the third test in a series of four tests in the same interval, was conducted within 2 hours after the second test with 23.2% seepage. In comparison, the first test conducted 20 days before the second test had a fairly consistent result of 22.6% seepage.

The seepage-threshold flux, defined as the flux of water that when introduced into the injection borehole results in zero seepage, was evaluated for the 10 zones that seeped in Section 6.2.2.1.

- The seepage-threshold fluxes measured at Niche 3650 range from 6.35E-09 to 4.31E-06 m/s or 200 to 136,000 mm/yr.

- The seepage-threshold data were evaluated and interpreted using analytical techniques derived for a homogenous, unsaturated porous medium derived by Philip et al. (1989) subject to the limiting assumptions discussed in Section 5.2.2.

Two types of flow paths were observed in the field during the mining operation, as described in Section 6.2.1.2. Estimates of the volumetric water content were produced in Section 6.2.2.3 using wetting-front arrival times recorded during the seepage tests. The α-values resulting from the analyses performed in Section 6.2.2.2 were used to estimate the water potentials of the fractures reported in Section 6.2.2.4. Water-potential estimates and the corresponding volumetric water contents were used to construct the fracture-water retention curves presented in Section 6.2.2.5. Examination of these plots indicates that:

- Fractures appear to drain very quickly, approaching a residual water content as low as 0.1 to 0.2% (Figure 6.2.2-3).

- Saturated water content or effective fracture porosity may be as high as 2.4%.

The approach of using short-term tests at Niche 3560 in ventilated conditions was replaced by long-term tests at both Niche 3107 and Niche 4788 under controlled high-humidity conditions. The series of Niche 4788 tests was more complete and was used by the seepage calibration model (CRWMS M&O 2001 [153045]) to calibrate and validate the model. The analytic solution approach presented in this AMR indicated that

- The seepage thresholds determined by the long-term tests are comparable to the seepage thresholds determined by short-term tests.

7.2.3 Constraints, Caveats, and Limitations of the Niche Seepage Test Results

The seepage test results at Niche 3566, including the determinations of the seepage thresholds, are based on multiple liquid-release tests conducted over short duration, with some of the rates high enough to induce artificial seepage. The tests were conducted in open-niche conditions with the humidity affected by the ventilation in the tunnel. The effects of evaporation can remove water from the rock through the vapor phase and may reduce the liquid seepage flux in determining the seepage threshold.

The tests at other niches are conducted over longer test periods, with some at lower release rates and under better control of ventilation and humidity effects. The same approaches will be used in tests at the lower lithophysal TSw unit. The constraints, caveats, and limitations of the currently available seepage test results in the middle nonlithophysal TSw unit should be carefully evaluated to assess their applicability in future use. The intended use of niche test data is for seepage process evaluation.

7.3 SUMMARY AND CONCLUSIONS OF TRACER-MIGRATION DELINATION AT NICHE 3650

Tracer distribution in cores after a liquid-release event at Niche 3650 was analyzed. The results of multiple sequences of short-term seepage tests showed that:

- The tracer migration from the latest test was localized and possibly confined within the 1.0 m × 1.6 m area directly below the liquid-release interval, with a vertical scale of about 0.7 m. This result is based mainly on analyses of iodine as a conservative tracer.

- Spatial distributions of other dye tracers resulting from early liquid-release tests consistently point to localized flow with limited lateral spreading of tracer migration. The previous liquid release and seepage tests with dyes were conducted over six months before the latest test.

Liquid-release tests reported in Section 6.2 indicated that post-excavation seepage water was captured in most cases directly beneath the test zone or in capture cells immediately adjacent to the interval. Flow-path observations during niche excavations generally showed that the dyes did not spread laterally to great extents (also see Section 6.2 and preliminary results of Niches 3566 and 3650 reported in Wang et al. 1999 [106146], pp. 329–332). Gravity-driven flow is the primary flow mechanism in fracture systems, either through individual fractures and/or through the fracture network connected to the release intervals. In Section 6.4 of this report, further laboratory tests of tracer sorption and fracture-matrix interactions are presented.

The absence of nonreactive tracers, especially iodine (introduced only at the latest pulse release), together with the localized spatial distributions of dyes long after the liquid releases, strongly suggested that the gravity-driven component was strong. Capillary imbibition and capillary barrier effects could promote lateral spreading. Longer-term tests with sampling over larger areas than the latest pulse test, as well as early liquid-release tests, could further quantify the migration and retention of tracers. Tracer-test results could be used to investigate the occurrence and significance of localized flow and to assess the mechanisms governing contaminant transport.

7.4 SUMMARY AND CONCLUSIONS ON TRACER PENETRATION AND WATER IMBIBITION INTO WELDED TUFF MATRIX

Field and laboratory tracer experiments have been conducted to investigate the flow partitioning between fracture flow and matrix imbibition in unsaturated conditions. During niche excavation, dye-stained rock samples were collected for laboratory analyses. Additional tuff samples collected from the potential repository horizon were machined as rock cores for laboratory studies of tracer penetration into the rock matrix under two initial water saturations. In the drift seepage tests using dye tracers, seepage-water samples were collected. A rock-drilling and sampling technique was developed to profile the tracer concentration in the rock matrix over distance.

- For rock samples, the sorbing dye-tracer penetration depths are on the order of several millimeters from the flowing fractures.

- In well-controlled laboratory tracer-imbibition tests under both high and low initial water saturations, the concentration profiles of sorbing dyes lag behind the nonreactive bromide front, with the travel distance for dyes being a few millimeters over the contact time of about 18 hours.

- The bromide front lags significantly behind the moisture front at high initial water saturation of 75.8%. The front is comparable to the moisture front in the rock core at the initial water saturation of 12.5%.

- Retardation of sorbing tracers increases with a decrease in saturation, as measured in the dry core and in the wet core, verifying the functional relationship between retardation and water content.

- Core measurements can be used to measure retardation factors in *in situ* conditions to check the results of batch experiments using crushed tuff in saturated conditions.

- The flow partitioning data with 92% fracture flow and 8% matrix imbibition were derived independently from seepage water sampled in drift seepage tests conducted after niche excavation and laboratory analyses of dye-stained samples collected during niche excavation.

Data presented in Section 6.4 revealed interesting processes, especially at the interface boundary region between the core bottom and the water reservoir, simulating the contact of flowing fracture with adjoining tuff matrix. Data of flow partitioning, front separation, and tracer retardation can be used for validation of fracture-matrix interaction and fracture flow models.

7.5 SUMMARY AND CONCLUSIONS OF SINGLE-HOLE PERMEABILITY DISTRIBUTIONS AND CROSSHOLE CONNECTIVITY ANALYSES

Crosshole analyses of pneumatic air-permeability test data are presented for Niche 4788, Alcove 6, and Alcove 4. Crosshole connectivity analyses for Niche 4788 are used in the seepage tests in this intensely fractured zone. The pneumatic air-permeability test results were used for interval selection and test interpretation in the series of tests conducted for fracture flows and fracture-matrix interactions in TSw at Alcove 6 and for fault and matrix flows in PTn in Alcove 4. The main results from permeability distribution and crosshole analyses are:

- Welded-tuff test sites have distinct flow paths clearly identified by crosshole analyses from isolated injection intervals to observation intervals.

- The fracture flow connections are predominately one-way, with an injection interval inducing response in an observation interval, but the interval not necessarily detecting injection into the original observation interval.

- The PTn test bed in Alcove 4 has many more connections than the corresponding TSw sites in niches and in Alcove 6. Weaker connections were trimmed out to reveal the stronger connections.

- The argillic layer in the test bed was shown from crosshole analyses to be a nearly impermeable barrier.

- Stronger connections were associated with a fault in the test bed at Alcove 4. A high-permeability zone near the end of the test block was identified by the air-permeability results and crosshole analyses.

7.6 SUMMARY AND CONCLUSIONS OF FRACTURE FLOW IN FRACTURE-MATRIX TEST BED AT ALCOVE 6

Fracture flow data were collected in a slotted test bed located at Alcove 6 of ESF within the TSw. With a slot below injection zones, it was possible to quantify both the inflow into the system and outflow at the lower boundary, and to better evaluate the flow field in underground test conditions.

In this field study, techniques developed to investigate flow in fractured welded tuffs were evaluated. Results from field tests suggest that *in situ* characterization of certain fundamental flow parameters (such as travel times, percolation, and seepage rates) can be achieved with this approach.

The test results revealed aspects of flow in unsaturated, fractured systems and provided insight towards the conceptualization of flow through unsaturated and fractured rock formations. The Alcove 6 test is the first and only test conducted in the ESF on unsaturated fractured tuff with attempts to take liquid mass conservation explicitly into account. In field tests, it is frequently difficult to control the boundaries and liquid can flow to unknown domains. Transient data collected at Alcove 6 also contribute to the evaluation of unsaturated flow in fractured tuffs. Some of the test result interpretations require additional analyses and modeling. The main focus currently is to present the data and to stimulate credible, not speculative, interpretations.

Several series of liquid-release tests were conducted with localized injections of liquid into a low permeability zone and into a high permeability zone along a borehole. The major test results were:

- For all injections into both LPZ and HPZ, changes in electrical resistance and psychrometer readings were detected in two monitoring boreholes ~0.6 m below the point of injection.

- For the LPZ tests, water did not seep into the slot located 1.65 m below.

- Liquid-release rate into the LPZ was observed to steadily decrease by two orders of magnitude (from >30 to < 0.1 ml/minute) over a period of 24 hours.

- In the HPZ, liquid-release rates under constant-head conditions were significantly higher (~100 ml/minute), with intermittent changes observed in the intake rate.

- For injection tests in HPZ, water was observed to drip into the slot in 3 to 7 minutes at high injection rates of ~28 to ~100 ml/min, in 1 hour at the low injection rate of 14 ml/min, and in 5 hours at the lowest rate of 5 ml/min.

- During the course of each test, seepage rates measured in the slot showed intermittent responses despite constant-head or constant-rate conditions imposed at the input boundary.

- The percentage of cumulative volume of water recovered in the slot was observed to increase in most tests, approaching steady-state values after ~10 liters of water had been injected.

- A maximum of 80% of the injected water was recovered for high-rate injection tests.

- The saturated volumes of fracture flowpaths were estimated for each test from measurements of fluid volume before wetting front arrivals and from measurements of drainage volume into the slot after termination of injection. The flowpath volumes were found to increase from <0.2 liter initially to ~1.0 liter during recovery, with some stepped increments of 0.1 to 0.3 liter observed.

- Plug-flow process was observed with tracer analyses. "New" water replaced "old" water from the previous test.

The stepped and intermittent changes could be associated with heterogeneous distribution of storage volumes in the connected fracture flow paths, in the dead-end fractures, and in the rock matrix blocks. The test results from Alcove 6 could be used to evaluate fracture flows and fracture-matrix interactions.

7.7 SUMMARY AND CONCLUSIONS OF FLOW THROUGH THE FAULT AND MATRIX IN THE TEST BED AT ALCOVE 4

Fault and matrix flow data were collected in a test bed located in the PTn at Alcove 4 in the ESF. Using a series of horizontal boreholes, the intake rates and plume travel times in various locations within the test bed were determined.

These test results revealed aspects of flow in a fault located within the nonwelded tuffs and provided insights into the flow properties of the PTn. A series of localized liquid-release tests helped determine that:

- Intake rates within a fault located in the PTn decreased as more water was introduced into the release zone (i.e., from an initial value of ~200 ml/min to ~50 ml/min after 193 liters of water entered the injection zone).

- The travel time of the wetting front resulting from water released in the fault decreased when the fault was wet (i.e., in closely timed tests, the plume traveled faster in subsequent releases).

- Over time, the hydrologic properties of the fault appear to be altered, with water traveling along the fault at significantly slower rates.

- The matrix adjacent to the fault imbibed water that was introduced into the fault. Changes in saturation were seen more than 1.0 m from the point of release.

- The intake rates and wetting front travel times in the matrix were significantly slower than in the fault. Water released into the matrix was observed to travel 0.45 m in 14 days.

7.8 SUMMARY AND CONCLUSIONS OF WATER-POTENTIAL MEASUREMENTS IN THE NICHES

Psychrometer measurements in the ESF suggest that significant variability in water potentials between and within the three niches. The main observations are:

- The extent to which ventilation effects may have penetrated the rock is possibly greater than 3 m.

- Two possible zones were observed to have significantly high water potentials in Niche 3566. The first was observed at the end of the middle borehole. The second was detected 6.25 m along borehole A in Niche 3566. Borehole A was drilled from the niche toward the Sundance fault.

- There was large variability (-15 and -84 m) in the short distance of 0.9 m between two boreholes at Niche 3107.

- In the zone beyond where ventilation effects of the ESF were observed (i.e., at 10 m depths), Niche 3566 (with potential 0.4 to –13 m) appeared to be wetter than Niche 3650 (with potential –1 to –39 m).

These potential measurements were conducted before the bulkhead closed in Niche 3566 and before seepage measurements in Niches 3650 and 3107. The data are presented for future comparisons with potential measurements elsewhere in the ESF, including the Cross Drift.

7.9 SUMMARY AND CONCLUSIONS OF MONITORING THE CONSTRUCTION-WATER MIGRATION

The sensors in a borehole below the starter tunnel of the Cross Drift detected signals associated with wetting-front migration. No seepage was observed in the ESF Main Drift at the cross-over point. The specific observations are

- At the starter tunnel, three events were observed along the borehole below the starter tunnel at depths close to 10 m. The ponding event that occurred on March 8, 1998 increased water-potential values up to a depth of 8.65 m (17.3 m along the borehole). During this event, the magnitude of the disturbance decreased further into the borehole, with an interesting aberration observed at a depth of 9.4 m: the change in water potentials was significantly larger than the expected trend.

- At different times during the monitoring period, the impact on changes in water-potential values occurred at different locations along the borehole. Early in March 1998, the large impact was restricted to close to the borehole collar, while by early April, 1998, this impact was relatively larger—between 9.4 and 11.4 m.

- One concern that could arise from the use of a slanting borehole to measure wetting-front migration is the possibility of the bore cavity short-circuiting flow paths. For this particular investigation, this short-circuiting does not appear to be happening, as indicated by the analysis of recovery responses observed at the depth of 5.2 m. Here, the response to a wetting event was negligible when compared with other psychrometers close to this location (above and below), suggesting that this zone was well isolated (hydraulically) from the adjacent zones and did not detect the wetting front.

- The response of the electrical resistivity probes when compared with the performance of psychrometers suggests that these probes (with their current design) can be effectively used as a qualitative tool to detect the arrival (or departure) of wetting fronts. Unlike psychrometers, these probes are relatively inexpensive, easy to maintain, and have a low failure rate. These advantages make them particularly useful for extensive down-hole monitoring applications in fractured-rock environments such as found at Yucca Mountain.

- At the cross-over point, no seepage was observed, nor were wetting-front signals detected at the cross-over point when the Cross Drift TBM passed over the ESF Main Drift. The TBM apparently did not use enough water to induce dripping into the Main Drift, 17.5 m below. The confirmation of no seepage at the cross-over point establishes the lower limit for the drift-to-drift flow and drift seepage processes associated with construction-water usage.

In the potential repository at Yucca Mountain, performance-confirmation drifts are planned to be located above (or below) the waste emplacement drifts to monitor the waste-induced impacts. It is therefore important to evaluate the drift-to-drift migration, drift seepage, and wetting-front detection to assess the potential impacts. The experience in the integrated monitoring station at the cross-over point (with seepage collection trays, water-potential and wetting-front sensors, and thermal/visual imaging devices) can be applied to future testing and monitoring tasks.

7.10 SUMMARY AND CONCLUSIONS OF ANALYSES OF CONSTRUCTION EFFECTS

Some observations of ESF moisture conditions are presented. From the observations:

- The newly excavated drift has high humidity conditions detected near the TBM.

- The relative humidity gradient near the end of the tunnel was greater than the gradient close to the entrance in the month after the excavation.

In the ongoing moisture study of bulkheaded sections in the ECRB Cross Drift, observations were as follows:

- Water-potential measurements in boreholes suggest that the formation (in tuff matrix) is still relatively dry up to a depth of 0.5–1.0 m.

- Moisture conditions (relative humidity and temperature) respond to bulkhead entries and TBM power fluctuations relatively quickly.

- Wet spots were observed and liquid water was collected in sections, with the water likely originating from condensation, based on chemical analyses of clean water collected. Isotopic signatures indicate that water collected has undergone an evaporation shift.

7.11. SUMMARY AND CONCLUSIONS OF SYSTEMATIC HYDROLOGICAL CHARACTERIZATION ALONG ECRB CROSS DRIFT

Hydrological characterization of the lower lithophysal zone of the Topopah Spring welded tuff unit has been initiated in the ECRB Cross Drift, using the systematic approach of testing at regular intervals. Data and analyses from several sets of completed tests performed in two low-angle boreholes are presented in the Section 6.11. The results to date indicate that:

- Small fractures (less than 1-m in length) are well connected, giving rise to air-permeability values on the order of 10^{-11} m^2. The connected fractures probably constitute the main contribution to fast paths for liquid flow.

- In the transient process of establishing the fast paths between the water release (at a vertical distance ranging from 1 to 5 meters above the drift) to the drift ceiling, some water imbibes into the rock matrix and some seeps into the lithophysal cavities. Out of the available storage porosity of 0.125 of the lithophysal cavities, about 20% to 50% participates in taking in water introduced when the rate of injection is tens of milliliters per minute. When the water-release rate is an order of magnitude higher, water flow occurs mainly in the fractures, having little participation from the matrix or lithophysal cavities during the time period it takes to intersect the drift.

- Under steady-state conditions, water introduced from one to several meters above the drift flows down toward the drift not in a uniform plume, but in preferential paths. A fraction of the water would miss the drift because of nonuniform flow from fracture heterogeneity, and a fraction of water would be diverted around the drift because of capillary effects. The former component of nonintersecting flow is controlled by geometry and is likely independent of the water-release rate. Data to date show that of the volume of water introduced, about half is noninteresecting and never enters into the drift.

- An estimate is made of the injection rate (from a borehole of a given area at a given distance above the drift) below which there is no seepage into the drift. Based on the discussion in Section 6.11.3.3 for borehole LA1, we arrive at a value of 15 ml/min for a projected borehole area of 0.13 m^2 at an average height of 1.3 m above the drift.

- Because of the low humidity inside the Cross Drift, and because of the drift ventilation system, effects of evaporation must be considered in interpreting seepage data from systematic testing. Relative humidity measurements and open-pan evaporation measurements were incorporated into the systematic-testing equipment system, following

the completion of the first set of tests (when the significance of evaporation was first noted).

The fully automated feature of the systematic-testing equipment has served investigators well. There were some prolonged periods when field problems with the ventilation system prevented the physical presence of investigators who were relying exclusively on being able to control the test from off-site.

As for all field-testing programs, the initial sets of measurements revealed many unforeseen items that provide insight into modification and improvement of the equipment system and testing protocol. Systematic testing is at a stage where all major experimental problems have been worked out, and it is anticipated that continual testing in many locations at regularly spaced intervals along the Cross Drift will proceed. Such testing will be productive in providing hydrological characteristics of the heterogeneous lower lithophysal unit.

DTN: LB0110SYST0015.001 is technical product output from the analysis presented in Section 6.11 of this AMR.

7.12 SUMMARY AND CONCLUSIONS OF DRIFT-TO-DRIFT TEST BETWEEN ALCOVE 8 AND NICHE 3107

From preliminary stages in the Fault tests in Alcove 8-Niche 3107, we have obtained early test data that describes the response of the system to releases of water under constant-head conditions. Specifically:

- Infiltration rates along the fault reached quasi-steady state conditions ~45 days after water was introduced to the infiltration zones, and the infiltration rates varied at different locations along the fault.
- Observations of saturation changes in borehole 10 indicate the velocity of the wetting front vertically along the fault to be ~0.58 m/s (i.e., 20 m traveled in 34 days).
- Seepage observations indicate that quasi-steady state conditions may have been reached two months after the initial releases into the fault.
- Radar data collected thus far in support of the Alcove8—Niche 3107 infiltration experiment suggests that this method is appropriate for investigating subsurface anomalies that may be related to moisture migration.

7.13 SUMMARY AND CONCLUSIONS OF BUSTED BUTTE UNSATURATED ZONE TRANSPORT TEST

The Unsaturated Zone Transport Test at Busted Butte was designed to address uncertainties associated with flow and transport in the UZ site-process models for Yucca Mountain. The UZTT is comprised of three tightly integrated efforts: the field test, a parallel laboratory program, and assessment and validation of computational models used for site Performance Assessment. This document presents the results, to date, of the field test and associated laboratory analyses. The model assessment and validation is reported in U0100 AMR.

The design of the UZTT began in 1997. Injection of tracers for Phase 1 began in April 1998, and Phase 2 injection was completed in October 2000. The mineback excavation of Phase 2 continued in 2001. Results to date provide important information for the unsaturated zone transport performance of Calico Hills hydrologic units of Yucca Mountain, with the following key conclusions:

- Flow and transport in the Calico Hills hydrologic units (Tac and Tptpv1) is strongly capillary dominated, as observed from fluorescein distributions in the Phase 1A test.
- Fractures at Busted Butte do not act as fast flow paths, as observed in Phase 1A. However, they appear to play a role as a barrier or permeability contrast boundary.
- Heterogeneity appears to have a significant effect on flow, as observed in Phase 1A for layer contact and in Phase 2 for fault.
- Breakthrough times of nonreactive bromide are approximately linear with travel distance.
- Sorption can delay chemical transport, as shown from the breakthrough curves of lithium.

8. INPUTS AND REFERENCES

The following is a list of the references cited in this document. Column 1 represents the unique six digit numerical identifier, which is placed in the text following the reference callout (e.g., CRWMS M&O 2000 [144054]). The purpose of these numbers is to assist the reader in locating a specific reference. Within the reference list, multiple sources by the same author (e.g., CRWMS M&O 2000) are sorted alphabetically by title.

8.1 CITED DOCUMENTS

106071 Andreini, M.S. and Steenhuis, T.S. 1990. "Preferential Paths of Flow Under Conventional and Conservation Tillage." *Geoderma, 46*, 85-102. Amsterdam, The Netherlands: Elsevier Science Publishers B.V. TIC: 245381.

100029 Barr, D.L.; Moyer, T.C.; Singleton, W.L.; Albin, A.L.; Lung, R.C.; Lee, A.C.; Beason, S.C.; and Eatman, G.L.W. 1996. *Geology of the North Ramp —Stations 4+00 to 28+00, Exploratory Studies Facility, Yucca Mountain Project, Yucca Mountain, Nevada*. Denver, Colorado: U.S. Geological Survey. ACC: MOL.19970106.0496.

156269 Bear, J. 1972. *Dynamics of Fluids in Porous Media*. Environmental Science Series. Biswas, A.K., ed. New York, New York: Elsevier. TIC: 217356.

155682 Bouwer, H. 1966. "Rapid Field Measurement of Air Entry Value and Hydraulic Conductivity of Soil as Significant Parameters in Flow System Analysis." *Water Resources Research, 2*, (4), 729-738. [Washington, D.C.]: American Geophysical Union. TIC: 225260.

106088 Braester, C. 1973. "Moisture Variation at the Soil Surface and the Advance of the Wetting Front During Infiltration at Constant Flux." *Water Resources Research, 9*, (3), 687-694. Washington, D.C.: American Geophysical Union. TIC: 242383.

107386 Broxton, D.E.; Chipera, S.J.; Byers, F.M., Jr.; and Rautman, C.A. 1993. *Geologic Evaluation of Six Nonwelded Tuff Sites in the Vicinity of Yucca Mountain, Nevada for a Surface-Based Test Facility for the Yucca Mountain Project*. LA-12542-MS. Los Alamos, New Mexico: Los Alamos National Laboratory. ACC: NNA.19940224.0128.

154874 BSC (Bechtel SAIC Company) 2001. *Analysis of Geochemical Data for the Unsaturated Zone*. ANL-NBS-HS-000017 REV 00 ICN 01. Las Vegas, Nevada: Bechtel SAIC Company. ACC: MOL.20010405.0013.

154622 BSC (Bechtel SAIC Company) 2001. *Geologic Framework Model Analysis Model Report*. MDL-NBS-GS-000002 REV 00 ICN 02. Las Vegas, Nevada: Bechtel SAIC Company. ACC: MOL.20010313.0505.

155051 BSC (Bechtel SAIC Company) 2001. *Technical Work Plan for Unsaturated Zone (UZ) Flow and Transport Process Model Report.* TWP-NBS-HS-000001 REV 01. Las Vegas, Nevada: Bechtel SAIC Company. ACC: MOL.20010404.0007.

157053 BSC (Bechtel SAIC Company) 2001. *Technical Work Plan for: Subsurface Performance Testing For License Application (LA) For the Fiscal Year 2001*. TWP-EBS-MD-000009 REV 03. Las Vegas, Nevada: Bechtel SAIC Company. ACC: MOL.20010628.0246.

157107 BSC (Bechtel SAIC Company) 2001. *Technical Work Plan for: Unsaturated Zone Flow, Transport, and Coupled Processes Process Model Report.* TWP-NBS-HS-000003 REV 00. Las Vegas, Nevada: Bechtel SAIC Company. Submit to RPC URN-0987

156609 BSC (Bechtel SAIC Company) 2001. *Unsaturated Zone Flow Patterns and Analysis*. MDL-NBS-HS-000012 REV 00. Las Vegas, Nevada: Bechtal SAIC Company. ACC: MOL.20011029.0315.

101433 Buesch, D.C. and Spengler, R.W. 1998. "Character of the Middle Nonlithophysal Zone of the Topopah Spring Tuff at Yucca Mountain." *High-Level Radioactive Waste Management, Proceedings of the Eighth International Conference, Las Vegas, Nevada, May 11-14, 1998*. Pages 16-23. La Grange Park, Illinois: American Nuclear Society. TIC: 237082.

100106 Buesch, D.C.; Spengler, R.W.; Moyer, T.C.; and Geslin, J.K. 1996. *Proposed Stratigraphic Nomenclature and Macroscopic Identification of Lithostratigraphic Units of the Paintbrush Group Exposed at Yucca Mountain, Nevada*. Open-File Report 94-469. Denver, Colorado: U.S. Geological Survey. ACC: MOL.19970205.0061.

131513 Bussod, G.Y.; Coen, K.; and Eckhardt, R.C. 1998. *LA Testing Status Report: Busted Butte Unsaturated Zone Transport Test FY 98*. SPU85M4. Los Alamos, New Mexico: Los Alamos National Laboratory. TIC: 246363.

155695 Bussod, G.Y.; Turin, H.J.; and Lowry, W.E. 1999. *Busted Butte Unsaturated Zone Transport Test: Fiscal Year 1998 Status Report*. LA-13670-SR. Los Alamos, New Mexico: Los Alamos National Laboratory. TIC: 250657.

156902 Cook, P. 2001. Drift Scale Seepage Test. Scientific Notebook YMP-LBNL-JSW-PJC-6.2. ACC: MOL.20011105.0080.

156876 CRWMS M&O (Civilian Radioactive Waste Management System Management and Operating Contractor) 1999. *Exploratory Studies Facility, Cross Drift Alcove #8 Plan and Sectio*ns. BABEAF000-01717-2100-40312 REV 00. Las Vegas, Nevada: CRWMS M&O. ACC: MOL.19990608.0041.

145771 CRWMS M&O 2000. *Analysis of Hydrologic Properties Data*. ANL-NBS-HS-000002 REV 00. Las Vegas, Nevada: CRWMS M&O. ACC: MOL.19990721.0519.

144426 CRWMS M&O 2000. *Calibrated Properties Model*. MDL-NBS-HS-000003 REV 00 Las Vegas, Nevada: CRWMS M&O. ACC: MOL.19990721.0520.

141187 CRWMS M&O 2000. *Conceptual and Numerical Models for UZ Flow and Transport*. MDL-NBS-HS-000005 REV 00. Las Vegas, Nevada: CRWMS M&O. ACC: MOL.19990721.0526.

138860 CRWMS M&O 2000. *Geologic Framework Model (GFM3.1).* MDL-NBS-GS-000002 REV 00 ICN 01. Las Vegas, Nevada: CRWMS M&O. ACC: MOL.20000121.0115.

141400 CRWMS M&O 2000. *In Situ Field Testing of Processes*. ANL-NBS-HS-000005 REV 00. Las Vegas, Nevada: CRWMS M&O. ACC: MOL.20000504.0304.

138960 CRWMS M&O 2000. *Mineralogical Model (MM3.0).* MDL-NBS-GS-000003 REV 00 ICN 01. Las Vegas, Nevada: CRWMS M&O. ACC: MOL.20000120.0477.

144331 CRWMS M&O 2000. *Radionuclide Transport Models Under Ambient Conditions.* MDL-NBS-HS-000008 REV 00. Las Vegas, Nevada: CRWMS M&O. ACC: MOL.19990721.0529.

153314 CRWMS M&O 2000. *Seepage Model for PA Including Drift Collapse*. MDL-NBS-HS-000002 REV 01. Las Vegas, Nevada: CRWMS M&O. ACC: MOL.20010221.0147.

151940 CRWMS M&O 2000. *Unsaturated Zone Flow and Transport Model Process Model Report*. TDR-NBS-HS-000002 REV 00 ICN 02. Las Vegas, Nevada: CRWMS M&O. ACC: MOL.20000831.0280.

122797 CRWMS M&O 2000. *UZ Flow Models and Submodels.* MDL-NBS-HS-000006 REV 00. Las Vegas, Nevada: CRWMS M&O. ACC: MOL.19990721.0527.

154291 CRWMS M&O 2001. *Abstraction of Drift Seepage*. ANL-NBS-MD-000005 REV 01. Las Vegas, Nevada: CRWMS M&O. ACC: MOL.20010309.0019

153045 CRWMS M&O 2001. *Seepage Calibration Model and Seepage Testing Data*. MDL-NBS-HS-000004 REV 01. Las Vegas, Nevada: CRWMS M&O. ACC: MOL.20010122.0093.

154024 CRWMS M&O 2001. *Unsaturated Zone and Saturated Zone Transport Properties (U0100).* ANL-NBS-HS-000019 REV 00 ICN 1. Las Vegas, Nevada: CRWMS M&O. ACC: MOL.20010201.0026.

156869 Descour, J.M.; Hanna, K.; Conover, D.; and Hoekstra, B. 2001. *Seismic Tomography Technology for the Water Infiltration Experiment.* TDR-EBS-MD-000017 REV00. Las Vegas, Nevada: Bechtel SAIC Company. ACC: MOL.20010508.0194.

100551 DOE (U.S. Department of Energy) 1998. *License Application Plan and Costs.* Volume 4 of *Viability Assessment of a Repository at Yucca Mountain*. DOE/RW-0508. Washington, D.C.: U.S. Department of Energy, Office of Civilian Radioactive Waste Management. ACC: MOL.19981007.0031.

100550 DOE (U.S. Department of Energy) 1998. *Total System Performance Assessment.* Volume 3 of *Viability Assessment of a Repository at Yucca Mountain*. DOE/RW-0508. Washington, D.C.: U.S. Department of Energy, Office of Civilian Radioactive Waste Management. ACC: MOL.19981007.0030.

149540 DOE (U.S. Department of Energy) 2000. *Quality Assurance Requirements and Description*. DOE/RW-0333P, Rev. 10. Washington, D.C.: U.S. Department of Energy, Office of Civilian Radioactive Waste Management. ACC: MOL.20000427.0422.

100147 Flint, A.L.; Hevesi, J.A.; and Flint, L.E. 1996. *Conceptual and Numerical Model of Infiltration for the Yucca Mountain Area, Nevada*. Milestone 3GUI623M. Denver, Colorado: U.S. Geological Survey. ACC: MOL.19970409.0087.

100033 Flint, L.E. 1998. *Characterization of Hydrogeologic Units Using Matrix Properties, Yucca Mountain, Nevada*. Water-Resources Investigations Report 97-4243. Denver, Colorado: U.S. Geological Survey. ACC: MOL.19980429.0512.

101173 Freeze, R.A. and Cherry, J.A. 1979. *Groundwater*. Englewood Cliffs, New Jersey: Prentice-Hall. TIC: 217571.

106099 Ghuman, B.S. and Prihar, S.S. 1980. "Chloride Displacement by Water in Homogeneous Columns of Three Soils." *Soil Science Society of America Journal, 44*, (1), 17-21. Madison, Wisconsin: Soil Science Society of America. TIC: 246698.

105787 GSA (Geological Society of America) 1991. *Rock Color Chart with Genuine Munsell Color Chips*. Boulder, Colorado: Geological Society of America. TIC: 242285.

156557 Hinds, J. 2000. Percolation and Seepage. Scientific Notebook YMP-LBNL-JSW-JJH-1. ACC: MOL.20000307.0066; MOL.20000419.0645..

156539 Hu, M.Q. 1999. Characterization of Yucca Mountain Percolation in the Unsaturated Zone-ESF Study. Scientific Notebook YMP-LBNL-JSW-QH-1. ACC: MOL.19991013.0463.

156540 Hu, M.Q. 1999. Characterization of Yucca Mountain Percolation in the Unsaturated Zone-ESF Study. Scientific Notebook YMP-LBNL-JSW-QH-1A. ACC: MOL.20000107.0345.

156541 Hu, M.Q. 1999. Characterization of Yucca Mountain Percolation in the Unsaturated Zone-ESF Study. Scientific Notebook YMP-LBNL-JSW-QH-1B. ACC: MOL.20000107.0346.

156542 Hu, M.Q. 1999. Characterization of Yucca Mountain Percolation in the Unsaturated Zone-ESF Study. Scientific Notebook YMP-LBNL-JSW-QH-1C. ACC: MOL.19991210.0212.

155691 Hu, M.Q. 1999. Characterization of Yucca Mountain Percolation in the Unsaturated Zone-ESF Study. Scientific Notebook YMP-LBNL-JSW-QH-1D. ACC: MOL.19991013.0467.

156473 Hu, M.Q. 2000. Characterization of Yucca Mountain Percolation in the Unsaturated Zone-ESF Study. Scientific Notebook YMP-LBNL-JSW-QH-1E. ACC: MOL.19991013.0468; MOL.20010201.0419.

106105 Klinkenberg, L.J. 1942. "The Permeability of Porous Media to Liquids and Gases." *Drilling and Production Practice 1941*. New York, New York: American Petroleum Institute. TIC: 217454.

101700 LeCain, G.D. 1995. *Pneumatic Testing in 45-Degree-Inclined Boreholes in Ash-Flow Tuff Near Superior, Arizona*. Water-Resources Investigations Report 95-4073. Denver, Colorado: U.S. Geological Survey. ACC: MOL.19960715.0083.

104158 Lipman, P.W. and McKay, E.J. 1965. *Geologic Map of the Topopah Spring SW Quadrangle, Nye County, Nevada*. Geologic Quadrangle Map GQ-439. Denver, Colorado: U.S. Geological Survey. TIC: 212352.

149850 Mongano, G.S.; Singleton, W.L.; Moyer, T.C.; Beason, S.C.; Eatman, G.L.W.; Albin, A.L.; and Lung, R.C. 1999. *Geology of the ECRB Cross Drift - Exploratory Studies Facility, Yucca Mountain Project, Yucca Mountain, Nevada*. [Deliverable SPG42GM3]. Denver, Colorado: U.S. Geological Survey. ACC: MOL.20000324.0614.

101269 Moyer, T.C. and Geslin, J.K. 1995. *Lithostratigraphy of the Calico Hills Formation and Prow Pass Tuff (Crater Flat Group) at Yucca Mountain, Nevada*. Open-File Report 94-460. Denver, Colorado: U.S. Geological Survey. ACC: MOL.19941208.0003.

100162 Moyer, T.C.; Geslin, J.K.; and Flint, L.E. 1996. *Stratigraphic Relations and Hydrologic Properties of the Paintbrush Tuff Nonwelded (PTn) Hydrologic Unit, Yucca Mountain, Nevada*. Open-File Report 95-397. Denver, Colorado: U.S. Geological Survey. ACC: MOL.19970204.0216.

134132 Muskat, M. 1982. *The Flow of Homogeneous Fluids through Porous Media*. Boston, Massachusetts: International Human Resources Development Corporation. TIC: 208295.

156558 Oldenburg, C. 2000. Percolation and Seepage. Scientific Notebook YMP-LBNL-JSW-CMO-1. ACC: MOL.20000922.0075.

155696 Peterman, Z.E. and Cloke, P.L. 2001. "Geochemical Homogeneity of Tuffs at the Potential Repository Level, Yucca Mountain, Nevada." *"Back to the Future - Managing the Back End of the Nuclear Fuel Cycle to Create a More Secure Energy Future," Proceedings of the 9th International High-Level Radioactive Waste Management Conference (IHLRWM), Las Vegas, Nevada, April 29-May 3, 2001*. La Grange Park, Illinois: American Nuclear Society. TIC: 247873.

106498 Peterman, Z.E.; Spengler, R.W.; Singer, F.R.; and Dickerson, R.P. 1993. "Isotopic and Trace Element Variability in Altered and Unaltered Tuffs at Yucca Mountain, Nevada." *High Level Radioactive Waste Management, Proceedings of the Fourth Annual International Conference, Las Vegas, Nevada, April 26-30, 1993*. 2, 1940-1947. La Grange Park, Illinois: American Nuclear Society. TIC: 208542.

106133 Philip, J.R. 1986. "Linearized Unsteady Multidimensional Infiltration." *Water Resources Research, 22*, (12), 1717-1727. Washington, D.C.: American Geophysical Union. TIC: 239826.

156974 Philip, J.R. 1989. "The Scattering Analog for Infiltration in Porous Media." *Reviews of Geophysics, 27*, (4), 431-448. Washington, D.C.: American Geophysical Union. Copyright Requested Library Tracking Number-251332

105743 Philip, J.R.; Knight, J.H.; and Waechter, R.T. 1989. "Unsaturated Seepage and Subterranean Holes: Conspectus, and Exclusion Problem for Circular Cylindrical Cavities." *Water Resources Research, 25*, (1), 16-28. Washington, D.C.: American Geophysical Union. TIC: 239117.

134083 Porro, I. and Wierenga, P.J. 1993. "Transient and Steady-State Transport through a Large Unsaturated Soil Column." *Ground Water, 31*, (2), 193-200. Dublin, Ohio: National Ground Water Association. TIC: 246899.

106141 Pullan, A.J. 1990. "The Quasilinear Approximation for Unsaturated Porous Media Flow." *Water Resources Resources, 26*, (6), 1219-1234. Washington, D.C.: American Geophysical Union. TIC: 239824.

155683 Raats, P.A.C. and Gardner, W.R. 1971. "Comparison of Empirical Relationships Between Pressure Head and Hydraulic Conductivity and Some Observations on Radially Symmetric Flow." *Water Resources Research, 7*, (4), 921-928. [Washington, D.C.]: American Geophysical Union. TIC: 239815.

155697 Russo, R.E.; Mao, X.; Borisov, O.V.; and Liu, H. 2000. "Laser Ablation in Atomic Spectroscopy." *Encyclopedia of Analytical Chemistry*. Meyers, R.A., ed. Pages 9485-9506. Chichester, England: John Wiley & Sons. TIC: 250479.

155692 Salve, R. 1999. Fracture Flow, Fracture-Matrix Interaction. Scientific Notebook YMP-LBNL-JSW-RS-1. ACC: MOL.19991013.0470.

156547 Salve, R. 1999. Fracture Flow, Fracture-Matrix Interaction. Scientific Notebook YMP-LBNL-JSW-RS-1A. ACC: MOL.19991013.0471.

156555 Salve, R. 1999. Measurements of Moisture Potential in P Tunnel Calico Hills using Tensiometers and Psychrometers. Scientific Notebook YMP-LBNL-JW-1.2A. ACC: MOL.19991013.0473.

156552 Salve, R. 1999. Measurements of Moisture Potential in P Tunnel/Calico Hills using Tensiometers and Psychrometers. Scientific Notebook YMP-LBNL-JW-1.2. ACC: MOL.20000215.0229.

156548 Salve, R. 2000. Percolation and Seepage. Scientific Notebook YMP-LBNL-JSW-RS-2. ACC: MOL.20000908.0236.

100075 Sawyer, D.A.; Fleck, R.J.; Lanphere, M.A.; Warren, R.G.; Broxton, D.E.; and Hudson, M.R. 1994. "Episodic Caldera Volcanism in the Miocene Southwestern Nevada Volcanic Field: Revised Stratigraphic Framework, 40Ar/39Ar Geochronology, and Implications for Magmatism and Extension." *Geological Society of America Bulletin, 106*, (10), 1304-1318. Boulder, Colorado: Geological Society of America. TIC: 222523.

106143 Selby, S.M., ed. 1975. *CRC Standard Mathematical Tables*. 23rd Edition. Cleveland, Ohio: CRC Press. TIC: 247118.

149146 Soll, W.E. 1997. Busted Butte Modeling, UZ Transport Modeling Notebook #1 (LA-EES-5-NBK-98-018). SN-LANL-SCI-048-V1. ACC: MOL.19991221.0369.

156561 Stepek, J. 2000. Characterization of Yucca Mountain Percolation in the Unsaturated Zone - ESF Study. Scientific Notebook YMP-LBNL-JSW-JS-1. ACC: MOL.19991013.0476; MOL.20010724.0086.

147703 SubTerra 1998. *Final Report, TRW Environmental Safety Systems, Inc., Busted Butte Test Facility*. Project: 97-35. Kirkland, Washington: SubTerra, Inc. TIC: 247628.

156563 Trautz, R.C. 1999. Moisture Monitoring in the ESF (Phase 2)/Drift Seepage Test. Scientific Notebook YMP-LBNL-RCT-1. ACC: MOL.20000306.0470; MOL.20001121.0084.

156903 Trautz, R.C. 2001. Moisture Monitoring in the ESF (Phase 2)/Drift Seepage Test. Scientific Notebook YMP-LBNL-RCT-2. ACC: MOL.20011030.0706.

157022 Trautz, R.C. 2001. Moisture Monitoring in the ESF (Phase 2)/Drift Seepage Test. Scientific Notebook YMP-LBNL-RCT-3. ACC: MOL.20011116.0083.

157161 Trautz, R.C. and Wang, J.S.Y. 2000. "Evaluation of Seepage into an Underground Opening Using Small-Scale Field Experiments, Yucca Mountain, Nevada." *SME Annual Meeting, February 28-March 1, 2000, Salt Lake City, Utah. Preprint 00-57*, Littleton, Colorado: Society for Mining, Metallurgy, and Exploration. On Order Library Tracking Number-251422

156530 Wang, J. 1997. Characterization of Yucca Mountain Percolation in the Unsaturated Zone - ESF Study. Scientific Notebook YMP-LBNL-JSW-6. ACC: MOL.19991013.0459.

156534 Wang, J. 1997. Characterization of Yucca Mountain Percolation in the Unsaturated Zone - ESF Study. Scientific Notebook YMP-LBNL-JSW-6A. ACC: MOL.19991013.0460.

156538 Wang, J. 1999. Characterization of Yucca Mountain Percolation in the Unsaturated Zone - ESF Study. Scientific Notebook YMP-LBNL-JSW-6B. ACC: MOL.19991013.0461.

153449 Wang, J. 1999. Characterization of Yucca Mountain Percolation in the Unsaturated Zone - ESF Study. Scientific Notebook YMP-LBNL-JSW-6C. ACC: MOL.19991013.0462.

156559 Wang, J. 2000. Characterization of Yucca Mountain Percolation in the Unsaturated Zone - Exploratory Shaft Facility Study. Scientific Notebook YMP-LBNL-JSW-4.3. ACC: MOL.19991018.0187; MOL.20000808.0010.

104366 Wang, J.S.Y. and Elsworth, D. 1999. "Permeability Changes Induced by Excavation in Fractured Tuff." *Rock Mechanics for Industry, Proceedings of the 37th U.S. Rock Mechanics Symposium, Vail, Colorado, USA, 6-9 June 1999*. Amadei, B.; Kranz, R.L.; Scott, G.A.; and Smeallie, P.H., eds. 2, 751-757. Brookfield, Vermont: A.A. Balkema. TIC: 245246.

106793 Wang, J.S.Y. and Narasimhan, T.N. 1993. "Unsaturated Flow in Fractured Porous Media." Chapter 7 of *Flow and Contaminant Transport in Fractured Rock*. Bear, J.; Tsang, C-F.; and de Marsily, G., eds.. San Diego, California: Academic Press. TIC: 235461.

101309 Wang, J.S.Y.; Flint, A.L.; Nitao, J.J.; Chesnut, D.A.; Cook, P.; Cook, N.G.W.; Birkholzer, J.; Freifeld, B.; Flint, L.E.; Ellet, K.; Mitchell, A.J.; Homuth, E.F.; Griego, G.J.; Cerny, J.A.; and Johnson, C.L. 1996. *Evaluation of Moisture Evolution in the Exploratory Studies Facility*. Milestone TR31K6M. Berkeley, California: Lawrence Berkeley National Laboratory. ACC: MOL.19961231.0089.

106146 Wang, J.S.Y.; Trautz, R.C.; Cook, P.J.; Finsterle, S.; James, A.L.; and Birkholzer, J. 1999. "Field Tests and Model Analyses of Seepage into Drift." *Journal of*

Contaminant Hydrology, 38, (1-3), 323-347. New York, New York: Elsevier. TIC: 244160.

106150 Warrick, A.W.; Biggar, J.W.; and Nielsen, D.R. 1971. "Simultaneous Solute and Water Transfer for an Unsaturated Soil." *Water Resources Research, 7,* (5), 1216-1225. Washington, D.C.: American Geophysical Union. TIC: 245674.

106152 White, I. and Sully, M.J. 1987. "Macroscopic and Microscopic Capillary Length and Time Scales from Field Infiltration." *Water Resources Research, 23,* (8), 1514-1522. Washington, D.C.: American Geophysical Union. TIC: 239821.

149733 YMP (Yucca Mountain Site Characterization Project) 2000. *Q-List*. YMP/90-55Q, Rev. 6. Las Vegas, Nevada: Yucca Mountain Site Characterization Office. ACC: MOL.20000510.0177.

Software Cited

147402 CRWMS M&O 1999. *Software routine: ECRB-XYZ V.03*. V.03. PC. 30093-V.03.

152835 Lawrence Berkeley National Laboratory 02/06/1998. *Software Code: EARTHVISION-2*. V4.0. SGI. STN: 30035-2.

8.2 CODES, STANDARDS, REGULATIONS, AND PROCEDURES

66 FR 55732. *Disposal of High-Level Radioactive Wastes in a Proposed Geologic Repository at Yucca Mountain, NV*. Final Rule 10 CFR Part 63. Readily available.

AP-2.21Q, Rev. 1, BSCN 1. *Quality Determinations and Planning for Scientific, Engineering, and Regulatory Compliance Activities*. Washington, D.C.: U.S. Department of Energy, Office of Civilian Radioactive Waste Management. ACC: MOL.20010212.0018.

AP-3.10Q, Rev. 2, ICN 5. *Analyses and Models*. Washington, D.C.: U.S. Department of Energy, Office of Civilian Radioactive Waste Management. ACC: MOL.20011126.0261.

AP-12.1Q, Rev. 0, ICN 1. *Control of Measuring and Test Equipment and Calibration Standards*. Washington, D.C.: U.S. Department of Energy, Office of Civilian Radioactive Waste Management. ACC: MOL.20010327.0025.

AP-SI.1Q, Rev. 3, ICN 2, ECN 1. *Software Management*. Washington, D.C.: U.S. Department of Energy, Office of Civilian Radioactive Waste Management. ACC: MOL.20011030.0598.

AP-SV.1Q, Rev. 0, ICN 2. *Control of the Electronic Management of Information*. Washington, D.C.: U.S. Department of Energy, Office of Civilian Radioactive Waste Management. ACC: MOL.20000831.0065.

QAP-2-3, Rev. 10, BSCN 2. *Classification of Permanent Items*. Washington, D.C.: U.S. Department of Energy, Office of Civilian Radioactive Waste Management. ACC: MOL.20010212.0283.

YMP-LBNL-QIP-SV.0 Rev. 2, Mod. 0. *Management of YMP-LBNL Electronic Data*. Berkeley, California: Lawrence Berkeley National Laboratory. ACC: MOL.20001108.0155.

YMP-LBNL-TIP/GP 5.0 Rev. 0, Mod. 0. *Ground Penetrating Radar Data Acquisition*. Berkeley, California: Lawrence Berkeley National Laboratory. ACC: MOL.19990205.0129.

8.3 SOURCE DATA, LISTED BY DATA TRACKING NUMBER

157119 GS010608312242.003. Crossover Alcove/Seepage into Niches 3; Trench Fault Infiltration Using Permeameters from March 5, 2001 to May 31, 2001. Submittal date: 06/28/2001.

106059 GS960908314224.020. Analysis Report: Geology of the North Ramp - Stations 4+00 to 28+00 and Data: Detailed Line Survey and Full-Periphery Geotechnical Map - Alcoves 3 (UPCA) and 4 (LPCA), and Comparative Geologic Cross Section - Stations 0+60 to 28+00. Submittal date: 09/09/1996.

135119 GS970208312242.001. Moisture Monitoring in the ESF, Oct. 1, 1996 through Jan. 31, 1997. Submittal date: 02/19/1997.

135123 GS970708312242.002. Moisture Monitoring in the ESF, Feb. 1, 1997 through July 31, 1997. Submittal date: 07/18/1997.

105978 GS970808312232.005. Deep Unsaturated Zone Surface-Based Borehole Instrumentation Program Data from Boreholes USW NRG-7A, UE-25 UZ#4, UE-25 UZ#5, USW UZ-7A and USW SD-12 for the Time Period 1/1/97 - 6/30/97. Submittal date: 08/28/1997.

105980 GS971108312232.007. Deep Unsaturated Zone Surface-Based Borehole Instrumentation Program Data from Boreholes USW NRG-7A, UE-25 UZ #4, UE-25 UZ #5, USW UZ-7A and USW SD-12 for the Time Period 7/1/97 - 9/30/97. Submittal date: 11/18/1997.

135181 GS980308312242.001. Time Domain Reflectometry Measurements in the South Ramp of the ESF, August 1, 1997 to January 4, 1998. Submittal date: 03/04/1998.

135163 GS980308312242.002. Heat Dissipation Probe Measurements in the South Ramp of the ESF, August 1, 1997 to January 31, 1998. Submittal date: 03/09/1998.

135180 GS980308312242.003. Physical Properties of Borehole Samples from the ESF South Ramp (ESF Station 59+65M to ESF Station 76+33M). Submittal date: 03/16/1998.

107172 GS980308312242.004. Water Potential Measurements Using the Filter Paper Technique for Borehole Samples from the ESF North Ramp (ESF Station 7+27 M to ESF Station 10+70 M) and the ESF South Ramp (ESF Station 59+65 M to 76+33 M). Submittal date: 03/19/1998.

107165 GS980308312242.005. Physical Properties of Lexan-Sealed Borehole Samples from the PTN Exposure in the ESF North Ramp (ESF Station 7+27 M to ESF Station 10+70 M). Submittal date: 03/11/1998.

105982 GS980408312232.001. Deep Unsaturated Zone Surface-Based Borehole Instrumentation Program Data from Boreholes USW NRG-7A, UE-25 UZ #4, USW NRG-6, UE-25 UZ #5, USW UZ-7A and USW SD-12 for the Time Period 10/01/97 - 03/31/98. Submittal date: 04/16/1998.

135170 GS980908312242.018. Physical Properties of Borehole Core Samples from ESF-MD-NICHE3566#1, ESF-MD-NICHE3566#2, ESF-MD-NICHE3566#3A, ESF-MD-NICHE3566LT#1, ESF-MD-NICHE3566LT#2, ESF-MD-NICHE3566LT#3, ESF-MD-NICHE3566LT#4, ESF-MD-NICHE3566LT#5, and ESF-MD-NICHE3566LT#6. Submittal date: 09/03/1998.

135172 GS980908312242.020. Physical Properties of Borehole Core Samples from ESF-MD-NICHE3650#1, ESF-MD-NICHE3650#2, ESF-MD-NICHE3650#3, ESF-MD-NICHE3650#4, ESF-MD-NICHE3650#5, ESF-MD-NICHE3650#6, and ESF-MD-NICHE3650#7. Submittal date: 09/05/1998.

135157 GS980908312242.022. Water Potentials Measured with Heat Dissipation Probes in Twenty-One Drill Holes in Niche 1 (ESF-NICHE3566) from 11/04/97 to 07/31/98. Submittal date: 09/11/1998.

135132 GS980908312242.024. Moisture Monitoring in the ESF, August 1, 1997 to July 31, 1998. Submittal date: 09/15/1998.

135176 GS980908312242.028. Physical and Hydrologic Properties of Borehole Core Samples from ESF-SAD-GTB#1. Submittal date: 09/16/1998.

135175 GS980908312242.029. Physical and Hydrologic Properties of Borehole Core Samples from ESF-NDR-MF#1, ESF-NDR-MF#2, and ESF-NDR-MF#4 in Alcove 6 of the ESF. Submittal date: 09/17/1998.

135224 GS980908312242.030. Physical Properties of Borehole Core Samples from ESF-ECRB-SLANT#2. Submittal date: 09/17/1998.

107177 GS980908312242.032. Physical and Hydrologic Properties of Borehole Core Samples and Water Potential Measurements Using the Filter Paper Technique for Borehole Samples from ESF-LPCA-PTN#1 and ESF-LPCA-PTN#2 in Alcove 4. Submittal date: 09/17/1998.

107168 GS980908312242.033. Physical and Hydrologic Properties of Borehole Core Samples and Water Potential Measurements Using the Filter Paper Technique for Borehole Samples from ESF-UPCA-PTN#1 in Alcove 3 of the ESF. Submittal date: 09/17/1998.

135133 GS980908312242.035. Moisture Monitoring in the ECRB, 04/08/98 to 07/31/98. Submittal date: 09/24/1998.

119820 GS980908312242.036. Water Potentials Measured with Heat Dissipation Probes in ECRB Holes from 4/23/98 to 7/31/98. Submittal date: 09/22/1998.

156505 GS981208312232.002. Deep UZ Surface-Based Borehole Instrumentation Program Data from Boreholes USW NRG-7A, UE-25 UZ#4, USW NRG-6, UE-25 UZ#5, USW UZ-7A and USW SD-12 for the Time Period 4/1/98 through 9/30/98. Submittal date: 12/03/1998.

107185 GS990308312242.007. Laboratory and Centrifuge Measurements of Physical and Hydraulic Properties of Core Samples from Busted Butte Boreholes UZTT-BB-INJ-1, UZTT-BB-INJ-3, UZTT-BB-INJ-4, UZTT-BB-INJ-6, UZTT-BB-COL-5 and UZTT-BB-COL-8. Submittal date: 03/22/1999.

108409 GS990408314224.006. Full-Periphery Geologic Maps for Station 20+00 to 26+81, ECRB Cross Drift. Submittal date: 09/09/1999.

109822 GS990708312242.008. Physical and Hydraulic Properties of Core Samples from Busted Butte Boreholes. Submittal date: 07/01/1999.

152631 GS990908314224.010. Geology of the ECRB Cross Drift: Graphical Data. Submittal date: 09/14/1999.

157100 LA0112WS831372.001. Busted Butte UZ Transport Test: Phase II Collection Pad Tracer Loading. Submittal date: 12/06/2001. URN-0985

157115 LA0112WS831372.002. Busted Butte UZ Transport Test: Phase II Collection Pad Tracer Concentrations. Submittal date: 12/06/2001. URN-0986

157106 LA0112WS831372.003. Busted Butte UZ Transport Test: Phase II Normalized Collection Pad Tracer Concentrations. Submittal date: 12/06/2001. URN-0984

122739 LA9909WS831372.001. Busted Butte UZ Transport Test: Phase I Collection Pad Extract Concentrations. Submittal date: 09/29/1999.

122741 LA9909WS831372.002. Busted Butte UZ Transport Test: Phase I Collection Pad Tracer Loading and Tracer Concentrations. Submittal date: 09/30/1999.

140089 LA9909WS831372.015. ICPAES Porewater Analysis for Rock Samples from Busted Butte, NV. Submittal date: 10/01/1999.

140093 LA9909WS831372.016. ION Chromatography Porewater Analysis for Rock Samples from Busted Butte, NV. Submittal date: 09/30/1999.

140097 LA9909WS831372.017. pH of Porewater of Rock Samples from Busted Butte, NV. Submittal date: 09/30/1999.

140101 LA9909WS831372.018. Gravimetric Moisture Content of Rock Samples from Busted Butte, NV. Submittal date: 09/30/1999.

147156 LA9910WS831372.008. Busted Butte UZ Transport Test: Gravimetric Moisture Content and Bromide Concentration in Selected Phase 1A Rock Samples. Submittal date: 11/03/1999.

147157 LA9910WS831372.009. QXRD Data for UZTT-Busted Butte Samples. Submittal date: 11/03/1999.

156586 LA9912WS831372.001. Sorption of Fluorinated Benzoic Acids and Lithium on Rock Samples Form Busted Butte, NV. Submittal date: 02/22/2000.

122730 LAJF831222AQ98.007. Chloride, Bromide, and Sulfate Analyses of Salts Leached from ECRB-CWAT#1, #2, and #3 Drill Core. Submittal date: 09/09/1998.

149214 LB00032412213U.001. Busted Butte Ground Penetrating Radar Data Collected June 1998 through February 2000 at the Unsaturated Zone Transport Test (UZTT): GPR Velocity Data. Submittal date: 03/24/2000.

153141 LB00090012213U.001. Air K Testing in Borehole SYBT-ERCB-LA#2 at CS 17+26 in Cross Drift. Submittal date: 11/03/2000.

153154 LB00090012213U.002. Liquid Release Tests from Borehole SYBT-ECRB-LA#2 at CS 17+26 in Cross Drift. Submittal date: 11/09/2000.

153144 LB0010NICH3LIQ.001. Niche 3107 Seepage Test. Submittal date: 11/02/2000.

153145 LB0010NICH4LIQ.001. Niche 4788 Seepage Test. Submittal date: 11/02/2000.

153155 LB0011AIRKTEST.001. Air Permeability Testing in Niches 3566 and 3650. Submittal date: 11/08/2000.

153460 LB0011CO2DST08.001. Isotope Data for CO2 from Gas Samples Collected from Hydrology Holes in Drift-Scale Test. Submittal date: 12/09/2000.

154586 LB0012AIRKTEST.001. Niche 5 Air K Testing 3/23/00-4/3/00. Submittal date: 12/21/2000.

146878 LB002181233124.001. Air Permeability and Pneumatic Pressure Data Collected Between October 27, 1999 through November 7, 1999 from Niche 5 (ECRB Niche 1620) of the ESF. Submittal date: 02/18/2000.

155681 LB0102NICH5LIQ.001. Niche 5 Seepage Tests - Pre Excavation. Submittal date: 02/28/2001.

156888 LB0108CO2DST05.001. Concentration Data for CO2 from Gas Samples Collected from Hydrology Holes in Drift-Scale Test - May and August 1999, April 2000, January and April 2001. Submittal date: 08/27/2001. URN-0988

156912 LB0110A8N3GPRB.001. Alcove 8/Niche 3 GPR Baseline Data. Submittal date: 11/12/2001. URN-0970

157001 LB0110A8N3LIQR.001. Preliminary Observations from the Fault Test at Alcove8/Niche3. Submittal date: 11/12/2001. URN-0971

156905 LB0110AK23POST.001. AK2 and AK3 Post-Excavation Air-K. Submittal date: 11/12/2001. URN-0972

156904 LB0110AKN5POST.001. Niche 5 (1620 in ECRB) Post-Excavation Air-K. Submittal date: 11/12/2001. URN-0973

156913 LB0110BSTBTGPR.001. Busted Butte GPR Data. Submittal date: 11/12/2001. URN-0974

157169 LB0110COREPROP.001. Lab Measurements of 14 Matrix Cores. Submittal date: 11/12/2001. URN-0975

156886 LB0110ECRBH2OA.001. ECRB Water Analyses. Submittal date: 11/12/2001. URN-0976

156887 LB0110ECRBH2OI.001. Isotope Data for Water Samples Collected from the ECRB. Submittal date: 11/12/2001. URN-0977

156883 LB0110ECRBH2OP.001. Water Potential Data From Three Locations in the ECRB. Submittal date: 11/12/2001. URN-0978

156878 LB0110ECRBLIQR.001. Systematic Testing in ECRB-SYBT-LA#1, 12/20/2000. Submittal date: 11/12/2001. URN-0979

156879 LB0110ECRBLIQR.002. Systematic Testing in ECRB-SYBT-LA#1, 2/28/2001. Submittal date: 11/12/2001. URN-0980

156877 LB0110ECRBLIQR.003. Systematic Testing in ECRB-SYBT-LA#2, 10/23/2000. Submittal date: 11/12/2001. URN-0981

156885 LB0110ECRBRHTB.001. Moisture Monitoring at Four Locations in the ECRB. Submittal date: 11/12/2001. URN-0982

156979 LB0110TUFTRACR.001. Using Laser Ablation to Study Tracer Movement in Tuff. Submittal date: 11/12/2001. URN-0983

105793 LB960800831224.001. Relative Humidity, Temperature, and Pressure in ESF Monitoring Stations. Submittal date: 08/23/1996.

105794 LB970300831224.001. Moisture Data Report from October, 1996 to January, 1997. Submittal date: 03/13/1997.

105796 LB970801233124.001. Moisture Monitoring Data Collected at ESF Sensor Stations. Submittal date: 08/27/1997.

105798 LB970901233124.002. Moisture Monitoring Data Collected at Stationary Moisture Stations. Submittal date: 09/30/1997.

105800 LB980001233124.001. Water Potential Measurements in Niches 3566, 3650, and 3107 of the ESF. Submittal date: 04/23/1998.

136583 LB980001233124.004. Liquid Release Test Data from Niche 3566 and Niche 3650 of the ESF in Milestone Report, "Drift Seepage Test and Niche Moisture Study: Phase 1 Report on Flux Threshold Determination, Air Permeability Distribution, and Water Potential Measurement. Submittal date: 11/23/1999.

105818 LB980101233124.002. Post-Excavation Permeability Data Collected from Niche 3650 of the ESF. Submittal date: 11/04/1998.

105592 LB980901233124.003. Liquid Release and Tracer Tests in Niches 3566, 3650, 3107, and 4788 in the ESF. Submittal date: 09/14/1998.

105855 LB980901233124.004. Pneumatic Pressure and Air Permeability Data from Alcove 6 in the ESF. Submittal date: 09/14/1998.

105856 LB980901233124.009. Pneumatic Pressure and Air Permeability Data from Alcove 4 in the ESF. Submittal date: 09/14/1998.

105858 LB980901233124.014. Borehole Monitoring at the Single Borehole in the ECRB and ECRB Crossover Point in the ESF. Submittal date: 09/14/1998.

136593 LB980901233124.101. Pneumatic Pressure and Air Permeability Data from Niche 3107 and Niche 4788 in the ESF from Chapter 2 of Report SP33PBM4: Fracture Flow and Seepage Testing in the ESF, FY98. Submittal date: 11/23/1999.

110828 LB980912332245.001. Air Injection Data from Niche 3107 of the ESF. Submittal date: 09/30/1998.

105593 LB980912332245.002. Gas Tracer Data from Niche 3107 of the ESF. Submittal date: 09/30/1998.

105888 LB990601233124.001. Seepage Data Feed to UZ Drift-Scale Flow Model for TSPA-SR. Submittal date: 06/18/1999.

106051 LB990601233124.003. Seepage Data Feed to UZ Drift-Scale Flow Model for TSPA-SR. Submittal date: 06/18/1999.

155694 LB990901233124.001. Alcove 6 Tracer Tests for AMR U0015, "In Situ Field Testing of Processes." Submittal date: 11/01/1999.

146883 LB990901233124.002. Alcove 6 Flow Data for AMR U0015, "In Situ Field Testing of Processes." Submittal date: 11/01/1999.

155690 LB990901233124.003. Tracer Lab Analyses of Dye Penetration in Niches 3650 and 4788 of the ESF for AMR U0015, "In Situ Field Testing of Processes." Submittal date: 11/01/1999.

123273 LB990901233124.004. Air Permeability Cross-Hole Connectivity in Alcove 6, Alcove 4, and Niche 4 of the ESF for AMR U0015, "In Situ Testing of Field Processes". Submittal date: 11/01/1999.

146884 LB990901233124.005. Alcove 4 Flow Data for AMR U0015, "In Situ Field Testing of Processes". Submittal date: 11/01/1999.

135137 LB990901233124.006. Moisture Data from the ECRB Cross Drift for AMR U0015, "In Situ Testing of Field Processes". Submittal date: 11/01/1999.

146601 LB991220140160.019. Values from Referred Literature Used as Input in AMR U0060, "Radionuclide Transport Models Under Ambient Conditions". Submittal date: 03/14/2000.

147168 LL990612704244.098. ERT Data for Busted Butte. Submittal date: 06/21/1999. Submit to RPC URN-0386

103769 MO9901MWDGFM31.000. Geologic Framework Model. Submittal date: 01/06/1999.

150300 MO0004GSC00167.000. As-Built Coordinate of Boreholes in the Test Alcove and Running Drift, Busted Butte Test Facility (BBTF). Submittal date: 04/20/2000.

151029 MO0006J13WTRCM.000. Recommended Mean Values of Major Constituents in J-13 Well Water. Submittal date: 06/07/2000.

153777 MO0012MWDGFM02.002. Geologic Framework Model (GFM2000). Submittal date: 12/18/2000.

156941 MO0107GSC01069.000. ESF Niche #4 (Niche 4788) Borehole As-Built Information. Submittal date: 07/19/2001.

8.4 OUTPUT DATA, LISTED BY DATA TRACKING NUMBER

LB0110AIRK0015.001. Developed Data for Air-K Tests. Submittal date: to be submitted with this AMR.

LB0110LIQR0015.001. Developed Data for Liquid Release/Seepage Tests and Systematic Testing. Submittal date: to be submitted with this AMR.

LB0110NICH4LIQ.001. Niche 4788 Ceiling - Wetting Front Data. Submittal date: to be submitted with this AMR.

LB0110SYST0015.001. Developed Data for Systematic Test. Submittal date: to be submitted with this AMR.

INTENTIONALLY LEFT BLANK

ATTACHMENT I

AUTOMATED AIR INJECTION SYSTEM

INTENTIONALLY LEFT BLANK

ATTACHMENT I AUTOMATED AIR INJECTION SYSTEM

The pneumatic-testing equipment is a specially designed packer system fabricated to take specific testing needs into account. Many boreholes at several sites need to be tested in a controlled fashion to allow site-to-site and borehole-to-borehole comparisons to be meaningful. For determination of connectivity between boreholes, all permutations of injection and response zones at a site need to be examined, so the boreholes must be instrumented for simultaneous measurements. In heterogeneous rock, such as that at the ESF, it is difficult to compensate for variations in results caused by different test configurations such as test interval length or test scale. It is therefore important to keep the testing as consistent as possible by varying only one parameter when performing the tests, namely the location of the test zones. These needs were accommodated not only in the design and operation of the packer system, but also in planning the borehole patterns and drilling. To ensure that the air permeability of unaltered rock would be measured, boreholes were drilled dry and at low speed, a process that minimizes damage to the formation and thereby allows the packer systems to be placed along the entire length of each borehole.

I.1 AUTOMATIC PNEUMATIC INJECTION PACKERS

In light of the need for consistency, the same packer design is used for injection and observation. This approach is amenable to the automation and remote control necessary for establishing consistent testing regimens and accommodating the large number of tests. Inflatable rubber sealing bladders on a packer string can be manipulated independently and divide a borehole into 14 different possible zones over the length of the string. Zone resolution is 0.3 meter, and the bladders cover the entire length of the string. This configuration allows 4.8 meters of borehole to be covered by one string. One 3.2-mm-diameter port for pressure measurement and one 6.4-mm-diameter port for air injection service each zone. Up to seven boreholes can be instrumented at one time. The packer inflation and air-injection lines can all be controlled automatically. A modular design allows partial dismantling of the packer strings in the field for repair or work in tight quarters. Figure I-1 shows a diagram of part of a packer assembly.

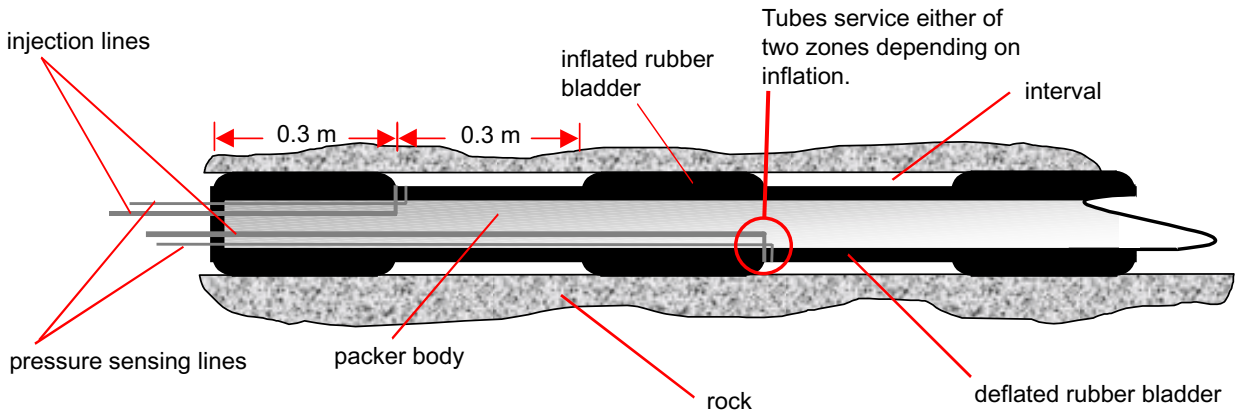

Figure I-1. Schematic Sketch of Automatic Packer Design.

If the bladders are all inflated at once, then the packer string would seal the entire section of borehole occupied by the string. However, by inflating every other bladder and allowing the remainder to remain deflated, an alternating sequence of open and closed (sealed) intervals is produced. Depending on the injection control valves, an open interval becomes either an observation zone used to monitor pressure, or it becomes the injection zone where air is introduced under pressure during a test. Once tests have been performed with these open zones, the inflated bladders are deflated, and deflated bladders are inflated, causing those zones that were once closed to become open and those that were originally open to become closed. In this manner, close to the entire length of the packer string is usable for testing every 0.3 meters without having to move the string. By changing the zones on the injection packer independently from those on the observation packers, there are four possible zone configurations available during a given packer installation. All permutations of these injection and observation positions are used to ensure that all positions within each observation borehole are allowed a chance to respond to a given injection zone. Figure I-2 shows schematically how this process is implemented. The observation packer zones are usually changed in unison because the locations of the observation zones are thought not to perturb the flow field significantly. Permutations between them would cause only second-order effects in the response system.

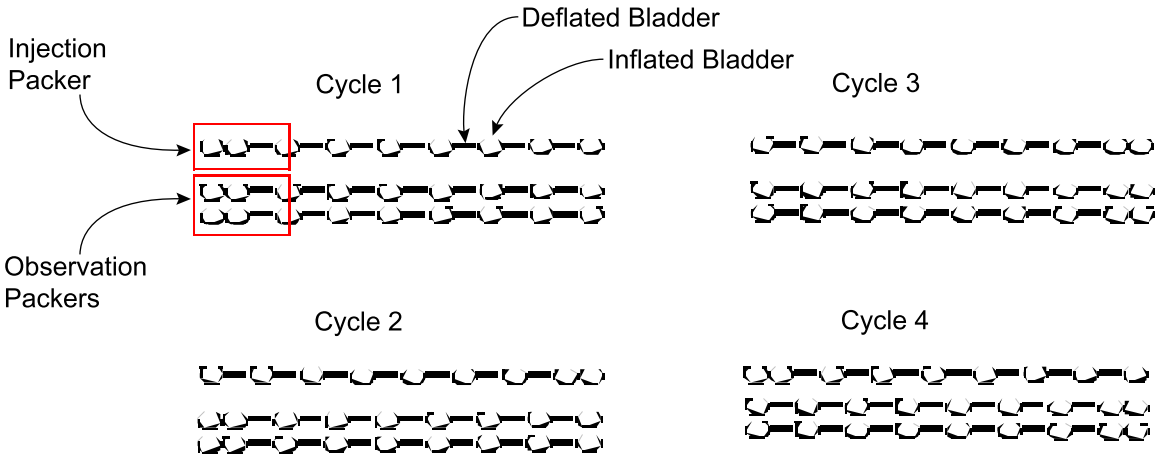

Figure I-2. Schematic Illustration of the Permutation Scheme for Automatic Packers.

I.2 AIR-INJECTION FLOW INSTRUMENTATION

Pressure monitoring for each zone was accomplished using pressure transducers accurate to a resolution of 0.3 kilopascals (kPa). Mass flow controllers (MFCs) with voltage control and output were used to inject a constant mass-flow rate of air during each permeability test. Four sizes of these controllers, from 1 to 500 standard liters per minute (SLPM), were employed to span the anticipated flow-rate ranges. The pressure transducer and MFC outputs were continually monitored and digitally recorded throughout testing, using a 27-bit voltmeter and an accompanying computer. Time resolution for the data from all sources was set nominally at five seconds.

I.3 INITIAL SETUP IN TESTING REGIMEN

Initially, by performing some manually operated tests for a given site, the operator determined under what conditions steady-state was reached and at what injection pressure packer leak-by could occur. (Leak-by is the condition of injected air forcing its way past the packer and breaking its seal with the rock.) The information from these initial tests was used to plan the automatic controls. The operator determined packer leak-by pressure by observing the pressure response in the observation zones axially adjacent to the injection zone. When leak-by occurs, a distinct and sudden pressure response occurs in the guard zone as the packer seal with the borehole is broken. The packer inflation pressure was set at roughly 240 kPa above the ambient pressure to ensure adequate contact with the borehole without risk of damage to the rubber bladders. The leak-by pressure at this inflation was usually about 138 kPa above the ambient pressure, depending on rock conditions, and the limit for any injection pressure was typically set to 80 kPa above the ambient pressure

I.4 AUTOMATION AND MULTI-RATE APPROACH

Utilization of the automatic controls ensured that the tests would reach steady state yet allow them to be completed in minimal time. In addition, automation enabled testing to be run 24 hours a day. The automation scheme allotted a minimum time to every individual injection test. This time period allowed enough data points to be collected to determine the slope of the injection pressure response. Steady state was defined in the automation routine as when the slope of pressure change over time is less than a certain set point for the recent readings. If, after the minimum time, the criterion of steady state had not been met, the test was allowed to continue until it had been met. Pauses between tests left time to monitor recovery pressure. Any excess pressure was bled off from all zones for sufficient time to allow residual pressure in the formation to reach ambient conditions at the site before further testing. Confirmation of this bleed-off was seen in all cases.

The automation routine allowed multiple flow rates at each test interval and also ensured that injection pressure did not exceed the packer leak-by pressure. The test would be shut off if the injection pressure came within about 60% of the packer leak-by pressure and the data automatically annotated to note that steady state had not been attained. To save time, injections at higher rates would not be attempted in a zone with this situation. Conversely, if pressure in an injection zone did not rise above a certain threshold value after a short time, then the test at this rate was cut short and a higher flow rate test attempted. The multi-rate strategy ensured that, by utilizing higher flow rates, highly permeable injection intervals would more likely have sufficient pressure to generate a measurable response in the observation intervals. It also ensured that, by using low flow rates, the very tight intervals could be measured without possible interference of packer leak-by. Theoretically, the same permeability value should result for a given interval location, regardless of the flow rate used. Small differences in permeability may result at different flow rates and between repeat tests, possibly caused by movement of residual water within the fractures. In the case of water redistribution, permeability will be seen to go up slightly for higher rates as testing progresses, with injection pressures overcoming the capillary forces holding the water in the formation. A small decrease of apparent permeability with increasing flow rate can be seen in areas that are drier on account of turbulence at higher air

injection rate. Any large discrepancy between permeabilities at different flow rates and in repeat tests for a given zone can be attributed to compromised packer sealing. The maximum flow rate that did not cause the zone pressure to exceed the packer leak-by pressure during a test was chosen for the purposes of single-hole permeability calculation and for cross-hole response detection.

ATTACHMENT II

COMPUTATION TABLES FOR NICHE STUDIES

INTENTIONALLY LEFT BLANK

ATTACHMENT II. COMPUTATION TABLES FOR NICHE STUDIES

Table II-1. Computation of Aspect Ratio (depth to lateral distance)

Observed Dye Observed	Injection Borehole	Injection Interval (m)	Mass Injected (g)	Input Maximum Lateral Distance (m)	Input Maximum Penetration Depth (m)	Output Ratio of Depth to Lateral Dist.
Niche 3566 (Tptpmn)						
FD&C Red No. 40	M	2.13 - 2.44	941.7	0.73	1.52	2.08
Acid Yellow 7	M	2.77 - 3.05	120.3	0.16	0.3	1.90
FD&C Blue No. 1	M	4.57 - 4.88	474	0.30	1.3	4.33
Niche 3650 (Tptpmn)						
FD&C Red No. 40	UL	7.01 - 7.31	694.5	0.99	1.42	1.43
FD&C Blue No. 1	UM	4.27 - 4.57	675.8	0.58	1.68	2.90
FD&C Red No. 40	UM	4.88 - 5.18	937.4	0.28	0.86	3.07
FD&C Blue No. 1	UM	6.70 - 7.01	438.7	1.05	1.82	1.74
FD&C Red No. 40	UR	1.52 - 1.82	369.9	0.76	1.41	1.86
FD&C Blue No. 1	UR	2.13 - 2.43	999.8	0.32	2.57	8.03
Sulfo Rhodamine B	ML	4.88 - 5.18	151.6	0.08	0.02	0.25
Sulfo Rhodamine B	ML	6.7 - 7.01	170.9	0.25	1.02	4.06
Niche 3107 (Tptpmn)						
Green	B1.5	3.35-3.66	391.3	0.54	0.87	1.61
FD&C Blue No. 1	UM	4.88-5.18	111.7	0.27	1.19	4.41
Niche 4788 (Tptpmn)						
FD&C Red No. 40	UM	4.27-4.57	151.1	0.31	0.955	3.08
Green	UM	4.88-5.18	401.8	0.51	1.79	3.50
FD&C Blue No. 1	UM	6.40-6.70	1019.7	0.78	1.25	1.61
						Ave. Tptpmn = 2.87
Niche CD1620 (Tptpll)						
Green	#1	1.48-1.78	1184.7	0.76	1.25	1.64
Rhodamine	#1	2.54-2.84	1342.8	0.22	1.37	6.23
Green	#1	3.31-3.61	804.7	0.21	0.28	1.33
Rhodamine	#1	4.54-4.84	826.9	0.15	0.19	1.27
FD&C Blue No. 1	#1	5.44-5.74	1001.8	0.33	0.18	0.55
Rhodamine	#1	6.54-6.84	1041.3	0.16	0.07	0.44
FD&C Blue No. 1	#1	7.58-7.88	1555.9	0.17	0.18	1.06
Rhodamine	#1	8.54-8.84	1142.2	0.26	0.15	0.58
						Ave. Tptpll = 1.64
A	**B**	**C**	**D**	**E**	**F**	**G**

A through E from DTN: LB980001233124.004 [136583] for Niches 3566 and 3650.
A through E from DTN: LB980901233124.003 [105592] for Niches 3107 and 4788.
A through E from DTN: LB0102NICH5LIQ.001 [155681] for Niches 3107 and 4788.
D for Niche CD1620 are reported in kg and converted to g in table by multiplying by 1000 g/kg
G = F/E
Ave. Tptpmn and Ave. Tptpll computed using Excel 2000 arithmetic average (AVE) function.

Table II-2. Computation of Distance from Borehole to Niche Ceiling at Niche 4788, a Niche Study

Niche	Borehole & Depth (m)	Input Vertical distance from horizontal scanline to borehole UM (m)	Input Elevation of borehole UM at collar (m)	Input Elevation of borehole collar (m)	Output Difference in elevation between borehole and UM (m)	Output Elevation of borehole collar above horizontal scanline (m)	Input Borehole Inclination minutes	Input Borehole Inclination seconds	Output Borehole inclination (radians)	Output Sine(J)	Output Cosine(J)	Input Local horizontal coordinate for borehole collar (m)
4788	UL 7.62-7.93	1.505	1096.57	1096.58	0.01	1.515	-41	-13	-0.0120	-0.0120	0.9999	4.17
	UM 6.10-6.40	1.505	1096.57	1096.57	0.00	1.505	-41	-23	-0.0120	-0.0120	0.9999	4.87
	UR 5.18-5.48	1.505	1096.57	1096.57	0.00	1.505	-10	-26	-0.0030	-0.0030	1.0000	5.82
A	**B**	**C**	**D**	**E**	**F**	**G**	**H**	**I**	**J**	**K**	**L**	**M**

C a horizontal scanline or datum measured along the center line of the niche was used to relate known survey stations to the boreholes and a local coordinate system setup inside the niche. Nodes spaced 0.6 X 0.6 m apart were marked on the niche ceiling using the frame holding the seepage capture trays as the basis for the grid – see scientific notebook YMP-LBNL-RCT-2 (Trautz 2001 [156903], p. 36) for details.

D, E from survey data DTN: MO0107GSC01069.000 [156941]

F=E-D

G=C+F

H, I from survey data DTN: MO0107GSC01069.000 [156941]

K=sin(J)

L=cos(J)

M from survey data DTN: MO0107GSC01069.000 [156941], local coordinate system see note for T & U.

Table II-2. Computation of Distance from Borehole to Niche Ceiling at Niche 4788, a Niche Study (Continued).

Niche	Input Distance along inclined borehole from collar to start of test interval (m)	Input Distance along inclined borehole from collar to end of test interval (m)	Output Distance along inclined borehole from collar to center of test interval (m)	Output Vertical distance from borehole collar to the center of test interval (m)	Output Vertical distance from horizontal scanline to center of test interval (m)	Output Local horizontal coordinate for center of test interval (m)	Input Local horizontal coordinate for start of capture node (m)	Input Local horizontal coordinate for end of capture node (m)	Input Vertical distance from horizontal scanline to ceiling above start node (m)	Input Vertical distance from horizontal scanline to ceiling above end node (m)	Output Interpolated vertical distance from horizontal scanline to the ceiling beneath the center of the test interval (m)	Output Distance from borehole bottom to Ceiling (m)
4788	7.62	7.93	7.775	-0.09	1.42	11.944	11.905	11.905	0.81	0.84	0.820	0.60
	6.10	6.40	6.25	-0.08	1.43	11.12	10.955	11.26	0.84	0.855	0.848	0.58
	5.18	5.48	5.33	-0.02	1.49	11.15	10.615	11.905	0.76	0.73	0.748	0.74
	N	**O**	**P**	**Q**	**R**	**S**	**T**	**U**	**V**	**W**	**X**	**Y**

N and O from DTN: LB0010NICH4LIQ.001 [153145]

P = N+(O-N)/2

Q=K*P

R=G+Q

S=M+(P*L)

T, U represent local coordinates. They are horizontal distances from the ESF centerline taken parallel to the niche axis to the starting node and ending node of the capture system, respectively, that bracket the center of the overlying test interval, S. Note that the center of the interval lies between two nodes at the same horizontal coordinate, 11.905 m, for UL 7.62-7.93. Values from sci. notebook YMP-LBNL-RCT-2 (Trautz 2001 [156903], p. 36).

V,W are the vertical distances from the horizontal scanline plane to the ceiling of the niche at the start and end node at the horizontal coordinate T and U, respectively. Values from scientific notebook YMP-LBNL-RCT-2 (Trautz 2001 [156903], pp. 36, 38, 40, 41).

X is the interpolated distance to ceiling determined using V and W. X = V+(W-V)*(S-T)/(U-T) except for UL 7.62-7.93 where X = V+(W-V)*(0.3-0.2)/0.3 and 0.3 is the distance between nodes (2,12) and (3,12).

Y = R-X

Table II-3a. Computation of Liquid Release Flux for Post-Excavation Seepage Tests at Niche 3107, Niche Studies

Borehole	Depth (m)	Test Name	Input Liquid-release rate Qs (kg/s)	Input Seepage percentage y' (%)	Computed Cross-sectional area A (m^2)	Output Liquid-release flux qs (m/s)	Output Liquid-release flux qs (mm/yr)
UM	4.88-5.18	Test #1 3/4/99	1.4266E-05	0	0.053	2.67E-07	8420
		Test #1 4/7/99	9.7304E-05	--	0.053	1.82E-06	57430
		Test #1 4-27-99	3.9897E-05	5.465	0.053	7.47E-07	23548
		Test #1 4-30-99	1.4113E-05	0	0.053	2.64E-07	8330
		Test #1 5/6/99	9.0739E-05	47.271	0.053	1.70E-06	53555
		Test #1 9-21-99	8.39647E-05	42.975	0.053	1.57E-06	49557
		Test #1 9-23-99	8.7576E-05	46.08	0.053	1.64E-06	51689
		Test #1 9-27-99	9.0044E-05	59.5915	0.053	1.69E-06	53145
		Test #1 10-11-99	9.03981E-05	70.0857	0.053	1.69E-06	53354
A	**B**	**C**	**D**	**E**	**F**	**G**	**H**

UM = upper middle

A through E from DTN LB0010NICH3LIQ.001 [153144]

F through H computed in Excel 2000 spreadsheet using formulae below:

F = wetted area of borehole up to return port of packers = $[2\pi-(2\text{Arccosine}(d/r))]hr$ where d = nominal vertical distance from center of borehole to return port on packer system = 2.54 cm r = nominal radius of borehole = 3.81 cm = 0.0381 m h = nominal test interval length = 1 ft = 0.3048 m

G = D*(1000 g/kg)/(1,000,000 g/m^3 *F) = D/(1000*F), where density of water is assumed = 1,000,000 g/m^3

H = G *(1000 mm/m)*(86400 s/day)*(365 days/year)

Table II-3b. Computation of Liquid Release Flux for Post-Excavation Seepage Tests at Niche 4788, Niche Studies

Borehole	Depth (m)	Test Name	Input Liquid-release rate Q_s (kg/s)	Input Seepage percentage y' (%)	Computed Cross-sectional area A (m^2)	Output Liquid-release flux q_s (m/s)	Output Liquid-release flux q_s (mm/yr)
UL	7.62-7.93	Test #1 11/3/99	8.8095E-05	24.159	0.053	1.65E-06	51995
		Test #1 11-30-99 Niche 4788	4.9246E-05	17.964	0.053	9.22E-07	29066
		Test #1 01-24-00	7.81146E-06	0.000	0.053	1.46E-07	4610
		Test #1 6-26-2000	1.91662E-05	14.4488	0.053	3.59E-07	11312
UM	6.10-6.40	Test #1 Niche 4788 11/16/99	9.16384E-05	35.383	0.053	1.72E-06	54086
		Test #1 Niche 4788 12-10-99	3.91451E-05	23.405	0.053	7.33E-07	23104
		Test #1 02-09-2000	8.819E-06	0	0.053	1.65E-07	5205
		Test #1 3-10-2000	9.681E-06	0	0.053	1.81E-07	5714
		Test #1 3-14-2000	8.8479E-06	0	0.053	1.66E-07	5222
		Test #1 06-08-2000	2.0489E-05	8.5381	0.053	3.83E-07	12093
UR	5.18-5.48	Test #1 Niche 4788 12/7/99	9.00855E-05	68.6623	0.053	1.69E-06	53170
		Test #1 1/5/2000	3.79689E-05	56.4895	0.053	7.11E-07	22410
		Test #1 02-14-2000	8.80016E-06	11.092	0.053	1.65E-07	5194
A	**B**	**C**	**D**	**E**	**F**	**G**	**H**

UL = upper left

UM = upper middle

UR = upper right

A through E from DTN LB0010NICH4LIQ.001 [153145]

F through H computed in Excel 2000 spreadsheet using formulae below:

F = wetted area of borehole up to return port of packers = $[2\pi-(2\text{Arccosine}(d/r))]hr$ where:

d = nominal vertical distance from center of borehole to return port on packer system = 2.54 cm

r = nominal radius of borehole = 3.81 cm = 0.0381 m

h = nominal test interval length = 1 ft = 0.3048 m

G = D*(1000 g/kg)/(1,000,000 g/m^3 *F) = D/(1000*F), where density of water is assumed = 1,000,000 g/m^3

H = G *(1000 mm/m)*(86400 s/day)*(365 days/year)

Table II-4. Summary of Regression Equations and Computation of Seepage Threshold Fluxes (K o*) and Saturated Hydraulic Conductivities (K l), a Niche Study

Niche	Borehole & Depth (m)	Output Linear regression equation	Input Data points	Output Correlation coefficient (R2)	Input Slope	Input intercept	Output/Input Seepage threshold flux Ko* (m/s)	Output Seepage threshold flux Ko* (mm/yr)	Input Air permeability k (m2)	Output Saturated hydraulic conductivity Kl (m/s)
3107	UM 4.88-5.18	$y = 30.440Ln(K_o) + 456.085$	8	0.820	30.440	456.085	3.11E-07	9.81E+03	NA	NA
3650	UL 7.01-7.32	$y = 0.6833Ln(K_o) + 8.5742$	2	NR	--	--	3.55E-06	1.12E+05	--	8.98E-05
	UL 7.62-7.92	$y = 5.7394Ln(K_o) + 92.627$	3	0.979	--	--	9.80E-08	3.09E+03	--	1.51E-04
	UM 4.27-4.57	$y = 5.2757Ln(K_o) + 79.443$	4	0.921	--	--	2.89E-07	9.11E+03	--	2.62E-05
	UM 4.88-5.18	$y = 2.304Ln(K_o) + 31.767$	3	0.975	--	--	1.03E-06	3.25E+04	--	2.52E-03
	UM 5.49-5.79	$y = 5.8876Ln(K_o) + 87.528$	4	0.963	--	--	3.50E-07	1.10E+04	--	2.16E-05
	UR 4.27-4.57	$y = 0.314Ln(K_o) + 4.3283$	2	NR	--	--	1.03E-06	3.25E+04	--	4.08E-05
	UR 4.88-5.18	$y = 0.3165Ln(K_o) + 4.3751$	2	NR	--	--	9.92E-07	3.13E+04	--	9.87E-05
	UR 5.49-5.79	$y = 28.419Ln(K_o) + 351.09$	2	NR	--	--	4.31E-06	1.36E+05	--	1.71E-05
	UR 6.10-6.40	$y = 4.2169Ln(K_o) + 79.596$	2	NR	--	--	6.35E-09	2.00E+02	--	3.01E-05
	UR 6.71-7.01	$y = 10.574Ln(K_o) + 165.28$	3	0.974	--	--	1.63E-07	5.14E+03	--	2.28E-04
4788	UL 7.62-7.93	$y = 9.273Ln(K_o) + 148.119$	4	0.929	9.273	148.119	1.16E-07	3.65E+03	2.51E-12	2.46E-05
	UM 6.10-6.40	$y = 15.697Ln(K_o) + 243.611$	4	0.980	15.697	243.611	1.82E-07	5.74E+03	2.50E-11	2.45E-04
	UR 5.18-5.48	$y = 25.415Ln(K_o) + 410.285$	3	0.970	25.415	410.285	9.75E-08	3.07E+03	4.00E-13	3.92E-06
A	B	C	D	E	F	G	H	I	J	K

NA = not available, the test could not be completed as planned because of rock properties outside the equipment's measurable range.

NR = not reported because two data points result in perfect correlation (R^2 =1.0), therefore, correlation coefficient is meaningless Intermediate computations not performed for Niche 3650 because they were performed in earlier technical products using the same formulae / methods shown below. Output shown in Table for Niche 3650 was obtained directly from TDMS except where noted.

C for Niche 3650 from DTN LB980001233124.004 [136583]

C for Niche 3107 and 4788 computed below using Excel 2000 built-in Regression Analysis Tool pack (see Tables II-4b - II-4e). y = predicted seepage percentage (%). Derived from measured seepage percentages (y') in Table II-4a (E). K_o = net downward liquid-release flux (m/s) from regression model. Derived from computed liquid-release fluxes ($\ln[q_s]$) in Table II-4a (G).

D = number of data points used in linear regression

E for Niche 3650 from DTN: LB980001233124.004 [136583]

E for Niche 3107 and 4788 = correlation coefficient from Excel 2000 built-in Regression Analysis Tool pack (see Tables II-4b - II 4e). F = slope of regression line C

G = intercept of regression line C

H for Niche 3650 from DTN: LB980901233124.003 [105592]

H for Niche 3107 and 4788 are computed by setting y=0 in C and solving $K_o(0) = K_{o^*} = \exp(-G/F)$

I = 1000 mm/m * 86400 s/day * 365 days/year for all the niches

J for Niche 3107 and 4788 from DTN: LB990601233124.001 [105888]

K = J * (100*100 cm^2/m^2) * 980 m/s/cm^2; the conversion factor 980 is from Freeze and Cherry 1979 [101173].

K for Niche 3650 from DTN LB980901233124.003 [105592]

Table II-4a. Data Used in Linear Regression Analysis (y' vs. ln q_s)

Niche	Borehole	Depth (m)	Test name	Input Seepage percentages y' (%)	Input Liquid-release flux q_s (m/s)	Output Natural log of liquid release flux ln(q_s)
3107	UM	4.88-5.18	Test #1 3/4/99	0.0	2.67E-07	-15.136
			Test #1 4-27-99	5.5	7.47E-07	-14.108
			Test #1 4-30-99	0.0	2.64E-07	-15.147
			Test #1 5/6/99	47.3	1.70E-06	-13.286
			Test #1 9-21-99	43.0	1.57E-06	-13.364
			Test #1 9-23-99	46.1	1.64E-06	-13.321
			Test #1 9-27-99	59.6	1.69E-06	-13.294
			Test #1 10-11-99	70.1	1.69E-06	-13.290
4788	UL	7.62-7.93	Test #1 11/3/99	24.2	1.65E-06	-13.315
			Test #1 11-30-99 Niche 4788	18.0	9.22E-07	-13.897
			Test #1 01-24-00	0.0	1.46E-07	-15.738
			Test #1 6-26-2000	14.4	3.59E-07	-14.841
	UM	6.10-6.40	Test #1 Niche 4788 11/16/99	35.4	1.72E-06	-13.276
			Test #1 Niche 4788 12-10-99	23.4	7.33E-07	-14.127
			Test #1 3-14-2000	0.0	1.66E-07	-15.614
			Test #1 06-08-2000	8.5	3.83E-07	-14.774
	UR	5.18-5.48	Test #1 Niche 4788 12/7/99	68.7	1.69E-06	-13.293
			Test #1 1/5/2000	56.5	7.11E-07	-14.157
			Test #1 02-14-2000	11.1	1.65E-07	-15.619
A	**B**	**C**	**D**	**E**	**F**	**G**

A through F from Table II-3a and Table II-3b

G = ln(F)

Table II-4b. Linear Regression Summary (Output) for Niche 3107 UM 4.88-5.18

ANOVA								
	df	***SS***	***MS***	***F***	***Significance F***			
Regression	1	4500.737	4500.737	27.411	0.002			
Residual	6	985.173	164.195					
Total	7	5485.910						
	Coefficients	***Standard Error***	***t Stat***	***P-value***	***Lower 95%***	***Upper 95%***	***Lower 95.0%***	***Upper 95.0%***
Intercept	456.085	80.759	5.647	0.001	258.474	653.695	258.474	653.695
X Variable 1	30.440	5.814	5.236	0.002	16.214	44.667	16.214	44.667

All output shown in this table was obtained using Microsoft Excel 2000 built-in regression analysis tool pak.

Intercept = y-intercept of linear regression equation

X Variable 1 = slope of linear regression equation

Data used in regression analysis are from Table II-4a.

Regression Statistics: Multiple R = 0.906; R Square = 0.820; Adjusted R Square = 0.790; Standard Error = 12.814; Number of Observations = 8.

Table II-4c. Linear Regression Summary (Output) for Niche 4788 UL 7.62-7.93

ANOVA								
	df	***SS***	***MS***	***F***	***Significance F***			
Regression	1	292.815	292.815	26.353	0.036			
Residual	2	22.223	11.111					
Total	3	315.038						
	Coefficients	***Standard Error***	***t Stat***	***P-value***	***Lower 95%***	***Upper 95%***	***Lower 95.0%***	***Upper 95.0%***
Intercept	148.119	26.152	5.664	0.030	35.597	260.640	35.597	260.640
X Variable 1	9.273	1.806	5.133	0.036	1.501	17.045	1.501	17.045

All output shown in this table was obtained using Microsoft Excel 2000 built-in regression analysis tool pak.

Intercept = y-intercept of linear regression equation

X Variable 1 = slope of linear regression equation

Data used in regression analysis are from Table II-4a.

Regression Statistics: Multiple R = 0.964; R Square = 0.929; Adjusted R Square = 0.894; and number of Observations = 4.

Table II-4d. Linear Regression Summary (Output) for Niche 4788 UM 6.10-6.40

ANOVA								
	df	***SS***	***MS***	***F***	***Significance F***			
Regression	1	724.849	724.849	99.295	0.010			
Residual	2	14.600	7.300					
Total	3	739.449						
	Coefficients	***Standard Error***	***t Stat***	***P-value***	***Lower 95%***	***Upper 95%***	***Lower 95.0%***	***Upper 95.0%***
Intercept	243.611	22.798	10.685	0.009	145.517	341.704	145.517	341.704
X Variable 1	15.697	1.575	9.965	0.010	8.919	22.474	8.919	22.474

All output shown in this table was obtained using Microsoft Excel 2000 built-in regression analysis tool pak.

Intercept = y-intercept of linear regression equation

X Variable 1 = slope of linear regression equation

Data used in regression analysis are from Table II-4a.

Regression Statistics: Multiple R = 0.990; R Square = 0.980; Adjusted R Square = 0.970; Standard Error = 2.702; Number of Observations = 4

Table II-4e. Linear Regression Summary (Output) for Niche 4788 UR 5.18-5.48

ANOVA								
	df	***SS***	***MS***	***F***	***Significance F***			
Regression	1	1785.798	1785.798	32.263	0.111			
Residual	1	55.352	55.352					
Total	2	1841.150						
	Coefficients	***Standard Error***	***t Stat***	***P-value***	***Lower 95%***	***Upper 95%***	***Lower 95.0%***	***Upper 95.0%***
Intercept	410.285	64.381	6.373	0.099	-407.747	1228.317	-407.747	1228.317
X Variable 1	25.415	4.474	5.680	0.111	-31.438	82.268	-31.438	82.268

All output shown in this table was obtained using Microsoft Excel 2000 built-in regression analysis tool pak.

Intercept = y-intercept of linear regression equation

X Variable 1 = slope of linear regression equation

Data used in regression analysis are from Table II-4a.

Regression Statistics: Multiple R = 0.985; R Square = 0.970; Adjusted R Square = 0.940; Standard Error = 7.440; Number of Observations = 3

Table II-5. Computation of Θ-Values, a Niche Study

Niche	Borehole & Depth (m)	Input Seepage threshold flux K_{o*} (m/s)	Input Saturated hydraulic conductivity K_l (m/s)	Intermediate Output K_{o*} / K_l (dim.less)	Intermediate Output Inverse of dimensionless potentials $[\vartheta_{max}(s)]^{-1}$	Output Sorptive number α (m^{-1})	Output Capillary strength α^{-1} (m)	Output Error (%)
3650	UL 7.01-7.32	3.55E-06	8.98E-05	--	--	11.7	0.0855	--
	UL 7.62-7.92	9.80E-08	1.51E-04	--	--	771.9	0.0013	--
	UM 4.27-4.57	2.89E-07	2.62E-05	--	--	44.4	0.0225	--
	UM 4.88-5.18	1.03E-06	2.52E-03	--	--	1225.5	0.0008	--
	UM 5.49-5.79	3.50E-07	2.16E-05	--	--	29.9	0.0334	--
	UR 4.27-4.57	1.03E-06	4.08E-05	--	--	18.8	0.0532	--
	UR 4.88-5.18	9.92E-07	9.87E-05	--	--	48.8	0.0205	--
	UR 5.49-5.79	4.31E-06	1.71E-05	--	--	1.4	0.71	--
	UR 6.10-6.40	6.35E-09	3.01E-05	--	--	2373.7	0.0004	--
	UR 6.71-7.01	1.63E-07	2.28E-04	--	--	699.2	0.0014	--
4788	UL 7.62-7.93	1.16E-07	2.46E-05	4.70E-03	4.70E-03	105.4	0.0095	-3.66E-04
	UM 6.10-6.40	1.82E-07	2.45E-04	7.43E-04	7.43E-04	672.3	0.0015	-1.80E-04
	UR 5.18-5.48	9.75E-08	3.92E-06	2.49E-02	2.49E-02	19.1	0.0523	-9.41E-05
Theoretical limit						521.7	0.0019	
A	B	C	D	E	F	G	H	I

Intermediate computations not performed for Niche 3650 because they were performed in other technical products using the same formulae shown below. Output shown in Table for Niche 3650 was obtained directly from TDMS except where noted.

C from Table II-4 (H)

D from Table II-4 (K)

E = C/D

F = $1/(2*G+2-(1/G)) = [\vartheta_{max}(s)]^{-1}$, where ϑ_{max} is defined by Equation (84) and s is defined by Equation (14) in Philip et al. 1989 [105743]. In our case, $s = 0.5*\alpha*r = 0.5*\alpha*2 = \alpha$ since the nominal radius of the niche (r) is approximately 2 meters.

G = α, sorptive number, where α is selected such that absolute value of Error (i.e., column I) is < 1E-03 %

G for Niche 3650 from DTN: LB980901233124.003 [105592]

G (Theoretical limit) = α = maximum sorptive number = $(2*\rho*g/\gamma)^{1/2}$, where ρ = density of water assumed equal to 1000 kg/m3, g = acceleration of gravity 9.8 m/s2, and γ = surface tension of water assumed equal to 0.072 kg/s2

Equation G (theoretical limit) can be derived by substituting the maximum aperture (β_{max}) that can sustain a fluid meniscus because of capillary forces ($\beta_{max} = (2\gamma/\rho g)^{1/2}$) into the capillary height of rise equation $2\alpha^{-1} = 2\gamma/(\rho\gamma\beta_{max})$.

Expression for β_{max} from Wang and Narasimhan 1993 [106793]. Expression for capillary height of rise equation from Philip 1989 [156974].

H = $1/G = \alpha^{-1}$, capillary strength of the porous medium computed for all niches

I = $100*(E-F)/E$, Note that $K_{o*} / K_l = [\vartheta_{max}(s)]^{-1}$ as noted in Section 3.4 of Philip et al. 1989 [105743].

Table II-6. Computed Values of the Maximum Dimensionless Potential, Θ max

Output K_l (mm/yr)	Input K_l (m/s)	Input s (dim.less)	Input 2s (dim.less)	Output/Input ϑ_{max} (dim.less)	Output $[\vartheta_{max}]^{-1}$ (dim.less)	Output/Input K_{o*} (m/s)	Output K_{o*} (mm/yr)
3.154E+01	1.000E-09	521.7	1043.5	1045.50	9.56E-04	9.56E-13	3.02E-02
4.730E+01	1.500E-09			1045.50	9.56E-04	1.43E-12	4.52E-02
6.307E+01	2.000E-09			1045.50	9.56E-04	1.91E-12	6.03E-02
9.461E+01	3.000E-09			1045.50	9.56E-04	2.87E-12	9.05E-02
1.261E+02	4.000E-09			1045.50	9.56E-04	3.83E-12	1.21E-01
1.577E+02	5.000E-09			1045.50	9.56E-04	4.78E-12	1.51E-01
1.892E+02	6.000E-09			1045.50	9.56E-04	5.74E-12	1.81E-01
2.208E+02	7.000E-09			1045.50	9.56E-04	6.70E-12	2.11E-01
2.523E+02	8.000E-09			1045.50	9.56E-04	7.65E-12	2.41E-01
2.838E+02	9.000E-09			1045.50	9.56E-04	8.61E-12	2.71E-01
3.154E+02	1.000E-08			1045.50	9.56E-04	9.56E-12	3.02E-01
4.730E+02	1.500E-08			1045.50	9.56E-04	1.43E-11	4.52E-01
6.307E+02	2.000E-08			1045.50	9.56E-04	1.91E-11	6.03E-01
9.461E+02	3.000E-08			1045.50	9.56E-04	2.87E-11	9.05E-01
1.261E+03	4.000E-08			1045.50	9.56E-04	3.83E-11	1.21E+00
1.577E+03	5.000E-08			1045.50	9.56E-04	4.78E-11	1.51E+00
1.892E+03	6.000E-08			1045.50	9.56E-04	5.74E-11	1.81E+00
2.208E+03	7.000E-08			1045.50	9.56E-04	6.70E-11	2.11E+00
2.523E+03	8.000E-08			1045.50	9.56E-04	7.65E-11	2.41E+00
2.838E+03	9.000E-08			1045.50	9.56E-04	8.61E-11	2.71E+00
3.154E+03	1.000E-07			1045.50	9.56E-04	9.56E-11	3.02E+00
4.730E+03	1.500E-07			1045.50	9.56E-04	1.43E-10	4.52E+00
6.307E+03	2.000E-07			1045.50	9.56E-04	1.91E-10	6.03E+00
9.461E+03	3.000E-07			1045.50	9.56E-04	2.87E-10	9.05E+00
1.261E+04	4.000E-07			1045.50	9.56E-04	3.83E-10	1.21E+01
1.577E+04	5.000E-07			1045.50	9.56E-04	4.78E-10	1.51E+01
1.892E+04	6.000E-07			1045.50	9.56E-04	5.74E-10	1.81E+01
2.208E+04	7.000E-07			1045.50	9.56E-04	6.70E-10	2.11E+01
2.523E+04	8.000E-07			1045.50	9.56E-04	7.65E-10	2.41E+01
2.838E+04	9.000E-07			1045.50	9.56E-04	8.61E-10	2.71E+01
3.154E+04	1.000E-06			1045.50	9.56E-04	9.56E-10	3.02E+01
4.730E+04	1.500E-06			1045.50	9.56E-04	1.43E-09	4.52E+01
6.307E+04	2.000E-06			1045.50	9.56E-04	1.91E-09	6.03E+01
9.461E+04	3.000E-06			1045.50	9.56E-04	2.87E-09	9.05E+01
1.261E+05	4.000E-06			1045.50	9.56E-04	3.83E-09	1.21E+02
1.577E+05	5.000E-06			1045.50	9.56E-04	4.78E-09	1.51E+02
1.892E+05	6.000E-06			1045.50	9.56E-04	5.74E-09	1.81E+02
2.208E+05	7.000E-06			1045.50	9.56E-04	6.70E-09	2.11E+02
2.523E+05	8.000E-06			1045.50	9.56E-04	7.65E-09	2.41E+02
2.838E+05	9.000E-06			1045.50	9.56E-04	8.61E-09	2.71E+02

Table II-6. Computed Values of the Maximum Dimensionless Potential, Θ max (Continued)

Output K_l (mm/yr)	Input K_l (m/s)	Input s (dim.less)	Input 2s (dim.less)	Output/Input ϑ_{max} (dim.less)	Output $[\vartheta_{max}]^{-1}$ (dim.less)	Output/Input K_{o*} (m/s)	Output K_{o*} (mm/yr)
3.154E+05	1.000E-05			1045.50	9.56E-04	9.56E-09	3.02E+02
4.730E+05	1.500E-05			1045.50	9.56E-04	1.43E-08	4.52E+02
6.307E+05	2.000E-05			1045.50	9.56E-04	1.91E-08	6.03E+02
9.461E+05	3.000E-05			1045.50	9.56E-04	2.87E-08	9.05E+02
1.261E+06	4.000E-05			1045.50	9.56E-04	3.83E-08	1.21E+03
1.577E+06	5.000E-05			1045.50	9.56E-04	4.78E-08	1.51E+03
1.892E+06	6.000E-05			1045.50	9.56E-04	5.74E-08	1.81E+03
2.208E+06	7.000E-05			1045.50	9.56E-04	6.70E-08	2.11E+03
2.523E+06	8.000E-05			1045.50	9.56E-04	7.65E-08	2.41E+03
2.838E+06	9.000E-05			1045.50	9.56E-04	8.61E-08	2.71E+03
3.154E+06	1.000E-04			1045.50	9.56E-04	9.56E-08	3.02E+03
4.730E+06	1.500E-04			1045.50	9.56E-04	1.43E-07	4.52E+03
6.307E+06	2.000E-04			1045.50	9.56E-04	1.91E-07	6.03E+03
9.461E+06	3.000E-04			1045.50	9.56E-04	2.87E-07	9.05E+03
1.261E+07	4.000E-04			1045.50	9.56E-04	3.83E-07	1.21E+04
1.577E+07	5.000E-04			1045.50	9.56E-04	4.78E-07	1.51E+04
1.892E+07	6.000E-04			1045.50	9.56E-04	5.74E-07	1.81E+04
2.208E+07	7.000E-04			1045.50	9.56E-04	6.70E-07	2.11E+04
2.523E+07	8.000E-04			1045.50	9.56E-04	7.65E-07	2.41E+04
2.838E+07	9.000E-04			1045.50	9.56E-04	8.61E-07	2.71E+04
3.154E+07	1.000E-03			1045.50	9.56E-04	9.56E-07	3.02E+04
4.730E+07	1.500E-03			1045.50	9.56E-04	1.43E-06	4.52E+04
6.307E+07	2.000E-03			1045.50	9.56E-04	1.91E-06	6.03E+04
9.461E+07	3.000E-03			1045.50	9.56E-04	2.87E-06	9.05E+04
1.261E+08	4.000E-03			1045.50	9.56E-04	3.83E-06	1.21E+05
1.577E+08	5.000E-03			1045.50	9.56E-04	4.78E-06	1.51E+05
1.892E+08	6.000E-03			1045.50	9.56E-04	5.74E-06	1.81E+05
2.208E+08	7.000E-03			1045.50	9.56E-04	6.70E-06	2.11E+05
2.523E+08	8.000E-03			1045.50	9.56E-04	7.65E-06	2.41E+05
2.838E+08	9.000E-03			1045.50	9.56E-04	8.61E-06	2.71E+05
3.154E+08	1.000E-02			1045.50	9.56E-04	9.56E-06	3.02E+05
A	**B**	**C**	**D**	**E**	**F**	**G**	**H**

Refer to Philip et al. (1989 [105743]) for an explanation of nomenclature.

A=B*1000 mm/m * 86400 s/day * 365 days/year; dim.less = dimensionless

B = saturated hydraulic conductivity whose values are arbitrary set in this column to span the range of values measured during air k tests performed at Niches 3650 and 4788.

C = G (Theoretical limit) from bottom of Table II-5.

D = 2*C

E = 2s +2 -1/s

F = 1/E

G = B*F

H = G*1000 mm/m * 86400 s/day * 365 days/year.

Table II-7. Computation of Estimated Water Potentials, a Niche Study

Niche	Borehole Depth (m)	Test Name	Input Liquid release flux q_s (m/s)	Input Saturated hydraulic conductivity K_l (m/s)	Input Alpha value α (m^{-1})	Output Absolute value of the water potential $x\psi x$ (m)
3650	UL 7.62-7.92	Test #2 1-6-98	9.49E-06	1.51E-04	771.9	3.59E-03
	UL 7.62-7.92	Test #1 2-12-98	1.89E-06	1.51E-04	771.9	5.68E-03
	UL 7.62-7.92	Test #1 3-4-98	2.33E-07	1.51E-04	771.9	8.39E-03
	UM 4.27-4.57	Test 5 Niche 3650 (11-13-97)	3.78E-05	2.62E-05	44.4	8.26E-03
	UM 4.27-4.57	Test #1 12-3-97	9.42E-06	2.62E-05	44.4	2.30E-02
	UM 4.27-4.57	Test #2 12-3-97	9.47E-06	2.62E-05	44.4	2.29E-02
	UM 4.27-4.57	Test #1 1-7-98	8.82E-07	2.62E-05	44.4	7.64E-02
	UM 4.27-4.57	Test #2 2-10-98	3.09E-07	2.62E-05	44.4	1.00E-01
	UM 4.88-5.18	Test 1 Niche 3650 (11-12-97)	5.41E-05	2.52E-03	1225.5	3.13E-03
	UM 4.88-5.18	Test #1 12-4-97	9.49E-06	2.52E-03	1225.5	4.56E-03
	UM 4.88-5.18	Test #2 12-5-97	2.70E-06	2.52E-03	1225.5	5.58E-03
	UM 4.88-5.18	Test #1 1-8-98	8.75E-07	2.52E-03	1225.5	6.50E-03
	UM 4.88-5.18	Test #1 3-6-98	2.48E-07	2.52E-03	1225.5	7.53E-03
	UM 5.49-5.79	Test 4 Niche 3650 (11-13-97)	3.87E-05	2.16E-05	29.9	1.95E-02
	UM 5.49-5.79	Test #2 12-4-97	9.43E-06	2.16E-05	29.9	2.77E-02
	UM 5.49-5.79	Test #1 1-9-98	1.08E-06	2.16E-05	29.9	1.00E-01
	UM 5.49-5.79	Test #1 2-11-98	2.55E-07	2.16E-05	29.9	1.48E-01
	UR 6.71-7.01	Test #1 1-13-98	3.68E-06	2.28E-04	699.2	5.90E-03
	UR 6.71-7.01	Test #1 2-3-98	1.91E-06	2.28E-04	699.2	6.84E-03
	UR 6.71-7.01	Test #1 3-5-98	2.48E-07	2.28E-04	699.2	9.76E-03
4788	UL 7.62-7.93	Test #1 11/3/99	1.65E-06	2.46E-05	105.4	2.56E-02
	UL 7.62-7.93	Test #1 11-30-99 Niche 4788	9.22E-07	2.46E-05	105.4	3.12E-02
	UL 7.62-7.93	Test #1 6-26-2000	3.59E-07	2.46E-05	105.4	4.01E-02
	UL 7.62-7.93	Test #1 01-24-00	1.46E-07	2.46E-05	105.4	4.86E-02
	UM 6.10-6.40	Test #1 Niche 4788 11/16/99	1.72E-06	2.45E-04	672.3	7.38E-03
	UM 6.10-6.40	Test #1 Niche 4788 12-10-99	7.33E-07	2.45E-04	672.3	8.65E-03
	UM 6.10-6.40	Test #1 06-08-2000	3.83E-07	2.45E-04	672.3	9.61E-03
	UM 6.10-6.40	Test #1 3-14-2000	1.66E-07	2.45E-04	672.3	1.09E-02
	UR 5.18-5.48	Test #1 Niche 4788 12/7/99	1.69E-06	3.92E-06	19.1	4.41E-02
	UR 5.18-5.48	Test #1 1/5/2000	7.11E-07	3.92E-06	19.1	8.93E-02
	UR 5.18-5.48	Test #1 02-14-2000	1.65E-07	3.92E-06	19.1	1.66E-01
A	**B**	**C**	**D**	**E**	**F**	**G**

D for Niche 3650 from DTN: LB980901233124.003 [105592]; D for Niche 4788 computed in Table II-3b (G), respectively.

E from Table II-4 (K).

F from Table II-5 (G)

G = xln(D/E)/Fx; G for Niche 3650 from DTN: LB980901233124.003 [105592] using same formula

Table II-8. Computation of Estimated Water Content Change, Niche Studies

Niche	Depth (m)	Test Name	Input Liquid Release Flux q_s, (m/s)	Input Arrival Time of Wetting Front at Ceiling, t (s)	Input Distance to Ceiling z_p, (m)	Output Average Water Content Change $\theta_{ave} - \theta_n$ (m^3/m^3)
3650	UL 7.62-7.92	Test #2 1-6-98	9.49E-06	690	0.65	0.0101
	UL 7.62-7.92	Test #1 2-12-98	1.89E-06	570	0.65	0.0017
	UL 7.62-7.92	Test #1 3-4-98	2.33E-07	2610	0.65	0.0009
	UM 4.27-4.57	Test 5 Niche 3650 (11-13-97)	3.78E-05	416	0.65	0.0242
	UM 4.27-4.57	Test #1 12-3-97	9.42E-06	1008	0.65	0.0146
	UM 4.27-4.57	Test #2 12-3-97	9.47E-06	514	0.65	0.0075
	UM 4.27-4.57	Test #1 1-7-98	8.82E-07	8811	0.65	0.0120
	UM 4.27-4.57	Test #2 2-10-98	3.09E-07	13375	0.65	0.0063
	UM 4.88-5.18	Test 1 Niche 3650 (11-12-97)	5.41E-05	180	0.65	0.0150
	UM 4.88-5.18	Test #1 12-4-97	9.49E-06	298	0.65	0.0043
	UM 4.88-5.18	Test #2 12-5-97	2.70E-06	952	0.65	0.0040
	UM 4.88-5.18	Test #1 1-8-98	8.75E-07	6060	0.65	0.0082
	UM 4.88-5.18	Test #1 3-6-98	2.48E-07	21690	0.65	0.0083
	UM 5.49-5.79	Test 4 Niche 3650 (11-13-97)	3.87E-05	208	0.65	0.0124
	UM 5.49-5.79	Test #2 12-4-97	9.43E-06	420	0.65	0.0061
	UM 5.49-5.79	Test #1 1-9-98	1.08E-06	2750	0.65	0.0046
	UM 5.49-5.79	Test #1 2-11-98	2.55E-07	10130	0.65	0.0040
	UR 6.71-7.01	Test #1 1-13-98	3.68E-06	416	0.65	0.0024
	UR 6.71-7.01	Test #1 2-3-98	1.91E-06	626	0.65	0.0018
	UR 6.71-7.01	Test #1 3-5-98	2.48E-07	4457	0.65	0.0017
4788	UL 7.62-7.93	Test #1 11/3/99	1.65E-06	7057	0.60	0.0193
	UL 7.62-7.93	Test #1 11-30-99 Niche 4788	9.22E-07	3602	0.60	0.0055
	UL 7.62-7.93	Test #1 6-26-2000	3.59E-07	16445	0.60	0.0098
	UL 7.62-7.93	Test #1 01-24-00	1.46E-07	45697	0.60	0.0111
	UM 6.10-6.40	Test #1 Niche 4788 11/16/99	1.72E-06	16572	0.58	0.0489
	UM 6.10-6.40	Test #1 Niche 4788 12-10-99	7.33E-07	39938	0.58	0.0503
	UM 6.10-6.40	Test #1 06-08-2000	3.83E-07	50190	0.58	0.0331
	UM 6.10-6.40	Test #1 3-14-2000	1.66E-07	124800	0.58	0.0355
	UR 5.18-5.48	Test #1 Niche 4788 12/7/99	1.69E-06	4034	0.74	0.0092
	UR 5.18-5.48	Test #1 1/5/2000	7.11E-07	5707	0.74	0.0055
	UR 5.18-5.48	Test #1 02-14-2000	1.65E-07	24900	0.74	0.0055
A	**B**	**C**	**D**	**E**	**F**	**G**

D for Niche 3650 from DTN: LB980901233124.003 [105592]

D for Niche 4788 computed in Table II-3b (G), respectively.

E in hr:minute:second format for Niche 4788 from DTN: LB0010NICH4LIQ.001 [153145]

E conversion from hr:minute:second format to seconds = hours*3600+minutes*60+seconds in table

E in seconds for Niche 3650 from DTN: LB980901233124.003 [105592] using same conversion

F for Niche 3650 from scientific notebook YMP-LBNL-JSW-6c (Wang 1999 [153449], p. 84).

F for Niche 4788 from Table II-2

G = D*E/F for Niche 4788

G for Niche 3650 from DTN: LB980901233124.003 [105592] using same formula

ATTACHMENT III

COMPARISON OF LIQUID AND AIR-DERIVED SATURATED HYDRAULIC CONDUCTIVITIES

INTENTIONALLY LEFT BLANK

ATTACHMENT III COMPARISON OF LIQUID AND AIR-DERIVED SATURATED HYDRAULIC CONDUCTIVITIES

The liquid-release rate, Q_s, measured during each test (Section 6.2.1.3.1) was converted to a liquid-release flux, q_s, using the following equation:

$$q_s = \frac{Q_s}{A \rho_w} \quad \text{(Eq. III-1)}$$

where A is the cross-sectional area of flow and ρ_w is the density of water (set at 1.0E+6 g/m^3). The q_s data are tabulated in DTN: LB980001233124.004 [136583] for the seepage tests conducted at Niche 3650.

The cross-sectional area was derived by the water level that could rise to a maximum elevation of 0.0635 m in the borehole, equal to the maximum ponding depth within the borehole. The ponding depth is controlled by the elevation of the liquid-return line, which prevents the buildup of excess pressure in the test interval by allowing water to flow from the test interval back to the surface. If water rises to the level of the return line, then wetted area A is less than the surface area of the entire test interval and equal to that portion of the curved surface area of a right circular cylinder lying below the water line as follows (Selby 1975 [106143], pp. 12, 16):

$$A = \left[2\pi - \left(2\,\text{Arccosine}\left(d / r\right)\right)\right] h\, r \quad \text{(Eq. III-2)}$$

where d is equal to the vertical distance from the center of the cylinder to the water line (0.0254 m), r is equal to radius of the borehole (0.0381 m), and h is equal to the test interval length (0.3048 m). With these parameters, the cross-sectional area of flow A is equal to 5.343E-02 m^2.

With Assumptions 5.2-1 and 5.2-2 described in Section 5.2.1, we estimate the saturated hydraulic conductivity for liquid flow through the fractured porous medium by equating the air permeability (k) derived from the air-injection tests to the water permeability (k_l) of the porous medium. In turn, k_l is related to the saturated hydraulic conductivity (K_l) of a porous medium through the functional relation defined by Darcy's law (Freeze and Cherry 1979 [101173], Equation (2.28), p. 27):

$$K_l = \frac{k_l\, \rho_w g}{\mu} \quad \text{(Eq. III-3)}$$

where g is the acceleration of gravity and μ is the viscosity of water. Air-permeability values reported in DTN: LB980001233124.004 [136583] were converted to the equivalent saturated hydraulic conductivity values ($K_l \approx K_{air\text{-}sat}$) reported in DTN: LB980901233124.003 [105592] as shown in Scientific Notebook YMP-LBNL-JSW-6c (Wang 1999 [153449], p. 38). This conversion allows us to compare the $K_{air\text{-}sat}$ values to the q_s values, which are also summarized in

DTN: LB980901233124.003 [105592]. The q_s values were computed using Equation III-1 and the liquid-release rates (Q_s) from the pre-excavation tests performed at Niches 3566 and 3650 (DTN: LB980001233124.004 [136583]), the pre-excavation tests performed at Niches 3107 and 4788 (DTN: LB980901233124.003 [105592]), and the post-excavation seepage tests from Niche 3650 (DTN: LB980001233124.004 [136583]). [1]

Under slightly ponded conditions in the borehole (i.e., saturated conditions), q_s may initially exceed the saturated hydraulic conductivity of the test interval during the early stages of the test. During the later stages of the test, gravity-driven flow will dominate, a unit hydraulic gradient will be established near the borehole wall in the porous material, and q_s will approach K_l for the interval. Based on Assumption 5.2-2 in Section 5.2.1, gravity-driven flow is assumed to be the primary flow mechanism operating in fracture systems tested at Niche 3650. Therefore, one would expect capillary effects to be short-lived, and for all practical purposes the q_s for a given interval should be equal to K_l. Theoretically, q_s can exceed K_l if water ponds to a significant depth or is injected under high pressure, creating a steep hydraulic gradient within the porous material near the borehole wall. However, the packer system used in the seepage tests was designed so that water could not pond more than 0.0635 m; otherwise return flow to the surface would occur.

Return flow provides direct evidence that the liquid pumping rate exceeded the infiltration capacity of the test interval, implying that $q_s = K_l$, which in turn should equal $K_{air\text{-}sat}$, using the approximation that $K_{air\text{-}sat}$ is a reasonable estimate of K_l. The $K_{air\text{-}sat}$ and q_s values from DTN: LB980901233124.003 [105592] for those tests that exhibited return flow are plotted in Figure III-1, along with a solid line that represents the relation $K_{air\text{-}sat} = K_l = q_s$. A data point located above the solid line indicates that $K_{air\text{-}sat} > K_l$, and a data point below the solid line indicates that $K_{air\text{-}sat} < K_l$. One would expect the data values to fall on the $K_{air\text{-}sat} = q_s$ line if air-permeability and liquid-release tests are directly correlated.

Figure III-1 indicates that the data points are equally distributed above and below the $K_{air\text{-}sat} = q_s$ line, with the majority of points falling within a factor of 10 of $K_{air\text{-}sat} = q_s$. Therefore, the equivalent saturated hydraulic conductivity derived from the air-injection tests appears to approximately characterize the saturated hydraulic conductivity represented by q_s. The scattering of the individual data points around the line is a measure of the simplifying estimations, assumptions, and experimental uncertainties in relating air-flow processes with liquid-flow processes.

[1] The entire cross-sectional area of the borehole was used to compute the air-permeability values reported in LB980001233124.002 [136583] because gravitational effects on air are negligible and, thus, the entire cross-sectional area of the borehole is typically available for airflow. A smaller wetted area, as calculated by Equation III-2, was used to compute the liquid-release flux values.

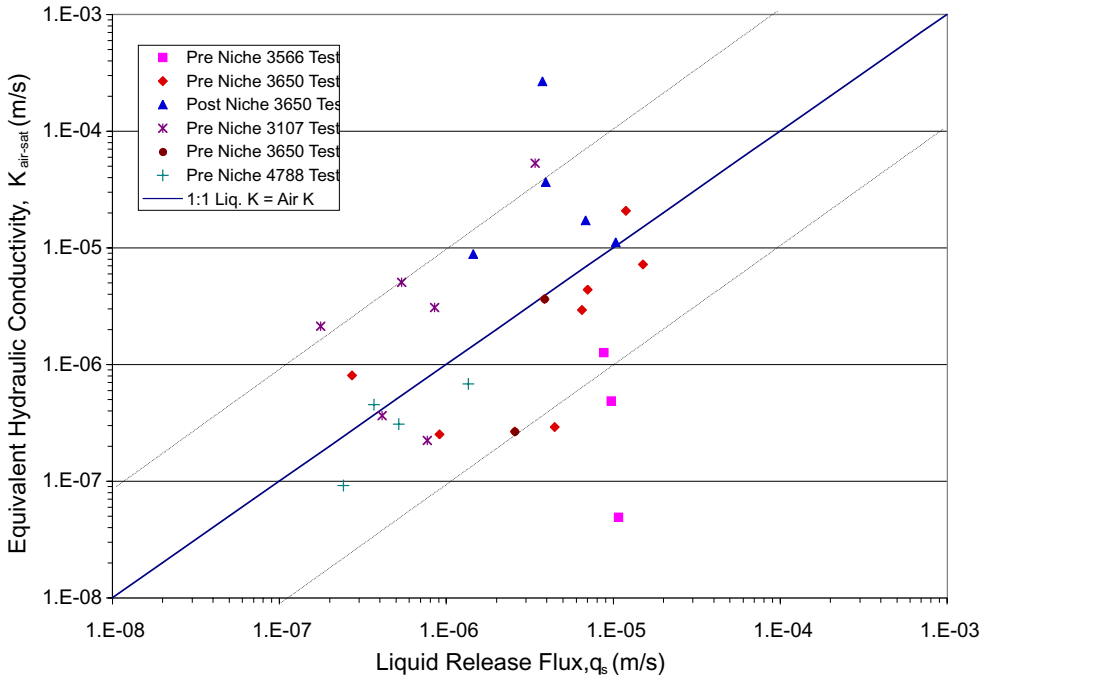

Figure III-1. Comparison of Liquid and Air-Derived Saturated Hydraulic Conductivities

INTENTIONALLY LEFT BLANK

ATTACHMENT IV

WATER CONTENT PROFILE EVALUATION

INTENTIONALLY LEFT BLANK

ATTACHMENT IV WATER CONTENT PROFILE EVALUATION

IV.1 EVALUATION OF ASSUMPTION OF ONE-DIMENSIONAL (1-D) FLOW

Large α-values calculated in Section 6.2.2.2 indicate that gravity-driven flow predominates in the fractures tested at Niche 3650. Although the large α-values of themselves do not collectively imply that flow is strictly 1-D, they do imply that limited lateral spreading of the wetting front in the fractures because of capillary forces will probably be negligible during the early stages of liquid release. Once the wetting front arrives at the niche ceiling, however, capillary forces become very important as water saturations begin to increase because of the capillary barrier, resulting in water being diverted laterally around the cavity. Therefore, flow will change from 1-D to 2-D or 3-D once the wetting front arrives at the ceiling. This implies that the θ_{ave} values calculated using Braester's model are no longer valid after the wetting front arrives at the niche ceiling.

Field observations made during the pre-excavation liquid release and post-excavation seepage tests provide stronger evidence that flow is roughly 1-D. Examination of Figure 6.2.1-2 described in Section 6.2.1.2 for the pre-excavation liquid-release tests shows that the average aspect ratio (i.e., depth to lateral distance traveled by the wetting front) is slightly less than 2 for the tests representing fracture networks and about 4.5 for the high-angle fracture data. This implies that for a 0.65-m travel distance, we would expect lateral spreading to be on average within 0.32 m of the borehole for the fractured network case and within 0.15 m for the near-vertical fracture case. The mean angle of wetting front migration is only 26° from the vertical (Arctan(0.32/0.65)). This analysis is supported further by two field observations made during the post-excavation seepage tests as described in Section 6.2.1.3.1: (1) the majority of water was typically captured in only one or two 0.305 × 0.305-m cells located directly beneath the test interval; (2) the wetting front typically arrived at the niche ceiling directly below the test zone.

IV.2 EVALUATION OF ASSUMPTION OF DOWNWARD TRANSLATION OF THE WETTED PROFILE AT CONSTANT VELOCITY

Earth scientists and engineers have recognized for a number of years that during infiltration tests the liquid-release rate approaches an asymptotic value equal to the hydraulic conductivity as time progresses. And in fact, steady moisture conditions are obtained rather rapidly in the vicinity of the source, typically with geometric mean of 1.7 hr when water is introduced at a water potential that is equal to or greater than zero (White and Sully 1987 [106152], pp. 1514, 1521). In our case, water is introduced at a flux that is often times much lower than the saturated hydraulic conductivity of the fractured interval and, therefore, reliance on generalities such as those in the preceding sentence may not be appropriate. Instead, the solution developed for unsteady multidimensional infiltration by Philip (1986 [106133], p. 1725) and summarized by White and Sully (1987 [106152], p. 1521) is used herein to determine the time to steady moisture conditions. In this manner we will check the validity of Assumption 5.2-5 in Section 5.2.3 on downward translation of wetting profile at constant velocity and determine whether the volumetric water contents presented in Section 6.2.2.3 are derived using an appropriate model.

Philip (1986 [106133]) developed an analytical solution for unsteady 2-D unsaturated flow from a buried horizontal cylinder into an infinite porous medium with uniform initial water content θ_n. We assume that this solution is also valid for flow through unsaturated, fractured media. Richards' equation was linearized with a constant D and the exponential relation between hydraulic conductivity and water potential, given by Equation 6.2.2-2 in Section 6.2.2.2. Philip (1986 [106133], p. 1719) found that regardless of the cavity shape and dimensionality of the flow field, the solution is approximately reducible to the product of the steady solution (ϑ_∞) and a function of dimensionless time (t_D) and radial coordinates (r_D dimensionless radius, $0 \le \varphi \le \pi$ polar angle) as follows:

$$\vartheta(r_D, \varphi; s; t_D) \approx G(r_D; s; t_D)\, \vartheta_\infty(r_D, \varphi; s; \infty) = G(r_D; s; t_D)\, \vartheta_\infty \qquad \text{(Eq. IV-1)}$$

Philip (1986 [106133]) defines ϑ, r_D, and t_D, by Equation (15), G by Equation (29), ϑ_∞ by Equation (62), and φ in Section 4 in his paper for flow from a buried horizontal cylinder. Equation IV-1 is valid for large s (the dimensionless characteristic cavity length defined by Equation 6.2.2-3 in Section 6.2.2.2) and for any value of t_D.

The significance of Equation IV-1 is that the function G ranges in value from 0 to 1. This implies that at large dimensional times (corresponding to large t_D) the unsteady solution approaches the steady solution ($G \rightarrow 1$). Using the same approach employed by Philip (1986 [106133], Section 8, p. 1725) for a spherical source, we computed the time to obtain 95% of the steady-state moisture conditions ($t_{D\ 95\%}$) for flow from a buried horizontal cylinder at a radial distance that is slightly larger than the borehole ($r_D = 1.1$) and at radial distance to the niche ceiling ($r_D = 17.1$ = 0.65 m / 0.0381 m). The details of the analysis can be found in Scientific Notebook YMP-LBNL-JSW-6c (Wang 1999 [153449], pp. 85-91) and the $t_{D\ 95\%}$ values are tabulated in DTN: LB980901233124.003 [105592] for each group of tests where seepage was observed.

The dimensional time ($t_{95\%}$) at which the moisture profile reaches 95% of its steady value can be calculated using $t_{D\ 95\%}$ (Philip 1986 [106133], Equation (15), p. 1718). Again, the details of the analysis can be found in Scientific Notebook YMP-LBNL-JSW-6c (Wang 1999 [153449], pp. 91–92) and the $t_{95\%}$ values are tabulated in Table IV-1 and DTN: LB980901233124.003 [105592], along with the time of arrival of the wetting front at the niche ceiling.

Examination of the $t_{95\%}$ values in Table IV-1 indicates that for all the tests, steady-state moisture conditions (i.e., constant θ) are reached near the borehole wall within 6 minutes (344 s) of starting the test and before pumping ceased (pumping times are tabulated in DTN: LB980001233124.004 [136583]). This demonstrates the original point of this discussion, that Assumption 5.2-5 in Section 5.2.3 on downward translation of wetting profile at constant velocity is valid. That is, q_s approached the unsaturated hydraulic conductivity of the fractured media, resulting in the downward migration of the wetted profile at a constant velocity within the time limit of each test. In addition, it is important to note that in all cases, steady-state moisture conditions are obtained near the borehole prior to the arrival of the wetting front. After the wetting front arrives at the ceiling, the moisture conditions will begin to change again near the release borehole as the water saturation increases because of the capillary barrier. Based on this analysis, the use of Equation 6.2.2-7 in Section 6.2.2.3 to estimate the change of volumetric water contents appears to be reasonable.

Table IV-1. Time to Steady-State Moisture Conditions

Borehole	Test Name	Test Date	Test Interval (m)	Time to Steady State[1]		Wetting Front[2] Arrival Time (hr)
				r_D = 1.1 (hr)	r_D = 17.1 (hr)	
Fracture Networks						
UR	Test #1 1-15-98	1/15/98	4.88-5.18	0.0129	0.691	0.497
	Test #1 2-6-98	2/6/98	4.88-5.18	0.0317	1.696	1.221
UL	Test #1 12-10-97	12/10/97	7.01-7.32	0.0012	0.127	0.067
	Test #1 1-6-98	1/6/98	7.01-7.32	0.0160	1.740	0.914
UR	Test #1 1-14-98	1/14/98	4.27-4.57	0.0200	1.580	0.936
	Test #1 2-5-98	2/5/98	4.27-4.57	0.0590	4.650	2.753
UM	Test 5 Niche 3650	11/13/97	4.27-4.57	0.0030	0.163	0.116
	Test 5 Niche 3650	12/3/97	4.27-4.57	0.0072	0.396	0.280
	Test #2 12-3-97	12/3/97	4.27-4.57	0.0037	0.202	0.143
	Test #1 1-7-98	1/7/98	4.27-4.57	0.0630	3.458	2.448
	Test #2 2-10-98	2/10/98	4.27-4.57	0.0957	5.249	3.715
UM	Test 4 Niche 3650	11/13/97	5.49-5.79	0.0014	0.088	0.058
	Test #2 12-4-97	12/4/97	5.49-5.79	0.0028	0.178	0.117
	Test #1 1-9-98	1/9/98	5.49-5.79	0.0186	1.164	0.764
	Test #1 2-11-98	2/11/98	5.49-5.79	0.0684	4.289	2.814
UR	Test #2 1-13-98	1/13/98	5.49-5.79	0.0005	0.527	0.150
	Test #2 2-10-98	2/10/98	5.49-5.79	0.0002	0.224	0.064
Individual or Small Groups of Vertical Fractures						
UM	Test 1 Niche 3650	11/12/97	4.88-5.18	0.0007	0.051	0.050
	Test #1 12-4-97	12/4/97	4.88-5.18	0.0011	0.085	0.083
	Test #2 12-5-97	12/5/97	4.88-5.18	0.0035	0.272	0.264
	Test #1 1-8-98	1/8/98	4.88-5.18	0.0225	1.729	1.683
	Test #1 3-6-98	3/6/98	4.88-5.18	0.0807	6.189	6.025
UR	Test #1 1-13-98	1/13/98	6.71-7.01	0.0018	0.122	0.116
	Test #1 2-3-98	2/3/98	6.71-7.01	0.0027	0.184	0.174
	Test #1 3-5-98	3/5/98	6.71-7.01	0.0195	1.307	1.238
UL	Test #2 1-6-98	1/6/98	7.62-7.92	0.0029	0.201	0.192
	Test #1 2-12-98	2/12/98	7.62-7.92	0.0024	0.166	0.158
	Test #1 3-4-98	3/4/98	7.62-7.92	0.0111	0.761	0.725
UR	Test #2 1-14-98	1/14/98	6.10-6.40	0.0030	0.267	0.267
	Test #1 2-4-98	2/4/98	6.10-6.40	0.0116	1.046	1.043

DTNs: [1] LB980901233124.003 [105592], [2] LB980001233124.004 [136583]

INTENTIONALLY LEFT BLANK

ATTACHMENT V

LABORATORY MEASUREMENTS OF RETARDATION AND FRONT SEPARATION

INTENTIONALLY LEFT BLANK

ATTACHMENT V LABORATORY MEASUREMENTS OF RETARDATION AND FRONT SEPARATION

Laboratory analyses are described for dyed samples collected from the niches and core samples for tracer retardation and front separation measurements.

V.1 WATER IMBIBITION

Rock cores, 5.08 cm in diameter and 2.0 cm in length, were used for the imbibition experiments to examine tracer penetration into the unsaturated rock matrix. Cores were cut and machined from a clean sample block from the same stratigraphic unit as the niche locations where tracer release tests were conducted. Porosity, bulk-density and particle-density measurements were based on the core dry weight at a temperature of 60^{o}C.

Partial saturation of cores was obtained by equilibrating cores within relative humidity chambers controlled by different saturated brines and/or water until they reached constant weights. Cores with two different levels of initial water saturation S_w, approximately 15% and 80%, were used in this work to investigate and compare tracer penetration behavior with respect to the saturation levels.

The core was hung inside a humidity-controlled chamber, with the core bottom submerged in a water reservoir containing tracers to a depth of about 1 mm. The core weight gain was continuously recorded by a data acquisition system. This study was designed to simulate the imbibition and penetration of tracers into the matrix from a continuously flowing fracture, modeled here as the core bottom. After a predetermined period of time (about 16–20 hrs), the core was lifted out of the reservoir, and the moisture front was usually examined. Rock sampling was immediately conducted as described below. The water contained about 10 g/l LiBr, 1 g/l FD&C Blue No. 1, and 1g/l Sulpho Rhodamine B. These tracers were selected to compare the behavior of nonreactive bromide with the dyes used in the field tracer work.

V.2 ROCK SAMPLING AND TRACER EXTRACTION

Tracer-stained rock samples were drilled, drill cuttings eluted, and the supernatant analyzed to profile tracer location and concentration. A mill (Bridgeport Series II) (Hu 1999 [156540], pp. 37–38) was used for drilling, with the rock sample firmly stabilized on the working platform and the rock surface covered with tape except for the location to be drilled. A series of drills of different sizes with flat-bottom, carbide-end mill cutters were used to sample different depths from the same location. The largest drill was used for the drilling at the rock surface, and the size gradually decreased with increased drilling depth to minimize carry-over powder contamination from previous depths. A tube was placed around the carbide-end mill cutter to reduce powder loss and to maximize sample recovery. The drilling was carried out slowly and steadily in 1 mm increments as indicated by a digital caliper (Mitutoyo, precision 0.01 mm).

Drill cuttings were collected at each 1-mm interval using a stainless steel needle attached to a stainless steel filter holder, connected to a vacuum source. The vacuum intensity was tested and adjusted before actual sample collection. Two pieces of cellulose nitrate membrane (with the membrane pore size of 0.45 μm) were used inside the filter holder to trap the sample powder.

The powder was suctioned and trapped into the collection device by pointing the needle to the drilled hole and applying the vacuum. Collected cuttings were transferred to an amber-glass vial before tracer extraction. Before drilling the next interval, the drilled hole was cleaned using an air stream just strong enough to remove any powder that might be left from the collection, and the cutter was cleaned with premoistened wipes and dried with a gentle air stream.

Samples of dye-stained rocks having a flat face were selected for rock drilling. Three samples were identified to be suitable for this work. The flat surfaces with dye stains were assumed to be fracture surfaces of active flow paths induced by dye water releases. For these three samples, no visible fracture coatings were observed.

Sampling of cylinder-shaped machined cores for the laboratory studies was performed from both the top and bottom of the core, first from the cleaner top (i.e., core side not in physical contact with liquid) to 16 mm, then from the bottom to 10 mm. This sampling scheme allows a comparison and evaluation of powder contamination of the drilling method. Drilling from the two sides was conducted so that the drill holes did not intersect each other.

Dye tracers were extracted from the drill cuttings into the aqueous phase by mixing 5 mL Nanopure water with 0.1 g of powder sample, mixing nominally for 15 seconds at the speed of 1,400 rpm. The mixture was then filtered, and the concentration of the tracer in the clear aqueous phase was measured. Either Gelman Supor® hydrophilic polyethersulfone membrane filter or Whatman cellulose nitrate membrane was used for the filtration. Testing showed negligible mass loss to both membranes for FD&C Blue No. 1 and Sulpho Rhodamine B.

Extraction efficiency was evaluated by spiking a known amount of tracers into the rock powder (<104 μm) for one day. The results show the extraction efficiency of 98.0 ± 4.6% (average plus and minus standard deviation, 5 replicates) for bromide, 94.1 ± 3.8% for FD&C Blue No. 1 (6 replicates), and 55.2 ± 0.7% for Sulpho Rhodamine B (7 replicates). The extraction procedure was not designed to be exhaustive for the maximum mass extraction. Relative comparisons with identical procedures were used in this study.

V.3 MEASUREMENT OF AQUEOUS TRACER CONCENTRATION

The aqueous concentration of FD&C Blue No. 1 dye was measured using a UV/vis Spectrophotometer (Hitachi, Model U-2001) at the characteristic wavelength of 630 nm. Sulpho Rhodamine B concentration was measured using a Spectrofluorophotometer (Shimadzu, Model RF-1501) at the excitation wavelength of 565 nm and emission wavelength of 590 nm. Depending upon the tracer concentration present in the samples, samples were diluted appropriately until the final solution measurement fell into the linear range of the calibration curve. Bromide concentration was measured by Ion Specific Electrode (Orion, Ionplus design) with the addition of ion strength adjuster with a volume ratio of 50:1. Background levels for all tracers were measured with powders from clean tuff samples. The clean powder was obtained from a clean rock sample that was crushed for size reduction to pass through a 104-μm opening sieve, similar to the powder size of the drill cuttings. Refer to the associated scientific notebook pages, Hu (1999 [156540], pp. 20–22, 37–48, 54, 68–82, 86–99, and 103–126), Hu (1999 [156541], pp. 9, 27, 42, 77, 118, 123–140, and 149), and Hu (1999 [156542], pp. 13, 17–25, 39–

41, 51–102, and 105–112), for detailed entries about instrument calibration and tracer measurements.

V.4 EVALUATION OF DRILLING TECHNIQUE

Tracer cross-contamination during drilling was evaluated by drilling from both the top and bottom for machined cores. For both drilling directions, measured tracer concentration are compared over distance in Figure V-1 for Core D with lower initial water saturation S_w and Figure V-2 for Core H with high initial S_w. Note that core bottom was the core side in physical contact with the tracer solution. For the lower S_w case, the tracer concentration is comparable for both drilling directions, showing no significant powder carry-over (Figures V-1a and V-1b). A slight difference at the 4–5 mm interval is observed in Figure V-1b for Sulpho Rhodamine B. This difference could be real since the fluorometer used for measurement had a low detection limit of about 0.021 mg/kg. Overall, the drilling technique yielded reliable concentration profile results.

For the case with the higher initial S_w, the difference in measured concentration from the two drilling directions is noticeable (Figure V-2a). After the tracer-rock contact and experiments were completed, the drilling was conducted first from the core top (cleaner side), then the core was inverted for the opposite drilling. Nominally, it took about 1 hour to finish drilling and sample collection for 10 depth intervals. The difference in concentrations shown in Figure V-2a for the two drilling directions may result from any or a combination of (1) gravitational flow during the second drilling phase, (2) heterogeneity, (3) flow resulting from exposure to the atmosphere, (4) evaporation loss resulting from heating caused by drilling. The spreading of tracer front at the high initial S_w makes the flow redistribution effects more pronounced than the case with sharp tracer front at low initial S_w. For Sulpho Rhodamine B, the difference is less evident (Figure V-2b). Results from the core top were utilized if the data were available.

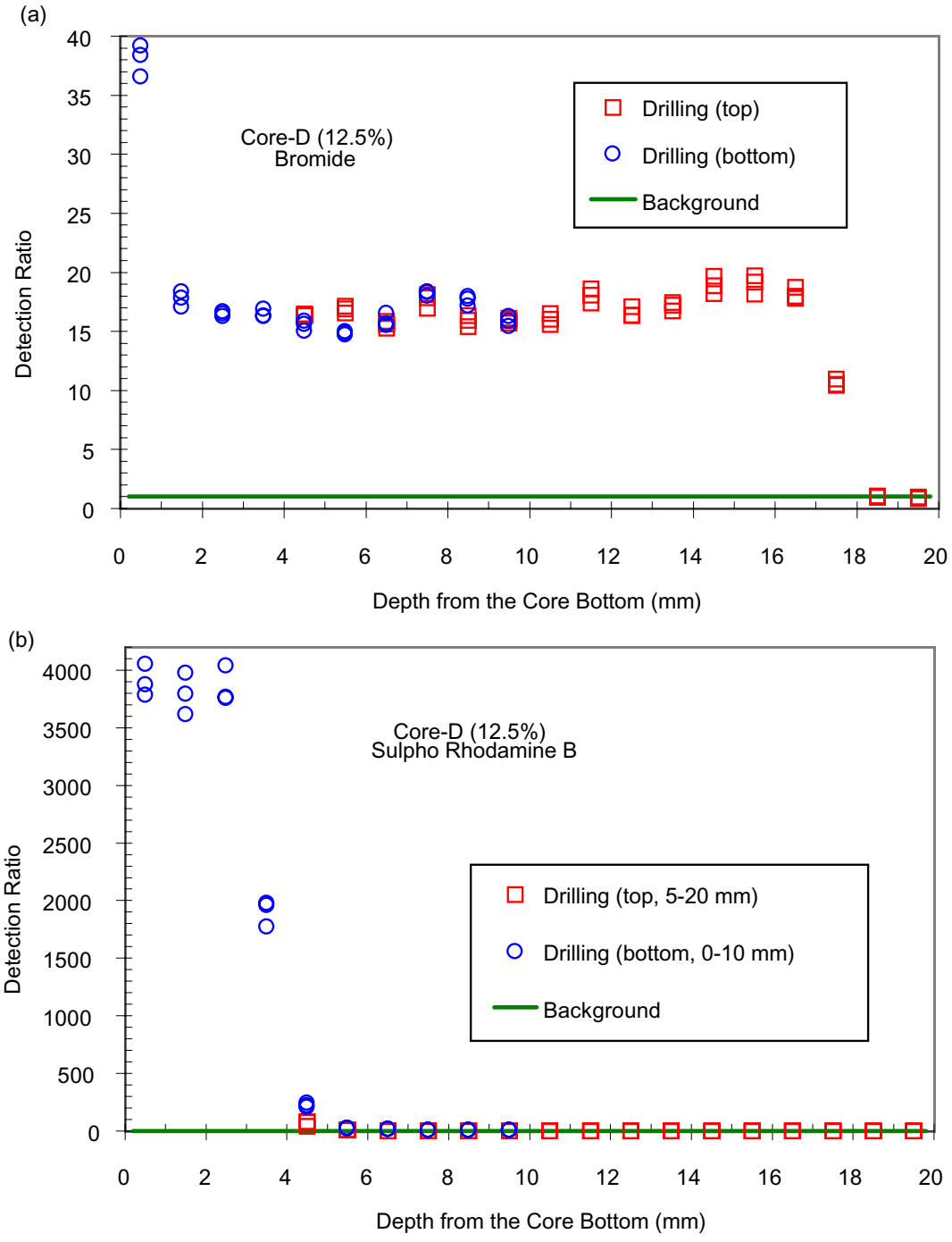

DTN: LB990901233124.003 [155690]

NOTE: The core ID and the initial core saturation (in parentheses) are presented in the figures.

Figure V-1. Comparison of Measured Detection Ratio from the Opposite Drilling Directions for Core D with Lower Initial S_w: (a) Bromide, (b) Sulpho Rhodamine B

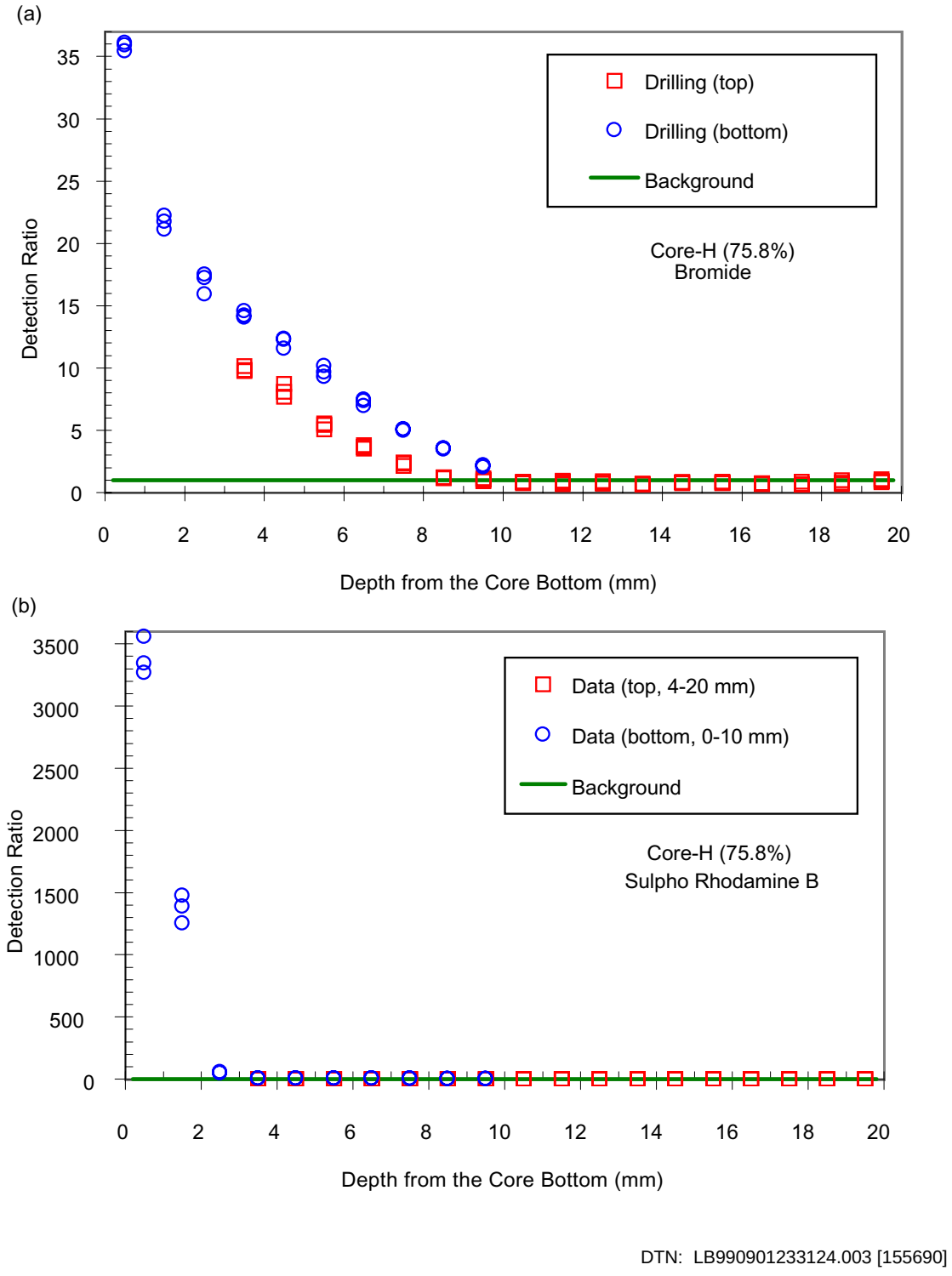

DTN: LB990901233124.003 [155690]

Figure V-2. Comparison of Measured Detection Ratio from the Opposite Drilling Directions for Core H with Higher Initial S_w: (a) Bromide, (b) Sulpho Rhodamine B

INTENTIONALLY LEFT BLANK

ATTACHMENT VI

FIELD EQUIPMENT FOR CONTROLLED WATER RELEASE, WETTING FRONT DETECTION AND SEEPAGE COLLECTION

INTENTIONALLY LEFT BLANK

ATTACHMENT VI FIELD EQUIPMENT FOR CONTROLLED WATER RELEASE, WETTING FRONT DETECTION AND SEEPAGE COLLECTION

Equipment for controlled release of water into isolated zones, borehole monitoring for changes in saturation and water potential, and collection of seepage in a excavated slot are presented for the new instruments developed for this field investigation of fracture flow and fracture matrix interaction.

VI.1 FLUID INJECTION

The liquid-release experiments required water to be injected into the formation over a 0.3-m zone in the borehole under constant-head or constant-rate conditions. The constant-head tests were conducted first to determine the maximum rates at which the zone could take in water. The subsequent set of experiments required that water be released to the formation at predetermined rates ranging from ~ 5 mL/min to ~ 100 mL/min. Both the constant-head method and the constant-rate method of injection were incorporated in the fluid-release apparatus. The main components of the fluid-release apparatus included an inflatable packer system for isolating the injection zone, a pump for delivering water, and a reservoir for providing a continuous supply of water (Figure VI-1a).

The inflation packer system consisted of two rubber packers, each 0.60 m long, connected to an inflation line (Figure VI-1b). Two stainless tubes (0.95 cm and 0.31 cm ID) passed through one of the packers to provide fluid (air and water) access into the injection zone. The 0.95-cm tube was used to deliver fluid into the injection zone, while the 0.31-cm tube was used as a siphon to remove excess water from the injection zone. Before liquid was released into the formation, the packer system was located to straddle the zone of interest (determined from air-permeability measurements) and then inflated to a pressure of ~ 200 kPa. The 0.95-cm ID stainless steel tube was then connected to a water supply line from a constant-head or a constant-rate system. During the entire period of injection, pressure in the inflation packers was continuously monitored to ensure that the injection zone remained isolated from adjacent zones of the borehole.

To capture the temporal variability in vertical flux of water from the injection zone, an automated liquid-release system was developed. This system allowed for continuous measurement of local liquid-release rates. The unit consisted of a storage tank (~ 4.5 liters) for water supply to a clear-acrylic, constant-head chamber. The chamber, 0.15 m ID and 0.30 m tall, served to maintain a constant head of water above the liquid-release surface within the injection zone (Figure VI-1c). The head maintenance was achieved with a level switch that activated the pump when the water level dropped below the control level. The control level was nominally set at or slightly above the elevation of the horizontal injection borehole. Two pressure transducers continuously recorded the height of water in each tank. A pulse damper was installed between the pump and tank to reduce any pulsating effects (caused by the pump) from migrating to the storage tank and influencing the pressure readings.

The constant-rate injection system included all the components used in the constant-head system without the constant-head chamber. To allow for easy regulation of flow rates in the field, the pump was calibrated before field deployment to relate flow rates with displayed numbers on a 10-turn speed control. In the field, the speed control was set at the desired flow rate before the

pump was activated. The actual flow rate was determined from transducers located at the bottom of the water reservoir. A data acquisition system was used to record changes in head of water (water level) in the reservoir.

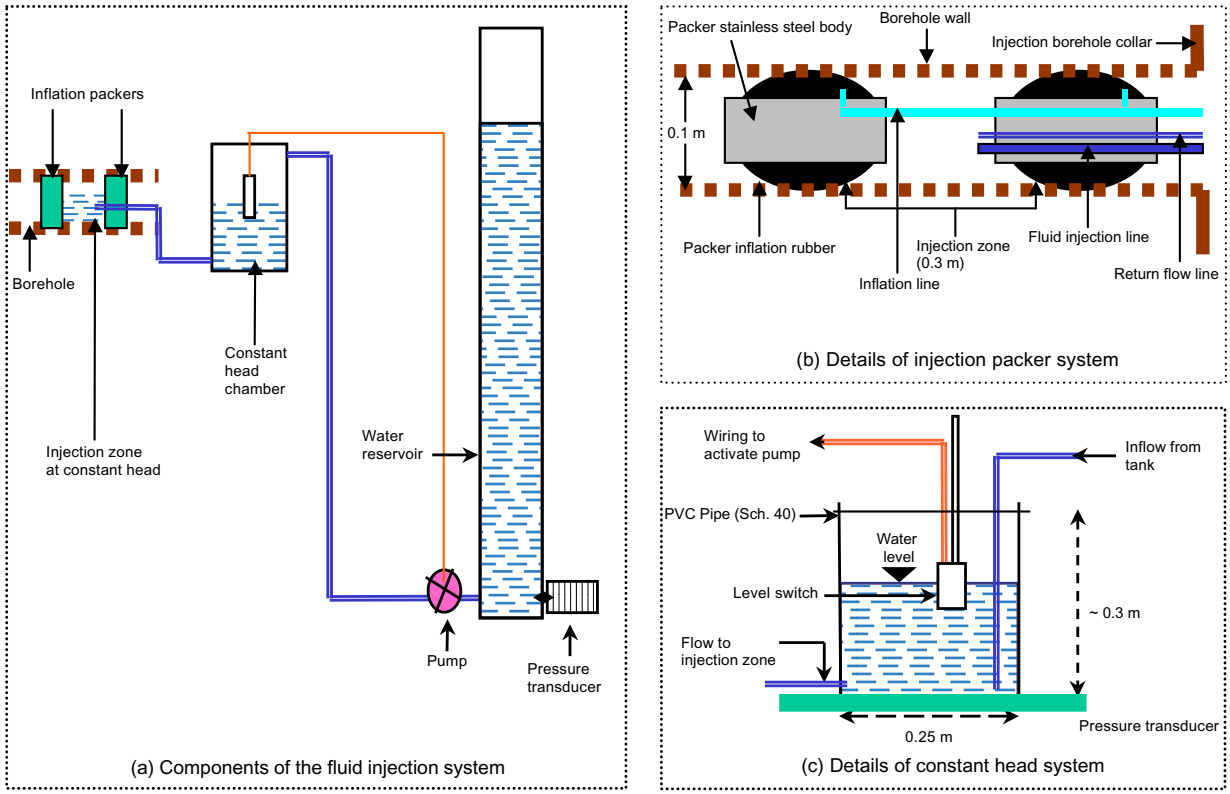

Figure VI-1. Schematic Illustration of Liquid Release System for Constant-Head and Constant-Rate Injections

VI.2 BOREHOLE MONITORING

In three monitoring boreholes (B, C and D in Figure 6.6.1-1), changes in saturation and water potential were measured continuously during the entire field investigation. Changes in saturation were measured with electrical-resistivity probes (ERPs) located at 0.25-m intervals along the 6.0-m length of each borehole. These ERPs consisted of two electrical leads sandwiched between pieces of filter paper. Water-potential measurements were made with psychrometers. With the multiplexing capabilities of the data logger (model CR7, Campbell Scientific Inc.), hourly measurements of up to 80 psychrometers (model PST-55, Wescor Inc.) were automated. The chromel-constantan junction in the psychrometer was cooled with an electric current to a temperature below dew point to first induce condensation, followed by evaporation without electric current. Temperature depression resulting from evaporation was recorded and used to determine water potentials in the vicinity of the psychrometers.

The psychrometers and ERP were housed in Borehole Sensor Trays (BSTs), installed along the length of each monitoring borehole (Figure VI-2a). The BSTs were fabricated from 0.10-m outside diameter (OD) PVC pipes, 3.0 m in section length. Each pipe section was cut lengthwise to produce a 0.075-m-wide curved tray (Figure VI-2b). On each tray, psychrometers were installed at 0.5-m intervals along the borehole while ERPs were located at 0.25-m intervals (Figures VI-2b and VI-2c). BST housing permitted immediate contact between ERPs and the borehole wall. The psychrometers were installed inside small cavities (0.005 m in diameter) perforated through the BST wall to measure water potentials of the rock. A steel spoon, 3.0 m long with the same configuration as the trays, was used to guide each BST to the assigned location along the borehole. Two BSTs were located along each section of borehole, one in contact with the top of the borehole and the other with the bottom. Each pair of BSTs was separated by a wedge that pressed the BSTs tight against the borehole wall. The double BST configuration improved the contacts between ERPs with the borehole wall and allowed two sensors, one on the upper BST and one on the lower BST, to detect wetting-front advances at each given location along the borehole.

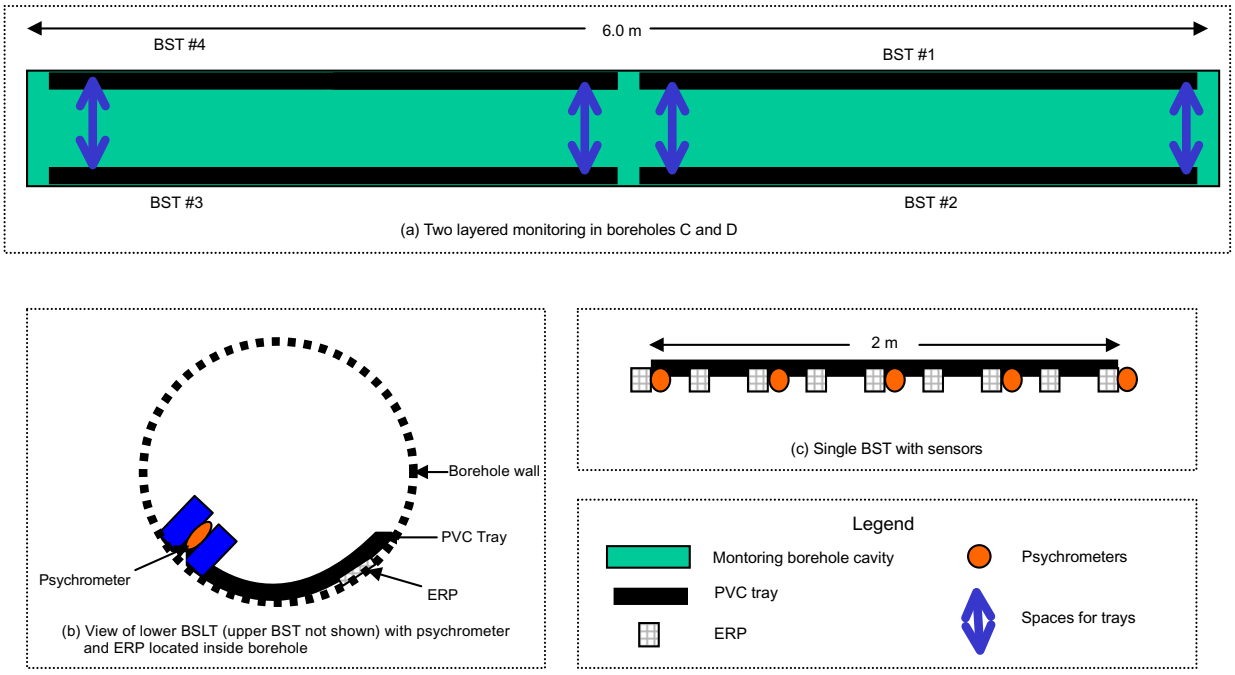

Figure VI-2. Schematic Illustration of Borehole Monitoring System

VI.3 SEEPAGE COLLECTION

To measure water seeping into the slot following liquid release into the injection borehole, a water collection system was designed to capture seepage from the slot ceiling (Figure VI-3). Design of this system was dictated by the slot geometry and locations of 'I' beam supports. A row of stainless steel trays was fabricated for each of the four accessible compartments between the I-beams. Each tray was an inverted pyramid 0.46 m long and 0.40 m wide and tapered to a

single point 0.20 m from the top. For each compartment, seven trays were assembled along a single steel frame, allowing for easy installation inside the slot. Water captured in the stainless steel trays was transferred into clear PVC collection bottles (0.076 m ID, 0.45 m tall). Water falling onto the trays was drained to the collection bottles through Teflon tubes (0.635 cm OD). An intermittent vacuum was applied to the collection bottles such that water stored on the trays or in Teflon tubes could be sucked into the collection bottles. The amounts of seepage water in the collection bottles were periodically recorded with sampling intervals determined in the field by the rates observed.

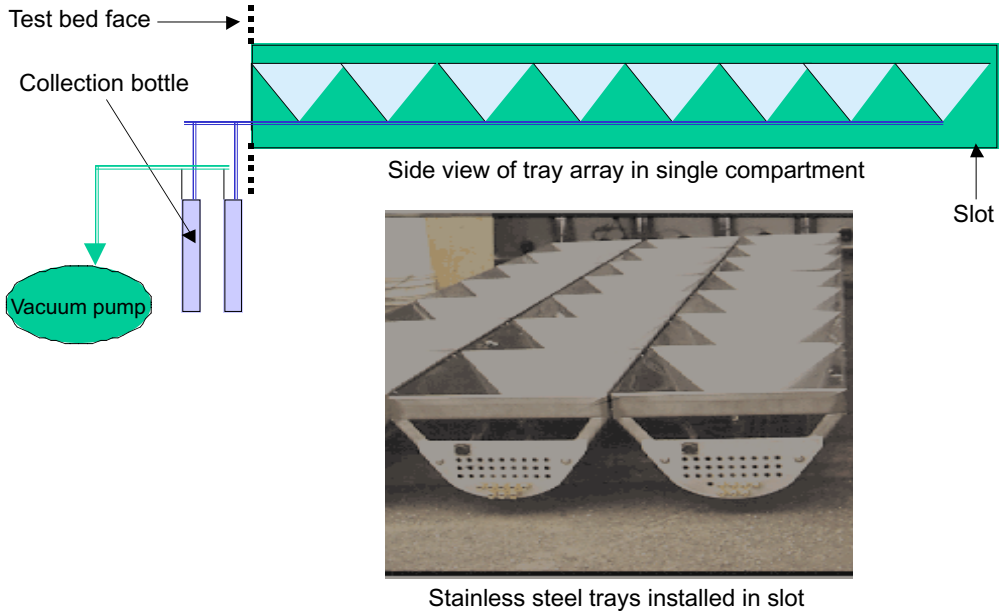

Figure VI-3. Schematic Illustration of Water Collection System Installed in Slot

ATTACHMENT VII

MEASUREMENT OF WATER POTENTIAL USING PSYCHROMETERS

INTENTIONALLY LEFT BLANK

ATTACHMENT VII MEASUREMENT OF WATER POTENTIAL USING PSYCHROMETERS

Prior to field use, all psychrometers were calibrated in the laboratory, using potassium chloride solutions (0.1-1.0 molal or mole of solute per 1000 grams of solvent). A second calibration was done in the laboratory after psychrometers had been used for field measurements, if feasible and practical. During the calibration procedure, psychrometers were isolated in an insulated box to minimize temperature fluctuations. Automated measurements were then made using the multiplexing capabilities of the CR7 data logger. When the psychrometers were observed to have reached equilibrium, they were removed from the calibration solution, washed in distilled water, air-dried, and immersed in the next solution. After calibrations were completed, all psychrometers were washed and air-dried before installation in the field.

During laboratory calibrations and preliminary field measurements, we noticed that the shape of the psychrometer output curve was significantly influenced by the size of the cooling voltage and cooling duration for a given water potential (Figure VII-1). This curve was also dramatically altered when the psychrometers became contaminated with dust particles (Figure VII-2). Given the high rate of failure of psychrometers in the field, it was therefore important to optimize both the cooling voltage and duration for a given water potential to help identify psychrometers that were contaminated or otherwise malfunctioning. Optimization was accomplished by increasing the cooling voltage and/or increasing the time over which the cooling voltage was applied until a well-defined plateau resulted for the psychrometer output. Data from contaminated or malfunctioning psychrometers are not for interpretation and are labeled as such in Salve (1999 [156552], pp. 103–152).

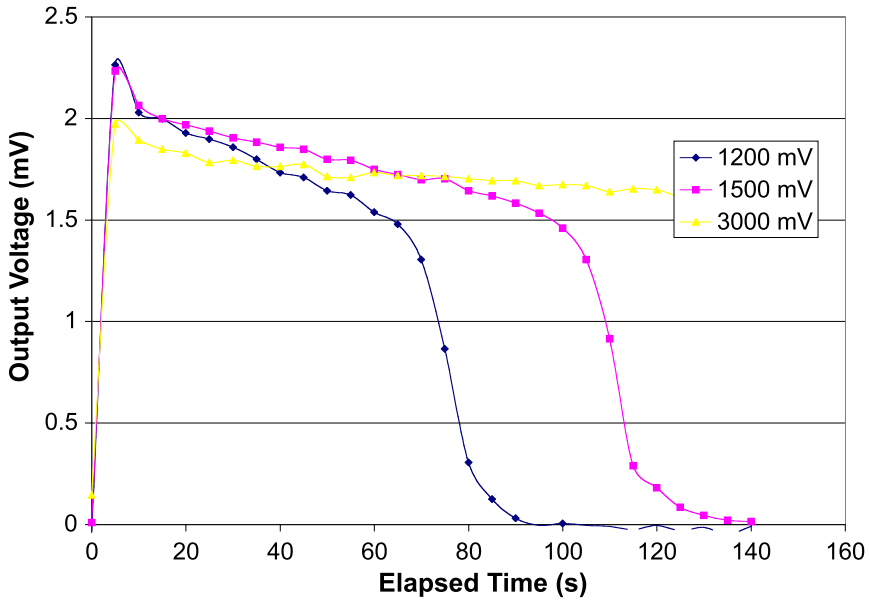

DTN: LB980001233124.001 [105800]

Figure VII-1. Effect of Cooling Current on Psychrometer Output Curve (PSY-732)

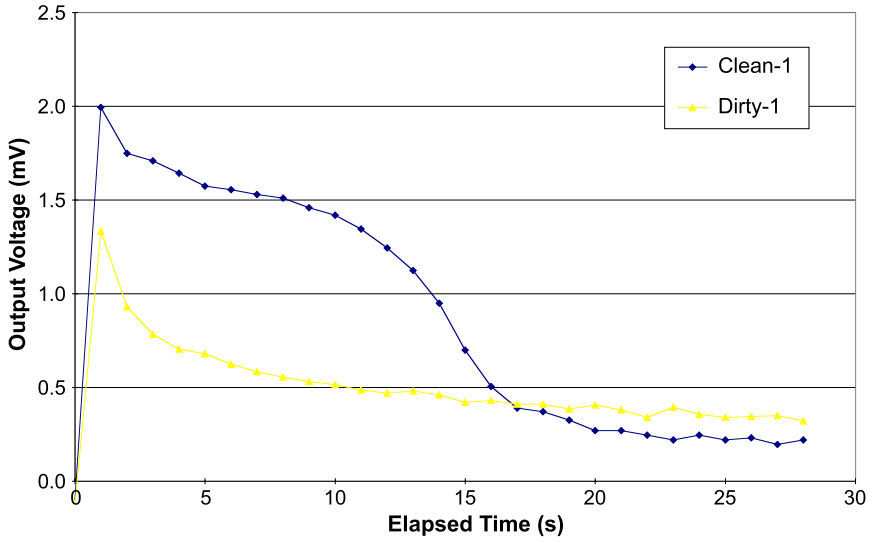

DTN: LB980001233124.001 [105800]

Figure VII-2. Effect of Dust Coating on Psychrometer Output Curve (PSY-731)

ATTACHMENT VIII

GEOLOGY, MINERALOGY, AND HYDROLOGIC PROPERTIES — BUSTED BUTTE APPLICABILITY

INTENTIONALLY LEFT BLANK

ATTACHMENT VIII GEOLOGY, MINERALOGY, AND HYDROLOGIC PROPERTIES — BUSTED BUTTE APPLICABILITY

The selection of southeastern Busted Butte, 8 km southeast of the potential repository area at Yucca Mountain, to site a field test facility was based on a presumption that the test results could be appropriately used in numerical studies of flow and transport in the Calico Hills Formation at Yucca Mountain (Bussod et al. 1999 [155695], p. 2). The presumption of applicability relies on the equivalence of stratigraphic units at Busted Butte and Yucca Mountain.

The Calico Hills section at southeastern Busted Butte, a thin distal residue of deposits, cannot completely represent the variability of the Calico Hills Formation below the potential nuclear waste repository. Because of this limitation, it is important to know more specifically what portion of the Calico Hills section occurs in the test facility. Existing and new data are examined here to document the extent of lithostratigraphic correspondence between the Busted Butte and Yucca Mountain sections. These studies focus on the portion of the Busted Butte section where tracer tests have been conducted.

VIII.1 Geology of the Busted Butte Test Facility

Busted Butte is a small (2.5 km by 1 km) north-trending mountain block primarily made up of thick, ignimbrite deposits of the Paintbrush Group. This fault-block uplift is bound by northeast- and north-trending normal faults, and it is split by a north-trending down-to-the-west normal fault that gives Busted Butte its distinctive appearance. The test facility is located within a small (300 to 350 m wide) horst on the southeast side of Busted Butte. Geologic units exposed in the vicinity of the test facility include, in ascending stratigraphic order: the Wahmonie Formation, the Calico Hills Formation, and the Topopah Spring Tuff (Figure VIII-1). The test facility is constructed in the Topopah Spring Tuff and the Calico Hills Formation. The Wahmonie Formation, which is not present below the potential repository, is also absent from the UZTT test block itself.

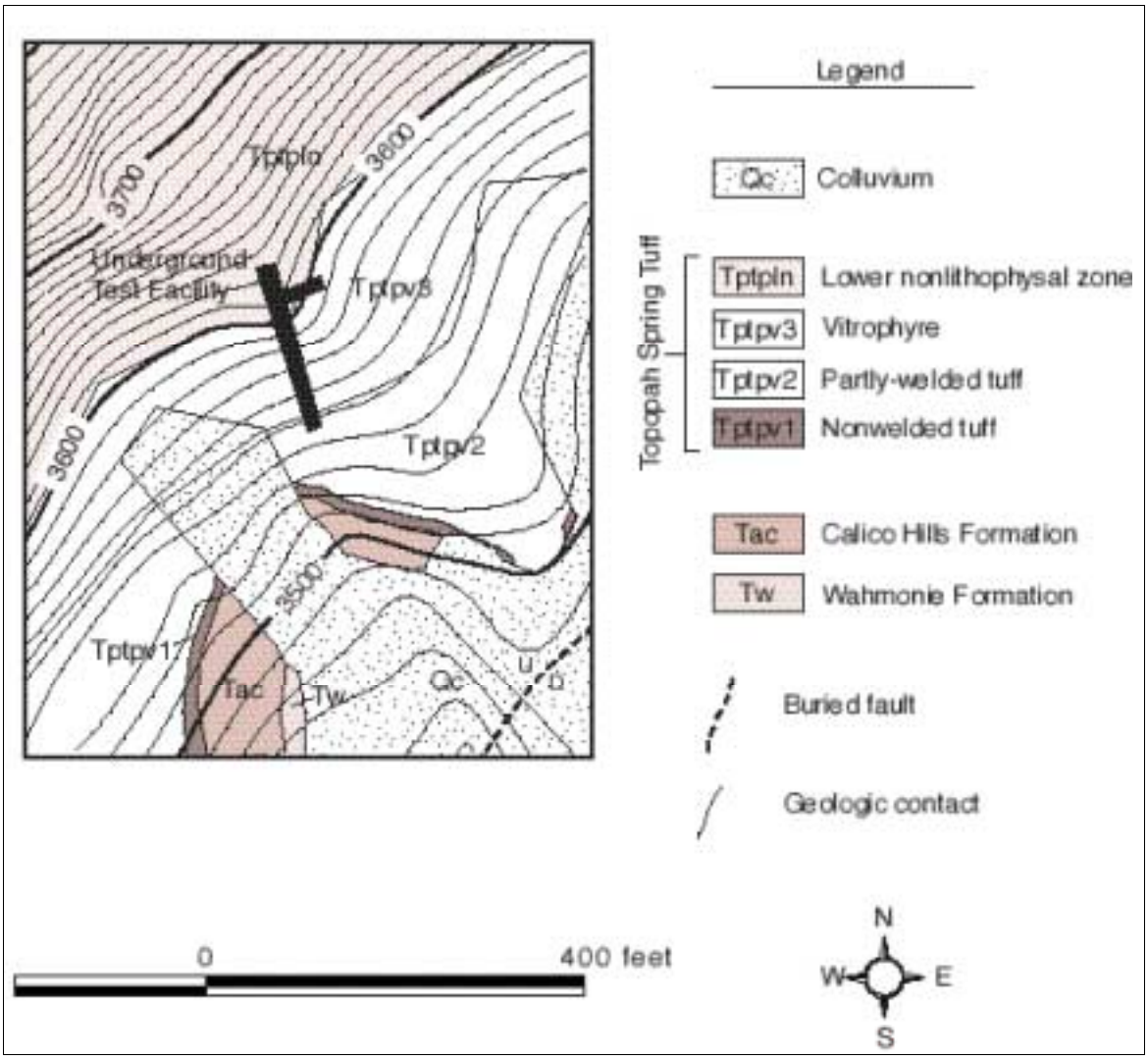

N/A - For illustration purposes only

NOTE: The plot is a geologic map of the area around the underground test facility in the southeastern part of Busted Butte. The contour interval is 10 feet. The tunnel entrance is at the southern end of the facility.

Figure VIII-1. Busted Butte Geologic Map (CRWMS M&O 2001 [154024], Figure 44)

VIII.2 Stratigraphic Setting of Busted Butte

The stratigraphic succession at Busted Butte was originally mapped by Lipman and McKay (1965 [104158]), who recognized the widespread principal units of the Paintbrush Group and small local exposures of underlying nonwelded tuffs not attributed to specific formations (undivided tuffs, Tt, according to their nomenclature). Broxton et al. (1993 [107386], pp. 6, 9) assigned the nonwelded tuffs to the Calico Hills Formation, the Wahmonie Formation, and the Prow Pass Tuff in order of increasing age and depth. This report follows the stratigraphic assignments of Broxton et al. (1993 [107386]), but all of the stratigraphic nomenclature has been updated from the original sources to the usage of Sawyer et al. (1994 [100075], Table 1).

The Calico Hills, Wahmonie, and Prow Pass tuffs were derived from different volcanic centers (Sawyer et al. 1994 [100075], Table 1). The pattern of decreasing unit thickness from north to south along Yucca Mountain (Moyer and Geslin 1995 [101269], Figure 3) is consistent with derivation of the Calico Hills pyroclastic material from an eruptive center north of the mountain (Sawyer et al. 1994 [100075], p. 1307). Thickness of the Calico Hills tuff decreases over a distance of about 13 km from more than 947.7 ft (288.86 m) at the northern end of Yucca Mountain (Moyer and Geslin 1995 [101269], Figure 3) to 21 ft (6.40 m) at the southeastern Busted Butte outcrop adjacent to the flow-and-transport test facility (Broxton et al. 1993 [107386], p. 9). At Raven Canyon, about 15 km southwest of Busted Butte, the Calico Hills Formation is absent and the Paintbrush Tuff rests on the Wahmonie Formation (Peterman et al. 1993 [106498], Figure 2).

VIII.3 Lithology of the Calico Hills Formation

The predominant rock types of the Calico Hills Formation in the Yucca Mountain area are an upper section of ash-flow and air-fall tuffs and a lower section of bedded tuffs and sandstones (Moyer and Geslin 1995 [101269], p. 5). All of these rocks originally consisted predominantly of glassy pyroclasts (volcanic ash, shards, and pumice clasts that formed as the lava was erupted and fragmented). The rocks also contained smaller amounts of phenocrysts (crystals from the lava) and lithic inclusions (crystalline or glassy rock fragments).

In the northeastern portion of the Yucca Mountain region, the glassy constituents of the Calico Hills tuffs have been altered to a mixture of zeolites (mostly clinoptilolite), smectite clay, and secondary silica. The Calico Hills Formation in the southeastern and southwestern Yucca Mountain region (including Busted Butte) remains mostly glassy, although some intervals contain appreciable amounts of smectite, clinoptilolite, and other secondary minerals. The areal distribution of zeolitic Calico Hills tuff is depicted in CRWMS M&O (2000 [138960], Figures 14 to 18). Areas of low zeolite content in the cited figures generally show where the tuff is vitric.

VIII.3.1 Informal Units of the Calico Hills Formation

An informal internal lithostratigraphy of the Calico Hills Formation devised by Moyer and Geslin (1995 [101269], pp. 5–9) provides a useful basis for comparing the Busted Butte and Yucca Mountain rock sections. The Calico Hills Formation is divided into five ash-flow/air-fall tuff units plus a bedded tuff and volcaniclastic sandstone (sand grains are mostly from volcanic rocks) at the base of the formation (Table VIII-1). Moyer and Geslin (1995 [101269], p. 5) speculated that each of the pyroclastic units may correspond to one of the five Calico Hills lava flows recognized east of Yucca Mountain. The majority of units (other than bedded tuff/sandstones) are laterally discontinuous, but pyroclastic unit 3 is present in most, and perhaps all, of the drill cores examined by Moyer and Geslin (1995 [101269], pp. 6, 8–9).

VIII.4 Criteria of Unit Identification

Positive recognition of the units depends heavily on observing the entire stratigraphic sequence in drill core or outcrop and identifying the distinctive contacts (boundaries) between adjacent units (Moyer and Geslin 1995 [101269], pp. 50–51). Moyer and Geslin (1995 [101269], pp. 5–8) also define typical values for color and for phenocryst content, lithic grains, and pumice clasts associated with each unit. Their summaries of chemical and mineralogic/petrographic data show

that the data for some of these parameters, taken alone, are sufficient only to distinguish the upper ash flow/air fall tuff section from the lower bedded tuff and sandstone. Within the ash flow/air fall section, however, the phenocryst data do not reliably distinguish among units 3, 4, and 5 because of the large overlaps in parameter-value populations (e.g., Moyer and Geslin 1995 [101269], Figures 4 and 5).

Drill hole USW GU-3 is the fully cored hole closest to Busted Butte. It is also the source of the only drill core studied by Moyer and Geslin (1995 [101269]) in which the Calico Hills section is vitric, like the section at Busted Butte. Unit identification in this hole was considered very ambiguous by Moyer and Geslin (1995 [101269], pp. 8–9) due to poor core recovery of the vitric Calico Hills interval. The main problem in making unit identifications in the Calico Hills section of drill core USW GU-3 is that contacts are missing because of incomplete core recovery. Moyer and Geslin (1995 [101269], pp. 8–9) tentatively recognized unit 3 and underlying bedded tuffs in this core, but did not rule out the presence of additional units. The absence of well-supported unit correlations in USW GU-3, along with a paucity of data from other drill sites where the Calico Hills Formation is vitric, increases the difficulty of comparison between Busted Butte and Yucca Mountain based solely on existing data.

The identification of lithostratigraphic units at southeastern Busted Butte is based on a combination of characteristics common to other locations where the units are exposed. Moyer and Geslin (1995 [101269], pp. 8, 10) noted lithologic similarities between the Calico Hills section exposed at Busted Butte and the USW GU-3 section, especially the presence of black, perlitic-glass lithic clasts [glass chunks with distinctive rounded surfaces, described by Moyer and Geslin (1995 [101269], p. 8) as “black obsidian” or “obsidian lithic clasts”]. The restricted occurrence of these clasts was considered a basis for identification and inter-site correlation of unit 3 by Moyer and Geslin (1995 [101269], p. 8). They did not have much data to support this interpretation because such data could only come from locations where the perlite clasts have escaped zeolitic alteration. At the time their report was produced, the USW GU-3 and USW UZ-14 cores were the only sources of data for vitric or partly vitric Calico Hills Formation.

As a follow-up to the observations and interpretations of Moyer and Geslin (1995 [101269]), new petrographic data on rock color, lithic-clast content, and black perlitic-clast content were collected for a vertical suite of samples from the Busted Butte test facility. Comparable data were collected for drill-hole samples from USW GU-3, USW H-5, and USW SD-12, all holes with predominantly vitric Calico Hills sections. These data are used to document the comparison of Calico Hills sections between Busted Butte and Yucca Mountain.

VIII.5 Evaluation of Petrographic Parameters

Because Moyer and Geslin (1995 [101269], pp. 8, 10) proposed that the Busted Butte section represents unit 3, efforts reported here concentrated on collection and evaluation of data most useful to distinguish unit 3 from other units of the Calico Hills Formation, particularly the adjacent units 2 and 4. Given that the Busted Butte section appears to contain only one pyroclastic-flow unit, the identification of that unit must be based on observable petrographic parameters without recourse to examination of the contacts of a multi-unit sequence. The parameters deemed to have the most characteristic values for unit 3 are the total lithic-clast content and the presence of black perlitic lithic clasts. Moyer and Geslin (1995 [101269], pp. 6–7) found that the lithic-clast content of unit 3 is in the range of 5 to 10 percent (excluding

localized zones of higher concentration), higher than the ranges of 1 to 5 percent in units 2 and 4. In keeping with the presumed usage of Moyer and Geslin (1995 [101269], p. 8), the lithic-clast abundances determined for this study include both crystalline and vitric lithic clasts. This usage differs from some published data (e.g., Broxton et al. 1993 [107386], p. 43) that include only crystalline clasts in the lithic-abundance determination.

VIII.6 Implications for Busted Butte Applicability

New data collected for this report confirm that the Calico Hills section exposed in the Busted Butte field test facility does not contain all the informal units of the formation that are present at Yucca Mountain. Given this limitation, correspondence of the Busted Butte test-facility section with unit 3 provides the best possible applicability because this is the unit of widest occurrence within the Yucca Mountain region. Unit 3 comprises at least one-third of the thickness of the Calico Hills Formation wherever the formation is predominantly vitric, based on the interpretations of Moyer and Geslin (1995 [101269], p. 8). In a lithostratigraphic sense, therefore, the Busted Butte section represents a substantial portion of the vitric Calico Hills Formation at Yucca Mountain. Correspondence of other rock properties, such as mineralogy or permeability, is a separate issue and not considered here.

Table VIII-1. Calico Hills Formation Lithostratigraphy

Unit 5 – Non- to partially welded, pumiceous pyroclastic-flow deposit
Slightly elongated pumice clasts; bimodal distribution of pumice clast sizes; 20 to 30 percent pumice. Light colored pumice clasts; moderate reddish-orange to grayish-pink matrix. Base marked by thinly bedded fall deposits.
Unit 4 – Nonwelded, pumiceous pyroclastic-flow deposit
Volcanic lithic clasts are large (20 to 70 mm), isolated orin swarms; prominent clasts of moderate reddish-orange tuff. Light colored pumice clasts; very pale orange to grayish orange-pink matrix. Lithic-poor sections appear similar to unit 2. Base marked by a heterolithologic sequence of fall deposits.
Unit 3 – Nonwelded, lithic-rich pyroclastic flow deposit
Lithic clasts comprise 5 to 10 percent, locally 10 to 30 percent (near the base and in several intervals within the unit); predominantly devitrified volcanic rocks with local obsidian. Grayish-orange to grayish-yellow or pinkish-gray matrix. The basal lithic-rich fallout is an excellent stratigraphic marker.
Unit 2 – Nonwelded, pumiceous pyroclastic-flow deposit
20 to 40 percent light colored pumice clasts; moderate pink or moderate orange-pink matrix. The fall deposit at the base of the unit contains porcelaneous ash layers.
Unit 1 – Nonwelded, lithic-rich pyroclastic-flow deposit
15 to 20 percent devitrified volcanic lithic clasts near base; lithic clasts decrease upward to 3 to 7 percent. Light colored pumice clasts; grayish orange-pink to light greenish-gray matrix; 7 to 12 percent phenocrysts.
Bedded tuff unit
Interbedded coarse-grained fallout deposits, pyroclastic-flow deposits (many reworked or with paleosols), and thinly bedded porcelaneous ash-fall deposits. Pyroclastic-flow deposits have 13 to 25 percent phenocrysts.
Basal sandstone unit
Massive to laminated, immature volcaniclastic sandstone; very pale orange to moderate red; medium to coarse grained; accumulations of argillic pumice clasts and rare sedimentary structures including load casts, pinch-and-swell structures, and flame structures. Locally interbedded with reworked pyroclastic-flow deposits.

Source: Moyer and Geslin (1995 [101269], Table 3).

As noted above, this analysis emphasizes the uppermost Calico Hills section present in the existing Busted Butte test facility. Information about the adjacent outcrop section collected by Broxton et al. (1993 [107386], pp. 9, 43) suggests that an additional informal unit other than

bedded tuff may be present below unit 3 at that site. This represents a potential opportunity for inter-unit Calico Hills flow-and-transport testing within an expanded Busted Butte facility.

VIII.7 Mineralogic Properties

Samples from outcrops were collected at the Busted Butte site for mineralogic and petrologic analysis. Mineralogic analysis of the units at Busted Butte were run using Quantitative X-ray Diffraction. Table VIII-2 delineates mineralogic content for the units at Busted Butte.

The samples from the Tptpv2 and Tptpv1 intervals show that the poorly welded to nonwelded vitric portions of the lower Topopah Spring Tuff at this site are largely unaltered, without zeolites but with modest smectite occurrences.

Table VIII-2. Rock Mineralogic Composition and Fe and Mn Oxide Contents in Stratigraphic Units Present in UZTT Phase-2 Block

Stratigraphic Unit: Borehole:		**Tptpv2 UZTT-BB-PH 1-7**	**Tptpv1 UZTT-BB-PH 1-3**	**Tac UZTT-BB-PH 1-4**
Smectite	(%)	8 ± 2	nd	18 ± 5
Kaolinite	(%)	2 ± 1	nd	nd
Mica	(%)	Trace	Trace	Trace
Quartz	(%)	1 ± 1	1 ± 1	6 ± 1
Opal-C	(%)	nd	1 ± 1?	nd
Cristobalite	(%)	nd	nd	1 ± 1
Calcite	(%)	nd	nd	Trace?
Hematite	(%)	nd	nd	1 ± 1
Feldspar	(%)	3 ± 1	4 ± 1	12 ± 2
Unidentified*	(%)	nd	nd	1 ± 1
Amorphous	(%)	86 ± 3	94 ± 2	61 ± 6

NOTE: nd = not detected
DTN: LA9910WS831372.009 [147157]

VIII.8 Hydrologic Properties

Samples of the Calico Hills Formation and Topopah Spring Tuff exposed in Busted Butte outcrops were used to determine the hydrologic properties of the formations in the test block. Table VIII-3 presents the mean and standard deviation for porosity, saturated conductivity, and van Genuchten parameters for samples taken from the three units at Busted Butte.

Table VIII-3. Hydrogeologic Properties of Busted Butte Units

Unit	# Samples	Porosity Mean	Porosity Std Dev	K_{sat} [m/s] Arith. Mean	K_{sat} [m/s] Std Dev	K_{sat} [m/s] Geom. mean
Tac	35	0.354	0.042	2.363E-05	1.720E-05	1.523E-05
Tptpv1	25	0.420	0.040	1.073E-05	1.853E-05	3.372E-06
Tptpv2	19	0.387	0.032	4.397E-06	4.387E-06	2.651E-06

Unit	# Samples	van Genuchten alpha [1/m] Mean	van Genuchten alpha [1/m] Std Dev	van Genuchten *n* Mean	van Genuchten *n* Std Dev
Tac	35	3.014	2.632	1.279	0.205
Tptpv1	25	0.685	0.365	1.385	0.278
Tptpv2	19	0.633	0.015	1.309	0.109

NOTE: Mean and standard deviation of values calculated from the following DTNs: GS990308312242.007 [107185];GS990708312242.008 [109822]

INTENTIONALLY LEFT BLANK